

# **Water in Earth's mantle: Metasomatism and melting**

## **Dissertation**

Zur Erlangung der Würde eines  
Doktors der Naturwissenschaften

- Dr. rer. nat. -

der Bayreuther Graduiertenschule für Mathematik und Naturwissenschaften

vorgelegt von

**Marija Putak Juriček**

aus Zagreb (Kroatien)

Bayreuth 2022

Die vorliegende Arbeit wurde in der Zeit von 03/2017 bis 03/2022 in Bayreuth am Bayerisches Geoinstitut unter Betreuung von Herrn Professor Dr. Hans Keppler angefertigt.

Vollständiger Abdruck der von der Bayreuther Graduiertenschule für Mathematik und Naturwissenschaften (BayNAT) der Universität Bayreuth genehmigten Dissertation zur Erlangung des akademischen Grades einer Doktorin der Naturwissenschaften (Dr. rer. nat.).

Dissertation eingereicht am: 21.02.2022

Zulassung durch das Leitungsgremium: 02.03.2022

Wissenschaftliches Kolloquium: 24.06.2022

Amtierender Direktor: Prof. Dr. Hans Keppler

Prüfungsausschuss:

Prof. Dr. Hans Keppler (Gutachter)  
Prof. Dr. Dan Frost (Gutachter)  
PD Dr. Gerd Steinle-Neumann (Vorsitz)  
Prof. Dr. Audrey Bouvier

# Table of contents

Summary .....	1
Zusammenfassung.....	4
1. Water in the mantle: An overview .....	7
1.1. The upper mantle water cycle .....	7
1.2. Motivation.....	9
1.3. Thesis structure .....	11
2. Amphibole stability in the upper mantle at reduced water activity .....	12
2.1. Introduction.....	12
2.2. Experimental methods .....	14
2.2.1. Starting materials and sample preparation .....	14
2.2.2. Piston cylinder experiments .....	17
2.2.3. Electron microscopy.....	18
2.2.4. X-ray diffraction.....	25
2.3. Results.....	29
2.3.1. Sample petrography.....	29
2.3.2. Amphibole stability at reduced water activity.....	30
2.3.3. Notes on experimental procedure.....	39
2.3.3.1. <i>The high pressure/low temperature amphibole stability limit</i> .....	39
2.3.3.2. <i>The low pressure/high temperature amphibole stability limit</i> .....	40
2.3.3.3. <i>Fluid mixing and the preheating procedures</i> .....	42
2.3.4. Mineral chemistry .....	43
2.3.4.1. <i>Amphibole compositions</i> .....	43
2.3.4.2. <i>Composition of other phases</i> .....	46
2.3.5. Mass balance calculation.....	47
2.3.6. Modelling amphibole stability in the upper mantle.....	50
2.4. Discussion .....	56
2.4.1. Amphibole stability in the upper mantle at reduced water activity.....	56
2.4.2. The role of nominally anhydrous minerals and implications of the model .....	57
3. Mantle metasomatism by sediment fluids in subduction zones .....	61
3.1. Introduction.....	61
3.1.1. Arc signature and the nature of the mobile slab component .....	62
3.1.2. The role of dilute sediment-derived hydrous fluids .....	65
3.2. Experimental methods .....	67

3.2.1. Starting materials and sample preparation .....	67
3.2.2. Piston cylinder experiments .....	69
3.2.3. Laser ablation inductively coupled plasma mass spectroscopy (LA-ICP-MS) .....	70
3.2.4. Electron microscopy .....	78
3.3. Results .....	79
3.3.1. Sample petrography .....	79
3.3.2. Mineral and fluid compositions .....	83
3.3.3. Trace element partition coefficients .....	89
3.3.4. Accessory minerals .....	101
3.3.5. Modelling the sediment trace element contribution in arc magmas .....	108
3.4. Discussion .....	121
3.4.1. The extended trace element partitioning dataset .....	121
3.4.2. Toward constraining subduction-related mantle metasomatism .....	122
4. Mantle melting at low water fugacity and the cryoscopic equation .....	126
4.1. Introduction .....	126
4.2. Experimental methods .....	130
4.2.1. Starting materials and sample preparation .....	130
4.2.2. Experiments in the internally heated gas pressure vessel (IHPV) .....	131
4.2.3. Fourier-transform infrared spectroscopy (FTIR) .....	134
4.3. Results .....	139
4.3.1. Solidus depression in the anorthite-diopside-H <sub>2</sub> O system at low water fugacity .....	140
4.3.2. Eutectic melt compositions .....	142
4.3.3. Thermodynamic description of the melting point depression in magmatic (silicate-H <sub>2</sub> O) systems at low water fugacity .....	150
4.3.3.1. Model 1: Defining the silicate molar unit .....	153
4.3.3.2. Model 2: Water speciation in haplobasaltic liquids .....	155
4.3.3.3. The enthalpy of fusion in the anorthite-diopside-H <sub>2</sub> O system .....	157
4.4. Discussion .....	158
4.4.1. Upper mantle melting and the cryoscopic equation .....	158
4.4.2. Implications of the updated melting model .....	163
4.4.2.1. Description of the melting model .....	163
4.4.2.2. Melting in the upper mantle .....	166
5. List of references .....	172
6. Supplement .....	197
6.1. Supplement I: Amphibole stability in the upper mantle .....	197
6.2. Supplement II: Mantle metasomatism by sediment fluids .....	216

7. Appendix: Kinetics of nanolite crystallization in alkaline silicate melts from the Eifel Volcanic Fields (Germany) .....	239
7.1. Introduction.....	239
7.2. Volcanic activity in the Eifel .....	240
7.3. Methods.....	242
7.4. Results.....	244
7.4.1. The FE-SEM study: an overview of nanolites in alkaline silicate melts.....	245
7.4.1.1. Ultramafic foidite samples.....	245
7.4.1.2. Mafic and intermediate samples .....	249
7.4.2. Oriented attachment of magnetite nanoparticles .....	252
7.5. Discussion .....	261
7.6. List of references.....	266

## Summary

This thesis investigates the role of water in generating some geochemical and geophysical features in the upper mantle that are thought to be related to melting and metasomatism.

Dehydration melting of amphibole has been proposed as a possible mechanism causing the lithosphere-asthenosphere boundary. However, the stability of amphibole under the reduced water activities expected in the upper mantle has never been thoroughly studied. Thus, the first part of the thesis addresses this problem by experiments under carefully controlled water activity. Piston cylinder runs were performed at 2 to 4.5 GPa and 900 to 1350 °C. Water activity was adjusted by diluting an excess hydrous fluid with molecular nitrogen, and the N<sub>2</sub>-H<sub>2</sub>O fluids were equilibrating with a synthetic oxide mixture of peridotite composition. Phase assemblages in the run products were studied by a combination of powder XRD and electron microscopy. Reducing water activity in the peridotite-H<sub>2</sub>O system had two effects on amphibole stability. With decreasing water activity, the amphibole stability limit is simultaneously depressed to lower pressures and elevated to higher temperatures, as a result of two distinctly different amphibole-out reactions. Melting was observed at the high-temperature amphibole-out boundary, but a solid-state decomposition reaction of amphibole occurred at the high-pressure stability limit. To further assess the stability of amphibole, a thermodynamic model including the effects of water dissolution in nominally anhydrous minerals was constructed. The model suggests that traces of amphibole may be common in the oceanic, but not in the continental lithosphere. In continental settings, the presence of amphibole is likely evidence for metasomatic water addition. Dehydration melting of amphibole may occur only under exceptional circumstances, and it therefore is not a plausible explanation for the seismic discontinuity at the lithosphere-asthenosphere boundary.

Subduction-related volcanism produces melts with distinct geochemical features. Some arc magmas bear a distinct ‘geochemical fingerprint’ of the subducted sediments. Sediment melts were therefore proposed as the main metasomatic agent in subduction zones. Piston cylinder experiments were performed in a sediment-H<sub>2</sub>O system at 2.5 to 4.5 GPa and temperatures of 600 and 700 °C to test if saline hydrous fluids may also transfer the sediment ‘geochemical fingerprint’

into the melt production zone, or if sediment melting is strictly required. Fluid salinities were varied between 0 and 7 wt.% Cl, and the diamond trap method was used to separate the fluid from solid metapelitic residues. The fluid and minerals in the run products were analyzed by LA-ICP-MS. With increasing salinity, the fluid/mineral partition coefficients for most trace elements, including LREE, were enhanced. Bulk fluid/sediment trace element partition coefficients were calculated and the composition of arc melts produced by hydrous mantle melting upon introduction of saline sediment-derived fluids was modelled. Comparison of the model melts with natural samples suggests that the most plausible agent of mass transfer in subduction zones is a saline sediment- and basalt-derived hydrous fluid mixture. Even a minor contribution of a saline sediment-derived fluid may be enough to explain the “sediment fingerprint” observed in natural samples.

Traces of water in the mantle may stabilize low-degree partial melts at the lithosphere-asthenosphere boundary. However, the relationship between the melt water content and the melting point depression in the peridotite-H<sub>2</sub>O system is not well constrained, as representatively low melt water concentrations are difficult to control in experiments. Moreover, the solidus in the peridotite-H<sub>2</sub>O system is hard to recognize and interpretations of run products may be highly subjective. A study in the anorthite-diopside-H<sub>2</sub>O system was designed to precisely determine the relationship between the melt water content and melting point depression. The haplobasaltic melts produced in this system are similar to tholeiites that are produced by partial melting of peridotite. However, as the anorthite-diopside-H<sub>2</sub>O system is eutectic, a large melt fraction is formed immediately at the solidus. This allows easy detection of incipient melting. All experiments were performed at water-saturated conditions at 0.02 to 0.2 GPa, to simulate low water fugacity, and temperatures between 1000 and 1500 °C, using a rapid-quench internally heated gas pressure vessel. One series of experiments was performed with a 1:1 mixture of pure pre-synthesized anorthite and diopside to determine the solidus depression as a function of water fugacity. In another series of experiments, large haplobasaltic glass cylinders were used to measure water solubility in the melt as determined by FTIR. The relationship between the melt water content and solidus depression, as determined in this study, was combined with previously published water mineral/basalt partition coefficients for major upper mantle phases. The resulting model of peridotite melting predicts low-degree partial melting along the oceanic lithosphere-asthenosphere

boundary with approximately 200 ppm of water in the bulk mantle. Additional melting point depression due to the presence of CO<sub>2</sub> may be required to form partial melt along the continental lithosphere-asthenosphere boundary.

## Zusammenfassung

Diese Dissertation untersucht die Rolle von Wasser bei der Bildung von Schmelzen und bei metasomatischen Prozessen im Mantel.

Dehydratations-Schmelzen von Amphibol wurde vorgeschlagen als eine mögliche Ursache für die Grenze zwischen Lithosphäre und Asthenosphäre. Die Stabilität von Amphibol unter den reduzierten Wasseraktivitäten im oberen Mantel wurde jedoch niemals sorgfältig untersucht. Im ersten Teil dieser Dissertation werden daher entsprechende Piston-Cylinder-Experimente beschrieben, die bei 2 bis 4.5 GPa und 900 bis 1350 °C unter sorgfältig kontrollierter Wasseraktivität ausgeführt wurden. Die Wasser-Aktivität wurde eingestellt, indem ein Wasserhaltiges Fluid mit N<sub>2</sub> verdünnt wurde. Ein synthetischer Peridotit wurde dann in Gegenwart von diesem N<sub>2</sub>-H<sub>2</sub>O-Fluid aus einer Oxid-Mischung auskristallisiert. Neugebildete Phasen in den Reaktionsprodukten wurden durch Röntgenbeugung und Elektronen-Mikroskopie identifiziert. Eine Verringerung der Wasser-Aktivität verschiebt das Stabilitätsfeld von Amphibol zu niedrigeren Drücken und zu höheren Temperaturen. Ursache hierfür sind zwei verschiedene Abbaureaktionen. Die Grenze des Stabilitätsfelds zu hohen Temperaturen wird definiert durch die Solidustemperatur, während die Amphibol-Stabilität zu hohem Druck durch eine Festkörper-Reaktion begrenzt wird. Um die Stabilität von Amphibol im Mantel vorherzusagen, wurde ein Modell entwickelt, das auch die Lösung von Wasser in nominal wasserfreien Mineralen berücksichtigt. Spuren von Amphibol sind wohl verbreitet in der ozeanischen, aber nicht in der kontinentalen Lithosphäre. Im subkontinentalen Mantel wird Amphibol wohl nur bei metasomatischer Zufuhr von Wasser gebildet. Dehydratations-Schmelzen von Amphibol kommt im Mantel nur unter sehr ungewöhnlichen Bedingungen vor und ist daher keine plausible Erklärung für die Grenze zwischen Lithosphäre und Asthenosphäre.

Vulkane oberhalb von Subduktionszonen produzieren Magmen mit einer charakteristischen Spurenelement-Zusammensetzung. In manchen Magmen findet man einen geochemischen „Fingerabdruck“ von subduzierten Sedimenten. Aus diesem Grund wurde vorgeschlagen, dass Sediment-Schmelzen das Hauptmedium für den Stofftransport von der subduzierten Platte in die

Zone der Schmelzbildung sind. Piston-Cylinder-Experimente wurden in einem Sediment-H<sub>2</sub>O-System bei 2,5 bis 4,5 GPa und 600 bis 700 °C durchgeführt, um zu testen, ob nicht salzhaltige Wasser-reiche Fluide ebenfalls den chemischen „Sediment-Fingerabdruck“ in den Magmen erzeugen könnten. Die Salzgehalte in den untersuchten Fluiden lagen zwischen 0 und 7 Gew. % Cl. Um die Fluide von den festen Mineralen in den Experimenten zu trennen, wurden Fallen aus Diamant-Pulver benutzt. Sowohl die abgeschreckten Fluide als auch die Minerale wurden mit LA-ICP-MS analysiert. Mit zunehmender Salinität steigen die Fluid/Mineral-Verteilungskoeffizienten der meisten Elemente (einschließlich der LREE) an. Gesamt-Gesteins/Fluid-Verteilungskoeffizienten wurden berechnet und die Zusammensetzung von Schmelzen wurde modelliert, die durch die Zufuhr von salzhaltigen Fluiden aus Sedimenten zum Mantel erzeugt werden. Der Vergleich der Modelle mit natürlichen Schmelzzusammensetzungen zeigt, dass der Stofftransport in den Subduktionszonen wahrscheinlich durch eine Mischung von salzhaltigen, Wasser-reichen Fluiden aus den subduzierten Basalten und den Sedimenten erfolgte. Bereits minimale Anteile von Fluiden aus Sedimenten können die typische „Sediment-Signatur“ in Magmen erzeugen.

Spuren von Wasser im Mantel könnten geringe Anteile von Teilschmelzen an der Lithosphäre-Asthenosphäre-Grenze stabilisieren. Die Beziehung zwischen dem Wassergehalt in den Teilschmelzen und der Schmelzpunkt-Erniedrigung im Peridotit-H<sub>2</sub>O-System ist jedoch nicht gut bekannt, da sich die entsprechenden niedrigen Wassergehalte in Experimenten nur schwer genau einstellen lassen. Darüber hinaus ist der Solidus im Peridotit-H<sub>2</sub>O-System schwer zu erkennen und die Interpretation von Versuchsprodukten in diesem System kann sehr subjektiv sein. Das System Anorthit-Diopsid-H<sub>2</sub>O wurde untersucht, um den Zusammenhang zwischen Wassergehalt in der Schmelze und Schmelzpunkterniedrigung genau zu bestimmen. Die in diesem System erzeugten „haplobasaltischen“ Schmelzen ähneln den Tholeiten, die beim Teilschmelzen von Peridotit entstehen. Da das Anorthit-Diopsid-System jedoch eutektisch ist, bilden sich große Schmelzmengen sofort am Solidus, so dass die Schmelztemperatur genau bestimmt werden kann. Alle Experimente wurden in einer „Rapid-Quench“ innenbeheizten Gasdruckapparatur bei 0,02 bis 0,2 GPa und 1000 bis 1500 °C ausgeführt, um niedrige Wasser-Fugazitäten zu simulieren. Eine Serie von Experimenten wurde mit einer Anorthit-Diopsid-Mischung (1:1) ausgeführt, um die Schmelzpunkterniedrigung als Funktion der Wasser-Fugazität zu bestimmen. In einer weiteren

Reihe von Experimenten wurden Glaszylinder aus „Haplobasalt“ benutzt, um die Wasserlöslichkeit in Schmelzen mit Hilfe von FTIR-Analysen zu messen. Die Beziehung zwischen Wassergehalt in der Schmelze und Schmelzpunkt-erniedrigung wurde kombiniert mit publizierten Daten über die Mineral/Basalt-Verteilungs-koeffizienten von Wasser unter den Bedingungen des oberen Mantels. Das resultierende Modell für die Schmelzbildung in Peridotit zeigt, dass bei einem Wassergehalt von etwa 200 ppm Schmelzbildung an der Grenze zwischen ozeanischer Lithosphäre und Asthenosphäre zu erwarten ist. Um Schmelze an der Lithosphäre-Asthenosphäre-Grenze unter Kontinenten zu bilden, ist möglicherweise eine zusätzliche Schmelzpunktniedrigung durch CO<sub>2</sub> notwendig.

## **1. Water in the mantle: An overview**

### **1.1. The upper mantle water cycle**

Water is the most abundant volatile in the upper mantle. Estimates of volatile contents in undegassed rapidly quenched MORB or in undegassed melt inclusions suggest that approximately 100 to 200 ppm of water may be present in most of the ambient upper mantle (Michael 1995; Danyushevsky et al., 2000; Saal et al., 2002). Similar ppm-level values were observed from measurements of water contents in exhumed mantle xenoliths (Kurosawa et al., 1997; Grant et al., 2007; Peslier et al., 2010, Demouchy and Bolfan-Casanova, 2016), although these estimates are not definitive, since partial dehydration may occur during exhumation. Michael (1995) noted that some mantle regions, such as the Mid Atlantic Ridge, appear to be more water enriched. Evidence from ophiolites and mantle xenoliths demonstrates that metasomatism may introduce additional volatile species and mobile elements to the upper mantle (Bailey, 1982; Frost, 2006). However, the term ‘mantle metasomatism’ is not well defined. The origins and types of metasomatic agents may vary greatly (O’Reilly and Griffin, 2012). Melts (silicate, carbonatite, sulfide), C-O-H (saline) fluids and supercritical fluids have all been proposed as viable upper mantle metasomatic agents. Based on textural evidence from natural samples, these liquids may presumably percolate along grain boundaries, or propagate in the mantle through cracks (O’Reilly and Griffin, 2012). The geographic extents of metasomatic events appear to vary as well. Lateral gradients in seismic and electrical properties in the upper mantle have been attributed to metasomatized mantle regions (Unsworth and Rondenay, 2012), possibly providing some constraint on their geographic distribution. These geophysical anomalies may have dimensions up to several hundred kilometers.

Water is stored in the upper mantle as OH<sup>-</sup> point defects in the structures of nominally anhydrous minerals (NAMs). Water solubility measurements in olivine (Kohlstedt et al., 1996; Zhao et al., 2004; Mosenfelder et al., 2006), pyroxene (Rauch and Keppler, 2002; Bromiley and Keppler, 2004; Mierdel et al., 2007) and garnet (Lu and Keppler, 1997) demonstrate that peridotite lithologies may dissolve several hundred to several thousand ppm of water at ambient mantle conditions. Nominally anhydrous minerals are, therefore, the principal water reservoir in the upper mantle. In addition, hydrous minerals – that may contain several wt.% of water – are sometimes observed as accessory phases in mantle xenoliths. The most common upper mantle hydrous phases

are mica and amphibole group minerals (Dawson and Powell, 1969; Dawson and Smith, 1982; Frost, 2006). Whether hydrous phases may be thermodynamically stable at typical (reduced) upper mantle water activities, or if they are predominantly products of metasomatic events, remains debated.

Some of the water in the present mantle may still be primordial, being inherited from the accretion of the Earth. Indeed, the overall similarity of terrestrial hydrogen isotope compositions with those of chondrites suggest that they are the main source of water on our planet, with contribution from comets being rather limited (Marty and Yokochi 2006). Some of the water initially contained in the solid Earth may have been lost by degassing during the magma ocean episode; however, the extent of this effect is difficult to quantify, as it strongly depends on the prevailing oxygen fugacity (Gaillard et al. 2022). Throughout Earth's history after the onset of plate tectonic regime, water was degassed from the mantle by magmatic activity. As water behaves incompatibly during partial melting (e.g. Hirschmann, 2006), all magmatic processes that extract melt from the upper mantle may efficiently return water to the Earth's surface. In the modern Earth, upper mantle degassing occurs by large-volume basaltic eruptions at mid-ocean-ridges, with contributions from arc volcanism, rifting and intraplate magmatic activity (Hirschman and Kohlstedt, 2012).

Water is being recycled into the upper mantle mainly by subduction-related processes. Traditionally, most of the slab water is thought to be lost at fore-arc conditions by the release of pore fluids through compaction and fracturing (Moore and Vrolijk, 1992). In contrast to this view, it was shown that water may infiltrate the mantle section of the slab along bending-related faults, and be carried past the fore-arc region by serpentized peridotites (Ranero et al., 2003). However, the global extent of slab mantle serpentization is poorly constrained (Kerrick, 2002). Various hydrous minerals are stable along typical slab geotherms (Schmidt and Poli, 1998). The hydrous phases may store water during continuous subduction, until they reach their respective stability limits, dehydrate and release a mobile fluid phase into the mantle wedge. Some of the initial slab water content may be transported deeper into the mantle by nominally anhydrous eclogite minerals (Lu and Keppeler, 1997; Bromiley and Keppeler, 2004). The mantle region above the slab is continuously metasomatized by infiltrating fluid. As a result, an increased mantle water content may be expected in the vicinity of subduction zones. Moreover, water could also be introduced

into the upper mantle from the transition zone (Hirschmann, 2006). The transition zone may be significantly more water-rich than the upper mantle (Pearson et al., 2014). Therefore, a plume rising from (or through) the transition zone may locally hydrate the surrounding upper mantle.

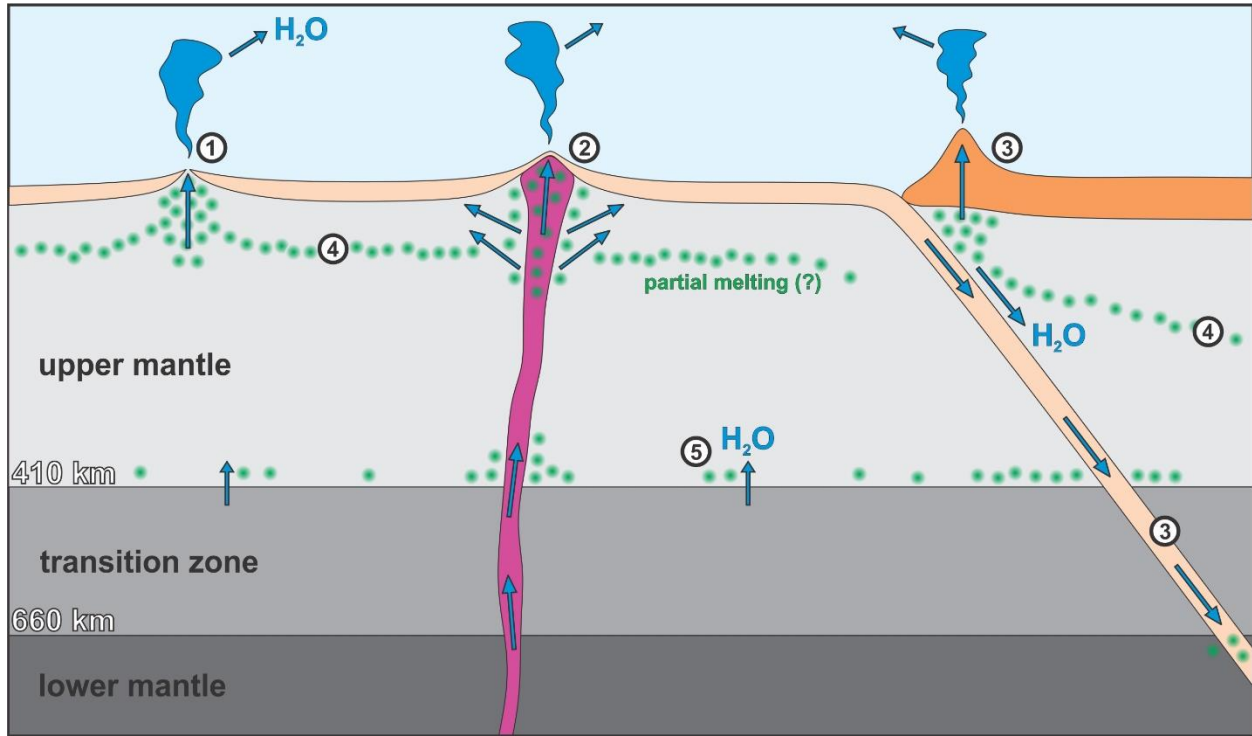


**Figure 1.1.1:** A simplified schematic of the upper mantle water cycle (modified after Hirschmann, 2006). The oceanic and continental crust are indicated in orange, the mantle is represented by different shades of gray, and a mantle plume is shown in purple. The blue arrows indicate plausible directions of water migration, and the green dots represent possible locations of hydrous partial melting in the mantle. 1) Mid-ocean-ridges: water is being extracted from the upper mantle by partial melting, and is returned to the surface. 2) Mantle plumes: water is introduced into the upper mantle via metasomatism, and simultaneously returned water to the surface by intracontinental magmatism. 3) Subduction zones: hydrated slabs and subduction-related metasomatism recycle water into the mantle; some of the subducted water returns to the surface via arc volcanism. 4) Possible partial melting at the lithosphere-asthenosphere boundary (LAB). 5) Possible partial melting at the boundary between hydrated regions of the transition zone and the bottom of the upper mantle (the 410 discontinuity).

## 1.2. Motivation

Even at trace concentrations, water may strongly influence the physical state of the mantle. In particular, water may help to stabilize silicate melts under conditions where otherwise no melting would occur. Water dissolution decreases the silicate activity in the melt, and melt may be stabilized at significantly lower temperatures than the dry solidus. As a result, low-degree partial melts may form at depths corresponding to the upper mantle low velocity zone (LVZ). The presence of low melt fractions could potentially explain the shear-wave velocity reductions

observed in the LVZ (Anderson and Sammis, 1969; Anderson and Spetzler, 1970). A partially molten seismic low velocity zone would also provide a channel of low viscosity below the plates, which appears to be an essential requirement for the development of plate tectonics on a planet (e.g. Höink et al., 2012) The effects of water on mantle melting may therefore be the key to understanding Earth's unique evolution.

The depths of melting and magma productivity beneath mid-ocean-ridges may also be influenced by the effect of water on the melting point depression of peridotite (Tenner et al., 2012). In addition, hydrous silicate melts have increased electrical conductivities and reduced viscosities (Richet et al., 1996; Ni et al., 2015) compared to dry systems. The presence of hydrous melts, aqueous fluids or supercritical fluids may therefore explain the electrical conductivity anomalies in the mantle (Unsworth and Rondenay, 2012), and the reduced viscosity of hydrous silicate melts may have implications for melt migration in the upper mantle (Kelemen et al., 1997). In addition, the relationship between silicate melt viscosity and degassing controls magma fragmentation processes at shallow crustal depths, and therefore determines the style of volcanic eruptions and their impact on the environment.

Water may directly alter physical properties of minerals as well. Hirth and Kohlstedt (1996) report that dissolution of water as OH<sup>-</sup> point defects may significantly lower the viscosity of olivine aggregates. The observed viscosity reduction due to the presence of trace amounts of water was proposed as an alternative explanation for the upper mantle low velocity zone, although this hypothesis was challenged by more recent studies (Fei et al., 2008).

Water-rich metasomatic phases are the main agents of mass transport in the upper mantle. Metasomatism is typically recognized as preferential enrichment in specific major and trace elements, and these chemical changes may or may not result in formation of additional accessory minerals (O'Reilly and Griffin, 2012). The observed element enrichment patterns are thought to depend on the type of metasomatic agent. For example, subduction-related metasomatism produces melts with distinct large ion lithophile element (LILE), light rare earth element (LREE), U, Th and Pb enrichments. Refractory elements (Ti, Nb, Ta, Zr, Hf) and heavy rare earth elements (HREE) are not as readily mobilized by the slab-derived metasomatic agent. Experimental studies

on trace element partitioning between residual slab lithologies and different high-pressure liquids are required to constrain the nature of the slab-derived metasomatic agent.

### **1.3. Thesis structure**

The thesis is structured in three main parts, which address different aspects of the role of water in the dynamics of the mantle:

- (i) One project investigates the stability of amphibole in the upper mantle at controlled conditions of reduced water activity (Chapter 2). This is important, since the production of hydrous melts by amphibole breakdown was proposed as another explanation for the upper mantle low velocity zone (Green et al., 2010).
- (ii) Metasomatic processes in subduction zones were studied as well (Chapter 3). It was experimentally tested whether the elemental and isotopic “sediment signature”, observed in some arc magmas, does indeed require chemical transport by sediment melts – as often assumed – or whether this signature may also be produced by saline aqueous fluids released from the sediments.
- (iii) The aim of the third project, presented in Chapter 4, was to precisely determine the effect of trace amounts of water on the melting point depression in the peridotite-H<sub>2</sub>O system. The results allow much more accurate predictions of melt stability in the low velocity zone.

In addition, a short-project was carried out in collaboration with the Department of Earth Science at Tohoku University (Japan). Pre-eruptive crystallization kinetics in alkaline melts from the Eifel were studied, and the conditions of magma ascent and fragmentation were constrained (Appendix).

## 2. Amphibole stability in the upper mantle at reduced water activity

### 2.1. Introduction

The stability of hydrous phases in the upper mantle has been a topic of interest ever since accessory mica and amphibole were observed in mantle xenoliths. But textural evidence from natural samples is not sufficient to determine if the exhumed hydrous phases are thermodynamically stable at upper mantle conditions, or if they are a product of secondary metasomatic events (Dawson and Smith, 1982). The stability of hydrous phases in the upper mantle therefore needs to be constrained by experiments.

Early experimental studies determined amphibole stability at H<sub>2</sub>O-saturated conditions – in the presence of excess hydrous fluid – and the stability limit was observed in the pressure range that generally corresponds to depths at which reduced seismic shear-wave velocities can be observed on a global scale (Lambert and Wyllie, 1968; Lambert and Wyllie, 1970). It was suggested that the formation of low-degree hydrous melts beyond the amphibole stability limit could explain the upper mantle low velocity zone (LVZ). Subsequent studies demonstrated that at upper mantle conditions, nominally anhydrous peridotite minerals may dissolve water as OH<sup>-</sup> point defects (Bell and Rossman, 1992). The estimated total water solubility in nominally anhydrous minerals (NAMs) is in the order of several hundred ppm by weight (Kohlstedt et al., 1996; Lu and Keppeler, 1997; Rauch and Keppeler, 2002; Mierdel and Keppeler, 2004; Bromiley et al., 2004; Bromiley and Keppeler, 2004; Mosenfelder et al., 2006; Mierdel et al., 2007). Since the upper mantle water content is likely limited to between 100 and 200 ppm (Ch. 1 and ref. therein), it is not clear if at realistically low water fugacity excess fluid may be available to form an additional hydrous phase.

The idea that amphibole dehydration melting may be occurring globally in the upper mantle was recently reconsidered by investigations of amphibole stability at very low nominal water concentrations (Green et al., 2010). This study proposed that shear-wave velocity reductions along the lithosphere-asthenosphere boundary (LAB) are due to partial melting at the amphibole-out boundary. This is essentially the interpretation proposed by the early experimental studies (e.g. Lambert and Wyllie, 1968). It should be noted, however, that the work from late '60s established the amphibole stability limit at lower pressures and temperatures than Green et al. (2010). As a

result, Lambert and Wyllie (1968) and Lambert and Wyllie (1970) may have been referring to shallower mid-lithospheric discontinuities (MLDs), instead of the lithosphere-asthenosphere boundary. Modern seismic methods allow distinction of the lithosphere-asthenosphere boundary from MLDs in both oceanic (Montagner and Burgos, 2019) and continental settings (Rader et al., 2015).

Low bulk water contents are experimentally difficult to control. Some uncertainties arise due to weighing errors and water evaporation during capsule welding. In addition, the noble metal sample containers generally preserve closed system conditions, but diffusion of hydrogen through capsule walls is possible at high temperature. This can be very difficult to detect, and depends largely on hydrogen permeability of both pressure medium and capsule materials (Matjuschkin et al., 2015). However, the most significant problem is likely the adsorption of atmospheric water on fine-grained starting materials. Keppler and Rauch (2000) showed that silicates and oxides may be contaminated by thousands of ppm of water, and that atmospheric contamination cannot be eliminated by drying. Thus, the actual bulk water contents in experimental studies tend to be higher than the nominal values.

Instead of attempting to maintain the starting materials dry and add ppm level water concentrations directly to the sample, a much more reliable approach for controlling water activity is to use a high bulk water content, and to introduce an additional inert component to the fluid phase. The additional component lowers the molar fraction of water in the fluid, and reduces water activity to H<sub>2</sub>O-undersaturated conditions. We decided to reinvestigate amphibole stability in the upper mantle using this experimental approach. Considering that very low nitrogen solubilities have been reported in upper mantle minerals (Li et al., 2013), we used molecular nitrogen to lower water activity in the fluid phase. The bulk water concentration was kept constant at 1 wt.% in all experiments, and the nitrogen content was adjusted to achieve a range of N<sub>2</sub>-H<sub>2</sub>O fluid compositions. The amphibole stability limit was determined in equilibrium with fluids that had molar fractions of water between 0.1 and 1 (H<sub>2</sub>O-saturated conditions). Based on reported water solubilities in nominally anhydrous minerals combined with estimates of bulk upper mantle water contents, we expect that fluids with mole fractions of water lower than  $\approx 0.3$  yield water activities representative of the upper mantle. The stability of amphibole in the upper mantle can then be

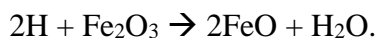
modelled using our new experimental data, taking into account the water solubility in nominally anhydrous minerals (Ch. 2.3.6).

## 2.2. Experimental methods

### 2.2.1. Starting materials and sample preparation

All experiments were performed using a synthetic peridotite oxide mixture. The bulk composition of the mixture is based on GEOROC database compilation of mantle xenoliths by Mandler and Grove (2016), and is considered representative of natural metasomatized peridotites (Table 2.2.1.).

Stoichiometric amounts of high-purity SiO<sub>2</sub>, TiO<sub>2</sub>, Al(OH)<sub>3</sub>, Cr<sub>2</sub>O<sub>3</sub>, MnO, Mg(OH)<sub>2</sub>, CaCO<sub>3</sub>, Na<sub>2</sub>CO<sub>3</sub>, K<sub>2</sub>CO<sub>3</sub> and NiO were weighed and ground under ethanol for 1 hour in an agate mortar. The iron-free mixture was then dehydrated and decarbonated in a Pt crucible at 1100 °C for 12 h. Separately, metallic Fe powder and Fe<sub>2</sub>O<sub>3</sub> were combined using the same procedure to produce an iron-bearing mixture with an initial 1:1 iron to oxygen stoichiometry. The iron mixture was annealed in a gas-mixing furnace for three days at 1050 °C and f<sub>O2</sub> between IW and MW buffers. The conditions for annealing the iron-bearing mixture were chosen to stabilize FeO and therefore to limit potential introduction of additional H<sub>2</sub>O to the samples during experiments via hydrogen diffusion through capsule walls by redox reaction:



The iron-free and iron-bearing mixtures were mixed and ground together under ethanol for an additional hour in an agate mortar. To promote garnet nucleation, 1 wt.% of natural garnet seeds was added as well, before the iron-free and iron-bearing mixtures were mechanically homogenized. The procedure described here is similar to that of Mandler and Grove (2016), with the exception of reducing the iron-bearing mixture at lower f<sub>O2</sub>.

To introduce H<sub>2</sub>O into the samples, brucite (Mg(OH)<sub>2</sub>) was used in the early experiments at high a<sub>H2O</sub>, as it allows the added water to be weighed more precisely and avoids possible water loss during capsule welding. In later experiments, distilled water was directly added to the samples. The main benefit of using H<sub>2</sub>O(l) is that fluid composition is established immediately at the beginning of the experiment, thus improving fluid circulation and mixing at run conditions and ensuring better equilibration, which is critical at reduced water activities where reaction kinetics

2. Amphibole stability in the upper mantle at reduced water activity

are noticeably slower. Silver azide ( $\text{AgN}_3$ ) was used as a source of molecular nitrogen in all experiments. To synthesize silver azide, stoichiometric amounts of silver nitrate ( $\text{AgNO}_3$ ) and sodium azide ( $\text{NaN}_3$ ) were dissolved in distilled water. Upon mixing the solutions, silver azide immediately precipitates. The silver azide was filtered off and washed with distilled water. For safety reasons, it was stored and loaded into the capsules as a suspension in water (see Keppler (1989) for further details).

**Table 2.2.1:** Bulk compositions of peridotite starting materials from this and several other experimental studies investigating amphibole stability in the upper mantle.

Oxide	This study	Mandler & Grove (2016)		MORB pyrolite	Niida & Green (1999)		
		fertile + met.comp.	depleted + met.comp.		Hawaiian pyrolite	Tinaquillo lherzolite	NHD peridotite
<b>SiO<sub>2</sub></b>	43.90	44.65	43.72	44.74	45.20	44.95	43.40
<b>TiO<sub>2</sub></b>	0.05	0.15	0.05	0.17	0.71	0.08	0.08
<b>Al<sub>2</sub>O<sub>3</sub></b>	1.80	3.87	1.79	4.37	3.54	3.22	2.00
<b>Cr<sub>2</sub>O<sub>3</sub></b>	0.42	0.37	0.42	0.45	0.43	0.45	0.30
<b>FeO</b>	8.00	8.14	7.97	7.55	8.47	7.66	8.60
<b>MnO</b>	0.13	0.14	0.13	0.11	0.14	0.14	0.13
<b>MgO</b>	43.00	37.70	42.82	38.57	37.50	40.03	43.10
<b>CaO</b>	1.70	3.38	1.69	3.38	3.08	2.99	1.80
<b>Na<sub>2</sub>O</b>	0.60	0.62	0.40	0.40	0.57	0.18	0.13
<b>K<sub>2</sub>O</b>	0.10	0.08	0.06	0.00	0.13	0.02	0.03
<b>NiO</b>	0.30	0.25	0.30	0.26	0.20	0.26	0.42

Cylindrical gold capsules (1 cm length, 5.0/4.6 mm outer/inner diameter) with flat lids were used to seal the samples in early experiments, since gold limits iron loss and hydrogen diffusion through the capsule wall at run conditions. However, for preparation of samples containing high gas-to-solid ratios, such as the ones used in low  $a_{\text{H}_2\text{O}}$  runs, it became necessary to replace the gold with the mechanically stronger  $\text{Pt}_{95}\text{Rh}_5$  capsules (5.0/4.4 mm outer/inner diameter) to prevent fluid loss during experiments. In runs at temperatures below 1250 °C, the inside of the PtRh capsules was lined with 1  $\mu\text{m}$  thick gold foil to reduce iron loss. In high-temperature experiments, the gold foil had to be removed entirely and silver azide was enclosed in open inner Pt envelopes to prevent melting of the outer PtRh capsules due to alloying with Au and Ag. All sample designs are shown in Figure 2.2.1.

## 2. Amphibole stability in the upper mantle at reduced water activity

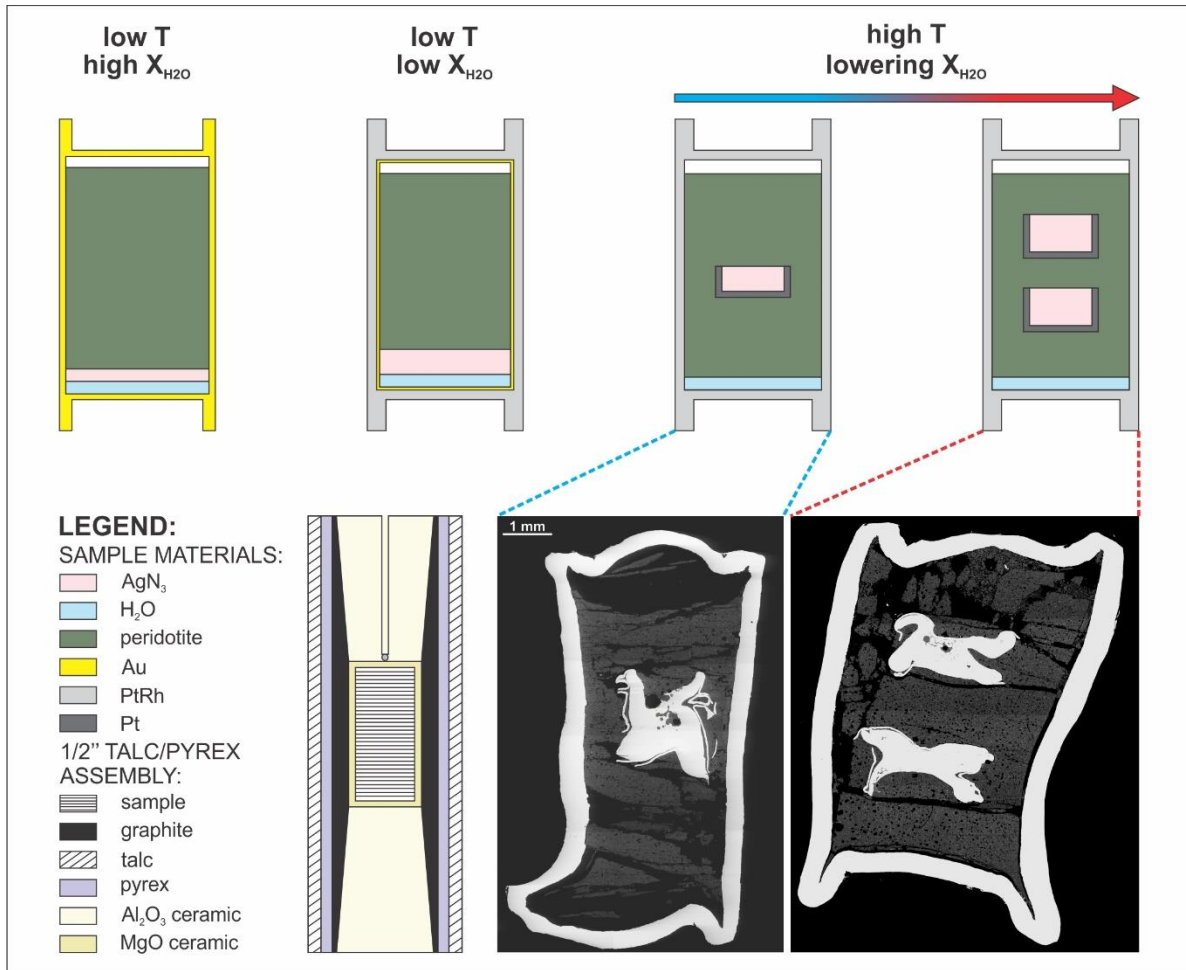


**Figure 2.2.1:** A summary of sample designs is shown in the top part of the figure. From left to right: gold capsules were used in runs at low temperatures and high water activities; experiments at low temperatures and low water activities were performed using mechanically stronger PtRh capsules to avoid fluid loss from samples with high gas-to-solid ratios; open inner Pt envelopes were introduced to prevent melting of outer capsules due to alloying with Au and Ag in runs at high temperature; the silver azide had to be divided between two smaller Pt envelopes in runs performed at both high temperature and low water activity – if only one larger inner container was used, the capsules typically collapsed in the middle and the fluid was lost. Representative BSE images of capsules recovered from high temperature runs are shown in the bottom right of the figure. The standard 1/2'' talc/pyrex assembly is shown in the bottom left of the figure.

Regardless of which sample design was used, the amount of water was kept constant in all experiments (1% by weight of the peridotite mixture) and the molar fraction of water in the  $N_2$ - $H_2O$  fluid was adjusted to the desired value by weighing in an appropriate amount of  $AgN_3$ . In  $H_2O$ -saturated experiments, no silver azide was added to the peridotite mixture. In early experiments,  $AgN_3$  was being decomposed in the piston cylinder press during heating. Later on, nitrogen-bearing samples capsules were routinely annealed in a 1 atm furnace before the experiments by slow heating from 100 to 350 °C over 16 to 20 h. The annealing procedure decomposes  $AgN_3$  in a controlled manner without rupturing the samples and helps to establish the desired fluid composition before the start of the experiment.

### 2.2.2. Piston cylinder experiments

The piston cylinder press is a common type of high-pressure apparatus used for routine experiments between 0.5 and 4 GPa, although some authors report reaching pressures as high as 7 GPa (Luedemann and Kennedy, 1968). The piston cylinder presses used by most experimental petrology laboratories today closely resemble the design developed by Boyd and England (1960).

The basic apparatus consists of a hydraulic ram ('master ram'), which pushes a tungsten carbide piston with a standard diameter of either ½" (12.70 mm) or ¾" (19.05 mm) into a steel-confined tungsten carbide pressure vessel, which has a cylindrical hole of an appropriate diameter. A second hydraulic ram (the 'endload') compresses the vessel in order to increase its effective tensile strength. The sample is located in the pressure vessel borehole and enclosed in an assembly of a solid pressure-transmitting medium (e.g. talc, pyrophyllite, boron nitride, NaCl, crushable ceramics, etc.), which is highly ductile at run conditions. The soft pressure medium transmits the pressure from the piston to the charge in a quasi-hydrostatic fashion. The nominal pressure applied to the sample can then be estimated as:

$$P_{nominal} = \frac{A_{ram}}{A_{piston}} \times P_{oil} \quad \text{Eq. 2.2.1.}$$

where  $P_{oil}$  and  $P_{nominal}$  are the oil pressure in the hydraulic master ram system and the nominal pressure applied to the sample, respectively.  $A_{ram}$  and  $A_{piston}$  are surface areas of the hydraulic master ram and of the tungsten carbide piston. Since the solid pressure medium supports shear stress, some pressure correction is necessary to account for the internal friction of the assembly materials. The friction correction is obtained by pressure calibration employing a well-defined thermodynamic equilibrium, such as the quartz/coesite transition. The actual pressure applied to the sample is then:

$$P_{actual} = P_{nominal} - P_{friction\ correction} \quad \text{Eq. 2.2.2.}$$

The temperatures in the piston cylinder apparatus can typically reach up to 2000 °C, and are achieved by resistive heating. To generate high temperatures, a strong current is passed through a thin graphite heater sleeve (the furnace), which is enclosed in the assembly materials. The steel casing surrounding the tungsten carbide pressure vessel is water-cooled during the experiment, in

order to retain the high tensile strength of the steel, and to allow fast quenching of the sample once the heater power is turned off.

All experiments were performed in an end-loaded piston cylinder apparatus (Boyd and England, 1960) at BGI using a 1/2" talc/pyrex assembly with crushable alumina spacers. The samples were enclosed in MgO capsule sleeves, which were dissolved in diluted HCl after the experiment to check for fluid leaks. The temperature was monitored by S-type thermocouples (Pt<sub>90</sub>Rh<sub>10</sub>/Pt), and controlled using a Eurotherm device.

The early experiments followed the standard hot-piston-in method (e.g. Johannes et al., 1971), where the samples were first compressed below target pressure and then heated at a rate of 100 °C/min. After the temperature had stabilized, the pressure was raised to target value. In later experiments, once several kbar of pressure was applied to the run charge, the temperature was raised to 400 °C and kept stable during compression to help maintain efficient fluid circulation throughout the capsule and to decompose silver azide, if the sample had not been annealed in the 1 atm furnace (Ch. 2.3.3.3). Pressure and temperature were then raised to target values following the hot-piston in method.

Both one-stage ('forward') and two-stage ('reverse') experiments were performed. In one-stage experiments, the samples were kept at target pressure and temperature for 3 to 10 days, depending on run conditions and water activity. Once the H<sub>2</sub>O-saturated amphibole stability limit had been determined by one-stage experiments, the two-stage experiments at reduced water activities were done by keeping the samples at target pressure and a temperature of 50 to 100 °C above the H<sub>2</sub>O-saturated stability limit for approximately one week to decompose metastable phases. Afterwards, the temperature was lowered to the target value at a rate of 100 °C/min, and the experiments were continued for an additional week. The two-stage procedure was necessary to avoid formation of metastable phases in runs at relatively low temperatures (Ch. 2.3.3.1).

### **2.2.3. Electron microscopy**

The scanning electron microscope (SEM) and the electron microprobe (EPMA) are two of the most common types of electron microscopes, widely used in modern geosciences for sample

imaging at micro- to nanometer scale, but also for chemical and structural analysis. The basic principles of operation of both SEM and EPMA are in many ways similar and can be described together, emphasizing the differences between instrument configurations when necessary. The EPMA is largely dedicated for quantitative chemical analysis, while SEM is more suitable for sample imaging. Since the two methods are complementary, both were used for run product examination in the course of this project. A summary of typical SEM/EPMA instrumentation, and its various applications in geology, is provided by Reed (2005).

Typical components of an electron microscope are: an electron source (electron gun), a vacuum pump system, a series of electron lenses and apertures (the column), a software-operated specimen stage, beam-deflection coils and multiple electron detectors for sample imaging, as well as X-ray spectrometers for chemical analysis (Fig. 2.2.2).

Different types of electron sources are commercially available. The most common and most affordable kind is the tungsten filament, a thin tungsten wire that is electrically heated to provide the electrons at the wire surface sufficient thermal energy so they could be extracted and accelerated along a difference in electrical potential of around 10-30 kV. An alternative to the tungsten filament are lanthanum and cerium hexaboride ( $\text{LaB}_6$  and  $\text{CeB}_6$ ) crystals, which provide a higher beam current and brightness. Field emission (FE) sources, sharply pointed tungsten electrodes, from which the electrons are extracted by a strong electric field, are becoming more common. They provide both a considerable increase in brightness, and a decrease in beam diameter relative to conventional thermionic sources, allowing higher spatial resolution. Source heating in FE guns is not strictly required, but is sometimes used for a more stable emission. Tungsten filaments are much better suited for operation in EPMA, where higher current is necessary and the sample-electron interaction volume, rather than the beam diameter, limits spatial resolution of the chemical analyses. Field emission sources are more advantageous for imaging purposes and are the preferred choice for most SEM systems. Tungsten filaments have the lowest vacuum requirements, while the FE sources can operate only in ultra-high vacuum. The vacuum system usually consists of a combination of rotary and oil diffusion or turbomolecular pumps, which work in series to maintain high vacuum. Evacuation is necessary to avoid source damage, and to reduce electron scattering by air particles.

Upon extraction from the source, the accelerated electrons pass through a series of condenser lenses and apertures. The condenser lenses are iron-shielded coils of copper wire that induce a strong magnetic field when a direct current is passed through them. The magnetic field focuses the electron beam. The electron deflection relative to the axis of the column is controlled by adjusting the lens current. The apertures – thin diaphragms with center holes of appropriate sizes – are located between electromagnetic lenses, and are used to limit the beam diameter. The final aperture determines the beam diameter and current on the specimen. Higher beam currents are desirable for chemical analysis, while lower currents and corresponding smaller beam diameters are required for high-resolution imaging. The final electromagnetic – objective – lens focuses the electron beam at the working distance. The lower part of the objective lens pole piece often has a smaller diameter to reduce the strength of the magnetic field in the vicinity of the sample but the geometry can differ, depending on instrument requirements. Objective lenses of electron microprobes typically have smaller dimensions and carry a stronger current than those of SEM systems to allow more space for other components, such as the mirrors of the optical microscope.

Electron microprobes require an optical microscope with a field of view coaxial to the electron beam. The focus of the optical system coincides with the sample stage height required for quantitative chemical analysis and is, thus, used to adjust the stage position in the z-direction. It can also be used for determining the electron beam position on the sample in the x-y plane by observing in-situ fluorescence on appropriate target minerals. Optical systems are rarely mounted on SEM systems, as precise control of the stage position is usually not necessary. The sample stages in both SEM and EPMA are fully automated and usually allow for different geometries of specimens and specimen holders to be attached and introduced into the sample chamber.

The interaction between the electron beam and the sample is fairly complex, generating a number of different signals, many of which can be detected with appropriate instrumentation. Backscattered and secondary electrons are the two signals most commonly used for sample imaging, while X-ray spectrometry provides information about chemical composition of the sample.

As the incident electrons pass by the atomic nuclei of sample material, the positive charge of the nuclei deflects the electrons from their original trajectory. This phenomenon is called Rutherford scattering. The degree of deflection is dependent on the incident electron energy, the charge of the nuclei and the minimum distance between the electron and nuclei. Some incident electrons may be deflected through an angle larger than  $90^\circ$  and exit the specimen. Others may go through several deflections before emerging from the sample surface in a similar manner. These so-called 'backscattered' electrons (BSE) can be detected either by a solid-state detector or a scintillator located directly above the sample. Since the deflection angle is dependent on the atomic number, the fraction of the backscattered electrons increases with increasing average atomic number of target materials. Therefore, in addition to textural studies, BSE images can provide information about the compositional contrast and volume proportions of different materials present in the specimen.

With some probability, incident electrons of energies exceeding the ionization potentials of atoms in the sample can eject secondary electrons through the specimen surface. These secondary electrons (SE) originate from the sample atoms located within several nanometers below the specimen surface and have very low energies, in the order of several eV. To be detected, the secondary electrons must first be captured by a metal grid, which is kept at a low positive potential. The grid guides the secondary electrons into the vicinity of the detector, while the higher energy backscattered electrons can pass by un-deflected. Secondary electrons are usually detected by a scintillator, which is metal coated and held at a positive potential an order of magnitude higher than the detector grid. Secondary electron yield is a function of the angle between the specimen surface and the electron beam, with more secondary electrons emerging from the surface as the sample tilt angle increases. Furthermore, if the sample is not polished, a larger proportion of secondary electrons is able to emerge from edges and protrusions on the specimen surface. Due to these effects, the secondary electron signal provides information on the topography of unpolished samples.

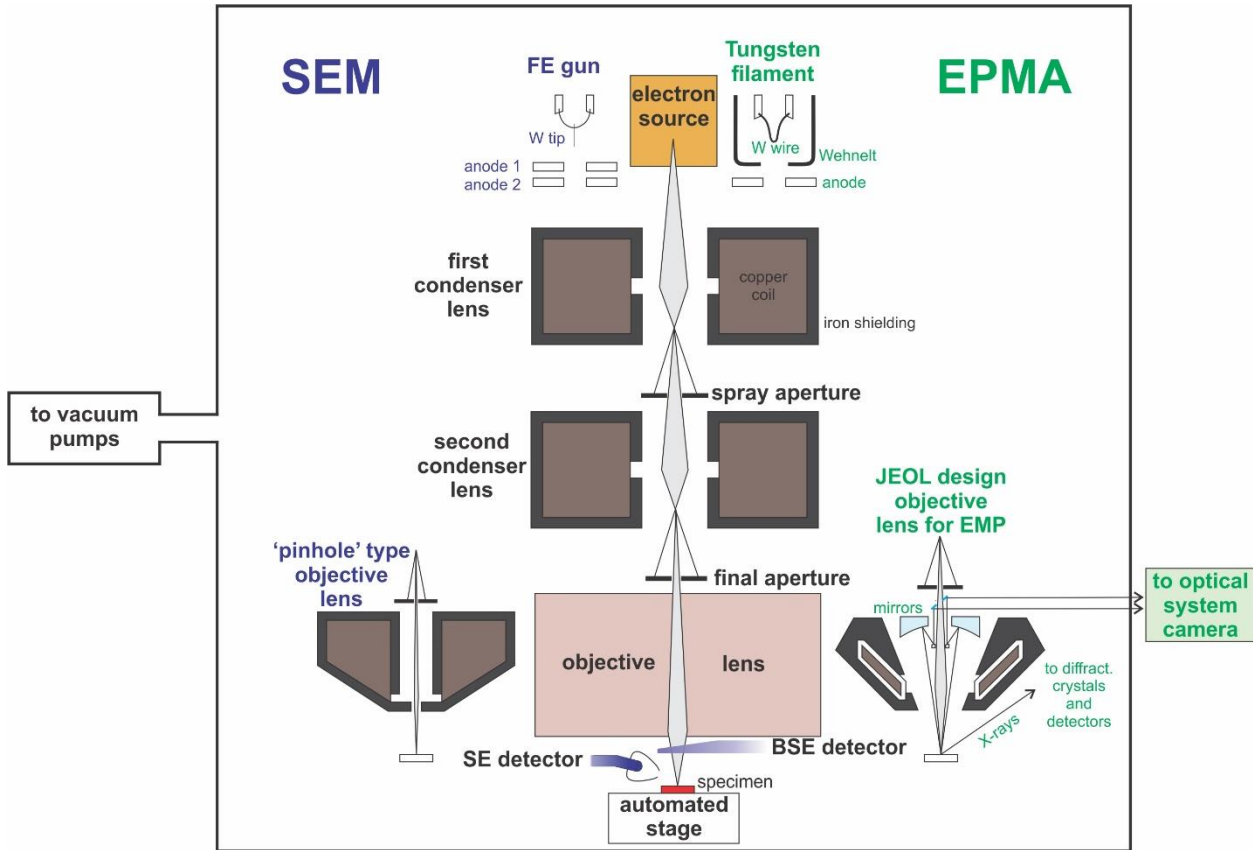


**Figure 2.2.2:** A simplified schematic view of electron microscopes. Common differences between the SEM (blue) and EPMA (green) instruments are shown.

Interaction of the electron beam with the sample also produces X-rays. The X-rays are emitted as a result of two different mechanisms (Fig. 2.2.3a). The incident electrons, scattered by the positively charged atomic nuclei in the sample, lose some of their energy as they decelerate and emit radiation in the X-ray energy range – the continuous spectrum (‘Bremsstrahlung’). Occasionally, an incident electron ejects an inner shell electron from a target atom. The higher energy level electrons of the target atom then fill the created vacancy, emitting characteristic X-rays of energies corresponding to the differences in energy levels between the initial and final states of the transitioning electrons. Atoms of each element can emit a series of characteristic X-rays of wavelengths that are unique to them. Therefore, the characteristic X-ray lines can be used to obtain information about the chemical composition of the sample. Two different designs of X-ray spectrometers are commonly used in electron microscopy: the energy-dispersive (EDS) and wavelength-dispersive (WDS) types.

Several kinds of EDS detectors are commercially available and all of them rely on devices capable of producing a pulsed electrical signal in which the height of output pluses is proportional to the X-ray photon energy. EDS detectors can simultaneously collect X-rays of all energies and produce a plot of X-ray intensity versus photon energy. The ED spectrometers usually provide only qualitative chemical analyses, but have the advantage of rapid data collection and are particularly suitable for initial investigation of specimens with complicated and unknown compositions.

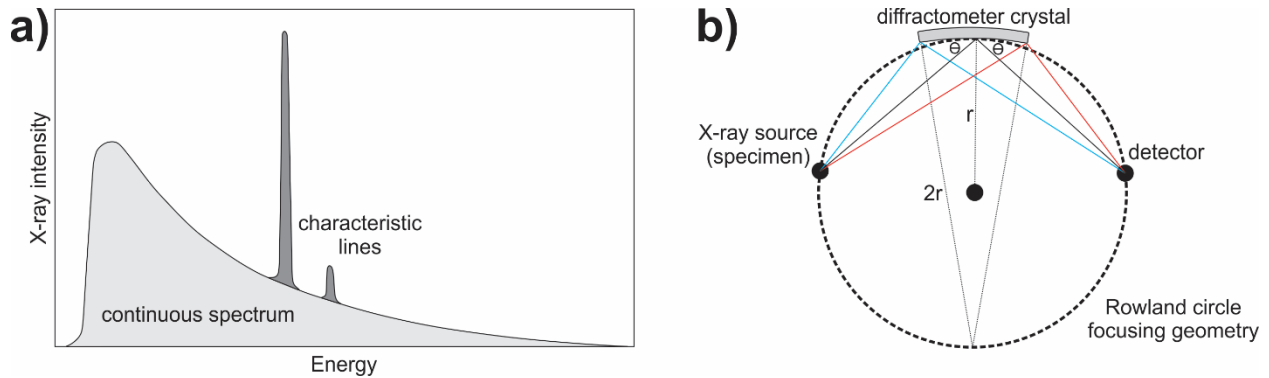


**Figure 2.2.3:** **a)** The generation of X-rays due to the interaction of incident electrons with the specimen. Scattering and deceleration of electrons by the positively charged atomic nuclei in the sample produce the continuous spectrum. The incident electrons may eject an inner shell electron from a target atom. The higher energy level electrons of the target atom fill the created vacancy, emitting characteristic X-ray lines. Characteristic line energies correspond to the differences in energy levels between the initial and final states of the transitioning electrons. **b)** A common configuration of the sample, diffractometer crystal and an X-ray detector in EPMA instruments during WDS analysis. The diffractometer crystal and the detector simultaneously move along the Rowland circle to achieve the focusing geometry for incident X-rays of different wavelengths.

WD spectrometers consist of a series of diffractometer crystals and several detectors, usually of the proportional counter type. Diffractometer crystals have well-defined structures with known interplanar spacings ( $d$ ). The characteristic X-rays emitted by the target materials diffract on the atomic layers of the crystals, according to the Bragg's law:

$$n\lambda = 2d\sin\theta \quad \text{Eq. 2.2.3.}$$

where  $n$  is the order of the reflection,  $\lambda$  the wavelength of the X-ray photon and  $\theta$  is the reflection angle. The atomic planes of the diffractometer crystals are curved, so all the points on the crystal could reflect X-rays of a specific wavelength towards the detector. If the sample, diffractometer crystal and the detector satisfy the focusing geometry, the recorded intensity of the characteristic X-ray line will be proportional to the concentration of its source element in the sample. An example of a common focusing geometry is shown in Figure 2.2.3b. During the measurement, the diffractometer crystal and detector both move to achieve the focusing geometries for different  $\theta$

and collect the intensities of a series of characteristic X-ray lines, one by one. WDS systems equipped with multiple crystals and detectors can simultaneously collect intensities at several wavelengths. The recorded X-ray intensities for a given beam current are lower in comparison to EDS, but the spectral resolution of WDS is much higher. While most SEM instruments come equipped only with EDS, electron microprobes usually have both EDS and WDS capabilities. In addition to the strict geometric requirements of WD spectrometers, to obtain a quantitative chemical analysis, calibration of characteristic X-ray line intensities against an external standard of known composition is necessary. Since the rates of X-ray production, as well as the absorption of the produced X-rays, depend on the mean atomic number of target material, a matrix correction is required to account for the differences between the properties of the standard and sample materials. Background corrections to remove the continuous spectrum are routinely performed, as well.

In the course of this study, a ZEISS-LEO 1530 Gemini FE-SEM at BGI was used for detailed examination of synthetic peridotite run products, prior to XRD and EPMA analysis. Samples were primarily checked for textural equilibrium and presence of amphibole and melt. In addition, SEM-EDS analyses proved useful in locating suitable mineral grains for subsequent EPMA-WDS measurement, which was helpful for obtaining quantitative compositions of accessory phases, such as phlogopite.

The JEOL JXA-8200 electron microprobe at BGI, equipped with a 5 WD spectrometer configuration was used for quantitative chemical analysis of all major minerals (olivine, pyroxenes, amphibole) in the produced synthetic lherzolites. Typically, between 5 and 10 high quality analyses were obtained per mineral phase in each sample. Whenever possible, minor and accessory phases (garnet, spinel, phlogopite) were analyzed as well. The measurements were performed with a focused beam (15  $\mu$ A current, 15 kV acceleration voltage). The PRZ matrix correction routine was used, and standardization materials were as follows: forsterite (Si), MnTiO<sub>3</sub> (Ti), spinel (Al), Cr metal (Cr), Fe metal (Fe), MnTiO<sub>3</sub> (Mn), enstatite (Mg), wollastonite (Ca), albite (Na), orthoclase (K) and Ni metal (Ni). Oxygen concentrations had not been analyzed, but were calculated assuming the common oxidation states of other elements. All iron is presumed to be ferrous (Fe<sup>2+</sup>). Moderately volatile alkali elements (Na, K) were analyzed in the first cycle of

the measurement, and shorter 8/10 seconds background/signal measurement times were used to limit the effects of evaporation under electron beam. Other elements were measured for 10/20 seconds on the background and signal, respectively.

#### **2.2.4. X-ray diffraction**

Powder X-ray diffraction (XRD) is a standard method for characterizing polycrystalline materials in science and industry, with many different possible applications including: crystal structure determination, identification of individual phases and phase mixtures (phase analysis), determination of phase proportions in a mixture, determination of crystallite size, measurements of solid solution compositions and measurements of thermodynamic properties of crystalline materials (compressibility, thermal expansivity). An introductory level information on X-ray powder diffraction methods is presented in numerous textbooks of mineralogy or physical chemistry (e.g. Atkins, 1982).

A brief description of typical instrumentation and powder phase analysis is presented. Other applications are not mentioned, as they are not relevant for the characterization of run products from this study. The main components of (powder) X-ray diffractometers are an X-ray source, an X-ray focusing system, a rotating sample stage, an X-ray detector, and a control unit (computer with suitable software).

The X-ray source consists of an anode and a cathode situated in an evacuated glass tube. The difference in potential between the cathode and anode is typically several kV and the cathode is usually a heated tungsten wire. Electrons are thermally emitted from the cathode and accelerated by the difference in potential. The extracted electrons collide with the anode, producing both the continuous spectrum and characteristic lines of the anode material (Ch. 2.2.3, Fig. 2.2.3a). Monochromatic radiation is desirable for general applications in (powder) XRD, so a foil of a suitable filter element that has an absorption edge between the  $K_{\alpha}$  and  $K_{\beta}$  lines of the anode material is usually placed in front of the X-ray source to suppress the  $K_{\beta}$  radiation. The  $K_{\alpha}$  radiation exits the tube through an X-ray transmissive material, usually a beryllium window. The filtered radiation exiting the tube is somewhat divergent and contains both  $K_{\alpha 1}$  and  $K_{\alpha 2}$  lines, as well as the continuous spectrum. Therefore, additional X-ray focusing is necessary for precise

measurement. The most common focusing systems use Johansson monochromator crystals. The monochromator crystals are curved along a set of lattice planes of well-defined interplanar spacing. As long as the X-ray source, the monochromator crystal and the sample satisfy the focusing geometry, all the points on the crystal reflect monochromatic radiation (characteristic  $K_{\alpha 1}$  line of the anode) towards the sample. Essentially the same principle is used for EPMA-WDS quantitative chemical analyses (Ch. 2.2.3, Fig. 2.2.3b). Other design solutions for obtaining a monochromatic X-ray beam exist, but are not described here.

An ideal sample for powder XRD should contain statistically oriented crystallites – all crystallographic orientations of a particular phase in the powder should be present in equal proportion in the X-ray beam interaction volume. If the sample is not sufficiently fine-grained, or if the grains in the sample have preferred orientation, the relative intensities of the reflections will not be representative. To improve the counting statistics, the sample stage is rotated during measurement as the sample is progressively tilted with respect to the incident X-ray beam.

The movement of the sample stage is coupled to the movement of the X-ray detector. For a sample tilt angle of  $\Theta$  with respect to the incident radiation, the detector is positioned at an angle of  $2\Theta$  (Fig. 2.2.4), in the direction of X-rays that are diffracted by lattice planes of crystallites in the powder. If the sample contains a phase with lattice spacing that satisfies the Bragg's law (Ch. 2.2.3., Eq. 2.2.1) for a given incidence angle ( $\Theta$ ), an intensity higher than the background is detected. The detector continuously records the intensity of the diffracted beam over the desired range of scattering angles ( $2\Theta$ ). The most common types of X-ray detectors are proportional counters and semiconductor-type detectors.

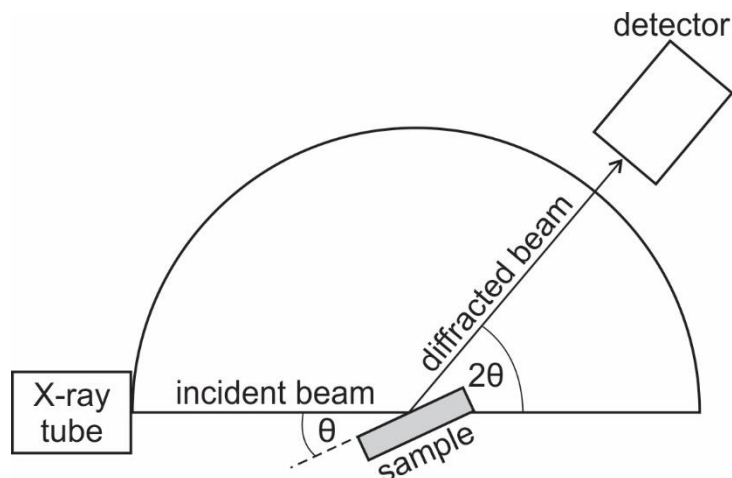


*Figure 2.2.4: Schematic measurement geometry of a (powder) X-ray diffractometer.*

The obtained diffraction pattern can then be compared to the available databases of X-ray powder diffraction data to obtain a qualitative phase analysis (e.g. Powder Diffraction File database). However, this approach, based on search by peak positions, may not always yield a satisfactory result. The potential downfalls are numerous – the reflection positions of solid solutions may depend on phase composition, reflections of different phases may overlap in multi-phase powders, diffraction patterns may contain artifacts related to instrument parameters, etc.

A more reliable approach is the Rietveld method (e.g. Young, 1993). In the Rietveld method, some initial crystal structure models are imported into an automated least-squares calculation routine. From the crystal structure models, the calculation routine estimates a theoretical reflection profile and compares it to the experimentally observed diffraction pattern. The entire diffraction pattern, including the positions and shapes of all reflections, is taken into account as a whole. If the agreement between the theoretical and observed diffraction profile is not satisfactory, a number of parameters in the calculation can be refined in subsequent steps until a best-fit is achieved. Different instrument parameters and structure model parameters (e.g. lattice constants, positions of atoms in the structure) are typically refined to fit the theoretical model to observation. More advanced fitting routines may include a number of additional, less common refinement parameters.

To confirm the presence or absence of monoclinic ( $C2/m$ ) amphibole in the run products, we obtained powder X-ray diffraction patterns of several samples. Approximately 20 to 50 mg of

## *2. Amphibole stability in the upper mantle at reduced water activity*

sample material was extracted from one halve of the longitudinally cut capsules, and was ground into a powder under ethanol, while the other halve was embedded in epoxy for electron microscopy.

All measurements were performed using a Philips X'Pert PRO diffractometer equipped with a Co  $K_{\alpha 1}$  ( $\lambda = 1.78897 \text{ \AA}$ ) radiation, monochromated with a symmetrically cut curved Johansson Ge (111) crystal and a Philips X'celerator detector. The data was collected at scattering angles ( $2\theta$ ) of 7 to  $90^\circ$  with exceptionally long acquisition times ( $0.017^\circ 2\theta$  increments and 1500 sec/step) to allow for detection of very low amphibole fractions.

Crystallographic information files (.cif) for amphibole, olivine, clinopyroxene and orthopyroxene structures were obtained from the American Mineralogist Crystal Structure Database (AMCSD). The .cif files were imported into Generalized Structure Analysis System (GSAS) software and the Rietveld method was used to fit the theoretical reflection profiles to the experimental diffraction patterns.

## 2.3. Results

Several series of experiments with different H<sub>2</sub>O-N<sub>2</sub> fluid compositions were performed at pressures of 2 to 4.5 GPa and temperatures between 900 and 1350 °C. To determine the amphibole stability field in the peridotite-H<sub>2</sub>O system at reduced water activity, fluid compositions were systematically varied between X<sub>H<sub>2</sub>O</sub>=1 (H<sub>2</sub>O-saturated) and 0.1 (H<sub>2</sub>O-understaturated conditions). The details of experimental conditions and procedures, as well as a summary of run product phase assemblages, are shown in Table 2.3.1. The variations in experimental procedures and materials (e.g. preheating, multiple stage runs) are explained in Chapters 2.2.1. and 2.2.2, but will be discussed further in the following text (Ch. 2.3.3).

### 2.3.1. Sample petrography

All run products have a lherzolite equilibrium assemblage consisting of olivine, clinopyroxene, orthopyroxene, ± amphibole, spinel (<3 GPa), ± garnet (>3 GPa) and ± phlogopite. Spinel often persists in the garnet stability field as a metastable phase. Complete decomposition of spinel occurred in only one experiment (3 GPa, 1250 °C, X<sub>H<sub>2</sub>O</sub>=0.25).

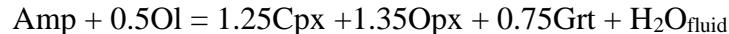
Sample grain size varies considerably (from >100 to <10 µm), depending mostly on X<sub>H<sub>2</sub>O</sub> in the fluid phase and run temperature. The effect of water activity on sample grain size is shown in Figure 2.3.1. (images a, c and e). The average grain size in the images decreases with decreasing X<sub>H<sub>2</sub>O</sub> in the fluid (a > c > e), despite the higher temperature in runs with lower water activity. All samples in the image panel 2.3.1. were produced by one-stage experiments, and the observed textures are representative of the given (P, T, X<sub>H<sub>2</sub>O</sub>) conditions. At constant X<sub>H<sub>2</sub>O</sub>, samples from two-stage runs retain grain sizes from the 1200 °C stage, and are usually coarser than those produced by “forward” experiments.

At water activities ≥ 0.25, a considerable modal proportion of amphibole is observed in the spinel stability field at temperatures <1100 °C. With increasing pressure and temperature, amphibole proportions generally decrease, while the clinopyroxene modes increase (see also Ch. 2.3.5). Phlogopite only appears in run products near or above amphibole stability limit. This observation was later confirmed by mass balance calculations (Ch. 2.3.5), which suggest that all the available K<sub>2</sub>O may dissolve in amphibole at low temperatures and pressures.

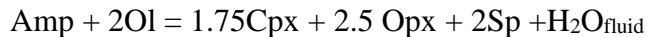
The onset of melting was defined by first appearance of melt pools along capsule walls and around open inner Pt capsules. The melt tends to quench into distinctive dendritic crystals surrounded by a Si-Na-K-rich glassy matrix (Fig. 2.3.1 b, d, f). Quenched glasses may occasionally contain dendritic amphibole, so no attempt was made to collect XRD data from the melted samples. The size of quench crystals generally decreases with decreasing pressure and  $X_{H_2O}$  in the fluid phase ( $b > d > f$ ). This observation is indirect evidence of lower water concentrations in the melt at lower pressures and water activities. Melts with higher water contents are expected to have lower viscosity and, therefore, produce more extensive quench crystallization. In only two experiments with fluid composition of  $X_{H_2O}=0.25$ , the melt quenched into fine-grained crystals (Fig. 2.3.1. f) that could be analyzed using EPMA by scanning the electron beam over several  $20 \times 20 \mu\text{m}$  areas. The obtained melt compositions are reported in Table 2.3.21. (Supplement I), but are not considered highly reliable.

### 2.3.2. Amphibole stability at reduced water activity

The high-temperature stability limit of amphibole is likely related to a melting reaction, where amphibole is consumed and a hydrous melt is formed. Since under water-saturated conditions, the hydrous melt contains more water than the amphibole, reducing water activity should destabilize the melt and extend amphibole stability to higher temperatures. On the other hand, the high-pressure stability limit of amphibole is a dehydration reaction involving solid phases and a supercritical vapor fluid phase, with amphibole on the side of the reactants and fluid on the side of the products. For the run products from this study, these reactions can be approximately balanced as:



in the garnet stability field and



in the spinel stability field. As the activity of water in the fluid decreases, the reaction should proceed to the right and the amphibole stability limit is expected to shift to lower pressures and temperatures.

## 2. Amphibole stability in the upper mantle at reduced water activity

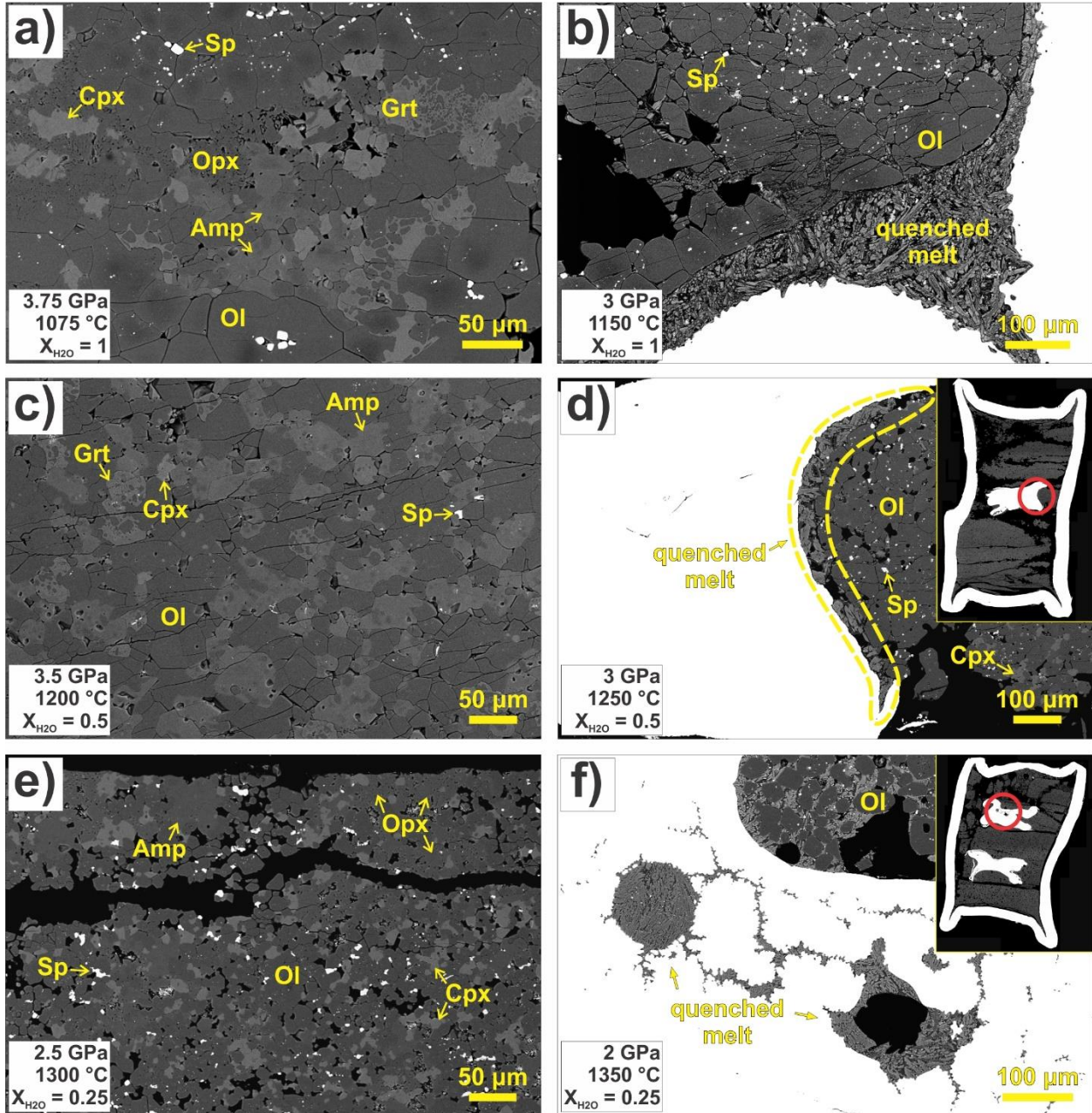


**Figure 2.3.1:** Representative run product BSE images. Textures of sub-solidus samples are shown in images **a** ( $X_{H_2O}=1$ ), **c** ( $X_{H_2O}=0.5$ ) and **e** ( $X_{H_2O}=0.25$ ). A gradual decrease in average grain size ( $a > c > e$ ) with decreasing water activity is typically observed. Textures of quenched melt pools are shown in images **b** ( $X_{H_2O}=1$ ), **d** ( $X_{H_2O}=0.5$ ) and **f** ( $X_{H_2O}=0.25$ ). The average size of quench precipitates decreases ( $b > d > f$ ) with decreasing pressure and water activity as a result of lower water concentrations in the melt. The bright pieces of platinum inside the capsules in images **d** and **f** were used to wrap the  $\text{AgN}_3$  (Ch. 2.2.1), which was used as  $\text{N}_2$  source.

In our experiments, amphibole was indeed destabilized toward lower pressures from above 4 to below 2 GPa at 1000 °C as the water activity in the fluid phase decreased from 1 to 0.1 (Fig. 2.3.2). At the same time, the high-temperature stability limit was shifted upwards. The observed effects are consistent with reactions of the types discussed above.

## 2. Amphibole stability in the upper mantle at reduced water activity

The position of amphibole stability limit in Figure 2.3.2. was determined by inspecting all run products for the presence of amphibole during FE-SEM observation. The samples synthesized at P-T conditions near the amphibole stability limit were additionally analyzed by powder XRD to confirm the result. The highest intensity reflections of monoclinic ( $C2/m$ ) amphibole structure are usually detected between  $30$  and  $45^\circ 2\theta$ . Since there is number of overlapping high-intensity pyroxene reflections in this  $2\theta$  range, diffraction patterns were also obtained from several samples containing abundant amphibole to allow easier identification of amphibole reflections (Fig. 2.3.3). The experimental reflection intensities were not reproduced in theoretical profiles obtained by Rietveld refinement, but the predicted and measured peak positions did generally agree. With decreasing amphibole fraction in the samples, relative intensities of several prominent reflections between  $30$  and  $45^\circ 2\theta$  become systematically lower, and the reflections finally disappear across the amphibole-out boundary (Fig. 2.3.3). The  $(110)$  amphibole reflection, at approximately  $12^\circ 2\theta$ , was particularly useful (Fig. 2.3.3), as it was readily detected even for low amphibole fractions.

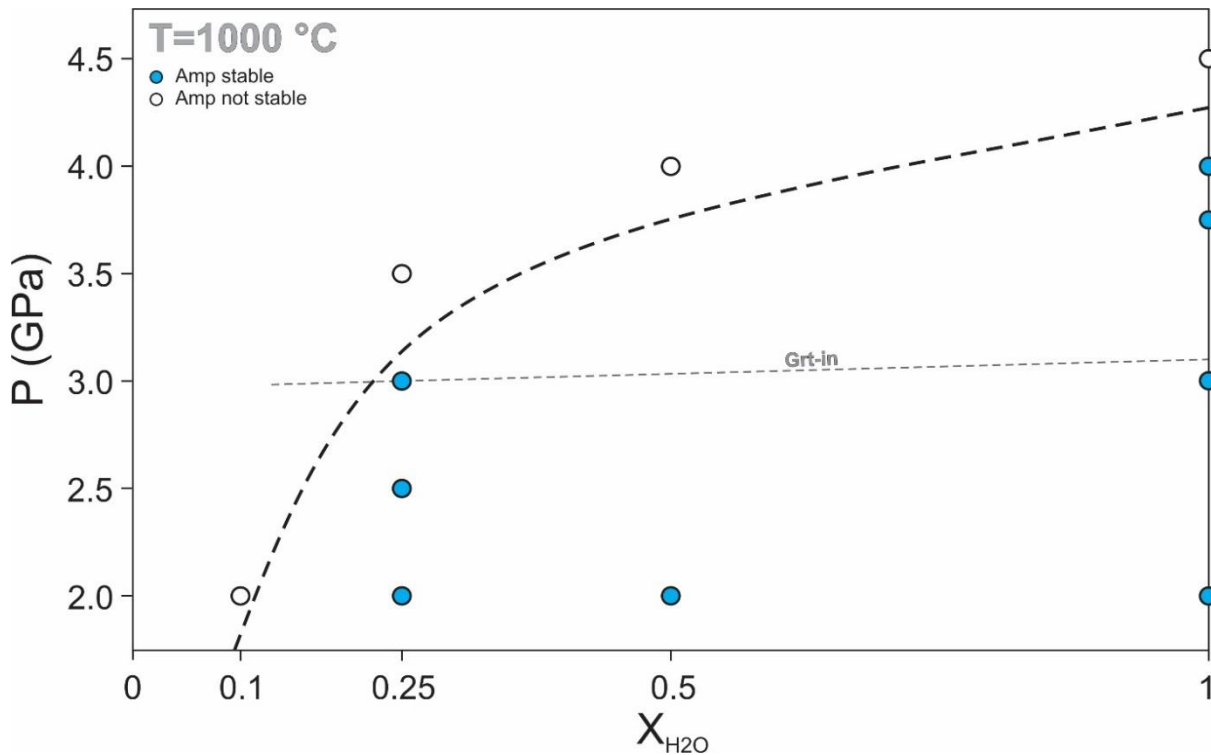


**Figure 2.3.2:** The approximate position of amphibole stability limit as a function of nominal  $X_{H_2O}$  in the fluid phase at constant temperature ( $1000^\circ\text{C}$ ). The effect shown in the figure is expected at low (sub-solidus) temperatures, where the amphibole-out reaction is a dehydration reaction involving amphibole and a supercritical  $H_2O$ -bearing fluid. This type of reaction governs amphibole stability at high pressure/low temperature.

2. Amphibole stability in the upper mantle at reduced water activity

**Table 2.3.1.** Summary of experimental conditions, procedures and the resulting phase assemblages. “Fwd/Rev” indicates either a “forward” one-stage experiment, or a “reverse” two-stage experiment with a 1200 °C first stage (to decompose metastable phases). Some samples were not preheated, whereas others underwent both preheating in a 1 atm furnace at 350 °C (to decompose AgN<sub>3</sub> before the experiment) and in piston-cylinder apparatus (to improve fluid mixing). Open inner Pt containers were introduced to isolate Ag from the PtRh in high temperature runs (to avoid outer capsule melting). Mineral name abbreviations: Amp – amphibole, Ol – olivine, Cpx – clinopyroxene, Opx – orthopyroxene, Sp – spinel, Grt – garnet, Phlog – phlogopite.

Sample	X <sub>H2O</sub>	P (GPa)	T (°C)	Fwd/Rev	Duration (h)		Preheating procedure		H <sub>2</sub> O source	Capsule material	Inner Pt container(s)	Phase assemblage
					at 1200 °C	at target T	350 °C at 1 atm	400 °C in PC				
C12	1	3	1050	Fwd	-	140	-	-	Mg(OH) <sub>2</sub>	Au	-	Amp, Ol, Cpx, Opx, Sp
C13	1	3.75	1000	Fwd	-	165	-	-	Mg(OH) <sub>2</sub>	Au	-	Amp, Ol, Cpx, Opx, Grt, Sp
C15	1	3	1100	Fwd	-	88	-	-	Mg(OH) <sub>2</sub>	Au	-	Amp, Ol, Cpx, Opx, Grt, Sp
C16	1	3.75	1075	Fwd	-	113	-	-	Mg(OH) <sub>2</sub>	PtRh, Au foil	-	Ol, Cpx, Opx, Grt, Sp, Phlog
C17	1	3	1150	Fwd	-	95	-	-	Mg(OH) <sub>2</sub>	PtRh, Au foil	-	Ol, Cpx, Opx, Grt, Sp, melt
C18	1	2	1125	Fwd	-	91	-	-	Mg(OH) <sub>3</sub>	PtRh, Au foil	-	Ol, Cpx, Opx, Sp
C19	1	3	1125	Fwd	-	89	-	-	Mg(OH) <sub>2</sub>	PtRh, Au foil	-	Amp, Ol, Cpx, Opx, Grt, Sp, melt
C20	1	3.75	1040	Fwd	-	119	-	-	Mg(OH) <sub>2</sub>	PtRh, Au foil	-	Amp, Ol, Cpx, Opx, Grt, Sp
C21	1	3.4	1100	Fwd	-	137	-	-	Mg(OH) <sub>2</sub>	PtRh, Au foil	-	Ol, Opx, Cpx, Grt, Sp
C22	1	2.5	1125	Fwd	-	113	-	-	Mg(OH) <sub>2</sub>	PtRh, Au foil	-	Amp, Ol, Cpx, Opx, Sp, melt
C23	1	2	1075	Fwd	-	112	-	-	Mg(OH) <sub>2</sub>	PtRh, Au foil	-	Amp, Ol, Cpx, Opx, Sp
C24	1	3.4	1075	Fwd	-	135	-	-	Mg(OH) <sub>2</sub>	PtRh, Au foil	-	Amp, Ol, Cpx, Opx, Grt, Sp, melt
C25	1	2	1100	Fwd	-	163	-	-	Mg(OH) <sub>2</sub>	PtRh, Au foil	-	Amp, Ol, Cpx, Opx, Sp, melt
C26	1	4	1000	Fwd	-	95	-	-	Mg(OH) <sub>2</sub>	PtRh, Au foil	-	Amp, Ol, Cpx, Opx, Grt, Sp
C27	1	2.5	1150	Fwd	-	116	-	-	Mg(OH) <sub>2</sub>	PtRh, Au foil	-	Amp, Ol, Cpx, Opx, Sp, melt
C28	1	4	1030	Fwd	-	115	-	-	Mg(OH) <sub>2</sub>	PtRh, Au foil	-	Amp, Ol, Cpx, Opx, Grt, Sp
C29	1	2	1000	Fwd	-	160	-	yes	H <sub>2</sub> O	PtRh, Au foil	-	Amp, Ol, Cpx, Opx, Sp
C30	1	3	1000	Fwd	-	144	-	yes	H <sub>2</sub> O	PtRh, Au foil	-	Amp, Ol, Cpx, Opx, Sp
C31	1	2	1000	Fwd	-	144	-	yes	H <sub>2</sub> O	PtRh, Au foil	-	Amp, Ol, Cpx, Opx, Sp
C32	1	4.5	1000	Fwd	-	100	-	-	H <sub>2</sub> O	PtRh	-	Ol, Cpx, Opx, Grt, Sp
C9N0.5	0.5	3	1125	Fwd	-	136	-	-	Mg(OH) <sub>2</sub>	PtRh, Au foil	-	Amp, Ol, Cpx, Opx, Grt, Sp
C10N0.5	0.5	2	1075	Fwd	-	139	-	-	Mg(OH) <sub>2</sub>	PtRh, Au foil	-	Amp, Ol, Cpx, Opx, Sp
C11N0.5	0.5	2.5	1125	Fwd	-	162	-	-	Mg(OH) <sub>2</sub>	PtRh, Au foil	-	Amp, Ol, Cpx, Opx, Sp
C12N0.5	0.5	3.5	1075	Fwd	-	159	-	-	Mg(OH) <sub>2</sub>	PtRh, Au foil	-	Amp, Ol, Cpx, Opx, Grt, Sp
C13N0.5	0.5	3	1125	Fwd	-	136	-	yes	Mg(OH) <sub>2</sub>	PtRh, Au foil	-	Amp, Ol, Cpx, Opx, Sp
C14N0.5	0.5	2	1100	Fwd	-	163	-	yes	Mg(OH) <sub>2</sub>	PtRh, Au foil	-	Amp, Ol, Cpx, Opx, Sp
C17N0.5	0.5	3.5	1075	Fwd	-	141	yes	yes	H <sub>2</sub> O	PtRh, Au foil	-	Amp, Ol, Cpx, Opx, Grt, Sp
C18N0.5	0.5	3.5	1075	Rev	165	163	yes	yes	H <sub>2</sub> O	PtRh, Au foil	-	Amp, Ol, Cpx, Opx, Grt, Sp
C19N0.5	0.5	3.5	900	Rev	161	144	yes	yes	H <sub>2</sub> O	PtRh, Au foil	-	Amp, Ol, Cpx, Opx, Sp
C20N0.5	0.5	2	1000	Fwd	-	168	yes	yes	H <sub>2</sub> O	PtRh, Au foil	-	Amp, Ol, Cpx, Opx, Sp
C21N0.5	0.5	3	1000	Fwd	-	148	yes	yes	H <sub>2</sub> O	PtRh, Au foil	-	Amp, Ol, Cpx, Opx, Sp
C23N0.5	0.5	3.5	1150	Fwd	-	91	yes	yes	H <sub>2</sub> O	PtRh, Au foil	-	Amp, Ol, Cpx, Opx, Grt, Phlog
C24N0.5	0.5	2.5	1200	Fwd	-	92	yes	yes	H <sub>2</sub> O	PtRh	yes	Amp, Ol, Cpx, Opx, Sp

2. Amphibole stability in the upper mantle at reduced water activity

Table 2.3.1. Continued.

Sample	X <sub>H2O</sub>	P (GPa)	T (°C)	Fwd/Rev	Duration (h)		Preheating procedure		H <sub>2</sub> O source	Capsule material	Inner Pt container(s)	Phase assemblage
					at 1200 °C	at target T	350 °C at 1 atm	400 °C in PC				
C25N0.5	0.5	3.5	1200	Fwd	-	91	yes	yes	H <sub>2</sub> O	PtRh	yes	Amp, Ol, Cpx, Opx, Grt, Sp, Phlog
C26N0.5	0.5	2.5	1250	Fwd	-	71	yes	yes	H <sub>2</sub> O	PtRh	yes	Ol, Cpx, Opx, Sp, melt
C27N0.5	0.5	4	1000	Rev	70	90	yes	yes	H <sub>2</sub> O	PtRh	yes	Ol, Cpx, Opx, Grt, Sp, Phlog
C29N0.5	0.5	3.5	1250	Fwd	-	40	yes	yes	H <sub>2</sub> O	PtRh	yes	Amp, Ol, Cpx, Opx, Grt, Sp, Phlog, melt
C30N0.5	0.5	3	1250	Fwd	-	41	yes	yes	H <sub>2</sub> O	PtRh	yes	Ol, Cpx, Opx, Grt, Sp, melt
C32N0.5	0.5	2	1200	Fwd	-	66	yes	yes	H <sub>2</sub> O	PtRh	yes	Amp, Ol, Cpx, Opx, Sp, Phlog
C1N0.75	0.25	2	900	Fwd	-	206	-	-	Mg(OH) <sub>2</sub>	PtRh, Au foil	-	Amp, Ol, Cpx, Opx, Sp
C5N0.75	0.25	2	1100	Fwd	-	164	-	yes	Mg(OH) <sub>2</sub>	PtRh, Au foil	-	Amp, Ol, Cpx, Opx, Sp
C13N0.75	0.25	3.5	1075	Fwd	-	139	yes (CSPV, 3kb)	yes	H <sub>2</sub> O	PtRh, Au foil	-	Amp, Ol, Cpx, Opx, Grt, Sp
C15N0.75	0.25	3.5	1075	Rev	167	145	yes	yes	H <sub>2</sub> O	PtRh, Au foil	-	Ol, Cpx, Opx, Grt, Sp, Phlog
C16N0.75	0.25	3.5	1000	Rev	139	189	yes	yes	H <sub>2</sub> O	PtRh, Au foil	-	Ol, Cpx, Opx, Grt, Sp, Phlog
C17N0.75	0.25	2	1100	Rev	70	212	yes	yes	H <sub>2</sub> O	PtRh, Au foil	-	Amp, Ol, Cpx, Opx, Grt, Sp
C18N0.75	0.25	2	1000	Rev	167	168	yes	yes	H <sub>2</sub> O	PtRh, Au foil	-	Amp, Ol, Cpx, Opx, Sp
C19N0.75	0.25	2	900	Rev	162	264	yes	yes	H <sub>2</sub> O	PtRh, Au foil	-	Amp, Ol, Cpx, Opx, Sp
C21N0.75	0.25	2	1050	Rev	164	170	yes	yes	H <sub>2</sub> O	PtRh, Au foil	-	Amp, Ol, Cpx, Opx, Sp
C22N0.75	0.25	3.5	900	Rev	170	160	yes	yes	H <sub>2</sub> O	PtRh, Au foil	-	Ol, Cpx, Opx, Grt, Sp, Phlog
C23N0.75	0.25	3	1000	Rev	186	168	yes	yes	H <sub>2</sub> O	PtRh, Au foil	-	Amp, Ol, Cpx, Opx, Grt, Sp, Phlog
C25N0.75	0.25	2.5	1000	Rev	187	168	yes	yes	H <sub>2</sub> O	PtRh, Au foil	-	Amp, Ol, Cpx, Opx, Sp
C29N0.75	0.25	3	1100	Rev	164	143	yes	yes	H <sub>2</sub> O	PtRh, Au foil	-	Amp, Ol, Cpx, Opx, Grt, Sp
C31N0.75	0.25	3	1200	Fwd	-	145	yes	yes	H <sub>2</sub> O	PtRh, Au foil	-	Amp, Ol, Cpx, Opx, Grt, Sp, Phlog
C32N0.75	0.25	2	1200	Fwd	-	163	yes	yes	H <sub>2</sub> O	PtRh, Au foil	-	Amp, Ol, Cpx, Opx, Sp, Phlog
C34N0.75	0.25	3	1250	Fwd	-	112	yes	yes	H <sub>2</sub> O	PtRh, Au foil	-	Amp, Ol, Cpx, Opx, Grt, Phlog
C41N0.75	0.25	3	1300	Fwd	-	71	yes	yes	H <sub>2</sub> O	PtRh	yes	Ol, Cpx, Opx, Grt, Sp, melt
C42N0.75	0.25	2	1250	Fwd	-	69	yes	yes	H <sub>2</sub> O	PtRh	yes	Amp, Ol, Cpx, Opx, Sp
C44N0.75	0.25	2	1300	Fwd	-	40	yes	yes	H <sub>2</sub> O	PtRh	yes	Amp, Ol, Cpx, Opx, Sp
C45N0.75	0.25	2	1350	Fwd	-	24	yes	yes	H <sub>2</sub> O	PtRh	yes	Ol, Cpx, Opx, Sp, melt
C48N0.75	0.25	2.5	1300	Fwd	-	66	yes	yes	H <sub>2</sub> O	PtRh	yes	Amp, Ol, Cpx, Opx, Sp
C49N0.75	0.25	2.5	1350	Fwd	-	19	yes	yes	H <sub>2</sub> O	PtRh	yes	Ol, Cpx, Opx, Sp, melt
C13N0.9	0.1	2	1100	Fwd	-	134	-	-	Mg(OH) <sub>2</sub>	Au	-	Amp, Ol, Cpx, Opx, Sp, Phlog
C16N0.9	0.1	2	1000	Rev	161	168	yes	yes	H <sub>2</sub> O	PtRh, Au foil	-	Ol, Cpx, Opx, Sp, Phlog
C18N0.9	0.1	2	900	Rev	162	121	yes	yes	H <sub>2</sub> O	PtRh, Au foil	-	Amp, Ol, Cpx, Opx, Sp

2. Amphibole stability in the upper mantle at reduced water activity

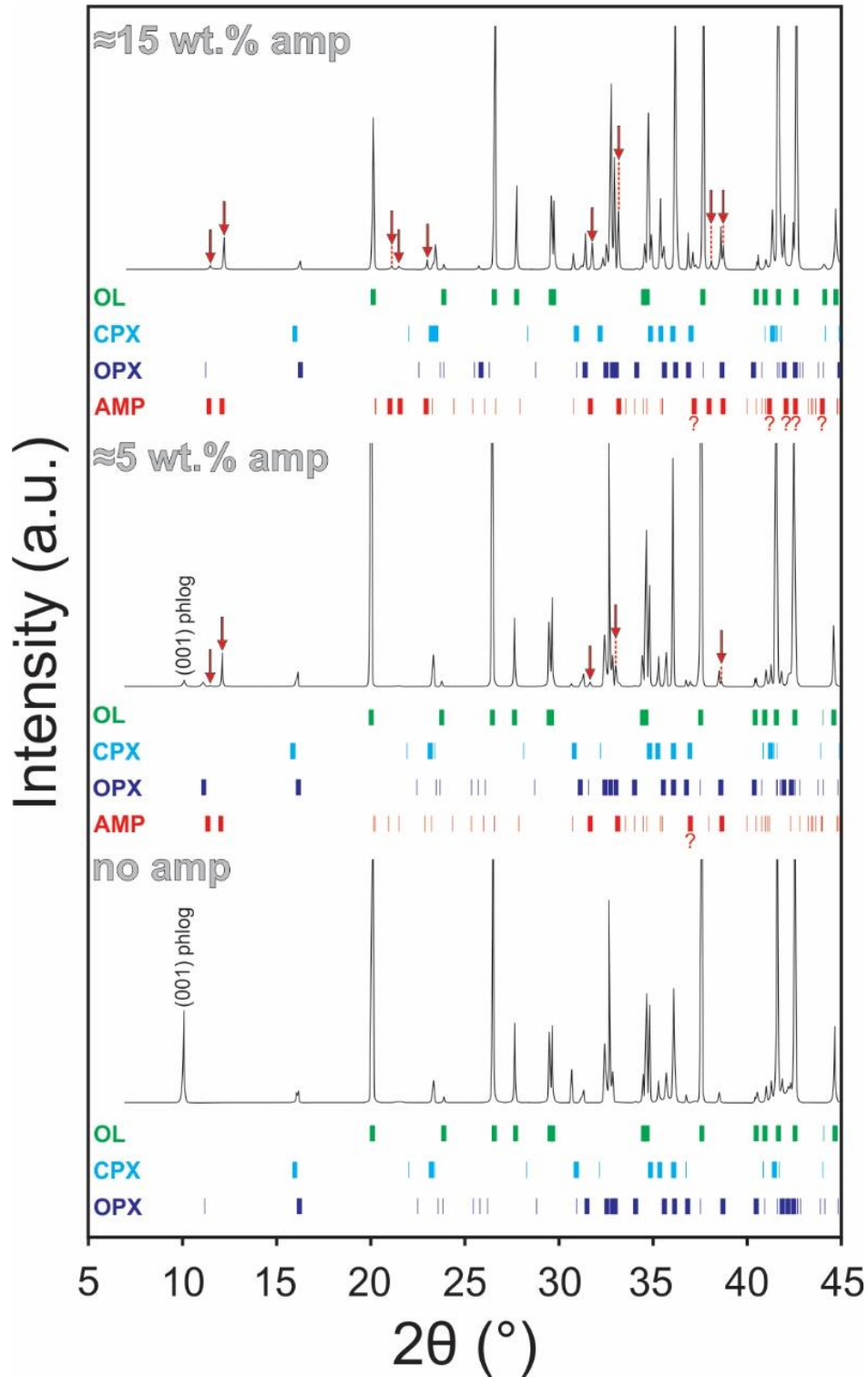


**Figure 2.3.3:** Powder X-ray diffraction patterns obtained from two samples containing different amphibole proportions – **C12** (3 GPa, 1050 °C,  $X_{H_2O}=1$ ,  $\approx 15$  wt.% amphibole) and **C23N0.75** (3 GPa, 1200 $\rightarrow$ 1000 °C,  $X_{H_2O}=0.25$ ,  $\approx 5$  wt.% amphibole) – and one sub-solidus sample outside the amphibole stability field (**C15N0.75**, 3.5 GPa, 1200 $\rightarrow$ 1075 °C,  $X_{H_2O}=0.25$ , no amphibole). Amphibole proportions indicated in the figure were estimated from mass balance calculations (Ch. 2.3.5). Reflections attributed to amphibole are emphasized by red arrows.

## 2. Amphibole stability in the upper mantle at reduced water activity

As already noted, the amphibole stability limit is displaced toward higher temperatures as the water activity decreases. Decreasing water activity of the fluid phase from approximately 1 to 0.25 had expanded the amphibole stability field from 1100 to 1300 °C at 2 GPa (Fig. 2.3.4). An important observation is the consistent appearance of melt across the amphibole-out at high temperature. The first detection of melt at the amphibole-out is unambiguous. As a result of high bulk water contents (1 wt.%) and limited water solubilities in the melt at H<sub>2</sub>O-undersaturated conditions, a large proportion of melt was stabilized in a narrow temperature range above the solidus. As a convenient byproduct of the method, the open inner Pt capsules, used to isolate silver from the outer capsule, often acted as melt traps making melt identification easier (Fig. 2.3.1). The solidus temperatures are clearly H<sub>2</sub>O activity dependent and shift to higher temperature with decreasing X<sub>H<sub>2</sub>O</sub> in the fluid phase, in agreement with theoretical expectation.

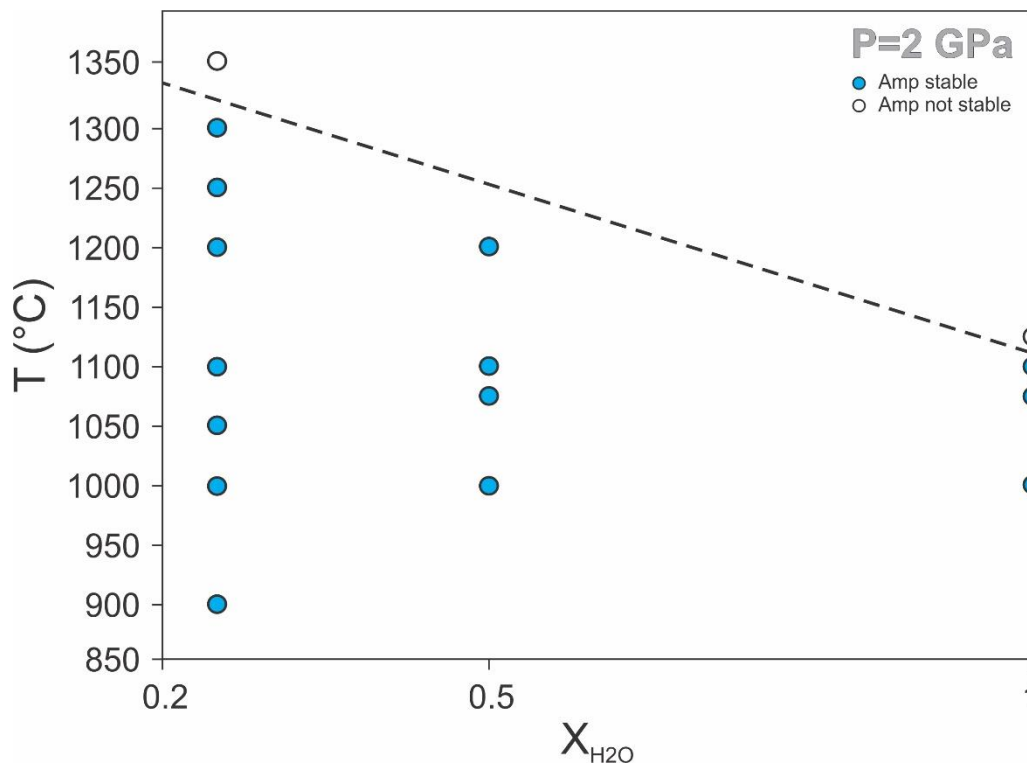


**Figure 2.3.4:** The approximate position of the high-temperature amphibole stability as function of X<sub>H<sub>2</sub>O</sub> in the fluid phase at constant pressure (2 GPa). The amphibole-out reaction in equilibrium with fluid compositions between X<sub>H<sub>2</sub>O</sub>=1 and 0.25 involves amphibole, a fluid phase (reactants) and a hydrous silicate melt (product). The simultaneous decrease of water activity in both the fluid phase and silicate melt stabilizes amphibole to higher temperature. This type of melting reaction is expected to govern amphibole stability at low pressure/high temperature.

## *2. Amphibole stability in the upper mantle at reduced water activity*

An effect similar to that observed here was reported by Holloway (1973), who investigated amphibole stability field in the pargasite-H<sub>2</sub>O-CO<sub>2</sub> system at pressures <1 GPa, where the CO<sub>2</sub> solubility in silicate melts is limited and water activity can be adjusted in the same manner as in this study. At pressures above 0.5 GPa, Holloway (1973) reports an expansion of the amphibole stability field toward higher temperatures with decreasing water activity.

In summary, reducing water activity in the peridotite-H<sub>2</sub>O system has a dual effect on amphibole stability. With decreasing  $X_{\text{H}_2\text{O}}$  in the fluid phase, the amphibole stability limit is simultaneously depressed to lower pressures and elevated to higher temperatures as a result of two distinctly different reactions occurring across the amphibole-out. A more comprehensive overview of the effect is shown in Figure. 2.3.5.

## 2. Amphibole stability in the upper mantle at reduced water activity

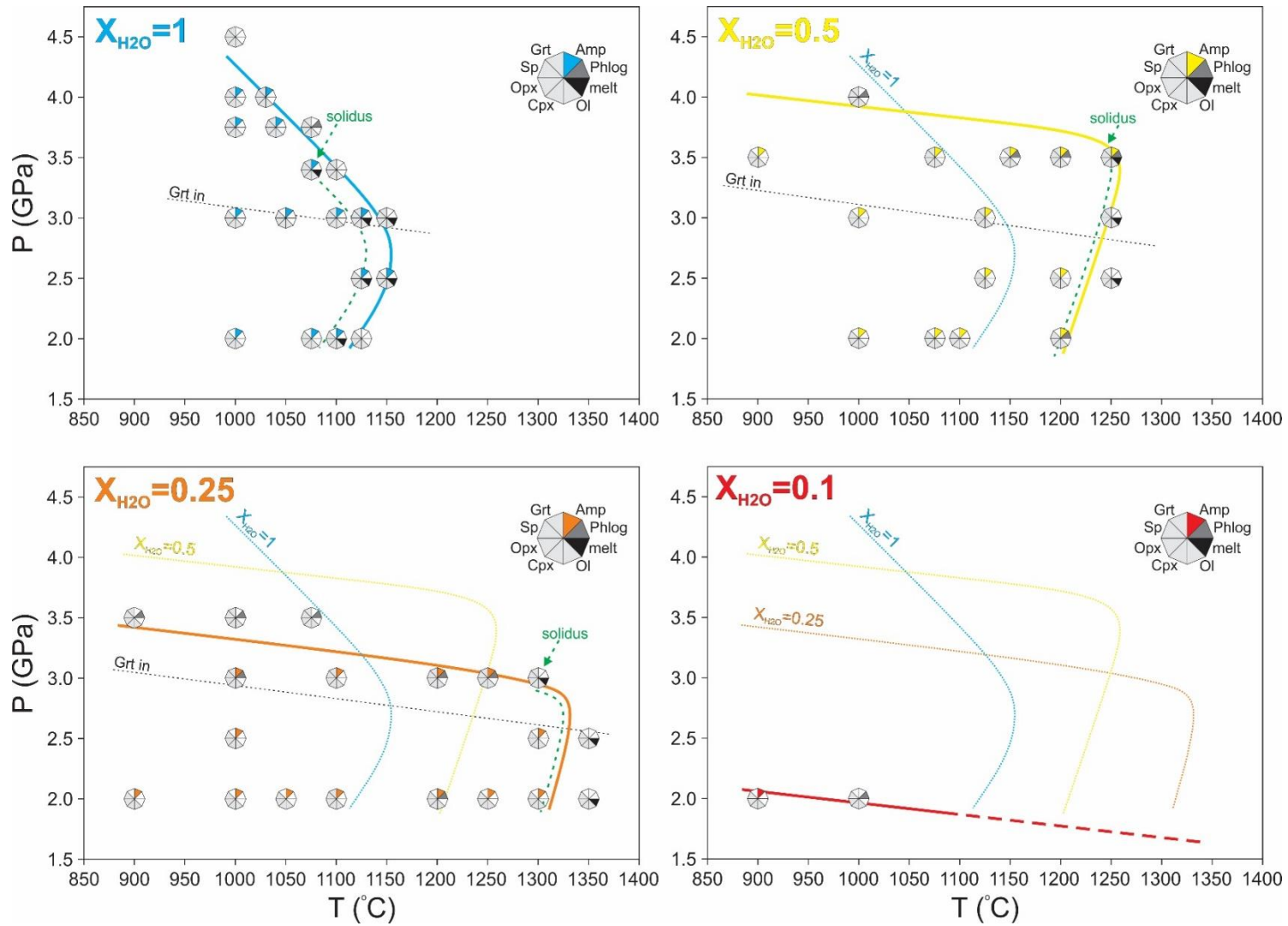


**Figure 2.3.5:** An overview of amphibole stability fields at nominal fluid compositions of  $X_{H_2O}=1$  (blue line),  $X_{H_2O}=0.5$  (yellow),  $X_{H_2O}=0.25$  (orange) and  $X_{H_2O}=0.1$  (red). A simultaneous depression of amphibole stability limit at high pressure/low temperature and expansion at low pressure/high temperature was observed as a result of two different reactions occurring across the amphibole-out (dehydration at HP/LT and melting at LP/HT). The effect is clearly summarized in the diagram showing the results in equilibrium with fluid composition  $X_{H_2O}=0.1$ , where the amphibole stability fields at varying water activities are plotted together. Observed mineral assemblages and approximate solidus positions are indicated as well (green dashed lines).

### 2.3.3. Notes on experimental procedure

#### 2.3.3.1. The high pressure/low temperature amphibole stability limit

The most challenging aspect of this study arises due to kinetic factors related to amphibole nucleation and decomposition in the peridotite-H<sub>2</sub>O system at low temperatures and reduced water activities. We observed that various monoclinic amphiboles nucleate easily during initial heating of the experiment. Due to sluggish reactions at reduced water activities, amphibole persists as a metastable phase throughout the run and, upon examination of the samples, no apparent effect of reducing water activity on amphibole stability field is observed. In reality, at low temperatures the amphibole-out should systematically shift to lower pressures with decreasing water activity, as discussed in Chapter 2.3.2. In one-stage experiments, the formation of metastable phases was a frequent problem, regardless of whether a preheating procedure was used – even a standard heating rate of 100 °C/min yielded the same result.

To overcome the problem, we resorted to performing two-stage experiments. If the run pressure was above the amphibole stability limit, the metastable phases would decompose during the (high-temperature) 1200 °C stage. If the target temperature was then lowered to within the stability field, amphibole readily nucleated again during the second (low-temperature) stage of the experiment, as demonstrated by the “reverse” runs at 2 GPa and  $X_{\text{H}_2\text{O}}=0.1$  at 900 °C and 1000 °C (Fig. 2.3.5). Newly nucleated amphibole was observed at target temperature of 900 °C, but not at 1000 °C. In the “forward” experiment at 1100 °C and same pressure and water activity (2 GPa,  $X_{\text{H}_2\text{O}}=0.1$ ), abundant metastable amphibole was produced (Table 2.3.1). Another demonstration of amphibole metastability is a pair of one- and two-stage experiments at 3.5 GPa, 1075 °C and  $X_{\text{H}_2\text{O}}=0.25$  – amphibole was detected in the sample from the “forward”, but not from the “reverse” run (Table 2.3.1).

At pressures above 2 GPa and temperatures higher than 1000 °C, the metastable phases were found to partially re-equilibrate with the rest of the assemblage, attaining chemical compositions similar to the previously reported upper mantle amphibole (i.e. near pargasite end-member). At lower pressures and temperatures, they presumably retained their initial composition, which is fairly close to the richterite ( $\text{Na}(\text{NaCa})\text{Mg}_5\text{Si}_8\text{O}_{22}(\text{OH})_2$ ) end-member (Fig. 2.3.6a), but may vary

depending on run duration and (P, T,  $X_{H_2O}$ ) conditions. Additionally, near-pargasite and near-richterite end-member amphiboles were observed to co-exist in one sample.

On the other hand, in two-stage experiments all phases tend to retain the 1200 °C chemistry if the target temperature is lower than 1050 °C. At a target temperature of 1100 °C, complete re-equilibration of mineral compositions is possible within a week-long second stage (see also Ch. 2.3.4).

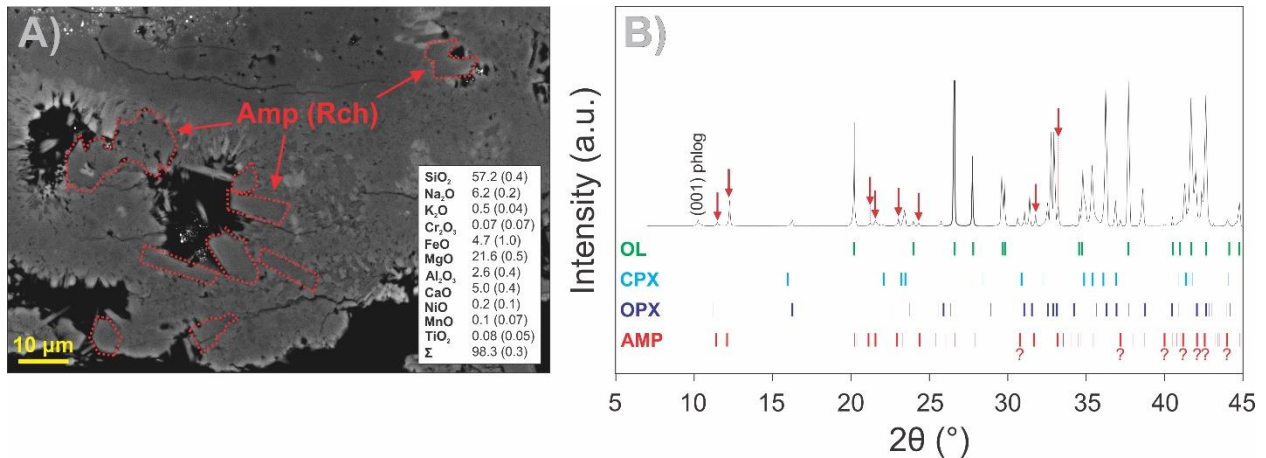


**Figure 2.3.6:** Characterization of the metastable near richterite end-member amphibole observed in one-stage run **C1N0.75** (2 GPa, 900 °C,  $X_{H_2O}=0.25$ ). **A)** An example of a BSE image and the obtained EPMA analysis of the metastable phase. **B)** Powder X-ray diffraction pattern showing several reflections consistent with monoclinic (C2/m) amphibole structure indicated by red arrows.

### 2.3.3.2. The low pressure/high temperature amphibole stability limit

Another methodological difficulty, which may severely influence the interpretation, is the definition of incipient melting. In studies focusing on amphibole stability in the upper mantle, a set of melting criteria based on the appearance of quench products along grain boundaries is often used (Ch. 2.1).

However, the appearance of interstitial quench products can be rather variable and, if applied to our samples, such melting criteria do not yield internally consistent solidus temperatures. This is demonstrated in Figure 2.3.7., where the interstitial quench products in two of our samples from H<sub>2</sub>O-saturated conditions at 3 GPa are shown. Based on the examples presented by Green et al. (2014), the likely interpretation would be that the sample in Figure 2.3.7a. had undergone low degree partial melting, while the sample in Figure 2.3.7b presumably contains quench products

## 2. Amphibole stability in the upper mantle at reduced water activity

precipitated from the fluid phase. However, the glassy melt-like precipitates (Fig. 2.3.7a) were found in a sample synthesized at 50 °C lower temperature than the one containing needle-like precipitates (Fig. 2.3.7b). These samples crystallized at 1000 and 1050 °C – 125 and 75 °C below the interpreted solidus, respectively. An increase in “melt” fraction with increasing temperature might be expected, but no appreciable change in the proportion of interstitial precipitates was detected in the temperature range between 1000 and 1125 °C.

Interstitial quench products can be readily observed in samples synthesized at H<sub>2</sub>O-saturated conditions ( $X_{\text{H}_2\text{O}}=1$ ), but are absent in most samples from low water activity runs ( $X_{\text{H}_2\text{O}}=0.25$  and 0.1). This is not unusual, as the total dissolved solid content of the fluid likely decreases with decreasing water activity.

We consider that all observed interstitial phases had precipitated solely from the fluid. The solidus was defined based on the first appearance of recognizable dendritic quench crystals in segregated melt pools (Ch. 2.3.1., Fig 2.3.1). Such textures clearly cannot be related to precipitation from the fluid phase. This approach may have led to some overestimation of solidus temperatures (<50 °C) as smaller melt pools may not have been detected in the (random) observed sample transects. However, the elevation of the solidus with decreasing water activity, which is crucial for the interpretation, appears internally consistent.

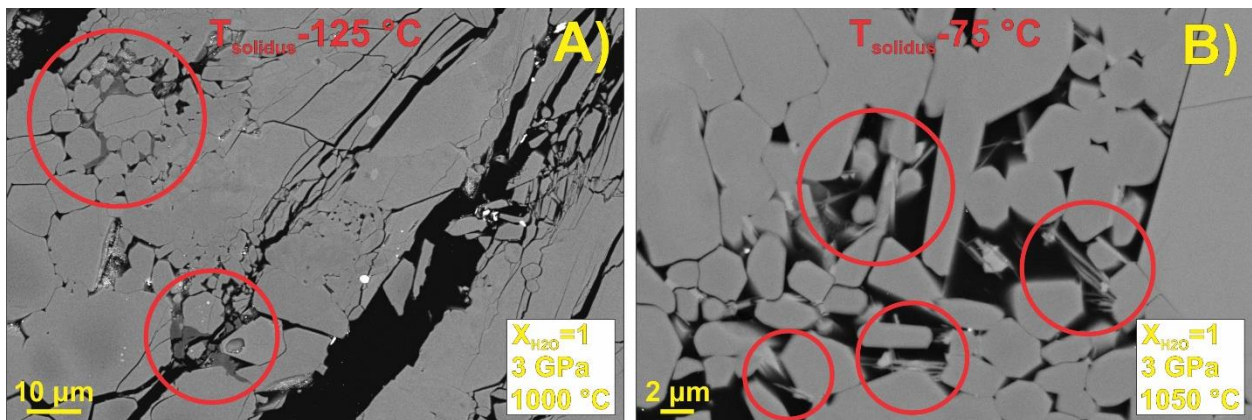


**Figure 2.3.7:** Representative BSE images of interstitial quench products from two samples synthesized at 3 GPa and 125 and 75 °C below the interpreted solidus (1125 °C). The sample from 1000 °C (A) contained both needle-like and glassy melt-like quench products, whereas only needle-like interstitial products were observed in the run products from 50 °C higher temperature (B). The appearance of quench products in image A may suggest solidus temperatures lower than 1000 °C at 3 GPa. Somewhat contradictory, needle-like interstitial phases in image B could be interpreted such that the H<sub>2</sub>O-saturated solidus at 3 GPa may be at temperature higher than 1050 °C.

### 2.3.3.3. Fluid mixing and the preheating procedures

The phase distribution in samples from the early experiments was somewhat inhomogeneous. It was assumed that this was a consequence of incomplete fluid mixing, even though studies of N<sub>2</sub>-H<sub>2</sub>O system at high pressures suggest complete miscibility between the two gases in the pressure and temperature range of our experiments (Constantino and Rice, 1991; Haefner et al., 2002). We suspected that the solid peridotite matrix may mechanically impede fluid circulation and create H<sub>2</sub>O-rich and N<sub>2</sub>-rich domains in the sample. It was presumed that amphibole could persist in the H<sub>2</sub>O-rich domains, as the issue of amphibole metastability was not understood at the time.

We gradually introduced the preheating routines. At first, we only decomposed AgN<sub>3</sub> in the piston cylinder press during compression between 0.5 GPa and target pressure by heating the run charge to 400 °C. The procedure maintains the fluid channels open, so once the water source decomposes (Mg(OH)<sub>2</sub>), a homogeneous fluid mixture should be obtained. Since decomposition of Mg(OH)<sub>2</sub> may be sluggish, we replaced the water source with H<sub>2</sub>O<sub>(l)</sub> so the desired fluid composition would be achieved at the beginning of the experiment. Finally, we discovered that AgN<sub>3</sub> may be thermally decomposed in a furnace at ambient pressure without explosion, as long as the heating rate is slow enough (>16 h from 100 to 350 °C) and the sample is contained in a thick-walled PtRh container that can withstand the internal gas pressure. The AgN<sub>3</sub> was indeed decomposed by this procedure, as the lids of capsules containing high gas proportion (X<sub>H<sub>2</sub>O</sub>=0.1) bent outward during preheating at ambient pressure.

The preheating did not eliminate metastable amphibole. Likely, this procedure is not strictly necessary for determining amphibole stability in the peridotite-H<sub>2</sub>O system at reduced water activities. However, phase distribution in the run products became homogeneous as preheating was introduced and, therefore, the routine was adopted in all subsequent experiments.

### 2.3.4. Mineral chemistry

The effect of temperature on mineral compositions was determined at 2 GPa in the spinel, and 3 GPa in the garnet stability field. A number of experiments were performed at 1000 and 1200 °C, allowing some insight into the effect of pressure on phase compositions. In two-stage experiments, we observed partial re-equilibration after the 1200 °C stage if the target temperature was below 1100 °C (Ch.2.3.3.1). For this reason, changes in amphibole chemistry with decreasing water activity could only be reliably observed in the spinel stability field at 2 GPa and 1100 °C, where a comparison between a “forward” and a “reverse” experiment demonstrated complete re-equilibration (Fig. 2.3.9).

#### 2.3.4.1. Amphibole compositions

Amphibole from this study had a wide range of Mg#, from 80.5 to 91.3. The amphibole synthesized at H<sub>2</sub>O-saturated conditions had relatively high Mg# ranging from 86.1 to 90.9 – values similar to previously reported amphibole compositions (e.g. Wallace and Green, 1991; Niida and Green, 1999). The Mg# of amphibole in our experiments increased with increasing pressure and decreasing water activity, and decreased with increasing temperature (Fig. 2.3.8. and 2.3.9). Only the amphibole from high temperature (>1200 °C) runs at H<sub>2</sub>O-understaurated conditions had Mg# lower than 85.

With increasing temperature, amphibole becomes more Al, K and Ti-rich, and the concentrations of Si and Ca in amphibole decrease (Fig. 2.3.8). In H<sub>2</sub>O-saturated experiments, Na content of amphibole increases with temperature, as reported in previous studies (e.g. Niida and Green, 1999). However, at H<sub>2</sub>O-undersaturated conditions, Na concentrations in amphibole are nearly constant (Fig. 2.3.8). Studies on natural high-Fe kaersutite and Ti-pargasite (Frost, 2006; Popp et al, 1995) report the highest thermal stability of amphibole in literature, up to 1200 °C. This, perhaps, suggests that the observed trends in chemistry (i.e. low Mg# and high Ti content) may be important in stabilizing amphibole to high temperatures. The low Mg# amphiboles are not necessarily quench products, crystallized from a melt phase, as previously suggested (Green et al., 2014).

2. Amphibole stability in the upper mantle at reduced water activity

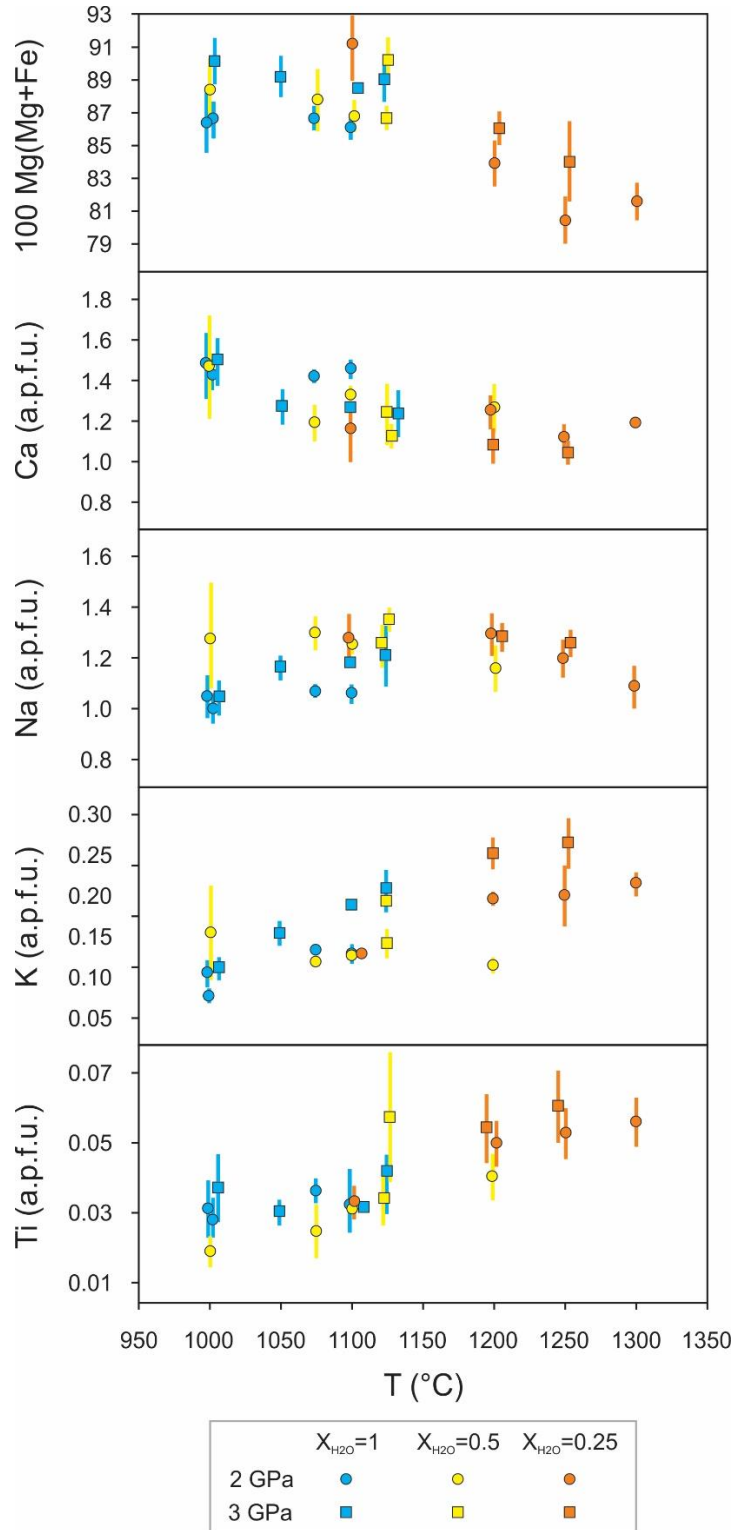


**Figure 2.3.8:** Amphibole composition as a function of temperature. Circles and squares represent measurements at 2 and 3 GPa, respectively. Some symbols were laterally shifted to avoid overlap. Only the results from “forward” runs are considered. Mg# of amphibole synthesized below 1150 °C agrees well with previously reported results (e.g. Nüda and Green, 1999). High temperature (>1200 °C) amphibole has Mg# lower than 85. At H<sub>2</sub>O-saturated conditions (blue), Na content in amphibole increases with temperature, as expected. At H<sub>2</sub>O-undersaturated conditions (yellow and orange), Na content in amphibole is nearly constant.

2. Amphibole stability in the upper mantle at reduced water activity

Concentrations of Na, K, and Ti in amphibole generally increase with increasing pressure, while the Ca and Fe contents become lower. The Si concentration in amphibole first decreases and then begins to increase with increasing pressure, with a minimum at the garnet-in boundary ( $\approx 3$  GPa). The observed effect of pressure on Al content in amphibole is complementary to that of Si. With increasing pressure, Al content in amphibole first increases and then decreases, with a maximum at  $\approx 3$  GPa. In addition, Na and Ca concentrations in amphibole as a function of pressure have a slight inflection at  $\approx 3$  GPa. These observations may suggest a coupled substitution  $\text{Na}^+ + \text{Si}^{4+} \leftrightarrow \text{Ca}^{2+} + \text{Al}^{3+}$  with changing pressure.

Decreasing  $X_{\text{H}_2\text{O}}$  in the fluid phase had some effect on amphibole chemistry as well (Fig. 2.3.9). With decreasing  $X_{\text{H}_2\text{O}}$  at constant pressure and temperature, amphibole became more Si and Na-rich, while the Ca and Al concentrations had decreased.

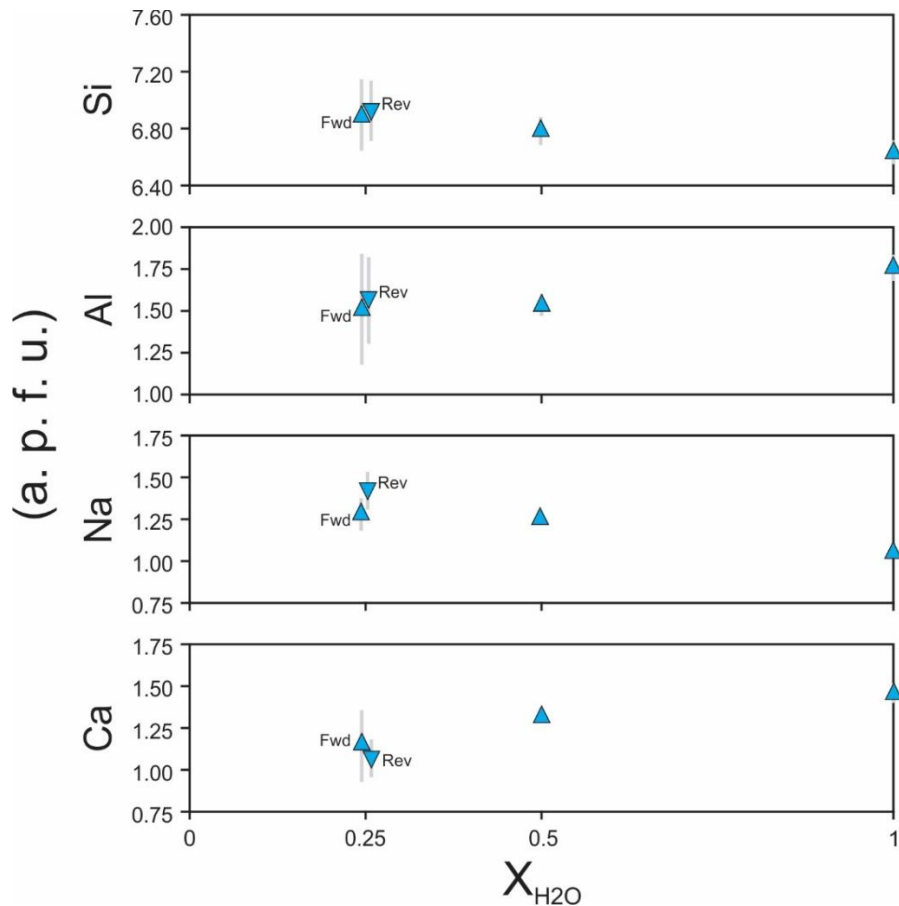


**Figure 2.3.9:** Amphibole composition as a function of water activity at 2 GPa and 1100 °C. Some symbols were laterally shifted to avoid overlap. Upward oriented triangles represent one-stage (“forward”) experiments, while the downward oriented ones indicate a two-stage (“reverse”) run. With decreasing water activity, a slight increase in Si and Na concentrations, as well as a decrease in Al and Ca contents in amphibole was observed. Larger variability in amphibole compositions at low water activity (error bars signify one standard deviation) may be related to sluggish reaction kinetics.

## 2. Amphibole stability in the upper mantle at reduced water activity

The fluid-soluble components, such as SiO<sub>2</sub> and Na<sub>2</sub>O, are expected to partition preferentially into the fluid phase. With decreasing water activity, their solubility in the fluid lowers and they dissolve more readily in solid phases. Therefore, both decreasing water activity and increasing pressure may affect the Na<sup>+</sup> + Si<sup>4+</sup> ↔ Ca<sup>2+</sup> + Al<sup>3+</sup> substitution such that more Na is incorporated in amphibole, and amphibole is stabilized at pressures above the spinel-garnet transition. This argument was used in previous studies (e.g. Green et al., 2010) to explain the presence of amphibole in samples with low nominal water contents, as “leaching” of alkalis into the fluid phase becomes limited at H<sub>2</sub>O-undersaturated conditions (Ch. 2.3.5). However, lowering water activity actually reduces the amphibole stability field, rather than extending it, as one would expect from the “leaching effect” alone (Ch. 2.3.2). “Alkali leaching” would only be relevant at H<sub>2</sub>O-saturated conditions with high bulk water contents (e.g. several wt.% of H<sub>2</sub>O). At high fluid/rock ratios, virtually all alkali may dissolve in the fluid and hydrous alkali-bearing phases can be destabilized. For example, Mandler and Grove (2016) observed this effect in their study. When the nominal bulk water content in their experiments was decreased from 3 to 0.65 wt.%, the stability limit of amphibole shifted to higher temperatures *and* pressures.

### 2.3.4.2. Composition of other phases

The Mg# of clinopyroxene from this study varied between 80.3 and 89.4 and increased with increasing temperature. Similar to amphibole, low Mg# clinopyroxene was observed only at temperatures above 1200 °C. No particular correlation between clinopyroxene Mg# and pressure was observed. Clinopyroxene chemistry changes systematically across the interpreted solidus temperatures. With increasing temperature, Al, Na, and Fe contents in clinopyroxene increase, and then somewhat decrease across the solidus. The Mg concentrations in clinopyroxene are nearly independent of temperature, but were observed to increase at the onset of melting.

No significant changes in olivine and orthopyroxene compositions were observed with changing pressure. The Mg# of olivine and orthopyroxene increased with temperature and were 90.1 to 93.7 and 90.5 to 92.3, respectively. In addition, increasing temperature lowered Si, and increased Al and Ca, contents in orthopyroxene.

The effects of pressure and temperature on phlogopite, garnet and spinel compositions could not be identified due to a limited number of analyses. However, phlogopite compositions were strongly influenced by pressure. A general increase in K and Si, and a decrease in Na and Al contents in phlogopite were observed with increasing pressure. The Mg# of phlogopite and garnet were 87.5 to 91.5 and 75.5 to 84.5, respectively. Phlogopite Mg# decreased, while the garnet Mg# increased with temperature. The spinels were iron-rich, with Mg# of approximately 30 to 45 and Cr# between  $\approx$  20 to 40.

### 2.3.5. Mass balance calculation

Mass fractions of olivine, clinopyroxene, orthopyroxene,  $\pm$  amphibole and  $\pm$  garnet were estimated from EPMA analyses of mineral compositions. Spinel was not considered in the mass balance, since it was often impossible to analyze due to its small grain size. Moreover, spinel occasionally showed heterogeneous composition in samples where it was measured. Mass balance was calculated for sub-solidus run products, and for the two samples where, as an exception, melt composition could be quantified. Negligible dissolution of solids in the fluid phase was assumed. As the estimate consistently yields a sum total of phase proportions between 97.2 and 100.9 wt.%, the simplifying assumptions made in the calculation appear reasonable. A summary of estimated mineral proportions is shown in Table 2.3.22. (Supplement I).

When phlogopite was observed, its proportion was estimated from the mass balance deficit of K<sub>2</sub>O. These estimates represent maximum plausible phlogopite proportions (up to 1.2 wt.%) In runs where no phlogopite was detected (i.e. at low temperatures in the spinel stability field), the entire K<sub>2</sub>O budget could be accounted for by the estimated amphibole proportions with the measured K<sub>2</sub>O concentrations in amphibole. Likewise, if Na<sub>2</sub>O was not constrained by the mass balance calculation, the bulk Na<sub>2</sub>O appeared to dissolve almost entirely in clinopyroxene and amphibole. The mass balance results give the overall impression of limited “alkali leaching” by the fluid phase.

The sum of FeO in olivine, clinopyroxene, orthopyroxene,  $\pm$  amphibole and  $\pm$  garnet indicates that less than 20 % of the total iron (expressed as FeO) may have been lost to capsule materials. In reality, a considerable proportion of iron was retained by spinel, such that this maximum possible iron loss is grossly overestimated.

## *2. Amphibole stability in the upper mantle at reduced water activity*

High proportions of amphibole (15 to 20 wt.%) persisted in all “forward” experiments below 1100 °C in the spinel stability field (Fig. 2.3.10). With increasing pressure, amphibole proportions decrease systematically. The reduction in amphibole proportion at high pressure is likely related to garnet nucleation, which can act as a considerable Al<sub>2</sub>O<sub>3</sub> sink. At low temperatures and with increasing pressure, the remaining amphibole is decomposed in a limited pressure range by a sub-solidus dehydration reaction.

At H<sub>2</sub>O-saturated conditions, approximately 10 wt.% of amphibole remains stable up to the solidus and is entirely consumed by dissolution of H<sub>2</sub>O in the melt in a narrow temperature range between 1100 and 1150 °C. At H<sub>2</sub>O-undersaturated conditions, as the run conditions approach the solidus, amphibole proportions decrease more systematically from >15 wt.% to 2-4 wt.% over a >100 °C temperature range (Fig. 2.3.10b and c).

The run products contained up to 12 wt.% of clinopyroxene, with a clear inverse-proportional relationship between the estimated clinopyroxene and amphibole modes. Olivine, orthopyroxene and garnet proportions were estimated to be 65 to 73 wt.%, 9 to 19 wt.% and up to 6 wt.%, respectively (Table 2.3.22, Supplement I).

2. Amphibole stability in the upper mantle at reduced water activity

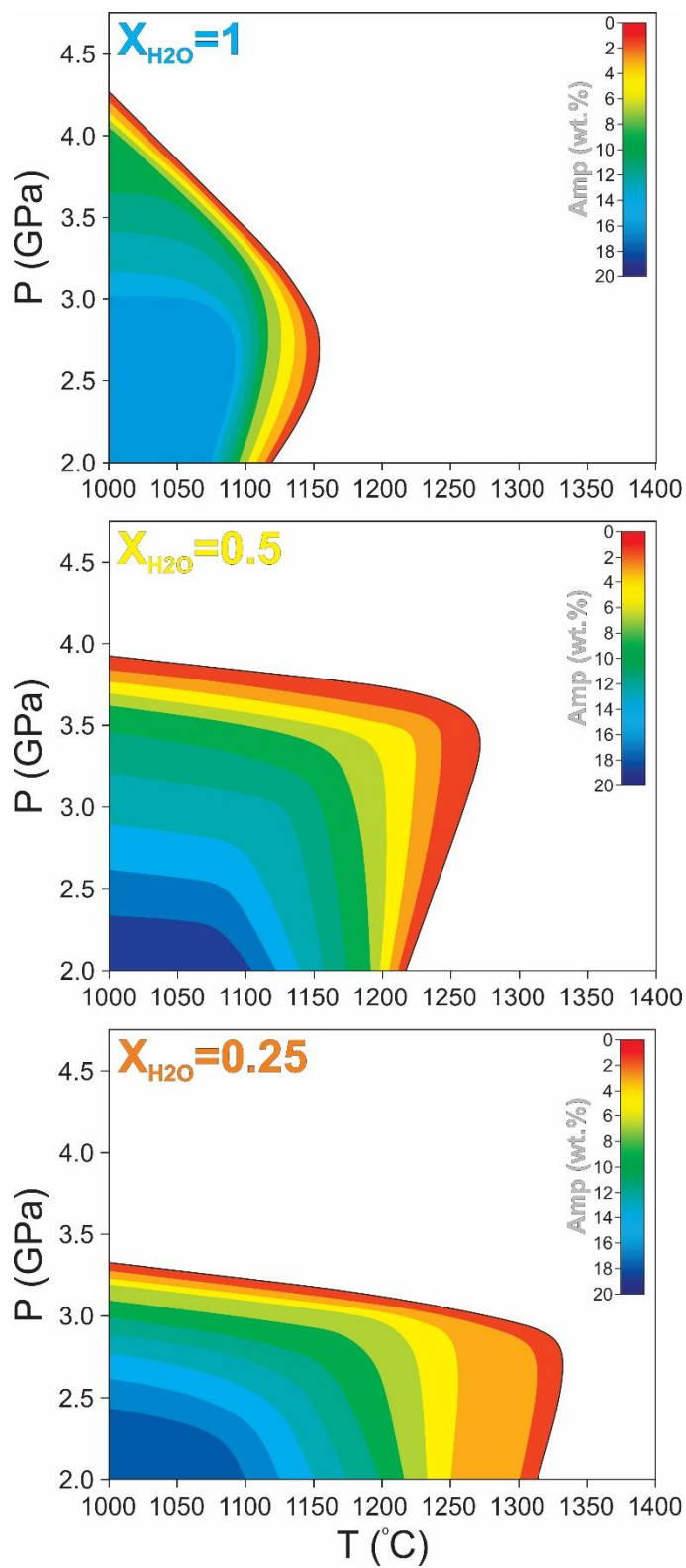


**Figure 2.3.10:** Idealized distribution of amphibole proportions (wt.%) in the run products from this study as a function of pressure and temperature.

### 2.3.6. Modelling amphibole stability in the upper mantle

Estimated amphibole proportions in the run products from this study (Fig. 2.3.10) are not representative of natural systems. The amphibole abundance in the upper mantle should be more limited. First, the bulk water content – 100 to 200 ppm in the depleted mantle (Michael, 1995; Danyushevsky et al., 2000; Saal et al., 2002) and potentially up to 900 ppm in the enriched mantle regions (Korenaga et al., 2016 and ref. therein) – would constrain the maximum amphibole proportions to  $\approx 1$  and  $\approx 4.5$  wt.% in the depleted and enriched mantle, respectively. Higher water contents may only be possible in subduction-related environments. Second, nominally anhydrous minerals (NAMs) may dissolve water in the order of several hundred ppm at upper mantle conditions, as suggested by experiments and studies of natural mantle xenoliths (Bolfan-Casanova and Keppler (2006) and ref. therein; Warren and Hauri, 2014). Most of the upper mantle water may reside in nominally anhydrous minerals co-existing with amphibole, which would further limit its abundance in the ambient mantle. Finally, under some (P, T,  $a_{\text{H}_2\text{O}}$ ) conditions, hydrogen solubility in nominally anhydrous minerals may be sufficiently high so that no modal amphibole is required to accommodate excess water. To investigate this, we used the existing data on hydrogen solubility in nominally anhydrous minerals to estimate upper mantle  $a_{\text{H}_2\text{O}}$  along average geotherms. The conditions of amphibole formation in the ambient mantle can then be constrained from the experimentally observed amphibole stability fields and the modeled  $a_{\text{H}_2\text{O}}$ -depth profiles.

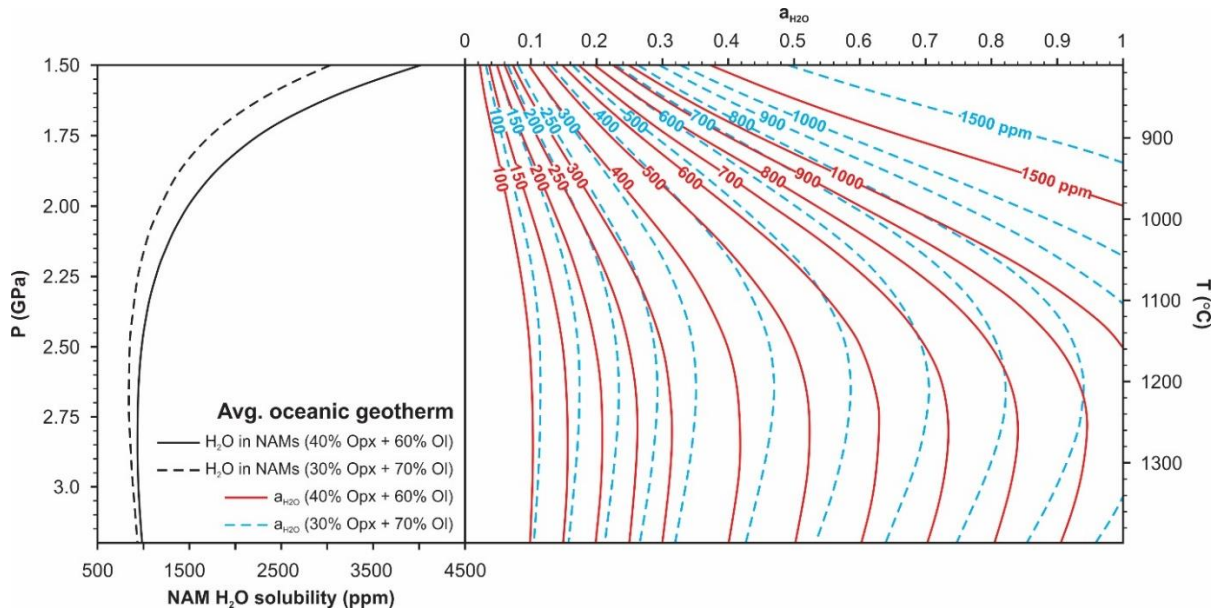


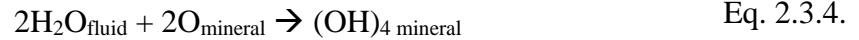
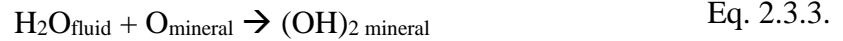
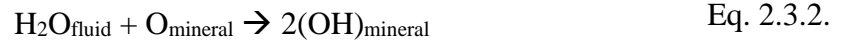
**Figure 2.3.11:** The estimates of  $\text{H}_2\text{O}$  solubility in model peridotites along an average oceanic geotherm are shown on the left-hand side of the figure. Mierdel et al. (2007) and Mosenfelder et al. (2006) calibrations were used to calculate  $\text{H}_2\text{O}$  solubility in orthopyroxene and olivine, respectively. The  $a_{\text{H}_2\text{O}}$ -depth profiles for a wide range of hypothetical mantle water contents are shown alongside the  $\text{H}_2\text{O}$  solubility estimates.

2. Amphibole stability in the upper mantle at reduced water activity

The water activity in the upper mantle is controlled by hydrogen solubility in major (nominally anhydrous) minerals – olivine and pyroxene. Water solubility may be defined as the equilibrium water concentration in a nominally anhydrous mineral at H<sub>2</sub>O-saturated conditions (i.e. co-existing with an aqueous fluid), and can be expressed by the general solubility formula:

$$c_{H_2O} = Af_{H_2O}^n \exp\left(-\frac{\Delta H^{1bar} + \Delta V^{solid}P}{RT}\right) \quad \text{Eq. 2.3.1.}$$

where A, n,  $\Delta H^{1bar}$  and  $\Delta V^{solid}$  are experimentally derived parameters,  $f_{H_2O}$  is water fugacity, R is the gas constant, P is pressure and T absolute temperature. The term A (ppm/bar) is a constant, while the exponent n denotes the nature of the hydrogen substitution mechanism in the mineral. Bolfan-Casanova and Keppler (2006) discuss that hydrogen may dissolve in nominally anhydrous minerals either as isolated (OH)<sup>-</sup> groups (Eq.2.3.2), OH-pairs (2.3.3) or the hydrogarnet (OH)<sub>4</sub> defects (2.3.4.), which can be described by the following reactions:



For example, the equilibrium constant for the reaction 2.3.3. is then:

$$K = \frac{a_{(OH)_2}}{f_{H_2O} a_O} \quad \text{Eq. 2.3.5.}$$

which implies the water solubility in a mineral is proportional to the water fugacity, yielding the exponent term n=1. For the reactions 2.3.2 and 2.3.4, the exponent terms would be 0.5 and 2, respectively. The term  $\Delta H^{1bar}$  (J/mol) is the enthalpy of the reaction at 1 bar, and  $\Delta V^{solid}$  (cm<sup>3</sup>/mol) represents the volume change of the solid related to dissolution of hydrogen in the structure.

Water solubility in upper mantle phases has been extensively investigated (Kohlstedt. et al., 1996; Lu and Keppler, 1997; Rauch and Keppler, 2002; Mierdel and Keppler, 2004; Bromiley et al., 2004; Bromiley and Keppler, 2004; Mosenfelder et al., 2006; Mierdel et al., 2007), and the parameters describing water solubility in olivine and orthopyroxene have been particularly well defined. Studies of mantle xenoliths have shown that olivine and orthopyroxene constitute

## 2. Amphibole stability in the upper mantle at reduced water activity

>90 wt.% of the lithospheric mantle (Maaløe and Aoki, 1977; Warren, 2016). Therefore, a model peridotite composed of these phases may be used for general considerations.

In the pressure range of interest (below the critical curve in the peridotite-H<sub>2</sub>O system), the upper mantle water activity may be approximated as:

$$a_{H_2O} \approx \frac{C_{H_2O,bulk}}{C_{H_2O,solubility}} \quad \text{Eq. 2.3.6.}$$

where  $C_{H_2O,bulk}$  is the hypothetical bulk water content of the mantle, and  $C_{H_2O,solubility}$  is the water solubility in nominally anhydrous peridotite minerals – sometimes referred to as the “water storage capacity”. The parameter  $C_{H_2O,solubility}$  was calculated along typical geotherms using Equation 2.3.1, and the existing calibrations for water solubility in olivine and orthopyroxene (Mosenfelder et al., 2006; Mierdel et al., 2007), as:

$$C_{H_2O,solubility} = F_{Ol}C_{H_2O,Ol} + F_{Opx}C_{H_2O,Opx} \quad \text{Eq. 2.3.7.}$$

where  $F_{Ol}$  and  $F_{Opx}$  represent olivine and orthopyroxene mass fractions, while  $C_{H_2O,Ol}$  and  $C_{H_2O,Opx}$  are the water solubilities in olivine and orthopyroxene at the given pressure and temperature. For a range of different hypothetical water contents, a first-order estimate of  $a_{H_2O}$ -depth profiles in the upper mantle was then obtained using Equation 2.3.6. As an example, a summary of the  $a_{H_2O}$ -depth profiles for an average oceanic geotherm and mantle water contents between 100 and 1500 ppm is shown in Figure 2.3.11.

Amphibole stability fields were experimentally observed at water activities of (approximately) 1, 0.5, 0.25 and 0.1 (Fig. 2.3.5). The stability limits for a range of intermediate water activities were obtained by interpolating between the experimental curves (Fig.2.3.12). The interpolation was linear on the x-axis (temperature). In the direction of the y-axis (pressure), logarithmic interpolation was used to estimate the stability limits for water activities between 0.1 and 0.5, whereas the stability limits between 0.5 and 1 were obtained by extending the linear interpolation on the x-axis at 2, 2.5, 3 and 3.5 GPa. The interpolation was then used to determine the P-T intersections of typical geotherms with the amphibole stability limits. The intersections constrain the maximum pressures of amphibole stability along the geotherms, as a function of water activity (Fig. 2.3.13).

2. Amphibole stability in the upper mantle at reduced water activity

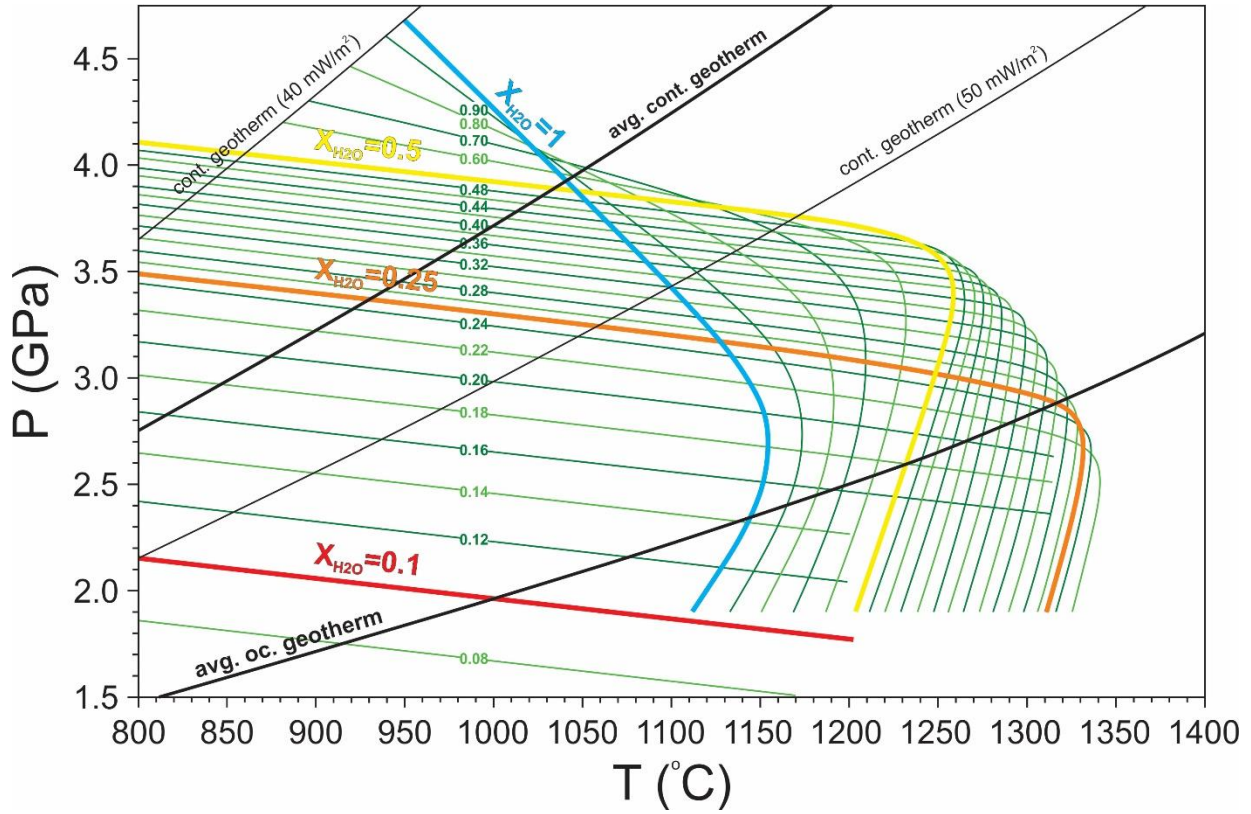


**Figure 2.3.12:** Interpolation of amphibole stability limits at intermediate water activities (green lines) between the experimentally derived curves at  $X_{H_2O}=1, 0.5, 0.25$  and  $0.1$  (blue, yellow, orange and red lines). Typical continental (Hasterok and Chapman, 2011) and oceanic (Schubert et al., 2001) geotherms are plotted for reference (black lines).

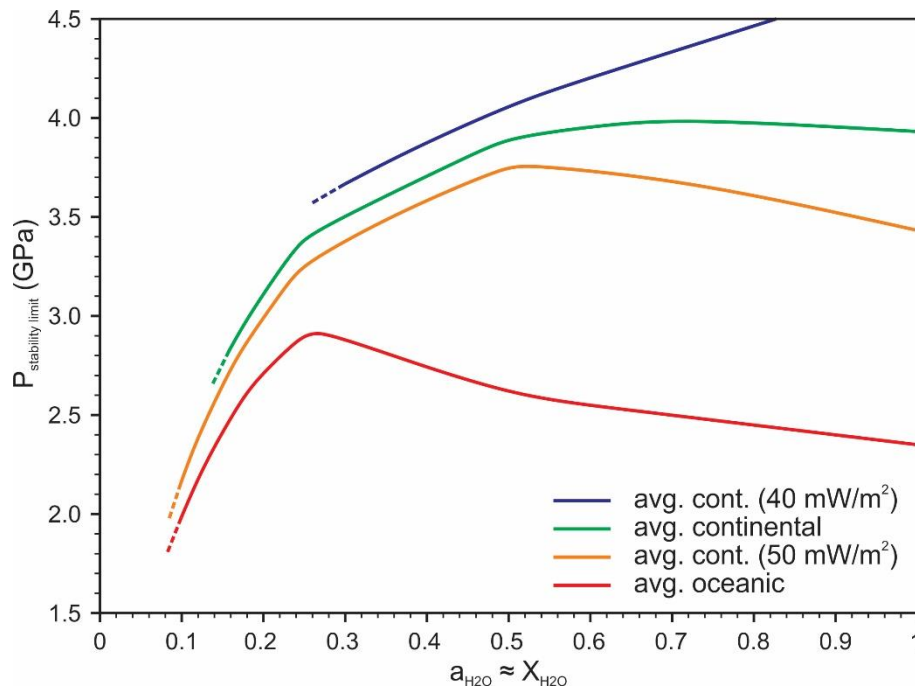


**Figure 2.3.13:** Maximum pressures of amphibole stability along different geotherms, as a function of water activity. The values were obtained from the  $P$ - $T$  intersections of average geotherms with the experimentally derived and interpolated amphibole stability limits at a range of water activities.

## 2. Amphibole stability in the upper mantle at reduced water activity

The  $a_{\text{H}_2\text{O}}$ -depth profiles along the geotherms (e.g. Fig. 2.3.11) were then correlated with the experimental maximum pressures of amphibole stability (Fig. 2.3.13). If the maximum pressure of amphibole stability exceeds the pressure along the geotherm at a corresponding water activity, it was assumed that amphibole may be stable under these (P, T,  $a_{\text{H}_2\text{O}}$ ) conditions. To illustrate the procedure, an example of a correlation is given for a 50 mW/m<sup>2</sup> continental geotherm and 300 ppm of water (Figure 2.3.14).

The complete summary of all correlations for different geotherms, hypothetical mantle water contents, and peridotite mineralogies is shown in Figure 2.3.15. The lower boundaries of amphibole formation intervals could not be constrained for high water contents (e.g. see case scenario of 30% Opx + 70% Ol in Figure 2.3.14). This would require experimental efforts at water activities lower than  $\approx 0.1$ , which may not be kinetically feasible.

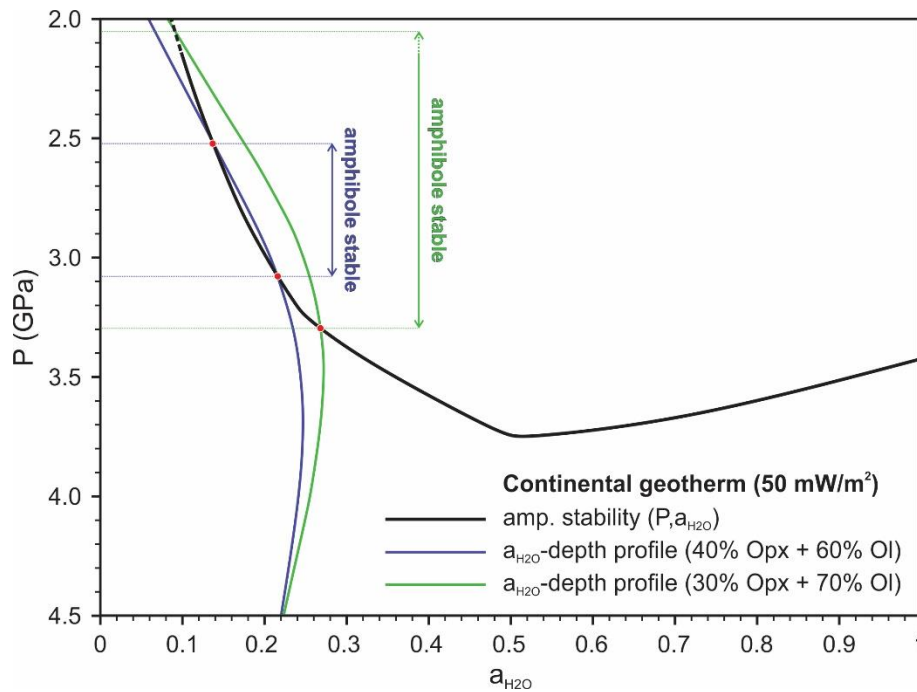


**Figure 2.3.14:** An example of the correlation of  $a_{\text{H}_2\text{O}}$ -depth profiles for a continental geotherm (50 mW/m<sup>2</sup>) and mantle water content of 300 ppm. Amphibole is stable in the pressure range where the maximum pressure of amphibole stability (black line) exceeds the pressure along the geotherm for a given  $a_{\text{H}_2\text{O}}$  (blue and green lines). Assuming a mineralogy of 40% Opx + 60% Ol yields a restricted interval of amphibole formation between 2.5 and 3.1 GPa. Decreasing the orthopyroxene proportion to 30% expands the amphibole stability interval to between 3.3 and  $\approx 2$  GPa; the amphibole stability below 2 GPa, 900 °C at  $a_{\text{H}_2\text{O}} \approx 0.1$  is not precisely known, so the lower boundary of the interval is not strictly constrained.

## 2. Amphibole stability in the upper mantle at reduced water activity

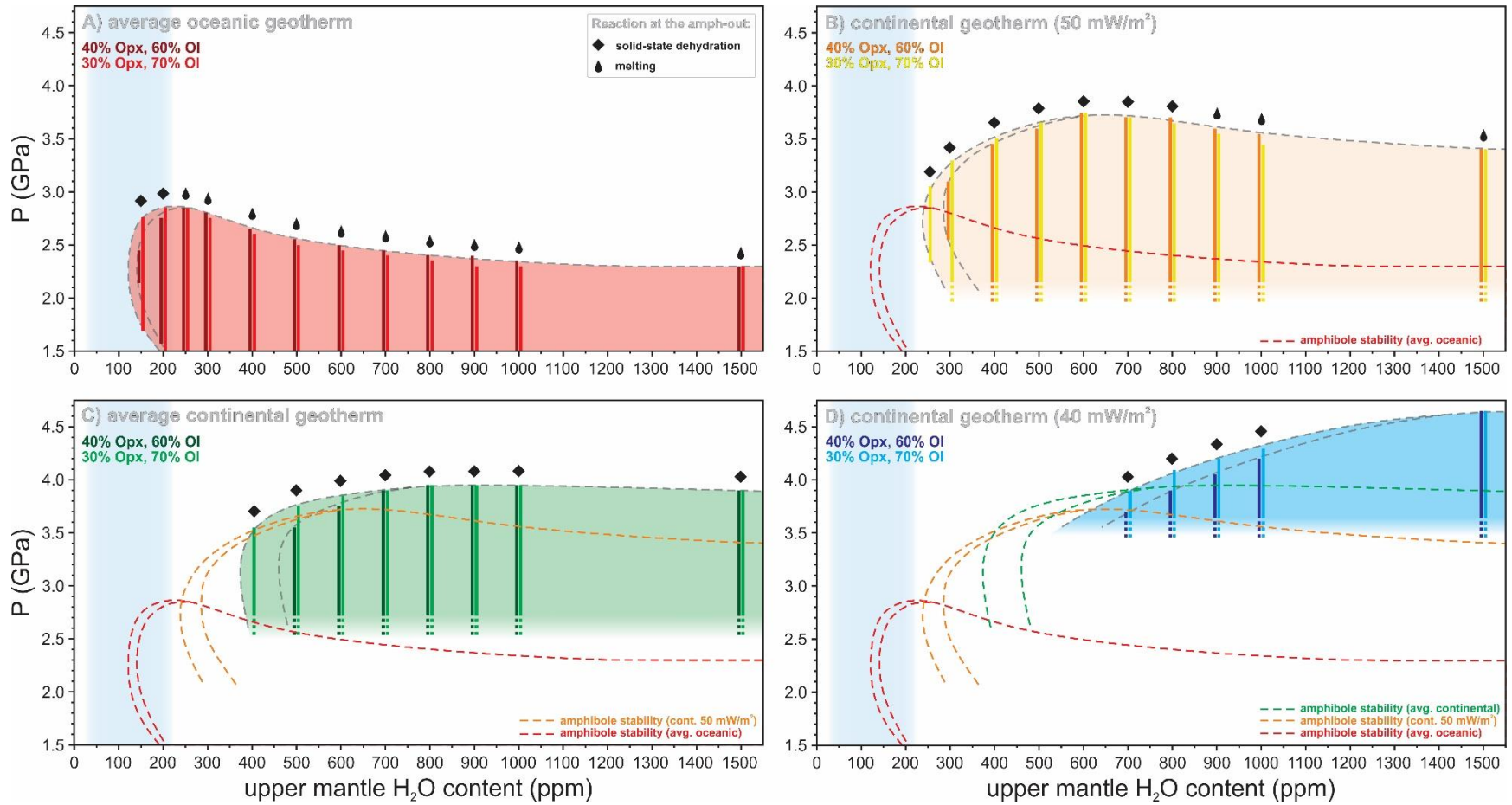


**Figure 2.3.15:** A summary of the estimated amphibole formation depth intervals along: **A)** an average oceanic geotherm; **B)** a warm continental (50 mW/m<sup>2</sup>) geotherm; **C)** an average continental geotherm; **D)** a cold (40 mW/m<sup>2</sup>) continental geotherm. Commonly accepted ambient upper mantle water contents (50 to 200 ppm) are indicated by the shaded light blue areas. The calculation is performed for higher hypothetical water contents as well, potentially representative of enriched mantle sources and subduction-related environments. The type of reaction at the amphibole stability limit is specified by the black symbols at the upper boundary of amphibole-bearing intervals; the “melt drop” shape signifies a melting reaction, while the “crystal” shape indicates solid-state dehydration of amphibole.

## 2.4. Discussion

### 2.4.1. Amphibole stability in the upper mantle at reduced water activity

At low temperatures ( $<1100$  °C), the amphibole stability limit is clearly displaced from above 4 to 2 GPa with reducing water activity (Ch. 2.3.2). To our knowledge, this effect has never been reported in the peridotite-H<sub>2</sub>O system. We extensively tested amphibole crystallization kinetics and concluded that metastable amphibole may persist at low temperatures, regardless of run duration (Ch. 2.3.3). The chemistry of metastable amphibole from ‘forward’ runs at pressures above 2 GPa is similar to the amphibole compositions reported by other experimental studies (Mengel and Green, 1989; Wallace and Green, 1991; Niida and Green, 1999; Fumagalli and Poli, 2005; Fumagalli et al., 2009; Tumiati et al., 2013; Green et al., 2014; Mandler and Grove, 2016; Saha et al., 2017). It is theoretically expected that amphibole should be destabilized with decreasing water activity at subsolidus conditions. However, the effect is difficult to detect due to the presence of the metastable phase, unless the reversed runs are performed.

Amphibole stability at high temperatures is limited by a melting reaction, and the amphibole stability field expands by more than 200 °C (from  $\approx 1100$  °C to  $\approx 1300$  °C) with decreasing water activity (Ch. 2.3.2). Due to several features of the experimental design, the onset of melting was easy to recognize in our run products (Ch. 2.3.2). In previous studies (Mengel and Green, 1989; Conceição and Green, 2004; Green et al., 2010), a more modest expansion of the amphibole stability field was observed as the nominal water contents were lowered. While the solidus was inferred to be at the amphibole-out boundary, the melting criteria in previous studies relied on textural and chemical characteristics of interstitial phases in the recovered run products (Ch. 2.3.3). In a subsequent publication, Green et al. (2014) elaborate on the experimental results of the previous study (Green et al., 2010). They report that one of the main criteria for melting was the appearance of iron-rich ‘lath-shaped’ amphibole (Mg#  $\approx 80$ ) in interstices of the coarse-grained olivine melt traps. The textures that develop in large interstitial spaces within olivine traps may not be comparable to those of phases that formed from the surrounding (powdered) starting materials. In addition, the ‘lath-shaped’ inosilicates, preferentially growing along fluid cavities, are not unusual. We observe them regularly in run products from ‘forward’ experiments (e.g. orthopyroxene in Fig. 2.3.1a), and some representative sample images are also provided by Saha et al. (2017). The Mg# of amphibole from our run products systematically decreases with

increasing temperature to approximately 80 (Ch. 2.3.4), and these crystals are clearly not quench-related, as they are often more coarse-grained than the surrounding phases (Ch. 2.3.1., Fig. 2.3.1e). The expansion of the amphibole stability field toward higher temperature may have been underestimated in previous studies due to a misinterpretation of quench products. Another possibility is that water activity in those studies was higher than expected, as a result of surface water adsorption in the powdered starting materials.

The experimental approach used in the present study offered several advantages. The bulk H<sub>2</sub>O and N<sub>2</sub> contents were high with respect to the weight of solid material. Thus, the fluid compositions were insensitive to common problems that are encountered when attempting to maintain low water concentrations (Ch. 2.1). Consistent control of water activity was possible. In addition, the method resolved most issues in discriminating metastable, quench and equilibrium phases with monoclinic (*C2/m*) amphibole structure. Finally, most of the subjectivity was removed from the interpretation by the use of XRD for phase identification in subsolidus samples, and due to the appearance of large segregated melt pools at near-solidus conditions.

The limited availability of water in the upper mantle may have a more complex effect on amphibole stability than previously thought. Already from the appearance of the phase diagrams (Ch. 2.3.2, Fig 2.3.5), it is apparent that most plausible geotherms intersect the amphibole stability fields in the subsolidus dehydration regime – no melt is expected at the amphibole-out boundary, at least not at typical upper mantle water activities. This casts serious doubts on the traditional view that amphibole dehydration melting could be the principal cause of reduced seismic velocities in the upper mantle (Ch. 2.1).

#### **2.4.2. The role of nominally anhydrous minerals and implications of the model**

Nominally anhydrous minerals may dissolve several hundred ppm of water at realistic upper mantle conditions, and excess water may not be available to stabilize an additional hydrous phase (Ch. 2.3.6). To properly model amphibole stability in the upper mantle, water solubilities in nominally anhydrous phases need to be taken into account. We used the published calibrations of water solubility in major nominally anhydrous peridotite minerals to estimate the water activity along several typical geotherms. The  $a_{\text{H}_2\text{O}}$ -depth profiles along the geotherms were then correlated

with the experimentally determined amphibole stability fields. We therefore constrained the depth intervals and minimum bulk water contents required to stabilize amphibole along particular geotherms (Ch. 2.3.6, Fig. 2.3.15).

Amphibole stability in the upper mantle is highly dependent on the geothermal gradient. Along steeper geothermal gradients, the amphibole may be stabilized in equilibrium with lower bulk water contents. The stability limit is reached at lower pressures, and the amphibole-out reaction is more likely to produce a hydrous melt (Fig. 2.3.15). This overall effect is related to two aspects of the model. Clearly, steeper geotherms intersect the amphibole stability limits at lower pressures and higher temperatures, so the probability of melting across the amphibole-out boundary is higher. Along hotter geotherms, amphibole will dehydrate at subsolidus conditions only if the water activity is very low. The other aspect of the model that governs amphibole stability in the upper mantle is the role of nominally anhydrous minerals. Hydrogen solubility in nominally anhydrous minerals – notably pyroxene – decreases with increasing temperature. At a constant bulk water content, the model will predict higher water activities along steeper geothermal gradients. Higher water activities promote formation of accessory amphibole at lower bulk water contents.

We estimated that along an average oceanic geotherm, accessory amphibole may indeed be stable in equilibrium with  $\approx 150$  ppm of water, as previously suggested (Green et al., 2010). However, considerably higher water contents ( $\approx 250$  ppm) are required to form hydrous melt at the amphibole-out boundary. Most estimates of water contents indicate that less than 200 ppm of water may be available in typical MORB source regions (Michael, 1995; Danyushevsky et al., 2000; Saal et al., 2002). We expect that the chemical reaction at the amphibole stability limit will be predominantly subsolidus dehydration. Melting across the amphibole-out boundary may be expected only in very young oceanic lithosphere, and in water-enriched regions (e.g. Mid-Atlantic ridge; Michael, 1995). In addition, the amphibole stability limit in the oceanic lithosphere is expected at depths between 75 and 85 km for a wide range of bulk water contents. In older ( $>50$  Ma) oceanic lithosphere, most of the geophysical observations estimate the lithosphere-asthenosphere boundary depths at  $>100$  km. Thus, dehydration melting at the

amphibole stability limit is unlikely to be a general explanation for the shear-wave velocity reduction at the lithosphere-asthenosphere boundary.

Less is known about the hydration state of the upper mantle under continents, as compared to oceanic regions. Very low water contents were measured in nominally anhydrous minerals from mantle xenoliths collected in continental settings (Kurosawa et al., 1997; Grant et al., 2007; Peslier et al., 2010; Demouchy and Bolfan-Casanova, 2016). This suggests that low bulk water contents, similar to those in an average MORB source, may be common in the ambient continental mantle. Likely, the only exceptions are metasomatized mantle regions. Evidence of metasomatism, related to subduction zones and intracontinental magmatism, is documented in literature (e.g. Frost, 2006), but the geographic extents and water contents of metasomatized mantle regions are not well known.

Mantle xenolith thermobarometry (Rudnick and Nyblade, 1999) suggests that geothermal gradients in the continental lithospheric mantle vary between the 50 and 40 mW/m<sup>2</sup> geotherms from the preferred geotherm family by Hasterok and Chapman (2011). We used the proposed model to estimate amphibole stability in the subcontinental mantle. High water solubility is expected in pyroxene at low temperatures (Mierdel et al., 2007). As a result, approximately 250 and 400 ppm of water is required to stabilize amphibole along hot and average continental geotherms, respectively. We do not predict accessory amphibole in the ambient continental lithosphere – the hydrous phases observed in exhumed mantle xenoliths from continental settings are almost certainly related to metasomatic addition of water. Along continental geotherms, the amphibole stability limit is estimated at depths between 100 and 140 km, and amphibole decomposes by a subsolidus reaction. Melting at the amphibole-out boundary may occur under exceptional circumstances along hot continental geotherms for very high bulk water contents ( $\approx 900$  ppm).

Selway et al. (2015) proposed that the presence of amphibole-rich layers may explain the mid-lithospheric-discontinuities observed in continental settings, even without the formation of hydrous melts. However, extremely high modal proportions of amphibole are required to achieve the observed shear-wave velocity reductions (Rader et al., 2015; Saha et al., 2017; Saha et al.,

## *2. Amphibole stability in the upper mantle at reduced water activity*

2021). In addition, this model implies regional to global percolation of metasomatic agents within the upper mantle. We hesitate to support this view, since there is no plausible mechanism for such widespread mantle metasomatism.

In conclusion, amphibole may be a common accessory mineral in the oceanic, but not continental lithosphere. In continental settings, the presence of amphibole is likely evidence for metasomatic water addition. Dehydration melting of amphibole may occur only exceptionally, and is not a good general explanation for seismic discontinuities in the upper mantle.

### 3. Mantle metasomatism by sediment fluids in subduction zones

#### 3.1. Introduction

Subduction related magmatism produces distinct geochemical features that are commonly observed in both intra-oceanic and continental volcanic arcs (Kelemen et al., 2005; Schmidt and Jagoutz, 2017). Arc magmas are selectively enriched in fluid-mobile (K, Cs, B, Rb, Sr) and depleted in fluid-insoluble (Nb, Ta, Ti, Zr, Hf) elements (Fig. 3.1.1). Another key characteristic of subduction related magmas is the systematic light rare-earth element (LREE) enrichment, relative to a MORB reference composition (Fig. 3.1.1).

The geochemical features of arc magmas are traditionally explained by the addition of a mobile slab component – a metasomatic agent capable of transporting fluid-soluble elements and LREE – to the melt source region in the overlying mantle wedge.

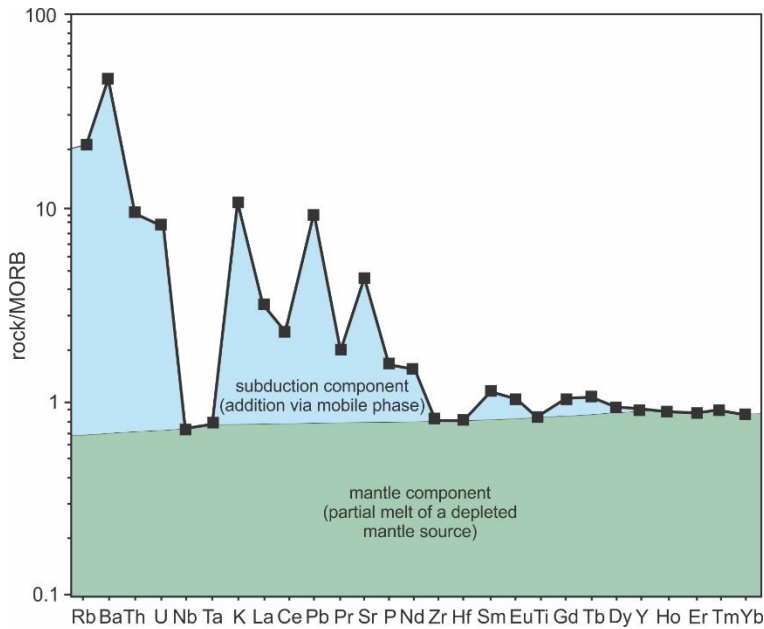


**Figure 3.1.1:** Idealized arc magma geochemistry (black squares), normalized to the MORB reference composition (after Pearce and Stern, 2006). The green field represents the component extracted from the depleted mantle wedge; the blue field shows the arc magma enrichments in fluid mobile elements and LREE, explained by the addition of a slab-derived metasomatic agent to the mantle melt source.

### 3.1.1. Arc signature and the nature of the mobile slab component

The nature of the mobile slab component is being debated due to uncertainties in the thermal structure of subduction zones. Newer numerical models generally predict temperatures between 700 and 900 °C near the slab top (Syracuse et al., 2011) at sub-arc depths. This temperature range encompasses the H<sub>2</sub>O-saturated solidi of metasediments and metabasalts. Furthermore, the miscibility gap between the silicate melts and hydrous fluids may close at sub arc-pressures in the sediment-H<sub>2</sub>O and basalt-H<sub>2</sub>O systems. Supercritical fluids are produced in the basalt-H<sub>2</sub>O system between 4 and 6 GPa (Kessel et al., 2005), and likely at lower pressures in sediment-H<sub>2</sub>O system (Shen and Keppler, 1997). As a result of uncertainties in the thermal structure of subduction zones and poor constraints on the P-T conditions of critical curves in the sediment-H<sub>2</sub>O system, silicate (sediment) melts, supercritical fluids and (saline) hydrous fluids have all been proposed as suitable slab-derived metasomatic agents (Hermann and Rubatto, 2009; Kessel et al. 2005; Keppler, 1996; Rustioni et al., 2019).

The source lithology of the mobile slab component is also being debated. The subducting sediments are 10 to 100 times enriched in trace elements, compared to the primitive mantle, and should significantly contribute to the slab trace element budget (Plank, 2013). The isotopic signals from natural samples indicate that involvement of subducted sedimentary material is necessary to produce the observed <sup>87</sup>Sr/<sup>86</sup>Sr ratio of many, and the <sup>207</sup>Pb/<sup>204</sup>Pb and <sup>206</sup>Pb/<sup>204</sup>Pb ratios of virtually all arc magmas (Nielsen and Marschall, 2017; White, 2013). The occurrence of the cosmogenic <sup>10</sup>Be isotope in arc magmas has also been linked to inputs from relatively young sediments (Tara et al., 1986). In addition, the δ<sup>7</sup>Li of Martinique lavas (Lesser Antilles) is exceptionally low and distinct from MORB, which allowed Tang et al. (2014) to infer 1 to 5 wt.% sediment addition to the mantle melt source. Hu et al. (2021), who recently studied the systematics of δ<sup>41</sup>K in Martinique lavas, found some evidence for a heterogeneity of metasomatic agents in Lesser Antilles, but most of the investigated samples confirmed the result of Tang et al. (2014). Further evidence of sediment recycling in subduction zones is provided by geochemical similarities between arc magmas and spatially related trench sediments. For example, Johnson and Plank (2000) and Plank (2005) noted the correlation between the sediment and arc Th/Rb and Th/La ratios, respectively. Finally, Plank and Langmuir (1993) studied elemental fluxes of Sr, Th and Ba, and observed a correlation between the sediment inputs and arc outputs.

Experimental studies on fluid/sediment and melt/sediment trace element partitioning suggest that sediment melts (or silicate-rich high-temperature supercritical fluids) may be a possible candidate for the slab-derived metasomatic phase (Johnson and Plank, 2000; Spandler et al., 2007; Hermann and Rubatto, 2009). Sediment melts from experimental studies could transport trace elements more readily than the dilute low-temperature fluids. The melts also had arc-like trace element abundances, largely due to the arc-like initial bulk composition of the recycled terrigenous component in the subducting sediments. If sediment melts were a main agent of chemical transport in subduction zones, this would constrain the slab-top temperatures to  $\geq 750$  °C, which is approximately the H<sub>2</sub>O-saturated solidus of crustal materials in the sub-arc pressure range (Tsuno and Dasgupta, 2012 and ref. therein). All previous studies assumed that a solidus can be defined in the sub-arc pressure range.

Sobolev and Brown (2019) argue that deep sediment subduction is a common geological process. However, the sedimentary veneer at the slab top may be relatively thin at sub-arc depths, as the sediments are scraped-off and accreted in the fore-arc region (e.g. Noda et al., 2020). The total thickness of the sedimentary column in the Tonga, Kermadec, Philippines, Ryukyu, Mexico, South Sandwich and Peru trenches is  $\leq 200$  m (Plank, 2013), and the proportion of sediments subducting past the fore-arc region may be negligible. Some typical subduction-related geochemical features are observed in arcs with both high and low sediment influx (Schmidt and Jagoutz, 2017), suggesting a common mechanism for the generation of the arc trace element enrichments. Experimental studies have demonstrated that basalt-derived fluids, in particular at elevated salinities, have distinctly arc-like trace element signatures (Kessel et al., 2005; Rustioni et al., 2019), which supports the idea of the predominantly basalt-sourced slab mobile phase, especially in subduction zones with low sediment influx.

Ever since Rüpke et al. (2004) proposed that hydrated slab mantle could transport significant water budgets, the interest in the role of serpentine dehydration in subduction zone processes had increased. The exhumed slab serpentinites have highly variable compositions and complex geological history, so it is difficult to draw conclusions about their contribution to the total trace element budget in subduction zones (Deschamps et al., 2013). In addition, the temperatures in the

slab mantle section may be as low as 400 to 500 °C. Only the most fluid-soluble trace elements will be mobile at these conditions (halogens, Cs and B), such that the role of serpentine-derived fluids in the production of the arc trace element signature may be limited.

Nielsen and Marschall (2017) recently made an interesting observation, based on the previously published compositions of natural arc magmas from several well-studied subduction zones. They argue that arc magma Nd/Sr and  $^{87}\text{Sr}/^{86}\text{Sr}$  ratios are not consistent with the extraction of either basalt-derived fluids or sediment melts (Fig. 3.1.2). Arc magmas typically display a wide range of Nd/Sr and a limited range of  $^{87}\text{Sr}/^{86}\text{Sr}$  ratios, with a number of samples plotting below the assumed mixing lines between the mantle and slab (basalt fluid and sediment melt) end-members (Fig. 3.1.2). Formation of hybrid sediment-basalt-peridotite *mélange* lithologies at the interface between the slab and mantle wedge, and their subsequent diapiric rise and melting in the sub-arc region, was invoked to reconcile the observations with the available experimental data on melt/sediment and fluid/basalt trace element partitioning. Codillo et al. (2018) tested the idea of the *mélange* model by performing melting experiments on mixtures of natural peridotite and sediment-dominated *mélange*. The sediment-dominated *mélange* had major and trace element composition similar to the GLOBal Subducting Sediment (GLOSS) (Plank, 2013). In order to generally reproduce typical arc magma chemistry, 5 to 15 % of the sediment-dominated *mélange* had to be admixed to the peridotite. Such high proportions of the sediment component in *mélange* lithologies would inevitably overwhelm the isotopic signals of the melt, and result in  $^{87}\text{Sr}/^{86}\text{Sr}$  ratios much higher than observed in arc magma. In addition, the Nd/Sr ratios of the produced melts were generally higher than in natural arc magma from the calc-alkaline series, and remained unchanged with respect to the bulk compositions. This suggests that *mélange* melting may not be able to efficiently lower the Nd/Sr ratio, after all. Both of these observations appear contradictory to the original argument presented by Nielsen and Marschall (2017).

Furthermore, Nielsen and Marschall (2017) use the  $^{87}\text{Sr}/^{86}\text{Sr}$  ratios of the altered oceanic crust to define the basalt-derived fluid end-member in their model. However, alteration of oceanic crust had not been systematically studied on a global scale (e.g. Kelley et al., 2003), and the extent to which it affects the bulk chemistry of subducting slabs is not known. The  $^{87}\text{Sr}/^{86}\text{Sr}$  ratio of the global MORB suite is relatively uniform, with the value of  $0.702819 \pm 0.000067$  (Gale et al.,

2013). If the  $^{87}\text{Sr}/^{86}\text{Sr}$  ratio of the average MORB were used, most arc magma compositions in Figure 3.1.2 would plot above the mixing line between the mantle and the basalt-derived fluid end-members.

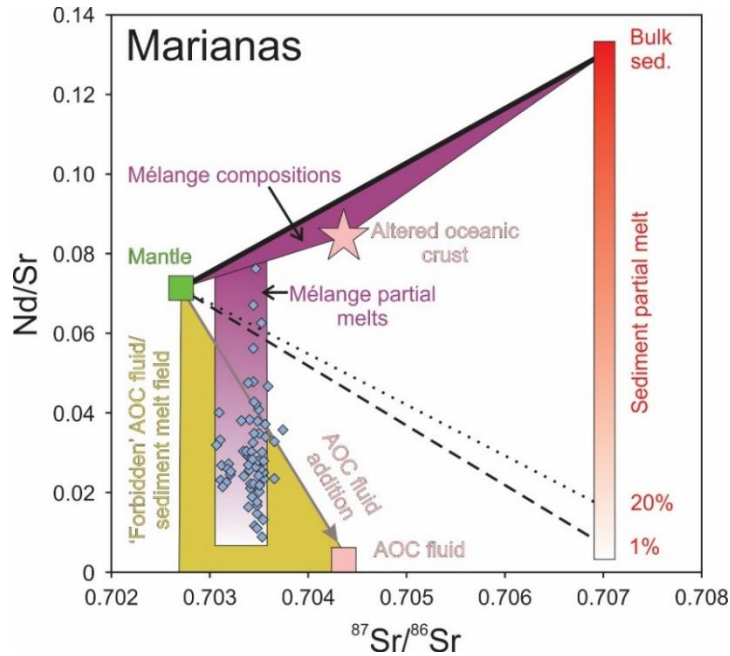


**Figure 3.1.2:** An example of the Nd/Sr –  $^{87}\text{Sr}/^{86}\text{Sr}$  discrimination diagram after Nielsen and Marschall (2017). Majority of the reported arc magma compositions from the Marianas plot below the mantle-AOC fluid and mantle-sediment melt mixing lines (the 'forbidden' field). A mechanical sediment-basalt-peridotite mixture of adequate isotopic composition is proposed to upwell into the mantle wedge and melt. Melting of the sediment component of the mélange lowers the Nd/Sr into the 'forbidden' field. Sr and Nd are not expected to fractionate during peridotite and basalt melting.

Thus, the traditional metasomatic models may very well explain the arc magma compositions. Rustioni et al. (2019) observed that the Nd/Sr ratio of basalt-derived fluids may increase with fluid salinity. The highly variable Nd/Sr ratios observed in nature may be related to trace element transport by fluids of different salinities, and mixing of sediment- and basalt-derived fluids could potentially explain the observed  $^{87}\text{Sr}/^{86}\text{Sr}$  ratios, without the need to invoke mélange diapirism.

### 3.1.2. The role of dilute sediment-derived hydrous fluids

Very few studies have investigated trace element partitioning between dilute low-temperature fluids and sediments (Johnson and Plank, 2000; Spandler et al., 2007; Hermann and Rubatto, 2009). The efforts to study fluid/sediment trace element partitioning were abandoned early on, in favor of sediment melts as the more likely candidate for the slab mobile phase (Ch.3.1.1). More

recently, Mallik et al. (2015) experimentally demonstrated that interaction of sediment melts with the mantle wedge produces ultrapotassic magmas, distinctly different from typical arc basalts. Also, as the isotopic signals of most arc magmas require some sediment input, but are not consistent with partial melting (Ch. 3.1.1, Fig. 3.1.2), the role of dilute low-temperature fluids in trace element transfer from sediments to arcs needs to be re-evaluated.

It is well established that the addition of chlorine enhances element solubility in hydrous fluids (Kawamoto, 2014; Keppler, 1996; Rustioni et al., 2019), but trace element partitioning in the sediment-H<sub>2</sub>O-NaCl system has never been investigated. Therefore, we measured trace element partition coefficients between saline fluids and metapelitic lithologies with GLOSS bulk composition to test whether or not such metasomatic agents could deliver the sediment geochemical fingerprint to the mantle melt production zone, without the need to invoke sediment melting.

## 3.2. Experimental methods

### 3.2.1. Starting materials and sample preparation

The starting material used in this study is a synthetic glass with a major element bulk composition similar to the average global subducted sediments (GLOSS) (Plank & Langmuir, 1998) and the upper continental crust (UCC) (Rudnick & Gao, 2003). The composition of the mixture is shown in Table 3.2.1., along with the starting materials used in some other notable studies on trace element partitioning between subduction zone fluids and crustal materials. GLOSS and UCC compositions are contained in the Table 3.2.1. as well, for comparison.

Major element oxides were added by weighing appropriate amounts of high purity  $\text{SiO}_2$ ,  $\text{Al}(\text{OH})_3$ ,  $\text{CaCO}_3$ ,  $\text{Fe}_2\text{O}_3$ ,  $\text{Mg}(\text{OH})_2$ ,  $\text{Na}_2\text{CO}_3$ ,  $\text{K}_2\text{CO}_3$  and  $\text{TiO}_2$ . Several fluid mobile trace elements were doped directly to the GLOSS mixture at this stage as well (Li, Be, B, Rb, Sr, Cs, Ba), to ensure sufficiently high concentrations in the final starting material. The GLOSS mixture was then mechanically homogenized under ethanol in an agate mortar for 1 h. The material was afterwards decarbonated and dehydrated in a platinum crucible for 5 h at 1100 °C, followed by chemical homogenization for 1 h at 1600 °C. The melt was quenched by dropping the crucible into distilled water. The resulting glass was crushed in a steel mortar and the remaining trace elements were added by mixing with 2 wt.% of a trace element-doped diopside glass in an agate mortar under ethanol for an additional hour. The doped diopside glass is from Rustioni et al. (2019), following the procedure described in Kessel et al. (2005). To overcome kinetic issues related to garnet nucleation, 1 wt.% of natural garnet seeds was added to the starting material, along with the doped glass. The final trace element content of the synthesized GLOSS material, as measured by LA-ICP-MS, is reported in Table 3.2.1.

The solutions that were introduced to the GLOSS starting material during sample preparation had initial compositions varying from distilled water to saline solutions, prepared by dissolving 5, 10, and 15 wt.% of high purity NaCl in distilled water. In one experiment phosphorous – which was omitted from the solid starting material – was subsequently added via the fluid by dissolving 5 wt.% of  $\text{H}_3\text{PO}_4$  in distilled water. With an initial fluid/GLOSS ratio of 0.3, this amount of  $\text{H}_3\text{PO}_4$  is equivalent to 1.1 wt.%  $\text{P}_2\text{O}_5$  by initial weight of the solid material.

### 3. Mantle metasomatism by sediment fluids in subduction zones

**Table 3.2.1:** The composition trace element-doped GLOSS starting material. LA-ICP-MS was used to analyze the synthetic GLOSS and diopside glasses. Values in the table are calculated from the LA-ICP-MS measurements. Several crustal reference compositions, as well as some natural and synthetic starting material from other experimental studies are shown for comparison. ‘synth.’ and ‘nat.’ indicate a synthetic or natural starting material from an experimental study; ‘ref.’ are crustal reference materials. ‘GLOSS’ stands for GLOBal Subducting Sediment, ‘UCC’ for Upper Continental Crust and ‘EPSM’ for Experimental Pelite Starting Material.

Crustal compositions	This study (GLOSS + 2 wt.% doped diopside glass)	GLOSS anhydrous (Plank & Langmuir, 1998)	GLOSS hydrous (Plank & Langmuir, 1998)	GLOSS II hydrous (Plank, 2013)	UCC (Rudnick & Gao, 2003)	EPSM anhydrous (Hermann & Spandler, 2008; Hermann & Rubatto, 2009)	EPSM (Li & Hermann, 2017)	natural red pelagic clay (Johnson & Plank, 1999)
synth./nat./ref	synth.	ref.	ref.	ref.	ref.	synth.	synth.	nat.
<b>Major elements (wt.%)</b>								
SiO <sub>2</sub>	64.60	65.28	58.57	56.60	66.62	68.83	63.56	53.23 - 54.43
TiO <sub>2</sub>	0.62	0.69	0.62	0.64	0.64	0.67	0.62	0.83 - 0.90
Al <sub>2</sub> O <sub>3</sub>	11.93	13.27	11.91	12.51	15.40	14.70	13.57	15.17
FeO	5.94	5.81	5.21	5.67	5.04	4.67	4.31	8.76 - 9.72
MnO	-	0.36	0.32	0.43	0.10	0.11	0.10	3.14 - 3.35
MgO	2.92	2.76	2.48	2.75	2.48	2.51	2.32	3.77 - 3.84
CaO	6.94	6.63	5.95	6.22	3.59	2.45	2.26	3.53 - 3.68
Na <sub>2</sub> O	3.21	2.71	2.43	2.50	3.27	2.62	2.42	4.63 - 5.87
K <sub>2</sub> O	2.51	2.27	2.04	2.21	2.80	2.94	2.71	2.80 - 3.42
P <sub>2</sub> O <sub>5</sub>	-	0.21	0.19	0.20	0.15	0.32	0.92	1.51 - 1.75
H <sub>2</sub> O	-	-	7.29	7.09	-	-	7.20	-
CO <sub>2</sub>	-	-	3.01	3.07	-	-	-	-
<b>Total</b>	<b>98.68</b>	<b>100.00</b>	<b>100.02</b>	<b>99.89</b>	<b>100.09</b>	<b>99.82</b>	<b>99.99</b>	<b>-</b>
<b>Trace elements (ppm)</b>								
Li	1037	-	-	45	21	-	37	49 - 54
Be	1033	-	-	2	2	-	6	2 - 3
B	1009	-	-	68	17	-	166	-
Rb	1282	64	57	84	84	225	64	50 - 54
Sr	1388	364	327	302	320	215	471	331 - 352
Y	36	33	30	33	21	60	32	410 - 451
Zr	26	145	130	129	193	202	117	259 - 273
Nb	72	10	9	9	12	57	72	17 - 18
Cs	1133	4	3	5	5	241	56	2
Ba	979	865	776	786	624	1170	867	700 - 803
La	207	32	29	29	31	163	63	243 - 267
Ce	762	64	57	58	63	68	98	333 - 360
Nd	217	30	27	28	27	60	63	304 - 325
Sm	220	7	6	6	5	66	61	66 - 70
Eu	216	2	1	1	1	61	58	15 - 16
Gd	243	6	5	6	4	58	59	72 - 78
Dy	238	6	5	5	4	55	63	63 - 68
Er	304	3	3	3	3	57	31	33 - 36
Yb	291	3	3	3	2	60	32	28 - 31
Lu	238	0.4	0.4	0.5	0.3	-	31	4 - 5
Hf	38	5	4	3	5	48	34	6 - 7
Ta	80	0.7	0.6	0.7	1	57	27	1
Pb	518	22	20	21	17	213	50	67 - 70
Th	104	8	7	8	11	238	31	8 - 9
U	132	2	2	2	3	532	35	2

The diamond trap method, originally proposed by Ryabchikov et al. (1989) and modified after Kessel et al. (2004), was used in this study to capture and separate the fluids from solid metapelitic residues. Samples were prepared by placing a thick layer of diamond powder between two layers of trace element doped starting material (Fig. 3.2.1). We used both a synthetic 10-20  $\mu\text{m}$  MEDIA, or a natural 40-60  $\mu\text{m}$  Alfa Aesar diamond powder. Approximately 30 to 40 wt.% of aqueous solution (relative to the solid starting material) were added. The solution was added either before the solids, or in two steps – before and after the diamond powder was introduced. The samples were sealed in 10 mm long Pt capsules with flat lids and a 5.0/4.6 mm outer/inner diameter. Observed weight losses during welding, presumably due to a combination of Pt spatter and fluid evaporation, were between 0.1 and 1.2 wt.% of the total added fluid and are, therefore, not a major concern.

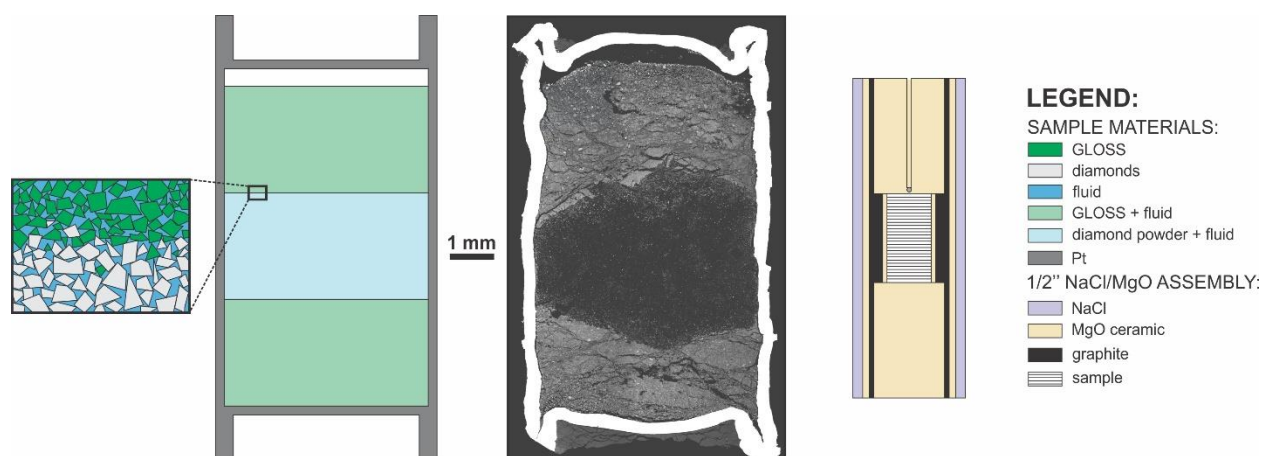


**Figure 3.2.1:** The samples were prepared by placing a thick layer of diamond powder between two layers of trace element-doped GLOSS starting material. The samples contained approximately 30 to 40 wt.% of aqueous solution, relative to the weight of the solid starting material. The aqueous solutions would usually permeate the solids, as shown of the left. A representative BSE image of a sample after the experiment is given for comparison. A schematic of the 1/2'' NaCl/MgO assembly is shown as well.

### 3.2.2. Piston cylinder experiments

A series of 12 to 19 day long piston cylinder experiments was performed at pressures between 2.5 and 4.5 GPa and temperatures of 600 and 700 °C. The experiments were started following the standard hot-piston-in procedure (Ch. 2.2.2.2.) after a long period of automatic compression, typically with >12 h duration. Long compression and decompression periods limit brittle deformation of the assembly materials, which can otherwise damage the Pt sample capsules and result in extensive fluid leaks.

Small crystal size was expected at the (low) temperatures of interest in this study. Therefore, once the temperature was raised to target value and had stabilized, a temperature cycling program was initiated to improve crystal growth. The effects of temperature oscillations on crystal growth are well understood (e.g. Erdmann and Keopke, 2016). The temperature cycling relies on Ostwald ripening. Upon heating above target temperature, small crystals and crystal nuclei are expected to dissolve entirely in the fluid phase. Upon cooling below the target temperature, the dissolved material is precipitated on the rims of larger grains, which had persisted throughout the upward cycle. The expected net result is that the sample recrystallizes to coarser grains, which can then be analyzed by means of LA-ICP-MS. The cycling program was also used by Rustioni et al. (2019), but had not been previously tested at temperatures as low as 600 °C.

The temperature was varied  $\pm 30$  °C around target in all 3.5 and 4.5 GPa runs. In some 2.5 GPa experiments, the cycle was only  $\pm 20$  °C. No notable difference in grain growth was observed between  $\pm 20$  °C and  $\pm 30$  °C cycles at 2.5 GPa. The grain size, however, improved significantly with increasing salinity. After 9 to 10 days (27 to 30 cycles of 8 h each), the temperature was kept stable for additional 3 to 9 days.

The recovered samples were frozen in liquid nitrogen and transferred to the freezer, where they were kept until fluid analysis. Upon freezing, ice, NaCl crystals and other precipitates may form in the diamond trap. Rapid freezing in liquid nitrogen should ensure formation of smaller ice, salt and precipitate crystals, and result in a more homogeneous diamond trap content.

### **3.2.3. Laser ablation inductively coupled plasma mass spectroscopy (LA-ICP-MS)**

Due to its high sensitivity for a wide array of elements, ICP-MS has found a broad range of applications for determining trace element concentrations and isotope ratios of various natural and synthetic geologic materials. ICP-MS in conjunction with a laser ablation sampling system has proven particularly useful, as it allows microanalysis of solid geologic samples with a spatial resolution adequate for most applications in petrology and mineralogy. The principal components of every LA-ICP-MS system are: laser, sample chamber, optical system for sample observation

during analysis, inductively coupled plasma torch, vacuum system, ion optics, mass analyzer and detector (Fig. 3.2.2).

Most common types of lasers in LA-ICP-MS systems are Nd:YAG solid state lasers (1064 nm, with possible higher harmonics at 266 nm) and ArF Excimer lasers (193 nm) (Longerich, 2008). Shorter wavelength laser light in the ultraviolet ablates geologic materials more efficiently, since most minerals absorb photons of the correspondingly higher energies better. Despite the higher cost, the Excimer lasers are, therefore, the universal choice of many laboratories. It is desirable that most of the energy delivered by the laser to the sample surface is expended on sample evaporation, rather than being transformed to heat the bulk of the specimen. The laser output is pulsed with a pulse width in the range of nanoseconds. Instead of delivering energy continuously, which would contribute to bulk sample heating, short pulses have been observed to reduce sample melting at the laser pit surface, a phenomena which is believed to cause element fractionation and should be avoided. More recently, femtosecond lasers have also been adopted for application in LA-ICP-MS. It has been reported that femtosecond pulses can further reduce element fractionation with respect to Excimer lasers (Horn, 2008). In addition to using a pulsed laser, the sample is ablated at a laser repetition rate of several to several dozen Hz.

The laser light is directed and focused onto the sample surface by a system of mirrors, prisms and lenses. The sample is contained in an air-tight chamber through which a carrier gas flows during measurement, transporting the evaporated sample aerosol via system of tubes into the plasma torch. The carrier gas is usually Ar, often admixed with a lighter component (such as He) to improve gas flow and sample flushing from the chamber (Günther and Koch, 2008). The precise locations for analysis can be determined by observing the sample using an optical microscope mounted on the instrument. To avoid directly looking at the sample during ablation, the optical system is typically accompanied by a monitor connected to a camera with a similar field of view as the microscope.

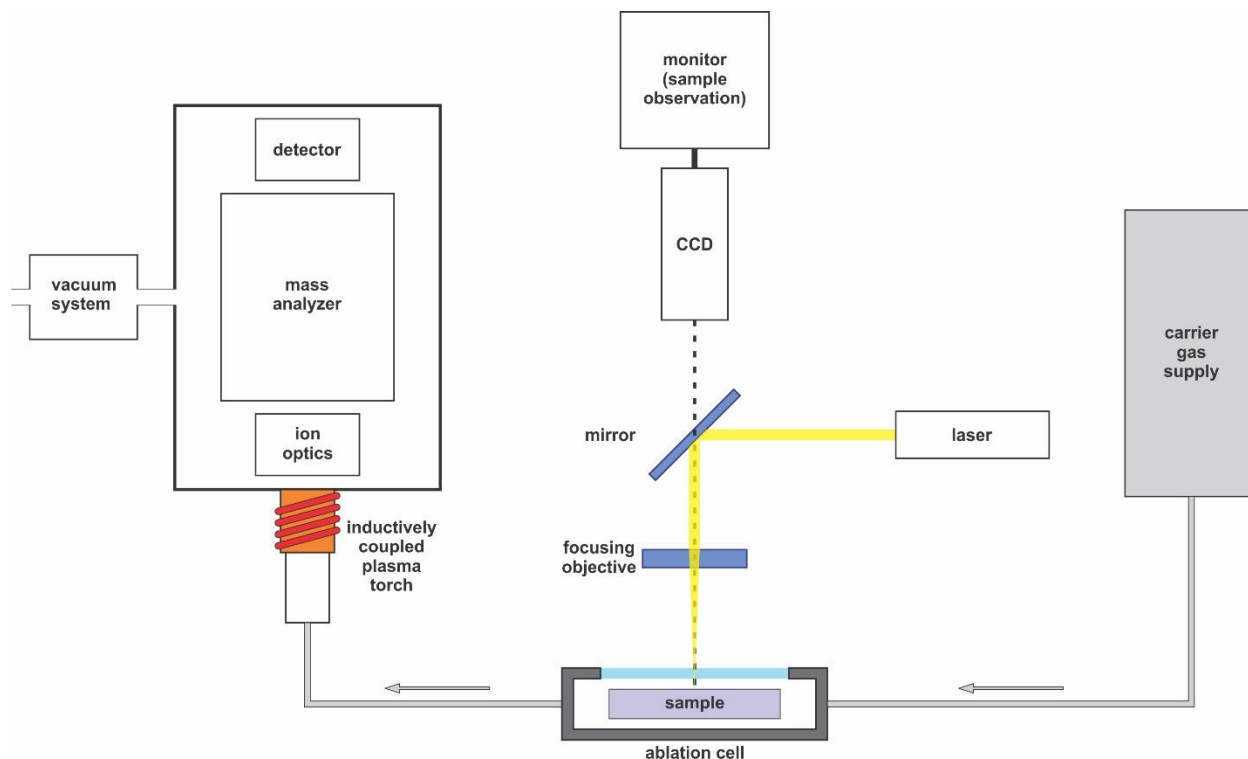


**Figure 3.2.2:** A simplified schematic view of the laser ablation inductively coupled plasma mass spectrometer (LA-ICP-MS).

An inductively coupled plasma torch generates energy sufficient for (nearly) complete ionization of the sample aerosol before it is carried into the mass spectrometer. The torch design is fairly universal in all ICP-MS systems (Longerich, 2008). The torch has a fused quartz casing which consists of several concentric tubes. The innermost tube is a capillary for sample introduction, while the Ar supply for plasma generation flows through the outer tubing. An additional stream of Ar gas is typically used to cool the outside of the torch. A copper load coil is located on one end of the fused quartz casing. A strong magnetic field is induced when a high-power radio frequency alternating current is passed through the load coil. Free electrons are initially introduced to the Ar flow by an electric spark. The electrons oscillate in the magnetic field and collide with and ionize Ar atoms, thus releasing thermal energy and producing further free electrons which maintain the plasma. Before entering the mass spectrometer, the ionized sample passes through a series of electrostatic ion lenses. Ion lenses accelerate and direct the ions into the mass spectrometer. Additionally, they are able to filter the majority of other types of particles which are generated in the plasma (free electrons, neutral particles).

The mass spectrometer itself consists of two main parts – the mass analyzer and ion detector(s). ICP-MS instruments for geoscience application usually have either quadrupole or sector mass analyzers. Longerich (2008) describes the working principles of both designs of mass analyzers, as well as the relevant detector types. Quadrupole mass analyzers consist of four conductive rods forming an ion channel. The opposing rods are electrically connected and oscillating currents are applied to one rod pair after the other. Depending on the characteristics the current applied to the rod pairs at a given time, only ions of a specific mass-to-charge ( $m/Z$ ) ratio will have favorable trajectories that allow them to pass through the channel. Ions of other  $m/Z$  are expected to collide with the rods. The entire range of  $m/Z$  of interest can be ‘scanned’ by gradually adjusting the power outputs of the rod pairs. The sector mass analyzers are comprised of two parts: the magnetic sector analyzer (MSA) and electrostatic sector analyzer (ESA). The magnetic sector analyzer consists of an electromagnet, which generates a magnetic field that deflects the ions from their trajectory. At any given time, only ions of specific  $m/Z$  have a deflection angle required to arrive at the position of the detector, while other ions collide with the inside of the flight tube. By gradual adjustment of the current through the electromagnet, a sequence of ions with different  $m/Z$  can be analyzed. In the electrostatic sector analyzer, the ions pass through an electric field with potential drop perpendicular to the ion flight path. When passing through the electric field, the heavier ions and singly charged ions are deflected less than the lighter and doubly charged ions. During measurement the potential drop in the electrostatic sector is adjusted to analyze ions of neighboring  $m/Z$ , while the magnetic field strength in the magnetic sector is changed to achieve the full range of  $m/Z$  of interest. Two types of sector instruments exist – single and multiple-collector sector ICP-MS. In single-collector instruments, ions pass first through MSA then ESA, while multiple-collector ICP-MS have an ESA-MSA configuration. Quadrupole and single-collector sector instruments are used for both elemental and isotope ratio measurements. Multiple-collector instruments are more suitable for specialized and precise isotope ratio measurements (Longerich, 2008).

Most common types of detectors used in LA-ICP-MS instruments are secondary/channel electron multipliers (SEM/CEM) and Faraday detectors. SEM/CEM detectors consist of a series of plates made from secondary emissive materials (e.g. BeO, MgO, PbO, GaP...). When an ion impacts the first plate, several secondary electrons are ejected towards the second plate. Each of these electrons

ejects several more secondary electrons from the second plate, thus gradually multiplying the output signal. The signal is detected at the final plate. Faraday detectors measure the ion currents directly. The incident ions create a net charge on the Faraday cup. The measured charge is proportional to the number of collected ions.

The ICP torch is kept at atmospheric pressure, but the chambers containing the ion lenses, mass analyzer and detectors must be held at successively lower pressures, since the ion mean free path in air is short. The vacuum system of the ICP-MS instruments usually consists of several turbomolecular pumps backed up by mechanical rotary pumps (Longerich, 2008).

Due to a number of factors (e.g. variations in gas flow, torch stability and laser intensity) the measurement conditions in LA-ICP-MS are rather unstable. For this reason, an external standard of well characterized composition must be used to regularly re-calibrate the instrument during measurements (the 'drift' correction). Depending on the mechanical properties of the sample, different volumes of various target materials can be ablated at constant measurement conditions. Therefore, a matrix correction is required to account for the differences in ablation rates of the sample materials with respect to those of the external standards. To compare relative ablation rates of the specimen and external standard, prior knowledge of the concentration of at least one internal standard element in the sample is necessary. The quantitative concentration of other analytes in the unknown can then be calculated as (Jackson, 2008):

$$C_{AN,sample} = C_{AN,cal} \frac{R_{AN,sample}}{R_{AN,cal}} \left( \frac{C_{IS,sample}}{R_{IS,sample}} \frac{R_{IS,cal}}{C_{IS,cal}} \right)$$

where:

$C_{AN,sample}$  – unknown concentration of analyte in the sample

$C_{AN,cal}$  – known concentration of analyte in the calibration material

$R_{AN,sample}$  – measured count rate of the analyte in the sample

$R_{AN,cal}$  – measured count rate of the analyte in the calibration material

$C_{IS,sample}$  – known concentration of the internal standard in the sample

$C_{IS,cal}$  – known concentration of the internal standard in the calibration material

$R_{IS,sample}$  – measured count rate of the internal standard in the sample

$R_{IS,cal}$  – measured count rate of the internal standard in the calibration material

While other calibration strategies exist, the combined use of an external and internal standard, as described above, is the most common procedure for obtaining quantitative trace element analyses. In addition to being ablated at different rates, the physical processes involved in ablation of various materials can also differ. For example, a range of size distributions and types of aerosol particles (quenched melt, mineral fragments, vapor condensates, etc.) can be expected when ablating different materials. The distribution of analytes between various types of aerosol particles is not homogeneous, nor are they transported into the plasma and ionized with equal efficiency. Layers of quenched melt and secondary phases can form on the laser pit walls and preferentially retain refractory elements, biasing the result in favor of more volatile analytes. These, and other types of processes which can fractionate elements (and isotopes) from one another during sample transport and ionization are described in detail by Sylvester (2008). The degree of fractionation for particular element (or isotope) pair in the external standard may not be the same as in the sample materials and this may lead to lower precision in measured concentrations of analytes that fractionate considerably with respect to the internal standard. Therefore, external standard and sample ‘matrix matching’ has merit, as it could minimize the effects of element fractionation.

Another common source of error in LA-ICP-MS measurements are interferences. Interferences can be due to formation of isobaric isotopes, polyatomic charged particles and doubly charged ions in the plasma, or due to tailing interferences (Wilschefschi and Baxter, 2019). Isobaric interferences are caused by isotopes of different elements that have the same mass. Some examples include  $^{58}\text{Fe}/^{58}\text{Ni}$ ,  $^{40}\text{Ca}/^{40}\text{Ar}$  and  $^{87}\text{Rb}/^{87}\text{Sr}$ . In addition to ions, various charged polyatomic particles may also form in the plasma. The polyatomic particles can be different oxides, carbides, nitrides, hydrides, hydroxides, argides, etc. Chlorides may also form if chlorine is present in the sample. Several random examples observed in practice include  $^{39}\text{K}/^{38}\text{Ar}^1\text{H}^+$ ,  $^{151}\text{Eu}/^{135}\text{Ba}^{16}\text{O}^+$  and  $^{47}\text{Ti}/^{12}\text{C}^{35}\text{Cl}^+$  (May and Wiedmeyer (1998) and references therein). Since the second ionization energies are always higher, the probability of formation of doubly charged ions in the plasma is low and this type of interference is usually not severe. Nevertheless, a doubly charged ion with a mass of 24 amu would have similar trajectories within the mass analyzer as a singly charged ion with a 12 amu mass. The tailing interferences, which are due to spectral overlap from adjacent  $m/Z$ , are thought to have limited effect on measurement precision and are often neglected.

All LA-ICP-MS analyses carried out in the course of this study were performed with a Perkin Elmer Elan DRC-e quadrupole ICP-MS, coupled with a Coherent 193 nm ArF GeolasPro Excimer laser. The aerosol carrier gas was He (0.4 L/min) with admixed H<sub>2</sub> (5 mL/min) for improved sensitivity. The instrument was tuned against thorium oxide (<0.1 %) and Ca<sup>2+</sup> (<0.25 %) production rates (Jochum et al., 2011). Assuming naturally occurring isotope abundances, element concentrations were obtained by measuring: <sup>7</sup>Li, <sup>9</sup>Be, <sup>11</sup>B, <sup>23</sup>Na, <sup>25</sup>Mg, <sup>27</sup>Al, <sup>30</sup>Si, <sup>31</sup>P, <sup>35</sup>Cl, <sup>39</sup>K, <sup>43</sup>Ca, <sup>49</sup>Ti, <sup>57</sup>Fe, <sup>85</sup>Rb, <sup>88</sup>Sr, <sup>89</sup>Y, <sup>90</sup>Zr, <sup>93</sup>Nb, <sup>133</sup>Cs, <sup>137</sup>Ba, <sup>139</sup>La, <sup>140</sup>Ce, <sup>146</sup>Nd, <sup>147</sup>Sm, <sup>153</sup>Eu, <sup>157</sup>Gd, <sup>163</sup>Dy, <sup>167</sup>Er, <sup>172</sup>Yb, <sup>175</sup>Lu, <sup>178</sup>Hf, <sup>181</sup>Ta, <sup>208</sup>Pb, <sup>232</sup>Th, <sup>238</sup>U. Used external standards include NIST SRM 610 and USGS GSE-1G synthetic reference glasses, as well as natural afghanite (Seo et al., 2011) for calibration of Cl concentrations.

Fluid compositions were analyzed in frozen state following the procedure developed by Kessel et al. (2004). Immediately after removing from the freezer, the samples were cut open by inserting a razor blade into a steel mould containing the run charge. The samples were then quickly enclosed in a Peltier-cooled laser ablation sample chamber. To maintain the fluid in frozen state during transfer from the freezer to the sample chamber, the capsules were occasionally immersed into liquid nitrogen. Earlier tests demonstrated that the temperature inside the sample chamber is maintained at approximately -30 °C during measurement (Rustioni et al., 2019). The fluids were analyzed by continuously scanning a 50 µm laser beam with a 7 Hz repetition rate across the diamond layer. A profile perpendicular to the diamond trap, and extending from one metapelite layer to the other, was always ablated first to observe the extent of starting material contamination at the diamond-metapelite interface. Afterward, one to two profiles parallel to the diamond layer were ablated until a pristine region of the fluid trap was located again. Major elements with low solubilities in the fluid (Mg, Al and Ca) proved most useful for selecting uncontaminated sections of the signals. Between 2 to 5 representative intervals, typically with a 20 to 40 sec durations, could be located in all diamond traps. After fluid measurement, the samples were mounted in epoxy, imaged in detail by FE-SEM and quantitative major element mineral analyses were obtained by EPMA (see Ch. 3.2.4.). To calculate fluid compositions in both Cl-bearing and non-Cl-bearing samples in a consistent way, a new calculation procedure that allows Cs to be used as internal standard was developed. As up to about 50 % of Cs can be retained by the metapelitic

assemblages, a correction for the weight of Cs in the solid phases is necessary, in addition to the standard correction for mass exchange between the solid and fluid. Mineral proportions in the solid residues can be obtained by mass balance calculation using EPMA measurements. Only major elements with low solubilities in the fluid (<1 wt.%) may be used for the mass balance. The Cs concentrations in minerals are later determined in the second step of LA-ICP-MS measurements. Additional corrections to the fluid composition may be performed as well, but are not strictly necessary as they have minor effect on the final result (e.g. correction for hydration of the solid residue). In Cl-bearing samples, fluid compositions were also routinely calculated using Cl as internal standard. It was assumed that Cl is perfectly incompatible and remains solely in the fluid (Keppler, 1996), so only the correction for mass exchange between the solid and fluid was performed. Excellent agreement was observed between these two approaches for calculating fluid composition.

Suitable areas for mineral analyses were located during FE-SEM observation (Ch. 3.2.4). Single crystals, coherent crystal aggregates and rims around garnet seeds that grew at run conditions were chosen for analysis, taking care to avoid grains suspected of containing fluid/mineral inclusions. Composite BSE images of samples were used to find the analysis spots again during the second LA-ICP-MS measurement. The optical system mounted on the LA-ICP-MS instrument does not allow precise phase identification and cannot resolve contamination with small fluid/mineral inclusions. However, with the aid of BSE images, it was possible to locate the desired grains by their shape and location in the sample. The minerals were analyzed by keeping the laser static over the target grain. Scanning the laser over grain surfaces during ablation was possible only occasionally. The laser beams had 6 to 14  $\mu\text{m}$  diameters with repetition rates between 4 and 6 Hz. Microprobe major element oxide concentrations were used as internal standards to calculate mineral compositions. The internal standards for determining mineral compositions were  $\text{SiO}_2$  (silicates), CaO (apatite) and  $\text{TiO}_2$  (rutile). Since FE-SEM images only provide information about the surface of the sample, and laser pits are three-dimensional, further data selection was necessary. Some unrepresentative mineral analyses could be eliminated based on signal appearance alone. Others were removed after the mineral compositions were calculated, if the major element concentrations did not agree with EPMA measurements. Usually, three or more representative

analyses of each major mineral could be obtained after adequate data filtering. Whenever possible, accessory minerals were analyzed as well.

#### **3.2.4. Electron microscopy**

After fluid analysis in frozen state by LA-ICP-MS (Ch. 3.2.3), all samples were examined in detail using a ZEISS-LEO 1530 Gemini FE-SEM at BGI. The main purpose of FE-SEM sessions was to locate suitable mineral grains (or mineral aggregates) for subsequent LA-ICP-MS trace element mineral analysis (Ch. 3.2.3.). A series of BSE images at different magnifications was obtained to create a composite of each sample. The general areas for LA-ICP-MS measurement were highlighted in low magnification images. High magnification images were then used to pinpoint locations of 10-15  $\mu\text{m}$  diameter grains/aggregates, which could not be otherwise found by the reflected light optical system mounted on the LA-ICP-MS. In addition, high imaging resolution of the FE-SEM was useful for avoiding grains and aggregates contaminated with small ( $<1 \mu\text{m}$ ) mineral and fluid inclusions. SEM-EDS analyses provided information about the mineral composition of the samples and gave useful insight into the solid-phase distribution of trace elements, which were occasionally detectable when present in sufficiently high concentrations.

In each sample, quantitative chemical analyses of all major and most accessory minerals were obtained by JEOL JXA-8200 electron microprobe at BGI. BSE composite images from FE-SEM examination were often used to find suitable locations for analysis. If the microprobe session was taking place before the LA-ICP-MS measurement, the areas designated for trace element analysis were avoided. The high current and long total measurement times required for EMP-WDS analyses would likely cause some fractionation of moderately volatile from refractory trace elements via electron beam evaporation.

All measurements were performed with a focused beam (15  $\mu\text{A}$  current and 15 kV acceleration voltage). Measurement times on the background and signal were 10/20 seconds for all elements. Alkali were analyzed in the first cycle of measurement. The following standards with a PRZ matrix correction routine were used for calibration: forsterite (Si),  $\text{MnTiO}_3$  (Ti), spinel (Al), Fe metal (Fe), enstatite (Mg), wollastonite (Ca), albite (Na) and orthoclase (K). Oxygen concentrations were calculated assuming the common oxidation states of other elements. Iron is reported as FeO.

### 3.3. Results

All experiments were performed at pressures of 2.5 to 4.5 GPa and temperatures of 600 to 700 °C (Fig. 3.3.1). More recent numerical models (e.g. Syracuse et al., 2010), as well as studies of exhumed Ultra-High-Pressure (UHP) terranes (Penniston-Dorland et al., 2015; Tsujimori et al., 2006), suggest these P-T conditions are representative of cold subduction geotherms.

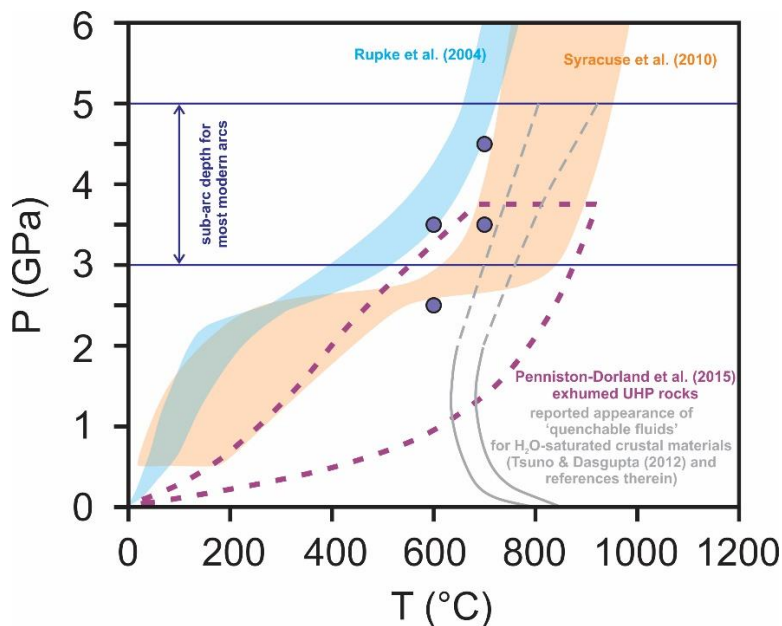


**Figure 3.3.1.** Experimental pressure and temperature conditions (circles) compared to the predicted sub-arc depths (Syracuse et al., 2010) and subduction geotherms according to well-known numerical models (Rüpke et al. (2004); Syracuse et al., 2010). Peak metamorphic conditions of exhumed UHP terranes (Penniston-Dorland et al., 2015) are shown as well.

At each P-T condition, the initial salinity of the fluid was varied (0, 5, 10, 15 wt.% NaCl) to investigate the effects of chlorine on trace element mobility in subduction zones. All experimental conditions and the resulting run product mineral assemblages are summarized in Table 3.3.1.

#### 3.3.1. Sample petrography

The equilibrium assemblage in 2.5 GPa and 600 °C experiments consisted of clinopyroxene, phengite, zoisite/clinozoisite and quartz. No overgrowth on garnet seed rims was observed and accessory phases in all runs were rutile and allanite. The grain size varied drastically with fluid salinity. The clinopyroxene, phengite and zoisite/clinozoisite grains in low salinity runs were only several hundred nm in size. In addition, FE-SEM observation revealed that different phases were often intergrown. The LA-ICP-MS analysis of minerals of geologic interest was not possible in experiments with 0 and 5 wt.% NaCl at 2.5 GPa and 600 °C. No results from these two runs are

### 3. Mantle metasomatism by sediment fluids in subduction zones

reported, but it is perhaps of some interest to note the current limitation of the experimental setup. Crystal aggregates of clinopyroxene, phengite and zoisite/clinozoisite of up to 30, 20 and 15  $\mu\text{m}$  in diameter, respectively, had formed in equilibrium with high salinity fluids (Fig. 3.3.2a and 3.3.2b) and were suitable for LA-ICP-MS analysis. Several zoned single-crystal clinopyroxene formed as well, growing along capsule walls.

**Table 3.3.1.** A summary of run conditions and resulting mineral assemblages. Mineral name abbreviations: Alla – allanite, Coe – coesite, Cpx – clinopyroxene, Grt – garnet, Laws – lawsonite, Pheng – phengite, Rut – rutile, Qtz – quartz, Ttn – titanite, Zo/Czo – zoisite/clinozoisite, Zrc – zircon. (\*) Solid phase not observed, but inferred from mass balance calculations. (\*\*\*) Phosphorous test experiment with 1.1 wt.%  $\text{P}_2\text{O}_5$  (per initial weight of solid material).

Run condition summary:								Mineral assemblage:		
Sample	time (h)	P (GPa)	T (°C)	T <sub>cycling</sub> (°C)	NaCl (wt.%)	Fluid (wt.%)	Diamond powder	Major minerals	Accessory minerals	
DT1	405	3.5	600	570-630, 30 periods	0	32	MEDIA synth. 10-20 $\mu\text{m}$	Cpx, Pheng, Laws, Coe	Rut, Alla	
DT2	399	3.5	600	570-630, 30 periods	5	30	MEDIA synth. 10-20 $\mu\text{m}$	Cpx, Pheng, Laws, Coe	Rut*, Alla	
DT3	405	3.5	600	570-630, 30 periods	10	28	MEDIA synth. 10-20 $\mu\text{m}$	Cpx, Pheng, Laws, Coe	Rut, Alla	
DT4	293	3.5	600	570-630, 30 periods	15	42	MEDIA synth. 10-20 $\mu\text{m}$	Cpx, Pheng, Laws, Coe	Rut*, Alla	
DT5	407	2.5	600	580-620, 30 periods	0	42	MEDIA synth. 10-20 $\mu\text{m}$	Cpx, Pheng, Zo/Czo, Qtz	Rut*, Alla	
DT6	333	2.5	600	580-620, 30 periods	15	43	MEDIA synth. 10-20 $\mu\text{m}$	Cpx, Pheng, Zo/Czo, Qtz	Rut, Alla	
DT7	360	3.5	600	570-630, 30 periods	0	30	MEDIA synth. 10-20 $\mu\text{m}$	Cpx, Pheng, Laws, Coe	Rut, Alla	
DT8	312	3.5	600	570-630, 30 periods	15	33	MEDIA synth. 10-20 $\mu\text{m}$	Cpx, Pheng, Laws, Coe	Rut, Alla	
DT9	455	3.5	600	570-630, 30 periods	5	30	MEDIA synth. 10-20 $\mu\text{m}$	Cpx, Pheng, Laws, Coe	Rut, Alla	
DT10	432	3.5	600	570-630, 30 periods	10	27	MEDIA synth. 10-20 $\mu\text{m}$	Cpx, Pheng, Laws, Coe	Rut*, Alla	
DT11	356	4.5	700	670-730, 30 periods	0	28	MEDIA synth. 10-20 $\mu\text{m}$	Cpx, Pheng, Grt, Laws, Coe	Rut, Alla	
DT12	307	4.5	700	670-730, 30 periods	5	32	MEDIA synth. 10-20 $\mu\text{m}$	Cpx, Pheng, Grt, Laws, Coe	Rut, Alla	
DT13	240	4.5	700	670-730, 30 periods	10	29	MEDIA synth. 10-20 $\mu\text{m}$	Cpx, Pheng, Grt, Laws, Coe	Rut, Alla	
DT14	429	4.5	700	670-730, 30 periods	15	31	MEDIA synth. 10-20 $\mu\text{m}$	Cpx, Pheng, Grt, Laws, Coe	Rut, Alla	
DT15	380	2.5	600	570-630, 30 periods	5	39	MEDIA synth. 10-20 $\mu\text{m}$	Cpx, Pheng, Zo/Czo, Qtz	Rut*, Alla	
DT16	357	2.5	600	570-630, 30 periods	10	39	MEDIA synth. 10-20 $\mu\text{m}$	Cpx, Pheng, Zo/Czo, Qtz	Rut, Alla	
***DT17	357	3.5	600	570-630, 30 periods	0	31	MEDIA synth. 10-20 $\mu\text{m}$	Cpx, Pheng, Grt, Laws, Coe	Rut, Alla, Ap	
DT20	260	3.5	700	---	15	31	MEDIA synth. 10-20 $\mu\text{m}$	Cpx, Pheng, Grt, Laws*, Coe	Rut, Alla	
DT21	308	3.5	700	---	0	30	Alfa Aesar nat. 40-60 $\mu\text{m}$	Cpx, Pheng, Grt, Laws, Coe	Rut, Alla, Ttn	
DT23	312	3.5	700	---	15	28	Alfa Aesar nat. 40-60 $\mu\text{m}$	Cpx, Pheng, Grt, Laws*, Coe	Rut, Alla, Zrc	
DT24	212	3.5	700	---	5	33	Alfa Aesar nat. 40-60 $\mu\text{m}$	Cpx, Pheng, Grt, Laws*, Coe	Rut, Alla	

A metamorphic assemblage of clinopyroxene, phengite, lawsonite and coesite (Fig. 3.3.2c and 3.3.2d), with accessory rutile and allanite, was found in all run products from 3.5 GPa and 600 °C. A very thin overgrowth (1-2  $\mu\text{m}$ ) on garnet seeds was observed in several phosphorous-free samples. In the phosphorous test experiment garnet had been stabilized by the addition of 1.1 wt.% of  $\text{P}_2\text{O}_5$  and overgrowth rims of up to 15  $\mu\text{m}$  thickness had developed around the seed crystals (Fig. 3.3.2e). At 3.5 GPa and 600 °C, lawsonite was always present as 50 to 100  $\mu\text{m}$  diameter single crystals. The single-crystal lawsonite occasionally displayed compositional zonation and sometimes contained mineral inclusions, which were avoided during LA-ICP-MS measurement. Clinopyroxene crystallized both as zoned single crystals and as crystal aggregates, while phengite was always present in aggregate form. Both clinopyroxene and phengite aggregates were up to approximately 30  $\mu\text{m}$  in diameter. The phosphorous test sample additionally contained 15 to 25  $\mu\text{m}$  single-crystal apatite.

### *3. Mantle metasomatism by sediment fluids in subduction zones*

In both 4.5 and 3.5 GPa experiments at 700 °C, the major minerals were clinopyroxene, phengite, garnet, lawsonite and coesite. The overgrowth rims on garnet seeds were up to 30 µm thick and numerous smaller newly nucleated garnets were present as well. Clinopyroxene and phengite crystallized as both aggregates and single crystals of a wide range of sizes (Fig. 3.3.2f, 3.3.2g and 3.3.2h). The clinopyroxene single crystals were usually zoned, while the phengite always appeared homogenous in BSE images. At 4.5 GPa, lawsonite formed aggregates (<15 µm) in low salinity runs and single crystals (5 to 40 µm) in the experiment with initial fluid NaCl content of 15 wt.%. At 3.5 GPa and 700 °C, a single approximately 500 µm diameter lawsonite grain had been observed growing on the capsule wall of one sample. No lawsonite was found in other samples from the same P-T conditions, but its presence could be inferred from mass balance calculations. In 4.5 GPa runs, the only accessory phases were rutile and allanite, while zircon and titanite were additionally observed at 3.5 GPa.

3. Mantle metasomatism by sediment fluids in subduction zones

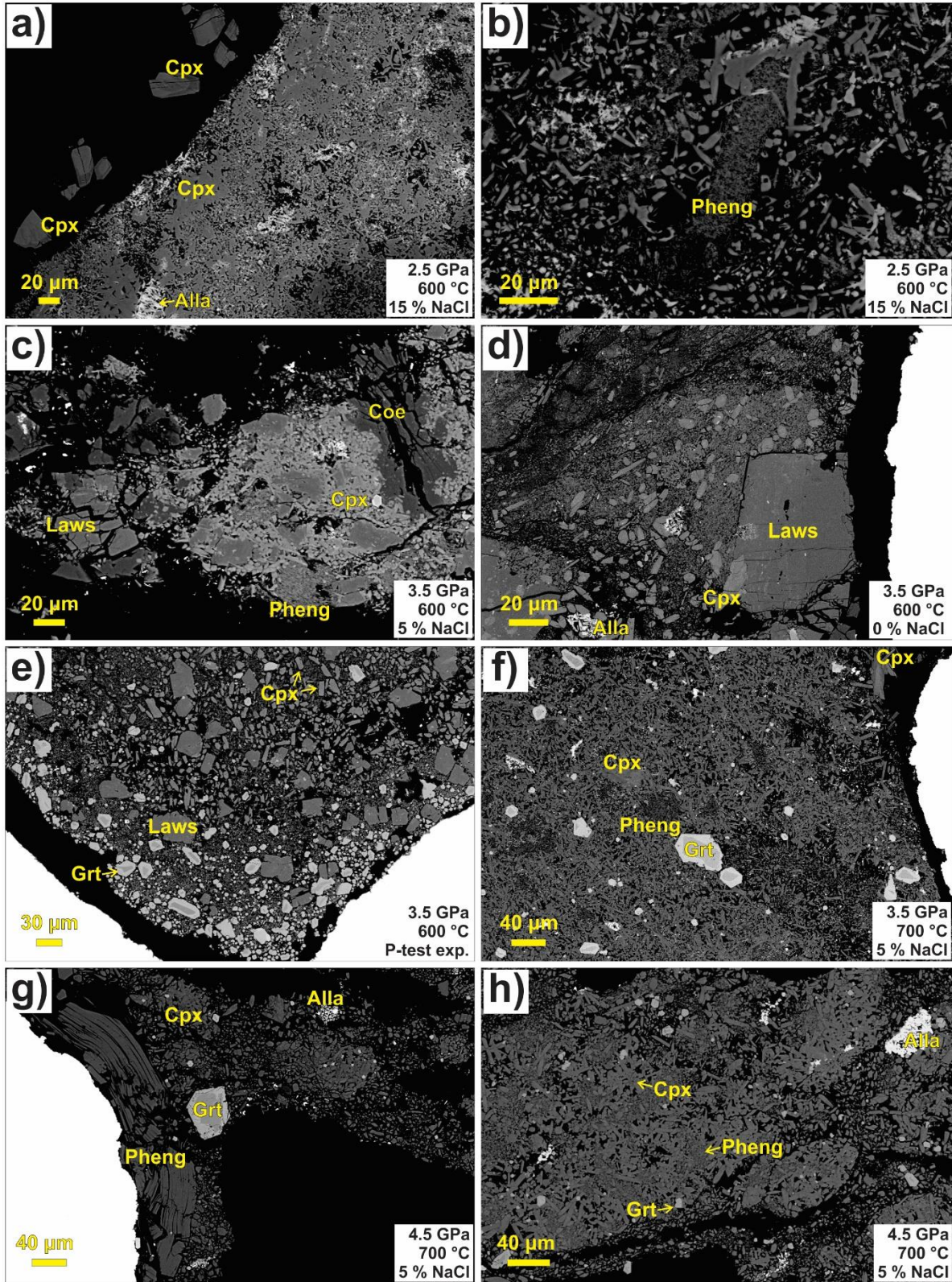


**Figure 3.3.2.** A panel of representative BSE images of samples from: 2.5 GPa and 600 °C (a and b), 3.5 GPa and 600 °C (c, d and e), 3.5 GPa and 700 °C (f), 4.5 GPa and 700 °C (g and h). Mineral name abbreviations: Alla – allanite, Coe – coesite, Cpx – clinopyroxene, Grt – garnet, Laws – lawsonite, Pheng – phengite.

### 3.3.2. Mineral and fluid compositions

Major element concentrations in solid phases, obtained by EPMA, are summarized in Tables 3.3.2. to 3.3.8. (Supplement II). The microprobe analyses totals are typically 1 to 3 wt.% below the hydrous stoichiometric ideals, which may be attributed to the trace element content. Mineral compositions were recalculated in terms of atoms per formula unit (a.p.f.u.) on the basis of 6, 12, 11 and 8 oxygen atoms for clinopyroxene, garnet, phengite and lawsonite, respectively. All iron was assumed to be ferrous.

The measured clinopyroxene compositions vary systematically with salinity. Due to introduction of additional sodium via the fluid, an increase in jadeite ( $\text{NaAlSi}_2\text{O}_6$ ) component from approximately 40 to 55 mol.% is observed with increasing fluid salinity (Fig. 3.3.3). Nevertheless, the sodium content of run product clinopyroxene from this study does not exceed the range observed in clinopyroxene from exhumed lawsonite eclogites of both pelitic and basaltic protoliths (Tsuji-mori et al., 2006).

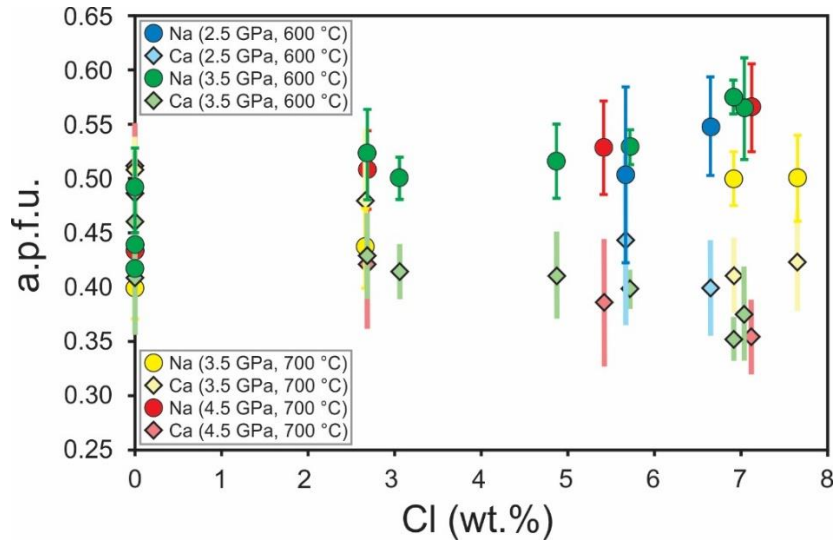
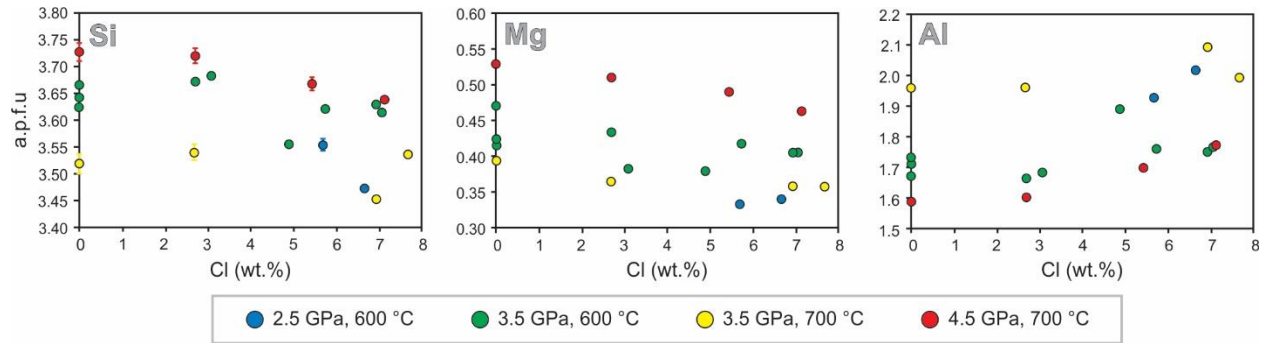


Figure 3.3.3. Clinopyroxene sodium and calcium contents as a function of fluid salinity.

Phengite compositions vary with pressure, temperature and salinity. The main compositional change appears to be a Tschermak type substitution  $\text{Si}^{4+} + \text{R}^{2+} = \text{Al}^{3+\text{IV}} + \text{Al}^{3+\text{VI}}$ , where  $\text{R}^{2+}$  is mostly  $\text{Mg}^{2+}$  (Fig. 3.3.4). The silicon and magnesium contents increase with pressure, but decrease

with temperature and salinity. Auzanneau et al. (2009), who investigated Ti in phengite as a geobarometer, have reported a similar pressure and temperature dependence of phengite compositions. The measured Ti concentrations in phengite decrease with pressure and increase with temperature, as expected, and generally agree with the proposed geobarometer. The K contents in phengites are  $0.8 \pm 0.04$  a.p.f.u. Additionally, up to 0.05 a.p.f.u. of Na+Ca was detected by microprobe analyses, suggesting up to 15 mol.% occupancy of the X-site by trace elements (presumably Rb, Cs and Ba).



**Figure 3.3.4.** Phengite silicon, magnesium and aluminum contents as a function of fluid salinity. Where no error bar (one standard deviation) is shown, the error is within the symbol.

The garnet compositions from the phosphorous bearing run at 3.5 GPa and 600 °C, as well as from the experiments at 4.5 GPa and 700 °C, agree with compositions of natural garnets (Fig. 3.3.5) from exhumed lawsonite eclogites (Tsuji-mori et al., 2006). The garnets in samples from 3.5 GPa and 700 °C runs are more Ca-rich, as compared to natural garnet compositions compiled by Tsuji-mori et al. (2006), perhaps due to an abrupt decrease in lawsonite proportion at these P-T conditions. In all samples, lawsonite compositions are close to its ideal stoichiometry ( $\text{CaAl}_2\text{Si}_2\text{O}_7(\text{OH})_2 \cdot \text{H}_2\text{O}$ ) without much variation with salinity, pressure and temperature.

Major and trace element concentrations in solid phases, as determined by LA-ICP-MS, are reported in Tables 3.3.9. to 3.3.15. (Supplement II). A comparison between major element mineral analyses by EPMA and LA-ICP-MS usually yields an agreement within  $\pm 20\%$  for most oxides. A systematic offset from the 1:1 line (Fig. 3.3.6) is typically observed, and attributed to element fractionation in the laser ablation system. However, the accuracy of the obtained trace element

mineral compositions should be satisfactory, since the partition coefficients are usually reported on logarithmic scale.

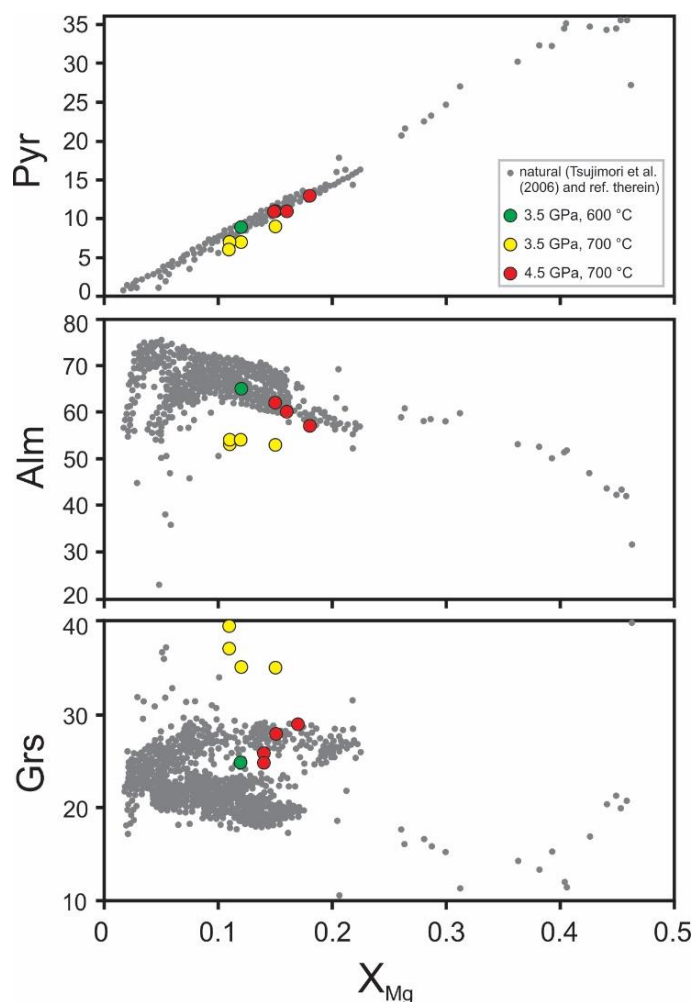


**Figure 3.3.5.** A comparison between natural (Tsuji-mori et al., 2006) and experimental (this study) garnet compositions from the pressure and temperature range of interest. End-member abbreviations: Pyr – pyrope, Alm – almandine, Grs – grossular.

In some instances, LA-ICP-MS analyses of minerals were accepted, even if they showed evidence for contamination by other phases. For example, rutile analyses may contain  $SiO_2$ , clearly suggesting contamination with a silicate phase. Since rutile is expected to accommodate orders of magnitude higher concentrations of Nb and Ta as compared to most silicates, only a negligible error in Nb and Ta partition coefficients would result from moderate silicate contamination.

### 3. Mantle metasomatism by sediment fluids in subduction zones

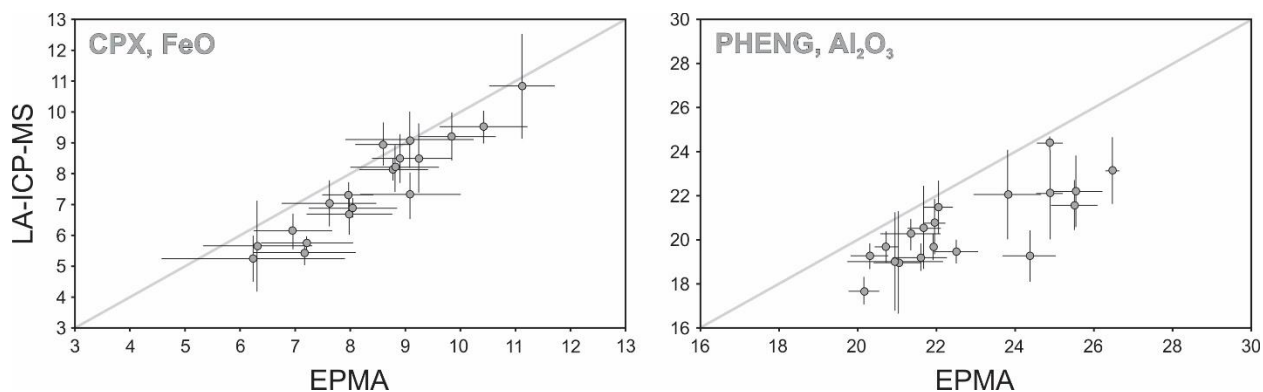


**Figure 3.3.6.** A comparison between LA-ICP-MS and EPMA measured FeO and Al<sub>2</sub>O<sub>3</sub> concentrations in clinopyroxene and phengite, respectively. LA-ICP-MS systematically underestimates most major element oxide concentrations in minerals.

The metapelitic mineral assemblages co-existed either with aqueous fluids or fairly dilute low-temperature supercritical fluids that had Total Dissolved Solid (TDS) contents between 5 and 30 wt.% (Fig 3.3.8). The exact position of the critical curve in the GLOSS-H<sub>2</sub>O system is presently unknown. Schmidt (2015) reports the second critical endpoint for crustal materials above 5 GPa, whereas some earlier in-situ observations in the albite-H<sub>2</sub>O system (Shen and Keppler, 1997) suggest complete miscibility between H<sub>2</sub>O and silicate melt may be possible above 2 GPa and 600 °C.

The initial fluid contents were kept within  $30 \pm 3$  wt.% in all 3.5 and 4.5 GPa samples, except for run “DT4” which initially contained 42 wt.% of fluid. All samples for 2.5 GPa experiments had higher initial fluid contents of  $40 \pm 3$  wt.% to improve grain growth. The overall solubility of major elements in the fluids was observed to decrease in the following order: SiO<sub>2</sub> > Na<sub>2</sub>O > K<sub>2</sub>O > CaO > FeO > Al<sub>2</sub>O<sub>3</sub> > MgO > TiO<sub>2</sub> (Fig. 3.3.8). The main constituent of the solid material dissolved in the fluid is SiO<sub>2</sub>, the concentrations of which vary between 5 and 15 wt.% without clear correlation with salinity. The solubilities of Na<sub>2</sub>O and K<sub>2</sub>O tend to increase with increasing salinity of the fluid. The K<sub>2</sub>O solubility in the fluid additionally exhibits a systematic increase with pressure and temperature. The reported fluid Na<sub>2</sub>O concentrations may be somewhat higher than in natural subduction zone fluids due to introduction of additional sodium via NaCl. However, mass balance calculations suggest that nearly all excess sodium from the fluid had reacted with solid residues, resulting in an increase in clinopyroxene mass proportion (Ch. 3.3.3), as well as an increase in jadeite component in clinopyroxene, with increasing salinity. The measured concentrations of

FeO, Al<sub>2</sub>O<sub>3</sub>, MgO and TiO<sub>2</sub> sporadically vary by one to two orders of magnitude and exhibit no correlation with increasing salinity. Previous studies (e.g. Audéat and Keppler, 2005) demonstrated that dissolution and re-precipitation of material at run conditions due to thermal gradients results in severe overestimation of element solubilities. The highest concentrations of FeO, Al<sub>2</sub>O<sub>3</sub>, MgO and TiO<sub>2</sub> measured in fluids from this study can likely be attributed to this methodological problem. The lowest measured values are thought to be closer to the true solubilities of these elements, and are in the order of a few hundred to a few thousand ppm for FeO and Al<sub>2</sub>O<sub>3</sub>, a few hundred ppm for MgO and dozens of ppm for TiO<sub>2</sub>. Concentrations of several trace elements (Be, Nb, Ta) in the fluid exhibit similar random variations, and may have been affected by crystal re-precipitation as well. The effects of increasing salinity, pressure and temperature on trace element mobility in the fluid phase are immediately apparent from the fluid compositions. For example, the concentrations of LILE and LREE in the fluids increase gradually with both metamorphic grade and salinity (Fig. 3.3.7).

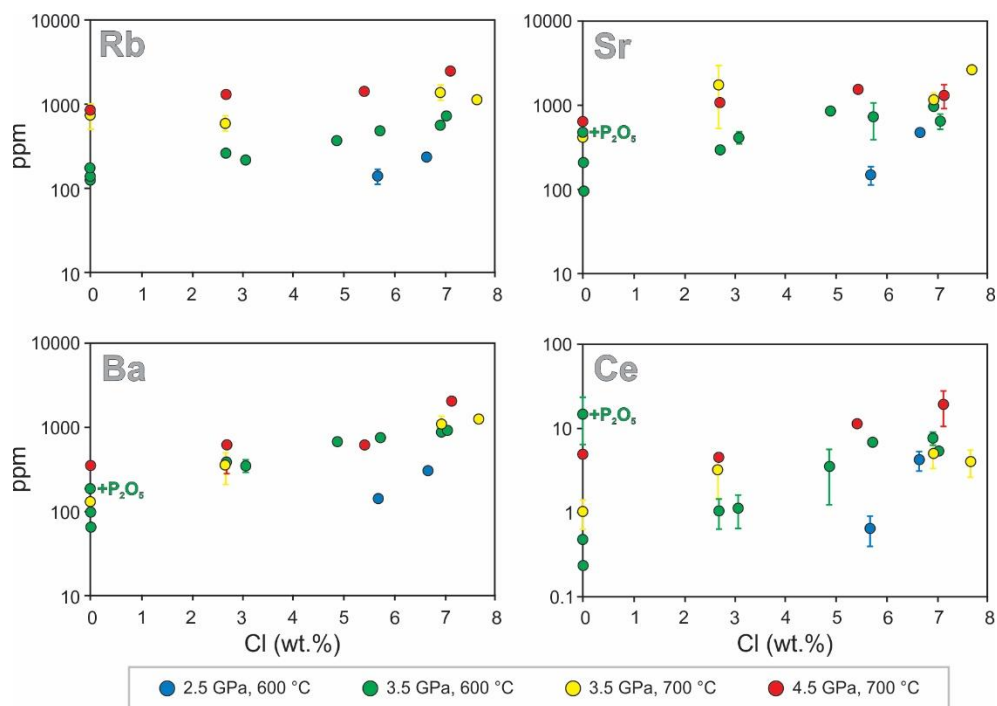


**Figure 3.3.7.** Concentrations of Rb, Sr, Ba and Ce in the fluid phase increase systematically with fluid salinity, pressure and temperature. When error bars (one standard deviation) are not indicated, the error is within the symbol.

### 3. Mantle metasomatism by sediment fluids in subduction zones

Phosphorous may also influence the properties of subduction zone fluids. Addition of 1.1 wt.% of  $P_2O_5$  in run “DT17” had dramatically increased  $SiO_2$  solubility in the fluid to nearly 50 wt.% (not shown in Fig. 3.3.8), while other major element concentrations remained similar as in phosphorous-free fluids. The solubilities of LREE were enhanced by the addition of phosphorous as well (Fig 3.3.7).

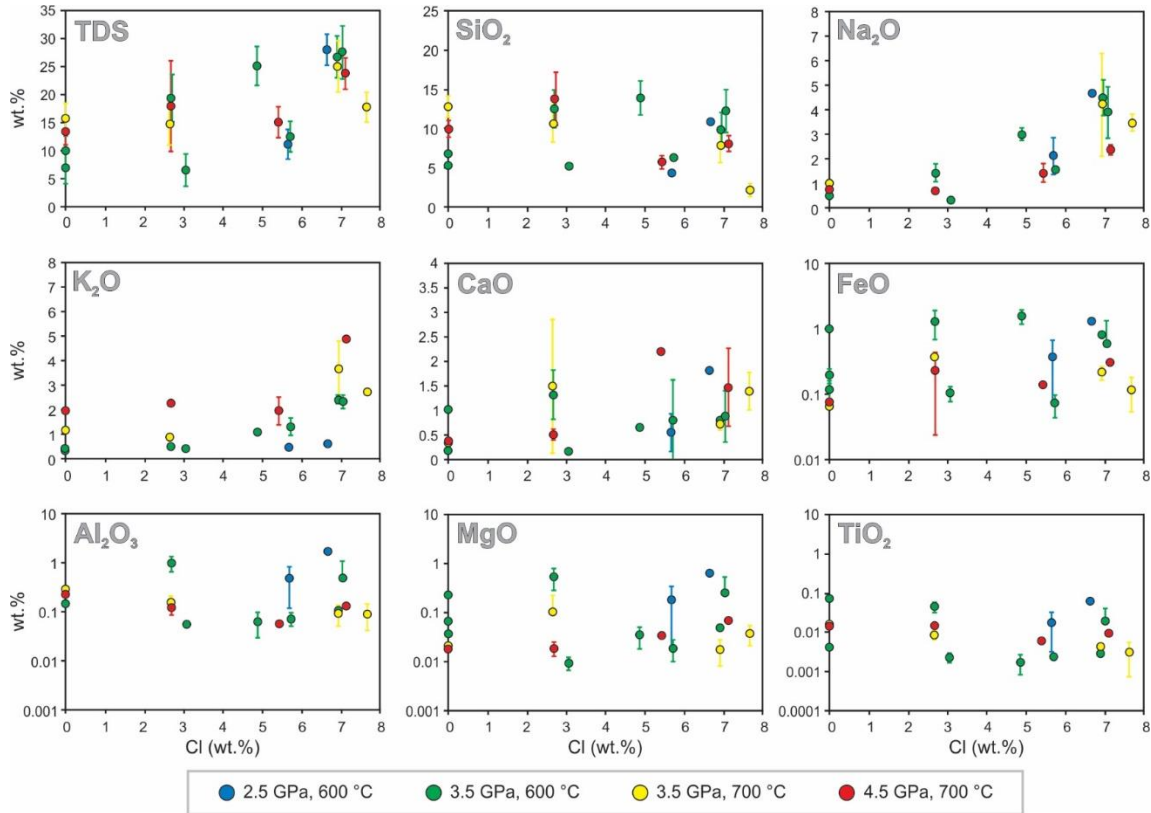


**Figure 3.3.8.** Major element oxide and Total Dissolve Solid (TDS) concentrations in the fluid phase as a function of fluid salinity. A positive correlation between salinity and  $Na_2O$ ,  $K_2O$  and  $CaO$  concentrations in the fluid is apparent. When the error bars (one standard deviation) are not indicated, the error is within the symbol.

### 3.3.3. Trace element partition coefficients

The fluid and mineral compositions, measured by LA-ICP-MS (Tables 3.3.9 to 3.3.16, Supplement II), were used to calculate the fluid/mineral trace element partition coefficients. Clinopyroxene may have an important role in the distribution of Li, Be and B between the fluid phase and metamorphic slab residues (Brenan et al., 1998). The Li, Be and B fluid/cpx partition coefficients measured in this study show no systematic dependence on fluid salinity or temperature. A noticeable increase in fluid/cpx partition coefficients for Be and B between pressures of 3.5 and 4.5 GPa at 700 °C was observed. The Rb, Cs, Sr, Ba and Pb fluid/cpx partition coefficients all systematically increase with temperature, but are not affected by pressure. In addition, an increase in fluid/cpx partition coefficients for Rb, Sr, Ba and Pb was observed with increasing fluid salinity. The measured Nb and Ta partition coefficients vary by an order of magnitude (Fig. 3.3.9). This may be related to re-precipitation of Nb and Ta in the diamond trap at run conditions (Ch. 3.3.2). However, due to the systematic change of clinopyroxene compositions with fluid salinity, the compatibility of Nb and Ta in run product clinopyroxene may also genuinely vary with the bulk sodium content of the samples. Baier et al. (2008) present a more comprehensive study of the solubility of Nb and Ta in clinopyroxene with compositions along the Di-Jd join. The order of magnitude of the lowest measured Nb and Ta fluid/cpx partition coefficients from this study (0.1 to 0.01) is in agreement with the values reported by Baier et al. (2008). With increasing salinity, the LREE fluid/cpx partition coefficients increase by about two orders of magnitude, likely due to the formation of chloride complexes in the fluid. The influence of chlorine on HREE partitioning is small in comparison (Fig. 3.3.9). The LREE fluid/cpx partition coefficients also generally increase with pressure and temperature.

A number of trace elements, which are otherwise fluid mobile, are strongly compatible in phengite. Therefore, the main interest in measuring fluid/phengite partition coefficients is to evaluate its role in fractionation of fluid mobile elements during progressive subduction. The fluid/pheng partition coefficients for several key trace elements are shown in Figure 3.3.10. The boron fluid/pheng partition coefficients are not clearly affected by either pressure, temperature or salinity. The Cs fluid/pheng partition coefficients increase with temperature, but are not affected by either salinity or pressure. The partitioning of Ba into the fluid increases abruptly between 2.5 and 3.5 GPa at

600 °C, but is otherwise mostly controlled by fluid salinity, which can increase the Ba fluid/pheng partition coefficients by up to two orders of magnitude.

The fluid/pheng partition coefficients for Rb increase systematically with pressure, temperature and salinity. Some positive correlation of Sr fluid/pheng partition coefficients with fluid salinity is observed, at least in runs < 4.5 GPa, but Sr partitioning into the fluid is mostly influenced by temperature. Fluid salinity has a clear effect on Pb fluid/pheng partition coefficients and some temperature dependence can be inferred as well.

Phengite is the main solid reservoir for B, Cs, Ba and Rb in the run product metapelitic residues, whereas considerable proportions of Sr and Pb were distributed between both phengite and lawsonite. In addition to clinopyroxene, phengite was the other significant reservoir for Li and Be. These observations – the order of element solubility in the fluid and the distribution of fluid mobile elements among different solid reservoirs – agree well with the descriptions of exhumed metapelites from the Catalina Schist (Bebout et al., 2007).

The lawsonite crystal structure contains favorable sites for Sr, Pb, U, Th and REE (Ch. 3.1). The lawsonite in most metapelitic residues from this study contained considerable proportions of Sr, Pb and REE, but the concentrations of Th and U were typically comparable to those detected in other major minerals. The Sr and Pb fluid/laws partition coefficients increase by about one order of magnitude with increasing chlorine content in the fluid. The REE are strongly retained by lawsonite, with partition coefficients of  $\leq 0.01$  for LREE and  $\leq 0.1$  for HREE (Fig. 3.3.11). The increase in fluid salinity results in a systematic increase of LREE fluid/laws partition coefficients. No clear effects of pressure and temperature on fluid/laws partition coefficients were observed. At 3.5 GPa and 700 °C, only one direct measurement of lawsonite composition was possible (experiment “DT21”). The lawsonite aggregate crystals in low salinity runs at 4.5 GPa and 700 °C were considerably contaminated with phengite and clinopyroxene. However, assuming that Nernst distribution law is applicable, the entire set of fluid/laws partition coefficients can be derived from the measured clinopyroxene/lawsonite partition coefficients and from the clinopyroxene and fluid compositions in individual runs.

3. Mantle metasomatism by sediment fluids in subduction zones

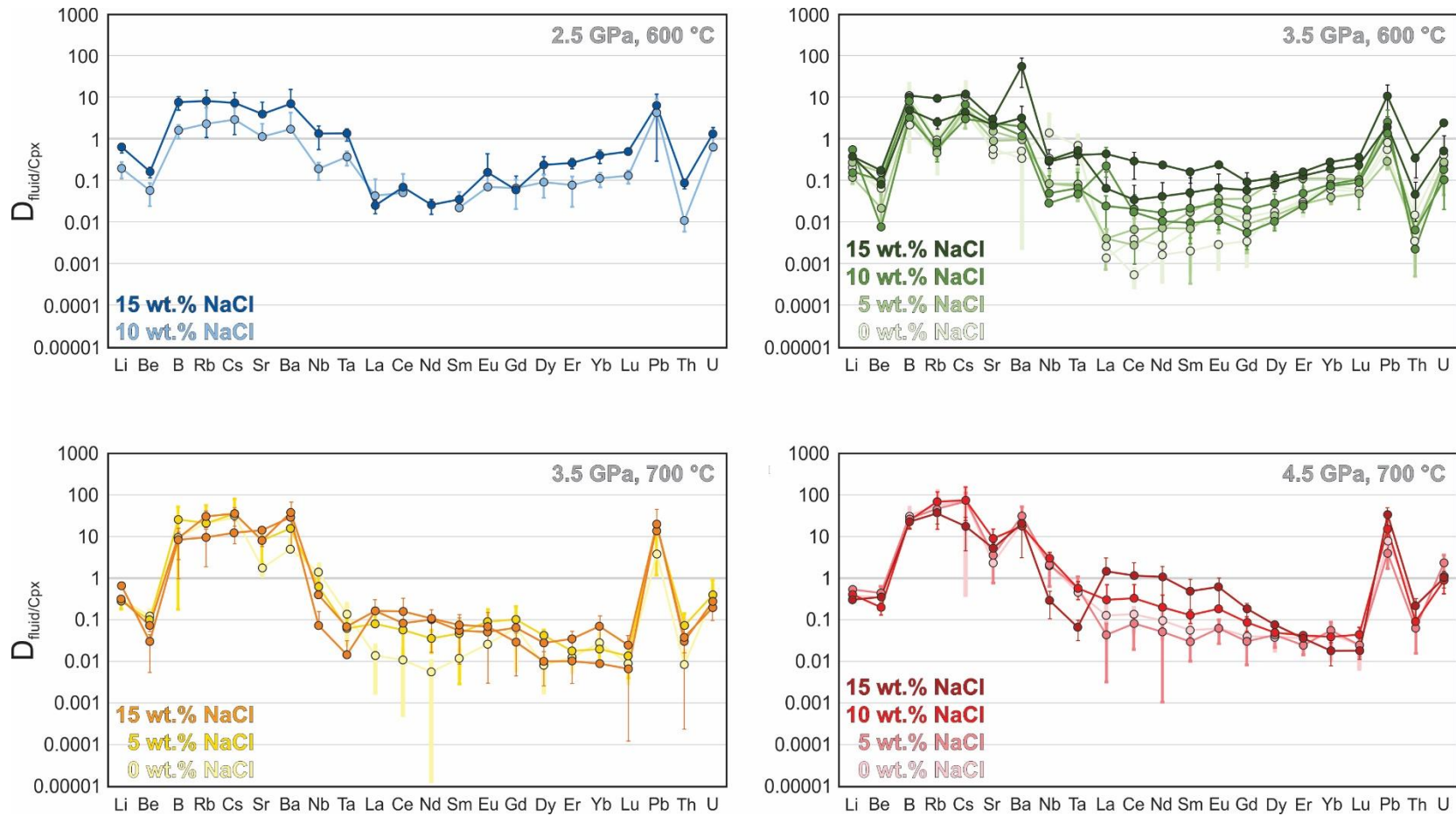


Figure 3.3.9: Experimentally measured fluid/cpx trace element partition coefficients.

3. Mantle metasomatism by sediment fluids in subduction zones

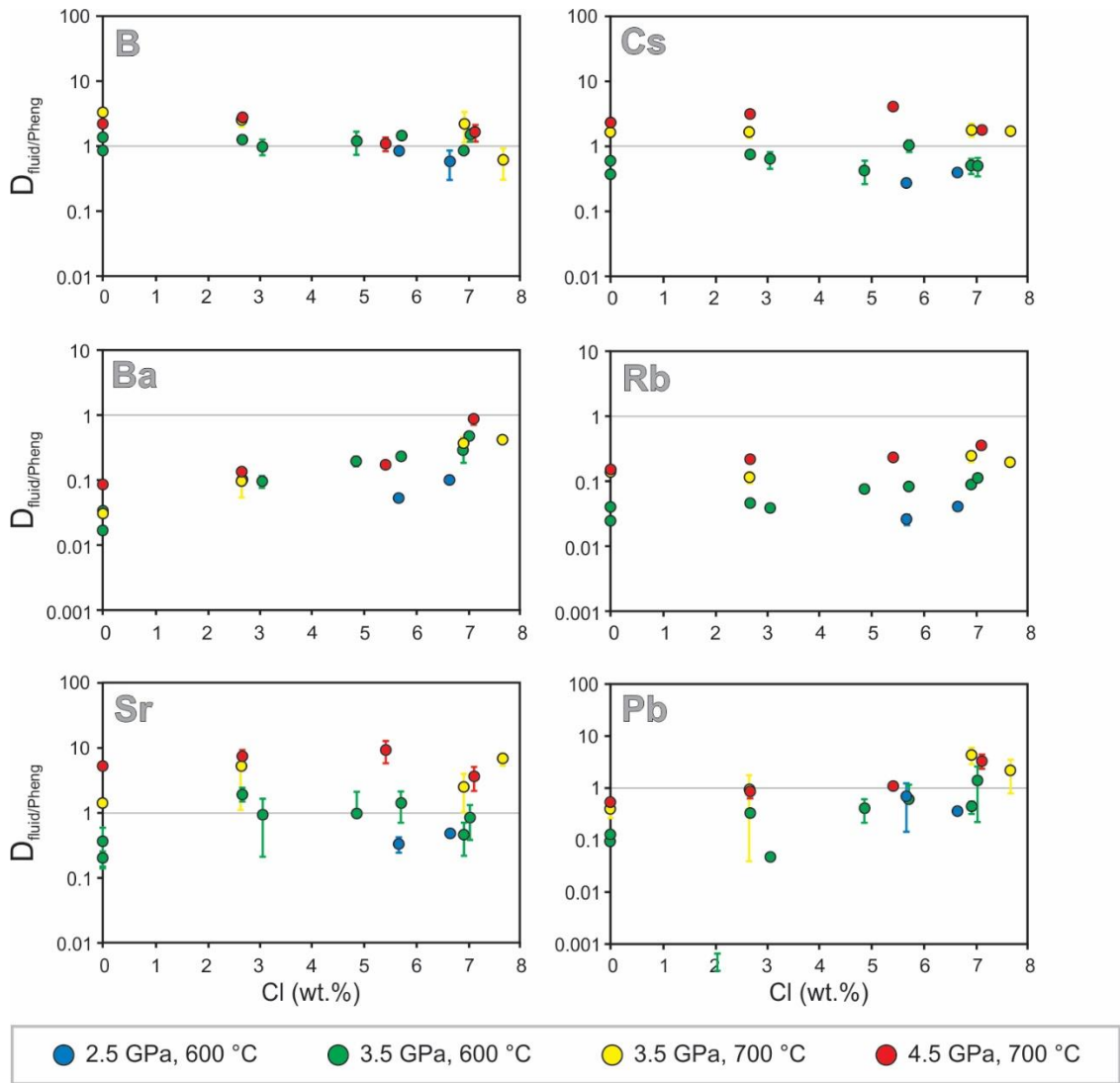
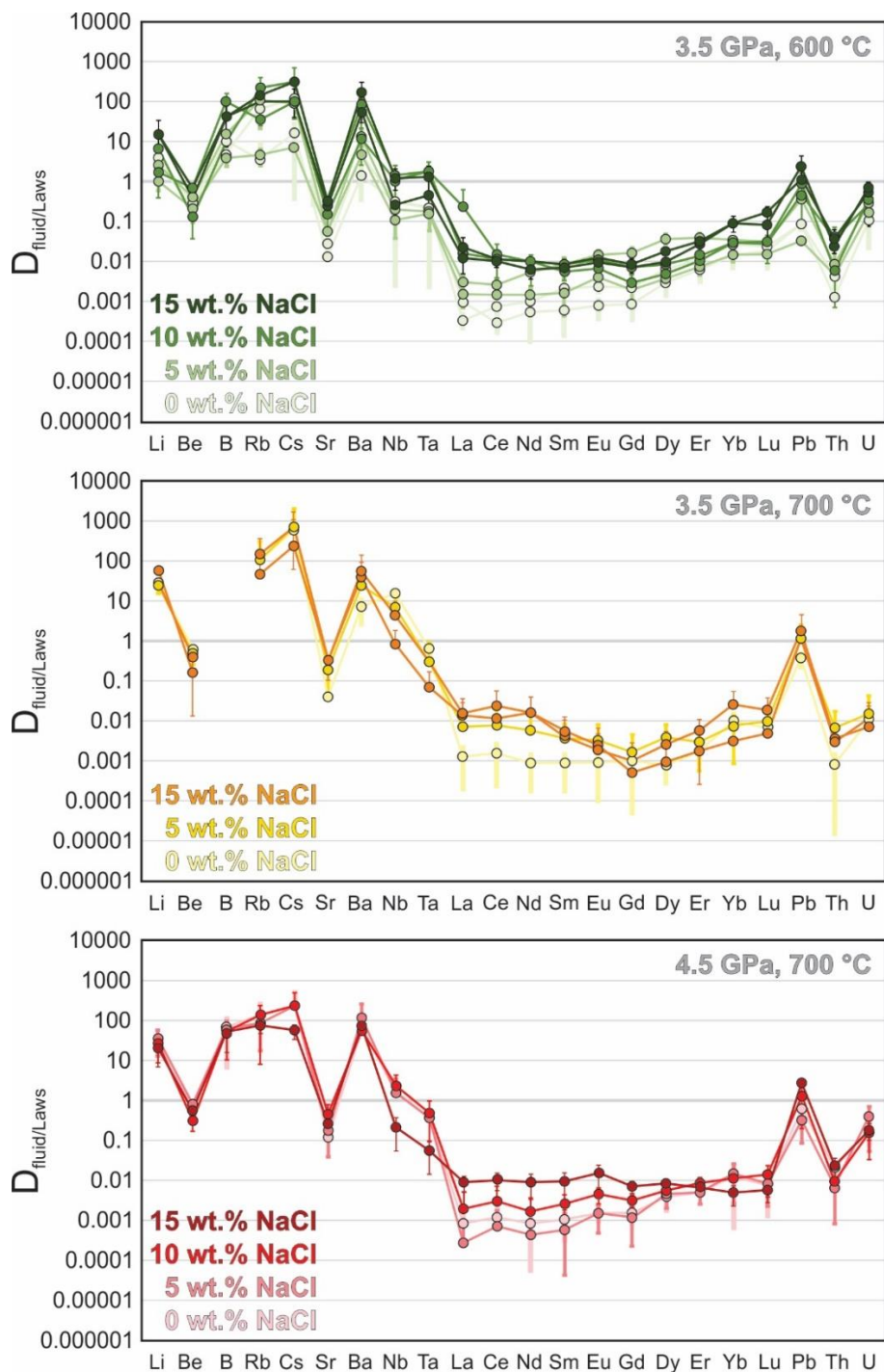


Figure 3.3.10: Experimentally measured fluid/pheng trace element partition coefficients as a function of fluid salinity.

The garnet, when stable, effectively retains HREE – the measured fluid/grt partition coefficients for HREE are  $\approx 0.001$  (Fig. 3.3.12). The addition of up to 8 wt.% of chlorine to the fluid increases LREE fluid/grt partition coefficients by one order of magnitude. As a result, the LREE fluid/grt partition coefficients approach 1 in equilibrium with high salinity fluids. The fluid/grt partition coefficients for several trace elements (Be, Rb, Cs, Ba) systematically increase with pressure by up to one order of magnitude.

### 3. Mantle metasomatism by sediment fluids in subduction zones



**Figure 3.3.11:** Experimentally measured fluid/laws trace element partition coefficients. The fluid/laws partition coefficients at 3.5 GPa and 700 °C with (initial) fluid salinities of 5 and 15 wt.% NaCl are derived from the clinopyroxene/lawsonite partition coefficient measured in equilibrium with chlorine free fluid and from the corresponding clinopyroxene and fluid compositions. The fluid/laws partition coefficients at 4.5 GPa and 700 °C with (initial) fluid salinities of 0, 5 and 10 wt.% NaCl are derived from the clinopyroxene/lawsonite partition coefficient measured in equilibrium with a fluid containing 15 wt.% NaCl (initially) and from the corresponding clinopyroxene and fluid compositions.

### *3. Mantle metasomatism by sediment fluids in subduction zones*

To be able to perform mass balance, and to determine the bulk fluid/rock partition coefficients, mass proportions of major minerals were estimated as a part of the iterative procedure for fluid composition calculation. In the first step, the major element oxides with low solubilities in the fluid are used to obtain the initial estimate of mineral proportions. For the Cpx + Pheng + Laws/Zo + Coe/Qtz assemblages, the mineral proportions are calculated from the concentrations of CaO, MgO and Al<sub>2</sub>O<sub>3</sub> in the minerals, assuming the solid residue behaved as a closed system for these elements at run conditions. EPMA mineral analyses were used for the calculation, and Coe/Qtz proportion was constrained from the sum of proportions of other solid phases. The initial mineral proportions and the LA-ICP-MS measurements of mineral compositions are then used to estimate the weight of Cs which was retained in the solids. The fluid composition is calculated using Cs as an internal standard, assuming the corrected Cs concentration in the fluid. The standard correction for mass exchange between the fluid and solid is included in the calculation. At 600 °C, up to approximately 50 % of Cs is stored in the solid phases, resulting in a half an order of magnitude correction of both major and trace element concentrations in the fluid. At 700 °C, typically < 30 % of Cs is dissolved in minerals. In the following steps of the calculation, the bulk CaO, MgO and Al<sub>2</sub>O<sub>3</sub> concentrations in the metamorphic residue are refined for dissolution in the fluid, and for the hydration of solid phases. The mineral mass proportions, the weight of Cs dissolved in minerals and the fluid composition are also re-calculated in each step.

To obtain mineral proportions in the Cpx + Pheng + Grt + Laws + Coe assemblages, FeO concentrations in minerals were used for the calculation as well. Iron absorption by platinum capsule walls was assumed to be limited at low temperatures.

Mass balance for major element oxides that were not constrained by the mineral proportion calculation can be evaluated. EPMA mineral compositions and LA-ICP-MS fluid compositions are used for the mass balance. The sum of measured weights of Na<sub>2</sub>O, K<sub>2</sub>O, SiO<sub>2</sub> and FeO in 600 °C samples are within -16 to +25 wt.%, 0 to +26 wt.%, -20 to -7 wt.% and -13 to +1 wt.%, respectively, compared to the theoretical totals. In samples from 700 °C, the measured weights of Na<sub>2</sub>O, K<sub>2</sub>O and SiO<sub>2</sub> are within -44 to +14 wt.%, -15 to +39 wt.% and -12 to +1 wt.% from the expected totals, respectively. Given the robust nature of the calculation, the observed chemical

zonation in solid phases and the intrinsic uncertainties in fluid composition measurements, these major element oxide totals are acceptable.

The mineral mass proportions are summarized in Figure 3.3.13. Lawsonite compositions remain constant with changing pressure, temperature and fluid salinity (Ch. 3.3.2). Therefore, the EPMA lawsonite composition from run “DT21” at 3.5 GPa and 700 °C could be used to estimate the proportions of major minerals in samples where lawsonite was not directly observed. This was necessary in order to obtain a realistic phengite proportion for the correction of fluid compositions. With increasing salinity of the fluid, the mass proportions of clinopyroxene increase to accommodate some of the excess sodium introduced by the addition of NaCl. Simultaneously, the coesite/quartz proportions decrease with increasing fluid salinity. The average phengite, lawsonite/zoisite and garnet proportions also decrease with increasing salinity, but these trends in mineralogy may not be statistically significant. The proportion of phengite is pressure dependent. In the investigated pressure range, the average phengite proportions systematically decrease from > 25 wt.% (per weight of the solid residue) at 2.5 GPa to between 15 and 20 wt.% at 4.5 GPa. The lawsonite proportions may decrease with increasing temperature. The low inferred proportion of lawsonite at 3.5 GPa and 700 °C suggests that these conditions are close to the lawsonite stability limit in the water-saturated GLOSS-H<sub>2</sub>O system. A summary of the calculated mineral mass proportions is presented in Table 3.3.17 (Supplement II).

For the following discussion, the major mineral mass proportions were averaged at each P-T condition to compensate for the changes in mineralogy due to excess sodium, and to isolate the effect of chlorine on bulk fluid/rock trace element partition coefficients. Simultaneously, the averaged mineral proportions generally capture the expected changes in mineralogy with increasing pressure and temperature. Therefore, some conclusions about the effect of metamorphic grade on bulk fluid/rock partition coefficients can be made as well. It should be noted that these bulk fluid/rock partition coefficients are representative of the experimental run products from this study, which had crystallized under water-saturated conditions and are a closed system.

### 3. Mantle metasomatism by sediment fluids in subduction zones

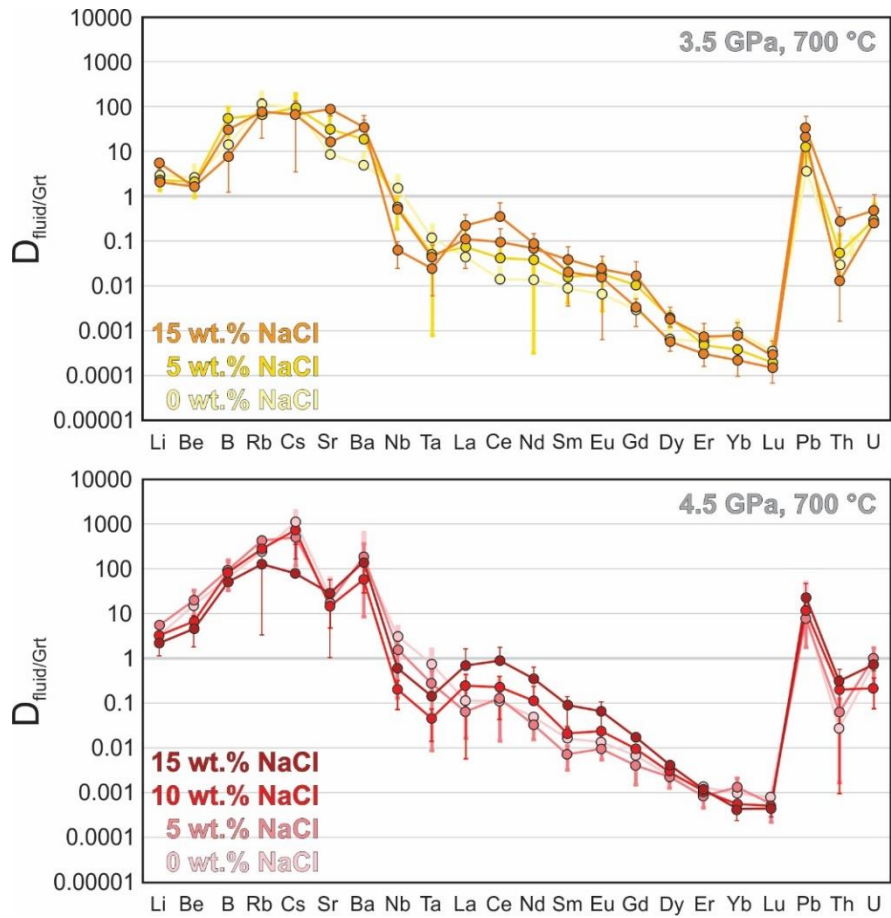


Figure 3.3.12: Experimentally measured fluid/grt trace element partition coefficients.

The bulk fluid/rock partition coefficients are calculated as:

$$D_{fluid/rock} = \frac{1}{\sum \frac{w_{mineral}}{D_{fluid/mineral}}} \quad \text{Eq. 3.3.1.}$$

where  $w_{mineral}$  are the calculated mineral mass proportions, averaged for each P-T condition. Note that in the following discussion, only the major minerals are considered. The effect of accessory phases on bulk fluid/rock partition coefficients will be discussed later (Ch. 3.3.4).

3. Mantle metasomatism by sediment fluids in subduction zones

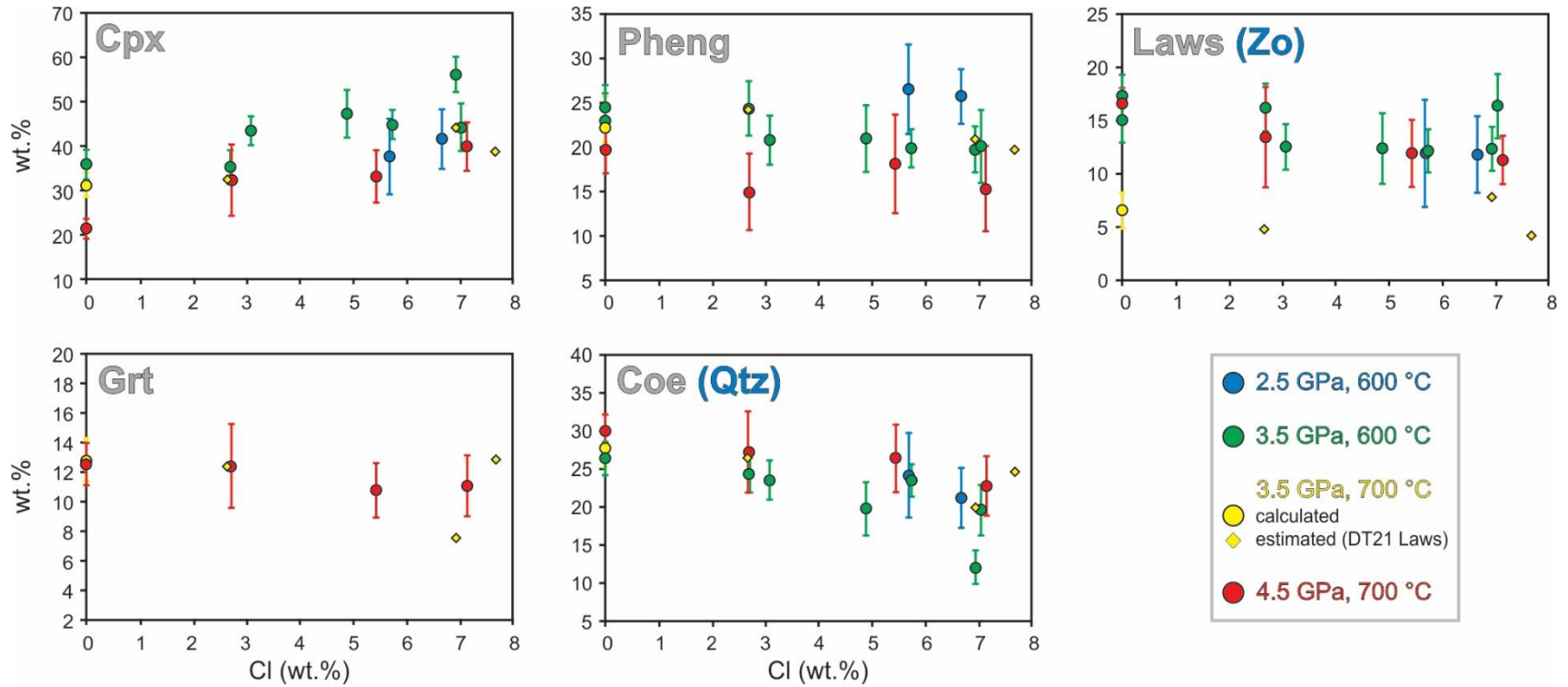


**Figure 3.3.13:** Mass proportions of major minerals in solid residues as a function of fluid salinity. The mineral proportions in some runs at 3.5 GPa and 700 °C are estimated using lawsonite composition from run “DT21” (see text for further explanation).

The effect of chlorine on Rb, Sr, Ba, Pb and LREE fluid/rock partition coefficients is systematic. At constant pressure and temperature (Fig. 3.3.14), the LREE fluid/rock partition coefficients are enhanced by up to two orders of magnitude by the addition of chlorine to the fluid, while the increase of fluid/rock partition coefficients is typically  $\leq$  one order of magnitude for the more fluid mobile elements. The partitioning of some elements (Li, Be, B, Cs) into the fluid is not enhanced by chlorine, but generally increases with pressure and temperature (Fig. 3.3.15). In addition to chlorine, fluid/rock partition coefficients of Rb, Sr, Ba and Pb are also significantly enhanced by the increase in pressure and/or temperature.

In equilibrium with low salinity fluids, the LREE fluid/rock partition coefficients are increased by one order of magnitude with increasing temperature (Fig. 3.3.15). At high fluid salinities, the increase of LREE fluid/rock partition coefficients due to the effect of temperature is only about half an order of magnitude (Fig. 3.3.15). The difference in LREE fluid/rock partition coefficients between 2.5 and 3.5 GPa at 600 °C is not attributed to a major change in fluid properties, but rather to a lawsonite dehydration reaction which forms zoisite. The zoisite in runs from 2.5 GPa co-exists with allanite, which has more than half an order of magnitude higher REE concentrations and could be visually distinguished in BSE images. The stabilization of garnet in samples from 700 °C lowers the fluid/rock HREE partition coefficients, compared to those measured in samples from 600 °C.

3. Mantle metasomatism by sediment fluids in subduction zones

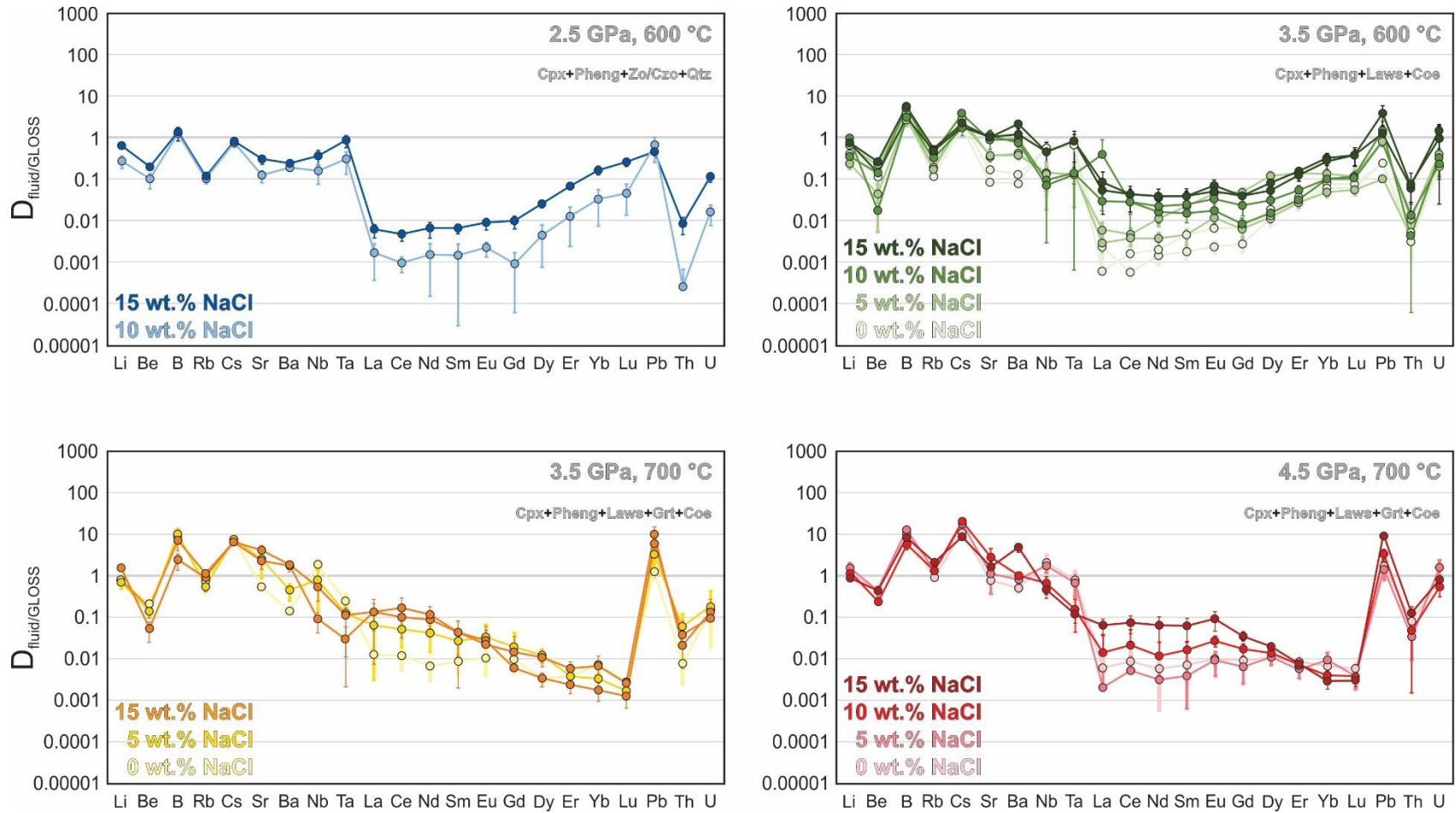


**Figure 3.3.14:** The effect of chlorine on the fluid/rock trace element partition coefficients at constant pressure and temperature. The effect of accessory phases is not considered in these diagrams.

3. Mantle metasomatism by sediment fluids in subduction zones

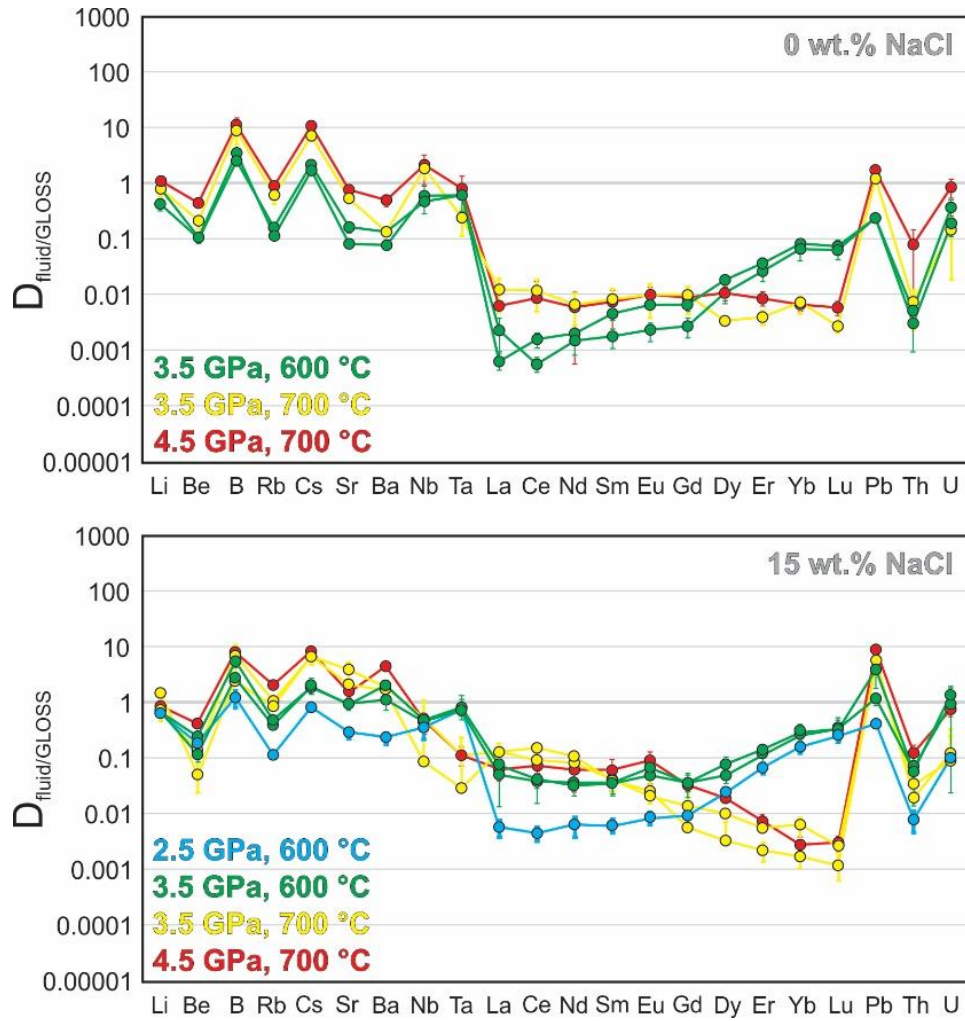


**Figure 3.3.15.** The effect of pressure and temperature on the fluid/rock trace element partition coefficients at constant salinity. The effect of accessory phases is not considered in these diagrams.

### 3.3.4. Accessory minerals

The compositions of accessory minerals were measured primarily for the purpose of trace element mass balance. Four examples of trace element mass balance are shown in Figure 3.3.16. The fluid/rock partition coefficients calculated for major mineral assemblages are compared to the fluid/rock partition coefficients for assemblages containing accessory phases. The fluid/rock partition coefficients can also be estimated through “mass balance” by subtracting the trace element content measured in the fluid from the initial trace element content of the doped solid material, thus obtaining the concentrations in the bulk rock. If the approach is sound, there should be a reasonable agreement between the “mass balance” and the calculated fluid/rock partition coefficients (with all accessory phases included).

In all four of the chosen samples (“DT4”, “DT6”, “DT14”, “DT20”), the only identified accessory phases are rutile and allanite. The proportions of rutile and allanite are estimated from the mass balance deficits of TiO<sub>2</sub> (EPMA) and La (LA-ICP-MS). The mass balance for Nb, Ta, Th, U and the remaining REE is unconstrained.

A mass balance deficit of Be in some samples (Fig. 3.3.16.) might be attributed to the presence of a Be-rich accessory phase, which was occasionally observed and its composition could be measured in some instances. The stoichiometry obtained from EPMA and LA-ICP-MS analyses (4.5 wt.% Be, 43 wt.% SiO<sub>2</sub> and 34 wt.% Al<sub>2</sub>O<sub>3</sub>) is similar to the chemical composition of euclase, a rare pegmatite mineral.

A mass balance excess of boron, ranging from +20 to +150 wt.%, is observed in all samples, but the source of contamination could not be confirmed. The other fluid mobile elements can be mass balanced with great success. The mass balance totals for Rb, Sr, Cs, Ba and Pb are in most cases within  $\pm 30$  wt.%, compared to theoretical totals. The similarity between the “mass balance approach” and fluid/rock partition coefficients calculated for major mineral assemblages suggests that these elements dissolved exclusively in the fluid and in major solid phases – no accessory minerals were formed to accommodate for doping. The excess Rb and Ba in sample “DT14” (Fig. 3.3.16) can be correlated with the highest mass balance excess of K<sub>2</sub>O (+39 wt.%, Ch. 3.3.3) and is perhaps related to an overestimation of phengite proportion in this sample.

### 3. Mantle metasomatism by sediment fluids in subduction zones

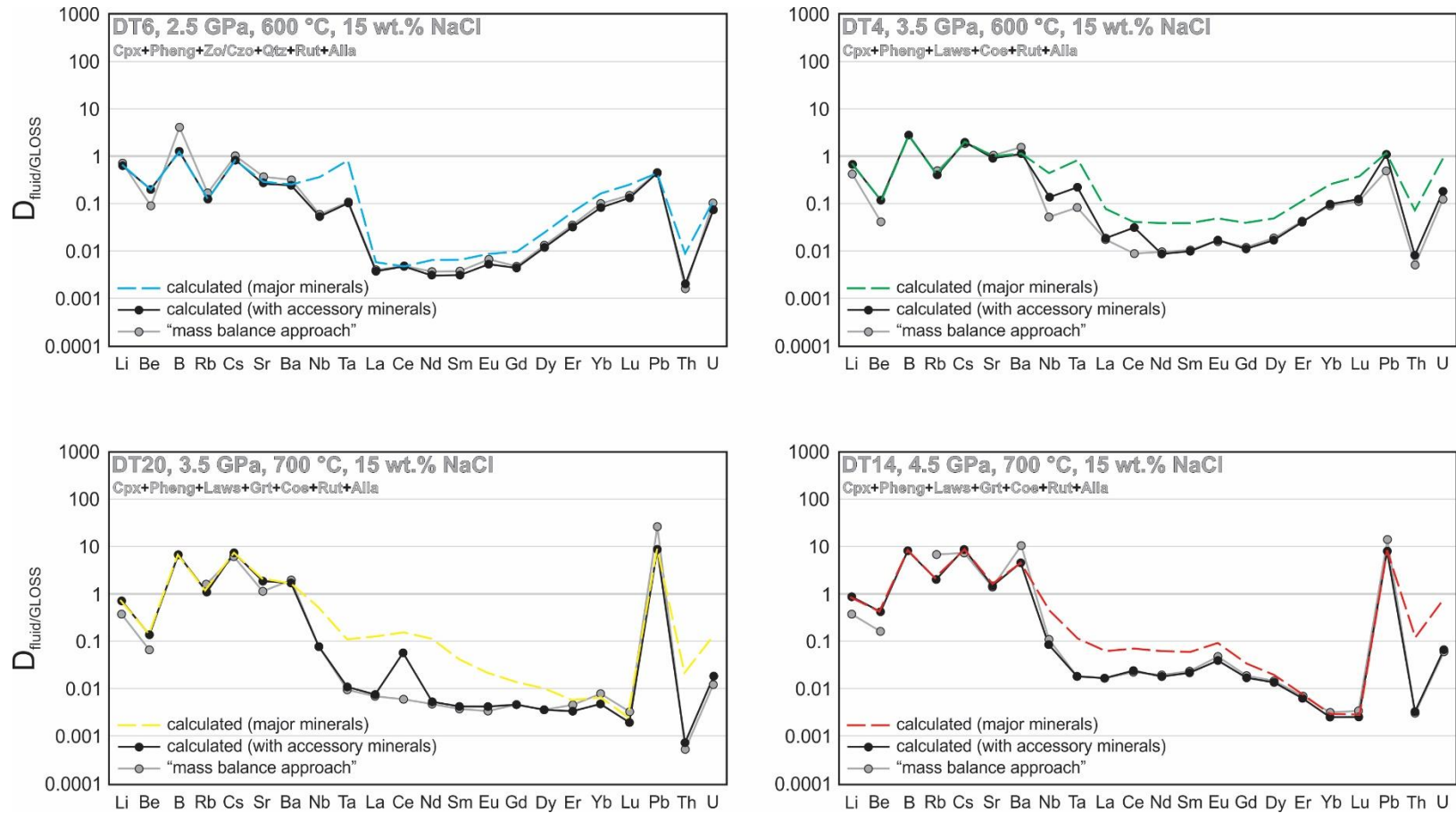


**Figure 3.3.16:** Four examples of trace element mass balance. The colored dashed lines indicate the fluid/rock partition coefficients shown in previous figures (Fig. 3.3.14. and 3.3.15). Black circles are the fluid/rock partition coefficients calculated using fluid/mineral partition coefficients of all identified major and accessory minerals. The grey circles represent the “mass balance approach” to fluid/rock partition coefficient calculation, which is based on the measured fluid compositions and the bulk solid residue trace element concentrations. A good fit between the “mass balance approach” and calculated values (with all accessory phases included) indicates a successful trace element mass balance. The difference between the “mass balance approach” and the calculated values for major mineral assemblages are mainly artifacts of trace element doping and subsequent spurious nucleation of trace element rich accessory phases.

A mass balance deficit of Nb and Ta was found in all samples from 3.5 GPa and 600 °C, suggesting consistent formation of an unknown additional Nb- and Ta-rich accessory phase. Under these conditions, rutile always contained nearly 100 wt.% TiO<sub>2</sub> when analyzed by EPMA, with Nb and Ta concentrations in the order of thousands of ppm. At all other P-T conditions, Nb and Ta could be mass balanced to within  $\pm 30$  wt.% from the expected value, indicating that rutile was the main reservoir for these elements. However, these rutiles often had low EPMA totals and contained in excess of 10 000 ppm of Nb and Ta, each. Similar Nb- and Ta-rich rutile had been observed by Kessel et al. (2005), but only in samples synthesized at high temperatures. In run “DT12” nearly pure rutile co-existed with Nb- and Ta-rich rutile grains. The single EPMA analysis of rutile composition from “DT12” contained approximately 100 wt.% TiO<sub>2</sub>, but the average Nb and Ta concentrations, obtained by LA-ICP-MS in other rutile grains, were 12 716 and 15 010 ppm, respectively (Table 3.3.14, Supplement II). In addition, the measurement errors of Nb and Ta concentrations in rutile from this sample are large, indicating a variation in composition (Table 3.3.14, Supplement II).

When the proportions of allanite inferred from the deficit of La are used for mass balance, a good agreement between the expected and measured totals for other REE, U and Th can be achieved (usually within  $\pm 50$  wt.%). Therefore, the allanite is thought to be the main reservoir for these trace elements. The only notable exception was Ce, which formed an unknown additional accessory phase in some samples (e.g. “DT4” and “DT20”). The inferred allanite proportions are typically 1 to 3 wt.%. This is realistic, given the starting material composition and the measured REE concentrations in allanite. The allanite composition may vary from one experiment to another. Some compositional heterogeneity in allanites within the same sample was observed as well (Table 3.3.13, Supplement II).

Variants of the “mass balance approach” were used in previous studies of trace element release from the subducted sediments (e.g. Spandler et al., 2007). For some fluid immobile elements, the differences in the “mass balance approach” and the calculated fluid/rock partition coefficients for major mineral assemblages vary from negligible (“DT6”) to more than one order of magnitude (“DT20”). This is a direct indication of the potential problems related to the use of the “mass balance approach” in combination with a starting material containing high trace element

abundancies. Such problems may arise both with doped synthetic mixtures (e.g. Spandler et al, 2007) and with natural trace element rich starting materials (e.g. Johnson and Plank, 1999).

The mass balance calculations presented here suggest that most trace elements can be successfully accounted for, provided all accessory phases are identified and analyzed by LA-ICP-MS. It also confirms the overall accuracy of the LA-ICP-MS mineral analyses and supports the iterative approach for calculating the mineral proportions and fluid compositions.

Hermann (2002) proposed that allanite controls REE distribution between the slab and the fluid phase. However, allanite may not be stable in natural eclogites at peak metamorphic conditions. In systems with naturally occurring trace element abundancies, allanite could be replaced by a small mass proportion of another epidote group mineral, one with order(s) of magnitude lower REE concentrations. For example, Carter et al. (2015) used natural oceanic crust as a starting material and found accessory epidote in a similar pressure and temperature range where Kessel et al. (2005), who used a doped MORB starting material, observed allanite. Nevertheless, the results of mass balance presented in Figure 3.3.16. indicate that allanite precipitation would have little influence on natural subduction zone fluid compositions. The concentrations of REE in the starting material from this study are approximately 10 to 100 times higher than the GLOSS average (Plank, 2013). Therefore, the maximum proportion of allanite in natural eclogites, and its ability to retain REE, should be at least one order of magnitude lower than in the experimental run products from this study (Fig. 3.3.16).

The residual rutile may retain considerable proportions of HFSE and could contribute to the overall Nb and Ta depletion in the fluid phase, relative to LILE and LREE (Brenan et al., 1994). The fluid/rutile partition coefficients for Nb and Ta measured at 3.5 GPa and 600 °C were between 0.01 and 0.001. Including rutile in the calculation caused up to half an order of magnitude decrease of the Nb and Ta fluid/rock partition coefficients. The estimated rutile proportions in solid residues from this study (0.2 to 0.5 wt.%) are likely representative of natural metasedimentary lithologies. The metabasalts have a higher bulk TiO<sub>2</sub> concentration (Gale et al., 2013) and may contain 1 to 2 wt.% of rutile. Therefore, in metabasaltic lithologies rutile may lower the Nb and Ta fluid/rock partition coefficients by up to one order of magnitude. In other experiments, the measured

fluid/rutile partition coefficients for Nb and Ta were between 0.001 and 0.00001, due to considerably higher Nb and Ta concentrations in rutile. The Nb- and Ta-rich variety of rutile could hypothetically lower the Nb and Ta fluid/rock partition coefficients by one order of magnitude in metasedimentary, and by two orders of magnitude in metabasaltic slab lithologies. However, the co-existence of both types of rutile in sample “DT12” may suggest one variety is metastable under the investigated conditions. Kinetic factors, which are beyond the scope of this study, might be involved in nucleation of Nb- and Ta-bearing accessory phases. If so, experimental estimation of the role of rutile in HFSE depletion might be susceptible to large uncertainties, especially when a doped starting material is used. Nevertheless, the results indicate that rutile precipitation is one of the causes of the negative “Nb-Ta anomaly” in subduction zone fluids.

It should be emphasized that the assumption of infinite dilution is neither valid for REE concentrations in allanite, nor for the Nb and Ta concentrations in Nb- and Ta-rich rutile observed in this study. Changing the bulk REE, Nb and Ta contents of the starting material would therefore likely influence the fluid/alla and fluid/rut partition coefficients to some degree, in response to changes in the activity coefficients of the trace elements in the accessory phases.

Apatite is a common accessory mineral in eclogites and its structure allows incorporation of a number of trace elements (Sr, Ba, REE, Pb, U, Th) of geochemical interest (Mao et al., 2016). To measure the composition of residual apatite and estimate its effect on trace element mobility in subduction zones, the fluid in run “DT17” was doped with phosphorous to introduce 1.1 wt.%  $P_2O_5$  (per weight of solid material) (Ch. 3.2.1).

### 3. Mantle metasomatism by sediment fluids in subduction zones

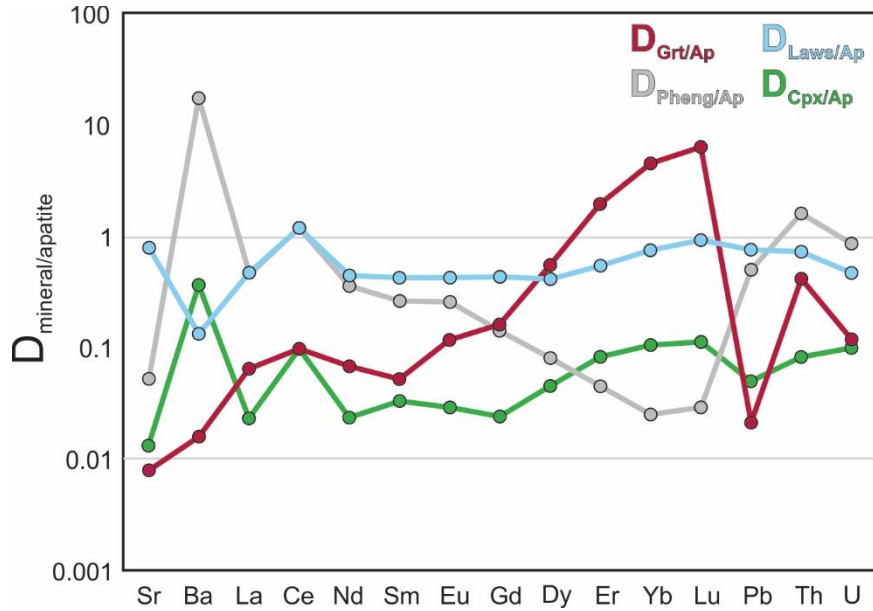


**Figure 3.3.17:** Experimentally determined mineral/apatite partition coefficients for relevant trace elements at 3.5 GPa and 600 °C. The measured partition coefficients are above 0.01, suggesting minor influence of apatite on the fluid composition.

The effect of apatite precipitation on fluid composition is negligible and this is immediately apparent from the mineral/apatite partition coefficients (Fig. 3.3.17). The proportion of apatite in slab lithologies is an order of magnitude lower compared to the proportions of other solid phases, so it cannot exert considerable control over the fluid composition unless fluid/apatite partition coefficients are at least two orders of magnitude lower than fluid/mineral partition coefficients for clinopyroxene, phengite, lawsonite and garnet. The results presented in Fig. 3.3.17. indicate that this is not the case – most of the measured mineral/apatite partition coefficients are higher than 0.01 for the trace elements of interest. In particular, there is very little trace element fractionation between apatite and lawsonite, which was the main host for Sr and REE in the experimental run products. In addition, a large proportion of phosphorous may dissolve in garnet at peak metamorphic conditions (Konzett, 2016), and in some subduction zones apatite may not precipitate at all.

The introduction of phosphorous into the system had two other significant consequences: 1) the trace element transport properties of the fluid phase were modified (Fig. 3.3.18) and 2) garnet was stabilized at 600 °C.

### 3. Mantle metasomatism by sediment fluids in subduction zones

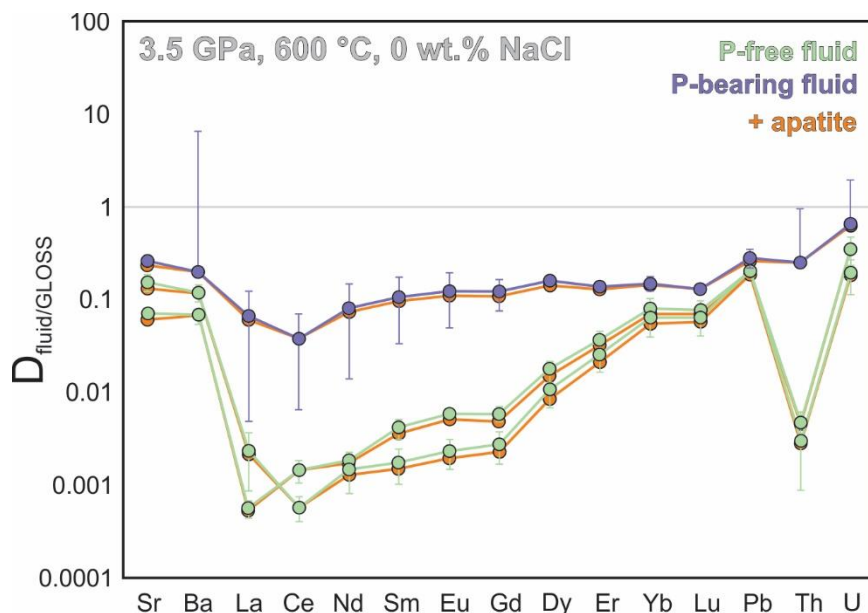


**Figure 3.3.18:** A comparison of fluid/rock partition coefficients for relevant trace elements measured in equilibrium with phosphorous free and phosphorous bearing fluids. Pressure, temperature and salinity were kept constant (3.5 GPa, 600 °C and 0 wt.% NaCl). The effect of apatite precipitation is shown as well.

Early test calculations demonstrated a good agreement between fluid compositions derived using Cs and B as internal standards. Due to B contamination, the concentrations of all elements in the fluid were slightly underestimated when it was used as internal standard. However, the factor of underestimation was usually less than two. An unknown Cs-bearing accessory mineral was observed in sample “DT17”. The precipitation of this phase disqualified Cs as internal standard for fluid composition calculation, and B was used instead (Table 3.3.16, Supplement II). The LREE fluid/mineral partition coefficients measured in “DT17” increased by nearly two orders of magnitude (Fig. 3.3.18) compared to phosphorous free runs at constant pressure (3.5 GPa), temperature (600 °C) and salinity (0 wt.% NaCl). In most subduction zones, the metabasalts and metapelites both contain around 0.2 wt.% P<sub>2</sub>O<sub>5</sub> (Gale et al., 2013; Plank, 2013) – an approximately 5 times lower concentration compared to “DT17”. Therefore, the effect of phosphorous on the properties of natural subduction zone fluids is expected to be smaller than indicated in Figure 3.3.18. Still, these results suggest that, despite the precipitation of accessory phosphates, the addition of phosphorous to the system may actually enhance the mobility of some trace elements.

### 3.3.5. Modelling the sediment trace element contribution in arc magmas

The experimental dataset was described mathematically to allow some extrapolation of the measured fluid/mineral partition coefficients, as well as to reduce random measurement errors. Expressing the fluid/mineral, instead of the fluid/rock partition coefficients, opens the opportunity to model different mineralogies. Estimating the compositions of sediment- and basalt-derived fluid mixtures is a particularly important avenue of future research.

The fluid/mineral trace element partition coefficients may be affected by changes in pressure, temperature and salinity (e.g. Keppler, 1996). The variation of measured fluid/mineral partition coefficients with these parameters was described by an equation of the type:

$$\ln(D) = a + \frac{b}{T} + cP + dCl + eTCl \quad \text{Eq. 3.3.2.}$$

where T is temperature in °C, P is pressure in GPa and Cl is salinity in wt.% of Cl in the fluid. For a number of trace elements, the effect of fluid salinity on fluid/mineral partition coefficients clearly decreases with increasing temperature. Therefore, the term eTCl was introduced to allow a more accurate prediction. All relevant fit parameters for major minerals (clinopyroxene, phengite, lawsonite and garnet) are summarized in Tables 3.3.18. to 3.3.21.

Rutile is assumed to be an empty reservoir for all trace elements, except Nb and Ta. The Nb and Ta fluid/mineral partition coefficients for rutile are primarily a function of temperature and the obtained fit parameters are:  $a_{Nb} = -13.67$ ,  $b_{Nb} = 2542$ ,  $c_{Nb} = 0.84$ ,  $d_{Nb} = 1.264$ ,  $e_{Nb} = -0.0021$ ,  $R^2_{Nb} = 0.73$ ,  $a_{Ta} = -32.85$ ,  $b_{Ta} = 12938$ ,  $c_{Ta} = 1.35$ ,  $d_{Ta} = 1.412$ ,  $e_{Ta} = -0.0022$  and  $R^2_{Ta} = 0.94$ .

If no clear effect of either pressure, temperature, or fluid salinity on a fluid/mineral partition coefficient was observed (typically accompanied by  $R^2 < 0.4$ ), an average of the experimental values was used in the model. The averaged fluid/mineral partition coefficients are also shown in Tables 3.3.18. to 3.3.21.

3. Mantle metasomatism by sediment fluids in subduction zones

**Table 3.3.28.** Fit parameters of the (P, T, Cl) regression model for fluid/clinopyroxene partition coefficients. The number of outliers is indicated by *number\**.

fluid/cpx	a	b	c	d	e	R <sup>2</sup>
Li	0.356 ± 0.153					
<sup>3*</sup> Be	-1.46	-2420	0.85	1.003	-0.0015	0.63
B	8.62	-5824	0.69	0.882	-0.0013	0.70
<sup>3*</sup> Rb	27.45	-17430	0.25	1.125	-0.0016	0.95
<sup>2*</sup> Cs	13.53	-8208	0.53	0.190	-0.0003	0.90
Sr	10.61	-6574	-0.08	0.501	-0.0004	0.87
<sup>1*</sup> Ba	22.48	-14157	0.05	1.485	-0.0019	0.90
<sup>3*</sup> Nb	0.723 ± 0.709					
<sup>2*</sup> Ta	0.295 ± 0.239					
La	7.34	-10810	1.19	2.778	-0.0035	0.81
Ce	11.48	-12886	0.90	2.896	-0.0037	0.83
Nd	0.84	-7336	1.44	1.655	-0.0019	0.88
Sm	2.09	-6375	0.82	1.506	-0.0018	0.78
Eu	5.82	-7484	0.44	1.936	-0.0025	0.65
<sup>1*</sup> Gd	11.23	-9027	-0.35	1.238	-0.0016	0.64
Dy	0.055 ± 0.026					
Er	0.062 ± 0.027					
Yb	0.105 ± 0.065					
Lu	0.116 ± 0.060					
Pb	17.223	-10401	-0.18	1.026	-0.0012	0.80
Th	6.260	-8852	0.83	2.157	-0.0030	0.46
<sup>2*</sup> U	-2.653	-2411	1.46	1.210	-0.0018	0.54

**Table 3.3.39.** Fit parameters of the (P, T, Cl) regression model for fluid/phengite partition coefficients. The number of outliers is indicated by *number\**.

fluid/pheng	a	b	c	d	e	R <sup>2</sup>
Li	9.01	-6784	0.54	0.885	-0.0014	0.71
<sup>2*</sup> Be	0.109 ± 0.044					
<sup>2*</sup> B	5.06	-3169	0.10	0.264	-0.0005	0.59
Rb	2.56	-4933	0.62	0.515	-0.0006	0.93
Cs	5.37	-4694	0.52	0.093	-0.0001	0.90
Sr	8.50	-7081	0.72	0.454	-0.0006	0.80
Ba	-5.86	-476	0.87	0.591	-0.0004	0.89
<sup>2*</sup> Nb	4.43	-4091	0.34	1.416	-0.0022	0.64
<sup>2*</sup> Ta	-3.18	629	0.51	2.497	-0.0038	0.85
<sup>2*</sup> La	28.72	-24484	1.35	4.328	-0.0058	0.80
<sup>1*</sup> Ce	23.00	-21749	1.57	3.745	-0.0047	0.84
<sup>3*</sup> Nd	14.52	-14635	0.91	2.537	-0.0034	0.85
<sup>1*</sup> Sm	8.87	-12454	1.66	2.537	-0.0034	0.83
<sup>1*</sup> Eu	13.64	-15529	1.79	3.154	-0.0041	0.83
<sup>3*</sup> Gd	6.13	-11187	2.03	2.364	-0.0033	0.83
<sup>3*</sup> Dy	-0.26	-6386	2.01	1.207	-0.0015	0.79
Er	0.750 ± 0.737					
Yb	0.959 ± 0.787					
Lu	2.938 ± 1.799					
Pb	8.92	-6804.783	0.003	0.523	-0.0004	0.80
<sup>2*</sup> Th	14.59	-14124.187	0.70	2.246	-0.0029	0.67
<sup>2*</sup> U	7.16	-7156.305	0.77	1.243	-0.0016	0.65

3. Mantle metasomatism by sediment fluids in subduction zones

**Table 3.3.20.** Fit parameters of the (P, T, Cl) regression model for fluid/lawsonite partition coefficients. The number of outliers is indicated by <sup>number\*</sup>.

fluid/laws	a	b	c	d	e	R <sup>2</sup>
Li	18.53	-10118	-0.20	0.309	-0.0004	0.79
Be	0.441 ± 0.180					
<sup>1*</sup> B	31.475 ± 23.009					
<sup>2*</sup> Rb	105.137 ± 47.148					
<sup>3*</sup> Cs	290.559 ± 202.190					
Sr	2.26	-4779	0.52	1.685	-0.0021	0.86
<sup>2*</sup> Ba	8.86	-7317	1.22	1.852	-0.0025	0.85
<sup>3*</sup> Nb	0.826 ± 0.654					
<sup>3*</sup> Ta	0.299 ± 0.171					
<sup>1*</sup> La	4.38	-4235	-1.37	1.561	-0.0018	0.84
Ce	5.21	-5443	-1.05	1.608	-0.0019	0.84
Nd	-0.59	-1320	-1.20	0.348	0.0000	0.82
Sm	-8.48	1651	-0.24	0.410	-0.0002	0.68
<sup>2*</sup> Eu	-10.16	2513	-0.08	-0.002	0.0005	0.77
<sup>3*</sup> Gd	-8.80	1046	0.10	0.474	-0.0004	0.84
<sup>3*</sup> Dy	-15.09	4072	0.77	0.188	-0.0001	0.72
<sup>2*</sup> Er	-15.15	4682	0.69	0.635	-0.0008	0.82
<sup>2*</sup> Yb	-8.51	2562	0.04	0.733	-0.0009	0.73
<sup>2*</sup> Lu	-9.37	2829	0.12	0.975	-0.0013	0.76
<sup>2*</sup> Pb	8.72	-6546	-0.06	1.366	-0.0017	0.88
<sup>2*</sup> Th	-10.77	2714	0.07	-0.023	0.0006	0.73
U	0.300 ± 0.169					

**Table 3.3.21.** Fit parameters of the (P, T, Cl) regression model for fluid/garnet partition coefficients. The number of outliers is indicated by <sup>number\*</sup>.

fluid/grt	a	b	c	d	e	R <sup>2</sup>
Li	2.956 ± 1.819					
Be	-4.12	-160	1.56	1.093	-0.0017	0.71
B	7.10	-4775	0.85	1.494	-0.0021	0.77
<sup>3*</sup> Rb	7.27	-4477	1.07	1.013	-0.0015	0.82
<sup>3*</sup> Cs	0.74	-2481	2.12	0.804	-0.0012	0.87
Sr	15.53	-8635	-0.15	2.099	-0.0028	0.80
<sup>2*</sup> Ba	-7.53	2174	1.94	1.931	-0.0026	0.76
Nb	12.18	-9636	0.56	3.045	-0.0048	0.58
<sup>3*</sup> Ta	-6.40	133	1.19	1.941	-0.0031	0.77
<sup>1*</sup> La	8.61	-10202	0.76	2.198	-0.0028	0.92
Ce	-3.75	-3686	1.40	1.500	-0.0017	0.89
Nd	0.09	-5086	0.84	0.971	-0.0010	0.86
<sup>1*</sup> Sm	-4.40	-406	0.06	0.564	-0.0005	0.62
<sup>1*</sup> Eu	-3.70	-1481	0.26	0.792	-0.0008	0.67
<sup>2*</sup> Gd	-0.05	-3394	-0.15	0.661	-0.0007	0.79
<sup>2*</sup> Dy	-13.32	2826	0.66	0.452	-0.0005	0.73
<sup>2*</sup> Er	0.0017 ± 0.0015					
Yb	0.0029 ± 0.0014					
Lu	0.0026 ± 0.0011					
<sup>2*</sup> Pb	5.23	-2063	-0.23	1.339	-0.0016	0.93
<sup>1*</sup> Th	-2.29	-4174	1.21	1.619	-0.0021	0.64
<sup>2*</sup> U	-6.87	3104	0.46	1.081	-0.0016	0.67

The goodness of fit between the experimental and interpolated data is demonstrated on the example of fluid/clinopyroxene partition coefficients at 4.5 GPa, 700 °C (Figure 3.3.19a). Pressure has relatively little effect on fluid/mineral partition coefficients in the investigated pressure range, so the interpolated values can also be compared to the 4 GPa and 700 °C data of Kessel et al. (2005). The calculated fit parameters were also used to extrapolate the fluid/clinopyroxene partition coefficients to 4.5 GPa and 800 °C. The extrapolated values were compared to the previously reported data from Kessel et al. (2005) at 4 GPa and 800 °C (Figure 3.3.19b). The relatively high level of reproducibility between this study and the study of Kessel et al. (2005) suggests that extrapolation of fluid/mineral partition coefficients by up to  $\pm 50$  °C should be fairly reliable. The values reported by Kessel et al. (2005) were not directly measured either, as a linear extrapolation of clinopyroxene compositions from higher temperatures was used to obtain the fluid/clinopyroxene partition coefficients at 700 and 800 °C. The good agreement of fluid/clinopyroxene partition coefficients between this study and that of Kessel et al. (2005) is quite remarkable, considering that the bulk compositions of the two series of experiments are different, with the Kessel et al. (2005) data being obtained in a metabasalt-fluid system.

3. Mantle metasomatism by sediment fluids in subduction zones

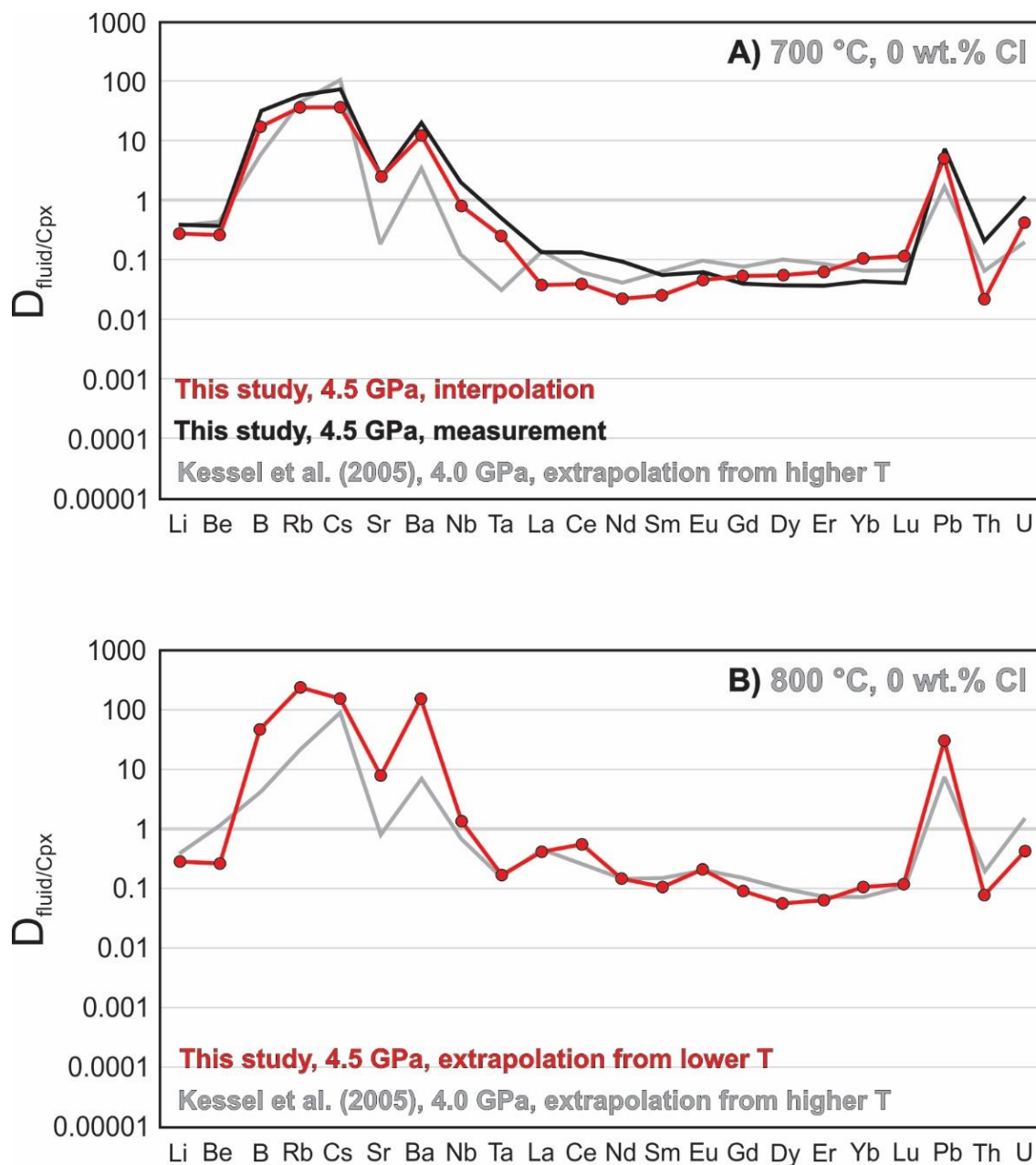


**Figure 3.3.19: a)** A comparison of the measured fluid/cpx partition coefficients from a single run (DT11) and the fluid/cpx partition coefficients calculated from the fitting parameters (interpolation). Previously reported fluid/cpx partition coefficients from similar P,T conditions (Kessel et al., 2005) are shown as well. **b)** A test extrapolation of the fluid/cpx partition coefficients compared to the previously reported data from similar P,T conditions (Kessel et al., 2005).

Mass balance calculations suggest that the water storage capacity of metapelitic residues from this study is between 1 and 3 wt.% in the relevant pressure and temperature range. In addition, some external fluid sources from the underlying lithologies are also likely. Schmidt and Poli (1998) offer a discussion on hydrous phases that may be stable in the basalt and peridotite layers of the slab. Therefore, slab fluid fractions of approximately 1 wt.% are thought to be plausible. If complete equilibration between the metapelitic residues and the slab fluid is assumed, the batch equilibrium equation can be used to obtain a first-order estimate of sediment-derived fluid compositions:

$$C_{fluid} = \frac{D_{fluid/GLOSS} C_{GLOSS}}{1 + F_{slab\ fluid} (D_{fluid/GLOSS} - 1)} \quad \text{Eq. 3.3.3.}$$

where  $C_{fluid}$  is the concentration of a given trace element in the fluid,  $D_{fluid/GLOSS}$  is the bulk fluid/metapelite partition coefficient,  $C_{GLOSS}$  is the concentration of a given trace element in the metapelitic residue and  $F_{slab\ fluid}$  is the fluid fraction in the slab. Varying the slab fluid fraction between 0.5 and 1.5 wt.% had nearly no effect on the estimated fluid compositions, so a constant value of 1 wt.% was assumed in the model. Fluid compositions were calculated using the trace element partition coefficients measured at 3.5 and 4.5 GPa for fluids containing 0 and 7 wt.% Cl. Measurements of trace element partition coefficients at 2.5 GPa and 600 °C suggest that most trace elements are not fluid mobile at fore-arc conditions, even in equilibrium with high salinity fluids. Only several elements (such as B, Cs and Pb) may be partially leached from the slab before reaching sub-arc depths. Studies of exhumed metasedimentary terranes (Bebout et al., 2007; Bebout et al., 2013; Busigny et al., 2003) suggest that very limited loss of fluid mobile elements can be expected in the fore-arc region, although Bebout et al. (2007) remarks on the systematic depletion of B and Cs with increasing metamorphic grade in different units of the Catalina Schist (California). Studies of natural samples generally support the results of our partitioning experiments. Therefore, the composition of trench sediments should be a fairly reasonable approximation of the trace element content of metapelitic residues at sub-arc depths. We used the GLOSS II composition – updated average GLObal Subducting Sediment (Plank, 2013) – to estimate the most plausible trace element concentrations in the fluid using Equation 3.3.3.

The obtained compositions of sediment-derived fluids were then admixed to the depleted mantle (Salters and Stracke, 2004) to calculate the bulk trace element concentrations in the metasomatized mantle melt source:

$$C_{mantle\ source} = F_{fluid}C_{fluid} + (1 - F_{fluid})C_{DM} \quad \text{Eq. 3.3.4.}$$

where  $C_{mantle\ source}$  is the concentration of a given trace element in the bulk metasomatized mantle source,  $F_{fluid}$  is the fluid fraction added to the depleted mantle and  $C_{DM}$  is the initial concentration of a given trace element in the depleted mantle (DM).

Wilson et al. (2014) suggest that considerable fluid focusing may occur in the high-permeability layers of the slab and along the contact of the slab with the overriding plate. This may result in a considerable increase in fluid fraction by the time the fluid reaches the mantle source, with respect to the initial fluid fraction in the slab. Since the extent of such fluid focusing mechanisms can be debated, the mantle melt source compositions were calculated for the addition of a wide range of fluid fractions (from 0.5 to 10 wt.%). The proportions of sediment trace element contributions in the mantle source are shown in Figure 3.3.20. The selected elements in the figure are those thought to be strongly recycled from sediments, based on the reported geochemical similarities with arc magmas: Sr, Th, Ba (Plank and Langmuir, 1993), Th/La (Plank, 2005), Th/Rb (Johnson and Plank, 2000),  $^{207}\text{Pb}/^{204}\text{Pb}$ ,  $^{206}\text{Pb}/^{204}\text{Pb}$  (White, 2013),  $^{10}\text{Be}$  (Tara et al., 1986) and  $^7\text{Li}$  (Tang et al., 2014). The sediment additions to the mantle source are calculated as:

$$sed.\ contrib. = \frac{F_{fluid}C_{fluid}}{F_{fluid}C_{fluid} + (1 - F_{fluid})C_{DM}} 100 \quad \text{Eq. 3.3.5.}$$

where the notation is the same as in Equation 3.3.4.

At temperatures above 700 °C most of B, Cs and Pb in the mantle source may originate from sediments, regardless of fluid salinity and even for a rather small fraction of sediment-derived fluid ( $\approx 0.5$  wt.%) addition. This model also suggests very efficient recycling of Rb, Ba and U – for most of the calculated mantle source compositions, more than 50 % of the total budget of these elements was derived from the sediment layer of the slab. Moderately high transfer efficiency of Li, Be, Sr and Th by aqueous fluids can be expected as well. Arc melts are likely to contain only a moderate to low proportion of LREE from sediments. The recycling of Li, Be, Sr, Th and LREE

appears to be strongly dependent on fluid salinity and/or the fraction of sediment-derived fluid in the mantle source.

To estimate the trace element composition of primitive arc melts, batch equilibrium was assumed to model partial melting of the metasomatized mantle source:

$$C_{melt} = \frac{\frac{C_{mantle\ source}}{D_{peridotite/melt}}}{1 + F_{melt} \left( \frac{1}{D_{peridotite/melt}} - 1 \right)} \quad \text{Eq. 3.3.6.}$$

where  $C_{melt}$  is the concentration of a given trace element in the primitive arc melt,  $F_{melt}$  is the melt fraction and  $D_{peridotite/melt}$  is the bulk partition coefficient of a given trace element between peridotite residue and basaltic melt.

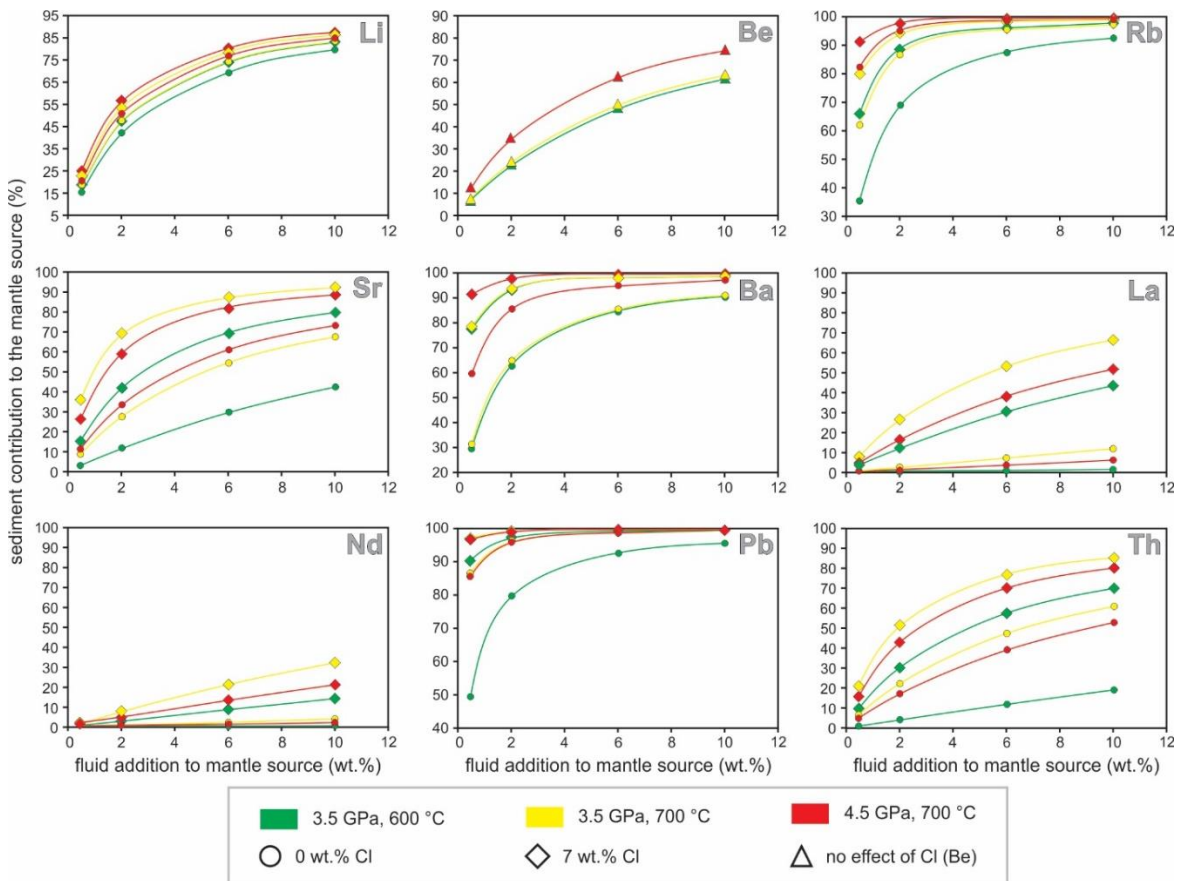


**Figure 3.3.20:** Estimated sediment contributions to the mantle melt source. The values in the figure were obtained using the partition coefficients from the (P, T, Cl) regression model. A wide range of sediment-derived fluid additions is assumed (0.5 to 10 wt.%). The most efficient recycling rate is observed for Pb – and similar recycling trends are obtained for B and Cs (not shown). Rb, Ba (and U; not shown) in arc melts are also expected to be strongly affected by fluids from the sediment layer of the slab. The transfer efficiency of Li, Be, Sr and Th from sediments are high to moderate under a wide range of model parameters, while LREE contributions may vary from moderate to negligible, depending on fluid salinity and fluid fraction.

Observations of the electrical conductivity structure in the mantle wedge as well as the results of experimental studies and thermodynamic models (Hata and Uyeshima, 2015; Kushiro, 2007; Schmidt and Jagoutz, 2017) suggest that the assumption of sub-arc melt fractions between 5 and 15 wt.% should be realistic. Literature data on mineral/basalt trace element partitioning was used to calculate the bulk  $D_{\text{peridotite/melt}}$  of a model peridotite containing 70 wt.% olivine, 20 wt.% orthopyroxene, 5 wt.% clinopyroxene and 5 wt.% garnet. The list of literature references for mineral/basalt partition coefficients and the  $D_{\text{peridotite/melt}}$  used in the model are shown in Tables 3.3.22. and 3.3.23. (Supplement II), respectively.

It should be emphasized that mantle source compositions in this calculation contain no contribution from basalt-derived fluids. In this model, which is a likely hypothetical end-member, the metasomatic agent is a fluid that equilibrated exclusively with the sediment layer of the slab.

The obtained melt compositions were compared to natural primitive arc magmas (Figures 3.3.21. to 3.3.24). The field of natural arc magma in the figures encompasses the “arc average” primitive melt compositions that were estimated by Schmidt and Jagoutz (2017) using the GEOROC database. To complete the dataset, the abundances of Li, Be, B and Cs in primitive arc melts were additionally compiled, also from the GEOROC database. Both the modelled melt compositions and the compositions of natural samples were normalized to the depleted mantle of Salters and Stracke (2004).

3. Mantle metasomatism by sediment fluids in subduction zones

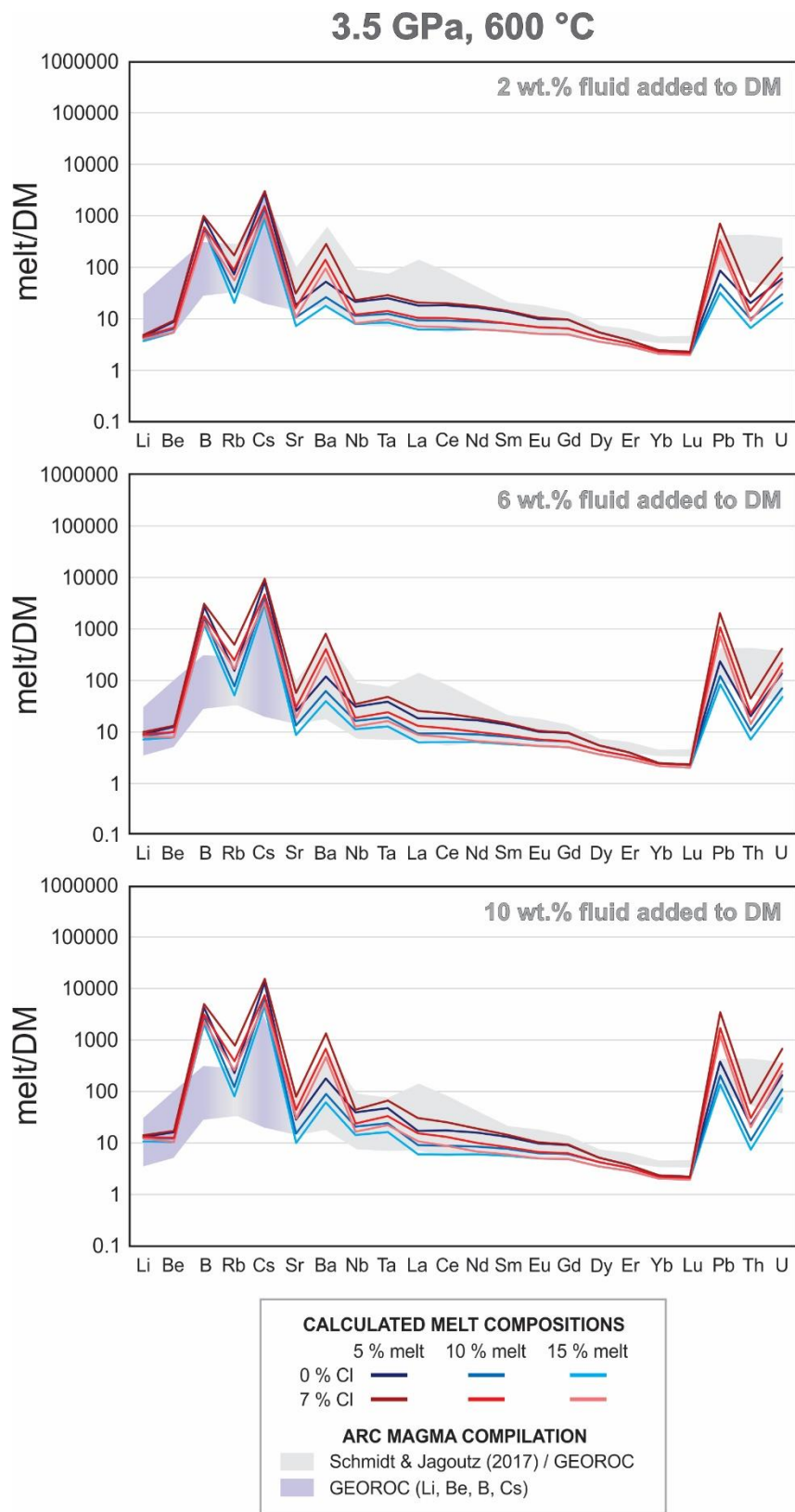


**Figure 3.3.21:** Compositions of primitive arc melts produced by partial melting of a mantle source metasomatized by sediment-derived fluids extracted from the slab at 3.5 GPa and 600 °C. Fluid salinities of 0 and 7 wt.% Cl were assumed. Melt compositions were estimated for fluid additions between 2 and 10 wt.% and melt fractions of 5, 10 and 15 wt.%.

3. Mantle metasomatism by sediment fluids in subduction zones

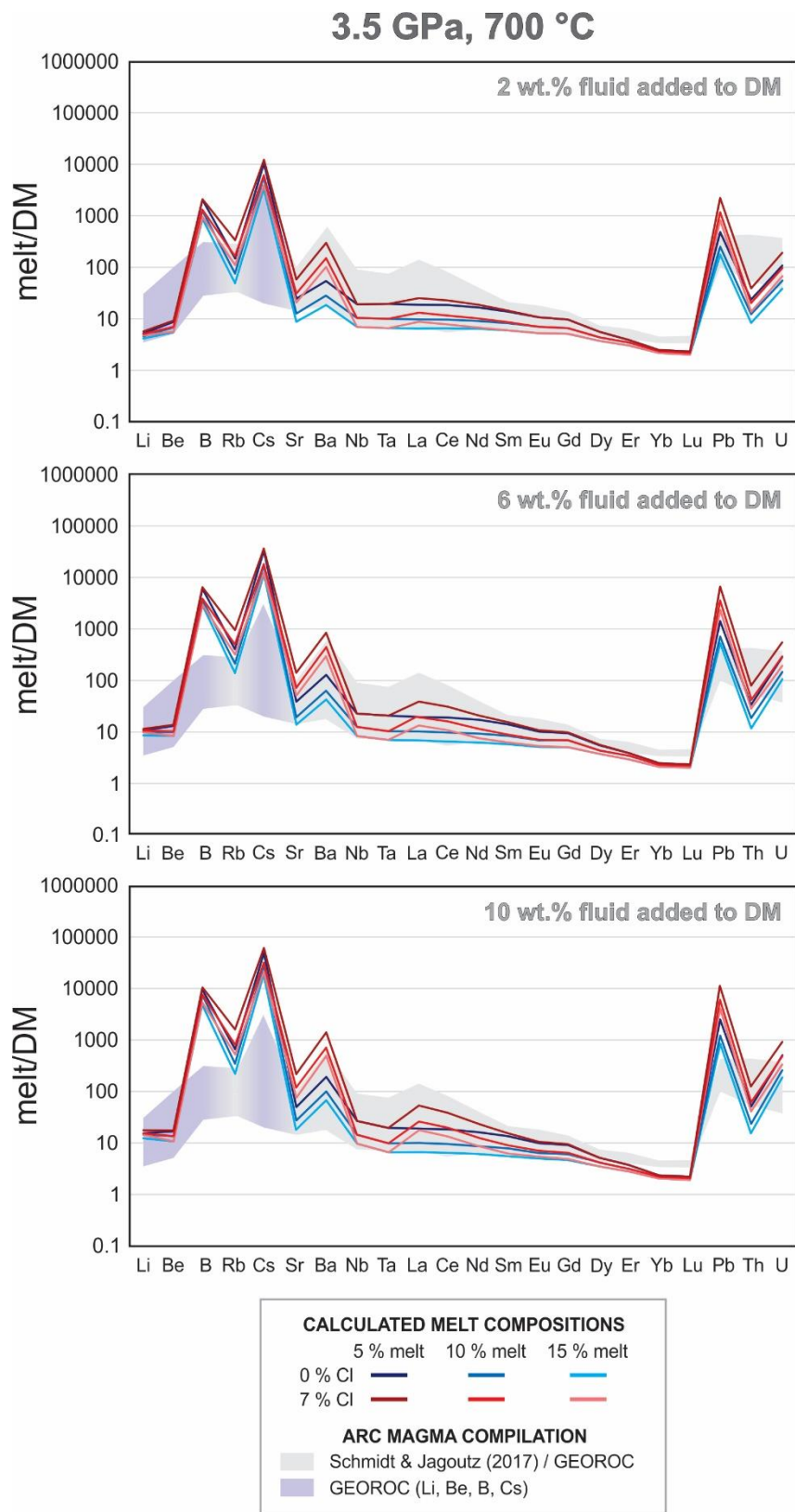


**Figure 3.3.22:** Compositions of primitive arc melts produced by partial melting of a mantle source metasomatized by sediment-derived fluids extracted from the slab at 3.5 GPa and 700 °C. Fluid salinities of 0 and 7 wt.% Cl were assumed. Melt compositions were estimated for fluid additions between 2 and 10 wt.% and melt fractions of 5, 10 and 15 wt.%.

3. Mantle metasomatism by sediment fluids in subduction zones

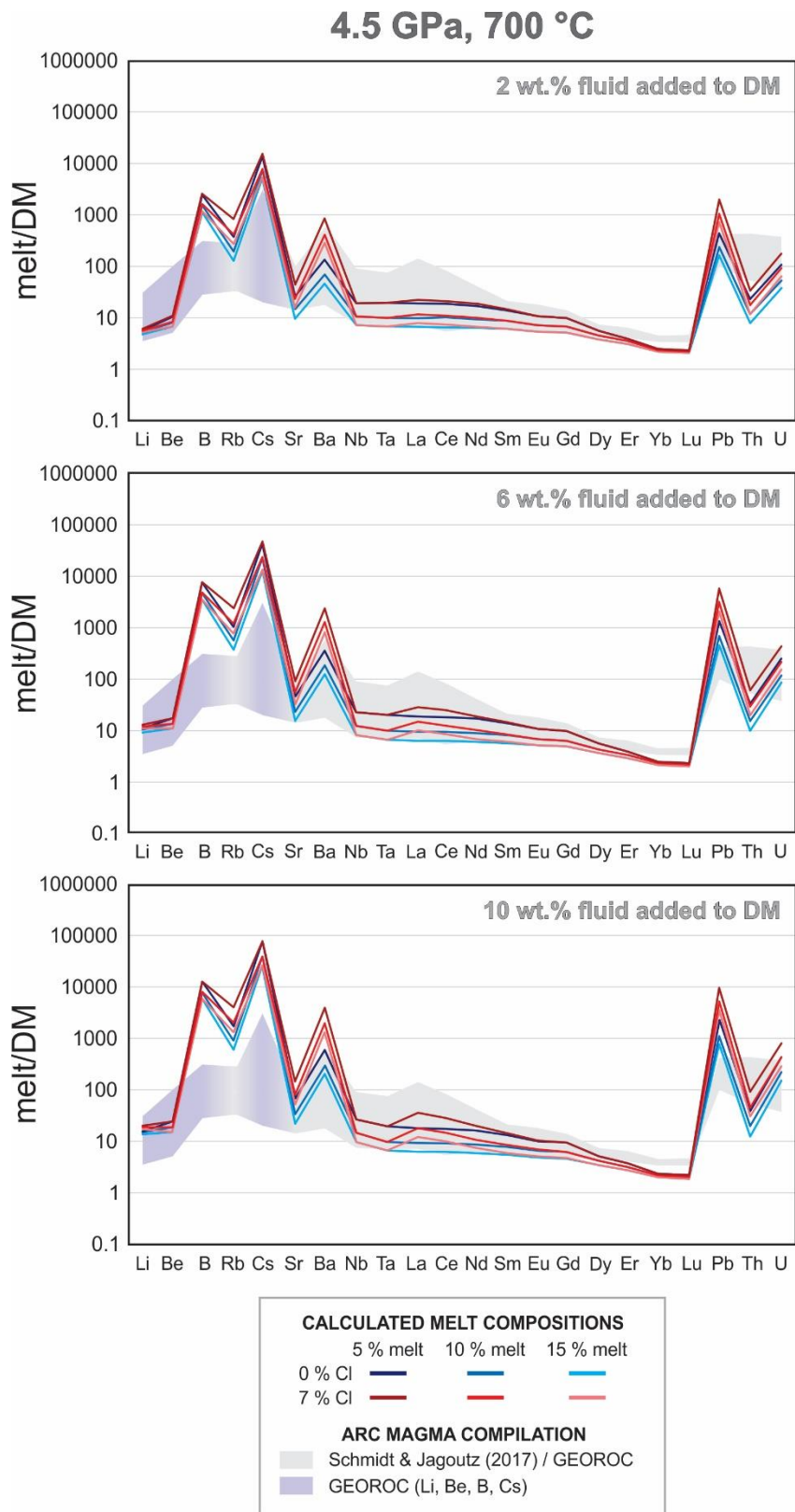


**Figure 3.3.23:** Compositions of primitive arc melts produced by partial melting of a mantle source metasomatized by sediment-derived fluids extracted from the slab at 4.5 GPa and 700 °C. Fluid salinities of 0 and 7 wt.% Cl were assumed. Melt compositions were estimated for fluid additions between 2 and 10 wt.% and melt fractions of 5, 10 and 15 wt.%.

3. Mantle metasomatism by sediment fluids in subduction zones

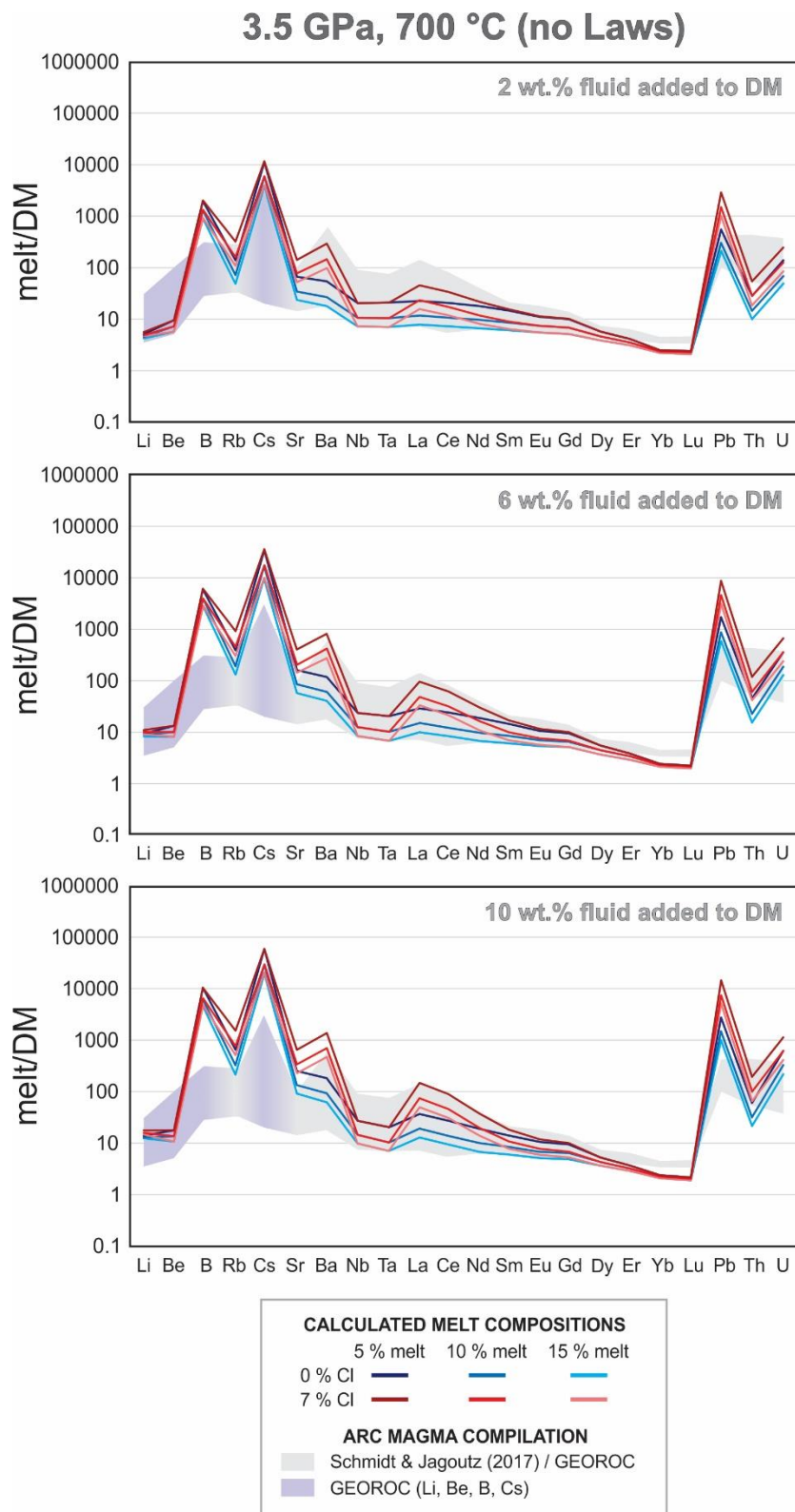


**Figure 3.3.24:** Compositions of primitive arc melts produced by partial melting of a mantle source metasomatized by fluids extracted from lawsonite-free metapelites at 3.5 GPa and 700 °C. Fluid salinities of 0 and 7 wt.% Cl were assumed. Melt compositions were estimated for fluid additions between 2 and 10 wt.% and melt fractions of 5, 10 and 15 wt.%. Melts contain considerably higher abundances of Sr and LREE as compared to melt compositions from Figure 3.3.22.

### 3.4. Discussion

#### 3.4.1. The extended trace element partitioning dataset

In order to constrain the nature of the slab-derived mobile phase, an extensive dataset of trace element partitioning between different high-pressure liquids and residual slab lithologies is necessary. Over the last several decades, experimental studies have gradually expanded the dataset by measuring mineral/melt (e.g. Klemme et al., 2002; Carter et al., 2015) and fluid/mineral partition coefficients for Cl-free (Kessel et al., 2005) and saline aqueous and supercritical fluids (Rustioni et al., 2019, 2021) in the basalt-H<sub>2</sub>O system. Some melt/rock and fluid/rock partition coefficients were also determined in equilibrium with sediment bulk compositions (Johnson and Plank, 2000; Spandler et al., 2007; Hermann and Rubatto, 2009), although some of these early data sets may have suffered from experimental and analytical problems. We now provide a new extensive data set for the sediment-H<sub>2</sub>O system, including the fluid/mineral partition coefficients for saline aqueous and supercritical fluids.

Kessel et al. (2005) argue that fluid properties in the basalt-H<sub>2</sub>O and sediment-H<sub>2</sub>O systems should be generally similar, and the same fluid/mineral partition coefficients may be used to model fluid release from both slab lithologies. However, the miscibility gap between the aqueous fluid and silicate melt likely closes at fore-arc conditions for the sediment-H<sub>2</sub>O system (Shen and Keppeler, 1995; Bureau and Keppeler, 1999). At constant conditions, the fluid equilibrating with sediments may dissolve more solid material, compared to the fluid equilibrating with a basalt composition (Keppeler, 2017). The new data allow a preliminary test of these hypotheses. Indeed, there is a surprising similarity between the fluid/cpx (Ch. 3.3.5, Fig. 3.3.19) and fluid/garnet trace element partition coefficients, measured in equilibrium with sediment (this study) and basalt bulk compositions (Kessel et al., 2005).

The existing fluid/cpx and fluid/garnet partition coefficient datasets were expanded with direct measurements of sediment lithologies at 600 and 700 °C in the sub-arc pressure range (2.5 to 4.5 GPa), and in equilibrium with representative fluid salinities (0 to 7 wt.% Cl). In addition, we provide the fluid/mineral trace element partitioning data for the co-existing lawsonite and phengite. The potential role of these phases in subduction zone processes was previously discussed in literature (Melzer and Wunder, 2000; Wunder et al., 2005; Schmidt et al., 2004; Martin and

Hermann, 2014; Vitale Brovarone et al., 2014), mainly due to the compatibility of REE and LILE elements in lawsonite and phengite structures, respectively.

The role of lawsonite on trace element re-distribution in subduction zones was tested using the partitioning data from 3.5 GPa and 700 °C. For this exercise, lawsonite was ‘removed’ from the metapelitic residue by re-distributing its mass proportion (6 wt.%) in equal parts between other major minerals, and the melt compositions were re-calculated (Ch. 3.3.5, Fig. 3.3.24). If a lawsonite-free metapelitic slab residue is assumed, the model predicts appreciably higher Sr and LREE partitioning into the fluid phase. This is also reflected in the resulting melt compositions, which have a much more prominent Nb-Ta anomaly and are more enriched in Sr, as compared to the model that assumes 6 wt.% of lawsonite in the slab residue.

We also present the first measurements of the fluid/phengite partition coefficients for an extensive suite of trace elements – until now, only data for Rb and Cs were available in literature (Melzer and Wunder, 2000). Since phengite may exert considerable control over the fractionation and release of LILE elements from the slab, the fluid/phengite partition coefficients are essential to test different models of arc magma generation.

### **3.4.2. Toward constraining subduction-related mantle metasomatism**

Growing databases of trace element and isotope compositions of natural arc magmas provide key constraints for resolving the compositions and extraction conditions of the slab-derived mobile phase. The experimental trace element partitioning data can be used to calculate the theoretical composition of primitive arc melts, and the results can then be compared with natural samples (Ch. 3.3.5). A plausible model should be able to reconcile trace element fractionation and abundances, isotopic compositions and across-arc geochemical variations observed in nature.

Simple one-step fluid release models may be a good starting point toward constraining these processes. Rustioni et al. (2021) already calculated the composition of primitive arc melts, generated by hydrous peridotite melting in presence of saline basalt-derived fluids. While mantle metasomatism by saline basalt-derived fluids explains the arc magma trace element signature, the model of Rustioni et al. (2021) does not offer an explanation for the sometimes pervasive sediment

isotopic signatures observed in natural samples. Thus, we used the new partitioning data from this study to test another end-member scenario – partial peridotite melting induced by the addition of sediment-derived saline fluid (Ch. 3.3.5). No contribution from basalt fluids is considered in this model.

The predicted Li, Be, Sr, Ba, Nb, Ta, REE and U concentrations in the theoretical melts overlap with the observed range of natural arc magma (Ch. 3.3.5, Fig. 3.3.22 to 3.3.24). With the exception of Th/U ratio, the predicted element fractionation also resembles natural compositions. The Th-U fractionation in our models is more prominent than observed in natural samples. However, this fractionation is expected to be strongly dependent on oxygen fugacity, which was not controlled in our experiments. In addition, phosphorous may increase Th solubility in the fluid, and thus reduce the Th-U fractionation, compared to the phosphorous-free systems (Ch. 3.3.4).

The sediment source is extremely trace element enriched. As a result, the model usually yields higher-than-natural abundances of B, Rb, Cs and Pb. We conclude that mixing and dilution with basalt-derived fluids is likely to lower the abundances of these elements into the naturally occurring range. Mixing of basalt- and sediment-derived fluids may also reconcile the isotopic composition of natural samples. For example, our model predicts different relative transfer rates for Pb and Sr (Ch. 3.3.5, Fig. 3.3.20). At constant fluid extraction conditions, Pb is transported much more efficiently than Sr. If basalt- and sediment-derived fluid mixing is assumed, this could explain the simultaneous strong  $^{207}\text{Pb}/^{204}\text{Pb}$  and  $^{206}\text{Pb}/^{204}\text{Pb}$  (White, 2013) and weak  $^{87}\text{Sr}/^{86}\text{Sr}$  (Nielsen and Marschall, 2017) sediment signatures in arc magma. More refined additional models will explore the plausible mixing ratios of sediment- and basalt-derived fluids by combining the reported isotopic compositions from natural samples with the experimental trace element partitioning data. Overall, our data suggest that the Pb isotopic signature may be produced by the addition of a small fraction of sediment-derived fluid to the mantle zone of melting. Neither the trace element abundances, nor the isotopic signatures of most arc magmas, require the addition of sediment melts.

The minimum extraction temperatures of slab-derived fluids transporting trace elements can be generally constrained to be between 600 and 700 °C. The model predicts that extraction of saline

fluids at temperature of 700 °C would produce melt compositions with Nb-Ta depletion, relative to LILE and LREE (Ch. 3.3.5, Fig. 3.3.22 to 3.3.24). This is a prominent geochemical feature of nearly all arc magmas (Ch. 3.1) – only few arcs worldwide produce melts that do not exhibit the negative “Nb-Ta anomaly” (Schmidt and Jagoutz, 2017). However, neither chlorine-free nor saline fluids released from the slab at 600 °C would have the appropriate Nb/LREE and Ta/LREE ratios to produce the Nb-Ta anomaly (Ch. 3.3.5, Fig. 3.3.21). The relative proportions of lawsonite and garnet in the slab residue may have a major influence on the LREE enrichment of the primitive arc melts (Fig. 3.3.24). Even if a garnet-rich slab residue – more representative of the metabasalts – is assumed (59 wt.% clinopyroxene, 39 wt.% garnet and 2 wt.% rutile; after Rustioni et al., 2021), the partitioning data from 600 °C still do not produce the necessary trace element fractionation. The Nb/LREE and Ta/LREE ratios in the average MORB composition are  $\approx 1$  (Gale et al., 2013). Thus, at 600 °C neither the sediments nor basalts could release a fluid that would generate arc melts with pronounced Nb-Ta anomalies.

It was previously suggested that the lower temperature limit for mobile phase extraction from the slab should be between 700 and 800 °C. These arguments assume that sediment melts should be the principal metasomatic agent in subduction zones (Johnson and Plank, 1999; Spandler et al., 2007; Hermann and Rubatto, 2009). Thus, the proposed lower temperature limit corresponds to the H<sub>2</sub>O-saturated sediment solidus. We emphasize that the position of the critical curve in the sediment-H<sub>2</sub>O system is not well constrained, so what is perceived as a defined ‘solidus’ in experimental studies may, in reality, be the transition from a dilute to a concentrated supercritical fluid. Moreover, our study shows that saline fluids may transfer a typical “sediment signature” from subducted sediments to arc magmas, which invalidates most geochemical arguments for sediment melting.

In addition, Nielsen and Marschall (2017) show that most arc magmas plot below the mixing line between the mantle and sediment melt end-members in the Nd/Sr – <sup>87</sup>Sr/<sup>86</sup>Sr diagram, which effectively disqualifies sediment melts as the predominant slab-derived metasomatic agent (Ch. 3.1.). An experimental study by Mallik et al. (2015) additionally supports this conclusion, as interaction between sediment melt and the mantle wedge produces ultrapotassic magmas that are distinct from a typical primitive arc basalt. Rather, the H<sub>2</sub>O-saturated sediment solidus may place

### *3. Mantle metasomatism by sediment fluids in subduction zones*

an upper temperature limit on the conditions of mobile phase extraction from the slab. However, this proposed upper temperature limit is not strict. Sediment melting, although apparently rare, may indeed be possible in some subduction zones. For example, ultrapotassic volcanism, consistent with mantle metasomatism by sediment melts, has been observed in the Sunda arc (Mallik et al., 2015, and ref. therein).

## 4. Mantle melting at low water fugacity and the cryoscopic equation

### 4.1. Introduction

A global seismic shear wave velocity reduction has been observed at depths corresponding to the lithosphere-asthenosphere boundary (LAB) (Anderson, 1989), and the origin of this discontinuity is still debated (Ch. 2.1). The observed effects could be explained by the presence of low-degree partial melt (Anderson and Sammis, 1969; Anderson and Spetzler, 1970), but the upper mantle temperatures generally do not exceed the dry peridotite solidus. With the exception of plate boundaries and plume-related settings, melting is therefore not expected throughout the upper mantle. To reconcile this, it was proposed that trace amounts of water may be able to significantly depress the melting point of peridotite (Mierdel et al., 2007). Volatile species, such as water and CO<sub>2</sub>, are highly incompatible in mineral structures and partition preferentially into silicate melts. The dissolution of trace volatiles in silicate liquids may therefore be able to induce melting at ambient upper mantle temperatures.

However, a number of mechanisms that do not involve melting could also explain significant shear-wave velocity reductions. Some of the proposed explanations include: contrasting mechanical properties of dry and hydrated olivine (Hirth and Kohlstedt, 1996; Karato and Jung, 1998), elastically accommodated grain boundary sliding (Karato, 2012), thermal and grain-size variation effects (Faul and Jackson, 2005), and seismic anisotropy (e.g. Yuan and Romanowicz, 2010). It remains debated whether the shear-wave velocity reductions at the lithosphere-asthenosphere boundary are related to partial melting or not.

In an effort to constrain the nature of the lithosphere-asthenosphere boundary, considerable experimental work was dedicated to investigate the melting point depression of peridotite in presence of trace volatiles. The effects of water (Hirschmann et al., 2009 and ref. therein) and CO<sub>2</sub> (Dasgupta et al, 2007) were studied separately, and also together (Hirschmann, 2010). The combined effect of 100 ppm of water and 60 ppm of CO<sub>2</sub> was suggested to induce melting (<0.1 % melt fraction) at the oceanic lithosphere-asthenosphere boundary. The estimated effect was largely due to the contribution of CO<sub>2</sub> to the melting point depression of peridotite, and the result was not entirely conclusive, as larger melt fractions may be required to explain the reduction in shear wave

velocities at the lithosphere-asthenosphere boundary. We hypothesize that the current models underestimate the effect of water on the melting point depression due to the difficulty in detecting small fractions of hydrous melt in conventional high-pressure experiments. The aim of this study is to reinvestigate the role of water in upper mantle melting using an alternative experimental approach.

Because of the adsorption of water on fine-grained starting materials (Ch. 2.1), the effects of ppm-level water concentrations on peridotite melting cannot be investigated directly. Instead, experiments may be performed at H<sub>2</sub>O-saturated conditions and low pressures, in order to precisely determine the effect of low water fugacities on melting temperatures. The effect of trace amounts of water on incipient melting can then be modelled from experimentally established dry and H<sub>2</sub>O-saturated solidus temperatures, measurements of water contents in near-solidus melts, and mineral/melt water partition coefficients ( $D_{H_2O}^{min/melt}$ ) for major peridotite minerals (Ch. 4.4.2).

Experiments in the peridotite-H<sub>2</sub>O system are complicated by difficulties in recovering pristine silicate glasses from high pressures. Low viscosity silicate liquids, like the hydrous basalts that form by partial melting of peridotite, tend to precipitate crystalline products upon quenching. This issue persists even at very rapid quench rates (>100 °C), and is progressively more problematic at higher target pressures. With increasing pressure, water solubility in silicate melts increases. Melt viscosity may be lowered by orders of magnitude due to the dissolution of water (Richet et al., 1996), and crystal nucleation is accelerated under these conditions (Davis et al., 1997). As a result, the recovery of crystal-free hydrous basaltic glasses becomes more challenging at high pressure. Very high melt fractions quench into obvious melt pools that contain recognizable dendritic crystals (e.g. Ch. 2.3., Fig. 2.3.1), but low-degree partial melts are very difficult to identify (Green, 2014). At high pressures, the subsolidus hydrous fluid can dissolve wt.% of silicate materials. The silicate solubility in hydrous fluids abruptly decreases upon quenching, and interstitial quench products may form (e.g. Ch. 2.3., Fig. 2.3.7). Visual discrimination of low-degree partial melts from subsolidus fluid precipitates is highly subjective. Thus, the H<sub>2</sub>O-saturated solidus temperatures are poorly constrained in the peridotite-H<sub>2</sub>O system. In particular, we suspect that most studies of hydrous peridotite systems may be overestimating the H<sub>2</sub>O-saturated melting temperatures, as only high-degree partial melts are readily recognizable in quenched samples. This

could lead to a systematic underestimation of the effect of water on the melting point depression in peridotite.

Quenched basaltic melts from high pressure experiments are often too inhomogeneous to be analyzed with high accuracy (e.g. Tenner et al., 2009). The published melt analyses from the peridotite-H<sub>2</sub>O system provide only a robust estimate of melt compositions. This introduces uncertainties in direct determination of total water contents in near-solidus melts, but also complicates the measurement of  $D_{H_2O}^{min/melt}$ . The estimation of  $D_{H_2O}^{min/melt}$  is further impaired by limited mineral grain size of typical piston-cylinder and multi-anvil run products. The small grains may be analyzed using SIMS (Koga et al., 2003), but these measurements may overestimate  $D_{H_2O}^{min/melt}$ , as SIMS does not discriminate between hydroxyl groups dissolved in mineral structures and water that is associated with defects, fluid inclusions and grain boundaries. Despite these uncertainties, mineral/melt water partition coefficients were extensively measured, and some general estimates are available from literature compilations.

The relationship between the melting point depression ( $\Delta T$ ) and the corresponding total water contents in near-solidus basaltic melt ( $c_{H_2O, total}$ ) remains poorly constrained. A thermodynamically meaningful description of the melting point depression of silicate-H<sub>2</sub>O systems requires information on the melt structure at high temperatures, as well as on the dissolution mechanisms of water in the silicate liquid phase (Ch. 4.4.2). This information may be obtained only from in-situ spectroscopic studies of silicate melts, which are relatively rare and only available for felsic compositions (e.g. Shen and Keppler, 1995). As a result, there is no consensus on how to reliably describe the  $\Delta T - c_{H_2O, total}$  relationship in silicate-H<sub>2</sub>O systems. An alternative possibility is to ‘calibrate’ the cryoscopic equation (Ch. 4.3.3, Eq. 4.3.13) against an experimental dataset of the  $\Delta T - c_{H_2O, total}$  pairs, by adjusting the assumptions about water dissolution mechanisms and the silicate melt structure, until a reasonable fit to the experimental observation is achieved (Hirschmann et al., 2009). However, if the experimental dataset is not of high quality, the resulting thermodynamic characterization of the melting point depression will be flawed. Ultimately, the experimental data determine the result of the melting model (Ch. 4.4.2).

We designed a study to precisely measure the  $\Delta T - c_{\text{H}_2\text{O},\text{total}}$  relationship in basaltic melts. The “haplobasalt” anorthite-diopside- $\text{H}_2\text{O}$  system was used for this purpose, as this is an eutectic system (Osborn, 1942), which produces high melt fractions immediately above the solidus. Unlike in the peridotite- $\text{H}_2\text{O}$  system, where identifying near-solidus melts is challenging, initial melting temperatures may be determined with a high degree of confidence. The compositions of haplobasaltic melts in the anorthite-diopside system are similar to tholeites, such that the effect of water on the solidus of these melts should be similar to that in the peridotite- $\text{H}_2\text{O}$  system.

The solubility of water in silicate liquids increases with water fugacity (e.g. Mysen, 2014). Thus, to determine the  $\Delta T - c_{\text{H}_2\text{O},\text{total}}$  curve for realistically low melt water contents, the water fugacity at run conditions needs to be controlled to low values. One possibility to do so is by diluting a co-existing hydrous fluid phase with an additional inert component, such that  $\text{H}_2\text{O}$ -understaurated conditions are achieved (Ch. 2.1). However, water fugacity can also be limited at  $\text{H}_2\text{O}$ -saturated conditions by maintaining low confining pressures. Thus, a rapid-quench internally-heated pressure vessel is a particularly suitable choice for this type of study. It allows direct and precise control of low confining pressures, avoiding uncertainties related to pressure calibration in solid pressure medium devices. In addition, the temperature can be precisely controlled, as thermal gradients along the entire sample can be effectively eliminated (Ch. 4.2.2).

Two types of experiments were carried out to determine the  $\Delta T - c_{\text{H}_2\text{O},\text{total}}$  relationship. The ‘solidus depression’ runs are classical melting experiments performed at  $\text{H}_2\text{O}$ -saturated conditions and varying low pressure (0.02 – 0.2 GPa). As the name suggests, the purpose of these runs is to precisely determine the  $\text{H}_2\text{O}$ -saturated solidus temperatures – and therefore the  $\Delta T$  – as a function of pressure (Ch. 4.3.1). The other type of experiments – the ‘ $\text{H}_2\text{O}$  solubility’ runs – are designed to measure water solubility in haplobasaltic melt, as a function of pressure and temperature. Extrapolating the water solubility in the melt to near-solidus conditions yields the total water contents ( $c_{\text{H}_2\text{O},\text{total}}$ ) that correspond to the experimentally observed  $\Delta T$ . The new results were used to construct a more accurate model for the effect of water on the melting point of mantle peridotite.

## 4.2. Experimental methods

### 4.2.1. Starting materials and sample preparation

For determining the melting point in the anorthite-diopside-H<sub>2</sub>O system as a function of pressure and melt water content ('solidus depression' runs), we used a 1:1 (by weight) mixture of synthetic anorthite and diopside powder.

For the synthesis of anorthite, stoichiometric amounts of Ca(OH)<sub>2</sub>, Al(OH)<sub>3</sub> and SiO<sub>2</sub> were ground under ethanol in an agate mortar. The mixture was dehydrated inside a platinum crucible by slowly heating to 1100 °C overnight. The crucible was then transferred to a high-temperature furnace and rapidly heated to 1600 °C. After that, it was very slowly cooled to 1350 °C over four days. However, when the crucible was removed from the furnace, the content was still completely molten, despite being far below the equilibrium melting temperature. When it was then placed on a cold surface, needle-like anorthite crystals nucleated at the bottom of the crucible. The crucible was returned to the furnace at 1450 °C and cooled to 1350 °C over five hours. This yielded an aggregate of cm-sized, elongated anorthite crystals. The purity was checked by XRD.

To synthesize diopside, a mixture of high purity CaCO<sub>3</sub>, Mg(OH)<sub>2</sub> and SiO<sub>2</sub> was homogenized in an agate mortar under ethanol. The un-decarbonated mixture was sealed together with 10 wt.% of distilled H<sub>2</sub>O, into several large 3.5 cm long gold capsules with a 5.0/4.6 mm outer/inner diameter. Both capsule ends were closed with a triple weld. The capsules were kept at 3 kbar and 700 °C for approximately 10 days in externally heated cold-seal pressure vessels in order to crystallize diopside. The resulting run products were analyzed by XRD, which revealed minor carbonate impurities. To dissolve the carbonates, diopside powders were submerged in 10% HNO<sub>3</sub> for an hour at room temperature. Nitric acid was afterward removed by repeated flushing with distilled H<sub>2</sub>O. The purity of the diopside powders was then confirmed using XRD. The typical size of the crystals was 5-10 μm.

For the 'H<sub>2</sub>O solubility' experimental series, we synthesized synthetic glass with the reported 1 bar anorthite-diopside eutectic melt composition (Osborn, 1942). High purity CaCO<sub>3</sub>, Al(OH)<sub>3</sub>, Mg(OH)<sub>2</sub> and SiO<sub>2</sub> were combined in an agate mortar under ethanol and subsequently decarbonated and dehydrated at 1110 °C for 12 h to produce a mixture with a stoichiometry of

An<sub>41</sub>Di<sub>59</sub> (wt.%). The sintered material was melted at 1400 °C for 2 h. To avoid formation of cracks in the resulting glass, the melt was not quenched in water, but allowed to slowly cool in air over several minutes. Glass cylinders with a 3.2 mm diameter and 3 mm height were cored out from the synthesized glass. The use of large mm-sized glass cylinders limits H<sub>2</sub>O diffusion from the melt upon quenching, and is more suitable for ‘H<sub>2</sub>O solubility’ experiments than the anorthite-diopside powder.

All starting materials were enclosed in 2 cm long platinum capsules with a 3.5/3.2 mm outer/inner diameter, along with an adequate amount of distilled H<sub>2</sub>O to ensure saturation at run conditions. The capsules were sealed with triple welds.

#### **4.2.2. Experiments in the internally heated gas pressure vessel (IHPV)**

The basic working principles of internally heated gas pressure vessels (IHPVs) are described. For more information, an in-depth review of a variety of existing IHPV designs is presented by Holloway (1971). Although an IHPV capable of operating at 3 GPa had been developed (Birch et al, 1957), in most facilities this apparatus is typically used to reach pressures of up to 1 GPa. The gas pressure is measured directly by a manufacturer-attested gauge. This is an important advantage over using a solid pressure media apparatus, in which considerable uncertainty in pressure must be acknowledged due to simplifying assumptions made during pressure calibrations. The IHPV can routinely reach temperatures as high as 1500 °C, and the thermal gradients along a several cm long furnace hotspots are typically only a few °C. In comparison, the reported thermal gradients in solid media apparatus are usually in the order of dozens of °C over a much smaller sample volume (e.g. Pickering et al., 1998).

Internally heated gas pressure vessels are thick-walled large-volume steel chambers capable of confining the entire furnace, along with the sample, at high pressure. The steel body of the vessel is continuously cooled during operation by circulating water in an outer cooling jacket. The water-cooling extends the available pressure and temperature range as compared to externally heated cold-seal pressure vessels.

A typical high-pressure system consists of a pressure medium gas bottle, a pressurization apparatus (diaphragm compressor and one or several hydraulic pressure intensifiers), and the vessel itself (Fig. 4.2.1). High pressure tubing connects the individual components of the system, and a series of high-pressure valves allow different sections of the pipeline to be disconnected or engaged as necessary. The most common choice of pressure medium for experiments up to 1 GPa is argon gas. Diaphragm compressors are sufficient to achieve target pressures up to 0.3 GPa, while the use of hydraulic intensifiers is typically required in the pressure range between 0.3 and 1 GPa.

Gas-tight seals secure the openings at the top and the bottom of the vessel. Avoiding gas leaks is challenging at high pressures, and several different seal designs had been developed to overcome this issue. In all variations of the design, the seal packing, consisting of a series of ductile washers, is held on the end of a long steel stem. The seal packing and the stem are supported in place against the vessel wall with a large closure plug. Due to the specific geometry of the stem and seal packing – which can vary considerably between different designs (Holloway, 1971) – the ductile washers of the packing deform against the vessel wall when pressure is applied to the chamber, eventually creating a gas-tight barrier.

The system used at Bayerisches Geoinstitut consists of a commercial autoclave made by Harwood Engineering (Walpole, MA, USA). The autoclave is rated to 150 000 psi, which translates to more than 1 GPa. It consists of a double-shell of steel, with the inner shell being made of the Republic A 286 steel, which is highly resistant to hydrogen. The autoclave is closed by inverse Bridgman seals using Pb rings and Teflon rings of Bal seal design. Cone seals insulated by Kynar (a Teflon-like polymer) are used to pass electrical wires through the closure plugs. Argon is used as a pressure medium, and is compressed to 0.3 GPa using a Nova Swiss membrane compressor; higher pressures to 1 GPa may be reached by using a hydraulic intensifier.

The autoclave is operated in vertical orientation. The furnace used consists of two-zone winding of Mo-wire on an alumina tube support. The furnace is surrounded by alternating layers of zirconia felt and Ni foil as insulation; the Ni foil is used for blocking thermal radiation. The outermost layer of insulation consists of alumina cloth and is included in a steel jacket that is attached to the upper closure plug of the autoclave, allowing rapid exchange of the entire heater.

#### 4. Mantle melting at low water fugacity and the cryoscopic equation

The sample holder and thermocouples are attached to the lower closure plug of the autoclave. The sample is suspended on a 0.1 mm thick platinum wire, which can be fused by a short voltage pulse, such that the sample drops into the cold zone of the autoclave for quenching. Two S-type thermocouples located 15 mm apart, situated above and below the sample, are used to measure and control temperature. Two Eurotherm controllers are used to separately control the power supply to the two furnace windings, such that temperature gradients can be minimized. Pressure is continuously measured by a Harwood manganin cell.

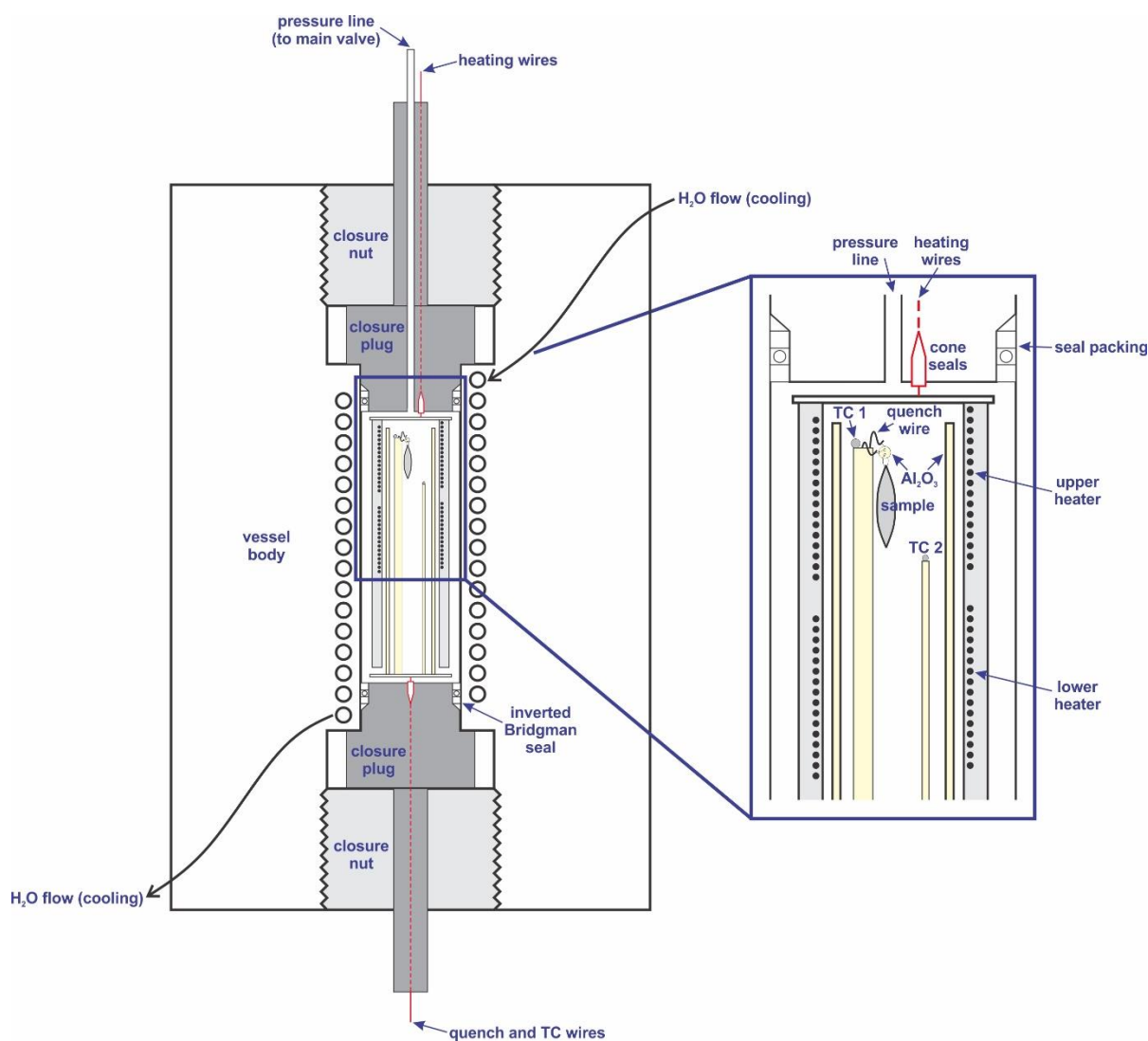


**Figure 4.2.1:** A simplified schematic of a rapid-quench internally heated pressure vessel. The vessel is in vertical (operating) position. A typical rapid quench mechanism is shown on the right-hand side. The sample is suspended on a 0.1 mm platinum wire, which is fused at the end of the experiment. The sample drops into the cold spot of the pressurized chamber, located below the lower heater.

Before each experiment, the pressure was increased above the target value using the membrane compressor. Once a gas-tight seal was formed, the samples were slowly heated over a period of 30 to 90 min, and pressure adjustments (gas release) were made as necessary, to avoid overshooting target pressure and temperature. The pressure in all experiments remained within  $\pm 50$  bar, with respect to the target value. Temperature gradients along the sample length remained  $\pm 2$  °C throughout all experiments. An isobaric rapid quench was attempted at the conclusion of all experiments. Success of the rapid-quench was evaluated based on 1 to 5 bar pressure increases upon fusing the quench wire, or by the sample location within the chamber after the experiment.

#### 4.2.3. Fourier-transform infrared spectroscopy (FTIR)

Fourier-transform infrared spectroscopy (FTIR) can be used to study the structures of gases, liquids and solids. In addition, light absorption by the sample correlates with the true concentration of chemical species in the investigated material. With proper calibration for matrix effects, quantitative chemical analyses using FTIR are possible.

The principles of FTIR spectroscopy are described by Griffiths and Haseth (2007). A typical two-beam interferometer, based on the design of Michaelson (1891), consists of a light source, an interferometer and a detector (Fig. 4.2.2). Different light sources are typically used to cover the entire spectral range of interest (infrared to ultraviolet). Common light sources include xenon arc lamps in the UV/visible range, tungsten lamps in the near-infrared (NIR) to visible, SiC rods glowing at about 800 °C (globars) in the mid-infrared (MIR), and mercury discharge lamps in the far-infrared (FIR) spectral range.

The interferometer is the essential part of the instrument. The polychromatic (unmodulated) light enters the interferometer where it is partially reflected from, and partially transmitted through a semi-transparent mirror – the beamsplitter. One light beam is reflected by a fixed mirror, and the other is reflected by a moving mirror (Fig. 4.2.2). The two ‘split’ beams re-combine at the beamsplitter. Because one mirror moves at a constant velocity (usually in  $\text{cm}\cdot\text{s}^{-1}$ ), there will be a difference in the optical path between the two beams (retardation), equal to  $2(AB-AC)$ , see

Figure 4.2.2. Depending on the optical path difference, either constructive or destructive interference will occur upon re-combination of the two beams.

For monochromatic light of a given wavelength, the constructive and destructive interference would alternate over time during the constant movement of the mirror, and the intensity of the beam would be modulated. The modulation frequency would depend on the wavelength of the light, and the velocity of the mirror. In other words, light of a given wavelength would be characterized by its modulation frequency when the mirror velocity is known. The detector measures light intensity as a function of time (the interferogram). For a monochromatic source, the modulation frequency can be directly determined from the interferogram, and therefore the wavelength of the incident light – and its intensity – can be estimated.

However, a realistic FTIR light source is polychromatic, and a Fourier transformation has to be used to convert the complex modulated signal, produced by the mirror movement, into a spectrum of light intensity versus frequency or wavenumber. By comparing a background measurement (without sample) to a measurement with a sample inserted into the path of the modulated beam, an absorption spectrum can be obtained. Absorbance is defined as:

$$A(\nu) = \log \frac{I_0(\nu)}{I(\nu)} \quad \text{Eq. 4.2.1.}$$

where  $A$  is the absorbance,  $I_0$  is the measured intensity of the incident beam during background measurement without sample,  $I$  is the measured intensity of the light transmitted through the sample, and  $\nu$  is the wavenumber.

The position of the mirror is monitored using laser interferometry, by passing a laser (usually a HeNe laser; 0.633  $\mu\text{m}$ ) through the same interferometer as used for the infrared absorption measurement. The beamsplitter is a transparent material with a reflecting coating, and it should ideally reflect 50%, and transmit the other 50% of the incident light, over the entire spectral range of interest. However, no material is optically transparent from the far-infrared to ultraviolet, so different materials need to be used. Typical beamsplitter materials are: Al-coated quartz in the UV, quartz with dielectric coating in the visible, Si-coated  $\text{CaF}_2$  in the NIR, Ge-coated KBr in the MIR, and Mylar or antimony sulfide in the FIR spectral range.

Three types of detectors are used in commercial systems. Pyroelectric detectors (such as deuterated triglycine sulfate – DTGS) operate at room conditions and measure the surface charge produced in a pyroelectric material as a function of the incident light intensity. Liquid nitrogen cooled semiconducting detectors are also widely used, as they have improved sensitivity and allow shorter measurement times. Semiconducting detectors measure the change in electrical resistivity due to the absorption of incident photons by the detector material. Mercury cadmium telluride (MCT) is a common example of a semiconducting detector. For measurements in the far-infrared, extremely sensitive liquid helium cooled silicon or germanium bolometers need to be used. These detectors monitor minute changes in temperature of the Si (or Ge) crystal due to absorption of the incident light.

For small specimens, an all-reflecting microscope with Cassegrain reflectors can be used to position the samples in the beam path, and the field of view may be limited by an aperture of appropriate size.

Light absorption by the sample occurs when the frequency of incident light equals to the vibration frequency of chemical species that are present in the sample. This is evident in the absorption spectrum as absorption ‘bands’ at particular wavenumbers. According to the Lambert-Beer law, for light of a given wavelength, the intensity of the transmitted radiation decays exponentially with increasing sample thickness, and the concentration of the absorbing chemical species (Eq. 4.2.2):

$$I = I_0 e^{-\varepsilon^* c d} \quad \text{Eq. 4.2.2.}$$

$$\ln \frac{I_0}{I} = \varepsilon^* c d \quad \text{Eq. 4.2.3.}$$

$$A = \log \frac{I_0}{I} = \varepsilon c d \quad \text{Eq. 4.2.4.}$$

where  $\varepsilon^*$  is the molar absorption coefficient,  $\varepsilon$  is the decadic molar absorption coefficient,  $c$  is the concentration of the absorbing chemical species (mol/L), and  $d$  is sample thickness (cm). If the absorption band is characterized by peak height, then the (linear) molar absorption coefficient is expressed in  $\text{Lmol}^{-1}\text{cm}^{-1}$ . If the absorption band is represented by its integral area, then the absorbance is no longer dimensionless, but is expressed in  $\text{cm}^{-1}$ , and the (integral) molar absorption coefficient has the unit of  $\text{Lmol}^{-1}\text{cm}^{-2}$ .

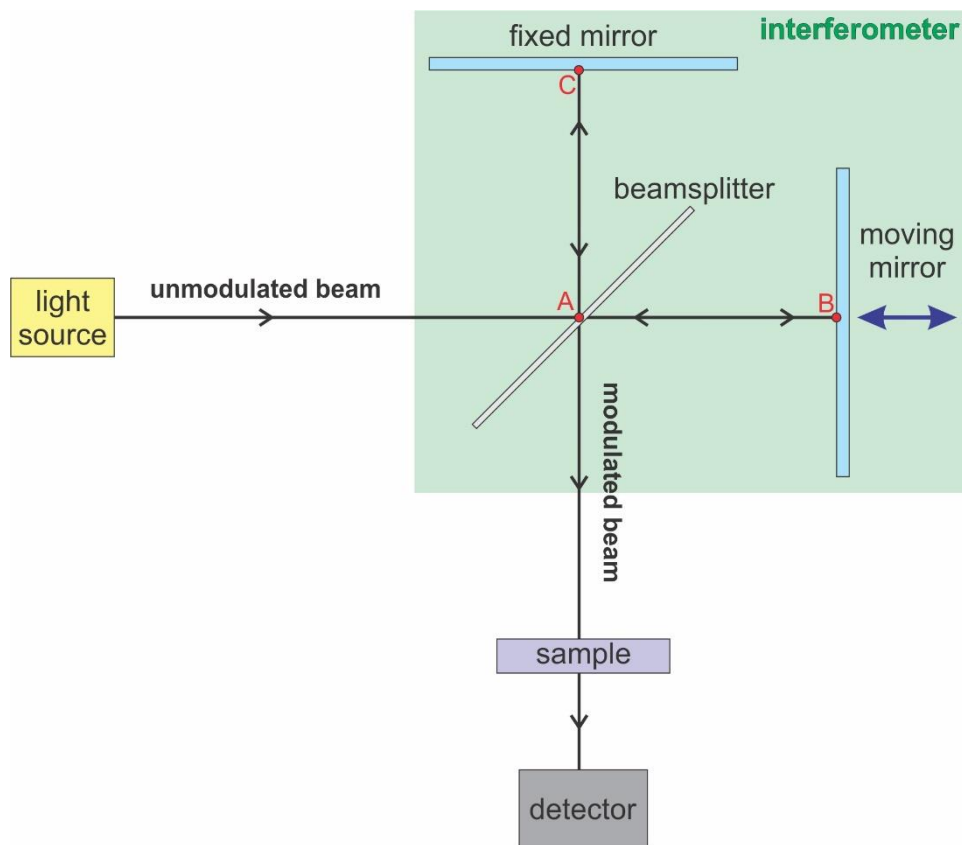


Figure 4.2.2: A simplified schematic of a Michelson-type interferometer.

In this project, FTIR was used for quantitative analysis of total water contents in haplobasaltic glasses (Ch. 4.3.2). Water dissolves in silicate melts as both molecular water and hydroxyl groups (Stolper, 1982). In order to measure the total water content in silicate glasses and melts, it is standard practice to use near-infrared absorption bands at  $5200\text{ cm}^{-1}$  and  $4500\text{ cm}^{-1}$  to quantify the concentrations of both dissolved species –  $\text{H}_2\text{O}$  and  $\text{OH}^-$ , respectively (Ch. 4.3.2). The combination band at  $5200\text{ cm}^{-1}$  results from the simultaneous excitation of two fundamental modes of water molecules (bending and stretching vibrations at  $1600$  and  $3600\text{ cm}^{-1}$ , respectively). The band at  $4500\text{ cm}^{-1}$  is the combination of O-H stretching ( $3500\text{ cm}^{-1}$ ) and X-OH stretching vibrations ( $1000\text{ cm}^{-1}$ ), where X is a cation in the silicate melt (Malfait, 2009; Le Losq et al., 2015).

The infrared spectra were measured with a Bruker IFS 120 Fourier-transform infrared spectrometer, coupled to an all-reflecting Bruker IRscope I microscope. The instrument contains a permanently aligned Michelson-type interferometer with a  $30^\circ$  angle of incidence on the beamsplitter. Mirror retardation is monitored with a frequency stabilized HeNe laser, and the

instrument optic system is evacuated. All measurements were performed with a tungsten light source, a Si-coated CaF<sub>2</sub> beam-splitter and a narrow-band mercury cadmium telluride (MCT) detector. Two hundred scans were accumulated per spectra, with 1 cm<sup>-1</sup> resolution. The spectra were obtained from mm-size glass fragments, doubly-polished to approximately 285 to 300 μm thickness. Quantitative results were calculated from the 4500 cm<sup>-1</sup> and 5200 cm<sup>-1</sup> absorption bands. Molar absorption coefficients were calibrated against water weight loss from the recovered and dried samples (Ch. 4.3.2).

### 4.3. Results

Pressure and temperature conditions, experiment duration and run procedure details are summarized in Table 4.3.1.

**Table 4.3.1.** Run summary with details of experimental conditions and materials. ‘Experiment type’ indicates whether the focus of the run was determination of solidus (eutectic) temperature at reduced water fugacity, or measurement of H<sub>2</sub>O solubility in the melt phase. ‘+’ is a confirmed rapid quench; ‘±’ indicates no observed pressure increase upon quenching, but the capsule was recovered from the cold spot; ‘-’ is a confirmed slow quench.

Sample	P (GPa)	T (°C)	t(h)	Rapid quench	Starting material	Experiment type	Phases
ADS15	0.02	1250	24	+	50:50 An-Di mixture, H <sub>2</sub> O	solidus depression	An, melt
ADS16	0.02	1150	8	-	50:50 An-Di mixture, H <sub>2</sub> O	solidus depression	An, Di
ADS17	0.05	1180	25	+	50:50 An-Di mixture, H <sub>2</sub> O	solidus depression	An, Di
ADS18	0.05	1100	24	+	50:50 An-Di mixture, H <sub>2</sub> O	solidus depression	An, Di
ADS21	0.1	1120	25	+	50:50 An-Di mixture, H <sub>2</sub> O	solidus depression	An, Di
ADS22	0.1	1040	46	+	50:50 An-Di mixture, H <sub>2</sub> O	solidus depression	An, Di
ADS23	0.15	1070	23	+	50:50 An-Di mixture, H <sub>2</sub> O	solidus depression	An, Di
ADS24	0.15	990	22	+	50:50 An-Di mixture, H <sub>2</sub> O	solidus depression	An, Di
ADS25	0.2	1020	72	±	50:50 An-Di mixture, H <sub>2</sub> O	solidus depression	An, Di
ADS26	0.2	940	25	+	50:50 An-Di mixture, H <sub>2</sub> O	solidus depression	An, Di
ADS27	0.02	1200	24	-	50:50 An-Di mixture, H <sub>2</sub> O	solidus depression	An, Di
ADS28	0.05	1230	24	±	50:50 An-Di mixture, H <sub>2</sub> O	solidus depression	An, melt
ADS29	0.1	1180	24	-	50:50 An-Di mixture, H <sub>2</sub> O	solidus depression	An, melt
ADS30	0.15	1140	24	+	50:50 An-Di mixture, H <sub>2</sub> O	solidus depression	An, Di, melt
ADS31	0.2	1100	24	+	50:50 An-Di mixture, H <sub>2</sub> O	solidus depression	An, Di
ADS32	0.02	1225	24	±	50:50 An-Di mixture, H <sub>2</sub> O	solidus depression	An, Di, melt
ADS33	0.05	1205	24	±	50:50 An-Di mixture, H <sub>2</sub> O	solidus depression	An, Di, melt
ADS34	0.1	1150	24	+	50:50 An-Di mixture, H <sub>2</sub> O	solidus depression	An, Di, melt
ADS35	0.15	1110	24	+	50:50 An-Di mixture, H <sub>2</sub> O	solidus depression	An, Di
ADS36	0.2	1130	24	+	50:50 An-Di mixture, H <sub>2</sub> O	solidus depression	An, Di, melt
ADS37	0.02	1213	25	±	50:50 An-Di mixture, H <sub>2</sub> O	solidus depression	An, Di, melt
ADS38	0.05	1192	31	+	50:50 An-Di mixture, H <sub>2</sub> O	solidus depression	An, Di, melt
ADS39	0.1	1135	24	+	50:50 An-Di mixture, H <sub>2</sub> O	solidus depression	An, Di, melt
ADS40	0.15	1125	24	+	50:50 An-Di mixture, H <sub>2</sub> O	solidus depression	An, Di, melt
ADS41	0.2	1115	30	+	50:50 An-Di mixture, H <sub>2</sub> O	solidus depression	An, Di, melt
ADS42	0.02	1207	24	±	50:50 An-Di mixture, H <sub>2</sub> O	solidus depression	An, Di, melt
ADS43	0.05	1186	24	+	50:50 An-Di mixture, H <sub>2</sub> O	solidus depression	An, Di, melt
ADS44	0.1	1128	24	+	50:50 An-Di mixture, H <sub>2</sub> O	solidus depression	An, Di
ADS45	0.15	1117	23	+	50:50 An-Di mixture, H <sub>2</sub> O	solidus depression	An, Di
ADS46	0.2	1107	27	+	50:50 An-Di mixture, H <sub>2</sub> O	solidus depression	An, Di, melt
ADS56	0.02	1350	5	±	glass cylinder, H <sub>2</sub> O	H <sub>2</sub> O solubility	melt
ADS57	0.05	1350	4	±	glass cylinder, H <sub>2</sub> O	H <sub>2</sub> O solubility	melt
ADS58	0.1	1350	5	-	glass cylinder, H <sub>2</sub> O	H <sub>2</sub> O solubility	melt
ADS59	0.15	1350	5	±	glass cylinder, H <sub>2</sub> O	H <sub>2</sub> O solubility	melt
ADS60	0.2	1350	5	±	glass cylinder, H <sub>2</sub> O	H <sub>2</sub> O solubility	melt
ADS64	0.1	1250	5	±	glass cylinder, H <sub>2</sub> O	H <sub>2</sub> O solubility	melt
ADS65	0.1	1350	5	+	glass cylinder, H <sub>2</sub> O	H <sub>2</sub> O solubility	melt
ADS66	0.1	1450	5	±	glass cylinder, H <sub>2</sub> O	H <sub>2</sub> O solubility	melt

### 4.3.1. Solidus depression in the anorthite-diopside-H<sub>2</sub>O system at low water fugacity

After recovery from the pressure vessel, the samples were dried at 150 °C to confirm the presence of excess water. The returns after drying were >80 wt.% of the nominal initial water content. We conclude that H<sub>2</sub>O-saturated conditions were achieved in all experiments. The dry sample material was either in the form of a loose powder, sintered angular fragments, or compact and rounded fragments. The sintered and compact fragments were embedded in epoxy and examined in detail using a FE-SEM. Representative sample images are shown in Figure 4.3.1. The sintered fragments contained both anorthite and diopside (Fig. 4.3.1. a and b). Formation of melt pools (typically <15 µm in diameter) and recrystallization of diopside (occasionally also anorthite) could be identified in some of the sintered samples (Fig. 4.3.1b). Compact fragments, clearly indicative of partial melting, always contained an equilibrium assemblage of anorthite and melt. Extensive quench precipitation was observed in high degree partial melts from compact fragments (Fig. 4.3.1c). According to qualitative EDS analyses, the dendritic quench precipitates are likely Al-bearing clinopyroxene with compositions close to diopside end-member.

The solidus was defined at the first appearance of melt pools co-existing with both anorthite and diopside (e.g. Fig. 4.3.1b). The results from the ‘solidus depression’ experimental series are summarized in Figure 4.3.2a, where blue and white circles indicate the run conditions and observed phase assemblages, and the orange lines mark the inferred solidus temperatures. The pressure and temperature conditions of ‘H<sub>2</sub>O solubility’ experimental series are shown in Figure 4.3.2a as well, indicated by yellow circles. Figure 4.3.2b. is a compilation of literature data on dry and H<sub>2</sub>O-saturated solidi in the An-Di system, combined with data points from this study (Osborn, 1942; Yoder, 1965; Presnall et al., 1978).

The melting point is systematically depressed to lower temperatures with increasing pressure and melt water content. At 0.2 GPa (corresponding melt water content of 4.87 wt.%, see Ch. 4.3.2) the melting point is lowered by approximately 200 °C, with respect to the dry An-Di system (Fig. 4.3.2).

4. Mantle melting at low water fugacity and the cryoscopic equation

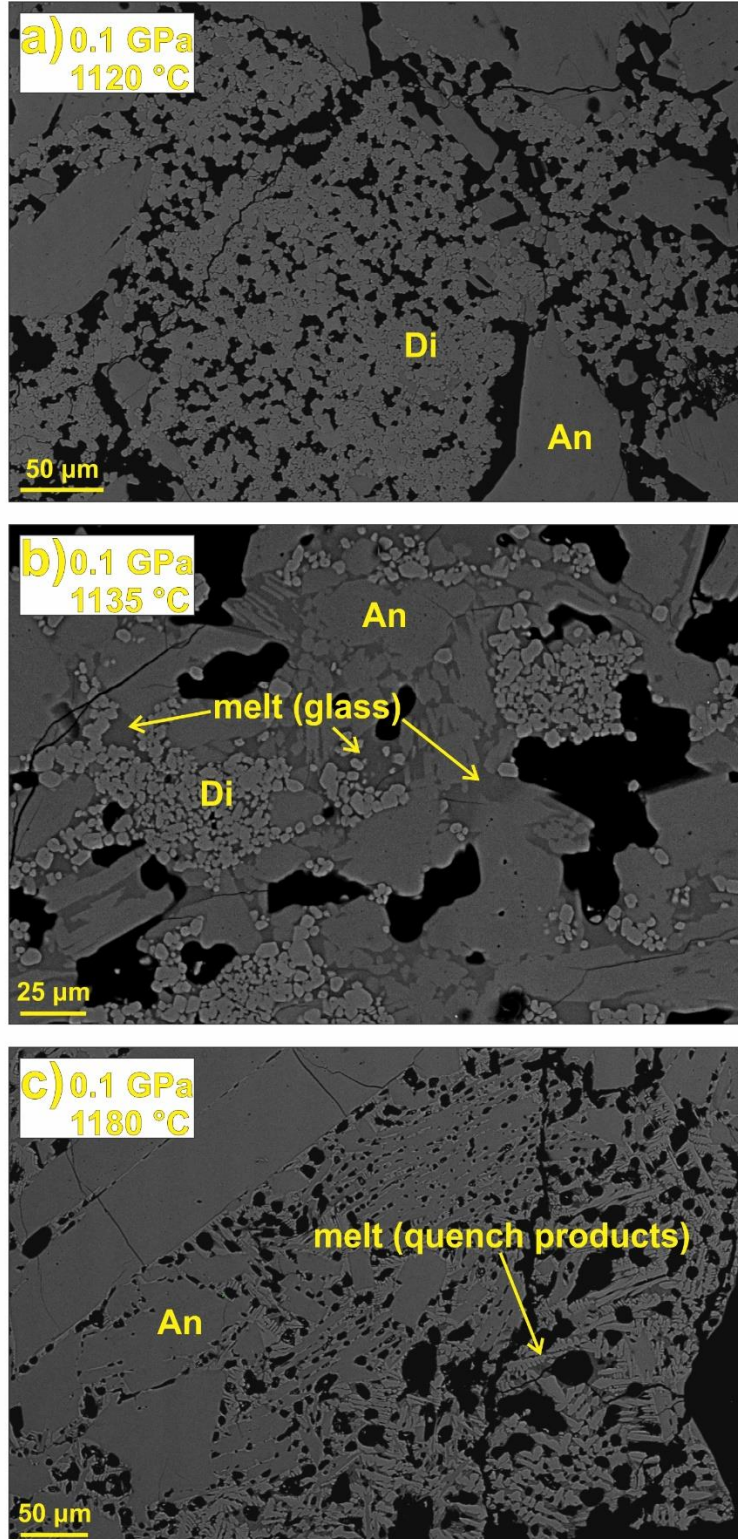


**Figure 4.3.1:** Representative BSE images, demonstrating the progression from subsolidus conditions (a) to a near-solidus assemblage consisting of An+Di+melt (b), and an above-solidus assemblage of one solid phase (An) co-existing with high degree partial melt (c). Recovered high degree partial melts (c) always contained quench precipitates, regardless of the quench rate.

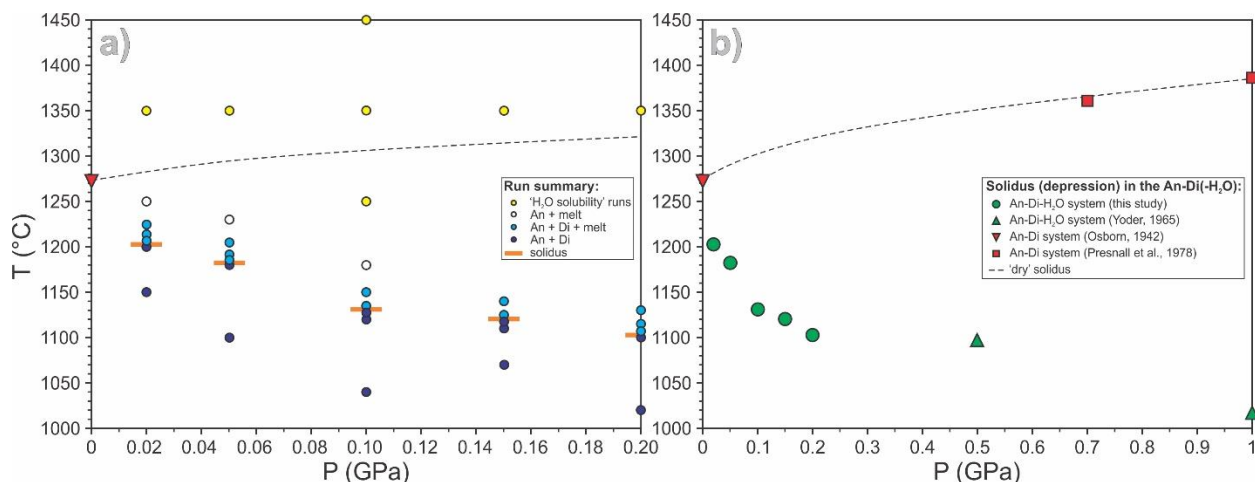


**Figure 4.3.2:** *a*) A summary of experimental conditions; white and blue circles are the ‘solidus depression’ experimental series and the yellow circles are the ‘H<sub>2</sub>O solubility’ runs. Solidus temperatures are indicated by horizontal orange lines. An increase in the melting point depression with increasing pressure and melt water content can be observed. At 0.2 GPa (corresponding melt water content of 4.87 wt.%, Ch.4.3.2) the melting point is lowered by approximately 200 °C. *b*) A literature compilation of eutectic temperatures in the An-Di (dry) and An-Di-H<sub>2</sub>O (H<sub>2</sub>O-saturated) systems.

### 4.3.2. Eutectic melt compositions

The ‘H<sub>2</sub>O solubility’ experimental series consists of two sets of experiments. One set of experiments was performed at a constant temperature of 1350 °C (Fig. 4.3.4. and Fig. 4.3.5) to determine water solubility in haplobasaltic melts as a function of pressure. Another set of experiments was performed at a constant pressure of 0.1 GPa to isolate the effect of temperature on water solubility in the melt phase. All runs from the ‘H<sub>2</sub>O solubility’ series were performed above the liquidus temperature.

The mm-size glass cylinders that were used in the ‘H<sub>2</sub>O solubility’ experimental series have a small surface area, thus limiting atmospheric water contamination. Therefore, the total water contents, initially sealed into the run charges, should be reliably known. The capsules were weighed before and after welding to check for water evaporation. Only minor welding weight loss (<2 % of the nominal water content) was tolerated. After experiment, the samples from the ‘H<sub>2</sub>O solubility’ series were dried at 150 °C and the weight of excess water was recorded. The total water concentrations in haplobasaltic glasses ( $C_{\text{H}_2\text{O},\text{total}}$ ) could be determined from the excess water weight measurements.

The glasses were bubble-free, and the weighing method gave internally consistent total water concentrations. Only sample ADS56 (0.15 GPa, 1350 °C) yielded anomalously low total water

concentration, attributed to entrapment of water in an isolated bubble. The glasses from lower pressure experiments ( $\leq 0.1$  GPa) were clear. In experiments at 0.15 and 0.2 GPa, the top sections of glass cylinders had milky appearance due to precipitation of  $\mu\text{m}$ -size quench crystals, but the bottom parts were clear and could be used to prepare the double-polished thin sections for subsequent FTIR measurements.

Total water contents were additionally determined by Karl-Fischer titration (KFT). However, glass fragments were extremely brittle, and would often suddenly fracture and fall out of the furnace hot-spot during sample heating and degassing. This resulted in anomalously low total water concentrations. The measurements that were deemed reliable are shown in Table 4.3.2, along with the values from the weighing method.

**Table 4.3.2:** A summary of the estimated total water concentrations in haplobasaltic glasses from the ‘H<sub>2</sub>O solubility’ experimental series. The FTIR-measured values, calculated with linear molar absorption coefficients calibrated from the weighing method, were used to estimate eutectic melt compositions. Runs ADS56 to 60 were performed at constant temperature and runs ADS64 to 66 at constant pressure, to determine water solubility in the melt as a function of pressure and temperature, respectively. ‘\*’ indicates an anomalously low value, possibly related to entrapment of H<sub>2</sub>O in an isolated bubble. ‘-’ represents anomalously low values due to glass fragmentation during measurement. ‘#’ values calculated using the molar absorption coefficients for Fe-bearing basalts (Shishkina et al., 2010); the obtained total water contents are approximately 17 % lower, as compared to those estimated using the calibrated molar absorption coefficients.

Sample	P (GPa)	T (°C)	C <sub>H<sub>2</sub>O,total</sub> (wt.%)			
			weighing	KFT	FTIR	FTIR <sup>#</sup>
ADS56	0.02	1350	0.99	1.24	<b>0.94</b>	0.77
ADS57	0.05	1350	1.91	2.31	<b>2.02</b>	1.66
ADS58	0.1	1350	2.86	-	<b>2.89</b>	2.40
ADS59	0.15	1350	*	-	<b>3.88</b>	3.23
ADS60	0.2	1350	4.44	4.57	<b>4.53</b>	3.82
ADS64	0.1	1250	2.89	-	<b>2.96</b>	2.46
ADS65	0.1	1350	2.76	-	<b>2.62</b>	2.17
ADS66	0.1	1450	2.77	2.82	<b>2.68</b>	2.22

The total water concentrations, derived from the weighing method, were used to calibrate the molar absorption coefficients for the near-infrared OH<sup>-</sup> (4500 cm<sup>-1</sup>) and H<sub>2</sub>O (5200 cm<sup>-1</sup>) bands in haplobasaltic glasses. The density of anhydrous glass, required for the calibration, was estimated

to be  $2767 \pm 28$  g/L, based on ten pycnometer measurements. The glass density was corrected for water dissolution using the relationship (Behrens et al., 2009):

$$\rho = \rho_{anhyd} - 22.1 \cdot c_{H_2O,total} \quad \text{Eq. 4.3.1.}$$

where  $\rho$  is the density of hydrous glass (g/L),  $\rho_{anhyd}$  is the density of anhydrous glass (g/L) and  $c_{H_2O,total}$  is the total water concentration in the glass (wt.%). The results of the calibration are shown in plots of normalized absorbances (Figure 4.3.3.)

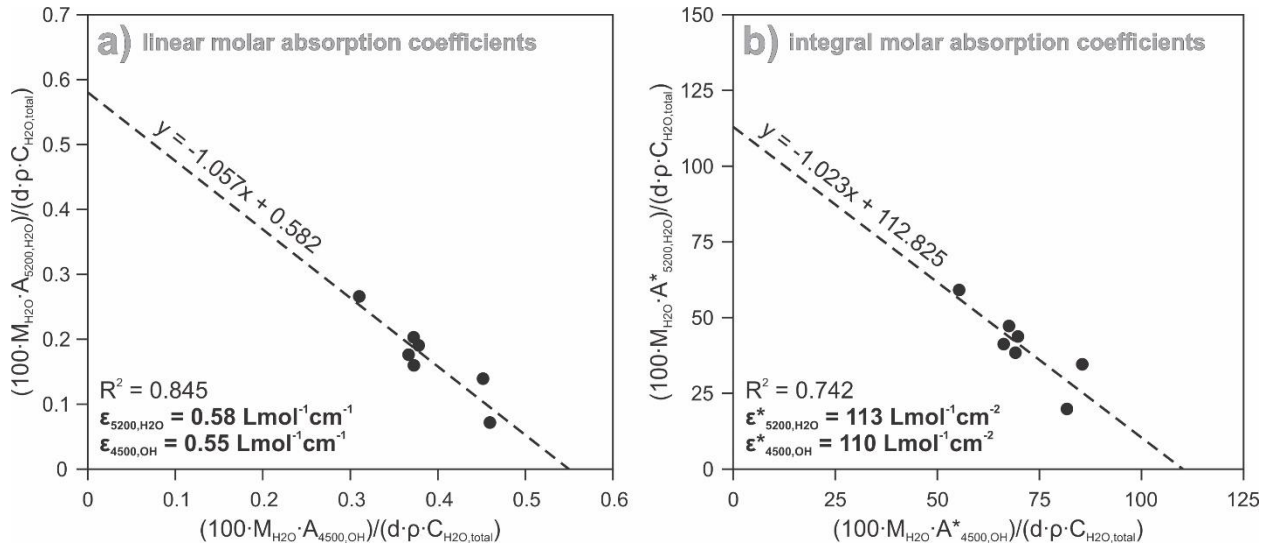


**Figure 4.3.3:** Plots of normalized absorbances for the OH<sup>-</sup> (4500 cm<sup>-1</sup>) and H<sub>2</sub>O (5200 cm<sup>-1</sup>) bands in haplobasaltic glasses. The absorption coefficients are determined from the x- and y-axis intercepts. Results are shown for both linear (a) and integral (b) absorption coefficients.

For the 5200 cm<sup>-1</sup> band of molecular H<sub>2</sub>O, a linear absorption coefficient of 0.58 liter mol<sup>-1</sup>cm<sup>-1</sup> and an integral absorption coefficients of 113 liter mol<sup>-1</sup> cm<sup>-2</sup> was obtained. For the 4500 cm<sup>-1</sup> band of OH<sup>-</sup>, the values are 0.55 liter mol<sup>-1</sup> cm<sup>-1</sup> and 110 liter mol<sup>-1</sup> cm<sup>-2</sup>. The linear extinction coefficients are similar to, but slightly smaller than the data reported by Shishkina et al. (2010) for tholeiitic glasses.

The concentrations of OH<sup>-</sup> and H<sub>2</sub>O species in haplobasaltic glasses were calculated using the calibrated molar absorption coefficients according to the Lambert-Beer law (Ch. 4.2.3):

$$c_{OH} = \frac{100 \cdot M_{H_2O} \cdot A_{OH}}{\rho \cdot d \cdot \epsilon_{OH}} \quad \text{Eq. 4.3.2.}$$

$$c_{H_2O} = \frac{100 \cdot M_{H_2O} \cdot A_{H_2O}}{\rho \cdot d \cdot \epsilon_{H_2O}} \quad \text{Eq. 4.3.3.}$$

and the final values of the total water concentrations were obtained as:

$$c_{H_2O, total} = c_{OH} + c_{H_2O} \quad \text{Eq. 4.3.4.}$$

where  $c_{OH}$ ,  $c_{H_2O}$  and  $c_{H_2O, total}$  are water and water species concentrations (wt.%),  $M_{H_2O}$  is the molar mass of water (g/mol),  $A_{OH}$  and  $A_{H_2O}$  are the FTIR-measured absorbances of the given species,  $\rho$  is the density of hydrous glass (g/L),  $d$  is the thickness of the double-polished thin sections (cm), and  $\epsilon_{OH}$  and  $\epsilon_{H_2O}$  are the linear molar absorption coefficients of the  $4500 \text{ cm}^{-1}$  and  $5200 \text{ cm}^{-1}$  water bands.

The results of FTIR measurements (Table 4.3.2) were then used to estimate near-solidus (eutectic) total water concentrations in haplobasaltic melts. Examples of representative FTIR spectra are shown in Figure 4.3.4.

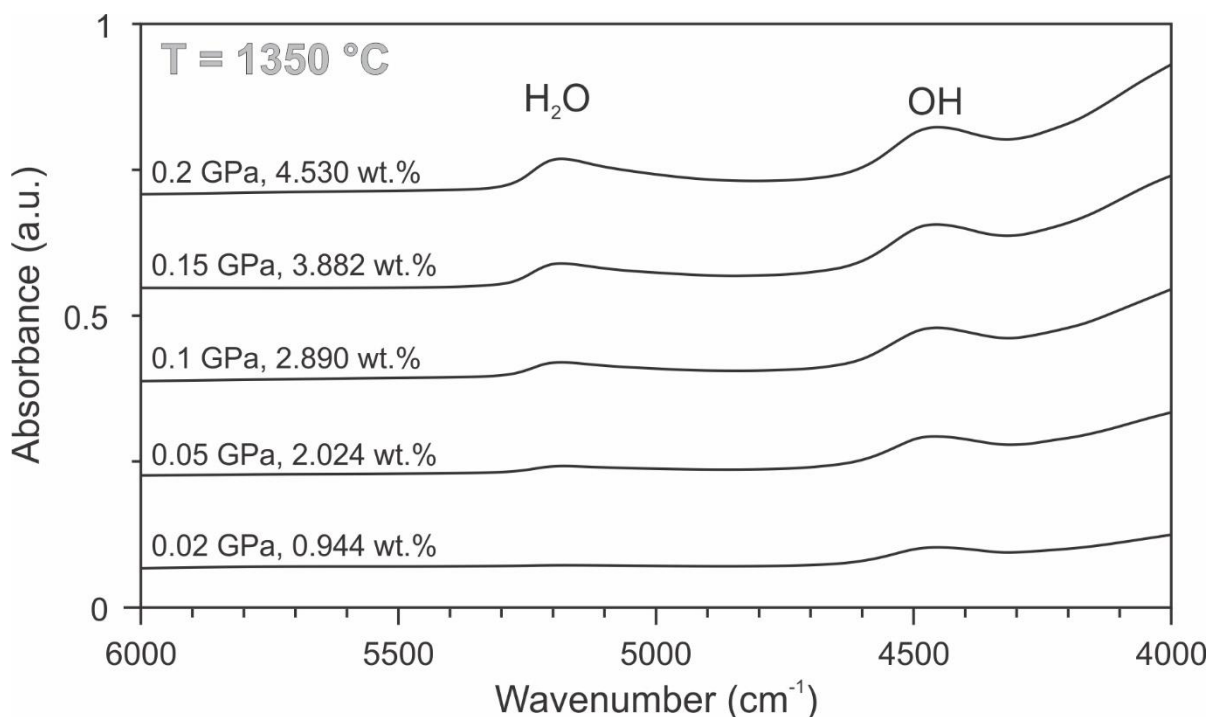


**Figure 4.3.4:** Representative near-infrared spectra of haplobasaltic glasses at constant temperature (1350 °C) from 0.02 to 0.2 GPa. Sample thickness was 284 to 302  $\mu\text{m}$ . The spectra are not background-corrected, but vertically offset for clarity. The water concentrations shown in the figure represent the total water contents (Eq. 4.3.4); the values are from Table 4.3.2.

#### 4. Mantle melting at low water fugacity and the cryoscopic equation

At low pressures, water solubility in silicate melts increases with the square root of water fugacity (e.g. Mysen, 2014). In the pressure range of interest (<0.2 GPa) and at temperatures above 1000 °C,  $f_{H_2O} \approx$  confining pressure. Therefore, the water solubility measurements from the set of experiments at constant temperature (1350 °C) can be fitted to a square root function (Fig. 4.3.5a), as:

$$c_{H_2O,total} = aP^{0.5} \quad \text{Eq. 4.3.5.}$$

where  $P$  is pressure (GPa),  $a$  is an experimentally derived parameter and  $c_{H_2O,total}$  is the total water concentration (wt.%) measured in the glasses by FTIR.

The effect of temperature on water solubility in haplobasaltic melts can be described as (Fig. 4.3.5b):

$$\ln\left(\frac{c_{H_2O,total}}{\text{wt. \%}}\right) = b + c \cdot 10^3 \cdot \frac{1}{T} \quad \text{Eq. 4.3.6.}$$

where  $c_{H_2O,total}$  is the total water concentration (wt.%),  $T$  is absolute temperature (K), and  $b$  and  $c$  are experimentally derived parameters. The  $dc_{H_2O,total}/dT$  was assumed to be independent of pressure. The melt total water concentration was extrapolated to the experimentally observed solidus temperatures (Fig. 4.3.5c) using Equation 4.3.6. The extrapolated total water concentrations are shown in Figure 4.3.5c. and in Table 4.3.3.

#### 4. Mantle melting at low water fugacity and the cryoscopic equation

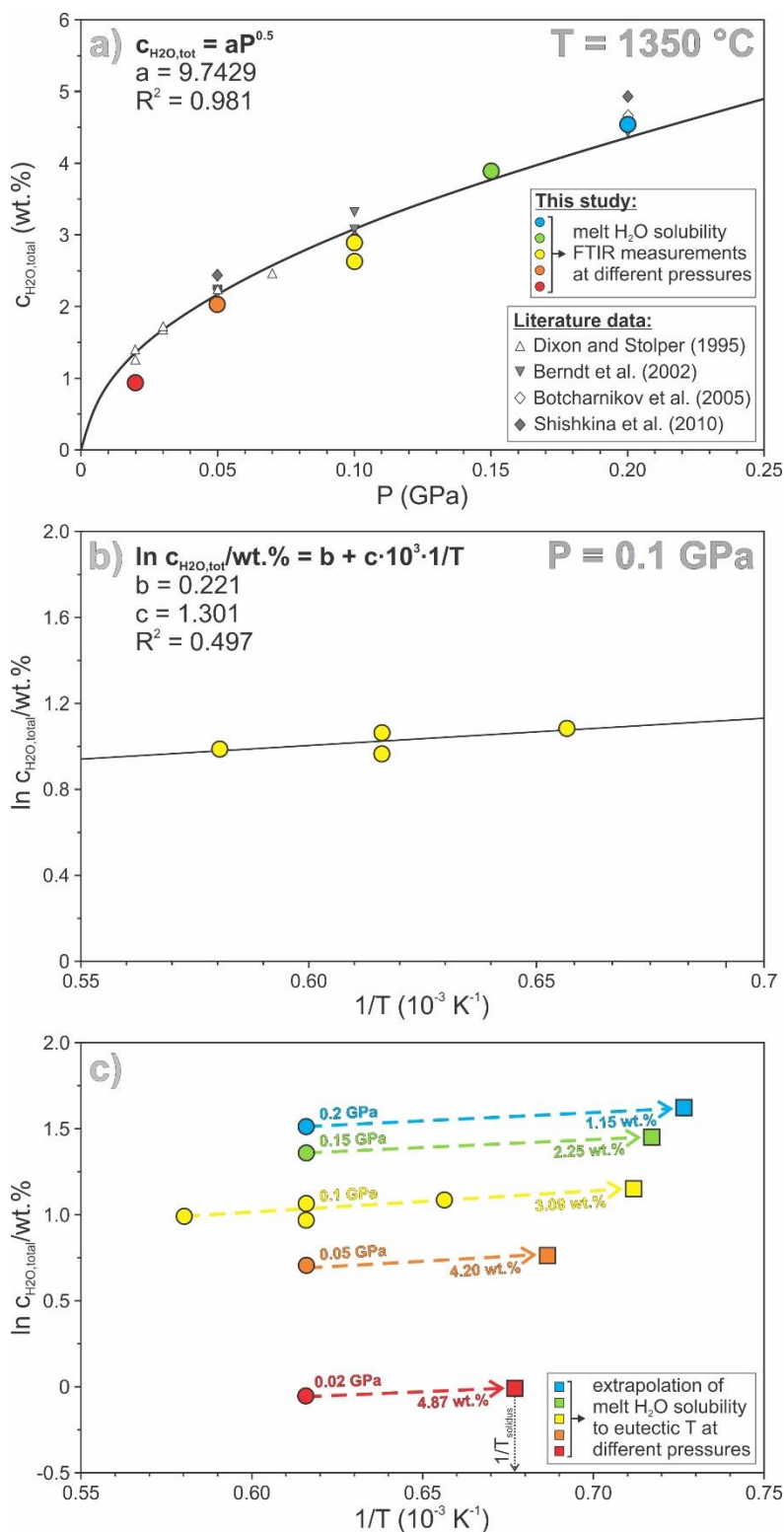


**Figure 4.3.5:** **a)** Water solubility in haplobasaltic melt as a function of pressure. Data is compared to previously published FTIR measurements of water solubility in various iron-bearing basaltic melts; the data compilation is after Shishkina et al. (2010). **b)** Water solubility in haplobasaltic melt as a function of temperature. **c)** Extrapolation of water solubility in the melt phase to the experimentally observed solidus (eutectic) temperatures. The values are extrapolated from the experimental data points, not from the fit to Eq. 4.3.5; a constant change in water solubility in the melt with decreasing temperature ( $c=1.301$ ) is assumed in the pressure range of interest.

An attempt was made to directly measure the composition of eutectic melts in samples from the ‘solidus depression’ series, where both anorthite and diopside co-existed with the melt phase. The melt pools were often small (<15 μm) and not fully equilibrated with the surrounding crystals. A gradient in atomic number contrast between the center and rim of the melt pools could sometimes be observed in BSE images. A direct EPMA measurement of the eutectic melt composition was possible only in sample ADS36 (0.2 GPa, 1130 °C). The composition of the melt was approximately An<sub>59</sub>Di<sub>41</sub>, on anhydrous basis.

The proportion of the An component in eutectic melts is expected to increase with pressure (Yoder, 1965). To constrain the effect of pressure on eutectic melt compositions in the An-Di-H<sub>2</sub>O system, the EPMA measurement from sample ADS36 was combined with previously published data (Osborn, 1942; Yoder, 1965) (Fig. 4.3.6).

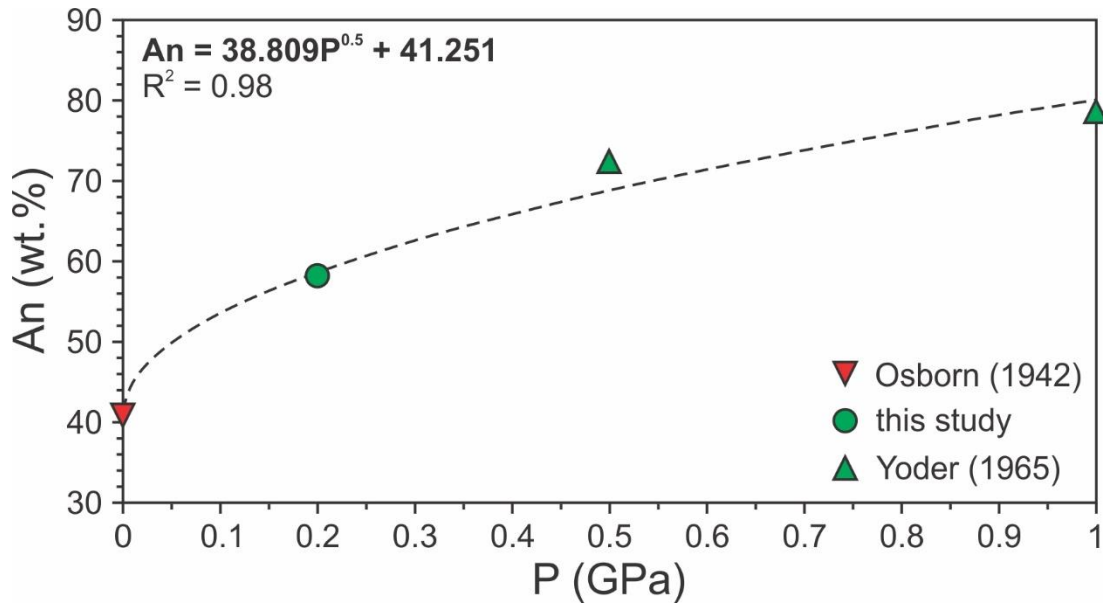


**Figure 4.3.6:** Experimentally observed eutectic melt compositions in the An-Di-H<sub>2</sub>O system, expressed as wt.% of anorthite component on anhydrous basis.

The total water contents, extrapolated to solidus temperatures (Fig. 4.3.5c), and melt compositions on anhydrous basis (Fig. 4.3.6) were used to estimate the major element oxide concentrations in eutectic melts at different pressures from 0.02 to 0.2 GPa. The eutectic melt compositions, normalized to 100 wt.%, are shown in Table 4.3.3.

4. Mantle melting at low water fugacity and the cryoscopic equation

**Table 4.3.3:** The estimated eutectic melt compositions in the An-Di-H<sub>2</sub>O system at 0.02 to 0.2 GPa, normalized to 100% by weight. ‘\*’ values calculated from the relationship given in Figure 4.3.6. ‘\*\*’ value based on direct EPMA measurement. ‘\*\*\*’ values represent the FTIR measurements of total water concentrations (from Table 4.3.2 and Fig. 4.3.5a and 4.3.5b), extrapolated to solidus temperatures (Fig. 4.3.5c).

<b>An (wt.%)</b>	<b>47*</b>	<b>50*</b>	<b>54*</b>	<b>56*</b>	<b>59**</b>
<b>T<sub>solidus</sub> (°C)</b>	<b>1203</b>	<b>1183</b>	<b>1131</b>	<b>1121</b>	<b>1103</b>
<b>P (GPa)</b>	<b>0.02</b>	<b>0.05</b>	<b>0.1</b>	<b>0.15</b>	<b>0.2</b>
<b>SiO<sub>2</sub></b>	49.14	48.23	47.34	46.56	45.89
<b>Al<sub>2</sub>O<sub>3</sub></b>	17.03	17.91	19.18	19.66	20.57
<b>CaO</b>	22.93	22.51	22.09	21.73	21.41
<b>MgO</b>	9.75	9.10	8.30	7.85	7.26
<b>H<sub>2</sub>O***</b>	<b>1.15</b>	<b>2.25</b>	<b>3.09</b>	<b>4.20</b>	<b>4.87</b>
<b>Σ</b>	100.00	100.00	100.00	100.00	100.00

### 4.3.3. Thermodynamic description of the melting point depression in magmatic (silicate-H<sub>2</sub>O) systems at low water fugacity

In a pure silicate (dry) system, the equilibrium condition at the solidus is simply:

$$G_s = G_l \quad \text{Eq. 4.3.7.}$$

where  $G_s$  and  $G_l$  are the Gibbs free energies of pure silicate solid(s) and pure silicate liquid, respectively. The solubility of water in (nominally anhydrous) minerals is limited. For low bulk water contents that are representative of upper mantle conditions, nearly all of the available water is expected to dissolve in the incipient melt. Thus, the liquid phase will no longer be pure, and, assuming ideal mixing between water and the silicate component, the equilibrium condition at the solidus is:

$$G_s = G_l + RT \ln X_{\text{silicate}} \quad \text{Eq. 4.3.8.}$$

where  $R$  is the ideal gas constant,  $T$  is absolute temperature and  $X_{\text{silicate}}$  is the mole fraction of the silicate component in the liquid phase. As a consequence of water dissolution in the melt, the stability field of the liquid phase expands and the melting point is depressed to lower temperature. Melting point depressions of several hundred degrees in silicate-H<sub>2</sub>O systems have been reported already in early experimental studies (e.g. Tuttle and England, 1955).

Equation 4.3.8. can be re-arranged as:

$$\frac{G_s - G_l}{RT} = \ln X_{\text{silicate}} \quad \text{Eq. 4.3.9.}$$

The Gibbs-Helmholtz equation states that (at constant pressure):

$$\frac{\partial \left( \frac{G}{T} \right)}{\partial T} = -\frac{H}{T^2} \quad \text{Eq. 4.3.10.}$$

Differentiating Equation 4.3.9. with respect to temperature, and using the Gibbs-Helmholtz equation (Eq. 4.3.10) to solve the left-hand side of the expression, one obtains:

$$\frac{H_l - H_s}{RT^2} = \frac{\Delta H_{\text{fus,silicate}}}{RT^2} = \frac{d \ln X_{\text{silicate}}}{dT} \quad \text{Eq. 4.3.11.}$$

where  $H_s$  and  $H_l$  are the enthalpies of pure silicate solid(s) and pure silicate liquid, respectively, and  $\Delta H_{\text{fus,silicate}}$  is the enthalpy of fusion of the dry system. Equation 4.3.11. can be integrated between the limits for pure silicate ( $X_{\text{silicate}}=1$ ,  $T=T_{\text{dry}}$ ) and the silicate-H<sub>2</sub>O system ( $X_{\text{silicate}}$ ,  $T$ ):

4. Mantle melting at low water fugacity and the cryoscopic equation

$$\frac{\Delta H_{fus,silicate}}{R} \int_{T_{dry}}^T \frac{dT}{T^2} = \int_1^{X_{silicate}} d \ln X_{silicate} \quad \text{Eq. 4.3.12.}$$

where  $T_{dry}$  is the solidus temperature of the dry system, and  $T$  is the solidus temperature of the silicate- $H_2O$  system at a given  $X_{silicate}$ . This implies the assumption that  $\Delta H_{fus,silicate}$  is constant over the temperature range of interest, between  $T_{dry}$  and  $T$ . The integration yields:

$$\frac{\Delta H_{fus,silicate}}{R} \left( \frac{1}{T_{dry}} - \frac{1}{T} \right) = \ln X_{silicate} \quad \text{Eq. 4.3.13.}$$

In conventional use, the expression above describes ideal (dilute) solutions; no chemical interaction between the solvent and the solute is assumed.

However, Stolper (1982) proposed that water dissolution in silicate liquids is a chemical reaction:



where  $H_2O_{melt}$  and  $OH_{melt}$  are the water species dissolved in the melt, and  $O_{melt}$  are the bridging oxygen atoms. This hypothesis was supported by consistent FTIR and NMR spectroscopic observations of both molecular water and hydroxyl groups in quenched silicate glasses. A similar relationship between the measured concentrations of hydroxyl and molecular water species, versus the total water concentrations, was found in quenched rhyolitic, basaltic and albite glasses.

This hypothesis was later confirmed by in-situ FTIR spectroscopic studies of water solubility in haplogranitic melts (Nowak and Behrens, 1995; Shen and Keppler, 1995). The equilibrium constant for the reaction 4.3.14. was directly measured, and was shown to be strongly dependent on temperature. The water speciation (at constant total water content) did not significantly change with pressure (Shen and Keppler, 1995). Both studies noted that speciation changes occur even during very fast quenching, and the speciation at original magmatic temperatures is not preserved in the glass. The equilibrium of reaction 4.3.14. is strongly shifted to the right in the high-temperature melt phase, with respect to the glass phase, causing the earlier studies of water speciation in quenched products to underestimate the concentration of hydroxyl species at run conditions.

Due to the observed chemical interaction between water and the silicate component, reaction 4.3.14. is expected to contribute to the overall enthalpy of fusion of the silicate-H<sub>2</sub>O system, and the expression 4.3.13. will not strictly hold. However, regardless of the actual value for the enthalpy of fusion in a silicate-H<sub>2</sub>O system, a linear relationship between  $\ln X_{\text{silicate}}$  and  $1/T$  is predicted by Equation 4.3.13:

$$\ln X_{\text{silicate}} = d + e \frac{1}{T} \quad \text{Eq. 4.3.15.}$$

where parameters  $d$  and  $e$  are:

$$d = \frac{\Delta H_{\text{fus}}}{R} \frac{1}{T_{\text{dry}}} \quad \text{Eq. 4.3.16.}$$

$$e = - \frac{\Delta H_{\text{fus}}}{R} \quad \text{Eq. 4.3.17.}$$

the enthalpy of fusion is now for the hydrous system ( $\Delta H_{\text{fus}} \neq \Delta H_{\text{fus,silicate}}$ ).

We precisely determined the melting point depressions ( $T$ ) and the corresponding near-solidus melt compositions ( $X_{\text{silicate}}$ ) in the anorthite-diopside-H<sub>2</sub>O system at a range of total melt water contents (Ch. 4.3.1. and 4.3.2.). Taking Equation 4.3.13. into consideration, the data is expected to plot along a straight line in the  $\ln X_{\text{silicate}} - 1/T$  plot, provided the  $X_{\text{silicate}}$  is correctly defined. The mole fraction of the silicate component in the liquid phase is:

$$X_{\text{silicate}} = 1 - X_{\text{H}_2\text{O}} - X_{\text{OH}} \quad \text{Eq. 4.3.18.}$$

where  $X_{\text{H}_2\text{O}}$  and  $X_{\text{OH}}$  are the mole fractions of the respective water species in the melt *at run conditions*. Given what is known about the water speciation change occurring upon quench (Nowak and Behrens, 1995; Shen and Keppler, 1995), the  $X_{\text{H}_2\text{O}}$  and  $X_{\text{OH}}$  need to be estimated from the equilibrium constant of reaction 4.3.14., run condition temperature, and the total water concentration in the quenched glasses.

Another problem in defining the  $X_{\text{silicate}}$  is the question of how to formulate one molar unit of a silicate melt. How many oxygen atoms should be assigned to a single molar unit to accurately describe the average lifetime of short-range ordering in a silicate liquid at high temperature?

#### 4.3.3.1. Model 1: Defining the silicate molar unit

To address the issue of the appropriate definition of a silicate molar unit, we begin with a simplified model, assuming complete dissociation of water in the melt as hydroxyl groups. At high temperatures and low total water concentrations, hydroxyl groups are expected to be the dominant species. Since these conditions are met in the anorthite-diopside-H<sub>2</sub>O system below 0.2 GPa, the assumption of all-hydroxyl-group water speciation should be a fairly good first approximation.

The molar weights of the silicate unit on 1-, 3-, 4- and 8-oxygen basis were calculated from the known near-solidus melt compositions (Ch. 4.3.2.), and were used to estimate the  $X_{H_2O, total}$ . The  $X_{H_2O, total}$  is the mole fraction of measured total water content in haplobasaltic glasses, expressed as molecular water. It is assumed that one mole of total water measured in the glass phase had previously formed two moles of hydroxyl groups in the melt at run conditions:

$$X_{OH} = 2X_{H_2O, total} \quad \text{Eq. 4.3.19.}$$

therefore, the final estimate of  $X_{silicate}$  is:

$$X_{silicate} = 1 - X_{OH} \quad \text{Eq. 4.3.20.}$$

The experimentally observed solidus temperatures (Ch. 4.3.1) were plotted against the sets of  $X_{silicate}$  values that were derived assuming 1-, 3-, 4- and 8-oxygen silicate molar units. The parameters  $d$  and  $e$  (Eq. 4.3.16. and 4.3.17) were obtained from simple linear regression. The results of the model are summarized in Table 4.3.4. The fit of  $\ln X_{silicate} - 1/T$  plot to a linear function gradually deteriorates with increasing molar weight of the silicate unit (Fig. 4.3.7), and for large molar units the dry melting temperature (Osborn, 1942) deviates from the trend defined by the solidus temperatures in the presence of water. This suggests that the silicate melt structure is best approximated by the assumption of a small 1-oxygen molar unit.

**Table 4.3.4:** A summary of results for Model 1. Complete dissociation of water as hydroxyl groups at run conditions is assumed. Different silicate molar units (containing 1, 3, 4 and 8 bridging oxygen atoms) are tested for goodness-of-fit to Equation 4.3.13. The fit of  $\ln X_{\text{silicate}} - 1/T$  plot to a linear function deteriorates with increasing molar weight of the silicate unit. The 1-oxygen molar unit provides the best approximation of silicate liquid structure at high temperature. ‘ $\approx$ ’ denotes the variation in near-solidus melt compositions with increasing pressure and total water content (Ch. 4.3.2, Table 4.3.3).

Silicate unit:	M (g/mol)	a	b	R <sup>2</sup>
1 oxygen	$\approx 35$	-2462	1.604	0.9497
3 oxygen	$\approx 106$	-7576	4.938	0.9458
4 oxygen	$\approx 141$	-10341	6.744	0.9418
8 oxygen	$\approx 283$	-25833	16.919	0.8897

This result is consistent with in-situ <sup>29</sup>Si NMR spectroscopic observations of silicate liquids. Already at several hundred degrees above glass transition temperatures, Stebbins (1995) describes rapid exchange of Si atoms between different coordination sites within the melt structure. Thus, the existence of large polymer-like molar units, containing multiple bridging oxygens, seems unlikely.

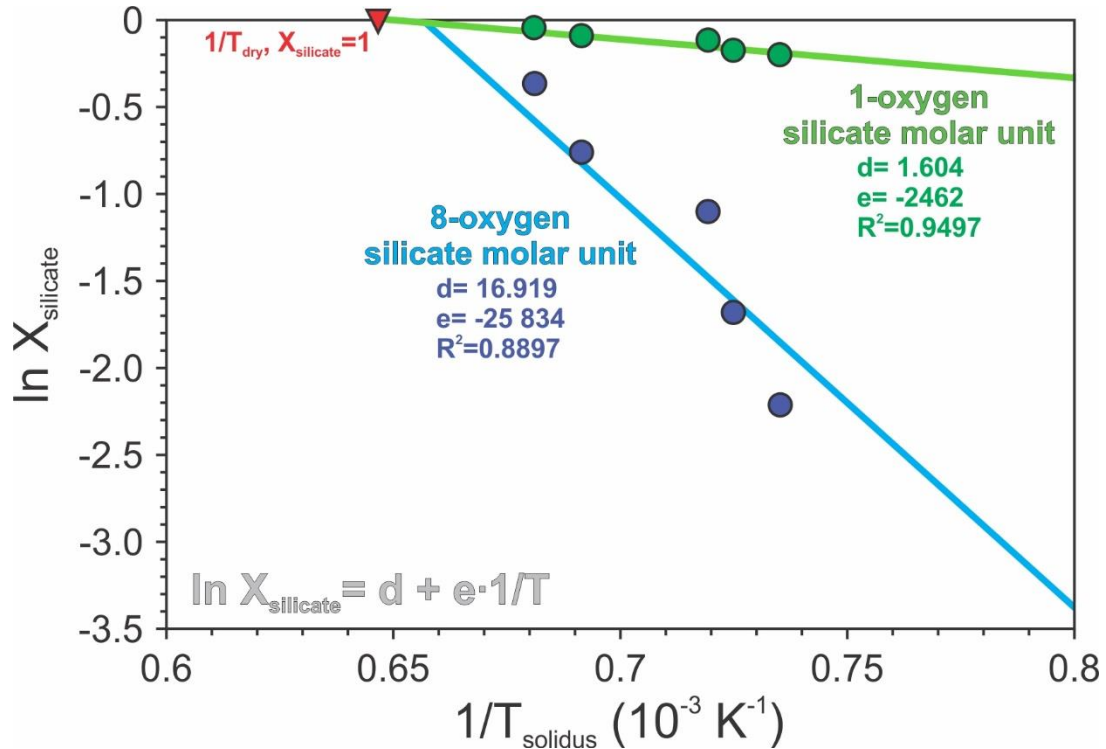


**Figure 4.3.7:** The  $\ln X_{\text{silicate}} - 1/T$  plot for Model 1. The results for the assumption of a 1-oxygen (green) and 8-oxygen (blue) silicate molar unit are compared. With increasing molar weight of the silicate unit, the fit to a straight line deteriorates and the dry melting temperature (Osborn, 1942) deviates from the trend defined by the hydrous experiments. The smallest silicate molar unit, containing one bridging oxygen, is the best approximation of the silicate melt structure at run conditions.

4.3.3.2. Model 2: Water speciation in haplobasaltic liquids

If the water speciation in silicate melts is governed by the reaction 4.3.14:



an equilibrium constant can be written:

$$K = \frac{(X_{OH})^2}{X_{H_2O}} \quad \text{Eq. 4.3.21.}$$

and

$$X_{H_2O, total} = X_{H_2O} + \frac{1}{2}X_{OH} \quad \text{Eq. 4.3.22.}$$

where, as before, the  $X_{H_2O}$  and  $X_{OH}$  are the mole fractions of the water species at run conditions, and the  $X_{H_2O, total}$  is the mole fraction of molecular water measured in the quenched glasses. For simplicity,  $X_O$  is included in the value of  $K$ .

For any equilibrium constant  $K$ , Equations 4.3.21. and 4.3.22. can be solved for  $X_{H_2O}$  and  $X_{OH}$ , and thus for the corresponding  $X_{silicate}$  (Eq. 4.3.18). A silicate molar unit on 1-oxygen basis is used throughout Model 2. Since no in-situ measurements of the equilibrium constant  $K$  are available for basaltic melts, the following approach was adopted. The equilibrium constant can be described as (Nowak and Behrens, 1995; Shen and Keppler, 1995):

$$\ln K = f + g \frac{1}{T} \quad \text{Eq. 4.3.23.}$$

where parameters  $f$  and  $g$  are:

$$f = \frac{\Delta S^0}{R} \quad \text{Eq. 4.3.24.}$$

$$g = -\frac{\Delta H^0}{R} \quad \text{Eq. 4.3.25.}$$

and  $\Delta S^0$  and  $\Delta H^0$  are the standard state entropy and enthalpy of the water speciation reaction in the silicate melt. If a fixed  $g$  is chosen, the y-axis intercept  $f$  can be adjusted to yield  $X_{H_2O}$ ,  $X_{OH}$  and  $X_{silicate}$  that result in a best-fit of the  $\ln X_{silicate} - 1/T$  plot to a straight line (for the given slope  $g$ ). Equilibrium constants were calculated, and  $\ln X_{silicate} - 1/T$  plots were generated, for a range of values of the parameter  $g$ .

#### 4. Mantle melting at low water fugacity and the cryoscopic equation

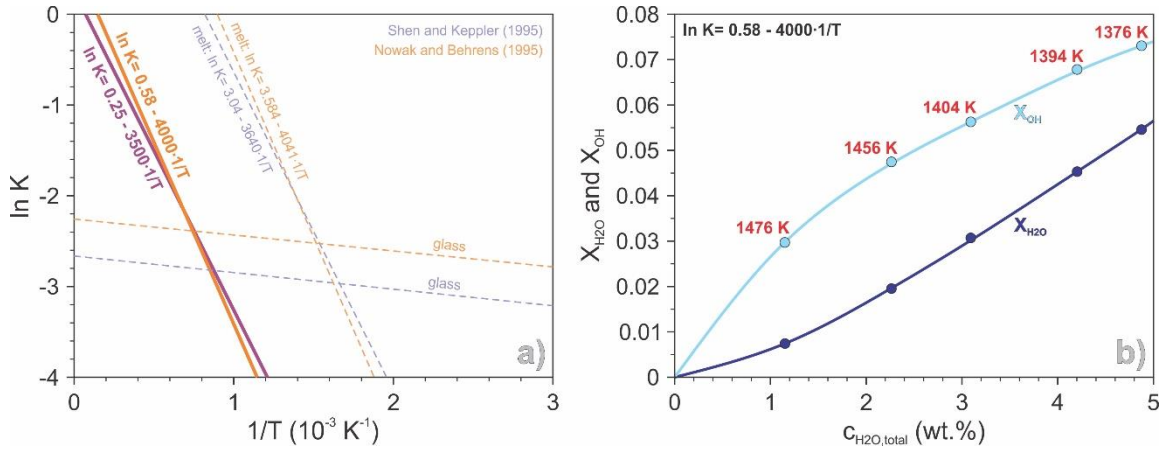


**Figure 4.3.8:** **a)** The preferred temperature-dependent equilibrium constants ( $K$ ) for the water speciation reaction in haplobasaltic melt (bold lines), compared to the results of previous in-situ measurements of  $K$  in haplogranitic bulk compositions (dashed lines). **b)** Water speciation of near-solidus melts in the anorthite-diopside- $\text{H}_2\text{O}$  system, expressed in mole fractions of molecular water and hydroxyl groups versus total melt water content (in wt.%). The estimated water speciation corresponds to the preferred equilibrium constant  $\ln K = 0.58 - 4000 \cdot 1/T$ .

Assuming a temperature dependent equilibrium constant for the water speciation reaction in the melt phase improves the fit of experimental data to a linear function in the  $\ln X_{\text{silicate}} - 1/T$  plots. However, since the water is mostly dissociated in the melt at run conditions as hydroxyl groups (assumption from Model 1), only a modest improvement of the fit, from  $R^2 = 0.9497$  to  $0.96 < R^2 < 0.97$ , occurs upon introducing the water speciation model (Fig. 4.3.9).

A similar goodness-of-fit can be obtained for a range of  $g$  values. Due to the limitations of this approach, we could not precisely constrain the temperature dependence of the equilibrium constant  $K$  in haplobasaltic melt. Shen and Keppler (1995) note that the standard state enthalpy for the water speciation reaction in the melt phase (i.e. parameter  $g$ ), obtained by their measurements, is very similar to the one from Nowak and Behrens (1995), despite the significantly higher alkali and lower silica content of the melt from the latter study. It is suggested that  $\Delta H^0$  may be fairly insensitive to the bulk composition of the silicate liquid. In addition, it is known that the water speciation in quenched silicate glasses is similar across the range of natural magmatic compositions (Stöpler, 1982). We, therefore, assume a parameter  $g$  based on the previous in-situ measurements in haplogranitic melts (Fig. 4.3.8a).

4.3.3.3. The enthalpy of fusion in the anorthite-diopside-H<sub>2</sub>O system

The enthalpy of fusion for the dry 50:50 mixture of anorthite and diopside was calculated following DeYoreo et al. (1995). Calorimetric measurements of heat contents of pure anorthite from Richet and Bottinga (1984), and of pure diopside from Lange et al. (1991) were used. The calculation yielded  $\Delta H_{\text{fus,silicate}}$  for the dry system of 19 kJ/mol (on 1-oxygen basis).

The enthalpy of fusion for the hydrous system can also be derived from parameter  $e$  (Eq. 4.3.17) of the preferred  $\ln X_{\text{silicate}} - 1/T$  fit from Model 2. The estimated  $\Delta H_{\text{fus}}$  for the hydrous system is 14 kJ/mol. This is reasonably close to the value for the dry system. The difference could be due to the enthalpy of mixing of water with the silicate melt.

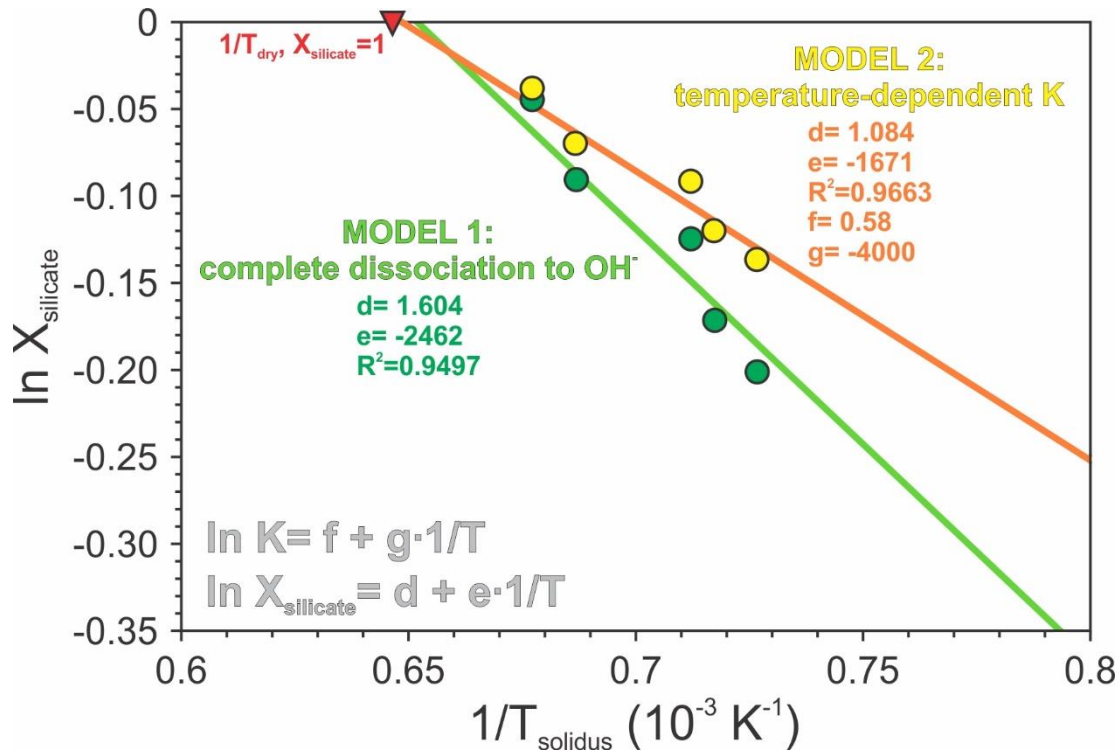


**Figure 4.3.9:** A comparison of  $\ln X_{\text{silicate}} - 1/T$  plots for Model 1 (green) and Model 2 (orange). A silicate molar unit containing one bridging oxygen is assumed in both examples. The Model 1 plot is the same as in Figure 4.3.7, but the y-axis range is adjusted to show more detail. Introducing temperature-dependent water speciation in Model 2 results in an improved fit to a linear function and the dry melting point is predicted within 5 °C of the experimental observation (Osborn, 1942).

#### 4.4. Discussion

In Chapter 4.1. we argued that many melting experiments in the peridotite-H<sub>2</sub>O system, performed using solid-medium high-pressure devices, systematically underestimate the effects of water on the melting point depression. The difficulties in recovering pristine basaltic glasses from high-pressures are well established in literature, and recognizing low degrees of partial melting in the run products is subjective (Ch. 4.1).

Our experiments in the haplobasalt anorthite-diopside-H<sub>2</sub>O system were designed to avoid these challenges. Since this is a eutectic system, large quantities of melt form immediately at the solidus and are easy to recognize. We observed the formation of basaltic melts with a total water content of 3 to 5 wt.% at approximately 50 °C lower temperatures, as compared to previous estimates from studies of hydrous peridotites (Fig. 4.4.1). This result is in good agreement with the theoretical expectation, and the implications are discussed in the following chapter. Notably, while the scatter in the hydrous peridotite dataset is considerable, some data points, particularly those from experiments performed at lower pressures, do agree with our observation.

##### 4.4.1. Upper mantle melting and the cryoscopic equation

Aubaud et al. (2004) suggested that the relationship between melting point depression and total melt water content may be described using the cryoscopic approach:

$$T = \frac{1}{\left( \frac{1}{T_{dry}} - \frac{R}{\Delta H_{fus,silicate}} \ln(1 - X_{OH}) \right)} \quad \text{Eq. 4.4.1.}$$

The expression above is essentially a re-arrangement of Equation 4.3.13, with the assumption of complete dissolution of water in the melt as hydroxyl groups, and  $X_{silicate}$  expressed through  $X_{OH}$ . It is apparent from the thermodynamic model presented in this study (Ch. 4.3.3) that there is considerable ambiguity in the definition of  $X_{silicate}$ . Unless the  $\Delta T - c_{H_2O,total}$  relationship is constrained by a high-quality experimental dataset, the  $X_{silicate}$  may not be properly defined. As a result, the cryoscopic prediction may severely deviate from the actual melting point depression, particularly at high total melt water contents.

Hirschmann et al. (2009) attempted to address this issue, and calibrated the cryoscopic equation against the existing experimental dataset (Fig. 4.4.1). As in the original model (Aubaud et al., 2004), an assumption of complete dissociation of water into hydroxyl groups was made. Indeed, this may be a fairly good approximation of water speciation in basaltic melts at high temperatures and low total water contents.

Hirschmann et al. (2009) used the calorimetric measurements on a dry peridotite assemblage from Kojitani and Akaogi (1997), and defined the silicate molar unit on the basis of simple oxides (e.g. SiO<sub>2</sub>, Al<sub>2</sub>O<sub>3</sub>, MgO, etc.) with a mean molar weight of 59 g/mol. The dry peridotite solidus was estimated, not from the difference in dry and hydrous incipient melting temperature, but from the difference in temperature required to stabilize a given melt fraction in dry and hydrous systems, respectively (Katz et al., 2003). The dry melting temperatures, required to stabilize melt fractions equivalent to those observed in hydrous peridotite studies, were interpolated from literature data (Baker and Stolper, 1994; Robinson et al., 1998; Walter, 1998). This combination of parameters resulted in a good empirical agreement with the experimental dataset that was available at the time, based solely on hydrous peridotite studies (Fig. 4.4.1).

We adopted a somewhat different approach. To avoid making the intrinsic assumptions of the cryoscopic equation, mainly related to the chemical interaction between water and silicate liquids (Ch. 4.3.3; also discussed by Hirschmann et al., 2009), we do not use literature values of  $\Delta H_{\text{fus,silicate}}$  to predict hydrous melting temperatures for a range of total melt water contents. Instead, we tested which approach for calculating  $X_{\text{silicate}}$  yields a linear  $\ln X_{\text{silicate}} - 1/T$  relationship, as required by Equation 4.3.13. This relationship should also include the point defined by the dry melting temperature and  $X_{\text{silicate}}=1$ . This type of modelling was not possible in previous studies due to the scatter in the hydrous peridotite melting temperatures (Fig. 4.4.1).

From the results of Model 1 (Ch. 4.3.3.1), which assumes all water is dissociated in the melt as hydroxyl groups, we are now able to demonstrate that a silicate unit containing one oxygen atom represents the best approximation of silicate liquid structure at high temperatures. The variation of Model 1 using a 1-oxygen silicate unit predicts a dry melting temperature within 25 °C of the

experimental observation (Osborn, 1942), and the goodness-of-fit of  $\ln X_{\text{silicate}} - 1/T$  pairs to the theoretical linear function is  $R^2=0.9497$ .

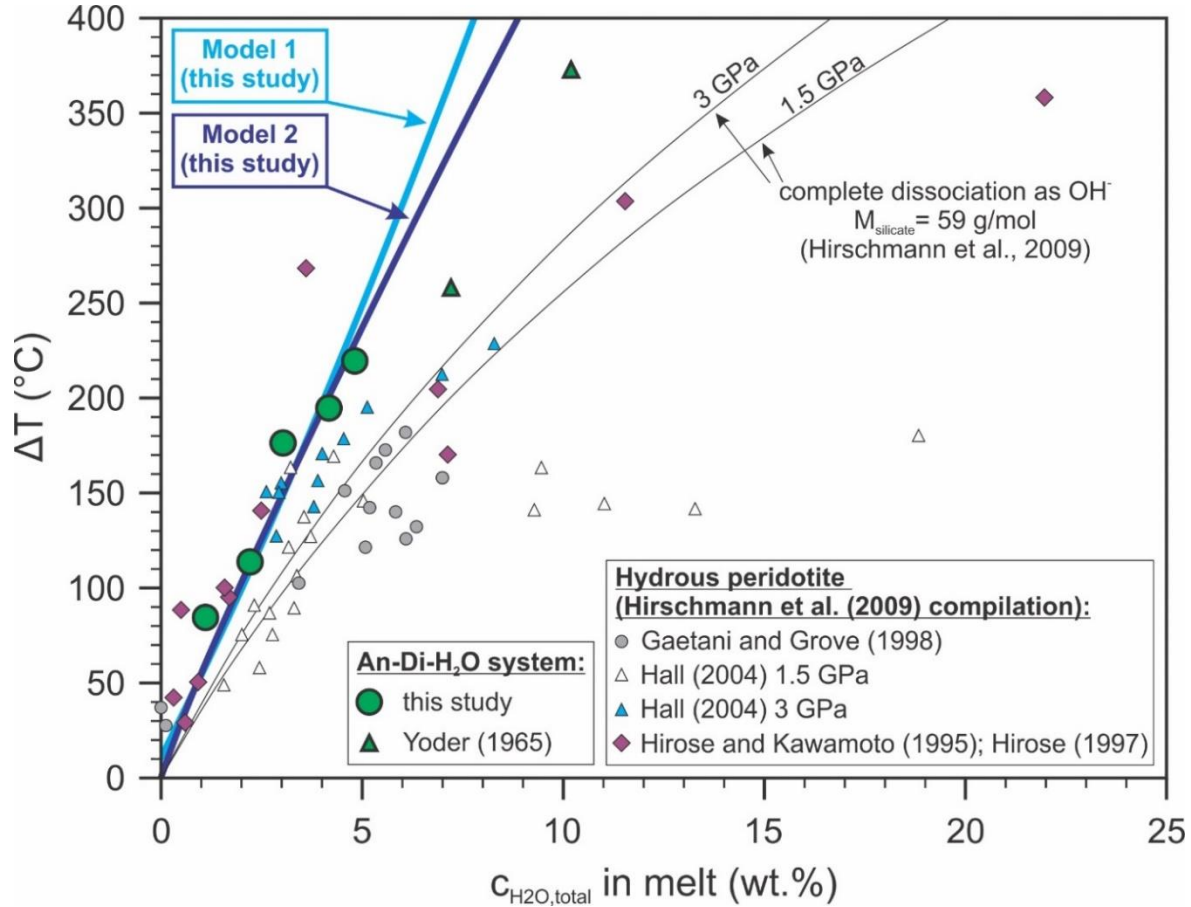


**Figure 4.4.1:** The melting point depression in the peridotite-H<sub>2</sub>O system, expressed as a function of total water content in near-solidus basaltic melt. The anorthite-diopside-H<sub>2</sub>O system dataset includes the results from this study (direct measurements) and literature data (water content was extrapolated from 0.02-0.2 GPa to 0.5-1 GPa; hydrous solidi temperatures are direct measurements taken from Yoder, 1965). The hydrous peridotite dataset (as compiled by Hirschmann et al., 2009) is shown for comparison. The  $\Delta T - c_{\text{H}_2\text{O},\text{total}}$  relationships predicted by our modelling are indicated by the bold blue lines. Model 1 (light blue) assumes complete dissociation of water in the melt as hydroxyl groups. Model 2 (dark blue) assumes that water is dissolved in the melt as both hydroxyl groups and molecular water, and uses a temperature-dependent equilibrium constant for the water speciation reaction  $\text{H}_2\text{O}_{\text{melt}} + \text{O}_{\text{melt}} \leftrightarrow \text{OH}_{\text{melt}}$ . The equilibrium constant is not strictly constrained by Model 2 – the result shown in the figure are our preferred values, supported by in-situ measurements performed on haplogranitic melts (Nowak and Berhens, 1995; Shen and Keppler, 1995). Both Model 1 and Model 2 curves are calculated assuming a 1-oxygen silicate molar unit (35 g/mol). The Hirschmann et al. (2009) calibration of the cryoscopic equation to the hydrous peridotite dataset is shown for comparison (black lines).

We attempted to refine the model further by acknowledging that silicate liquids may incorporate both hydroxyl groups and molecular water (Ch. 4.3.3.2). With increasing total melt water content, and with the corresponding decrease in solidus temperature, the proportion of molecular water in the melt increases. Thus, Model 2 agrees very well with Model 1 at low water contents, but

deviates from it for higher concentrations (Fig. 4.4.1). Compared to Model 1, Model 2 yields a higher goodness-of-fit of  $\ln X_{\text{silicate}} - 1/T$  plot to a linear function ( $R^2=0.9663$ ), and the dry melting temperature is now predicted within 5 °C of the experimental observation. The improvement with respect to Model 1 suggests that this approach has merit. However, even in the strictly controlled environment of this study, some minor inaccuracies in experimentally observed solidi, generally believed to be <15 °C, yielded a similar goodness-of-fit for a range of assumed parameters. Therefore, we could not precisely constrain the equilibrium constant of the water speciation reaction in basaltic melts. The curve in Figure 4.4.1. is our preferred solution, somewhat based on previous in-situ measurements of water speciation in haplogranitic melts (Ch. 4.3.3.2).

The data from Yoder (1965) on solidus temperatures in the anorthite-diopside-H<sub>2</sub>O system at 0.5 and 1 GPa were added to Figures 4.4.1. and 4.4.2. by extrapolating total melt water contents in near-solidus melts. The pressure and temperature dependence of water solubility in the melt, as determined from this study (Fig. 4.3.5), was used in the extrapolation. The extrapolation yields total water contents of 7.2 and 10.2 wt.% at 0.5 and 1 GPa, respectively. The solidus temperatures are 1096 °C at 0.5 GPa, and 1015 °C at 1 GPa (Yoder, 1965). It should be noted that the melting point depressions observed by Yoder (1965) are generally higher than those derived from the hydrous peridotite studies.

The prediction of Model 2 does not accurately reproduce the data points from the study by Yoder (1965). The most likely reason is that at higher water contents, major changes in water speciation occur and the fraction of molecular H<sub>2</sub>O in the melt becomes significant. This would necessarily reduce the melting point depression. Introducing a different set of parameters in Model 2 is, in principle, able to fit a curve through the entire experimental data set for the anorthite-diopside-H<sub>2</sub>O system. However, this results in a somewhat reduced goodness-of-fit of the  $\ln X_{\text{silicate}} - 1/T$  relationship to a linear function ( $0.95 < R^2 < 0.96$ ). The best fit after introducing the two additional data points corresponds to:  $\ln K = 1.036 - 4000 \cdot 1/T$  and  $\ln X_{\text{silicate}} = 1.306 - 2004 \cdot 1/T$  ( $R^2 = 0.9549$ ). The dry melting temperature is then predicted at 1260 °C, 14 °C lower than the experimental observation (Osborn, 1942). We do not recommend to use this equation, as the water contents corresponding to the solidus data by Yoder (1965) were not constrained by direct measurements in the 0.5 to 1 GPa pressure range.

A rigorous thermodynamic treatment of the melting point depression in silicate-H<sub>2</sub>O systems is useful, as it can provide insights into the structure of hydrous silicate liquids. However, for practical purposes, more simple empirical equations may also be used.

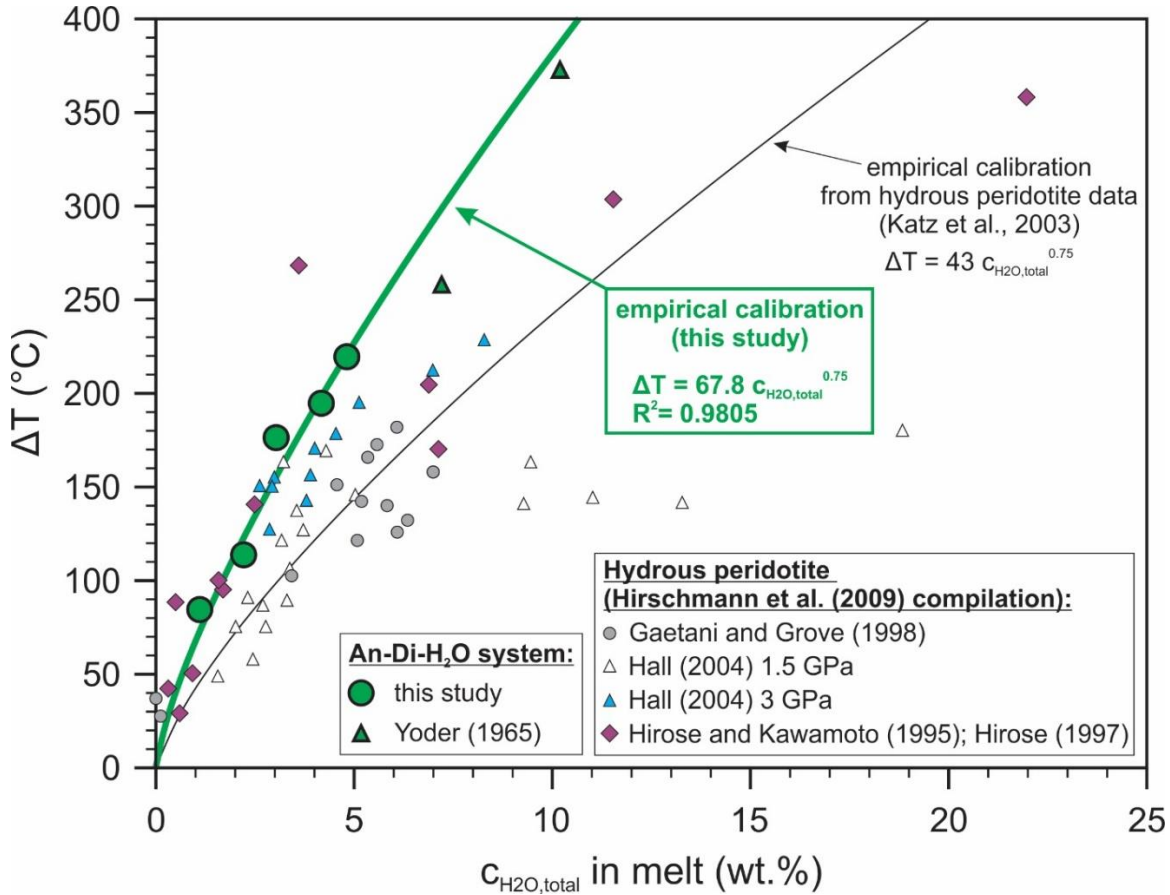


**Figure 4.4.2:** The melting point depression in the peridotite-H<sub>2</sub>O system, expressed as a function of total water content in near-solidus basaltic melt. The anorthite-diopside-H<sub>2</sub>O system dataset includes the results from this study (direct measurements) and the literature data (water content was extrapolated from 0.02-0.2 GPa to 0.5-1 GPa; hydrous solidi are direct measurements taken from Yoder, 1965). The hydrous peridotite dataset (as compiled by Hirschmann et al., 2009) is shown for comparison. The empirical calibration of the  $\Delta T - c_{\text{H}_2\text{O},\text{total}}$  relationship, based on the data from this study, is indicated by the bold green line. The literature data (Yoder, 1965) is not included in the regression analysis. The Katz et al. (2003) preferred empirical fit, based mostly on the data from Hirose and Kawamoto (1995) and Gaetani and Grove (1998), is shown for comparison.

Katz et al. (2003) proposed such a simple empirical relationship:

$$\Delta T = h (c_{\text{H}_2\text{O},\text{total}})^i \quad \text{Eq. 4.4.2.}$$

where the total melt water content is given directly in wt.%, and the parameters  $h$  and  $i$  are determined from the best-fit to the experimental data. Their preferred values were  $h=43$  and  $i=0.75$ ,

and the calibration was based mainly on the data from Hirose and Kawamoto (1995) and Gaetani and Grove (1998).

This type of equation successfully describes our dataset, as well (Fig. 4.4.2). For exponent values  $i \approx 0.75$ , the fit becomes particularly good ( $R^2 > 0.98$ ). Interestingly, the relationship also reproduces the Yoder (1965) data points more closely than Model 2, although this is likely coincidental. The Yoder (1965) data were not included to constrain the regression line shown in Figure 4.4.2. Due to its simplicity, this approach for estimating the  $\Delta T - c_{\text{H}_2\text{O, total}}$  relationship may be preferred for some purposes, although it does not have any theoretical foundation.

#### **4.4.2. Implications of the updated melting model**

The effect of water on the melting point depression of peridotite is more substantial than previously thought (Ch. 4.4.1). The existing model, used by Hirschmann et al. (2009) to evaluate the possibility of melting at upper mantle depths, can now be updated with the new calibration of the  $\Delta T - c_{\text{H}_2\text{O, total}}$  relationship (Fig. 4.4.1. and 4.4.2). The melting model is described only in general terms. For details of the model parametrization see Hirschmann et al. (2009).

##### *4.4.2.1. Description of the melting model*

To understand whether melting is plausible at upper mantle depths, is it first necessary to determine the total water contents of the hypothetical incipient peridotite melts. These values of total melt water contents can be estimated from the published water partition coefficients between peridotite minerals and basaltic melts.

The mineral/melt water partition coefficients depend on pressure and temperature, possibly also on water activity, if the water dissolution mechanisms in the mineral and melt are not the same (Keppler and Bolfan-Casanova, 2006). A number of experimental measurements are available, but the effects of pressure and temperature (and water activity) on peridotite/melt water partitioning are not well constrained. Thus, Hirschmann et al. (2009) introduced some simplifications. Constant values for olivine/melt and garnet/melt water partition coefficients – averages from literature data compilation – were used in the model.

Studies of water solubility in nominally anhydrous minerals suggest that most of the upper mantle water may be stored in pyroxene (Rauch and Keppler, 2002; Bromiley and Keppler, 2004; Mierdel et al., 2007). Therefore, the parametrization of pyroxene/melt water partition coefficients is particularly important for estimating the water content of hypothetical low-degree peridotite melt. The experimentally measured clinopyroxene/melt and orthopyroxene/melt water partition coefficients are generally of the same order of magnitude over a wide range of pressures; Warren and Hauri (2014) report an average  $D_{H_2O}^{cpx/opyx}$  of  $1.3 \pm 0.3$  from a number of experimental studies. Therefore, in the proposed melting model Hirschmann et al. (2009) treat the clinopyroxene/melt and orthopyroxene/melt water partition coefficients together. The pyroxene/melt water partition coefficients increase systematically with  $Al_2O_3$  content of pyroxenes, and a review of the published data indicates that  $Al_2O_3$  concentrations in pyroxenes vary strongly with pressure. The highest  $Al_2O_3$  (and water) concentrations in pyroxenes are reported at low pressures (<3.5 GPa). These observations are generally supported by water solubility measurements in Al-saturated enstatite (Mierdel et al., 2007). Hirschmann et al. (2009) express the  $Al_2O_3$  concentration in pyroxene as a function of pressure, and the pyroxene/melt water partition coefficient as a function of the  $Al_2O_3$  content in pyroxene. This allows calculation of pressure-dependent pyroxene/melt water partition coefficient. The effects of temperature on water and aluminium solubility in pyroxene are not taken into account.

Pressure-dependent mineral modes were used in the calculation (after Irifune and Isshiki (1998); Stixrude and Lithgow-Bertelloni, 2005, 2007), and a pressure-dependent bulk peridotite/melt water partition coefficient was calculated as:

$$D_{H_2O}^{per/melt} = \sum D_{H_2O}^{min/melt_i} X_i \quad \text{Eq. 4.4.3.}$$

where  $D_{H_2O}^{per/melt}$  is the bulk peridotite/melt water partition coefficient,  $D_{H_2O}^{min/melt_i}$  is the mineral/melt partition coefficient for mineral  $i$ , and the  $X_i$  is mass fraction of mineral  $i$ . The total water content of hypothetical upper mantle melts is estimated from the batch equilibrium equation (Ch. 3.3.5, Eq. 3.3.5). For incipient melt ( $F_{melt}=0$ ), the expression 3.3.5. is simplified and the hypothetical melt water concentration is obtained by dividing the bulk mantle water content by  $D_{H_2O}^{per/melt}$ . The  $D_{H_2O}^{per/melt}$  values after Hirschmann et al. (2009), and the corresponding water

concentrations in the hypothetical incipient melt are shown in Figure 4.4.3a. A bulk water content of 200 ppm is assumed in the given example.

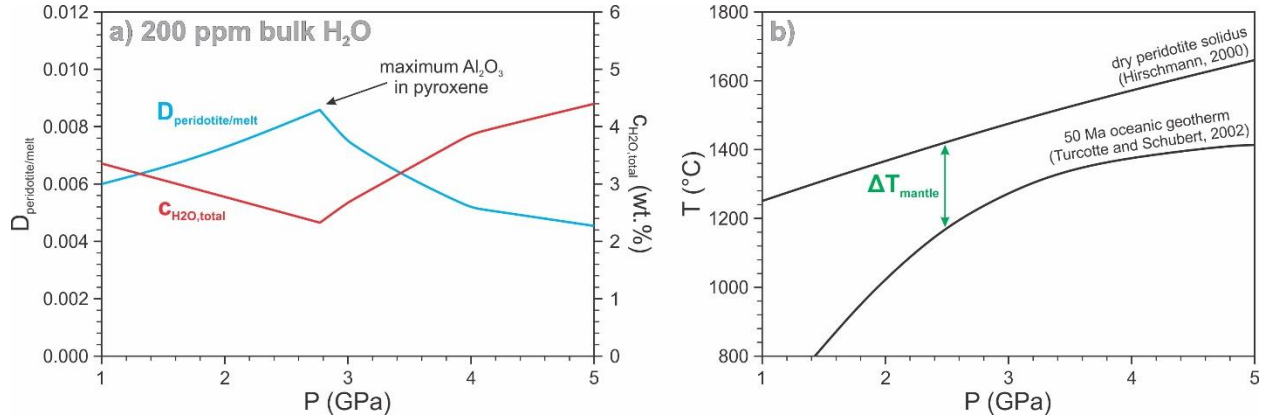


**Figure 4.4.3:** **a)** Peridotite/melt water partition coefficients (blue line) as a function of pressure (after Hirschmann et al., 2009); hypothetical incipient melt water contents ( $F_{\text{melt}}=0$ ), calculated using the shown peridotite/melt water partition coefficients, and assuming a bulk water content of 200 ppm (red line). **b)** An example of  $\Delta T_{\text{mantle}}$  (green) for the 50 Ma oceanic geotherm (after Turcotte and Schubert, 2002) assuming the dry peridotite solidus after Hirschmann (2000).

The remaining issue is whether the estimated water concentrations in hypothetical incipient melts can depress the peridotite solidus sufficiently for the melting to occur along some typical geotherm. The difference between the dry peridotite solidus temperatures and geotherm temperatures is calculated:

$$\Delta T_{\text{mantle}}(P) = T_{\text{dry}}(P) - T_{\text{geotherm}}(P) \quad \text{Eq. 4.4.4.}$$

where  $T_{\text{dry}}(P)$  and  $T_{\text{geotherm}}(P)$  are the dry peridotite solidus and geotherm temperatures, respectively, and the  $\Delta T_{\text{mantle}}(P)$  is the pressure-dependent difference between the solidus and geotherm temperatures (Fig. 4.4.3b).

The new calibration of the  $\Delta T - C_{\text{H}_2\text{O, total}}$  relationship (Fig. 4.4.1. and 4.4.2) can now be applied to reevaluate the role of water in upper mantle melting. The pressure-dependent  $\Delta T_{\text{mantle}}$  and the updated  $\Delta T - C_{\text{H}_2\text{O, total}}$  relationship (this study) can be used to calculate the minimum melt water contents sufficient to induce melting along a chosen geotherm. Equation 4.4.2 was inverted to express  $C_{\text{H}_2\text{O, total}}$  as a function of  $\Delta T_{\text{mantle}}$ . The minimum melt water contents required to induce melting along a particular geotherm are also a function of pressure. Melt may be stabilized in the pressure range where the water content of hypothetical incipient melt (derived from Eq. 4.4.3. and

3.3.5) exceeds the minimum melt water content required for melting (inverse function of Eq. 4.4.2). An example is shown in Figure 4.4.4.

#### 4.4.2.2. Melting in the upper mantle

To gain more insight into the potential existence of a stable melt layer at the oceanic lithosphere-asthenosphere boundary (LAB), we estimated the minimum melt water contents required to induce melting along a 50 Ma oceanic geotherm (Turcotte and Schubert, 2002). All calculation parameters are after Hirschmann et al. (2009), except for the  $\Delta T - c_{\text{H}_2\text{O},\text{total}}$  relationship, which is updated from the results of this study. The melt water contents sufficient for incipient melting exhibit a minimum of approximately 3.8 wt.% at pressures between 3 and 4 GPa. This depth range generally corresponds to the minimum of water solubility in peridotite minerals (Mierdel et al., 2007), and to the predicted decrease in pyroxene and increase in garnet modes with pressure (Irifune and Isshiki (1998); Stixrude and Lithgow-Bertelloni, 2005, 2007) (Fig. 4.4.4). The updated melting model predicts that 215 ppm of bulk water may be sufficient to induce melting along a typical oceanic geotherm, whereas the previous parametrization required close to 300 ppm (Fig. 4.4.4).

We constrained the effect of water on the melting point depression in the peridotite-H<sub>2</sub>O system, but the model requires a number of other input parameters that introduce uncertainty to the result. To explore how the choice of parameters affects the outcome of the model, the calculation from Figure 4.4.4. was repeated by systematically replacing the values preferred by Hirschmann et al. (2009) with other literature sources.

Figure 4.4.5. contains a summary of this exercise. The  $\Delta T - c_{\text{H}_2\text{O},\text{total}}$  relationship, as determined from this study, is used throughout all variations of the model shown in Figure 4.4.5. (Panels 4.4.5a to 4.4.5e). Most variations of the model predict incipient melting with  $200 \pm 20$  ppm of water at depths that generally correspond to the globally observed shear wave velocity reduction in the oceanic upper mantle.

4. Mantle melting at low water fugacity and the cryoscopic equation

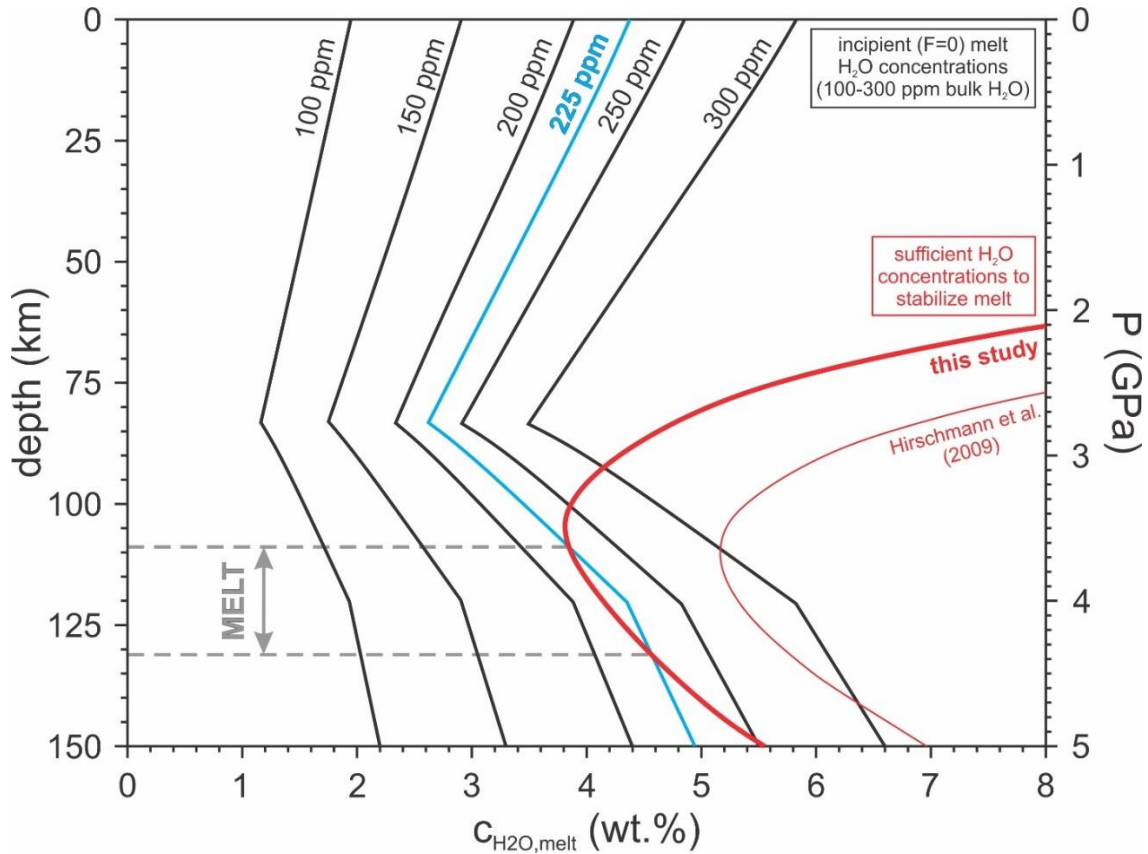


**Figure 4.4.4:** An example of the melting model results. All model parameters are after Hirschmann et al. (2009), except for the  $\Delta T - c_{H_2O, total}$  relationship (this study). The bold red line indicates minimum melt water contents required to induce melting along a 50 Ma oceanic geotherm (Schubert and Turcotte, 2002). Melting may occur in the depth interval where the hypothetical incipient melt water contents exceed the minimum melt water contents sufficient for melting. Given a bulk mantle water content of 225 ppm (blue), melting depths are estimated between 110 and 130 km (grey). The result of the previous model, which uses the  $\Delta T - c_{H_2O, total}$  relationship based on hydrous peridotite studies (thin red line), is shown for comparison; melting is predicted in a similar depth range, but for a considerably higher bulk water content (300 ppm).

Measurements of  $H_2O/Ce$  ratios in rapidly quenched MORB glasses from various locations along the global mid-ocean-ridge system suggest that a depleted upper mantle source typically contains 100 to 200 ppm of bulk water, with several estimates ranging from  $142 \pm 85$  ppm (Siqueiros spreading center, Saal et al., 2002) to as high as  $\approx 280$  ppm (Mid-Atlantic ridge, Michael, 1995).

The minimum bulk water contents required for melting, estimated from different variations of the melting model (Fig. 4.4.5), overlap considerably with the reported upper mantle water contents (Michael, 1995; Danyushevsky et al., 2000; Saal et al., 2002).

This model considers the isolated effect of water on the melting point depression of peridotite, but the depleted mantle source likely contains trace amounts of  $CO_2$  ( $<100$  ppm), as well. Dasgupta et

al. (2007) suggest that additional depression of the melting point should be expected, as a result of the combined effect of water and CO<sub>2</sub> dissolution in silicate liquids. Therefore, the extent of partial melting predicted from the updated melting model (Fig. 4.4.5) is likely only a minimum estimate. Partial melting is a viable explanation of the low velocity zone observed in the oceanic upper mantle.

The lithosphere-asthenosphere boundary in the continental lithosphere is reported at depths of approximately 80-150 km in younger regions, and 180-250 km under cratons (Aulbach, 2019; Sun et al., 2019). Based on mantle xenolith geothermobarometry, the  $\Delta T_{mantle}$  may exceed 350 °C in most cratonic localities (Rudnick and Nyblade, 1999). Given the updated  $\Delta T - \text{CH}_2\text{O}_{total}$  relationship, more than 7 wt.%, and possibly as much as 9 wt.%, of water in the silicate liquid might be necessary to induce melting at the cratonic lithosphere-asthenosphere boundary, assuming an average continental geotherm (Hasterok and Chapman, 2011). Bulk water contents of approximately 300 ppm (or more) may be required to produce such melt compositions.

In active margin settings, as well as under some cratons (e.g. Tanzania) the geothermal gradients may be more similar to those in the oceanic crust. If the melting model is applied to a 50 mW/m<sup>2</sup> geotherm (Hasterok and Chapman, 2011), the  $\Delta T_{mantle}$  reach a minimum of approximately 200 °C in a narrow depth range around 130 to 140 km, and some melting may be possible at melt water concentrations of approximately 4.3 wt.% and for bulk water contents slightly higher than 200 ppm. According to the updated model, melting at the continental lithosphere-asthenosphere boundary in active margins is plausible. However, the lithosphere-asthenosphere boundary under most cratons may have a different origin, or may require additional melting point depression due to CO<sub>2</sub>.

#### 4. Mantle melting at low water fugacity and the cryoscopic equation

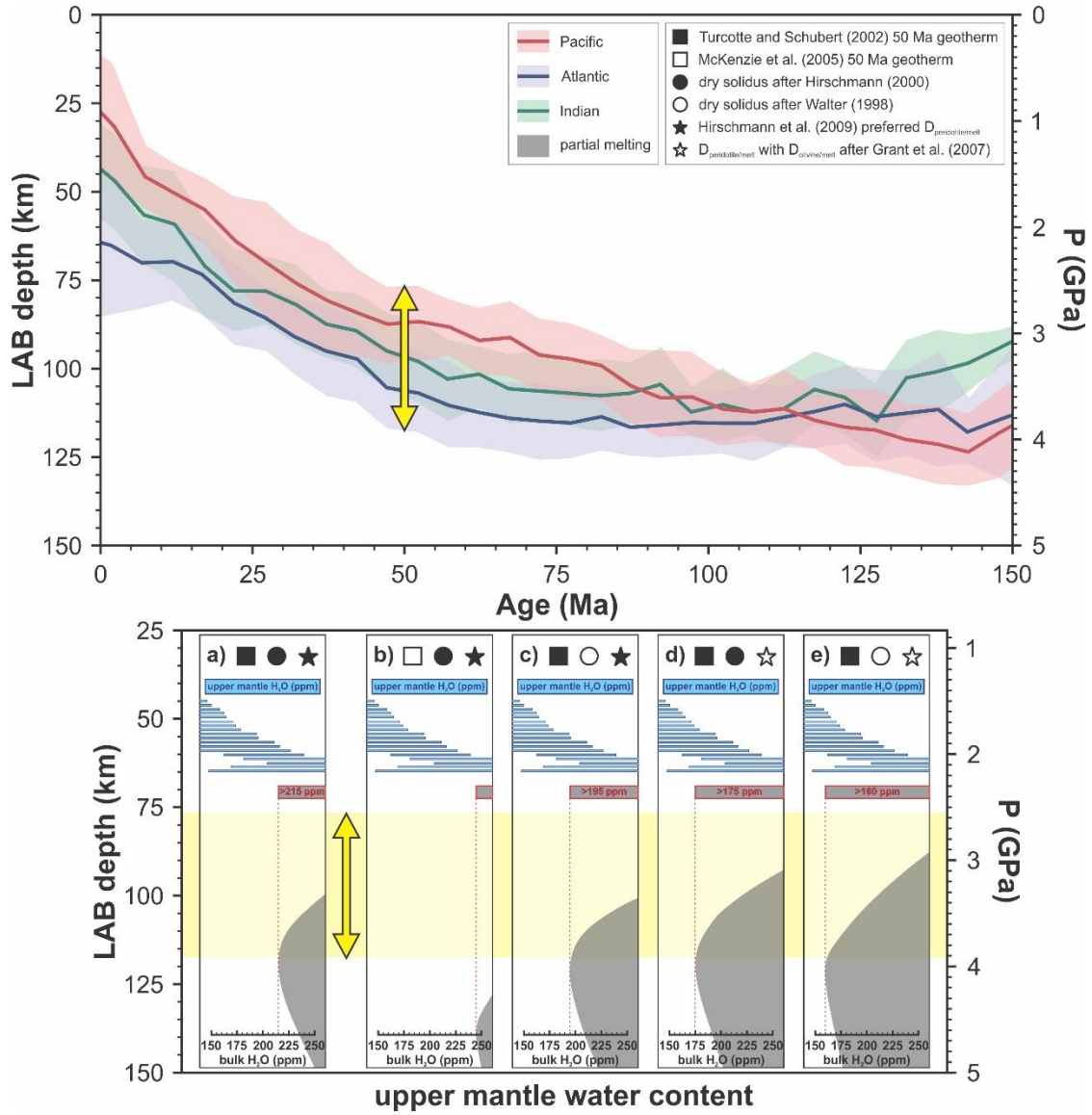


**Figure 4.4.5:** A summary of the melting model results with implications for the origin of the oceanic lithosphere-asthenosphere boundary. The red, blue and green bold lines are the average observed LAB depths in the Pacific, Atlantic and Indian oceans (respectively) as a function of lithospheric plate age; the corresponding shaded areas are one standard deviation (after Montagner and Burgos, 2019). The yellow area and arrows indicate the observed LAB depths for the 50 Ma lithosphere. **Panels a) to e):** Melting depth intervals for a range of bulk mantle water contents and different model parameters. The vertical axis in all panels is depth, with the same scale as the global y-axis. The horizontal axis is bulk mantle water content in ppm. H<sub>2</sub>O/Ce estimates of the upper mantle water content from 18 locations around the global MOR system are indicated within each panel in blue (Michael, 1995; Danyushevsky et al., 2000; Saal et al., 2002) **Panel a)** Same model parameters used by Hirschmann et al. (2009), except for the  $\Delta T - \text{CH}_{2\text{O},\text{total}}$  relationship (this study). **Panel b)** Same model parameters as in Panel a), except for the geothermal gradient, which is now after the plate cooling model of Stein and Stein (1992) and McKenzie et al. (2005). **Panel c)** Same model parameters as in Panel a), except for the dry peridotite solidus, which is now after Walter (1998). **Panel d)** Same model parameters as in Panel a), except for the peridotite/melt water partition coefficients, which are now calculated using the olivine/melt water partition coefficient of 0.002 (Grant et al., 2007). **Panel e)** Model variation combining the  $\Delta T - \text{CH}_{2\text{O},\text{total}}$  relationship from this study, the 50 Ma oceanic geotherm after Turcotte and Schubert (2002), dry peridotite solidus after Walter (1998) and the peridotite/melt water partition coefficients calculated using the olivine/melt water partition coefficient from Grant et al. (2007).

The results presented here are supported by literature reviews of seismic data. Fischer et al. (2010) examined the results of various seismic studies. They concluded that the steep velocity gradients observed at the LAB in oceanic and active margin settings require a compositional contrast and/or melting, and cannot be explained by thermal gradients alone. However, compositional contrasts and/or melting are not necessarily required to reproduce the more gradual velocity gradients attributed to cratonic lithosphere-asthenosphere boundaries.

The updated melting model may have implications for the generation of mid-ocean-ridge-basalts (MORB). Mid-ocean-ridge-basalts are characterized by globally occurring isotope, major and trace element signatures that are conventionally related to melt extraction from a garnet-bearing source. However, a number of mechanisms were invoked to explain these geochemical observations, and many of them do not require partial melting of garnet lherzolites (Krein et al., 2020 and ref. therein). It is, therefore, unclear whether the garnet signatures observed in global MORB suites can truly be attributed to partial melting in the garnet stability field.

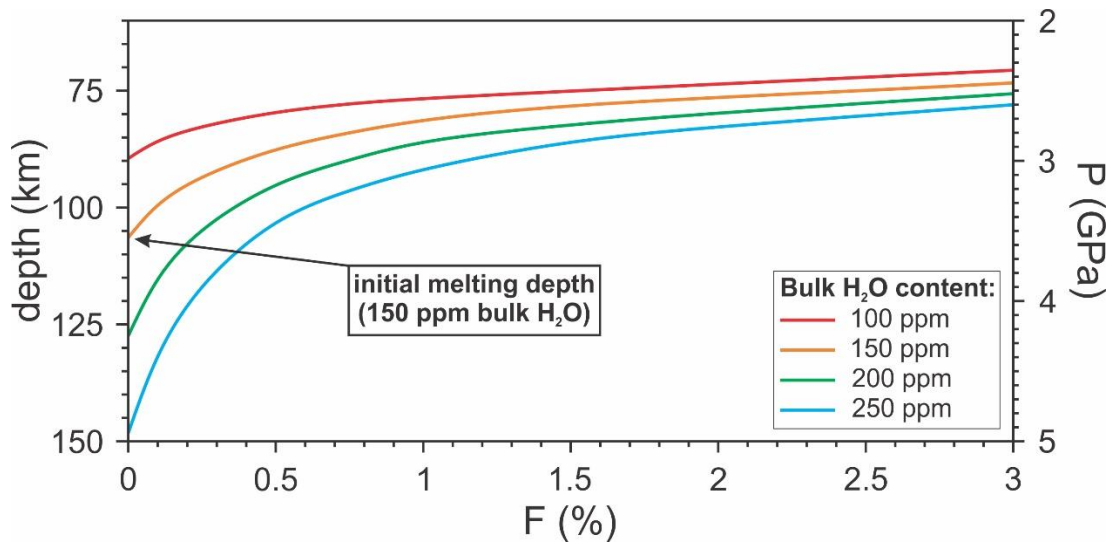


**Figure 4.4.6:** Initial melting depths and estimated melt fractions under mid-ocean-ridges, assuming bulk mantle water contents between 100 and 250 ppm. All model parameters are after Hirschmann et al. (2009), except for the  $\Delta T - CH_{2O, total}$  relationship (this study). The  $\Delta T_{mantle}$  are calculated from the average ridge adiabat after Stixrude and Lithgow-Bertelloni (2007). Incipient melting depths are greater or equal to 90 km. Approximately 1 to 2 wt.% of melt may be sourced from the garnet stability field. Other combinations of model parameters may yield higher melt fractions in the same depth range for a given bulk water content.

If the updated melting model is applied to an average mid-ocean-ridge adiabat (Stixrude and Lithgow-Bertelloni, 2007), incipient melting is predicted at depths greater or equal to 90 km

(Fig. 4.4.6) for bulk water contents higher than 100 ppm. Assuming the spinel-garnet transition occurs at  $\approx 2.5$  GPa at typical ridge adiabat temperatures (Klemme and O'Neill, 2000), the model suggests that 1 to 2 wt.% of partial melt may indeed be sourced from the garnet stability field. This result may be able to reconcile the ubiquitous garnet geochemical signatures in MORB, without invoking additional mechanisms. We do not rule out the possibility of more complex melting scenarios – such as melt extraction from garnet pyroxenite veins in the spinel stability field (Hirschmann and Stolper, 1996) – or neglect that these geochemical signatures may be explained by metasomatic events (e.g. Donnelly et al, 2004). In fact, some case studies provide compelling evidence for local to regional plume-ridge metasomatic interactions (Yang et al, 2017).

## 5. List of references

Anderson, D. L., Sammis, C. (1970). Partial melting in the upper mantle. *Physics of the Earth and Planetary Interiors*, 3, 41-50.

Anderson, D.L. (1989). *Theory of the Earth*. Blackwell Scientific, Boston.

Anderson, D.L., Spetzler, H. (1970). Partial melting and the low-velocity zone. *Physics of the Earth and Planetary Interiors*, 4(1), 62-64.

Atkins, P.W. (1982). *Physical chemistry*. Freeman & Company, W&H.

Aubaud, C., Hauri, E.H., Hirschmann, M.M. (2004). Hydrogen partition coefficients between nominally anhydrous minerals and basaltic melts. *Geophysical Research Letters*, 31.

Audétat, A., Keppler, H. (2005). Solubility of rutile in subduction zone fluids, as determined by experiments in the hydrothermal diamond anvil cell. *Earth and Planetary Science Letters*, 232, 393-402.

Aulbach, S. (2019). Cratonic Lithosphere Discontinuities: Dynamics of Small-Volume Melting, Metacratonization, and a Possible Role for Brines. *AGU Geophysical Monograph Series, Lithospheric Discontinuities*, 177-203.

Auzanneau, E., Schmidt, M.W., Vielzeuf, D., D Connolly, J. (2009). Titanium in phengite: a geobarometer for high temperature eclogites. *Contributions to Mineralogy and Petrology*, 159, 1-24.

Baier, J., Audétat, A., Keppler, H. (2008). The origin of the negative niobium tantalum anomaly in subduction zone magmas. *Earth and Planetary Science Letters*, 267(1-2), 290-300.

## 5. List of references

Bailey, D. (1982). Mantle metasomatism — continuing chemical change within the Earth. *Nature*, 296, 525–530.

Baker, M.B., Stolper, E.M. (1994). Determining the composition of high-pressure mantle melts using diamond aggregates. *Geochimica et Cosmochimica Acta*, 58, 2811-2827.

Bebout, G., Bebout, A.E., Graham, C.M. (2007). Cycling of B, Li, and LILE (K, Cs, Rb, Ba, Sr) into subduction zones: SIMS evidence from micas in high-P/T metasedimentary rocks. *Chemical Geology*, 239, 284-304.

Bebout, G.E., Agard, P., Kobayashi, K., Moriguti, T., Nakamura, E. (2013). Devolatilization history and trace element mobility in deeply subducted sedimentary rocks: Evidence from Western Alps HP/UHP suites. *Chemical Geology*, 342, 1–20.

Behrens, H., Misiti, V., Freda, C., Vetere, F., Botcharnikov, R.E., Scarlato, P. (2009). Solubility of H<sub>2</sub>O and CO<sub>2</sub> in ultrapotassic melts at 1200 and 1250 °C and pressure from 50 to 500 MPa. *American Mineralogist* 94, 105–120.

Bell, D.R., Rossman, G.R. (1992). Water in Earth's Mantle: The Role of Nominally Anhydrous Minerals. *Science*, 255(5050), 1391-1397.

Berndt, J., Liebske, C., Holtz, F., Freise, M., Nowak, M., Ziegenbein, D., Hurkuck, W., Koepke, J. (2002). A combined rapid-quench and H<sub>2</sub>-membrane setup for internally heated pressure vessels: Description and application for water solubility in basaltic melts. *American Mineralogist*, 87, 1717 - 1726.

Botcharnikov, R.E., Koepke, J., Holtz, F., McCammon, C., Wilke, M. (2005). The effect of water activity on the oxidation and structural state of Fe in a ferro-basaltic melt. *Geochimica et Cosmochimica Acta* 69, 5071–5085.

## 5. List of references

Boyd, F. R., England, J. L. (1960). Apparatus for phase-equilibrium measurements at pressures up to 50 kilobars and temperatures up to 1750°C. *Journal of Geophysical Research*, 65 (2), 741-748.

Brenan, J.M., Ryerson, F.J., Shaw, H.F. (1998). The role of aqueous fluids in the slab-to-mantle transfer of boron, beryllium, and lithium during subduction: experiments and models. *Geochimica et Cosmochimica Acta*, 62, 3337-3347.

Brenan, J.M., Shaw, H.F., Phinney, D.L., Ryerson, F.J. (1994). Rutile-aqueous fluid partitioning of Nb, Ta, Hf, Zr, U and Th: implications for high field strength element depletions in island-arc basalts. *Earth and Planetary Science Letters*, 128, 327-339.

Bromiley, G. D., Keppler, H. (2004). An experimental investigation of hydroxyl solubility in jadeite and Na-rich clinopyroxenes. *Contributions to Mineralogy and Petrology*, 147(2), 189-200.

Bromiley, G., Keppler, H., McCammon, C., Bromiley, F., Jacobsen, S. (2004). Hydrogen solubility and speciation in natural, gem-quality chromian diopside. *American Mineralogist*, 89(7), 941-949.

Brovarone, A.V., Alard, O., Beyssac, O., Martin, L., Picatto, M. (2014). Lawsonite metasomatism and trace element recycling in subduction zones. *Journal of Metamorphic Geology*, 32, 489-514.

Bureau, H., & Keppler, H. (1999). Complete miscibility between silicate melts and hydrous fluids in the upper mantle: experimental evidence and geochemical implications. *Earth and Planetary Science Letters*, 165, 187-196.

Busigny, V., Cartigny, P., Philippot, P., Ader, M., Javoy, M. (2003). Massive recycling of nitrogen and other fluid-mobile elements (K, Rb, Cs, H) in a cold slab environment: evidence from HP to UHP oceanic metasediments of the Schistes Lustrés nappe (western Alps, Europe). *Earth and Planetary Science Letters*, 215, 27-42.

## 5. List of references

Carter, L.B., Skora, S., Blundy, J., Hoog, J.C., Elliott, T. (2015). An Experimental Study of Trace Element Fluxes from Subducted Oceanic Crust. *Journal of Petrology*, 56, 1585-1606.

Chaussudon, M., Libourel, G. (1993). Boron partitioning in the upper mantle: An experimental and ion probe study. *Geochimica et Cosmochimica Acta*, 57, 5053-5062.

Codillo, E., Le Roux, V., Marschall, H.R. (2018). Arc-like magmas generated by mélange-peridotite interaction in the mantle wedge. *Nature Communications*, 9.

Conceição, R.V., Green, D.H. (2004). Derivation of potassic (shoshonitic) magmas by decompression melting of phlogopite+pargasite lherzolite. *Lithos*, 72, 209-229.

Costantino, M., Rice, S.F. (1991). Supercritical phase separation in water-nitrogen mixtures. *The Journal of Physical Chemistry*, 95, 9034-9036.

Danyushevsky, L. V., Eggins, S.M., Falloon, T.J., Christie, D. M. (2000). H<sub>2</sub>O Abundance in Depleted to Moderately Enriched Mid-ocean Ridge Magmas; Part I: Incompatible Behaviour, Implications for Mantle Storage, and Origin of Regional Variations. *Journal of Petrology*, 41, 8, 1329–1364.

Dasgupta, R., Hirschmann, M.M., Smith, N.D. (2007). Water follows carbon: CO<sub>2</sub> incites deep silicate melting and dehydration beneath mid-ocean ridges. *Geology*, 35, 135-138.

Davis, M.J., Ihinger, P.D., Lasaga, A.C. (1997). Influence of water on nucleation kinetics in silicate melt. *Journal of Non-crystalline Solids*, 219, 62-69.

Dawson, J., Smith, J. (1982). Upper-mantle amphiboles: A review. *Mineralogical Magazine*, 45(337), 35-46.

Dawson, J.B., Powell, D.G. (1969). Mica in the upper mantle. *Contributions to Mineralogy and Petrology*, 22, 233–237.

## 5. List of references

- Demouchy, S., Bolfan-Casanova, N. (2016). Distribution and transport of hydrogen in the lithospheric mantle: A review. *Lithos*, 240-243, 402-425.
- Deschamps, F., Godard, M., Guillot, S., Hattori, K. (2013). Geochemistry of subduction zone serpentinites: A review. *Lithos*, 178, 96-127.
- DeYoreo, J. J., Lange, R. A., Navrotsky, A. (1995). Scanning calorimetric determinations of the heat contents of diopside-rich systems during melting and crystallization. *Geochimica et Cosmochimica Acta*, 59, 13, 2701-2707.
- Dixon, J., Stolper, E.M., Holloway, J.R. (1995). An Experimental Study of Water and Carbon Dioxide Solubilities in Mid-Ocean Ridge Basaltic Liquids. Part I: Calibration and Solubility Models. *Journal of Petrology*, 36, 1607-1631.
- Donnelly, K.E., Goldstein, S.L., Langmuir, C.H., Spiegelman, M. (2004). Origin of Enriched Ocean Ridge Basalts and Implications for Mantle Dynamics. *Earth and Planetary Science Letters*, 226, 347-366.
- Dunn, T., Şen, C. (1994). Mineral/matrix partition coefficients for orthopyroxene, plagioclase, and olivine in basaltic to andesitic systems: A combined analytical and experimental study. *Geochimica et Cosmochimica Acta*, 58, 717-733.
- Erdmann, M. Koepke, J. (2016). Experimental temperature cycling as a powerful tool to enlarge melt pools and crystals at magma storage conditions. *American Mineralogist*, 101(4), 960-969.
- Faul, U.H., Jackson, I. (2005). The seismological signature of temperature and grain size variations in the upper mantle. *Earth and Planetary Science Letters*, 234, 119-134.
- Fei, H., Wiedenbeck, M., Yamazaki, D., Katsura, T. (2008). Small effect of water on upper-mantle rheology based on silicon self-diffusion coefficients. *Nature*, 498, 213–215.

## 5. List of references

Fischer, K.M., Ford, H.A., Abt, D.L., Rychert, C.A. (2010). The Lithosphere- Asthenosphere Boundary. *Annual Review of Earth and Planetary Sciences*, 38, 551-575.

Frost, D.J. (2006). The Stability of Hydrous Mantle Phases. *Reviews in Mineralogy and Geochemistry*, 62, 243–271.

Fumagalli, P., Poli, S. (2005). Experimentally Determined Phase Relations in Hydrous Peridotites to 6.5 GPa and their Consequences on the Dynamics of Subduction Zones. *Journal of Petrology*, 46(3), 555–578.

Fumagalli, P., Zanchetta, S., Poli, S. (2009). Alkali in phlogopite and amphibole and their effects on phase relations in metasomatized peridotites: a high-pressure study. *Contributions to Mineralogy and Petrology*, 158, 723.

Gaetani, G.A., Grove, T.L. (1998). The influence of water on melting of mantle peridotite. *Contributions to Mineralogy and Petrology*, 131, 323-346.

Gaillard, F., Bernadou, F., Roskosz, M., Ali Bouhifd, M., Marrocchi, Y., Iacono-Marziano, G., Moreira, M., Scaillet, B., Rogerie, G. (2022). Redox controls during magma ocean degassing. *Earth and Planetary Science Letters*, 577, 117255.

Gale, A.D., Dalton, C.A., Langmuir, C.H., Su, Y., Schilling, J. (2013). The mean composition of ocean ridge basalts. *Geochemistry Geophysics Geosystems*, 14, 489-518.

Grant, K., Ingrin, J., Lorand, J.P., Dumas, P. (2007). Water partitioning between mantle minerals from peridotite xenoliths. *Contribution to Mineralogy and Petrology*, 154, 15-34.

Grant, K.J., Kohn, S.C., Brooker, R.A. (2007). The partitioning of water between olivine, orthopyroxene and melt synthesised in the system albite-forsterite-H<sub>2</sub>O. *Earth and Planetary Science Letters*, 260, 227-241.

## 5. List of references

Green, D., Hibberson, W., Kovács, I., Rosenthal, A. (2010). Water and its influence on the lithosphere–asthenosphere boundary. *Nature*, 467, 448–451 (2010).

Green, D.H. (2015). Experimental petrology of peridotites, including effects of water and carbon on melting in the Earth's upper mantle. *Physics and Chemistry of Minerals*, 42, 95-122.

Green, D.H., Hibberson, W.O., Rosenthal, A., Kovács, I.J., Yaxley, G.M., Falloon, T.J., Brink, F.J. (2014). Experimental Study of the Influence of Water on Melting and Phase Assemblages in the Upper Mantle. *Journal of Petrology*, 55, 2067-2096.

Griffiths, P. R., De Haseth, J. A. (2007). *Fourier transform infrared spectrometry* (Vol. 171). John Wiley & Sons.

Günther, D., Koch, J. (2008). Formation of aerosols generated by laser ablation and their impact on elemental fractionation in LA–ICP–MS. *Laser Ablation ICP-MS in the Earth Sciences: Current Practices and Outstanding Issues* (Ed. Sylvester), Mineralogical Association of Canada, Short Course Volume 40.

Haefner, A., Aranovich, L., Connolly, J., Ulmer, P. (2002). H<sub>2</sub>O activity in H<sub>2</sub>O-N<sub>2</sub> fluids at high pressure and temperature measured by the brucite-periclase equilibrium. *American Mineralogist*, 87(7), 822-828.

Hall, L. (1999). The effect of water on mantle melting. Unpublished Ph.D. Thesis. Bristol University, 159 pp.

Hart, S.R., Brooks, C. (1974). Clinopyroxene-matrix partitioning of K, Rb, Cs, Sr and Ba. *Geochimica et Cosmochimica Acta*, 38, 1799-1806.

Hart, S.R., Dunn, T. (1993). Experimental cpx/melt partitioning of 24 trace elements. *Contributions to Mineralogy and Petrology*, 113, 1-8.

## 5. List of references

Hasterok, D., Chapman, D.S. (2011). Heat production and geotherms for the continental lithosphere. *Earth and Planetary Science Letters*, 307, 59-70.

Hata, M., Uyeshima, M. (2015). Temperature and melt fraction distributions in a mantle wedge determined from the electrical conductivity structure: Application to one nonvolcanic and two volcanic regions in the Kyushu subduction zone, Japan. *Geophysical Research Letters*, 42, 2709–2717.

Hauri, E.H., Wagner, T., Grove, T.L. (1994). Experimental and natural partitioning of Th, U, Pb and other trace elements between garnet, clinopyroxene and basaltic melts. *Chemical Geology*, 117, 149-166.

Hermann, J. (2002). Allanite: thorium and light rare earth element carrier in subducted crust. *Chemical geology*, 192(3-4), 289-306.

Hermann, J., Rubatto, D. (2009). Accessory phase control on the trace element signature of sediment melts in subduction zones. *Chemical Geology*, 265, 512-526.

Hermann, J., Spandler, C. (2008). Sediment Melts at Sub-arc Depths: an Experimental Study. *Journal of Petrology*, 49, 717-740.

Hirose, K. (1997). Melting experiments on lherzolite KLB-1 under hydrous conditions and generation of high-magnesian andesitic melts. *Geology*, 25, 42-44.

Hirose, K., Kawamoto, T. (1995). Hydrous partial melting of lherzolite at 1 GPa: The effect of H<sub>2</sub>O on the genesis of basaltic magmas. *Earth and Planetary Science Letters*, 133, 463-473.

Hirschmann, M.M., Kohlstedt, D. (2012). Water in Earth's mantle. *Physics Today*, 65, 40-45.

## 5. List of references

Hirschmann, M.M. (2000). Mantle solidus: Experimental constraints and the effects of peridotite composition. *Geochemistry Geophysics Geosystems*, 1.

Hirschmann, M.M. (2006). Water, melting, and the deep Earth H<sub>2</sub>O cycle. *Annual Review of Earth and Planetary Sciences*, 34:1, 629-653.

Hirschmann, M.M. (2010). Partial melt in the oceanic low velocity zone. *Physics of the Earth and Planetary Interiors*, 179, 60–71.

Hirschmann, M.M., Stolper, E.M. (1996). A possible role for garnet pyroxenite in the origin of the "garnet signature" in MORB. *Contributions to Mineralogy and Petrology*, 124 (2), 185-208.

Hirschmann, M.M., Tenner, T.J., Aubaud, C., Withers, A.C. (2009). Dehydration melting of nominally anhydrous mantle: The primacy of partitioning. *Physics of the Earth and Planetary Interiors*, 176, 54-68.

Hirth, G., Kohlstedt, D.L. (1996). Water in the oceanic upper mantle: implications for rheology, melt extraction and the evolution of the lithosphere. *Earth and Planetary Science Letters*, 144, 93-108.

Höink, T., Lenardic, A., Richards, M. (2012). Depth-dependent viscosity and mantle stress amplification: implications for the role of the asthenosphere in maintaining plate tectonics. *Geophysical Journal International*, 191, 1, 30–41.

Holloway, J.R. (1971). *Internally Heated Pressure Vessels. Research Techniques for High Pressure and High Temperature*, Springer.

Holloway, J.R. (1973). The system pargasite-H<sub>2</sub>O-CO<sub>2</sub>: a model for melting of a hydrous mineral with a mixed-volatile fluid—I. Experimental results to 8 kbar. *Geochimica et Cosmochimica Acta*, 37, 651-666.

## 5. List of references

Horn, I. (2008). Comparison of femtosecond and nanosecond laser interactions with geologic matrices and their influence on accuracy and precision of LA–ICP–MS data. *Laser Ablation ICP-MS in the Earth Sciences: Current Practices and Outstanding Issues* (Ed. Sylvester), Mineralogical Association of Canada, Short Course Volume 40.

Hu, Y., Tneg, F.Z., Chauvel, C. (2021). Potassium isotopic evidence for sedimentary input to the mantle source of Lesser Antilles lavas. *Geochimica et Cosmochimica Acta*, 295, 98–111.

Irifune, T., Isshiki, M. (1998). Iron partitioning in a pyrolite mantle and the nature of the 410-km seismic discontinuity. *Nature*, 392, 702-705.

Jackson, S. (2008). Calibration strategies for elemental analysis by LA–ICP–MS. *Laser Ablation ICP-MS in the Earth Sciences: Current Practices and Outstanding Issues* (Ed. Sylvester), Mineralogical Association of Canada, Short Course Volume 40.

Johannes, W., Bell, P.M., Mao, H.K., Boettcher, A.L., Chipman, D.W., Hays, J.F., Newton, R.C., Seifert, F. (1971). An interlaboratory comparison of piston-cylinder pressure calibration using the albite-breakdown reaction. *Contributions to Mineralogy and Petrology*, 32, 24–38.

Johnson, K.T. (1998). Experimental determination of partition coefficients for rare earth and high-field-strength elements between clinopyroxene, garnet, and basaltic melt at high pressures. *Contributions to Mineralogy and Petrology*, 133, 60-68.

Johnson, M.C., Plank, T. (2000). Dehydration and melting experiments constrain the fate of subducted sediments. *Geochemistry Geophysics Geosystems*, 1, 1007.

Karato, S. (2012). On the origin of the asthenosphere. *Earth and Planetary Science Letters*, 321, 95-103.

Karato, S., Jung, H. (1998). Water, partial melting and the origin of the seismic low velocity and high attenuation zone in the upper mantle. *Earth and Planetary Science Letters*, 157, 193-207.

## 5. List of references

Katz, R. F., Spiegelman, M., Langmuir, C.H. (2003). A new parameterization of hydrous mantle melting. *Geochemistry Geophysics Geosystems* 4(9), 1073.

Kawamoto, T., Mibe, K., Bureau, H., Reguer, S., Mocuta, C., Kubsy, S., Thiaudière, D., Ono, S., Kogiso, T. (2014). Large-ion lithophile elements delivered by saline fluids to the sub-arc mantle. *Earth, Planets and Space*, 66, 1-11.

Keken, P.V., Syracuse, E.M., Abers, G.A., Fischer, K.M. (2009). The global range of subduction zone thermal models: consequences for slab devolatilization. *Physics of the Earth and Planetary Interiors*, 183, 73–90.

Kelemen, P.B., Hanghøj, K., Greene, A.R. (2005). One View of the Geochemistry of Subduction-Related Magmatic Arcs, with an Emphasis on Primitive Andesite and Lower Crust. *Treatise on Geochemistry*, 3, 749-806.

Kelemen, P.B., Hirth, G., Shimizu, N., Spiegelman, M., Dick, H.J. (1997). A review of melt migration processes in the adiabatically upwelling mantle beneath oceanic spreading ridges. *Proceedings of The Royal Society A Mathematical Physical and Engineering Sciences*, 355(1723), 283-318.

Kelley, K.A., Plank, T., Ludden, J., Staudigel, H. (2003). Composition of altered oceanic crust at ODP Sites 801 and 1149. *Geochemistry Geophysics Geosystems*, 4, 8910.

Kennedy, A., Lofgren, G.E., Wasserburg, G.J. (1993). An experimental study of trace element partitioning between olivine, orthopyroxene and melt in chondrules: equilibrium values and kinetic effects. *Earth and Planetary Science Letters*, 115, 177-195.

Keppler, H. (1989). A new method for the generation of N<sub>2</sub>-containing fluids in high pressure experiments. *European Journal of Mineralogy*, 1, 135–137.

## 5. List of references

Keppler, H. (1996). Constraints from partitioning experiments on the composition of subduction-zone fluids. *Nature*, 380, 237-240.

Keppler, H. (2017). Fluids and trace element transport in subduction zones. *American Mineralogist*, 102, 20 - 5.

Keppler, H., Bolfan-Casanova, N. (2018). Thermodynamics of Water Solubility and Partitioning. *Reviews in Mineralogy and Geochemistry, Water in Nominally Anhydrous Minerals*, 193-230.

Keppler, H., Rauch, M. (2000). Water solubility in nominally anhydrous minerals measured by FTIR and  $^1\text{H}$  MAS NMR: the effect of sample preparation. *Physics and Chemistry of Minerals*, 27(6), 371-376.

Kerrick, D. (2002). Serpentine seduction. *Science*, 298, 1344– 1345.

Kessel, R., Schmidt, M.W., Ulmer, P., Pettke, T. (2005). Trace element signature of subduction-zone fluids, melts and supercritical liquids at 120–180 km depth. *Nature*, 437, 724-727.

Kessel, R., Ulmer, P., Pettke, T., Schmidt, M. W., Thompson, A.B. (2004). A novel approach to determine high-pressure high-temperature fluid and melt compositions using diamond-trap experiments. *American Mineralogist*, 89, 1078–1086.

Klemme, S., Blundy, J., Wood, B.J. (2002). Experimental constraints on major and trace element partitioning during partial melting of eclogite. *Geochimica et Cosmochimica Acta*, 66, 3109-3123.

Klemme, S., O'Neill, H. (2000). The near-solidus transition from garnet lherzolite to spinel lherzolite. *Contributions to Mineralogy and Petrology*, 138, 237-248.

Koga, K.T., Hauri, E.H., Hirschmann, M.M., Bell, D.R. (2003). Hydrogen concentration analyses using SIMS and FTIR: Comparison and calibration for nominally anhydrous minerals. *Geochemistry Geophysics Geosystems*, 4.

## 5. List of references

- Kohlstedt, D., Keppler, H., Rubie, D. (1996). Solubility of water in the  $\alpha$ ,  $\beta$  and  $\gamma$  phases of  $(\text{Mg,Fe})_2\text{SiO}_4$ . *Contributions to Mineralogy and Petrology*, 123, 345–357.
- Kojitani, H., Akaogi, M. (1997). Melting enthalpies of mantle peridotite: calorimetric determinations in the system  $\text{CaO-MgO-Al}_2\text{O}_3\text{-SiO}_2$  and application to magma generation. *Earth and Planetary Science Letters*, 153(3-4), 209-222.
- Konzett, J. (2016). From phosphates to silicates and back: an experimental study on the transport and storage of phosphorus in eclogites during uplift and exhumation. *American Mineralogist*, 101, 1756 - 1768.
- Korenaga, J., Planavsky, N. J., Evans, D. (2017). Global water cycle and the coevolution of the Earth's interior and surface environment. *Philosophical transactions. Series A, Mathematical, physical, and engineering sciences*, 375:20150393.
- Krein, S.B., Behn, M.D., & Grove, T.L. (2020). Origins of Major Element, Trace Element, and Isotope Garnet Signatures in Mid-Ocean Ridge Basalts. *Journal of Geophysical Research*, 125.
- Kurosawa, M., Yurimoto, H., Sueno, S. (1997). Patterns in the hydrogen and trace element compositions of mantle olivines. *Physics and Chemistry of Minerals*, 24, 385–395.
- Kushiro I. (2007). Origin of magmas in subduction zones: a review of experimental studies. *Proceedings of the Japan Academy, Series B, Physical and biological sciences*, 83(1), 1–15.
- Lambert, I., Wyllie, P. (1968). Stability of Hornblende and a Model for the Low Velocity Zone. *Nature*, 219, 1240–1241.
- Lambert, I.B., Wyllie, P.J. (1970). Low-Velocity Zone of the Earth's Mantle: Incipient Melting Caused by Water. *Science*, 169, 764-766.

## 5. List of references

Lange, R. A., De Yoreo, J. J., Navrotsky, A. (1991). Scanning calorimetric measurement of heat capacity during incongruent melting of diopside. *American Mineralogist*, 76, 904-912.

Le Losq, C., Cody, G.D., Mysen, B.O. (2015). Complex IR spectra of OH<sup>-</sup> groups in silicate glasses: Implications for the use of the 4500 cm<sup>-1</sup> IR peak as a marker of OH<sup>-</sup> groups concentration. *American Mineralogist*, 100, 945 - 950.

Li, H., Hermann, J. (2017). The effect of fluorine and chlorine on trace element partitioning between apatite and sediment melt at subduction zone conditions. *Chemical Geology*, 473, 55–73.

Li, Y., Wiedenbeck, M., Shcheka, S.S., Keppler, H. (2013). Nitrogen solubility in upper mantle minerals. *Earth and Planetary Science Letters*, 377, 311-323.

Longerich, H. (2008). Laser ablation–inductively coupled plasma–mass spectrometry (LA–ICP–MS); an introduction. *Laser Ablation ICP-MS in the Earth Sciences: Current Practices and Outstanding Issues* (Ed. Sylvester), Mineralogical Association of Canada, Short Course Volume 40.

Lu, R., H. Keppler (1997). Water solubility in pyrope to 100 kbar. *Contributions to Mineralogy and Petrology*, 129, 35–42.

Luedemann, H. D., Kennedy, G. C. (1968). Melting curves of lithium, sodium, potassium, and rubidium to 80 kilobars. *Journal of Geophysical Research*, 73(8), 2795– 2805.

Maaløe, S., Aoki, K.I. (1977). The major element composition of the upper mantle estimated from the composition of lherzolites. *Contributions to Mineralogy and Petrology*, 63(2), 161-173.

Malfait, W.J. (2009). The 4500 cm<sup>-1</sup> infrared absorption band in hydrous aluminosilicate glasses is a combination band of the fundamental (Si,Al)-OH and O-H vibrations. *American Mineralogist*, 94, 849 - 852.

## 5. List of references

- Mallik, A., Nelson, J., Dasgupta, R. (2015). Partial melting of fertile peridotite fluxed by hydrous rhyolitic melt at 2–3 GPa: implications for mantle wedge hybridization by sediment melt and generation of ultrapotassic magmas in convergent margins. *Contributions to Mineralogy and Petrology*, 169, 1-24.
- Mandler, B. E., Grove, T.L. (2016). Controls on the stability and composition of amphibole in the Earth's mantle. *Contributions to Mineralogy and Petrology*, 171(8-9).
- Mao, M., Rukhlov, A.S., Rowins, S.M., Spence, J., Coogan, L.A. (2016). Apatite Trace Element Compositions: A Robust New Tool for Mineral Exploration. *Economic Geology*, 111(5), 1187–1222.
- Martin, L.A.J., Hermann, J., Gauthiez-Putallaz, L., Whitney, D.L., Vitale Brovarone, A., Fornash, K.F., Evans, N.J. (2014). Lawsonite geochemistry and stability – implication for trace element and water cycles in subduction zones. *Journal of Metamorphic Geology*, 32: 455-478.
- Marty, B., Yokochi, R. (2006). Water in the Early Earth. *Reviews in Mineralogy and Geochemistry*, 62, 421–450.
- Matjuschkin, V., Brooker, R.A., Tattitch, B., Blundy, J.D., Stamper, C.C. (2015). Control and monitoring of oxygen fugacity in piston cylinder experiments. *Contrib Mineral Petrol* 169, 9.
- May, T.W., Wiedmeyer, R.H. (1998). A Table of Polyatomic Interferences in ICP-MS. *Atomic Spectroscopy*, 19, 150-155.
- McKenzie, D., Jackson, J., Priestley, K. (2005). Thermal structure of oceanic and continental lithosphere. *Earth and Planetary Science Letters*, 233, 337-349.
- Melzer, S., Wunder, B. (2000). Island-arc basalt alkali ratios: Constraints from phengite-fluid partitioning experiments. *Geology*, 28(7), 583-586.

## 5. List of references

Mengel, K., Green, D.H. (1989). Stability of amphibole and phlogopite in metasomatized peridotite under water-saturated and water-understaturated conditions. Proceedings of the fourth international kimberlite conference, Kimberlites and related rocks, 1(7).

Michael, P. (1995). Regionally distinctive sources of depleted MORB: Evidence from trace elements and H<sub>2</sub>O. Earth and Planetary Science Letters, 131, 301-320.

Michelson, A. A. (1891). On the application of interference-methods to spectroscopic measurements.—I. The London, Edinburgh, and Dublin Philosophical Magazine and Journal of Science, 31:191, 338-346.

Mierdel, K., Keppler, H. (2004). The temperature dependence of water solubility in enstatite. Contributions to Mineralogy and Petrology, 148(3), 305-311.

Mierdel, K., Keppler, H., Smyth, J.R., Langenhorst, F. (2007). Water Solubility in Aluminous Orthopyroxene and the Origin of Earth's Asthenosphere. Science, 315 (5810), 364-368.

Montagner, J.P., Burgos, G. (2019). Lithospheric and Asthenospheric Structure Below Oceans from Anisotropic Tomography. AGU Geophysical Monograph Series, Lithospheric Discontinuities, 55-69.

Moore, J.C., & Vrolijk, P.J. (1992). Fluids in accretionary prisms. Reviews of Geophysics, 30, 113-135.

Mosenfelder, J. L., Deligne, N. I., Asimow, P. D., Rossman, G. R. (2006). Hydrogen incorporation in olivine from 2–12 GPa. American Mineralogist, 91, 2-3, 285-294.

Mysen, B.O. (2014). Water-melt interaction in hydrous magmatic systems at high temperature and pressure. Progress in Earth and Planetary Science, 1, 1-18.

## 5. List of references

- Ni, H., Hui, H., Steinle-Neumann, G. (2015). Transport properties of silicate melts. *Reviews of Geophysics*, 53, 715–744.
- Nielsen, S.G., & Marschall, H.R. (2017). Geochemical evidence for mélangé melting in global arcs. *Science Advances*, 3.
- Niida, K., Green, D.H. (1999). Stability and chemical composition of pargasitic amphibole in MORB pyroxene under upper mantle conditions. *Contributions to Mineralogy and Petrology*, 135, 18-40.
- Noda, A., Koge, H., Yamada, Y., Miyakawa, A., Ashi, J. (2020). Subduction of trench-fill sediments beneath an accretionary wedge: Insights from sandbox analogue experiments. *Geosphere*, 16, 953-968.
- Nowak, M., Behrens, H. (1995). The speciation of water in haplogranitic glasses and melts determined by in situ near-infrared spectroscopy. *Geochimica et Cosmochimica Acta*, 59, 3445-3450.
- O'Reilly, S.Y., Griffin, W.L. (2012). Mantle metasomatism. *Lecture Notes in Earth System Sciences: Metasomatism and the Chemical Transformation of Rock*, 471-533.
- Osborn, E.F. (1942). The system  $\text{CaSiO}_3$ -diopside-anorthite. *American Journal of Science*, 240(11), 751-788.
- Pearce, J.A., Stern, R.J. (2013). Origin of Back-Arc Basin Magmas: Trace Element and Isotope Perspectives. *Geophysical monograph*, 166, 63-86.
- Pearson, D., Brenker, F., Nestola, F., McNeill, J., Nasdala, L., Hutchison, M.T., Matveev, S., Mather, K., Silversmit, G., Schmitz, S., Vekemans, B., Vincze, L. (2004). Hydrous mantle transition zone indicated by ringwoodite included within diamond. *Nature*, 507, 221–224.

## 5. List of references

Penniston-Dorland, S.C., Kohn, M.J., Manning, C.E. (2015). The Global Range of Subduction Zone Thermal Structures from Exhumed Blueschists and Eclogites: Rocks Are Hotter than Models. *Earth and Planetary Science Letters*, 428, 243-254.

Peslier, A., Woodland, A., Bell, D., Lazarov, M. (2010). Olivine water contents in the continental lithosphere and the longevity of cratons. *Nature* 467, 78–81.

Pickering, J.M., Schwab, B.E., Johnston, A.D. (1998). Off-center hot spots: Double thermocouple determination of the thermal gradient in a 1.27 cm (1/2 in.) CaF<sub>2</sub> piston-cylinder furnace assembly. *American Mineralogist*, 83, 228–235.

Plank, T. (2005). Constraints from Thorium/Lanthanum on Sediment Recycling at Subduction Zones and the Evolution of the Continents. *Journal of Petrology*, 46, 921-944.

Plank, T. (2013). The Chemical Composition of Subducting Sediments. *Treatise on Geochemistry*, 4, 607-629.

Plank, T., Langmuir, C.H. (1993). Tracing trace elements from sediment input to volcanic output at subduction zones. *Nature*, 362, 739-743.

Plank, T., Langmuir, C.H. (1998). The chemical composition of subducting sediment and its consequences for the crust and mantle. *Chemical Geology*, 145, 325-394.

Popp, R.K., Virgo, D., Yoder, H.S., Hoering, T.C., Phillips, M.W. (1995). An experimental study of phase equilibria and Fe oxy-component in kaersutitic amphibole: implications for the  $f_{\text{H}_2}$  and  $a_{\text{H}_2\text{O}}$  in the upper mantle. *American Mineralogist*, 80, 534-548.

Presnall, D.C., Dixon, S.A., Dixon, J.R., O'donnell, T.H., Brenner, N.L., Schrock, R.L., Dycus, D.W. (1978). Liquidus phase relations on the join diopside-forsterite-anorthite from 1 atm to 20 kbar: Their bearing on the generation and crystallization of basaltic magma. *Contributions to Mineralogy and Petrology*, 66, 203-220.

## 5. List of references

- Rader, E., Emry, E., Schmerr, N., Frost, D., Cheng, C., Menard, J., Yu, C.-Q., Geist, D. (2015). Characterization and Petrological Constraints of the Midlithospheric Discontinuity. *Geochemistry, Geophysics, Geosystems*, 16, 3484–3504.
- Ranero, C., Phipps, M. J., McIntosh, K., Reichert, C. (2003). Bending-related faulting and mantle serpentinization at the Middle America trench. *Nature*, 425, 367–373.
- Rauch, M., Keppler, H. (2002). Water solubility in orthopyroxene. *Contributions to Mineralogy and Petrology*, 143, 525–536.
- Reed, S.J.B. (2005). *Electron Microprobe Analysis and Scanning Electron Microscopy in Geology*, 2nd Edition. Cambridge University Press.
- Richet, P., Bottinga, Y. (1984). Anorthite, andesine, wollastonite, diopside, cordierite and pyrope: thermodynamics of melting, glass transitions, and properties of the amorphous phases. *Earth and Planetary Science Letters*, 67, 415-432.
- Richet, P., Lejeune, A.M., Holtz, F., Roux, J. (1996). Water and the viscosity of andesite melts. *Chemical Geology*, 128, 185-197.
- Robinson, J. A. C., Wood, B. J., Blundy, J. D. (1998). The beginning of melting of fertile and depleted peridotite at 1.5 GPa. *Earth and Planetary Science Letters*, 155, 1, 97-111.
- Rudnick, R., Nyblade, A. (1999). The thickness and heat production of Archean lithosphere: constraints from xenolith thermobarometry and surface heat flow. In: Fei, Y., Bertka, C., Mysen, B. (Eds.), *Mantle Petrology: Field Observations and High Pressure Experimentation: a Tribute to Francis R. (Joe) Boyd*. Special Pub: Geochem. Soc., 6.
- Rudnick, R.L., Gao, S. (2014). Composition of the Continental Crust. *Treatise on Geochemistry*, 4, 1-51.

## 5. List of references

Rüpke, L.H., Morgan, J.P., Hort, M., Connolly, J.A. (2004). Serpentine and the subduction zone water cycle. *Earth and Planetary Science Letters*, 223, 17-34.

Rustioni, G., Audéat, A., Keppler, H. (2019). Experimental evidence for fluid-induced melting in subduction zones. *Geochemical Perspectives Letters*.

Rustioni, G., Audéat, A., Keppler, H. (2021). The composition of subduction zone fluids and the origin of the trace element enrichment in arc magmas. *Contributions to Mineralogy and Petrology*, 176.

Ryabchikov, I.D., Orlova, G.P., Kalenchuk, G.Y., Ganeyev, I.I., Udovkina, N.G., Nosik, L.P. (1989). Reactions of spinel lherzolite with H<sub>2</sub>O-CO<sub>2</sub> fluids at 20 kbar and 900 °C. *Geochemistry International*, 26, 56–62.

Saal, A., Hauri, E., Langmuir, C., Perfit, M.R. (2002). Vapour undersaturation in primitive mid-ocean-ridge basalt and the volatile content of Earth's upper mantle. *Nature* 419, 451–455.

Saha, S., Dasgupta, R., Tsuno, K. (2018). High pressure phase relations of a depleted peridotite fluxed by CO<sub>2</sub>-H<sub>2</sub>O-bearing siliceous melts and the origin of Mid-Lithospheric Discontinuity. *Geochemistry, Geophysics, Geosystems*, 19, 595– 620.

Saha, S., Peng, Y., Dasgupta, R., Mookherjee, M., Fischer, K.M. (2021). Assessing the presence of volatile-bearing mineral phases in the cratonic mantle as a possible cause of mid-lithospheric discontinuities. *Earth and Planetary Sciences Letters*, 553:116602.

Salters, V.J., Longhi, J., Bizimis, M. (2002). Near mantle solidus trace element partitioning at pressures up to 3.4 GPa. *Geochemistry Geophysics Geosystems*, 3, 1-23.

Salters, V.J., Stracke, A. (2003). The Composition of the Depleted Mantle. *Geochemistry, Geophysics, Geosystems*, 5, 5.

## 5. List of references

Schmidt, M. W., Jagoutz, O. (2017). The global systematics of primitive arc melts. *Geochemistry, Geophysics, Geosystems*, 18, 2817– 2854.

Schmidt, M.W., Poli, S. (1998). Experimentally based water budgets for dehydrating slabs and consequences for arc magma generation. *Earth and Planetary Science Letters*, 163, 361-379.

Schmidt, M.W., Vielzeuf, D., Auzanneau, E. (2004). Melting and dissolution of subducting crust at high pressures: the key role of white mica. *Earth and Planetary Science Letters*, 228, 65-84.

Schubert, G., Turcotte, D., Olson, P. (2001). *Mantle Convection in the Earth and Planets*. Cambridge: Cambridge University Press.

Selway, K., Ford, H.A., Kelemen, P.B. (2015). The seismic mid-lithosphere discontinuity. *Earth and Planetary Science Letters*, 414, 45-57.

Seo J.H., Guillong M., Aerts M., Zajacz Z., Heinrich C.A. (2011). Microanalysis of S, Cl, and Br in fluid inclusions by LA-ICP-MS. *Chemical Geology*, 284, 35-44.

Shen, A., Keppler, H. (1995). Infrared spectroscopy of hydrous silicate melts to 1000 °C and 10 kbar: Direct observation of H<sub>2</sub>O speciation in a diamond-anvil cell.

Shen, A.H., Keppler, H. (1997). Direct observation of complete miscibility in the albite–H<sub>2</sub>O system. *Nature*, 385, 710-712.

Shishkina, T.A., Botcharnikov, R., Holtz, F., Almeev, R.R., Portnyagin, M. (2010). Solubility of H<sub>2</sub>O- and CO<sub>2</sub>-bearing fluids in tholeiitic basalts at pressures up to 500 MPa. *Chemical Geology*, 277, 115-125.

Sobolev, S.V., Brown, M. (2019). Surface erosion events controlled the evolution of plate tectonics on Earth. *Nature*, 570, 52-57.

## 5. List of references

Spandler, C., Mavrogenes, J., Hermann, J. (2007). Experimental constraints on element mobility from subducted sediments using high-P synthetic fluid/melt inclusions. *Chemical Geology*, 239, 228–249.

Stebbins, J.F. (1995). Dynamics and structure of silicate and oxide melts; nuclear magnetic resonance studies. *Reviews in Mineralogy and Geochemistry*, 32, 191-246.

Stein, C., Stein, S.P. (1992). A model for the global variation in oceanic depth and heat flow with lithospheric age. *Nature*, 359, 123-129.

Stixrude, L.P., Lithgow-Bertelloni, C.R. (2005). Mineralogy and elasticity of the oceanic upper mantle: Origin of the low-velocity zone. *Journal of Geophysical Research*, 110.

Stixrude, L.P., Lithgow-Bertelloni, C.R. (2007). Influence of phase transformations on lateral heterogeneity and dynamics in Earth's mantle. *Earth and Planetary Science Letters*, 263, 45-55.

Stolper, E.M. (1982). The speciation of water in silicate melts. *Geochimica et Cosmochimica Acta*, 46, 2609-2620.

Sun, W., Kennett, B., Zhao, L., Fu, L.Y. (2019). Continental Lithospheric Layering Beneath Stable, Modified, and Destroyed Cratons from Seismic Daylight Imaging. *AGU Geophysical Monograph Series, Lithospheric Discontinuities*, 155-176.

Sylvester, P. (2008). Matrix effects in laser ablation ICP–MS. *Laser Ablation ICP-MS in the Earth Sciences: Current Practices and Outstanding Issues* ( Ed. Sylvester), Mineralogical Association of Canada, Short Course Volume 40.

Tang, M., Rudnick, R.L., Chauvel, C. (2014). Sedimentary input to the source of Lesser Antilles lavas: A Li perspective. *Geochimica et Cosmochimica Acta*, 144, 43-58.

## 5. List of references

Tenner, T. J., Hirschmann, M. M., Humayun, M. (2012). The effect of H<sub>2</sub>O on partial melting of garnet peridotite at 3.5 GPa. *Geochemistry, Geophysics, Geosystems*, 13.

Tenner, T.J., Hirschmann, M.M., Withers, A.C., Hervig, R.L. (2009). Hydrogen partitioning between nominally anhydrous upper mantle minerals and melt between 3 and 5 GPa and applications to hydrous peridotite partial melting. *Chemical Geology*, 262, 42-56.

Tera, F., Brown, L., Morris, J., Sacks, I.S., Klein, J., Middleton, R. (1986). Sediment incorporation in island-arc magmas: inferences from <sup>10</sup>Be. *Geochimica et Cosmochimica Acta*. 50, 535-550.

Tsujimori, T., Sisson, V.B., Liou, J.G., Harlow, G.E., & Sorensen, S.S. (2006). Very-low-temperature record of the subduction process: A review of worldwide lawsonite eclogites. *Lithos*, 92, 609-624.

Tsuno, K., Dasgupta, R. (2012). The effect of carbonates on near-solidus melting of pelite at 3 GPa: Relative efficiency of H<sub>2</sub>O and CO<sub>2</sub> subduction. *Earth and Planetary Science Letters*, 319, 185-196.

Tumiati, S., Fumagalli, P., Tiraboschi, C., Poli, S. (2012). An Experimental Study on COH-bearing Peridotite up to 3.2 GPa and Implications for Crust-Mantle Recycling. *Journal of Petrology*, 54, 453-479.

Turcotte, D.L., Schubert, G. (2002). *Geodynamics*. Cambridge University Press.

Tuttle, O.F., England, J.L. (1955). Preliminary report on the system SiO<sub>2</sub>-H<sub>2</sub>O. *GSA Bulletin*, 66(1), 149–152.

Unsworth, M., Rondenay, S. (2012). Mantle metasomatism. *Lecture Notes in Earth System Sciences: Metasomatism and the Chemical Transformation of Rock*, 535-598.

## 5. List of references

- Wallace, M., Green, D.H. (1991). The effect of bulk rock composition on the stability of amphibole in the upper mantle: Implications for solidus positions and mantle metasomatism. *Mineralogy and Petrology*, 44, 1–19.
- Walter, M.J. (1998). Melting of Garnet Peridotite and the Origin of Komatiite and Depleted Lithosphere. *Journal of Petrology*, 39, 29-60.
- Warren, J. M., Hauri, E. H. (2014). Pyroxenes as tracers of mantle water variations. *Journal of Geophysical Research: Solid Earth*, 119, 1851– 1881.
- Warren, J.M. (2016). Global variations in abyssal peridotite compositions. *Lithos*, 248, 193-219.
- White, W.M. (2013). *Geochemistry*. Wiley-Blackwell.
- Wilschefski, S.C., Baxter, M. (2019). Inductively Coupled Plasma Mass Spectrometry: Introduction to Analytical Aspects. *The Clinical biochemist. Reviews*, 40 3, 115-133.
- Wilson, C., Spiegelman, M., Keken, P.V., Hacker, B.R. (2014). Fluid flow in subduction zones: The role of solid rheology and compaction pressure. *Earth and Planetary Science Letters*, 401, 261-274.
- Wunder, B., Meixner, A., Romer, R.L., Wirth, R., Heinrich, W. (2005). The geochemical cycle of boron: Constraints from boron isotope partitioning experiments between mica and fluid. *Lithos*, 84, 206-216.
- Yang, A. Y., Zhao, T. P., Zhou, M. F., Deng, X. G. (2017). Isotopically enriched N-MORB: A new geochemical signature of off-axis plume-ridge interaction—A case study at 50° 28' E, Southwest Indian Ridge. *Journal of Geophysical Research: Solid Earth*, 122(1), 191-213.
- Yoder, H.S. (1965). Diopside-Anorthite-Water at Five and Ten Kilobars and Its Bearing on Explosive Volcanism. *Carnegie Institution Textbook*, 64, 1964-1965.

*5. List of references*

Young, R.A. (1993). *The Rietveld Method*. Oxford University Press.

Yuan, H., Romanowicz, B.A. (2010). Depth dependent azimuthal anisotropy in the western US upper mantle. *Earth and Planetary Science Letters*, 300, 385-394.

Zhao, Y. H., Ginsberg, S. B., Kohlstedt, D. L. (2004). Solubility of hydrogen in olivine: dependence on temperature and iron content. *Contributions to Mineralogy and Petrology*, 147(2), 155-161.

## 6. Supplement

### 6.1. Supplement I: Amphibole stability in the upper mantle

#### Amphibole compositions

**Table 2.3.2:** Amphibole compositions measured in run products from H<sub>2</sub>O-saturated experiments (initial fluid composition X<sub>H<sub>2</sub>O</sub>=1). ‘n.a.’ indicates that EPMA analyses were not obtained, but the phase was identified by powder XRD and/or SEM-EDS.

P (GPa)	2				2.5		3			
T (°C)	1000	1000	1075	1100	1125	1150	1000	1050	1100	1125
Fwd/Rev	Fwd	Fwd	Fwd	Fwd	Fwd	Fwd	Fwd	Fwd	Fwd	Fwd
Sample	C29	C31	C23	C25	C22	C27	C30	C12	C15	C19
SiO <sub>2</sub>	47.07 (2.28)	47.30 (1.56)	46.83 (0.82)	46.67 (0.60)	45.32 (0.62)	n.a.	47.11 (1.95)	47.10 (1.18)	46.41 (0.21)	47.17 (1.91)
Na <sub>2</sub> O	3.81 (0.31)	3.65 (0.20)	3.88 (0.09)	3.83 (0.14)	3.75 (0.13)	n.a.	3.81 (0.25)	4.20 (0.17)	4.28 (0.05)	4.38 (0.44)
K <sub>2</sub> O	0.58 (0.09)	0.42 (0.05)	0.73 (0.03)	0.71 (0.03)	0.89 (0.06)	n.a.	0.61 (0.08)	0.85 (0.08)	1.03 (0.01)	1.16 (0.12)
Cr <sub>2</sub> O <sub>3</sub>	0.52 (0.31)	0.35 (0.17)	0.94 (0.16)	0.56 (0.21)	0.91 (0.31)	n.a.	0.64 (0.26)	0.82 (0.17)	0.90 (0.03)	0.59 (0.21)
FeO	5.58 (0.65)	5.59 (0.27)	5.43 (0.22)	5.68 (0.41)	5.15 (0.31)	n.a.	4.58 (0.37)	4.98 (0.27)	5.08 (0.14)	5.02 (0.55)
MgO	19.95 (0.98)	20.42 (0.66)	19.85 (0.24)	19.80 (0.26)	19.32 (0.31)	n.a.	19.80 (0.80)	19.99 (0.59)	19.35 (0.09)	19.82 (0.70)
Al <sub>2</sub> O <sub>3</sub>	10.39 (2.09)	10.58 (1.53)	10.43 (0.36)	10.48 (0.48)	12.70 (0.49)	n.a.	11.24 (1.86)	10.31 (0.92)	11.68 (0.11)	10.75 (1.43)
CaO	9.72 (1.07)	9.43 (0.49)	9.31 (0.21)	9.54 (0.33)	9.25 (0.41)	n.a.	9.91 (0.78)	8.33 (0.56)	8.32 (0.08)	8.13 (0.99)
NiO	0.10 (0.05)	0.12 (0.04)	0.09 (0.04)	0.12 (0.03)	0.11 (0.04)	n.a.	0.11 (0.03)	0.15 (0.03)	0.12 (0.01)	0.14 (0.05)
MnO	0.09 (0.03)	0.09 (0.01)	0.09 (0.02)	0.08 (0.02)	0.09 (0.02)	n.a.	0.10 (0.02)	0.09 (0.01)	0.09 (0.00)	0.09 (0.02)
TiO <sub>2</sub>	0.26 (0.07)	0.29 (0.08)	0.34 (0.04)	0.30 (0.04)	0.35 (0.04)	n.a.	0.34 (0.09)	0.28 (0.03)	0.29 (0.00)	0.39 (0.05)
<b>Total</b>	98.06 (0.31)	98.24 (0.32)	97.93 (0.35)	97.77 (0.25)	97.85 (0.13)	n.a.	98.25 (0.27)	97.11 (0.43)	97.55 (0.14)	97.64 (0.27)

6. Supplement – Supplement I: Amphibole stability in the upper mantle

Table 2.3.2: Continued.

P (GPa)	3.4	3.75		4	
T (°C)	1075	1000	1040	1000	1030
Fwd/Rev	Fwd	Fwd	Fwd	Fwd	Fwd
Sample	C24	C13	C20	C26	C28
SiO <sub>2</sub>	47.35 (0.65)	48.82 (1.32)	48.19 (1.15)	51.67 (0.91)	48.70 (0.74)
Na <sub>2</sub> O	4.45 (0.19)	5.12 (0.24)	4.76 (0.24)	5.62 (0.31)	4.81 (0.23)
K <sub>2</sub> O	1.11 (0.10)	1.17 (0.13)	1.19 (0.09)	1.09 (0.11)	1.29 (0.12)
Cr <sub>2</sub> O <sub>3</sub>	0.75 (0.14)	0.67 (0.25)	0.65 (0.35)	0.51 (0.15)	0.58 (0.17)
FeO	4.92 (0.42)	4.22 (0.26)	4.73 (0.44)	3.37 (0.29)	4.65 (0.34)
MgO	19.71 (0.44)	20.22 (0.45)	19.91 (0.45)	20.86 (1.10)	20.41 (0.80)
Al <sub>2</sub> O <sub>3</sub>	11.00 (0.40)	8.99 (1.23)	9.71 (0.84)	7.48 (0.94)	8.82 (0.49)
CaO	7.97 (0.32)	7.25 (0.43)	8.07 (0.57)	6.39 (0.89)	7.23 (0.51)
NiO	0.11 (0.02)	0.14 (0.04)	0.10 (0.05)	0.13 (0.03)	0.12 (0.03)
MnO	0.09 (0.02)	0.09 (0.02)	0.08 (0.02)	0.09 (0.02)	0.08 (0.02)
TiO <sub>2</sub>	0.28 (0.04)	0.30 (0.06)	0.28 (0.04)	0.29 (0.07)	0.35 (0.05)
<b>Total</b>	97.75 (0.17)	97.00 (0.31)	97.66 (0.33)	97.87 (0.51)	97.03 (0.57)

Table 2.3.3: Amphibole compositions measured in run products from H<sub>2</sub>O-undersaturated experiments (initial fluid composition X<sub>H<sub>2</sub>O</sub>=0.5). ‘n.a.’ indicates that EPMA analyses were not obtained, but the phase was identified by powder XRD and/or SEM-EDS.

P (GPa)	2				2.5		3		
T (°C)	1000	1075	1100	1200	1125	1200	1000	1125	1125
Fwd/Rev	Fwd	Fwd	Fwd	Fwd	Fwd	Fwd	Fwd	Fwd	Fwd
Sample	C20N0.5	C10N0.5	C14N0.5	C32N0.5	C11N0.5	C24N0.5	C21N0.5	C9N0.5	C13N0.5
SiO <sub>2</sub>	48.35 (3.06)	49.16 (0.99)	47.74 (0.71)	45.33 (0.86)	46.57 (0.71)	44.63 (0.43)	n.a.	46.21 (1.45)	47.26 (0.55)
Na <sub>2</sub> O	4.63 (0.99)	4.73 (0.24)	4.53 (0.12)	4.15 (0.33)	4.62 (0.14)	4.15 (0.10)	n.a.	4.59 (0.34)	4.90 (0.16)
K <sub>2</sub> O	0.85 (0.34)	0.66 (0.04)	0.70 (0.04)	0.62 (0.05)	0.88 (0.07)	0.82 (0.05)	n.a.	0.78 (0.10)	1.07 (0.06)
Cr <sub>2</sub> O <sub>3</sub>	0.25 (0.15)	0.59 (0.16)	0.59 (0.29)	0.51 (0.17)	0.57 (0.19)	0.83 (0.14)	n.a.	0.84 (0.77)	0.51 (0.06)
FeO	4.78 (0.59)	5.15 (0.51)	5.49 (0.34)	6.64 (0.63)	6.12 (0.47)	6.73 (0.18)	n.a.	4.55 (0.30)	5.90 (0.35)
MgO	20.54 (0.99)	20.89 (0.54)	20.29 (0.33)	19.51 (0.70)	19.61 (0.28)	18.81 (0.11)	n.a.	19.75 (0.68)	19.85 (0.11)
Al <sub>2</sub> O <sub>3</sub>	8.50 (2.37)	8.26 (0.81)	9.13 (0.38)	11.43 (0.53)	10.76 (0.68)	11.79 (0.22)	n.a.	12.14 (1.79)	10.57 (0.43)
CaO	9.62 (1.85)	7.85 (0.60)	8.69 (0.30)	8.21 (0.77)	8.05 (0.19)	8.45 (0.28)	n.a.	8.17 (1.10)	7.36 (0.35)
NiO	0.13 (0.06)	0.15 (0.02)	0.13 (0.03)	0.12 (0.03)	0.12 (0.02)	0.13 (0.04)	n.a.	0.13 (0.09)	0.15 (0.04)
MnO	0.07 (0.02)	0.09 (0.02)	0.10 (0.01)	0.08 (0.02)	0.10 (0.02)	0.07 (0.01)	n.a.	0.10 (0.02)	0.07 (0.02)
TiO <sub>2</sub>	0.17 (0.04)	0.23 (0.07)	0.28 (0.03)	0.38 (0.07)	0.36 (0.05)	0.36 (0.04)	n.a.	0.54 (0.31)	0.31 (0.04)
<b>Total</b>	97.89 (0.25)	97.77 (0.21)	97.67 (0.27)	96.96 (0.42)	97.75 (0.40)	96.76 (0.28)	n.a.	97.80 (0.38)	97.68 (0.22)

6. Supplement – Supplement I: Amphibole stability in the upper mantle

Table 2.3.3: Continued.

P (GPa)	3.5						
T (°C)	900	1075	1075	1075	1150	1200	1250
Fwd/Rev	Rev	Fwd	Fwd	Rev	Fwd	Fwd	Fwd
Sample	C19N0.5	C12N0.5	C17N0.5	C18N0.5	C23N0.5	C25N0.5	C29N0.5
SiO <sub>2</sub>	n.a.	47.78 (1.36)	49.59 (2.81)	49.85 (0.85)	48.60 (0.46)	47.06 (0.76)	46.00 (0.11)
Na <sub>2</sub> O	n.a.	5.05 (0.36)	5.16 (0.51)	5.51 (0.35)	4.91 (0.37)	5.03 (0.16)	4.61 (0.15)
K <sub>2</sub> O	n.a.	0.99 (0.14)	0.86 (0.11)	1.25 (0.18)	1.41 (0.24)	1.41 (0.09)	1.59 (0.06)
Cr <sub>2</sub> O <sub>3</sub>	n.a.	0.78 (0.77)	0.28 (0.20)	0.73 (0.20)	1.18 (0.31)	0.98 (0.27)	0.49 (0.21)
FeO	n.a.	4.97 (0.30)	4.02 (0.45)	4.10 (0.11)	3.73 (0.38)	5.90 (0.36)	6.83 (0.14)
MgO	n.a.	19.87 (0.65)	20.82 (1.17)	20.48 (0.24)	20.38 (0.80)	19.09 (0.27)	18.65 (0.10)
Al <sub>2</sub> O <sub>3</sub>	n.a.	9.95 (1.03)	9.22 (2.98)	9.10 (0.36)	9.95 (0.35)	10.40 (0.66)	11.10 (0.17)
CaO	n.a.	7.11 (0.53)	7.17 (1.21)	6.45 (0.74)	6.39 (0.15)	6.26 (0.38)	6.91 (0.15)
NiO	n.a.	0.16 (0.06)	0.12 (0.06)	0.10 (0.05)	0.11 (0.05)	0.12 (0.04)	0.11 (0.04)
MnO	n.a.	0.09 (0.03)	0.09 (0.03)	0.09 (0.02)	0.07 (0.01)	0.08 (0.02)	0.06 (0.02)
TiO <sub>2</sub>	n.a.	0.37 (0.06)	0.43 (0.23)	0.55 (0.04)	0.60 (0.10)	0.46 (0.11)	0.42 (0.01)
Total	n.a.	97.14 (0.31)	97.74 (0.32)	98.22 (0.22)	97.33 (0.25)	96.80 (0.19)	96.77 (0.43)

Table 2.3.4: Amphibole compositions measured in run products from H<sub>2</sub>O-undersaturated experiments (initial fluid composition X<sub>H2O</sub>=0.25). ‘n.a.’ indicates that EPMA analyses were not obtained, but the phase was identified by powder XRD and/or SEM-EDS.

P (GPa)	2								2.5	
T (°C)	900	1000	1050	1100	1100	1200	1250	1300	1000	1300
Fwd/Rev	Rev	Rev	Rev	Fwd	Rev	Fwd	Fwd	Fwd	Rev	Fwd
Sample	C19N0.75	C18N0.75	C21N0.75	C5N0.75	C17N0.75	C32N0.75	C42N0.75	C44N0.75	C25N0.75	C48N0.75
SiO <sub>2</sub>	44.93 (1.42)	44.96 (0.77)	46.61 (0.68)	48.84 (1.79)	49.40 (1.46)	45.61 (0.72)	45.34 (0.45)	45.24 (0.54)	n.a.	44.95 (0.49)
Na <sub>2</sub> O	4.16 (0.47)	4.18 (0.22)	4.36 (0.39)	4.67 (0.35)	5.22 (0.40)	4.67 (0.31)	4.31 (0.27)	3.90 (0.30)	n.a.	4.13 (0.23)
K <sub>2</sub> O	1.19 (0.12)	1.26 (0.07)	0.91 (0.10)	0.72 (0.07)	0.82 (0.12)	1.07 (0.05)	1.10 (0.20)	1.17 (0.08)	n.a.	1.45 (0.09)
Cr <sub>2</sub> O <sub>3</sub>	0.65 (0.52)	0.58 (0.31)	1.13 (0.31)	0.63 (0.65)	0.38 (0.59)	0.85 (0.46)	0.48 (0.14)	0.55 (0.13)	n.a.	0.64 (0.26)
FeO	5.69 (0.35)	5.98 (0.47)	5.24 (0.50)	3.63 (0.94)	3.68 (0.67)	6.29 (0.36)	7.89 (0.29)	7.39 (0.14)	n.a.	6.71 (0.56)
MgO	18.69 (0.56)	18.57 (0.39)	19.94 (1.39)	21.28 (1.15)	20.96 (0.48)	18.48 (0.37)	18.23 (0.40)	18.43 (0.33)	n.a.	18.52 (0.14)
Al <sub>2</sub> O <sub>3</sub>	13.17 (1.63)	13.18 (0.95)	11.15 (0.86)	8.97 (1.91)	9.42 (1.70)	12.20 (0.81)	12.60 (0.46)	12.31 (0.53)	n.a.	12.19 (0.24)
CaO	8.53 (1.19)	8.51 (0.54)	7.87 (0.61)	7.65 (1.31)	7.04 (0.82)	8.15 (0.55)	7.29 (0.42)	7.71 (0.16)	n.a.	7.20 (0.12)
NiO	0.12 (0.04)	0.10 (0.04)	0.13 (0.03)	0.11 (0.05)	0.11 (0.06)	0.08 (0.04)	0.12 (0.05)	0.11 (0.04)	n.a.	0.15 (0.05)
MnO	0.09 (0.01)	0.09 (0.02)	0.08 (0.02)	0.09 (0.02)	0.09 (0.01)	0.08 (0.01)	0.08 (0.02)	0.07 (0.02)	n.a.	0.07 (0.01)
TiO <sub>2</sub>	0.47 (0.18)	0.60 (0.08)	0.51 (0.09)	0.31 (0.09)	0.31 (0.11)	0.46 (0.06)	0.49 (0.07)	0.52 (0.07)	n.a.	0.64 (0.10)
Total	97.68 (0.30)	98.00 (0.25)	97.94 (0.61)	96.89 (0.44)	97.43 (0.51)	97.95 (0.20)	97.93 (0.28)	97.41 (0.50)	n.a.	96.66 (0.34)

6. Supplement – Supplement I: Amphibole stability in the upper mantle

Table 2.3.4: Continued.

P (GPa)	3				3.5
T (°C)	1000	1100	1200	1250	1075
Fwd/Rev	Rev	Rev	Fwd	Fwd	Fwd
Sample	C23N0.75	C29N0.75	C31N0.75	C34N0.75	C13N0.75
SiO <sub>2</sub>	48.38 (0.26)	45.85 (0.69)	46.05 (0.70)	45.49 (0.67)	48.16 (2.27)
Na <sub>2</sub> O	5.20 (0.02)	4.78 (0.22)	4.64 (0.21)	4.53 (0.19)	5.19 (0.70)
K <sub>2</sub> O	0.99 (0.12)	1.40 (0.14)	1.39 (0.11)	1.45 (0.17)	1.04 (0.17)
Cr <sub>2</sub> O <sub>3</sub>	0.65 (0.00)	0.58 (0.10)	0.74 (0.35)	0.78 (0.20)	0.96 (0.78)
FeO	4.15 (0.16)	6.47 (0.24)	5.89 (0.37)	6.63 (0.18)	5.99 (1.10)
MgO	20.09 (0.24)	18.55 (0.31)	18.76 (0.29)	18.51 (0.69)	19.23 (1.25)
Al <sub>2</sub> O <sub>3</sub>	9.36 (0.17)	11.80 (0.61)	12.53 (0.53)	12.60 (0.50)	9.89 (1.33)
CaO	6.94 (0.54)	7.21 (0.41)	7.07 (0.57)	6.80 (0.38)	6.65 (1.71)
NiO	0.12 (0.05)	0.10 (0.04)	0.11 (0.03)	0.12 (0.04)	0.12 (0.04)
MnO	0.08 (0.00)	0.09 (0.02)	0.08 (0.02)	0.08 (0.02)	0.09 (0.03)
TiO <sub>2</sub>	0.51 (0.06)	0.43 (0.02)	0.50 (0.09)	0.56 (0.10)	0.28 (0.06)
<b>Total</b>	96.73 (0.97)	97.27 (0.18)	97.77 (0.26)	97.55 (0.32)	97.60 (0.75)

6. Supplement – Supplement I: Amphibole stability in the upper mantle

**Olivine compositions**

**Table 2.3.5:** Olivine compositions measured in run products from H<sub>2</sub>O-saturated experiments (initial fluid composition X<sub>H<sub>2</sub>O</sub>=1). ‘n.a.’ indicates that EPMA analyses were not obtained, but the phase was identified by powder XRD and/or SEM-EDS.

P (GPa)	2					2.5		3		
T (°C)	1000	1000	1075	1100	1125	1125	1150	1000	1050	1100
Fwd/Rev	Fwd									
Sample	C29	C31	C23	C25	C18	C22	C27	C30	C12	C15
SiO <sub>2</sub>	41.49 (0.22)	41.18 (0.09)	40.95 (0.19)	41.53 (0.16)	42.08 (0.23)	40.84 (0.18)	41.25 (0.17)	41.34 (0.28)	41.09 (0.22)	41.16 (0.59)
Na <sub>2</sub> O	0 (0)	0.01 (0.01)	0.01 (0.01)	0.01 (0.01)	0.01 (0.00)	0.01 (0.01)	0.02 (0.02)	0 (0)	0.01 (0.01)	0.02 (0.01)
K <sub>2</sub> O	0 (0)	0.01 (0.01)	0.01 (0.01)	0 (0)	0.01 (0.01)	0 (0)	0.01 (0.01)	0 (0)	0 (0)	0 (0)
Cr <sub>2</sub> O <sub>3</sub>	0.02 (0.02)	0.02 (0.02)	0.03 (0.03)	0.01 (0.01)	0.03 (0.03)	0.03 (0.04)	0.06 (0.03)	0.02 (0.02)	0 (0)	0.03 (0.03)
FeO	6.80 (1.68)	7.99 (0.20)	7.55 (0.32)	6.67 (1.49)	7.38 (1.78)	8.42 (0.36)	7.48 (0.47)	7.29 (1.11)	9.01 (0.28)	8.50 (0.22)
MgO	52.23 (1.36)	51.20 (0.15)	50.92 (0.14)	52.54 (1.29)	50.57 (1.43)	50.20 (0.43)	51.63 (0.53)	51.56 (1.07)	50.67 (0.33)	50.68 (0.26)
Al <sub>2</sub> O <sub>3</sub>	0.06 (0.14)	0.02 (0.01)	0.02 (0.01)	0.02 (0.01)	0.04 (0.05)	0.04 (0.04)	0.04 (0.03)	0.02 (0.01)	0.01 (0.01)	0.02 (0.01)
CaO	0.04 (0.02)	0.04 (0.01)	0.06 (0.01)	0.05 (0.02)	0.06 (0.02)	0.07 (0.02)	0.06 (0.01)	0.05 (0.05)	0.02 (0.02)	0.03 (0.01)
NiO	0.36 (0.12)	0.35 (0.01)	0.35 (0.06)	0.37 (0.05)	0.40 (0.10)	0.35 (0.05)	0.36 (0.08)	0.32 (0.11)	0.38 (0.05)	0.40 (0.04)
MnO	0.14 (0.03)	0.12 (0.02)	0.16 (0.02)	0.14 (0.03)	0.15 (0.03)	0.14 (0.02)	0.14 (0.02)	0.13 (0.03)	0.14 (0.03)	0.16 (0.01)
TiO <sub>2</sub>	0.01 (0.01)	0.01 (0.01)	0.01 (0.01)	0.01 (0.01)	0.02 (0.01)	0.01 (0.02)	0.01 (0.01)	0.02 (0.02)	0 (0)	0.02 (0.02)
Total	101.16 (0.25)	100.94 (0.13)	100.05 (0.28)	101.36 (0.21)	100.74 (0.36)	100.11 (0.17)	101.04 (0.18)	100.77 (0.30)	101.34 (0.13)	101.02 (0.40)

**Table 2.3.5:** Continued.

P (GPa)	3		3.4		3.75			4		4.5
T (°C)	1125	1150	1075	1100	1000	1040	1075	1000	1030	1000
Fwd/Rev	Fwd	Fwd	Fwd	Fwd	Fwd	Fwd	Fwd	Fwd	Fwd	Fwd
Sample	C19	C17	C24	C21	C13	C20	C16	C26	C28	C32
SiO <sub>2</sub>	41.12 (0.25)	40.94 (0.35)	41.34 (0.24)	40.73 (0.17)	39.86 (0.54)	40.86 (0.19)	40.79 (0.14)	40.64 (0.13)	40.80 (0.18)	n.a.
Na <sub>2</sub> O	0.02 (0.01)	0.02 (0.01)	0.02 (0.01)	0.03 (0.01)	0.02 (0.01)	0.01 (0.01)	0.02 (0.01)	0.01 (0.01)	0.02 (0.02)	n.a.
K <sub>2</sub> O	0.01 (0.01)	0 (0)	0.01 (0.01)	0.01 (0.01)	0 (0)	0 (0)	0 (0)	0 (0)	0 (0)	n.a.
Cr <sub>2</sub> O <sub>3</sub>	0.03 (0.03)	0.03 (0.03)	0.05 (0.04)	0.06 (0.03)	0.04 (0.04)	0.05 (0.03)	0.02 (0.03)	0.02 (0.03)	0.01 (0.02)	n.a.
FeO	7.95 (1.47)	7.63 (0.57)	8.02 (0.33)	7.58 (0.49)	9.71 (0.38)	8.57 (0.35)	8.16 (0.54)	9.35 (0.47)	9.11 (0.42)	n.a.
MgO	51.50 (1.03)	51.37 (0.47)	51.34 (0.43)	51.08 (0.40)	49.68 (0.38)	50.62 (0.21)	51.13 (0.59)	49.82 (0.46)	50.82 (0.29)	n.a.
Al <sub>2</sub> O <sub>3</sub>	0.05 (0.03)	0.03 (0.03)	0.04 (0.04)	0.05 (0.04)	0.10 (0.20)	0.01 (0.01)	0.02 (0.01)	0.01 (0.01)	0.01 (0.01)	n.a.
CaO	0.04 (0.01)	0.05 (0.01)	0.05 (0.01)	0.05 (0.02)	0.03 (0.02)	0.02 (0.02)	0.02 (0.01)	0.03 (0.02)	0.02 (0.01)	n.a.
NiO	0.37 (0.07)	0.39 (0.05)	0.36 (0.07)	0.33 (0.04)	0.39 (0.09)	0.43 (0.10)	0.41 (0.09)	0.39 (0.07)	0.44 (0.11)	n.a.
MnO	0.14 (0.03)	0.13 (0.01)	0.13 (0.02)	0.12 (0.02)	0.14 (0.03)	0.13 (0.02)	0.13 (0.03)	0.15 (0.04)	0.12 (0.02)	n.a.
TiO <sub>2</sub>	0.01 (0.01)	0.02 (0.01)	0 (0)	0.01 (0.01)	0.02 (0.01)	0.02 (0.01)	0.01 (0.01)	0 (0)	0.01 (0.01)	n.a.
Total	101.22 (0.56)	100.61 (0.42)	101.37 (0.37)	100.04 (0.26)	99.99 (0.68)	100.72 (0.41)	100.70 (0.47)	100.41 (0.34)	101.37 (0.31)	n.a.

6. Supplement – Supplement I: Amphibole stability in the upper mantle

**Table 2.3.6:** Olivine compositions measured in run products from H<sub>2</sub>O-undersaturated experiments (initial fluid composition X<sub>H<sub>2</sub>O</sub>=0.5). ‘n.a.’ indicates that EPMA analyses were not obtained, but the phase was identified by powder XRD and/or SEM-EDS.

P (GPa)	2				2.5			3		
T (°C)	1000	1075	1100	1200	1125	1200	1250	1000	1125	1125
Fwd/Rev	Fwd	Fwd	Fwd	Fwd	Fwd	Fwd	Fwd	Fwd	Fwd	Fwd
Sample	C20N0.5	C10N0.5	C14N0.5	C32N0.5	C11N0.5	C24N0.5	C26N0.5	C21N0.5	C9N0.5	C13N0.5
SiO <sub>2</sub>	40.93 (0.60)	40.67 (0.16)	40.42 (0.87)	41.19 (0.71)	40.60 (0.20)	41.28 (0.14)	41.31 (0.43)	n.a.	40.72 (0.32)	41.09 (0.12)
Na <sub>2</sub> O	0.02 (0.03)	0.01 (0.01)	0.01 (0.01)	0.01 (0.01)	0.01 (0.01)	0.02 (0.01)	0.05 (0.05)	n.a.	0.01 (0.01)	0.02 (0.01)
K <sub>2</sub> O	0 (0)	0 (0)	0 (0)	0 (0)	0 (0)	0.01 (0.01)	0.01 (0.01)	n.a.	0 (0)	0 (0)
Cr <sub>2</sub> O <sub>3</sub>	0.02 (0.02)	0.04 (0.03)	0.04 (0.04)	0.05 (0.05)	0.03 (0.02)	0.03 (0.03)	0.10 (0.07)	n.a.	0.04 (0.03)	0.02 (0.03)
FeO	8.54 (1.83)	8.34 (0.86)	8.55 (0.59)	6.75 (0.12)	8.20 (0.23)	6.97 (0.26)	6.68 (0.21)	n.a.	7.74 (2.16)	7.80 (0.26)
MgO	50.45 (2.07)	51.02 (0.86)	50.30 (1.15)	52.08 (0.77)	51.08 (0.35)	52.16 (0.13)	51.95 (0.82)	n.a.	52.24 (1.81)	51.70 (0.23)
Al <sub>2</sub> O <sub>3</sub>	0.03 (0.05)	0.04 (0.04)	0.01 (0.01)	0.03 (0.01)	0.03 (0.02)	0.03 (0.01)	0.13 (0.17)	n.a.	0.02 (0.02)	0.03 (0.01)
CaO	0.53 (1.02)	0.06 (0.03)	0.07 (0.02)	0.08 (0.01)	0.07 (0.01)	0.07 (0.02)	0.21 (0.36)	n.a.	0.07 (0.01)	0.04 (0.02)
NiO	0.40 (0.22)	0.35 (0.08)	0.36 (0.10)	0.35 (0.04)	0.41 (0.04)	0.36 (0.03)	0.40 (0.03)	n.a.	0.28 (0.07)	0.40 (0.10)
MnO	0.24 (0.10)	0.15 (0.04)	0.17 (0.03)	0.12 (0.02)	0.17 (0.02)	0.13 (0.02)	0.12 (0.02)	n.a.	0.17 (0.06)	0.14 (0.01)
TiO <sub>2</sub>	0.01 (0.01)	0.01 (0.01)	0.02 (0.02)	0.01 (0.01)	0.01 (0.01)	0.01 (0.01)	0.01 (0.01)	n.a.	0.02 (0.02)	0.01 (0.01)
Total	101.18 (0.41)	100.70 (0.26)	99.94 (2.64)	100.68 (1.50)	100.61 (0.24)	101.07 (0.15)	100.98 (0.19)	n.a.	101.31 (0.21)	101.26 (0.18)

**Table 2.3.6:** Continued.

P (GPa)	3	3.5						4	
T (°C)	1250	900	1075	1075	1075	1150	1200	1250	1000
Fwd/Rev	Fwd	Rev	Fwd	Fwd	Rev	Fwd	Fwd	Fwd	Rev
Sample	C30N0.5	C19N0.5	C12N0.5	C17N0.5	C18N0.5	C23N0.5	C25N0.5	C29N0.5	C27N0.5
SiO <sub>2</sub>	41.19 (0.11)	n.a.	40.81 (0.35)	40.46 (0.36)	41.09 (0.19)	41.02 (0.21)	41.09 (0.19)	41.24 (0.40)	n.a.
Na <sub>2</sub> O	0.03 (0.01)	n.a.	0.02 (0.01)	0.02 (0.01)	0.02 (0.01)	0.02 (0.01)	0.03 (0.01)	0.04 (0.01)	n.a.
K <sub>2</sub> O	0 (0)	n.a.	0.01 (0.01)	0 (0)	0 (0)	0 (0)	0 (0)	0.01 (0.01)	n.a.
Cr <sub>2</sub> O <sub>3</sub>	0.05 (0.03)	n.a.	0.04 (0.03)	0.05 (0.05)	0.05 (0.03)	0.04 (0.03)	0.03 (0.03)	0.07 (0.05)	n.a.
FeO	7.21 (0.10)	n.a.	8.51 (0.29)	8.62 (0.60)	7.88 (0.34)	8.46 (0.29)	7.34 (0.26)	7.21 (0.16)	n.a.
MgO	51.85 (0.23)	n.a.	51.37 (0.41)	50.76 (0.63)	51.71 (0.38)	51.20 (0.28)	51.88 (0.23)	51.58 (0.53)	n.a.
Al <sub>2</sub> O <sub>3</sub>	0.05 (0.02)	n.a.	0.03 (0.01)	0.24 (0.63)	0.03 (0.2)	0.02 (0.01)	0.02 (0.01)	0.06 (0.07)	n.a.
CaO	0.07 (0.01)	n.a.	0.04 (0.03)	0.06 (0.06)	0.05 (0.01)	0.04 (0.01)	0.04 (0.01)	0.07 (0.01)	n.a.
NiO	0.36 (0.04)	n.a.	0.35 (0.11)	0.24 (0.06)	0.32 (0.08)	0.36 (0.04)	0.35 (0.08)	0.37 (0.05)	n.a.
MnO	0.12 (0.02)	n.a.	0.13 (0.02)	0.15 (0.03)	0.14 (0.02)	0.11 (0.01)	0.12 (0.01)	0.11 (0.02)	n.a.
TiO <sub>2</sub>	0.01 (0.01)	n.a.	0.01 (0.01)	0.02 (0.02)	0.01 (0.01)	0.02 (0.02)	0.01 (0.02)	0.01 (0.01)	n.a.
Total	100.92 (0.26)	n.a.	101.32 (0.21)	100.62 (0.46)	101.30 (0.36)	101.29 (0.20)	100.92 (0.24)	101.04 (0.15)	n.a.

6. Supplement – Supplement I: Amphibole stability in the upper mantle

**Table 2.3.7:** Olivine compositions measured in run products from H<sub>2</sub>O-undersaturated experiments (initial fluid composition X<sub>H<sub>2</sub>O</sub>=0.25). ‘n.a.’ indicates that EPMA analyses were not obtained, but the phase was identified by powder XRD and/or SEM-EDS.

P (GPa)	2									2.5	
T (°C)	900	1000	1050	1100	1100	1200	1250	1300	1350	1000	1300
Fwd/Rev	Rev	Rev	Rev	Fwd	Rev	Fwd	Fwd	Fwd	Fwd	Rev	Fwd
Sample	C19N0.75	C18N0.75	C21N0.75	C5N0.75	C17N0.75	C32N0.75	C42N0.75	C44N0.75	C45N0.75	C25N0.75	C48N0.75
SiO <sub>2</sub>	40.66 (0.25)	40.84 (0.26)	41.08 (0.16)	40.65 (0.63)	40.36 (0.39)	40.75 (0.26)	42.21 (0.26)	41.73 (0.22)	41.85 (0.27)	n.a.	41.03 (0.22)
Na <sub>2</sub> O	0.02 (0.01)	0.02 (0.01)	0.02 (0.01)	0 (0)	0.01 (0.01)	0.02 (0.01)	0.04 (0.04)	0.02 (0.01)	0.02 (0.01)	n.a.	0.04 (0.01)
K <sub>2</sub> O	0 (0)	0 (0)	0 (0)	0 (0)	0 (0)	0 (0)	0 (0)	0 (0)	0 (0)	n.a.	0 (0)
Cr <sub>2</sub> O <sub>3</sub>	0.05 (0.02)	0.03 (0.02)	0.09 (0.08)	0.04 (0.03)	0.11 (0.18)	0.03 (0.02)	0.04 (0.02)	0.02 (0.02)	0.06 (0.05)	n.a.	0.04 (0.03)
FeO	8.15 (0.35)	7.88 (0.47)	8.05 (0.31)	8.88 (1.91)	8.79 (1.48)	8.54 (0.69)	6.42 (0.26)	6.84 (0.12)	6.39 (0.42)	n.a.	6.47 (0.12)
MgO	51.08 (0.30)	51.21 (0.43)	51.63 (0.48)	51.01 (1.87)	51.23 (1.37)	50.97 (0.80)	53.15 (0.87)	52.86 (0.21)	53.18 (0.45)	n.a.	52.20 (0.28)
Al <sub>2</sub> O <sub>3</sub>	0.03 (0.01)	0.03 (0.01)	0.03 (0.04)	0.02 (0.01)	0.19 (0.32)	0.02 (0.01)	0.11 (0.14)	0.05 (0.01)	0.07 (0.01)	n.a.	0.05 (0.01)
CaO	0.08 (0.01)	0.09 (0.01)	0.08 (0.02)	0.07 (0.02)	0.04 (0.02)	0.08 (0.02)	0.15 (0.12)	0.07 (0.01)	0.15 (0.02)	n.a.	0.11 (0.01)
NiO	0.35 (0.03)	0.35 (0.06)	0.42 (0.12)	0.31 (0.09)	0.32 (0.12)	0.35 (0.04)	0.37 (0.05)	0.35 (0.03)	0.33 (0.07)	n.a.	0.38 (0.05)
MnO	0.15 (0.02)	0.16 (0.02)	0.15 (0.01)	0.16 (0.04)	0.15 (0.02)	0.17 (0.03)	0.12 (0.01)	0.13 (0.01)	0.11 (0.01)	n.a.	0.12 (0.02)
TiO <sub>2</sub>	0.01 (0.01)	0.01 (0.01)	0.01 (0.01)	0.01 (0.01)	0.01 (0.01)	0.01 (0.01)	0.01 (0.01)	0.01 (0.01)	0.01 (0.01)	n.a.	0.01 (0.01)
Total	100.61 (0.27)	100.65 (0.33)	101.61 (0.35)	101.18 (0.56)	101.25 (0.35)	100.97 (0.53)	102.65 (0.15)	102.13 (0.30)	102.21 (0.52)	n.a.	100.47 (0.51)

**Table 2.3.7:** Continued.

P (GPa)	2.5	3					3.5			
T (°C)	1350	1000	1100	1200	1250	1300	900	1000	1075	1075
Fwd/Rev	Fwd	Rev	Rev	Fwd	Fwd	Fwd	Rev	Rev	Fwd	Rev
Sample	C49N0.75	C23N0.75	C29N0.75	C31N0.75	C34N0.75	C41N0.75	C22N0.75	C16N0.75	C13N0.75	C15N0.75
SiO <sub>2</sub>	n.a.	41.48 (0.84)	40.99 (0.28)	41.53 (0.09)	41.36 (0.11)	41.94 (0.13)	40.84 (0.16)	n.a.	41.09 (0.30)	41.19 (0.20)
Na <sub>2</sub> O	n.a.	0.04 (0.01)	0.02 (0.01)	0.02 (0.01)	0.04 (0.02)	0.04 (0.01)	0.03 (0.01)	n.a.	0 (0)	0.02 (0.01)
K <sub>2</sub> O	n.a.	0 (0)	0 (0)	0.01 (0.01)	0.03 (0.06)	0 (0)	0 (0)	n.a.	0 (0)	0 (0)
Cr <sub>2</sub> O <sub>3</sub>	n.a.	0.14 (0.11)	0.03 (0.02)	0.05 (0.01)	0.04 (0.03)	0.09 (0.04)	0.04 (0.03)	n.a.	0.05 (0.08)	0.03 (0.02)
FeO	n.a.	8.33 (0.28)	7.51 (0.30)	7.88 (0.42)	8.02 (0.42)	6.52 (0.07)	7.65 (0.59)	n.a.	7.62 (0.63)	7.42 (0.42)
MgO	n.a.	51.01 (1.08)	52.20 (0.25)	51.67 (0.32)	51.35 (0.57)	53.17 (0.16)	52.18 (0.72)	n.a.	52.12 (0.56)	51.45 (2.61)
Al <sub>2</sub> O <sub>3</sub>	n.a.	0.18 (0.15)	0.03 (0.02)	0.04 (0.01)	0.12 (0.21)	0.08 (0.01)	0.04 (0.02)	n.a.	0.05 (0.05)	0.79 (1.87)
CaO	n.a.	0.07 (0.04)	0.04 (0.02)	0.05 (0.01)	0.06 (0.02)	0.11 (0.01)	0.06 (0.02)	n.a.	0.05 (0.02)	0.15 (0.21)
NiO	n.a.	0.36 (0.05)	0.30 (0.06)	0.32 (0.05)	0.35 (0.04)	0.31 (0.05)	0.32 (0.08)	n.a.	0.28 (0.09)	0.31 (0.07)
MnO	n.a.	0.15 (0.02)	0.14 (0.01)	0.14 (0.01)	0.12 (0.01)	0.10 (0.02)	0.15 (0.02)	n.a.	0.14 (0.02)	0.13 (0.02)
TiO <sub>2</sub>	n.a.	0.04 (0.05)	0.01 (0.01)	0.01 (0.01)	0.01 (0.01)	0.01 (0.01)	0.02 (0.02)	n.a.	0.01 (0.01)	0.01 (0.01)
Total	n.a.	101.85 (0.07)	101.29 (0.19)	101.76 (0.25)	101.54 (0.20)	102.39 (0.09)	101.37 (0.44)	n.a.	101.44 (0.13)	101.54 (0.22)

**Clinopyroxene compositions****Table 2.3.8:** Clinopyroxene compositions measured in run products from H<sub>2</sub>O-saturated experiments (initial fluid composition X<sub>H<sub>2</sub>O</sub>=1). ‘n.a.’ indicates that EPMA analyses were not obtained, but the phase was identified by powder XRD and/or SEM-EDS.

P (GPa)	2					2.5		3		
T (°C)	1000	1000	1075	1100	1125	1125	1150	1000	1050	1100
Fwd/Rev	Fwd	Fwd	Fwd	Fwd	Fwd	Fwd	Fwd	Fwd	Fwd	Fwd
Sample	C29	C31	C23	C25	C18	C22	C27	C30	C12	C15
SiO <sub>2</sub>	54.22 (0.92)	n.a.	54.28 (0.77)	54.43 (1.14)	53.38 (0.72)	53.41 (0.33)	53.24 (0.41)	54.48 (0.5)	53.97 (0.86)	53.78 (0.95)
Na <sub>2</sub> O	0.88 (0.26)	n.a.	1.71 (0.08)	1.51 (0.39)	1.82 (0.06)	1.99 (0.14)	1.94 (0.11)	1.44 (0.12)	2.04 (0.51)	2.46 (0.07)
K <sub>2</sub> O	0 (0)	n.a.	0 (0)	0 (0)	0.01 (0.01)	0.01 (0.01)	0 (0)	0 (0)	0 (0)	0.01 (0.01)
Cr <sub>2</sub> O <sub>3</sub>	0.29 (0.13)	n.a.	0.71 (0.22)	0.46 (0.41)	0.89 (0.19)	1.14 (0.17)	1.03 (0.27)	0.49 (0.23)	0.58 (0.30)	1.08 (0.28)
FeO	3.62 (0.42)	n.a.	4.53 (0.49)	4.94 (0.58)	4.72 (0.58)	4.29 (0.21)	4.61 (0.33)	3.6 (0.29)	4.61 (0.23)	4.66 (0.05)
MgO	16.94 (0.65)	n.a.	16.97 (0.32)	17.36 (1.09)	16.77 (0.55)	16.24 (0.17)	16.38 (0.44)	16.68 (0.4)	16.67 (1.11)	15.74 (0.30)
Al <sub>2</sub> O <sub>3</sub>	2.31 (0.87)	n.a.	2.81 (0.30)	2.22 (1.43)	3.48 (0.55)	4.70 (0.23)	3.98 (0.37)	2.62 (0.32)	2.89 (1.34)	4.40 (0.17)
CaO	22.36 (1.19)	n.a.	19.25 (0.26)	19.27 (0.86)	18.76 (0.42)	18.34 (0.45)	18.37 (0.08)	20.5 (0.32)	18.57 (0.85)	17.90 (0.20)
NiO	0.05 (0.03)	n.a.	0.06 (0.02)	0.05 (0.03)	0.04 (0.02)	0.08 (0.02)	0.05 (0.02)	0.04 (0.04)	0.07 (0.05)	0.05 (0.02)
MnO	0.14 (0.03)	n.a.	0.13 (0.02)	0.18 (0.07)	0.12 (0.02)	0.12 (0.01)	0.12 (0.01)	0.15 (0.04)	0.14 (0.02)	0.14 (0.01)
TiO <sub>2</sub>	0.07 (0.03)	n.a.	0.07 (0.01)	0.06 (0.03)	0.12 (0.02)	0.13 (0.03)	0.09 (0.03)	0.09 (0.02)	0.10 (0.04)	0.09 (0.05)
Total	100.91 (0.41)	n.a.	100.56 (0.64)	100.52 (0.31)	100.16 (0.21)	100.49 (0.30)	99.82 (0.42)	100.15 (0.2)	99.66 (0.46)	100.33 (0.72)

**Table 2.3.8:** Continued.

P (GPa)	3		3.4		3.75			4		4.5
T (°C)	1125	1150	1075	1100	1000	1040	1075	1000	1030	1000
Fwd/Rev	Fwd	Fwd	Fwd	Fwd	Fwd	Fwd	Fwd	Fwd	Fwd	Fwd
Sample	C19	C17	C24	C21	C13	C20	C16	C26	C28	C32
SiO <sub>2</sub>	53.77 (0.23)	53.21 (0.66)	55.14 (0.41)	54.50 (0.55)	54.72 (0.33)	54.43 (0.33)	54.69 (0.17)	55.35 (0.79)	54.48 (0.17)	n.a.
Na <sub>2</sub> O	2.74 (0.08)	2.59 (0.29)	2.66 (0.49)	2.77 (0.22)	3.39 (0.35)	3.45 (0.20)	2.97 (0.27)	3.33 (1.27)	3.72 (0.17)	n.a.
K <sub>2</sub> O	0 (0)	0 (0)	0 (0)	0 (0)	0 (0)	0.01 (0.01)	0 (0)	0.01 (0.01)	0.01 (0.01)	n.a.
Cr <sub>2</sub> O <sub>3</sub>	0.93 (0.41)	1.02 (0.50)	0.93 (0.47)	0.98 (0.22)	0.34 (0.39)	0.79 (0.18)	0.55 (0.23)	0.58 (0.28)	0.89 (0.52)	n.a.
FeO	4.70 (0.78)	4.68 (0.47)	4.49 (0.58)	4.71 (0.56)	4.35 (0.32)	5.33 (0.08)	4.40 (0.40)	3.42 (0.34)	4.56 (0.68)	n.a.
MgO	15.68 (0.14)	16.4 (0.71)	16.56 (0.91)	16.15 (0.61)	15.72 (0.88)	15.06 (0.40)	16.44 (0.35)	14.75 (0.65)	14.82 (0.30)	n.a.
Al <sub>2</sub> O <sub>3</sub>	4.55 (0.47)	3.91 (0.66)	3.67 (1.28)	4.15 (0.36)	4.29 (0.31)	4.02 (0.23)	4.14 (0.13)	5.13 (1.01)	4.81 (0.56)	n.a.
CaO	17.67 (0.40)	17.03 (0.52)	16.82 (0.59)	17.17 (0.24)	16.13 (1.46)	16.71 (0.32)	16.54 (1.10)	17.73 (3.22)	15.98 (0.49)	n.a.
NiO	0.06 (0.02)	0.05 (0.01)	0.07 (0.01)	0.06 (0.04)	0.06 (0.03)	0.05 (0.04)	0.06 (0.02)	0.03 (0.03)	0.08 (0.03)	n.a.
MnO	0.13 (0.02)	0.13 (0.02)	0.16 (0.02)	0.12 (0.01)	0.13 (0.03)	0.12 (0.02)	0.17 (0.02)	0.14 (0.02)	0.13 (0.04)	n.a.
TiO <sub>2</sub>	0.12 (0.03)	0.07 (0.02)	0.08 (0.03)	0.09 (0.02)	0.21 (0.09)	0.13 (0.02)	0.08 (0.01)	0.14 (0.03)	0.15 (0.05)	n.a.
Total	100.37 (0.34)	99.14 (0.41)	100.61 (0.29)	100.74 (0.21)	99.38 (0.57)	100.11 (0.49)	100.07 (0.36)	100.65 (0.49)	99.63 (0.47)	n.a.

6. Supplement – Supplement I: Amphibole stability in the upper mantle

**Table 2.3.9:** Clinopyroxene compositions measured in run products from H<sub>2</sub>O-undersaturated experiments (initial fluid composition X<sub>H<sub>2</sub>O</sub>=0.5). ‘n.a.’ indicates that EPMA analyses were not obtained, but the phase was identified by powder XRD and/or SEM-EDS.

P (GPa)	2				2.5			3		
T (°C)	1000	1075	1100	1200	1125	1200	1250	1000	1125	1125
Fwd/Rev	Fwd	Fwd	Fwd	Fwd	Fwd	Fwd	Fwd	Fwd	Fwd	Fwd
Sample	C20N0.5	C10N0.5	C14N0.5	C32N0.5	C11N0.5	C24N0.5	C26N0.5	C21N0.5	C9N0.5	C13N0.5
SiO <sub>2</sub>	54.15 (0.64)	53.94 (0.73)	53.81 (0.58)	52.54 (0.82)	53.18 (0.64)	52.4 (0.45)	52.26 (0.64)	n.a.	53.69 (0.66)	53.68 (0.73)
Na <sub>2</sub> O	1.45 (0.35)	1.57 (0.52)	1.95 (0.49)	2.05 (0.25)	2.54 (0.48)	2.56 (0.12)	2.70 (0.29)	n.a.	2.27 (0.65)	3.34 (0.29)
K <sub>2</sub> O	0 (0)	0 (0)	0 (0)	0 (0)	0 (0)	0 (0)	0 (0)	n.a.	0 (0)	0 (0)
Cr <sub>2</sub> O <sub>3</sub>	0.02 (0.03)	0.64 (0.57)	0.83 (0.54)	0.67 (0.19)	0.79 (0.44)	0.85 (0.16)	0.76 (0.17)	n.a.	0.30 (0.67)	0.62 (0.27)
FeO	3.86 (0.60)	4.66 (1.01)	4.59 (0.46)	5.82 (0.31)	5.07 (0.76)	5.77 (0.16)	6.03 (0.34)	n.a.	3.95 (0.19)	6.08 (0.59)
MgO	16.42 (0.37)	17.73 (0.99)	16.86 (0.95)	16.81 (1.52)	16.17 (0.58)	16.00 (0.59)	16.56 (1.09)	n.a.	16.13 (0.32)	15.30 (0.51)
Al <sub>2</sub> O <sub>3</sub>	1.72 (0.29)	2.01 (1.01)	2.54 (0.59)	4.21 (0.91)	3.87 (0.29)	4.97 (0.55)	5.58 (0.83)	n.a.	4.20 (0.75)	4.48 (0.62)
CaO	22.23 (1.27)	18.69 (2.19)	18.71 (1.42)	17.21 (0.96)	17.18 (1.61)	16.71 (0.38)	15.11 (0.49)	n.a.	19.48 (1.85)	15.93 (1.28)
NiO	0.03 (0.02)	0.07 (0.04)	0.05 (0.05)	0.06 (0.04)	0.06 (0.04)	0.07 (0.02)	0.06 (0.02)	n.a.	0.03 (0.02)	0.06 (0.03)
MnO	0.13 (0.07)	0.14 (0.08)	0.16 (0.01)	0.12 (0.02)	0.13 (0.02)	0.09 (0.01)	0.11 (0.01)	n.a.	0.13 (0.03)	0.13 (0.01)
TiO <sub>2</sub>	0.06 (0.03)	0.06 (0.03)	0.07 (0.03)	0.11 (0.03)	0.11 (0.02)	0.12 (0.03)	0.13 (0.04)	n.a.	0.21 (0.11)	0.13 (0.06)
Total	100.11 (0.39)	99.56 (0.55)	99.61 (0.37)	99.64 (0.36)	99.16 (0.55)	99.58 (0.25)	99.34 (0.32)	n.a.	100.42 (0.43)	99.81 (0.24)

**Table 2.3.9:** Continued.

P (GPa)	3	3.5						4	
T (°C)	1250	900	1075	1075	1075	1150	1200	1250	1000
Fwd/Rev	Fwd	Rev	Fwd	Fwd	Rev	Fwd	Fwd	Fwd	Rev
Sample	C30N0.5	C19N0.5	C12N0.5	C17N0.5	C18N0.5	C23N0.5	C25N0.5	C29N0.5	C27N0.5
SiO <sub>2</sub>	52.69 (0.41)	n.a.	54.32 (0.40)	54.73 (0.51)	54.98 (0.39)	54.29 (0.37)	53.66 (0.31)	53.27 (0.31)	n.a.
Na <sub>2</sub> O	2.77 (0.27)	n.a.	2.86 (0.31)	2.59 (0.33)	3.96 (0.25)	4.24 (0.14)	3.98 (0.29)	3.55 (0.61)	n.a.
K <sub>2</sub> O	0 (0)	n.a.	0.01 (0.01)	0 (0)	0 (0)	0.01 (0.01)	0 (0)	0.01 (0.01)	n.a.
Cr <sub>2</sub> O <sub>3</sub>	0.92 (0.11)	n.a.	0.14 (0.07)	0.22 (0.23)	1.38 (0.57)	2.05 (0.43)	1.34 (0.40)	0.83 (0.39)	n.a.
FeO	5.66 (0.23)	n.a.	4.68 (0.48)	3.98 (0.77)	4.69 (0.46)	4.53 (0.44)	5.99 (0.38)	6.39 (0.67)	n.a.
MgO	16.05 (0.78)	n.a.	15.8 (0.59)	16.09 (0.54)	15.53 (0.23)	15.04 (0.31)	15.07 (0.52)	15.65 (1.08)	n.a.
Al <sub>2</sub> O <sub>3</sub>	5.82 (0.73)	n.a.	4.19 (0.47)	4.10 (0.51)	5.61 (0.41)	5.86 (0.43)	5.44 (0.47)	5.33 (0.57)	n.a.
CaO	15.51 (0.31)	n.a.	17.71 (1.81)	18.32 (1.33)	14.41 (0.64)	13.51 (0.48)	13.75 (0.51)	14.09 (1.03)	n.a.
NiO	0.04 (0.01)	n.a.	0.05 (0.04)	0.04 (0.04)	0.06 (0.04)	0.05 (0.02)	0.06 (0.03)	0.05 (0.04)	n.a.
MnO	0.11 (0.01)	n.a.	0.16 (0.09)	0.15 (0.06)	0.14 (0.01)	0.12 (0.02)	0.11 (0.02)	0.11 (0.01)	n.a.
TiO <sub>2</sub>	0.12 (0.03)	n.a.	0.17 (0.06)	0.19 (0.09)	0.15 (0.04)	0.17 (0.02)	0.13 (0.05)	0.13 (0.06)	n.a.
Total	99.75 (0.37)	n.a.	100.12 (0.30)	100.46 (0.42)	100.95 (0.21)	99.91 (0.16)	99.57 (0.25)	99.46 (0.42)	n.a.

6. Supplement – Supplement I: Amphibole stability in the upper mantle

**Table 2.3.10:** Clinopyroxene compositions measured in run products from H<sub>2</sub>O-undersaturated experiments (initial fluid composition X<sub>H<sub>2</sub>O</sub>=0.25). ‘n.a.’ indicates that EPMA analyses were not obtained, but the phase was identified by powder XRD and/or SEM-EDS.

P (GPa)	2									2.5	
T (°C)	900	1000	1050	1100	1100	1200	1250	1300	1350	1000	1300
Fwd/Rev	Rev	Rev	Rev	Fwd	Rev	Fwd	Fwd	Fwd	Fwd	Rev	Fwd
Sample	C19N0.75	C18N0.75	C21N0.75	C5N0.75	C17N0.75	C32N0.75	C42N0.75	C44N0.75	C45N0.75	C25N0.75	C48N0.75
SiO <sub>2</sub>	54.01 (1.02)	53.71 (0.86)	53.72 (0.74)	53.79 (0.77)	54.23 (0.64)	54.06 (0.84)	53.47 (0.27)	53.15 (0.42)	52.52 (0.19)	n.a.	52.13 (0.29)
Na <sub>2</sub> O	2.93 (0.48)	2.88 (0.16)	2.24 (0.62)	2.11 (0.17)	2.61 (0.38)	3.25 (0.55)	3.01 (0.24)	2.76 (0.39)	1.68 (0.16)	n.a.	3.32 (0.34)
K <sub>2</sub> O	0 (0)	0 (0)	0 (0)	0 (0)	0 (0)	0 (0)	0.01 (0.01)	0.01 (0.01)	0 (0)	n.a.	0 (0)
Cr <sub>2</sub> O <sub>3</sub>	1.16 (0.67)	1.36 (0.52)	0.74 (0.67)	0.24 (0.14)	0.19 (0.17)	1.05 (0.62)	0.67 (0.19)	0.67 (0.11)	0.56 (0.12)	n.a.	0.76 (0.14)
FeO	4.78 (0.44)	4.97 (0.46)	4.43 (0.49)	3.65 (0.62)	3.39 (0.89)	5.63 (0.53)	7.14 (0.25)	6.65 (0.26)	6.49 (0.13)	n.a.	6.66 (0.20)
MgO	16.84 (1.49)	16.54 (1.02)	15.89 (0.47)	17.23 (0.52)	16.32 (0.46)	16.17 (1.91)	16.37 (0.71)	16.67 (1.02)	18.51 (1.47)	n.a.	15.83 (0.48)
Al <sub>2</sub> O <sub>3</sub>	4.78 (1.12)	4.94 (0.73)	3.89 (0.56)	3.87 (0.65)	4.27 (0.63)	4.76 (0.81)	5.77 (0.60)	5.93 (0.81)	5.13 (0.54)	n.a.	6.45 (0.67)
CaO	15.41 (1.74)	15.76 (1.11)	19.36 (2.11)	18.22 (0.83)	18.36 (1.22)	15.35 (0.88)	13.83 (0.38)	14.42 (0.41)	15.23 (0.78)	n.a.	13.71 (0.63)
NiO	0.04 (0.03)	0.06 (0.02)	0.04 (0.04)	0.05 (0.02)	0.05 (0.02)	0.05 (0.02)	0.08 (0.03)	0.06 (0.03)	0.08 (0.04)	n.a.	0.06 (0.03)
MnO	0.13 (0.02)	0.12 (0.01)	0.11 (0.03)	0.13 (0.03)	0.17 (0.06)	0.14 (0.03)	0.12 (0.01)	0.11 (0.01)	0.11 (0.02)	n.a.	0.11 (0.01)
TiO <sub>2</sub>	0.16 (0.06)	0.15 (0.03)	0.13 (0.03)	0.08 (0.02)	0.16 (0.06)	0.12 (0.04)	0.19 (0.03)	0.18 (0.03)	0.08 (0.02)	n.a.	0.17 (0.05)
Total	100.29 (0.33)	100.54 (0.21)	100.59 (0.42)	99.42 (0.75)	99.79 (1.13)	100.62 (0.39)	100.70 (0.32)	100.66 (0.35)	100.44 (0.68)	n.a.	99.25 (0.34)

**Table 2.3.10:** Continued.

P (GPa)	2.5	3					3.5			
T (°C)	1350	1000	1100	1200	1250	1300	900	1000	1075	1075
Fwd/Rev	Fwd	Rev	Rev	Fwd	Fwd	Fwd	Rev	Rev	Fwd	Rev
Sample	C49N0.75	C23N0.75	C29N0.75	C31N0.75	C34N0.75	C41N0.75	C22N0.75	C16N0.75	C13N0.75	C15N0.75
SiO <sub>2</sub>	n.a.	54.56 (0.56)	53.76 (0.68)	53.60 (0.74)	53.55 (0.33)	53.81 (0.43)	53.19 (0.55)	n.a.	54.67 (0.46)	53.94 (0.39)
Na <sub>2</sub> O	n.a.	3.76 (0.21)	3.78 (0.21)	3.49 (0.74)	3.89 (0.28)	2.27 (0.36)	4.09 (0.67)	n.a.	3.92 (0.63)	4.16 (0.21)
K <sub>2</sub> O	n.a.	0 (0)	0 (0)	0 (0)	0 (0)	0 (0)	0 (0)	n.a.	0.01 (0.01)	0 (0)
Cr <sub>2</sub> O <sub>3</sub>	n.a.	1.23 (0.45)	0.28 (0.13)	0.33 (0.21)	1.05 (0.15)	0.96 (0.18)	0.72 (0.40)	n.a.	0.29 (0.35)	0.89 (0.29)
FeO	n.a.	4.99 (0.31)	5.43 (0.59)	5.23 (0.26)	6.11 (0.41)	5.98 (0.35)	5.82 (0.55)	n.a.	6.01 (0.51)	6.47 (0.64)
MgO	n.a.	16.30 (0.78)	14.95 (0.60)	14.62 (0.26)	15.53 (0.73)	19.11 (1.75)	14.36 (0.54)	n.a.	15.24 (0.54)	14.98 (0.45)
Al <sub>2</sub> O <sub>3</sub>	n.a.	6.05 (0.46)	6.33 (0.31)	6.73 (0.68)	6.92 (0.39)	5.45 (0.85)	6.04 (0.28)	n.a.	4.59 (0.86)	6.13 (0.29)
CaO	n.a.	13.39 (0.23)	15.14 (1.01)	16.18 (2.33)	13.02 (0.44)	12.62 (0.95)	14.77 (2.33)	n.a.	15.37 (1.87)	13.03 (0.81)
NiO	n.a.	0.05 (0.03)	0.04 (0.02)	0.05 (0.03)	0.06 (0.03)	0.05 (0.04)	0.04 (0.03)	n.a.	0.06 (0.04)	0.04 (0.04)
MnO	n.a.	0.14 (0.02)	0.14 (0.02)	0.12 (0.02)	0.12 (0.01)	0.13 (0.01)	0.12 (0.01)	n.a.	0.15 (0.03)	0.13 (0.01)
TiO <sub>2</sub>	n.a.	0.16 (0.05)	0.17 (0.03)	0.26 (0.03)	0.19 (0.03)	0.08 (0.02)	0.19 (0.03)	n.a.	0.11 (0.05)	0.19 (0.03)
Total	n.a.	100.68 (0.48)	100.05 (0.37)	100.64 (0.31)	100.48 (0.32)	100.52 (0.29)	99.38 (1.08)	n.a.	100.44 (0.74)	100.01 (0.39)

6. Supplement – Supplement I: Amphibole stability in the upper mantle

**Orthopyroxene compositions**

**Table 2.3.11:** Orthopyroxene compositions measured in run products from H<sub>2</sub>O-saturated experiments (initial fluid composition X<sub>H<sub>2</sub>O</sub>=1). ‘n.a.’ indicates that EPMA analyses were not obtained, but the phase was identified by powder XRD and/or SEM-EDS.

P (GPa)	2					2.5		3		
T (°C)	1000	1000	1075	1100	1125	1125	1150	1000	1050	1100
Fwd/Rev	Fwd	Fwd	Fwd	Fwd	Fwd	Fwd	Fwd	Fwd	Fwd	Fwd
Sample	C29	C31	C23	C25	C18	C22	C27	C30	C12	C15
SiO <sub>2</sub>	57.47 (0.37)	56.24 (0.79)	56.82 (0.31)	56.91 (0.43)	55.95 (0.13)	56.50 (0.31)	56.24 (0.48)	57.73 (0.57)	56.95 (0.80)	56.56 (1.21)
Na <sub>2</sub> O	0.08 (0.03)	0.06 (0.02)	0.13 (0.02)	0.08 (0.01)	0.15 (0)	0.16 (0.01)	0.18 (0.06)	0.08 (0.02)	0.17 (0.05)	0.18 (0.02)
K <sub>2</sub> O	0 (0)	0 (0)	0 (0)	0 (0)	0 (0)	0 (0)	0 (0)	0 (0)	0.01 (0.01)	0 (0)
Cr <sub>2</sub> O <sub>3</sub>	0.16 (0.08)	0.33 (0.08)	0.27 (0.09)	0.13 (0.05)	0.43 (0)	0.36 (0.04)	0.41 (0.17)	0.31 (0.31)	0.19 (0.10)	0.28 (0.16)
FeO	5.98 (0.26)	5.97 (0.17)	5.94 (0.27)	5.97 (0.18)	6.16 (0.02)	6.15 (0.24)	6.10 (0.27)	5.44 (0.75)	6.37 (0.43)	6.39 (0.39)
MgO	35.02 (0.29)	34.67 (0.29)	34.31 (0.32)	34.86 (0.25)	34.09 (0.02)	33.89 (0.13)	33.71 (0.52)	35.38 (0.78)	34.6 (0.64)	33.79 (0.31)
Al <sub>2</sub> O <sub>3</sub>	0.96 (0.37)	2.64 (0.82)	1.65 (0.32)	1.96 (0.44)	2.36 (0.12)	2.89 (0.45)	2.34 (0.46)	0.95 (0.41)	1.15 (0.59)	1.82 (0.64)
CaO	0.60 (0.09)	0.40 (0.10)	0.84 (0.07)	0.73 (0.08)	0.95 (0.01)	0.89 (0.03)	1.04 (0.24)	0.42 (0.11)	0.68 (0.22)	0.81 (0.21)
NiO	0.11 (0.04)	0.09 (0.04)	0.12 (0.03)	0.09 (0.04)	0.12 (0)	0.12 (0.03)	0.15 (0.04)	0.13 (0.05)	0.14 (0.08)	0.12 (0.04)
MnO	0.16 (0.02)	0.14 (0.02)	0.17 (0.02)	0.19 (0.01)	0.16 (0)	0.16 (0.01)	0.15 (0)	0.16 (0.03)	0.17 (0.04)	0.17 (0.01)
TiO <sub>2</sub>	0.02 (0.01)	0.03 (0.02)	0.04 (0.02)	0.02 (0.01)	0.03 (0)	0.04 (0.01)	0.03 (0.02)	0.02 (0.02)	0.01 (0.02)	0.03 (0.02)
Total	100.61 (0.2)	100.61 (0.32)	100.33 (0.17)	100.97 (0.24)	100.46 (0.07)	101.19 (0.18)	100.39 (0.26)	100.67 (0.14)	100.49 (0.25)	100.19 (0.71)

**Table 2.3.11:** Continued.

P (GPa)	3		3.4		3.75			4		4.5
T (°C)	1125	1150	1075	1100	1000	1040	1075	1000	1030	1000
Fwd/Rev	Fwd	Fwd	Fwd	Fwd	Fwd	Fwd	Fwd	Fwd	Fwd	Fwd
Sample	C19	C17	C24	C21	C13	C20	C16	C26	C28	C32
SiO <sub>2</sub>	56.37 (0.16)	55.86 (0.62)	57.17 (0.26)	56.45 (0.49)	56.55 (0.55)	56.67 (0.28)	56.66 (0.38)	57.61 (0.32)	57.03 (0.24)	n.a.
Na <sub>2</sub> O	0.18 (0.02)	0.24 (0.03)	0.23 (0.03)	0.24 (0.02)	0.25 (0.11)	0.21 (0.04)	0.24 (0.03)	0.24 (0.05)	0.23 (0.04)	n.a.
K <sub>2</sub> O	0 (0)	0.01 (0.01)	0 (0)	0 (0)	0.01 (0.01)	0.01 (0.01)	0 (0)	0 (0)	0 (0)	n.a.
Cr <sub>2</sub> O <sub>3</sub>	0.29 (0.13)	0.24 (0.09)	0.33 (0.08)	0.39 (0.05)	0.12 (0.09)	0.26 (0.05)	0.34 (0.11)	0.26 (0.16)	0.26 (0.08)	n.a.
FeO	6.12 (0.12)	6.22 (0.55)	6.25 (0.21)	5.77 (0.15)	6.22 (1.42)	6.01 (0.06)	5.95 (0.53)	5.83 (0.48)	6.01 (0.16)	n.a.
MgO	34.37 (0.23)	34.01 (0.73)	34.24 (0.21)	34.15 (0.33)	34.42 (1.51)	34.49 (0.31)	34.68 (0.43)	34.59 (0.67)	34.92 (0.38)	n.a.
Al <sub>2</sub> O <sub>3</sub>	2.38 (0.20)	2.13 (0.87)	1.87 (0.35)	2.34 (0.46)	1.01 (0.65)	1.54 (0.28)	1.48 (0.35)	1.01 (0.25)	1.36 (0.26)	n.a.
CaO	0.71 (0.03)	0.81 (0.22)	0.69 (0.03)	0.74 (0.06)	0.52 (0.29)	0.58 (0.11)	0.51 (0.08)	0.53 (0.25)	0.47 (0.06)	n.a.
NiO	0.09 (0.01)	0.14 (0.03)	0.12 (0.07)	0.12 (0.02)	0.19 (0.04)	0.12 (0.03)	0.13 (0.03)	0.15 (0.02)	0.11 (0.04)	n.a.
MnO	0.17 (0.01)	0.16 (0.04)	0.18 (0.02)	0.16 (0.01)	0.14 (0.04)	0.16 (0.02)	0.14 (0.01)	0.16 (0.05)	0.15 (0.02)	n.a.
TiO <sub>2</sub>	0.04 (0.02)	0.02 (0.01)	0.04 (0.01)	0.04 (0.01)	0.01 (0.01)	0.03 (0.01)	0.04 (0.02)	0.02 (0.01)	0.03 (0.02)	n.a.
Total	100.78 (0.16)	99.87 (0.23)	101.16 (0.14)	100.45 (0.33)	99.48 (0.49)	100.12 (0.23)	100.22 (0.33)	100.44 (0.29)	100.61 (0.16)	n.a.

6. Supplement – Supplement I: Amphibole stability in the upper mantle

**Table 2.3.12:** Orthopyroxene compositions measured in run products from H<sub>2</sub>O-undersaturated experiments (initial fluid composition X<sub>H<sub>2</sub>O</sub>=0.5). ‘n.a.’ indicates that EPMA analyses were not obtained, but the phase was identified by powder XRD and/or SEM-EDS.

P (GPa)	2				2.5			3		
T (°C)	1000	1075	1100	1200	1125	1200	1250	1000	1125	1125
Fwd/Rev	Fwd	Fwd	Fwd	Fwd	Fwd	Fwd	Fwd	Fwd	Fwd	Fwd
Sample	C20N0.5	C10N0.5	C14N0.5	C32N0.5	C11N0.5	C24N0.5	C26N0.5	C21N0.5	C9N0.5	C13N0.5
SiO <sub>2</sub>	57.54 (0.52)	56.59 (0.49)	57.05 (0.25)	55.00 (0.86)	55.61 (0.49)	54.81 (0.29)	54.24 (0.36)	n.a.	57.54 (0.34)	56.09 (0.27)
Na <sub>2</sub> O	0.16 (0.03)	0.19 (0.03)	0.19 (0.01)	0.21 (0.02)	0.23 (0.02)	0.24 (0.03)	0.33 (0.01)	n.a.	0.24 (0.03)	0.29 (0.03)
K <sub>2</sub> O	0 (0)	0 (0)	0 (0)	0 (0)	0 (0)	0 (0)	0 (0)	n.a.	0 (0)	0 (0)
Cr <sub>2</sub> O <sub>3</sub>	0.35 (0.14)	0.24 (0.04)	0.25 (0.05)	0.36 (0.10)	0.31 (0.06)	0.40 (0.07)	0.47 (0.08)	n.a.	0.16 (0.06)	0.28 (0.08)
FeO	6.35 (0.71)	6.07 (0.08)	6.11 (0.16)	6.06 (0.36)	6.33 (0.08)	6.18 (0.15)	6.21 (0.15)	n.a.	6.46 (0.25)	6.23 (0.09)
MgO	35.44 (0.64)	34.38 (0.22)	34.51 (0.20)	33.85 (0.67)	33.82 (0.20)	33.67 (0.32)	33.02 (0.25)	n.a.	34.53 (0.30)	34.21 (0.14)
Al <sub>2</sub> O <sub>3</sub>	0.34 (0.07)	1.08 (0.22)	1.01 (0.31)	3.64 (0.88)	2.24 (0.13)	3.68 (0.39)	4.46 (0.40)	n.a.	1.36 (0.41)	2.13 (0.09)
CaO	0.41 (0.08)	0.87 (0.07)	0.85 (0.15)	1.03 (0.25)	0.82 (0.03)	0.91 (0.10)	1.08 (0.16)	n.a.	0.68 (0.08)	0.73 (0.02)
NiO	0.17 (0.06)	0.15 (0.03)	0.11 (0.02)	0.11 (0.04)	0.16 (0.04)	0.09 (0.06)	0.12 (0.05)	n.a.	0.15 (0.03)	0.15 (0.06)
MnO	0.13 (0.02)	0.17 (0.01)	0.18 (0.01)	0.13 (0.01)	0.16 (0.02)	0.14 (0)	0.12 (0.01)	n.a.	0.17 (0.03)	0.18 (0.03)
TiO <sub>2</sub>	0.01 (0.01)	0.02 (0.01)	0.02 (0.01)	0.07 (0.02)	0.04 (0.01)	0.04 (0.02)	0.05 (0.02)	n.a.	0.03 (0.01)	0.06 (0.03)
<b>Total</b>	100.94 (0.75)	99.80 (0.41)	100.32 (0.21)	100.49 (0.35)	99.75 (0.47)	100.19 (0.26)	100.14 (0.28)	n.a.	101.35 (0.21)	100.39 (0.22)

**Table 2.3.12:** Continued.

P (GPa)	3	3.5						4	
T (°C)	1250	900	1075	1075	1075	1150	1200	1250	1000
Fwd/Rev	Fwd	Rev	Fwd	Fwd	Rev	Fwd	Fwd	Fwd	Rev
Sample	C30N0.5	C19N0.5	C12N0.5	C17N0.5	C18N0.5	C23N0.5	C25N0.5	C29N0.5	C27N0.5
SiO <sub>2</sub>	54.05 (0.39)	n.a.	56.68 (0.78)	57.25 (0.22)	56.56 (0.25)	56.68 (0.33)	55.85 (0.45)	54.72 (0.43)	n.a.
Na <sub>2</sub> O	0.32 (0.01)	n.a.	0.23 (0.04)	0.23 (0.02)	0.45 (0.21)	0.43 (0.03)	0.41 (0.03)	0.41 (0.04)	n.a.
K <sub>2</sub> O	0 (0)	n.a.	0 (0)	0 (0)	0.02 (0.05)	0 (0)	0 (0)	0 (0)	n.a.
Cr <sub>2</sub> O <sub>3</sub>	0.48 (0.08)	n.a.	0.38 (0.36)	0.25 (0.09)	0.46 (0.21)	0.66 (0.15)	0.57 (0.15)	0.51 (0.05)	n.a.
FeO	6.30 (0.22)	n.a.	6.01 (0.34)	6.45 (0.24)	5.56 (0.23)	5.50 (0.11)	5.94 (0.11)	6.11 (0.13)	n.a.
MgO	32.73 (0.32)	n.a.	34.74 (0.54)	34.63 (0.21)	34.10 (0.58)	34.13 (0.25)	33.92 (0.41)	33.04 (0.42)	n.a.
Al <sub>2</sub> O <sub>3</sub>	4.94 (0.48)	n.a.	1.63 (0.71)	1.17 (0.28)	2.23 (0.23)	2.22 (0.19)	2.73 (0.44)	4.05 (0.56)	n.a.
CaO	0.96 (0.09)	n.a.	0.45 (0.14)	0.60 (0.08)	0.74 (0.27)	0.71 (0.03)	0.72 (0.06)	1.02 (0.07)	n.a.
NiO	0.12 (0.04)	n.a.	0.21 (0.05)	0.17 (0.05)	0.11 (0.05)	0.14 (0.04)	0.11 (0.04)	0.10 (0.03)	n.a.
MnO	0.13 (0.01)	n.a.	0.13 (0.03)	0.17 (0.03)	0.15 (0.02)	0.12 (0.01)	0.13 (0.01)	0.12 (0.01)	n.a.
TiO <sub>2</sub>	0.05 (0.02)	n.a.	0.03 (0.02)	0.03 (0.04)	0.05 (0.03)	0.06 (0.01)	0.06 (0.01)	0.03 (0.02)	n.a.
<b>Total</b>	100.12 (0.26)	n.a.	100.54 (0.32)	100.98 (0.14)	100.47 (0.23)	100.69 (0.20)	100.48 (0.32)	100.15 (0.22)	n.a.

6. Supplement – Supplement I: Amphibole stability in the upper mantle

**Table 2.3.13:** Orthopyroxene compositions measured in run products from H<sub>2</sub>O-undersaturated experiments (initial fluid composition X<sub>H<sub>2</sub>O</sub>=0.25). ‘n.a.’ indicates that EPMA analyses were not obtained, but the phase was identified by powder XRD and/or SEM-EDS.

P (GPa)	2									2.5	
T (°C)	900	1000	1050	1100	1100	1200	1250	1300	1350	1000	1300
Fwd/Rev	Rev	Rev	Rev	Fwd	Rev	Fwd	Fwd	Fwd	Fwd	Rev	Fwd
Sample	C19N0.75	C18N0.75	C21N0.75	C5N0.75	C17N0.75	C32N0.75	C42N0.75	C44N0.75	C45N0.75	C25N0.75	C48N0.75
SiO <sub>2</sub>	56.72 (0.25)	55.36 (0.29)	56.66 (0.30)	56.58 (0.53)	56.64 (0.93)	56.72 (0.52)	55.67 (0.37)	55.49 (0.46)	55.43 (0.74)	n.a.	53.69 (0.27)
Na <sub>2</sub> O	0.37 (0.03)	0.33 (0.03)	0.33 (0.02)	0.21 (0.03)	0.21 (0.05)	0.37 (0.02)	0.39 (0.01)	0.34 (0.02)	0.29 (0.10)	n.a.	0.43 (0.01)
K <sub>2</sub> O	0 (0)	0 (0)	0 (0)	0 (0)	0 (0)	0 (0)	0 (0)	0 (0)	0 (0)	n.a.	0 (0)
Cr <sub>2</sub> O <sub>3</sub>	0.42 (0.15)	0.46 (0.18)	0.34 (0.03)	0.21 (0.06)	0.21 (0.17)	0.37 (0.07)	0.34 (0.05)	0.33 (0.04)	0.45 (0.04)	n.a.	0.38 (0.09)
FeO	5.80 (0.27)	6.08 (0.13)	5.58 (0.68)	6.49 (0.29)	6.41 (0.80)	6.03 (0.37)	6.15 (0.22)	6.28 (0.18)	6.14 (0.21)	n.a.	6.29 (0.13)
MgO	34.01 (0.23)	33.47 (0.35)	34.37 (0.50)	34.41 (0.35)	34.69 (0.67)	33.87 (0.38)	33.58 (0.31)	33.51 (0.26)	33.34 (1.21)	n.a.	32.53 (0.23)
Al <sub>2</sub> O <sub>3</sub>	2.24 (0.35)	3.41 (0.22)	2.40 (0.22)	0.94 (0.37)	1.22 (0.78)	2.11 (0.61)	4.21 (0.37)	4.29 (0.33)	3.85 (0.49)	n.a.	4.97 (0.35)
CaO	1.02 (0.18)	0.97 (0.08)	0.93 (0.05)	0.86 (0.21)	0.59 (0.19)	0.95 (0.11)	1.03 (0.12)	0.99 (0.04)	1.64 (0.48)	n.a.	1.04 (0.09)
NiO	0.12 (0.03)	0.12 (0.03)	0.11 (0.05)	0.13 (0.04)	0.12 (0.05)	0.12 (0.04)	0.11 (0.04)	0.12 (0.02)	0.12 (0.02)	n.a.	0.11 (0.03)
MnO	0.16 (0.02)	0.16 (0.01)	0.16 (0.02)	0.16 (0.02)	0.18 (0.04)	0.17 (0.01)	0.13 (0.01)	0.14 (0.02)	0.13 (0.02)	n.a.	0.13 (0.01)
TiO <sub>2</sub>	0.04 (0.02)	0.06 (0.02)	0.03 (0.02)	0.03 (0.01)	0.02 (0.01)	0.03 (0.01)	0.06 (0.02)	0.06 (0.03)	0.04 (0.03)	n.a.	0.06 (0.01)
<b>Total</b>	100.93 (0.17)	100.48 (0.43)	100.95 (0.16)	100.07 (0.36)	100.35 (0.31)	100.78 (0.15)	101.71 (0.20)	101.59 (0.28)	101.47 (0.73)	n.a.	99.68 (0.27)

**Table 2.3.13:** Continued.

P (GPa)	2.5	3					3.5			
T (°C)	1350	1000	1100	1200	1250	1300	900	1000	1075	1075
Fwd/Rev	Fwd	Rev	Rev	Fwd	Fwd	Fwd	Rev	Rev	Fwd	Rev
Sample	C49N0.75	C23N0.75	C29N0.75	C31N0.75	C34N0.75	C41N0.75	C22N0.75	C16N0.75	C13N0.75	C15N0.75
SiO <sub>2</sub>	n.a.	56.44 (0.71)	55.91 (0.49)	56.63 (0.74)	55.07 (0.38)	55.20 (0.35)	57.01 (0.53)	n.a.	57.76 (0.23)	56.69 (0.67)
Na <sub>2</sub> O	n.a.	0.43 (0.05)	0.42 (0.10)	0.51 (0.03)	0.51 (0.04)	0.41 (0.02)	0.52 (0.09)	n.a.	0.22 (0.06)	0.41 (0.06)
K <sub>2</sub> O	n.a.	0 (0)	0 (0)	0 (0)	0 (0)	0 (0)	0 (0)	n.a.	0 (0)	0 (0)
Cr <sub>2</sub> O <sub>3</sub>	n.a.	0.39 (0.12)	0.35 (0.06)	0.32 (0.07)	0.46 (0.05)	0.55 (0.14)	0.19 (0.10)	n.a.	0.31 (0.13)	0.29 (0.11)
FeO	n.a.	5.86 (0.24)	6.08 (0.29)	5.89 (0.19)	6.44 (0.10)	6.07 (0.34)	5.59 (0.48)	n.a.	5.32 (0.34)	6.02 (0.34)
MgO	n.a.	33.83 (0.48)	33.91 (0.48)	33.88 (0.78)	32.68 (0.34)	33.11 (0.32)	34.53 (0.48)	n.a.	35.73 (0.45)	34.04 (0.52)
Al <sub>2</sub> O <sub>3</sub>	n.a.	3.08 (0.83)	2.85 (0.54)	2.67 (0.85)	4.56 (0.52)	4.61 (0.39)	1.61 (0.74)	n.a.	0.86 (0.19)	2.33 (0.57)
CaO	n.a.	0.87 (0.08)	0.74 (0.19)	0.78 (0.06)	0.84 (0.13)	1.22 (0.11)	0.91 (0.31)	n.a.	0.32 (0.11)	0.77 (0.09)
NiO	n.a.	0.12 (0.03)	0.13 (0.03)	0.12 (0.04)	0.12 (0.05)	0.10 (0.04)	0.12 (0.06)	n.a.	0.18 (0.06)	0.15 (0.04)
MnO	n.a.	0.14 (0.02)	0.15 (0.01)	0.15 (0.02)	0.12 (0.01)	0.12 (0.02)	0.16 (0.04)	n.a.	0.12 (0.03)	0.14 (0.02)
TiO <sub>2</sub>	n.a.	0.06 (0.02)	0.06 (0.02)	0.06 (0.02)	0.07 (0.02)	0.04 (0.02)	0.03 (0.03)	n.a.	0.02 (0.01)	0.05 (0.01)
<b>Total</b>	n.a.	101.26 (0.26)	100.62 (0.35)	101.05 (0.23)	100.92 (0.31)	101.47 (0.36)	100.71 (0.32)	n.a.	100.90 (0.13)	100.93 (0.46)

6. Supplement – Supplement I: Amphibole stability in the upper mantle

**Garnet compositions**

**Table 2.3.14:** Garnet compositions measured in run products from H<sub>2</sub>O-saturated experiments (initial fluid composition X<sub>H<sub>2</sub>O</sub>=1). ‘n.a.’ indicates that EPMA analyses were not obtained, but the phase was identified by powder XRD and/or SEM-EDS.

P (GPa)	3			3.4		3.75			4		4.5
T (°C)	1100	1125	1150	1075	1100	1000	1040	1075	1000	1030	1000
Fwd/Rev	Fwd	Fwd	Fwd	Fwd	Fwd	Fwd	Fwd	Fwd	Fwd	Fwd	Fwd
Sample	C15	C19	C17	C24	C21	C13	C20	C16	C26	C28	C32
SiO <sub>2</sub>	42.27 (0.88)	42.37 (0.18)	41.81 (0.44)	42.65 (0.55)	42.51 (0.28)	42.45 (1.66)	43.24 (1.82)	42.16 (0.51)	41.42 (0.49)	41.86 (0.62)	n.a.
Na <sub>2</sub> O	0.06 (0.01)	0.03 (0.01)	0.03 (0.02)	0.09 (0.06)	0.04 (0)	0.10 (0.08)	0.41 (0.62)	0.05 (0.03)	0.06 (0.02)	0.09 (0.04)	n.a.
K <sub>2</sub> O	0 (0)	0 (0)	0 (0)	0 (0)	0 (0)	0 (0)	0.01 (0)	0 (0)	0 (0)	0.01 (0.01)	n.a.
Cr <sub>2</sub> O <sub>3</sub>	0.77 (0.26)	1.24 (0.26)	1.18 (0.28)	1.49 (0.50)	2.21 (0.62)	1.09 (0.42)	1.06 (0.43)	1.49 (0.49)	1.11 (0.28)	1.67 (1.49)	n.a.
FeO	8.81 (0.21)	8.40 (0.14)	8.37 (0.52)	8.66 (0.56)	8.05 (0.19)	8.85 (0.12)	8.76 (1.26)	9.05 (0.49)	8.40 (0.27)	9.31 (0.88)	n.a.
MgO	19.54 (0.15)	20.85 (0.43)	20.64 (0.64)	20.73 (0.97)	20.86 (0.55)	22.99 (4.03)	19.88 (0.89)	21.79 (3.22)	14.55 (2.92)	20.84 (1.09)	n.a.
Al <sub>2</sub> O <sub>3</sub>	21.40 (0.16)	21.49 (0.25)	21.56 (0.68)	20.49 (0.85)	20.50 (0.59)	20.43 (2.95)	19.66 (2.51)	20.49 (1.62)	19.81 (1.17)	22.11 (1.39)	n.a.
CaO	6.86 (0.54)	5.42 (0.21)	5.69 (0.68)	5.99 (0.56)	5.88 (0.38)	3.39 (1.12)	6.39 (1.47)	4.54 (1.05)	14.15 (4.58)	4.47 (1.31)	n.a.
NiO	0.03 (0.03)	0.04 (0)	0.01 (0.01)	0.02 (0.02)	0.03 (0.02)	0.05 (0.08)	0.42 (0.06)	0.02 (0.04)	0.02 (0.01)	0 (0)	0.04 (0.02)
MnO	0.46 (0.05)	0.49 (0.08)	0.39 (0.02)	0.42 (0.06)	0.41 (0.04)	0.38 (0.14)	0.42 (0.06)	0.44 (0.02)	0.41 (0.05)	0.42 (0.08)	n.a.
TiO <sub>2</sub>	0.29 (0.06)	0.16 (0.01)	0.19 (0.11)	0.27 (0.08)	0.17 (0.04)	0.13 (0.08)	0.22 (0.13)	0.18 (0.10)	0.52 (0.07)	0.25 (0.13)	n.a.
<b>Total</b>	100.54 (1.06)	100.54 (0.21)	99.89 (0.47)	100.84 (0.28)	100.67 (0.37)	99.91 (0.42)	100.11 (0.33)	100.24 (0.22)	100.45 (0.31)	101.11 (0.64)	n.a.

**Table 2.3.15:** Garnet compositions measured in run products from H<sub>2</sub>O-undersaturated experiments (initial fluid composition X<sub>H<sub>2</sub>O</sub>=0.5). ‘n.a.’ indicates that EPMA analyses were not obtained, but the phase was identified by powder XRD and/or SEM-EDS. ‘\*’ one analysis available.

P (GPa)	3		3.5						4	
T (°C)	1125	1250	900	1075	1075	1075	1150	1200	1250	1000
Fwd/Rev	Fwd	Fwd	Rev	Fwd	Fwd	Rev	Fwd	Fwd	Fwd	Rev
Sample	*C9N0.5	*C30N0.5	C19N0.5	C12N0.5	C17N0.5	C18N0.5	C23N0.5	C25N0.5	C29N0.5	C27N0.5
SiO <sub>2</sub>	42.22	42.55	n.a.	42.03 (0.45)	41.96 (0.21)	42.38 (0.37)	42.47 (0.21)	42.46 (0.31)	42.37 (0.98)	n.a.
Na <sub>2</sub> O	0.06	0.05	n.a.	0.07 (0.02)	0.05 (0.02)	0.05 (0.02)	0.06 (0.02)	0.06 (0.01)	0.11 (0.07)	n.a.
K <sub>2</sub> O	0	0	n.a.	0 (0)	0 (0)	0 (0)	0 (0)	0 (0)	0 (0)	n.a.
Cr <sub>2</sub> O <sub>3</sub>	0.30	1.13	n.a.	1.08 (0.86)	0.59 (0.46)	1.75 (1.31)	2.30 (0.79)	1.99 (0.45)	1.19 (0.55)	n.a.
FeO	7.98	7.84	n.a.	9.81 (2.29)	8.79 (0.81)	7.96 (1.02)	7.72 (0.11)	7.60 (0.41)	7.76 (0.63)	n.a.
MgO	21.98	21.50	n.a.	21.95 (2.42)	25.15 (4.97)	22.14 (0.49)	21.91 (0.32)	22.52 (0.52)	22.18 (0.53)	n.a.
Al <sub>2</sub> O <sub>3</sub>	23.36	21.46	n.a.	22.64 (1.03)	20.88 (3.50)	21.97 (0.99)	21.86 (0.64)	21.51 (0.73)	21.56 (0.44)	n.a.
CaO	4.44	5.88	n.a.	3.33 (1.59)	2.69 (0.38)	3.62 (0.65)	4.34 (0.20)	4.09 (0.45)	4.41 (0.40)	n.a.
NiO	0	0.01	n.a.	0.03 (0.03)	0.06 (0.05)	0.05 (0.06)	0.02 (0.02)	0.04 (0.02)	0.03 (0.02)	n.a.
MnO	0.44	0.33	n.a.	0.31 (0.11)	0.37 (0.11)	0.29 (0.08)	0.32 (0.01)	0.34 (0.02)	0.32 (0.03)	n.a.
TiO <sub>2</sub>	0.34	0.19	n.a.	0.24 (0.14)	0.14 (0.12)	0.23 (0.20)	0.25 (0.04)	0.17 (0.04)	0.18 (0.02)	n.a.
<b>Total</b>	101.12	100.95	n.a.	101.54 (0.32)	100.71 (0.87)	100.49 (0.32)	101.29 (0.23)	100.82 (0.81)	100.14 (2.45)	n.a.

6. Supplement – Supplement I: Amphibole stability in the upper mantle

**Table 2.3.16:** Garnet compositions measured in run products from H<sub>2</sub>O-undersaturated experiments (initial fluid composition X<sub>H<sub>2</sub>O</sub>=0.25). ‘n.a.’ indicates that EPMA analyses were not obtained, but the phase was identified by powder XRD and/or SEM-EDS.

P (GPa)	2		3				3.5			
T (°C)	1100	1000	1100	1200	1250	1300	900	1000	1075	1075
Fwd/Rev	Rev	Rev	Rev	Fwd	Fwd	Fwd	Rev	Rev	Fwd	Rev
Sample	C17N0.75	C23N0.75	C29N0.75	*C31N0.75	C34N0.75	C41N0.75	C22N0.75	C16N0.75	C13N0.75	C15N0.75
SiO <sub>2</sub>	n.a.	42.94 (0.17)	42.34 (0.50)	42.95	42.99 (0.20)	n.a.	42.66 (0.21)	n.a.	40.98 (1.82)	42.65 (0.36)
Na <sub>2</sub> O	n.a.	0.06 (0.01)	0.04 (0.01)	0.03	0.05 (0.01)	n.a.	0.06 (0.01)	n.a.	0.04 (0.02)	0.05 (0.01)
K <sub>2</sub> O	n.a.	0 (0)	0 (0)	0.01	0 (0)	n.a.	0 (0)	n.a.	0 (0)	0 (0)
Cr <sub>2</sub> O <sub>3</sub>	n.a.	0.89 (0.42)	1.01 (0.19)	0.88	0.83 (0.14)	n.a.	0.69 (0.52)	n.a.	0.89 (0.58)	0.83 (0.44)
FeO	n.a.	7.48 (0.25)	7.57 (0.81)	7.88	7.84 (0.17)	n.a.	7.35 (0.48)	n.a.	8.77 (0.72)	7.96 (0.81)
MgO	n.a.	22.33 (0.30)	22.23 (0.70)	22.80	23.06 (1.22)	n.a.	22.53 (0.40)	n.a.	25.84 (3.12)	22.25 (0.45)
Al <sub>2</sub> O <sub>3</sub>	n.a.	22.60 (0.43)	22.31 (0.34)	22.43	21.77 (0.75)	n.a.	22.71 (0.77)	n.a.	20.84 (4.24)	22.53 (0.45)
CaO	n.a.	4.58 (0.31)	4.85 (0.80)	4.11	4.30 (0.44)	n.a.	4.74 (0.98)	n.a.	3.31 (1.09)	4.25 (0.26)
NiO	n.a.	0.01 (0.01)	0.03 (0.02)	0.01	0.03 (0.03)	n.a.	0.04 (0.03)	n.a.	0.09 (0.07)	0.03 (0.03)
MnO	n.a.	0.35 (0.01)	0.40 (0.06)	0.38	0.33 (0.02)	n.a.	0.37 (0.06)	n.a.	0.35 (0.06)	0.45 (0.08)
TiO <sub>2</sub>	n.a.	0.25 (0.05)	0.22 (0.09)	0.13	0.17 (0.06)	n.a.	0.19 (0.04)	n.a.	0.16 (0.09)	0.18 (0.05)
Total	n.a.	101.53 (0.29)	101.04 (0.43)	101.61	101.41 (0.26)	n.a.	101.39 (0.31)	n.a.	101.32 (0.32)	101.22 (0.25)

**Spinel compositions**

**Table 2.3.17:** Spinel compositions measured in run products from H<sub>2</sub>O-saturated experiments (initial fluid composition X<sub>H<sub>2</sub>O</sub>=1).

P (GPa)	2					2.5
T (°C)	1000	1000	1075	1100	1125	1150
Fwd/Rev	Fwd	Fwd	Fwd	Fwd	Fwd	Fwd
Sample	C29	C31	C23	C25	C18	C27
SiO <sub>2</sub>	0.08 (0.02)	1.44 (0.76)	0.12 (0.04)	0.21 (0.23)	0.21 (0.14)	0.21 (0.09)
Na <sub>2</sub> O	0.01 (0.01)	0.01 (0)	0 (0)	0.02 (0.06)	0.02 (0.03)	0.02 (0.02)
K <sub>2</sub> O	0 (0)	0 (0)	0.01 (0)	0.01 (0.01)	0 (0)	0 (0)
Cr <sub>2</sub> O <sub>3</sub>	10.49 (5.41)	19.73 (0.45)	11.85 (5.49)	8.96 (2.83)	10.96 (7.64)	11.73 (7.24)
FeO	55.95 (5.78)	43.71 (0.91)	59.80 (5.62)	56.52 (5.31)	43.55 (3.90)	53.88 (6.77)
MgO	12.42 (2.79)	14.11 (0.11)	11.46 (0.36)	12.59 (1.25)	15.71 (2.13)	13.12 (0.29)
Al <sub>2</sub> O <sub>3</sub>	15.21 (8.41)	17.16 (0.22)	8.39 (0.21)	13.46 (5.55)	23.75 (10.15)	13.41 (0.74)
CaO	0.01 (0.01)	0.02 (0.02)	0 (0)	0 (0)	0.01 (0.02)	0 (0)
NiO	0.73 (0.17)	0.62 (0)	0.68 (0.16)	0.66 (0.10)	0.49 (0.06)	0.58 (0.11)
MnO	0.24 (0.06)	0.25 (0)	0.25 (0.02)	0.22 (0.03)	0.20 (0.05)	0.23 (0.02)
TiO <sub>2</sub>	0.63 (0.15)	0.55 (0.03)	0.47 (0.07)	0.58 (0.07)	0.38 (0.04)	0.53 (0.13)
Total	95.81 (1.40)	97.63 (0.95)	93.06 (0.24)	93.27 (0.84)	95.31 (1.29)	93.73 (0.31)

6. Supplement – Supplement I: Amphibole stability in the upper mantle

**Table 2.3.18:** Spinel compositions measured in run products from H<sub>2</sub>O-undersaturated experiments (initial fluid composition X<sub>H<sub>2</sub>O</sub>=0.5).

P (GPa)	2			2.5		3		3.5	
T (°C)	1075	1100	1200	1125	1200	1250	1125	1250	1250
Fwd/Rev	Fwd								
Sample	C10N0.5	C14N0.5	C32N0.5	C11N0.5	C24N0.5	C26N0.5	C13N0.5	C30N0.5	C29N0.5
SiO <sub>2</sub>	0.11 (0.04)	0.26 (0.42)	0.48 (0.31)	0.39 (0.53)	0.37 (0.18)	0.31 (0.06)	0.19 (0.04)	0.28 (0.11)	0.37 (0.13)
Na <sub>2</sub> O	0 (0)	0 (0)	0.01 (0.01)	0.02 (0.02)	0.01 (0.01)	0.02 (0.02)	0.01 (0.01)	0.01 (0)	0 (0)
K <sub>2</sub> O	0 (0)	0 (0)	0 (0)	0 (0)	0 (0)	0 (0)	0.01 (0)	0 (0)	0.01 (0.01)
Cr <sub>2</sub> O <sub>3</sub>	7.36 (5.37)	6.37 (3.67)	12.92 (2.25)	7.73 (5.80)	11.69 (2.85)	11.30 (1.58)	12.53 (3.38)	17.61 (4.79)	15.26 (1.27)
FeO	47.65 (7.98)	50.10 (2.08)	53.65 (1.37)	51.85 (4.51)	53.88 (3.21)	49.49 (0.67)	54.40 (6.27)	42.01 (3.41)	49.24 (1.33)
MgO	15.21 (0.91)	17.14 (1.54)	13.16 (0.38)	14.99 (1.94)	13.75 (0.73)	15.37 (0.20)	12.22 (2.27)	15.81 (0.18)	14.45 (0.23)
Al <sub>2</sub> O <sub>3</sub>	23.66 (3.98)	19.15 (2.72)	12.14 (0.73)	18.79 (4.84)	13.42 (1.31)	17.29 (0.78)	12.85 (8.25)	18.85 (1.46)	14.05 (0.31)
CaO	0 (0)	0.01 (0)	0.06 (0.05)	0 (0)	0.03 (0.02)	0.01 (0.01)	0.02 (0.02)	0.02 (0.01)	0.04 (0.03)
NiO	0.88 (0.20)	0.85 (0.31)	0.61 (0.06)	0.57 (0.07)	0.55 (0.05)	0.57 (0.07)	0.62 (0.04)	0.47 (0.05)	0.56 (0.01)
MnO	0.14 (0.04)	0.17 (0.03)	0.22 (0)	0.18 (0.04)	0.20 (0.01)	0.19 (0.02)	0.23 (0.04)	0.21 (0.02)	0.21 (0.01)
TiO <sub>2</sub>	0.79 (0.30)	0.81 (0.23)	0.45 (0.03)	0.67 (0.12)	0.51 (0.19)	0.40 (0.02)	0.78 (0.06)	0.40 (0.05)	0.27 (0.06)
<b>Total</b>	95.83 (1.16)	94.89 (0.32)	93.73 (0.66)	95.23 (1.17)	94.46 (0.41)	94.98 (0.35)	93.90 (1.98)	95.70 (0.05)	94.51 (0.44)

**Table 2.3.19:** Spinel compositions measured in run products from H<sub>2</sub>O-undersaturated experiments (initial fluid composition X<sub>H<sub>2</sub>O</sub>=0.25).

P (GPa)	2			2.5		3		3.5		
T (°C)	900	1000	1050	1100	1200	1300	1100	1300	1075	1075
Fwd/Rev	Rev	Rev	Rev	Fwd	Fwd	Fwd	Rev	Fwd	Fwd	Rev
Sample	C19N0.75	C18N0.75	C21N0.75	C5N0.75	C32N0.75	C48N0.75	C29N0.75	C41N0.75	C13N0.75	C15N0.75
SiO <sub>2</sub>	0.16 (0.03)	0.80 (0.15)	0.18 (0.08)	0.64 (0.55)	0.17 (0.14)	0.27 (0.02)	0.48 (0.44)	0.37 (0.10)	0.18 (0.13)	0.16 (0.02)
Na <sub>2</sub> O	0.02 (0.01)	0.01 (0)	0 (0)	0 (0)	0 (0)	0 (0)	0 (0)	0 (0)	0 (0)	0.01 (0.01)
K <sub>2</sub> O	0.01 (0)	0 (0)	0 (0)	0 (0)	0 (0)	0.01 (0.01)	0.01 (0.01)	0 (0)	0.01 (0.03)	0.01 (0)
Cr <sub>2</sub> O <sub>3</sub>	12.18 (11.32)	12.32 (10.41)	6.76 (2.46)	5.25 (4.01)	11.03 (6.92)	10.38 (3.12)	7.15 (5.12)	22.12 (1.39)	4.39 (5.89)	10.62 (2.02)
FeO	41.97 (10.43)	49.17 (1.92)	49.98 (1.73)	52.54 (5.97)	44.89 (5.99)	49.22 (3.42)	53.72 (9.81)	37.04 (2.00)	52.63 (5.14)	55.17 (8.26)
MgO	17.56 (3.58)	13.93 (1.41)	14.98 (0.59)	16.83 (2.71)	19.27 (2.16)	15.64 (1.06)	11.57 (6.01)	16.84 (0.29)	9.96 (3.93)	12.75 (2.67)
Al <sub>2</sub> O <sub>3</sub>	23.99 (6.48)	15.67 (9.61)	21.55 (1.78)	18.00 (3.31)	18.69 (5.27)	18.03 (5.53)	14.03 (12.66)	18.96 (1.18)	8.28 (10.85)	14.43 (8.40)
CaO	0.01 (0.01)	0.02 (0.01)	0 (0)	0 (0)	0.01 (0)	0.06 (0.05)	0 (0)	0.06 (0.06)	0.03 (0.03)	0.04 (0.04)
NiO	0.80 (0.42)	1.26 (0.98)	1.65 (0.20)	1.72 (0.41)	0.81 (0.38)	0.55 (0.03)	0.48 (0.34)	0.37 (0.03)	0.45 (0.25)	0.69 (0.05)
MnO	0.21 (0.11)	0.21 (0.13)	0.13 (0.03)	0.09 (0.02)	0.21 (0.05)	0.19 (0.02)	0.17 (0.07)	0.21 (0.02)	0.11 (0.03)	0.23 (0.03)
TiO <sub>2</sub>	0.84 (0.51)	0.97 (0.84)	1.12 (0.19)	0.63 (0.40)	0.61 (0.14)	0.42 (0.12)	7.51 (11.68)	0.25 (0.04)	18.82 (15.94)	0.90 (0.16)
<b>Total</b>	97.79 (1.36)	94.36 (0.51)	96.38 (0.24)	95.73 (1.18)	95.71 (1.12)	94.83 (0.79)	95.14 (2.39)	96.26 (0.72)	94.88 (1.35)	95.02 (1.57)

6. Supplement – Supplement I: Amphibole stability in the upper mantle

**Phlogopite and melt compositions**

**Table 2.3.20:** Phlogopite compositions. ‘n.a.’ indicates that EPMA analyses were not obtained, but the phase was identified by powder XRD and/or SEM-EDS.

‘\*’ one analysis available.

X <sub>H2O</sub>	1					0.5			0.25					
P (GPa)	3.75	2		3.5			4	2	3		3.5			
T (°C)	1075	1200		1150	1200		1250	1000	1200		1250	900	1000	1075
Fwd/Rev	Fwd	Fwd		Fwd	Fwd		Fwd	Rev	Fwd		Fwd	Rev	Rev	Rev
Sample	*C16	C32N0.5	C23N0.5	C25N0.5	C29N0.5	C27N0.5	C32N0.75	C31N0.75	C34N0.75	C22N0.75	C16N0.75	*C15N0.75		
SiO <sub>2</sub>	40.35	39.03 (0.26)	41.06 (0.26)	40.14 (0.26)	39.76 (0.12)	n.a.	38.46 (0.30)	39.52 (0.33)	39.19 (0.41)	n.a.	n.a.	39.77		
Na <sub>2</sub> O	0.77	2.08 (0.12)	0.75 (0.03)	0.88 (0.05)	0.95 (0.02)	n.a.	1.55 (0.08)	1.07 (0.02)	0.88 (0.06)	n.a.	n.a.	0.68		
K <sub>2</sub> O	9.00	7.08 (0.15)	8.85 (0.14)	8.79 (0.11)	8.83 (0.07)	n.a.	8.00 (0.10)	8.53 (0.04)	8.35 (0.54)	n.a.	n.a.	8.58		
Cr <sub>2</sub> O <sub>3</sub>	0.24	0.59 (0.26)	0.58 (0.22)	0.34 (0.22)	0.53 (0.12)	n.a.	0.61 (0.35)	0.81 (0.29)	0.73 (0.07)	n.a.	n.a.	0.71		
FeO	4.59	4.87 (0.94)	4.10 (0.26)	5.02 (0.49)	5.95 (0.20)	n.a.	5.82 (0.25)	5.56 (0.36)	6.22 (0.16)	n.a.	n.a.	5.41		
MgO	24.87	24.05 (0.16)	24.62 (0.24)	24.05 (0.38)	23.43 (0.31)	n.a.	23.05 (0.38)	23.22 (0.31)	23.62 (1.91)	n.a.	n.a.	23.35		
Al <sub>2</sub> O <sub>3</sub>	13.65	16.44 (0.16)	14.13 (0.09)	14.06 (0.14)	14.48 (0.11)	n.a.	17.01 (0.26)	15.97 (0.37)	14.93 (1.09)	n.a.	n.a.	15.41		
CaO	0	0 (0)	0 (0)	0 (0)	0 (0)	n.a.	0 (0)	0 (0)	0 (0)	n.a.	n.a.	0		
NiO	0.27	0.17 (0.02)	0.18 (0.05)	0.17 (0.05)	0.22 (0.04)	n.a.	0.19 (0.04)	0.27 (0.11)	0.22 (0.03)	n.a.	n.a.	0.29		
MnO	0.01	0.01 (0)	0.02 (0.01)	0.02 (0.01)	0.01 (0.01)	n.a.	0.03 (0)	0.03 (0.02)	0.03 (0.01)	n.a.	n.a.	0		
TiO <sub>2</sub>	0.40	0.42 (0.05)	0.68 (0.06)	0.72 (0.13)	0.66 (0.09)	n.a.	0.55 (0.03)	0.51 (0.04)	0.91 (0.06)	n.a.	n.a.	0.72		
<b>Total</b>	94.14	94.78 (0.58)	94.99 (0.43)	94.23 (0.79)	94.87 (0.30)	n.a.	95.30 (0.51)	95.53 (0.23)	95.12 (0.53)	n.a.	n.a.	94.92		

**Table 2.3.21:** Melt compositions measured in two run products from H<sub>2</sub>O-undersaturated experiments (initial fluid composition X<sub>H2O</sub>=0.25). Analyses were obtained by scanning the electron beam across multiple 20 x 20 µm areas.

P (GPa)	2	3
T (°C)	1350	1300
Fwd/Rev	Fwd	Fwd
Sample	C45N0.75	C41N0.75
SiO <sub>2</sub>	48.42 (1.66)	43.94 (0.96)
Na <sub>2</sub> O	2.52 (0.99)	3.76 (0.09)
K <sub>2</sub> O	0.60 (0.10)	1.01 (0.05)
Cr <sub>2</sub> O <sub>3</sub>	0.23 (0.05)	0.21 (0.02)
FeO	9.63 (0.53)	11.13 (0.38)
MgO	19.92 (8.42)	14.66 (0.43)
Al <sub>2</sub> O <sub>3</sub>	9.14 (1.70)	10.44 (0.31)
CaO	5.47 (3.04)	6.91 (0.40)
NiO	0.04 (0.05)	0.04 (0.03)
MnO	0.16 (0.03)	0.17 (0.03)
TiO <sub>2</sub>	0.28 (0.10)	0.53 (0.02)
<b>Total</b>	96.40 (1.42)	92.82 (1.68)

6. Supplement – Supplement I: Amphibole stability in the upper mantle

**Phase proportions**

**Table 2.3.22:** Phase proportions, as estimated from mass balance calculations, expressed in wt.% of the solid residues. Negligible dissolution of solids into the fluid phase is assumed in subsolidus samples. Mass balance was not performed when melt was observed, except in two samples where melt composition could be measured by EPMA (Table 2.3.21).

Sample	Fwd/Rev	X(H <sub>2</sub> O)	P (GPa)	T(°C)	W <sub>Ol</sub>	W <sub>Opx</sub>	W <sub>Cpx</sub>	W <sub>Amp</sub>	W <sub>Grt</sub>	W <sub>Phlog</sub>	W <sub>melt</sub>	Σ
C12	Fwd	1	3	1050	70.1	11.6	2.2	15.5				99.4
C13	Fwd	1	3.75	1000	71.7	11.7	6.4	7.4	3.6			100.9
C15	Fwd	1	3	1100	70.6	12.7	4.0	11.7	0.1			99.2
C16	Fwd	1	3.75	1075	68.6	14.9	9.2		5.8	1.1		99.6
C20	Fwd	1	3.75	1040	70.6	12.2	4.7	9.2	2.7			99.3
C21	Fwd	1	3.4	1100	68.5	18.8	9.9					97.2
C23	Fwd	1	2	1075	69.8	12.1	2.2	15.5				99.6
C26	Fwd	1	4	1000	72.9	10.5	3.6	8.5	4.4			99.9
C28	Fwd	1	4	1030	70.3	12.0	6.4	7.5	3.0			99.2
C29	Fwd	1	2	1000	65.9	15.2	0.8	15.7				97.6
C30	Fwd	1	3	1000	67.2	14.9	1.3	14.4				97.9
C31	Fwd	1	2	1000	67.5	15.5	3.1	12.2				98.3
C9N0.5	Fwd	0.5	3	1125	65.5	17.1	3.9	11.6				98.0
C10N0.5	Fwd	0.5	2	1075	69.3	9.5	0.5	20.4				99.8
C11N0.5	Fwd	0.5	2.5	1125	68.3	14.9	4.2	12.1				99.5
C12N0.5	Fwd	0.5	3.5	1075	68.3	14.0	5.7	8.6	2.1			98.7
C13N0.5	Fwd	0.5	3	1125	68.5	13.0	5.0	12.3				98.7
C14N0.5	Fwd	0.5	2	1100	70.1	11.5	0.6	18.3				100.4
C17N0.5	Fwd	0.5	3.5	1075	69.2	12.8	5.4	8.9	2.9			99.2
C23N0.5	Fwd	0.5	3.5	1150	70.8	11.5	10.0	3.6	2.8	0.6		99.2
C24N0.5	Fwd	0.5	2.5	1200	66.1	18.4	6.8	6.6				97.9
C25N0.5	Fwd	0.5	3.5	1200	68.8	13.4	9.8	4.2	2.2	0.5		98.8
C32N0.5	Fwd	0.5	2	1200	65.8	18.3	6.2	7.6		0.7		98.7
C18N0.5	Rev	0.5	3.5	1075	69.3	12.5	9.2	4.3	2.8			98.0
C5N0.75	Fwd	0.25	2	1100	68.9	10.8	1.7	18.2				99.5
C13N0.75	Fwd	0.25	3.5	1075	66.9	13.7	7.8	5.6	3.7			97.7
C31N0.75	Fwd	0.25	3	1200	69.6	13.5	7.2	7.5	0.1	0.1		97.9
C32N0.75	Fwd	0.25	2	1200	69.8	13.7	5.7	10.2		0.1		99.4
C34N0.75	Fwd	0.25	3	1250	71.1	12.5	11.1	3.7	0.0	0.6		99.0
C41N0.75	Fwd	0.25	3	1300	66.7	14.3	10.5				5.5	96.9
C42N0.75	Fwd	0.25	2	1250	66.8	14.9	9.7	4.8				96.3
C44N0.75	Fwd	0.25	2	1300	66.3	16.7	9.5	4.2				96.7
C45N0.75	Fwd	0.25	2	1350	66.0	13.7	7.7				9.6	97.0

6. Supplement – Supplement I: Amphibole stability in the upper mantle

Table 2.3.22: Continued.

Sample	Fwd/Rev	X(H <sub>2</sub> O)	P (GPa)	T (°C)	W <sub>Ol</sub>	W <sub>Opx</sub>	W <sub>Cpx</sub>	W <sub>Amp</sub>	W <sub>Grt</sub>	W <sub>Phlog</sub>	W <sub>mett</sub>	Σ
C48N0.75	Fwd	0.25	2.5	1300	67.1	18.0	11.8	1.2				98.1
C15N0.75	Rev	0.25	3.5	1075	70.5	12.3	11.9		3.5	1.2		99.3
C17N0.75	Rev	0.25	2	1100	67.5	14.7	5.5	8.7	2.4			98.9
C18N0.75	Rev	0.25	2	1000	68.6	16.3	7.1	6.7				98.7
C19N0.75	Rev	0.25	2	900	68.8	15.3	6.1	8.8				99.0
C21N0.75	Rev	0.25	2	1050	67.4	15.3	4.1	11.4				98.2
C22N0.75	Rev	0.25	3.5	900	66.9	16.5	10.2		4.0			97.7
C23N0.75	Rev	0.25	3	1000	71.7	10.4	9.6	4.6	2.0	0.6		98.9
C29N0.75	Rev	0.25	3	1100	67.3	16.0	8.2	6.1	0.5			98.0

## 6.2. Supplement II: Mantle metasomatism by sediment fluids

### Mineral compositions

**Table 3.3.2:** Clinopyroxene major element compositions, as measured by EPMA. ‘\*\*\*’ phosphorous test run with 1.1 wt.% of P<sub>2</sub>O<sub>5</sub> (per weight of solids) introduced via the fluid as diluted H<sub>3</sub>PO<sub>4</sub>.

P (GPa) / T (°C)	2.5 / 600				3.5 / 600						
Salinity (wt.% NaCl)	10	15	0	0	0	5	5	10	10	15	15
Sample	DT16	DT6	DT1	DT7	***DT17	DT2	DT9	DT3	DT10	DT4	DT8
SiO <sub>2</sub>	54.9 (0.5)	55.1 (0.2)	54.8 (1.4)	53.8 (0.3)	55.0 (0.4)	55.0 (0.8)	54.8 (0.5)	55.1 (0.9)	55.0 (0.6)	56.5 (0.2)	55.3 (0.5)
Na <sub>2</sub> O	7.1 (1.1)	7.8 (0.6)	5.9 (0.6)	6.1 (0.6)	6.9 (0.5)	7.1 (0.3)	7.4 (0.6)	7.3 (0.5)	7.5 (0.2)	8.3 (0.2)	8.0 (0.7)
K <sub>2</sub> O	0 (0)	0 (0)	0.1 (0.1)	0 (0)	0 (0)	0.2 (0.1)	0 (0)	0.1 (0.1)	0.1 (0.1)	0.1 (0.1)	0 (0)
CaO	11.3 (2.0)	10.3 (1.1)	11.7 (1.2)	12.2 (0.9)	10.4 (1.3)	10.6 (0.6)	10.9 (1.0)	10.5 (1.0)	10.2 (0.4)	9.2 (0.5)	9.6 (1.1)
FeO	9.1 (1.2)	8.6 (0.5)	9.2 (0.6)	11.1 (0.6)	9.8 (0.8)	8.9 (0.5)	10.4 (0.8)	8.8 (0.8)	8.8 (0.6)	8.0 (0.5)	9.1 (0.9)
MgO	5.2 (1.2)	4.7 (0.8)	5.0 (0.5)	5.4 (0.5)	5.4 (0.9)	4.5 (0.3)	4.7 (0.5)	4.7 (0.6)	4.5 (0.4)	4.2 (0.3)	4.9 (0.6)
Al <sub>2</sub> O <sub>3</sub>	10.8 (2.4)	11.9 (1.3)	10.9 (0.6)	9.3 (1.2)	10.8 (1.8)	11.9 (0.9)	10.6 (1.3)	11.6 (1.3)	12.4 (0.8)	13.0 (0.7)	11.7 (1.4)
TiO <sub>2</sub>	0.7 (0.3)	1.0 (0.3)	0.7 (0.1)	0.5 (0.1)	0.5 (0.2)	0.7 (0.1)	0.6 (0.1)	0.8 (0.2)	0.7 (0.1)	0.5 (0.1)	0.5 (0.1)
<b>Total</b>	99.2 (0.7)	99.4 (0.4)	98.3 (1.1)	98.6 (0.3)	98.9 (0.3)	98.8 (0.6)	99.4 (0.4)	98.8 (0.5)	99.2 (0.7)	99.7 (0.5)	99.1 (0.4)

**Table 3.3.2:** Continued.

P (GPa) / T (°C)	3.5 / 700				4.5 / 700			
Salinity (wt.% NaCl)	0	5	15	15	0	5	10	15
Sample	DT21	DT24	DT20	DT23	DT11	DT12	DT13	DT14
SiO <sub>2</sub>	54.5 (0.4)	55.4 (0.2)	54.8 (0.3)	56.1 (0.6)	55.4 (0.1)	55.7 (0.4)	55.9 (0.8)	56.2 (0.4)
Na <sub>2</sub> O	5.7 (0.4)	6.3 (0.5)	7.1 (0.4)	7.2 (0.6)	6.2 (0.5)	7.3 (0.5)	7.6 (0.6)	8.2 (0.6)
K <sub>2</sub> O	0 (0)	0 (0)	0 (0)	0 (0)	0 (0)	0 (0)	0 (0)	0 (0)
CaO	13.0 (0.7)	12.4 (1.7)	10.6 (0.9)	11.0 (1.2)	13.1 (1.0)	11.0 (1.5)	10.0 (1.5)	9.2 (0.9)
FeO	7.6 (0.9)	6.9 (0.7)	8.0 (0.8)	6.3 (1.0)	8.0 (0.8)	6.2 (1.7)	7.2 (0.9)	7.2 (0.8)
MgO	5.8 (0.5)	5.5 (1.1)	4.9 (0.6)	5.1 (0.6)	6.8 (0.8)	5.6 (1.5)	5.1 (0.8)	4.9 (0.5)
Al <sub>2</sub> O <sub>3</sub>	11.8 (1.0)	12.0 (1.5)	12.8 (1.3)	13.1 (1.3)	9.8 (0.7)	13.2 (2.1)	12.9 (1.7)	13.5 (1.3)
TiO <sub>2</sub>	0.5 (0.1)	0.6 (0.2)	0.6 (0.2)	0.5 (0.1)	0.4 (0.1)	0.5 (0.2)	0.4 (0.1)	0.3 (0.0)
<b>Total</b>	99.0 (0.5)	99.1 (0.5)	98.8 (0.7)	99.4 (0.6)	99.6 (0.4)	99.5 (0.7)	99.1 (0.5)	99.6 (0.2)

6. Supplement – Supplement II: Mantle metasomatism by sediment fluids

**Table 3.3.3:** Lawsonite and zoisite major element compositions, as measured by EPMA. ‘\*\*\*’ phosphorous test run with 1.1 wt.% of P<sub>2</sub>O<sub>5</sub> (per weight of solids) introduced via the fluid as diluted H<sub>3</sub>PO<sub>4</sub>. ‘-’ not observed, but inferred from mass balance calculations.

P (GPa) / T (°C)	2.5 / 600		3.5 / 600								
Salinity (wt.% NaCl)	10	15	0	0	0	5	5	10	10	15	15
Sample	DT16	DT6	DT1	DT7	***DT17	DT2	DT9	DT3	DT10	DT4	DT8
SiO <sub>2</sub>	39.9 (0.6)	38.7 (0.4)	38.7 (1.0)	38.4 (0.7)	38.4 (0.1)	39.4 (1.0)	39.0 (1.5)	38.7 (0.7)	39.1 (1.1)	38.3 (0.4)	38.2 (0.2)
Na <sub>2</sub> O	0.2 (0)	0.1 (0.1)	0.2 (0.3)	0.3 (0.2)	0 (0)	0.4 (0.4)	0.5 (0.5)	0.1 (0.2)	0.4 (0.4)	0 (0.1)	0.1 (0.1)
K <sub>2</sub> O	0.1 (0)	0 (0)	0 (0)	0 (0)	0 (0)	0 (0)	0 (0)	0.1 (0.2)	0 (0)	0 (0)	0 (0)
CaO	20.8 (0.4)	20.3 (0.4)	16.1 (0.4)	16.0 (0.2)	15.7 (0.2)	15.8 (0.4)	16.1 (0.5)	16.4 (0.4)	16.2 (0.4)	16.6 (0.4)	16.5 (0.2)
FeO	8.5 (0.2)	8.2 (0.6)	1.8 (0.4)	2.3 (0.3)	1.4 (0.1)	1.8 (0.5)	2.1 (0.6)	1.5 (0.1)	1.8 (0.7)	1.4 (0.3)	1.5 (0.2)
MgO	0.4 (0.1)	0.4 (0.1)	0.2 (0.3)	0.3 (0.2)	0.2 (0)	0.4 (0.3)	0.4 (0.4)	0.1 (0.1)	0.3 (0.3)	0.1 (0)	0.1 (0.1)
Al <sub>2</sub> O <sub>3</sub>	26.3 (0.4)	26.8 (0.4)	29.6 (1.1)	29.2 (0.7)	30.5 (0.2)	29.2 (1.4)	29.1 (1.3)	30.0 (0.6)	29.7 (1.5)	29.5 (1.0)	30.0 (0.7)
TiO <sub>2</sub>	0.6 (0.1)	0.5 (0.1)	0.7 (0.6)	0.4 (0.2)	0.3 (0.1)	0.5 (0.1)	0.5 (0.2)	0.7 (0.6)	0.4 (0.4)	1.1 (0.7)	0.5 (0.4)
<b>Total</b>	96.6 (0.9)	95.1 (1.1)	87.3 (0.8)	87.0 (0.8)	86.5 (0.1)	87.5 (0.8)	87.7 (1.5)	87.6 (0.9)	88.0 (1.0)	87.1 (0.7)	86.9 (0.3)

**Table 3.3.3:** Continued.

P (GPa) / T (°C)	3.5 / 700				4.5. / 700			
Salinity (wt.% NaCl)	0	5	15	15	0	5	10	15
Sample	DT21	DT24	DT20	DT23	DT11	DT12	DT13	DT14
SiO <sub>2</sub>	38.5 (0.1)	-	-	-	39.0 (0.2)	38.5 (0.3)	38.5 (0.5)	38.5 (0.3)
Na <sub>2</sub> O	0 (0)	-	-	-	0.1 (0)	0.1 (0)	0.3 (0.3)	0 (0)
K <sub>2</sub> O	0 (0)	-	-	-	0.1 (0.1)	0.1 (0.1)	0 (0)	0 (0)
CaO	16.0 (0.1)	-	-	-	16.1 (0.2)	15.8 (0.2)	15.9 (0.4)	16.4 (0.1)
FeO	0.3 (0)	-	-	-	0.9 (0.1)	0.8 (0.1)	1.0 (0.2)	0.9 (0.4)
MgO	0 (0)	-	-	-	0.2 (0)	0.2 (0.1)	0.3 (0.1)	0.1 (0)
Al <sub>2</sub> O <sub>3</sub>	31.6 (0.5)	-	-	-	30.1 (0.5)	30.6 (0.3)	29.6 (0.5)	30.8 (0.5)
TiO <sub>2</sub>	0.6 (0.3)	-	-	-	0.4 (0.1)	0.3 (0)	0.4 (0.1)	0.4 (0.2)
<b>Total</b>	87.0 (0.1)	-	-	-	86.8 (0.6)	86.3 (0.2)	86.0 (0.2)	87.1 (0.3)

6. Supplement – Supplement II: Mantle metasomatism by sediment fluids

**Table 3.3.4:** Phengite major element compositions, as measured by EPMA. ‘\*\*\*’ phosphorous test run with 1.1 wt.% of P<sub>2</sub>O<sub>5</sub> (per weight of solids) introduced via the fluid as diluted H<sub>3</sub>PO<sub>4</sub>.

P (GPa) / T (°C)	2.5 / 600		3.5 / 600								
Salinity (wt.% NaCl)	10	15	0	0	0	5	5	10	10	15	15
Sample	DT16	DT6	DT1	DT7	***DT17	DT2	DT9	DT3	DT10	DT4	DT8
SiO <sub>2</sub>	52.9 (0.6)	51.7 (0.4)	54.0 (0.7)	53.4 (0.6)	54.1 (0.4)	54.1 (0.9)	53.7 (0.3)	52.7 (0.2)	53.4 (0.7)	53.5 (0.4)	52.8 (0.4)
Na <sub>2</sub> O	0.2 (0)	0.3 (0)	0.4 (0.1)	0.2 (0.1)	0.1 (0.1)	0.2 (0.1)	0.1 (0)	0.2 (0)	0.2 (0.1)	0.1 (0)	0.1 (0)
K <sub>2</sub> O	8.9 (0.5)	9.0 (0.3)	9.8 (0.2)	9.9 (0.2)	8.8 (0.2)	9.7 (0.4)	10.2 (0.2)	9.4 (0.4)	9.6 (0.7)	9.5 (0.4)	10.0 (0.1)
CaO	0.3 (0.1)	0.6 (0.2)	0.3 (0.3)	0.1 (0.1)	0.1 (0.1)	0.2 (0.3)	0 (0)	0.4 (0.2)	0.1 (0.1)	0.8 (0.2)	0.3 (0)
FeO	3.6 (0.1)	3.5 (0.1)	4.2 (0.1)	4.4 (0)	4.1 (0.1)	4.2 (0.1)	4.2 (0.1)	3.5 (0)	4.1 (0.1)	3.7 (0.1)	3.9 (0)
MgO	3.3 (0.1)	3.4 (0.1)	4.1 (0.1)	4.2 (0.1)	4.7 (0.2)	3.8 (0.1)	4.3 (0.1)	3.8 (0.1)	4.1 (0.1)	4.0 (0.1)	4.0 (0)
Al <sub>2</sub> O <sub>3</sub>	24.3 (0.7)	25.5 (0.6)	20.9 (1.2)	21.7 (0.4)	21.6 (0.7)	21.0 (0.6)	20.7 (0.3)	23.8 (0.9)	22.0 (0.4)	21.9 (0.3)	21.9 (0.1)
TiO <sub>2</sub>	0.4 (0)	0.4 (0)	0.3 (0)	0.3 (0)	0.5 (0.4)	0.3 (0)	0.3 (0)	0.3 (0)	0.3 (0)	0.2 (0)	0.2 (0)
<b>Total</b>	94.1 (1.5)	94.3 (0.9)	94.0 (1.0)	94.1 (0.5)	93.9 (0.2)	93.5 (1.8)	93.5 (0.5)	94.0 (0.5)	93.8 (0.7)	93.7 (1.0)	93.2 (0.6)

**Table 3.3.4:** Continued.

P (GPa) / T (°C)	3.5 / 700				4.5 / 700			
Salinity (wt.% NaCl)	0	5	15	15	0	5	10	15
Sample	DT21	DT24	DT20	DT23	DT11	DT12	DT13	DT14
SiO <sub>2</sub>	52.6 (0.4)	52.9 (0.8)	51.4 (0.4)	53.4 (0.4)	55.6 (0.3)	55.4 (0.3)	54.2 (0.6)	54.3 (0.5)
Na <sub>2</sub> O	0.1 (0)	0.1 (0)	0.1 (0)	0.1 (0)	0 (0)	0 (0)	0 (0)	0 (0)
K <sub>2</sub> O	9.2 (0.2)	8.9 (0.2)	9.1 (0.1)	8.9 (0.2)	9.1 (0.3)	9.3 (0.1)	9.2 (0.1)	9.3 (0.3)
CaO	0.1 (0)	0.1 (0.2)	0.1 (0)	0.1 (0)	0 (0)	0 (0)	0.1 (0)	0 (0)
FeO	3.0 (0.3)	3.0 (0.2)	2.7 (0.2)	2.6 (0.2)	3.4 (0.1)	3.4 (0.2)	3.2 (0.4)	2.9 (0.2)
MgO	3.9 (0.3)	3.7 (0.2)	3.6 (0.1)	3.6 (0.1)	5.3 (0.3)	5.1 (0.2)	4.9 (0.2)	4.6 (0.1)
Al <sub>2</sub> O <sub>3</sub>	24.9 (0.3)	24.9 (0.3)	26.5 (0.2)	25.5 (0.7)	20.1 (0.4)	20.3 (0.5)	21.3 (0.8)	22.5 (0.6)
TiO <sub>2</sub>	0.5 (0.1)	0.5 (0)	0.4 (0)	0.5 (0)	0.5 (0)	0.5 (0.1)	0.4 (0)	0.3 (0)
<b>Total</b>	94.3 (0.2)	94.0 (0.8)	93.8 (0.5)	94.6 (0.5)	94.1 (0.4)	93.9 (0.3)	93.3 (0.3)	94.0 (0.7)

6. Supplement – Supplement II: Mantle metasomatism by sediment fluids

**Table 3.3.5:** Garnet major element compositions, as measured by EPMA. ‘\*\*\*’ phosphorous test run with 1.1 wt.% of P<sub>2</sub>O<sub>5</sub> (per weight of solids) introduced via the fluid as diluted H<sub>3</sub>PO<sub>4</sub>.

P (GPa) / T (°C)	3.5 / 600		3.5 / 700			4.5 / 700			
Salinity (wt.% NaCl)	0	0	5	15	15	0	5	10	15
Sample	***DT17	DT21	DT24	DT20	DT23	DT11	DT12	DT13	DT14
SiO <sub>2</sub>	37.2 (0.2)	37.5 (0.7)	37.9 (0.3)	37.8 (0.5)	38.2 (0.3)	37.8 (0.4)	37.9 (0.2)	37.4 (0.4)	38.1 (0.3)
Na <sub>2</sub> O	0.1 (0)	0.1 (0.1)	0.1 (0)	0.2 (0)	0.2 (0.1)	0.1 (0)	0.1 (0)	0.2 (0.1)	0.2 (0)
K <sub>2</sub> O	0 (0)	0 (0)	0 (0)	0 (0)	0 (0)	0 (0)	0 (0)	0 (0)	0 (0)
CaO	8.5 (0.4)	13.9 (1.3)	13.1 (0.7)	12.4 (0.4)	12.4 (0.7)	9.8 (0.7)	9.1 (0.7)	8.8 (1.3)	10.2 (0.6)
FeO	28.8 (0.3)	23.9 (1.3)	24.2 (0.5)	24.0 (0.4)	24.5 (1.0)	27.1 (1.0)	27.7 (0.7)	27.4 (1.0)	25.8 (0.7)
MgO	2.2 (0.1)	1.6 (0.3)	1.7 (0.3)	2.4 (0.2)	1.8 (0.2)	2.8 (0.4)	2.8 (0.3)	2.8 (0.2)	3.2 (0.2)
Al <sub>2</sub> O <sub>3</sub>	20.3 (0.3)	20.8 (0.2)	20.5 (0.3)	20.9 (0.2)	20.5 (0.3)	20.2 (0.4)	20.4 (0.3)	20.4 (0.2)	20.7 (0.3)
TiO <sub>2</sub>	0.7 (0)	1.0 (0.1)	0.9 (0.1)	0.5 (0.1)	0.8 (0.1)	0.9 (0.1)	1.0 (0.1)	0.8 (0.2)	0.7 (0.3)
<b>Total</b>	97.8 (0.3)	98.9 (0.5)	98.4 (0.3)	98.2 (0.6)	98.3 (0.4)	98.9 (0.6)	99.0 (0.3)	97.8 (0.6)	98.9 (0.2)

6. Supplement – Supplement II: Mantle metasomatism by sediment fluids

**Table 3.3.6:** Allanite major element compositions, as measured by EPMA. ‘\*\*\*’ phosphorous test run with 1.1 wt.% of P<sub>2</sub>O<sub>5</sub> (per weight of solids) introduced via the fluid as diluted H<sub>3</sub>PO<sub>4</sub>. ‘-’ not analyzed by EPMA, but observed by FE-SEM and analyzed by LA-ICP-MS.

P (GPa) / T (°C)	2.5 / 600		3.5 / 600								
Salinity (wt.% NaCl)	10	15	0	0	0	5	5	10	10	15	15
Sample	DT16	DT6	DT1	DT7	***DT17	DT2	DT9	DT3	DT10	DT4	DT8
SiO <sub>2</sub>	31.8 (0.6)	30.8 (0.3)	-	-	-	-	30.8 (0.1)	-	31.7 (0.1)	33.1 (2.6)	30.4 (0.4)
Na <sub>2</sub> O	0.3 (0.1)	0.3 (0.1)	-	-	-	-	0.2 (0)	-	0.3 (0.1)	0.2 (0.1)	0.2 (0.0)
K <sub>2</sub> O	0 (0)	0 (0)	-	-	-	-	0 (0)	-	0 (0)	0 (0)	0 (0)
CaO	12.1 (0.8)	11.1 (0.9)	-	-	-	-	10.1 (0.6)	-	11.4 (0.5)	12.8 (4.5)	10.0 (0.3)
FeO	7.9 (0.5)	7.9 (0.4)	-	-	-	-	8.6 (0.5)	-	10.4 (0.2)	9.0 (0.7)	10.9 (0.1)
MgO	1.1 (0.2)	0.9 (0.2)	-	-	-	-	1.8 (0.3)	-	0.9 (0.1)	1.0 (0.7)	1.1 (0.1)
Al <sub>2</sub> O <sub>3</sub>	18.3 (1.2)	17.2 (1.3)	-	-	-	-	16.5 (0.5)	-	17.6 (0.2)	18.7 (3.9)	16.1 (0.7)
TiO <sub>2</sub>	0.4 (0.1)	0.4 (0.1)	-	-	-	-	0.4 (0)	-	0.4 (0)	0.4 (0.1)	0.3 (0.1)
<b>Total</b>	<b>72.0 (2.6)</b>	<b>68.6 (2.6)</b>	-	-	-	-	<b>68.5 (1.1)</b>	-	<b>72.6 (0.7)</b>	<b>75.2 (9.5)</b>	<b>69.0 (1.3)</b>

**Table 3.3.6:** Continued.

P (GPa) / T (°C)	3.5 / 700				4.5 / 700			
Salinity (wt.% NaCl)	0	5	15	15	0	5	10	15
Sample	DT21	DT24	DT20	DT23	DT11	DT12	DT13	DT14
SiO <sub>2</sub>	31.3 (1.3)	31.4 (0.3)	30.8 (0.5)	31.8 (0.8)	32.3 (0.3)	31.6 (0.3)	31.8 (0.2)	32.3 (0.9)
Na <sub>2</sub> O	0.1 (0)	0.2 (0)	0.2 (0)	0.2 (0)	0.1 (0)	0.1 (0)	0.1 (0)	0.2 (0.1)
K <sub>2</sub> O	0 (0)	0 (0)	0 (0)	0 (0)	0 (0)	0 (0)	0 (0)	0 (0)
CaO	13.7 (1.9)	10.7 (0.6)	10.5 (0.8)	11.4 (1.4)	11.8 (0.9)	10.8 (0.8)	11.6 (1.1)	11.7 (1.1)
FeO	6.3 (0.2)	7.3 (1.0)	9.4 (0.4)	8.4 (0.5)	9.8 (0.8)	9.9 (0.6)	10.3 (0.7)	10.2 (0.3)
MgO	1.1 (0.3)	2.1 (0.2)	1.7 (0.4)	1.5 (0.6)	1.0 (0.4)	1.1 (0.2)	0.9 (0.2)	1.2 (0.4)
Al <sub>2</sub> O <sub>3</sub>	21.6 (1.6)	17.5 (0.7)	17.7 (0.7)	18.2 (1.5)	18.1 (0.9)	17.6 (0.8)	18.2 (0.8)	17.9 (1.5)
TiO <sub>2</sub>	0.3 (0)	0.4 (0)	0.4 (0)	0.3 (0)	0.4 (0)	0.5 (0)	0.4 (0.1)	0.4 (0)
<b>Total</b>	<b>74.5 (4.3)</b>	<b>69.7 (1.1)</b>	<b>70.8 (1.8)</b>	<b>71.9 (3.4)</b>	<b>73.7 (2.1)</b>	<b>71.7 (1.1)</b>	<b>73.4 (1.4)</b>	<b>73.9 (3.1)</b>

6. Supplement – Supplement II: Mantle metasomatism by sediment fluids

**Table 3.3.7:** Rutile major element compositions, as measured by EPMA. ‘\*\*\*’ phosphorous test run with 1.1 wt.% of P<sub>2</sub>O<sub>5</sub> (per weight of solids) introduced via the fluid as diluted H<sub>3</sub>PO<sub>4</sub>. ‘-’ not analyzed by EPMA, but observed by FE-SEM and/or analyzed by LA-ICP-MS. ‘(1)’ one analysis.

P (GPa) / T (°C)	2.5 / 600		3.5 / 600								
Salinity (wt.% NaCl)	10	15	0	0	0	5	5	10	10	15	15
Sample	DT16 (1)	DT6	DT1	DT7	***DT17	DT2	DT9	DT3 (1)	DT10	DT4	DT8
SiO <sub>2</sub>	0.1	-	-	-	0 (0)	-	-	0.8	-	-	0 (0)
Na <sub>2</sub> O	0	-	-	-	0 (0)	-	-	0.1	-	-	0 (0)
K <sub>2</sub> O	0	-	-	-	0 (0)	-	-	0.1	-	-	0 (0)
CaO	0.3	-	-	-	0.2 (0.1)	-	-	0.5	-	-	0.3 (0.1)
FeO	2.7	-	-	-	0.6 (0.1)	-	-	0.9	-	-	0.3 (0)
MgO	0	-	-	-	0 (0)	-	-	0	-	-	0 (0)
Al <sub>2</sub> O <sub>3</sub>	0	-	-	-	0 (0)	-	-	0.3	-	-	0 (0)
TiO <sub>2</sub>	97.3	-	-	-	99.6 (0.2)	-	-	97.9	-	-	101.3 (0.2)
<b>Total</b>	100.5	-	-	-	100.5 (0.1)	-	-	100.6	-	-	102.0 (0.1)

**Table 3.3.7:** Continued.

P (GPa) / T (°C)	3.5 / 700				4.5 / 700			
Salinity (wt.% NaCl)	0	5	15	15	0	5	10	15
Sample	DT21 (1)	DT24	DT20	DT23	DT11	DT12 (1)	DT13	DT14
SiO <sub>2</sub>	0.1	0.1 (0)	0.1 (0)	0.1 (0)	0.1 (0)	0	0.1 (0)	0.1 (0)
Na <sub>2</sub> O	0	0 (0)	0 (0)	0 (0)	0 (0)	0	0 (0)	0 (0)
K <sub>2</sub> O	0	0 (0)	0.1 (0.1)	0 (0)	0.1 (0)	0	0 (0)	0 (0)
CaO	0.4	0.3 (0.1)	0.1 (0)	0.3 (0.1)	0.2 (0)	0.2	0.3 (0.1)	0.3 (0)
FeO	1.9	1.7 (0)	2.2 (0.1)	1.8 (0)	2.6 (0.6)	0.3	2.4 (0.2)	2.1 (0.1)
MgO	0	0 (0)	0 (0)	0 (0)	0 (0)	0	0 (0)	0 (0)
Al <sub>2</sub> O <sub>3</sub>	0.5	0.6 (0)	0.7 (0)	0.6 (0)	0.5 (0)	0	0.6 (0)	0.6 (0.1)
TiO <sub>2</sub>	92.8	93.8 (0.6)	93.0 (0.4)	93.1 (1.3)	90.7 (2.0)	100.5	92.9 (0.5)	93.4 (0.8)
<b>Total</b>	95.8	96.5 (0.8)	96.1 (0.3)	95.8 (1.5)	94.3 (1.1)	100.9	96.3 (0.5)	96.4 (0.8)

6. Supplement – Supplement II: Mantle metasomatism by sediment fluids

**Table 3.3.8:** Major element compositions of other accessory phases, as measured by EPMA. ‘\*\*\*’ phosphorous test run with 1.1 wt.% of P<sub>2</sub>O<sub>5</sub> (per weight of solids) introduced via the fluid as diluted H<sub>3</sub>PO<sub>4</sub>. ‘(1)’ one analysis.

P (GPa) / T (°C)	3.5 / 600	3.5 / 700	
Salinity (wt.% NaCl)	0	0	15
Sample	***DT17	DT21	DT23 (1)
Mineral	Ap	Ttn	Zrc
SiO <sub>2</sub>	0.1 (0.1)	30.2 (0.7)	36.9
Na <sub>2</sub> O	0.1 (0)	0.1 (0.1)	0
K <sub>2</sub> O	0.1 (0.1)	0 (0)	0
CaO	53.1 (0.5)	27.0 (0.1)	0.1
FeO	0.5 (0.2)	0.4 (0.1)	0.1
MgO	0.1 (0)	0 (0)	0
Al <sub>2</sub> O <sub>3</sub>	0 (0)	3.1 (0.4)	0
TiO <sub>2</sub>	0 (0)	34.1 (0.4)	0
Total	54.0 (0.4)	95.0 (1.1)	37.1

6. Supplement – Supplement II: Mantle metasomatism by sediment fluids

**Table 3.3.9:** Clinopyroxene major and trace element compositions, as measured by LA-ICP-MS. ‘\*\*\*’ phosphorous test run with 1.1 wt.% of P<sub>2</sub>O<sub>5</sub> (per weight of solids) introduced via the fluid as diluted H<sub>3</sub>PO<sub>4</sub>. When no standard deviation is specified, then the measurement value was above detection limit in only one analysis. ‘b.d.l.’ below detection limit. ‘n.a.’ not analyzed.

P (GPa) / T (°C)	2.5 / 600				3.5 / 600						
Salinity (wt.% NaCl)	10	15	0	0	0	5	5	10	10	15	15
Sample	DT16	DT6	DT1	DT7	***DT17	DT2	DT9	DT3	DT10	DT4	DT8
Na <sub>2</sub> O	6.6 (0.5)	6.9 (0.5)	5.9 (0.5)	6.2 (0.3)	6.5 (0.6)	5.6 (0.5)	6.1 (0.3)	5.5 (0.5)	6.2 (0.1)	7.7 (0.4)	8.1 (0)
MgO	4.7 (0.5)	5.3 (0.7)	4.4 (0.3)	4.6 (0.5)	4.8 (0.9)	4.0 (0.3)	4.1 (0.1)	4.0 (0.3)	4.2 (0.2)	3.7 (0.2)	4.0 (0.1)
Al <sub>2</sub> O <sub>3</sub>	10.0 (1.4)	9.0 (1.1)	11.7 (0.8)	7.9 (1.9)	10.4 (1.6)	12.7 (1.1)	12.0 (0.6)	12.5 (1.2)	12.7 (0.5)	12.2 (0.5)	10.5 (0.7)
SiO <sub>2</sub> (int. standard)	55	55	55	55	55	55	55	55	55	55	55
K <sub>2</sub> O	0.4	b.d.l.	0.8 (0.5)	0.5 (0.4)	0.1 (0.1)	0.8 (0.3)	n.a.	1.4 (0.5)	n.a.	0.3 (0.1)	0.1 (0)
CaO	11.4 (1.3)	11.7 (0.7)	9.7 (0.9)	12.1 (4.3)	10.2 (1.7)	9.3 (1.4)	8.8 (0.9)	9.3 (0.8)	9.3 (0.7)	8.0 (0.3)	8.7 (0.3)
TiO <sub>2</sub>	0.6 (0.1)	0.4 (0.1)	0.6 (0.2)	0.4 (0.1)	0.4 (0.1)	0.7 (0.1)	0.7 (0.3)	0.8 (0.3)	0.8 (0.3)	0.4 (0)	0.4 (0)
FeO	9.1 (0.9)	8.9 (0.7)	8.5 (1.1)	10.8 (1.7)	9.2 (0.8)	8.5 (0.8)	9.5 (0.5)	8.2 (0.7)	8.1 (0.3)	7.3 (0.4)	7.3 (0)

Li	1199 (272)	932 (228)	1897 (262)	1542 (239)	1733 (219)	1409 (270)	1379 (177)	1350 (129)	1141 (57)	992 (97)	1061 (5)
Be	777 (146)	658 (179)	1262 (110)	718 (235)	653 (246)	2602 (2865)	775 (85)	2237 (2908)	725 (63)	604 (81)	577 (17)
B	569 (181)	173 (61)	778 (200)	146 (137)	293 (226)	511 (109)	344 (206)	621 (242)	331 (67)	383 (20)	275 (116)
Rb	60 (89)	28 (24)	360 (248)	151 (209)	63 (53)	369 (152)	527 (205)	614 (221)	586 (151)	221 (61)	75 (9)
Sr	135 (136)	128 (130)	354 (137)	223 (66)	137 (72)	276 (62)	330 (92)	365 (143)	323 (113)	471 (128)	219 (59)
Y	8 (9)	10 (4)	18 (9)	39 (13)	15 (4)	18 (10)	35 (17)	21 (8)	52 (13)	34 (15)	23 (1)
Zr	59 (39)	55 (14)	23 (12)	13 (10)	9 (3)	17 (3)	12 (5)	15 (4)	14 (9)	16 (3)	7 (3)
Nb	10 (5)	4 (2)	18 (7)	2 (4)	15 (18)	56 (60)	54 (68)	106 (103)	94 (36)	15 (8)	13 (14)
Cs	207 (238)	113 (93)	314 (86)	110 (137)	66 (52)	306 (84)	263 (93)	431 (175)	295 (84)	260 (102)	115 (31)
Ba	85 (133)	44 (57)	294 (202)	128 (126)	71 (60)	331 (140)	400 (202)	572 (253)	389 (133)	273 (243)	17 (11)
La	5 (8)	39	55 (41)	22 (23)	10 (10)	49 (33)	63 (36)	49 (28)	78 (59)	62 (80)	4 (3)
Ce	13 (24)	63	440 (206)	117 (149)	65 (65)	166 (122)	360 (192)	202 (103)	325 (258)	221 (274)	18 (11)
Nd	b.d.l.	37	58 (45)	53 (12)	13 (24)	35 (29)	66 (33)	48 (26)	91 (77)	56 (65)	5 (0)
Sm	10 (13)	27	60 (39)	38	22 (29)	46 (32)	61 (35)	46 (25)	75 (61)	51 (63)	10 (5)
Eu	5 (6)	11 (19)	70 (51)	37 (9)	25 (23)	53 (35)	64 (33)	62 (28)	86 (63)	58 (67)	15 (1)
Gd	3 (1)	23 (26)	70 (51)	38 (21)	26 (22)	52 (31)	82 (38)	63 (34)	82 (71)	59 (61)	25 (12)
Dy	9 (4)	16 (10)	71 (36)	127 (54)	60 (18)	78 (34)	96 (28)	86 (29)	101 (67)	66 (51)	53 (8)
Er	38 (19)	49 (14)	100 (41)	256 (123)	116 (30)	114 (37)	186 (85)	142 (26)	144 (67)	115 (41)	109 (6)
Yb	67 (14)	82 (28)	119 (27)	237 (112)	102 (34)	133 (27)	217 (134)	149 (35)	146 (85)	144 (71)	124 (5)
Lu	62 (9)	77 (12)	91 (18)	182 (71)	75 (34)	91 (21)	183 (137)	101 (16)	100 (42)	122 (72)	87 (10)
Hf	97 (74)	92 (50)	37 (13)	31 (15)	23 (9)	35 (14)	21 (6)	29 (5)	29 (20)	29 (4)	27 (2)
Ta	9 (3)	7 (2)	15 (8)	5 (3)	16 (21)	67 (84)	54 (73)	111 (111)	92 (41)	14 (7)	14 (15)
Pb	75 (64)	31 (29)	172 (92)	121 (40)	87 (51)	79 (24)	182 (53)	131 (40)	205 (94)	105 (69)	67 (22)
Th	4	2	19 (14)	6 (7)	4 (4)	13 (11)	24 (11)	18 (11)	49 (65)	14 (15)	1 (1)
U	3 (6)	11 (5)	56 (32)	47 (42)	16 (22)	29 (23)	46 (23)	37 (19)	60 (54)	34 (43)	8 (0)

6. Supplement – Supplement II: Mantle metasomatism by sediment fluids

Table 3.3.9: Continued.

P (GPa) / T (°C)	3.5 / 700				4.5 / 700			
Salinity (wt.% NaCl)	0	5	15	15	0	5	10	15
Sample	DT21	DT24	DT20	DT23	DT11	DT12	DT13	DT14
Na <sub>2</sub> O	6.3 (0.6)	6.1 (0.7)	7.3 (0.2)	7.3 (0.4)	6.8 (0.3)	6.6 (0.5)	7.9 (0.1)	8.6 (0.2)
MgO	4.7 (0.4)	5.0 (0.7)	4.0 (0.4)	4.0 (0.1)	5.3 (0.7)	4.8 (1.3)	4.6 (0.4)	4.0 (0.2)
Al <sub>2</sub> O <sub>3</sub>	12.0 (0.8)	10.5 (1.8)	12.0 (0.7)	12.2 (0.4)	11.1 (1.0)	12.1 (1.1)	13.0 (0.4)	13.2 (0.5)
SiO <sub>2</sub> (int. standard)	55	55	55	56	56	56	56	56
K <sub>2</sub> O	0.2 (0.2)	0.1 (0.1)	0.2 (0.1)	0.2 (0.1)	0.1 (0.1)	0.1 (0)	0.1 (0)	0.1 (0)
CaO	11.4 (0.6)	10.9 (1.3)	11.3 (1.9)	9.2 (0.5)	11.3 (1.5)	9.5 (1.4)	9.6 (1.2)	7.3 (0.1)
TiO <sub>2</sub>	0.5 (0.1)	0.4 (0.1)	0.4 (0.1)	0.5 (0.2)	0.4 (0.1)	0.4 (0.1)	0.4 (0.1)	0.4 (0)
FeO	7.0 (0.7)	6.1 (0.6)	6.9 (0.3)	5.6 (1.5)	6.7 (0.7)	5.2 (0.7)	5.4 (0.4)	5.7 (0.2)

Li	1693 (257)	1125 (248)	1195 (131)	1334 (162)	1560 (200)	1291 (400)	1294 (77)	1237 (64)
Be	1159 (347)	764 (147)	1000 (80)	890 (649)	813 (157)	543 (148)	667 (220)	478 (47)
B	233 (273)	84 (81)	367 (270)	169 (76)	78 (43)	123 (43)	76 (23)	175 (50)
Rb	33 (39)	28 (47)	45 (19)	113 (90)	14 (17)	28 (16)	21 (16)	66 (28)
Sr	246 (81)	221 (49)	142 (26)	196 (34)	275 (23)	309 (235)	173 (125)	252 (18)
Y	10 (6)	9 (5)	22 (14)	11 (6)	16 (8)	16 (12)	19 (4)	24 (8)
Zr	13 (12)	12 (7)	14 (6)	12 (9)	6 (3)	6 (2)	8 (12)	6 (1)
Nb	20 (12)	15 (27)	15 (16)	14 (15)	13 (15)	11 (7)	2 (1)	28 (17)
Cs	75 (116)	58 (71)	60 (29)	175 (78)	33 (33)	35 (23)	37 (29)	126 (93)
Ba	27 (29)	22 (23)	30 (25)	44 (13)	18 (8)	19 (15)	35 (37)	101 (84)
La	13 (11)	10 (8)	10 (1)	5 (5)	8 (3)	13 (11)	9 (11)	3 (3)
Ce	99 (86)	59 (35)	31 (33)	51 (51)	37 (15)	56 (42)	34 (38)	16 (16)
Nd	30 (30)	17 (9)	11 (1)	6 (4)	11 (7)	15 (14)	14 (14)	4 (3)
Sm	18 (11)	10 (9)	17 (4)	10 (5)	28 (8)	31 (16)	22 (5)	11 (7)
Eu	11 (11)	13 (10)	16 (9)	17 (17)	47 (10)	40 (21)	35 (4)	17 (6)
Gd	6 (5)	13 (7)	21 (16)	19 (11)	66 (10)	53 (28)	50 (19)	27 (8)
Dy	37 (28)	26 (9)	35 (18)	44 (28)	84 (41)	53 (24)	66 (12)	52 (13)
Er	57 (28)	39 (10)	45 (16)	58 (35)	94 (47)	55 (12)	45 (11)	67 (17)
Yb	53 (31)	35 (16)	35 (16)	66 (78)	54 (41)	39 (6)	28 (15)	56 (24)
Lu	54 (34)	24 (15)	35 (23)	52 (46)	41 (30)	27 (3)	18 (9)	49 (13)
Hf	39 (30)	19 (11)	20 (5)	17 (14)	14 (9)	18 (12)	3 (1)	8 (4)
Ta	13 (11)	16 (26)	12 (16)	18 (20)	13 (15)	8 (7)	2 (1)	24 (12)
Pb	28 (18)	27 (16)	65 (85)	62 (32)	37 (11)	30 (17)	32 (23)	33 (13)
Th	4 (5)	4 (3)	2	5	2 (1)	2 (1)	3 (4)	2 (1)
U	7 (7)	7 (6)	6 (4)	9 (9)	11 (2)	11 (3)	8 (4)	8 (4)

6. Supplement – Supplement II: Mantle metasomatism by sediment fluids

**Table 3.3.10:** Lawsonite and zoisite major and trace element compositions, as measured by LA-ICP-MS. ‘\*\*\*’ phosphorous test run with 1.1 wt.% of P<sub>2</sub>O<sub>5</sub> (per weight of solids) introduced via the fluid as diluted H<sub>3</sub>PO<sub>4</sub>. When no standard deviation is specified, then the measurement value was above detection limit in only one analysis. ‘b.d.l.’ below detection limit. ‘n.a.’ not analyzed. ‘-’ phase not observed, but inferred from mass balance calculations.

P (GPa) / T (°C)	2.5 / 600		3.5 / 600								
Salinity (wt.% NaCl)	10	15	0	0	0	5	5	10	10	15	15
Sample	DT16	DT6	DT1	DT7	***DT17	DT2	DT9	DT3	DT10	DT4	DT8
Na <sub>2</sub> O	0.9 (0.8)	0.4 (0.4)	0.3 (0.2)	0.5 (0.2)	0.1 (0.1)	0.5 (0.1)	0.6 (0.3)	0.4 (0.7)	0.1 (0.1)	0 (0)	0.5 (0.7)
MgO	0.7 (0.5)	0.5 (0.4)	0.3 (0.2)	0.4 (0)	0.2 (0)	0.4 (0.1)	0.4 (0.2)	0.3 (0.4)	0.1 (0.1)	0 (0)	0.3 (0.4)
Al <sub>2</sub> O <sub>3</sub>	19.6 (3.3)	18.5 (3.3)	25.7 (0.4)	25.8 (0.7)	29.6 (0.5)	25.6 (0.4)	26.3 (1.6)	25.1 (1.5)	28.5 (1.4)	28.2 (1.2)	27.2 (0)
SiO <sub>2</sub> (int. standard)	40	40	39	39	39	39	39	39	39	39	39
K <sub>2</sub> O	0.6 (0.5)	1.2	0 (0)	0 (0.2)	0 (0)	0.1 (0)	n.a.	0 (0)	n.a.	0 (0)	0
CaO	18.3 (4.3)	17.5 (4.7)	14.6 (0.9)	16.3 (0.5)	17.3 (0.8)	14.3 (1.4)	15.3 (1.0)	14.3 (1.2)	17.0 (0.5)	15.3 (0.5)	15.0 (3.0)
TiO <sub>2</sub>	0.3 (0)	0.4 (0.1)	0.8 (0.4)	0.5 (0.2)	1.0 (0.3)	0.7 (0.3)	0.7 (0.2)	0.8 (0.5)	0.7 (0.4)	1.1 (0.2)	0.7 (0.1)
FeO	7.8 (1.3)	6.5 (0.5)	2.3 (0.3)	2.4 (0.2)	1.5 (0.2)	1.5 (0.4)	2.2 (0.3)	1.6 (0.7)	1.3 (0.2)	1.1 (0.1)	1.5 (1.0)

Li	1496 (1553)	1282 (505)	112 (53)	144 (28)	31 (23)	155 (71)	149 (71)	112 (156)	105 (80)	27 (34)	147
Be	193 (150)	273	182 (59)	203 (23)	158 (47)	261 (145)	296 (75)	140 (78)	103 (15)	78 (18)	206 (211)
B	1599 (1090)	1281 (463)	351 (103)	160 (112)	237 (94)	409 (141)	105 (33)	203 (47)	27 (16)	48 (6)	58 (48)
Rb	360 (278)	507 (252)	3 (1)	40 (65)	8 (9)	49 (23)	3 (2)	2 (1)	14 (4)	6 (3)	5 (2)
Sr	9029 (2412)	8094 (2389)	7427 (1082)	7068 (962)	8273 (654)	6805 (1788)	5296 (1324)	2951 (470)	4741 (374)	2317 (189)	3070 (471)
Y	374 (71)	195 (70)	466 (405)	148 (69)	108 (21)	294 (80)	262 (218)	85 (12)	71 (18)	123 (29)	85 (33)
Zr	46 (42)	28 (6)	6 (3)	6 (3)	3 (1)	6 (4)	9 (4)	2 (2)	1 (0)	1 (1)	6 (5)
Nb	17 (12)	49 (34)	28 (27)	11 (9)	71 (52)	44 (45)	22 (17)	2 (1)	5 (3)	4 (3)	14 (18)
Cs	1347 (1034)	1491 (274)	11 (10)	72 (70)	25 (14)	215 (203)	17 (23)	4 (5)	20 (13)	11 (7)	5 (1)
Ba	420 (336)	1307 (1844)	22 (9)	47 (35)	26 (5)	76 (54)	28 (9)	7 (6)	62 (49)	5 (4)	17 (18)
La	1070 (695)	900 (203)	147 (144)	91 (30)	196 (59)	140 (31)	86 (44)	48 (21)	124 (26)	184 (50)	130 (21)
Ce	5178 (1299)	5631 (1163)	796 (334)	639 (218)	770 (123)	740 (63)	399 (95)	234 (103)	586 (140)	692 (143)	527 (99)
Nd	1200 (1101)	817 (213)	170 (139)	142 (46)	240 (59)	170 (39)	92 (40)	61 (35)	156 (44)	266 (51)	182 (79)
Sm	1206 (991)	856 (136)	199 (148)	143 (47)	290 (68)	194 (65)	127 (60)	81 (34)	196 (35)	335 (74)	218 (105)
Eu	1201 (411)	1148 (262)	265 (144)	209 (52)	360 (71)	242 (58)	161 (56)	106 (24)	230 (53)	397 (94)	258 (121)
Gd	1561 (1249)	846 (258)	282 (167)	238 (55)	469 (115)	233 (67)	186 (67)	125 (45)	239 (57)	448 (97)	291 (159)
Dy	1363 (1103)	892 (142)	379 (198)	359 (55)	559 (85)	284 (93)	273 (54)	179 (22)	336 (54)	519 (131)	366 (167)
Er	1768 (1349)	1086 (226)	598 (310)	571 (160)	759 (215)	419 (148)	539 (149)	339 (77)	495 (131)	545 (130)	457 (40)
Yb	1636 (1379)	1015 (273)	549 (279)	564 (194)	717 (267)	360 (105)	691 (197)	413 (201)	416 (186)	300 (95)	414 (228)
Lu	1263 (976)	699 (189)	416 (212)	468 (193)	602 (245)	304 (88)	630 (189)	370 (215)	341 (171)	175 (56)	373 (279)
Hf	54 (40)	42	7 (5)	10 (5)	6 (0)	10 (7)	14 (8)	11 (5)	10 (8)	8 (5)	11 (9)
Ta	22 (19)	38 (21)	32 (30)	15 (13)	68 (48)	37 (37)	21 (13)	3 (2)	3 (2)	6 (4)	13 (16)
Pb	2817 (831)	1646 (343)	1145 (165)	1157 (164)	1292 (185)	714 (112)	794 (199)	432 (63)	625 (27)	217 (11)	301 (72)
Th	1251 (1996)	146 (59)	52 (95)	21 (13)	34 (14)	20 (9)	18 (28)	3 (2)	19 (16)	17 (11)	16 (4)
U	1056 (577)	786 (230)	103 (75)	71 (23)	77 (24)	49 (15)	40 (40)	13 (8)	31 (23)	33 (26)	28 (11)

6. Supplement – Supplement II: Mantle metasomatism by sediment fluids

Table 3.3.10: Continued.

P (GPa) / T (°C)	3.5 / 700				4.5 / 700			
	0	5	15	15	0	5	10	15
Salinity (wt.%)	0	5	15	15	0	5	10	15
Sample	DT21	DT24	DT20	DT23	DT11	DT12	DT13	DT14
Na <sub>2</sub> O	0 (0)	-	-	-	-	-	-	0.1 (0)
MgO	0 (0)	-	-	-	-	-	-	0.1 (0)
Al <sub>2</sub> O <sub>3</sub>	28.5 (1.8)	-	-	-	-	-	-	29.9 (1.4)
SiO <sub>2</sub> (int. standard)	<b>39</b>	-	-	-	-	-	-	<b>39</b>
K <sub>2</sub> O	b.d.l.	-	-	-	-	-	-	0.1 (0)
CaO	14.8 (1.3)	-	-	-	-	-	-	16.3 (0.7)
TiO <sub>2</sub>	0.4 (0.2)	-	-	-	-	-	-	0.5 (0.2)
FeO	0.4 (0.1)	-	-	-	-	-	-	0.9 (0.2)
Li	19	-	-	-	-	-	-	19 (12)
Be	228 (65)	-	-	-	-	-	-	311 (82)
B	b.d.l.	-	-	-	-	-	-	85 (55)
Rb	7 (6)	-	-	-	-	-	-	33 (11)
Sr	11024 (1530)	-	-	-	-	-	-	5215 (309)
Y	107 (75)	-	-	-	-	-	-	80 (9)
Zr	b.d.l.	-	-	-	-	-	-	2 (1)
Nb	2	-	-	-	-	-	-	40 (29)
Cs	4 (4)	-	-	-	-	-	-	40 (16)
Ba	18 (12)	-	-	-	-	-	-	28 (10)
La	149 (113)	-	-	-	-	-	-	456 (53)
Ce	726 (552)	-	-	-	-	-	-	1944 (94)
Nd	200 (161)	-	-	-	-	-	-	547 (90)
Sm	246 (200)	-	-	-	-	-	-	618 (114)
Eu	326 (272)	-	-	-	-	-	-	739 (109)
Gd	340 (325)	-	-	-	-	-	-	752 (144)
Dy	401 (266)	-	-	-	-	-	-	501 (57)
Er	352 (203)	-	-	-	-	-	-	357 (41)
Yb	150 (72)	-	-	-	-	-	-	216 (84)
Lu	77 (33)	-	-	-	-	-	-	162 (70)
Hf	3	-	-	-	-	-	-	5 (2)
Ta	3 (0)	-	-	-	-	-	-	31 (22)
Pb	308 (78)	-	-	-	-	-	-	435 (58)
Th	47 (46)	-	-	-	-	-	-	16 (6)
U	198 (230)	-	-	-	-	-	-	52 (21)

6. Supplement – Supplement II: Mantle metasomatism by sediment fluids

**Table 3.3.11:** Phengite major and trace element compositions, as measured by LA-ICP-MS. ‘\*\*\*’ phosphorous test run with 1.1 wt.% of P<sub>2</sub>O<sub>5</sub> (per weight of solids) introduced via the fluid as diluted H<sub>3</sub>PO<sub>4</sub>. When no standard deviation is specified, then the measurement value was above detection limit in only one analysis. ‘b.d.l.’ below detection limit. ‘n.a.’ not analyzed.

P (GPa) / T (°C)	2.5 / 600				3.5 / 600						
Salinity (wt.% NaCl)	10	15	0	0	0	5	5	10	10	15	15
Sample	DT16	DT6	DT1	DT7	***DT17	DT2	DT9	DT3	DT10	DT4	DT8
Na <sub>2</sub> O	0.9 (0.1)	0.5 (0.1)	1.7 (0.7)	0.5 (0.3)	0.4 (0.1)	0.3 (0.1)	0.1 (0)	0.9 (0.2)	0.2 (0.1)	0.3 (0.3)	0.1 (0)
MgO	2.6 (0.2)	2.7 (0.1)	4.0 (0.5)	3.7 (0.3)	3.4 (0.4)	3.7 (0.3)	3.7 (0.1)	3.8 (0.2)	3.7 (0.1)	3.4 (0.1)	3.4 (0.4)
Al <sub>2</sub> O <sub>3</sub>	19.2 (0.1)	21.5 (1.1)	18.9 (2.2)	20.5 (1.9)	19.2 (0.6)	18.9 (2.3)	19.6 (0.7)	22.0 (2.0)	21.4 (0.9)	20.7 (1.1)	19.6 (0.6)
SiO <sub>2</sub> (int. standard)	53	55	55	55	54	55	55	55	55	55	55
K <sub>2</sub> O	10.0 (0.5)	10.6 (0.6)	8.2 (1.4)	11.0 (0.4)	10.0 (0.7)	10.4 (1.1)	n.a.	10.4 (0.5)	n.a.	10.6 (0.3)	11.7 (0.6)
CaO	1.1 (0.3)	b.d.l.	2.6 (1.7)	0.6 (0.8)	0.5 (0.4)	0.4 (0.3)	0.3 (0.1)	1.7 (0.9)	0.4 (0.3)	1.0 (0.3)	0.8 (0.2)
TiO <sub>2</sub>	0.3 (0.1)	0.3 (0)	0.3 (0.1)	0.3 (0)	0.2 (0)	0.3 (0)	0.2 (0)	0.3 (0)	0.2 (0)	0.2 (0)	0.2 (0.1)
FeO	3.7 (0.1)	3.2 (0.2)	5.5 (0.4)	4.2 (0.2)	4.0 (0.3)	4.3 (0.2)	4.0 (0.1)	4.1 (0.1)	3.7 (0.2)	3.6 (0.2)	3.7 (0.4)

Li	848 (348)	708 (165)	708 (158)	554 (290)	483 (147)	552 (245)	233 (43)	862 (588)	176 (48)	661 (265)	145 (26)
Be	447 (0)	516 (62)	1035 (173)	1195 (143)	825 (61)	1050 (239)	991 (59)	651 (201)	822 (107)	626 (187)	653 (212)
B	1105 (81)	2207 (1063)	1284 (121)	1784 (264)	1065 (329)	1574 (426)	1287 (164)	1671 (675)	1743 (297)	2232 (330)	1786 (401)
Rb	5229 (15)	5545 (290)	4066 (718)	5586 (206)	4720 (488)	5535 (395)	5509 (148)	4811 (556)	5602 (311)	6035 (327)	6240 (548)
Sr	448 (33)	1014 (148)	567 (328)	466 (110)	545 (249)	445 (336)	154 (34)	865 (960)	510 (118)	2154 (1094)	776 (400)
Y	46 (0)	b.d.l.	25 (19)	33 (5)	14 (9)	18 (10)	5 (3)	4 (13)	7 (6)	1 (1)	6 (3)
Zr	55 (76)	b.d.l.	3 (2)	1 (1)	2 (2)	1 (1)	1 (0)	2 (2)	1 (0)	2	1
Nb	25 (23)	14 (4)	11 (2)	16 (9)	7 (3)	19 (6)	12 (5)	7 (4)	10 (3)	7 (3)	6 (2)
Cs	2254 (375)	2086 (252)	2111 (468)	2931 (170)	3114 (304)	2280 (683)	2035 (213)	3142 (1183)	1914 (422)	2168 (544)	2619 (832)
Ba	2753 (74)	3065 (232)	3104 (564)	3944 (299)	3417 (197)	3714 (522)	3761 (158)	3481 (605)	3227 (464)	3075 (1142)	1954 (161)
La	36 (6)	4 (2)	90 (62)	148 (29)	192 (142)	124 (78)	31 (24)	10 (29)	89 (40)	2 (2)	53 (36)
Ce	234 (54)	27 (21)	517 (297)	804 (237)	788 (610)	512 (348)	137 (102)	37 (373)	183 (248)	3 (3)	221 (157)
Nd	39 (19)	b.d.l.	89 (61)	165 (47)	196 (147)	112 (65)	27 (23)	17 (17)	53 (54)	8 (3)	38 (24)
Sm	24 (2)	b.d.l.	81 (45)	165 (53)	179 (133)	106 (70)	27 (21)	4 (26)	46 (48)	3 (1)	49 (30)
Eu	48 (7)	8 (6)	112 (69)	161 (46)	218 (175)	121 (81)	28 (20)	9 (40)	57 (59)	2 (1)	47 (37)
Gd	33 (10)	b.d.l.	94 (54)	158 (55)	157 (119)	102 (67)	27 (16)	7 (34)	34 (44)	9 (1)	57 (43)
Dy	34 (9)	b.d.l.	88 (61)	127 (49)	108 (82)	75 (48)	21 (20)	5 (33)	40 (41)	3 (1)	41 (23)
Er	43 (3)	b.d.l.	82 (58)	104 (29)	63 (47)	43 (27)	17 (14)	11 (36)	32 (31)	5 (2)	32 (9)
Yb	37 (0)	b.d.l.	62 (44)	70 (20)	24 (16)	27 (15)	11 (9)	12 (29)	17 (14)	10 (7)	17 (11)
Lu	30 (16)	3 (1)	44 (34)	45 (15)	19 (13)	15 (9)	6 (4)	8 (25)	11 (10)	2 (1)	15 (11)
Hf	2 (1)	b.d.l.	7 (3)	1 (1)	1	1 (1)	1 (1)	3 (3)	2 (0)	2 (1)	2
Ta	19 (22)	4 (0)	4 (3)	7 (11)	2 (2)	7 (10)	3 (3)	3 (1)	3 (2)	2 (1)	1 (1)
Pb	454 (10)	518 (52)	728 (40)	1065 (21)	856 (34)	470 (101)	803 (40)	425 (191)	857 (405)	490 (147)	497 (101)
Th	6 (2)	b.d.l.	36 (23)	59 (19)	75 (57)	41 (25)	9 (7)	3 (4)	21 (16)	1	17 (16)
U	24 (8)	6 (0)	87 (56)	133 (52)	139 (106)	80 (56)	21 (16)	4 (29)	30 (35)	1 (1)	30 (26)

6. Supplement – Supplement II: Mantle metasomatism by sediment fluids

Table 3.3.11: Continued.

P (GPa) / T (°C)	3.5 / 700				4.5 / 700			
	0	5	15	15	0	5	10	15
Salinity (wt.% NaCl)	0	5	15	15	0	5	10	15
Sample	DT21	DT24	DT20	DT23	DT11	DT12	DT13	DT14
Na <sub>2</sub> O	0.1 (0)	0.1 (0.1)	0.2 (0)	0.2 (0.1)	0 (0)	0 (0)	0 (0)	0.1 (0)
MgO	3.3 (0.1)	2.9 (0.1)	2.9 (0.3)	2.8 (0.3)	4.2 (0.3)	4.4 (0.1)	4.0 (0.2)	3.5 (0.3)
Al <sub>2</sub> O <sub>3</sub>	24.4 (0.3)	22.1 (2.1)	23.1 (1.5)	22.2 (1.6)	17.6 (0.6)	19.2 (0.6)	20.2 (0.7)	19.4 (0.5)
SiO <sub>2</sub> (int. standard)	<b>53</b>	<b>53</b>	<b>52</b>	<b>53</b>	<b>54</b>	<b>55</b>	<b>54</b>	<b>54</b>
K <sub>2</sub> O	11.0 (0.5)	9.6 (0.8)	10.6 (0.4)	10.8 (0.6)	11.2 (0.3)	11.1 (0.2)	11.3 (0.1)	11.0 (0.3)
CaO	0.5	b.d.l.	b.d.l.	1.5	0.6	0.2	0.9 (0.1)	0.7
TiO <sub>2</sub>	0.5 (0)	0.3 (0)	0.3 (0)	0.4 (0.1)	0.4 (0)	0.5 (0)	0.3 (0)	0.3 (0.1)
FeO	2.6 (0.1)	2.5 (0.4)	2.2 (0.2)	2.4 (0.2)	3.2 (0.2)	3.3 (0.1)	2.6 (0.2)	2.6 (0.2)

Li	105 (3)	144 (58)	206 (40)	339 (112)	153 (44)	132 (29)	97 (20)	171 (13)
Be	957 (281)	1111 (333)	614 (122)	858 (149)	2070 (194)	2189 (307)	1698 (109)	1241 (189)
B	647 (55)	839 (99)	1417 (42)	2216 (421)	1117 (295)	1222 (118)	1697 (301)	2491 (681)
Rb	5347 (56)	5069 (511)	5428 (156)	5579 (164)	5474 (215)	5792 (86)	6022 (160)	6788 (649)
Sr	296 (43)	348 (119)	472 (263)	398 (91)	125 (10)	150 (26)	168 (57)	370 (95)
Y	2 (1)	2	1 (0)	2	1	0.2 (0.2)	1 (0)	0.9 (0.4)
Zr	2 (2)	1	5	3 (0)	0.4	0.3 (0)	b.d.l.	1.9 (1.3)
Nb	26 (3)	22 (6)	20 (0)	21 (2)	26 (4)	30 (4)	17 (7)	14 (1)
Cs	1368 (36)	1281 (251)	1138 (248)	1251 (183)	1099 (89)	787 (70)	653 (52)	1239 (81)
Ba	4349 (396)	3626 (692)	2994 (507)	3036 (223)	4174 (440)	4572 (366)	3545 (96)	2359 (195)
La	2 (2)	4 (5)	1	1 (0)	0.4 (0.3)	0.3 (0.1)	8 (5)	1.1 (1.0)
Ce	9 (12)	40	2 (1)	1 (0)	0.4 (0.2)	1.1 (1.2)	22 (5)	1.5 (1.4)
Nd	7	4 (3)	b.d.l.	8	b.d.l.	0.8 (0.3)	16 (13)	b.d.l.
Sm	5	13	b.d.l.	3 (1)	5	1.3 (1.3)	10 (7)	b.d.l.
Eu	3 (3)	6	1	1 (1)	0.4 (0)	0.8 (0.4)	7 (2)	1.1
Gd	6	14	b.d.l.	3	2 (1)	1.4	7 (3)	5 (0)
Dy	3	8	b.d.l.	1	0.6	1	4 (2)	0.9 (0.3)
Er	1	3	b.d.l.	2 (1)	1.2 (0.2)	1.3 (1.7)	2.0 (1.4)	b.d.l.
Yb	b.d.l.	3	6	b.d.l.	1.1	0.2	2.1 (0.3)	1.6 (1.0)
Lu	1	1	b.d.l.	b.d.l.	0.4 (0)	0.1 (0.1)	1.1 (0.9)	0.9 (0.8)
Hf	2	b.d.l.	7	b.d.l.	b.d.l.	0.2	1.3 (0.5)	b.d.l.
Ta	3	4 (1)	3 (2)	3 (1)	4 (1)	5 (1)	5 (5)	4 (4)
Pb	279 (18)	361 (237)	280 (17)	404 (57)	534 (82)	130 (27)	441 (52)	334 (25)
Th	1 (1)	1	2	b.d.l.	b.d.l.	0.1	3 (4)	0.5
U	5	4 (5)	1	0.5 (0.2)	4 (2)	2 (0)	3 (2)	3 (1)

6. Supplement – Supplement II: Mantle metasomatism by sediment fluids

**Table 3.3.12:** Garnet major and trace element compositions, as measured by LA-ICP-MS. ‘\*\*\*’ phosphorous test run with 1.1 wt.% of P<sub>2</sub>O<sub>5</sub> (per weight of solids) introduced via the fluid as diluted H<sub>3</sub>PO<sub>4</sub>. When no standard deviation is specified, then the measurement value was above detection limit in only one analysis. ‘b.d.l.’ below detection limit.

P (GPa) / T (°C)	3.5 / 600		3.5 / 700			4.5 / 700			
Salinity (wt.% NaCl)	0	0	5	15	15	0	5	10	15
Sample	***DT17	DT21	DT24	DT20	DT23	DT11	DT12	DT13	DT14
Na <sub>2</sub> O	0.2 (0)	0.1 (0)	0.1 (0)	0.3 (0.2)	0.2 (0)	0.2 (0)	0.1 (0)	0.2 (0.1)	0.5 (0.2)
MgO	2.2 (0.2)	1.5 (0.4)	1.9 (0.5)	2.1 (0.3)	1.9 (0.4)	2.2 (0.3)	2.4 (0.3)	2.0 (0.3)	2.9 (0.3)
Al <sub>2</sub> O <sub>3</sub>	17.2 (0.8)	17.2 (0.7)	18.7 (0.9)	18.0 (1.4)	17.7 (1.1)	15.7 (1.0)	16.5 (1.3)	14.6 (1.2)	18.1 (1.3)
SiO <sub>2</sub> (int. standard)	37	38	38	38	38	38	38	38	38
K <sub>2</sub> O	0.1 (0.1)	0.1 (0)	0 (0)	0.1 (0.1)	0.1 (0.1)	0 (0)	0 (0)	0 (0)	0
CaO	7.5 (1.3)	10.0 (1.7)	10.3 (1.3)	9.5 (1.3)	9.9 (1.3)	7.0 (1.3)	7.4 (1.6)	5.4 (1.3)	9.1 (1.5)
TiO <sub>2</sub>	0.5 (0.1)	0.7 (0.1)	0.7 (0.2)	0.4 (0.1)	0.6 (0.1)	0.6 (0.1)	0.6 (0.2)	0.6 (0.1)	0.6 (0.1)
FeO	23.0 (1.5)	22.4 (1.0)	21.9 (1.4)	21.4 (1.6)	23.6 (1.3)	21.8 (1.3)	22.9 (2.3)	21.0 (1.2)	24.1 (2.5)

Li	214 (34)	180 (77)	139 (40)	179 (25)	166 (41)	205 (39)	131 (31)	172 (60)	179 (82)
Be	18 (4)	54 (21)	37 (19)	50	17	22 (3)	13 (8)	21 (6)	40 (23)
B	277 (52)	152 (186)	41 (33)	107 (63)	175 (122)	41 (63)	38 (24)	24 (8)	82 (11)
Rb	6 (2)	7 (6)	9 (12)	18 (6)	16 (11)	3 (2)	3 (1)	5 (4)	21 (20)
Sr	82 (66)	54 (33)	59 (52)	74 (43)	33 (10)	33 (63)	62 (61)	108 (70)	49 (44)
Y	250 (57)	314 (390)	224 (98)	277 (48)	236 (72)	647 (576)	297 (232)	375 (340)	251 (68)
Zr	22 (6)	47 (19)	39 (13)	29 (12)	37 (17)	33 (12)	48 (13)	33 (20)	54 (12)
Nb	39 (21)	19 (4)	17 (11)	12 (15)	16 (8)	9 (7)	15 (14)	37 (23)	14 (10)
Cs	21 (10)	25 (22)	23 (26)	32 (23)	32 (30)	2 (2)	5 (4)	4 (2)	28 (30)
Ba	3	28	19 (20)	36 (21)	36 (16)	3 (9)	3 (3)	11 (5)	15 (5)
La	26 (31)	4 (2)	11 (14)	15 (10)	4 (3)	10 (15)	9 (6)	13 (12)	6 (6)
Ce	63 (25)	76 (61)	80 (69)	55 (35)	12 (13)	46 (89)	37 (32)	53 (42)	23 (27)
Nd	37 (37)	13 (7)	16 (16)	17 (13)	7 (3)	23 (32)	25 (11)	26 (32)	14 (9)
Sm	36 (38)	23 (6)	32 (20)	25 (14)	37 (16)	101 (29)	133 (52)	144 (33)	67 (8)
Eu	99 (55)	44 (7)	64 (22)	36 (13)	69 (14)	242 (47)	280 (95)	286 (39)	167 (29)
Gd	177 (104)	116 (15)	123 (37)	78 (25)	168 (15)	431 (75)	423 (167)	491 (49)	309 (42)
Dy	741 (179)	456 (45)	548 (182)	536 (64)	767 (54)	1439 (341)	1034 (417)	1183 (207)	1000 (188)
Er	2779 (590)	1250 (242)	1450 (350)	2157 (215)	2041 (436)	2592 (615)	1628 (550)	1947 (470)	2104 (328)
Yb	4374 (855)	1681 (391)	1859 (354)	3282 (292)	2699 (718)	2735 (620)	1697 (534)	2063 (540)	2563 (492)
Lu	4163 (753)	1438 (314)	1590 (370)	2953 (285)	2374 (618)	2197 (512)	1391 (401)	1682 (483)	2129 (339)
Hf	7 (6)	23 (17)	19 (9)	12 (2)	18 (9)	17 (9)	24 (18)	23 (14)	33 (12)
Ta	44 (4)	15 (5)	19 (19)	20 (20)	11 (6)	9 (10)	16 (14)	33 (22)	12 (12)
Pb	37 (29)	32 (34)	29 (28)	64 (46)	28 (19)	13 (15)	15 (12)	45 (15)	52 (54)
Th	19 (24)	1 (1)	6 (10)	5 (2)	1	14 (31)	2 (2)	1 (1)	1 (1)
U	19 (16)	5 (3)	9 (9)	7 (4)	4 (2)	18 (11)	26 (11)	33 (22)	13 (3)

6. Supplement – Supplement II: Mantle metasomatism by sediment fluids

**Table 3.3.13:** Allanite major and trace element compositions, as measured by LA-ICP-MS. ‘\*\*\*’ phosphorous test run with 1.1 wt.% of P<sub>2</sub>O<sub>5</sub> (per weight of solids) introduced via the fluid as diluted H<sub>3</sub>PO<sub>4</sub>. When no standard deviation is specified, then the measurement value was above detection limit in only one analysis. ‘b.d.l.’ below detection limit. ‘n.a.’ not analyzed. ‘(1)’ one analysis.

P (GPa) / T (°C)	2.5 / 600		3.5 / 600								
Salinity (wt.% NaCl)	10	15	0	0	0	5	5	10	10	15	15
Sample	DT16	DT6	DT1	DT7 (1)	***DT17 (1)	DT2	DT9	DT3	DT10	DT4	DT8
Na <sub>2</sub> O	0.4 (0.2)	0.2 (0)	1.3 (1.1)	4.4	1.1	1.5 (1.4)	0.4 (0.2)	0.3 (0.1)	0.5 (0.3)	0.8 (1.1)	0.3 (0.2)
MgO	0.8 (0.2)	0.5 (0.1)	1.1 (0.2)	2.9	0.6	1.2 (0.4)	1.1 (0.3)	0.6 (0.1)	1.1 (0.2)	1.1 (0.4)	0.9 (0.1)
Al <sub>2</sub> O <sub>3</sub>	15.7 (1.4)	16.9 (2.0)	11.8 (2.9)	8.0	13.5	9.2 (2.2)	15.0 (0.5)	16.1 (3.4)	15.3 (0.5)	14.8 (2.5)	11.6 (0.3)
SiO <sub>2</sub> (int. standard)	32	33	33	33	32	33	32	33	32	33	30
K <sub>2</sub> O	0.1 (0.1)	0.1 (0.1)	b.d.l.	0.7	0.7	0.1 (0)	n.a.	0.1 (0.1)	n.a.	0.1 (0)	0.3 (0.3)
CaO	11.1 (2.4)	11.5 (1.8)	10.6 (3.4)	9.1	10.8	5.8 (1.2)	8.4 (0.4)	9.4 (2.6)	9.9 (1.2)	10.1 (3.1)	5.4 (2.6)
TiO <sub>2</sub>	0.5 (0.6)	0.3 (0.1)	0.2 (0.1)	0.2	0.4	0.3 (0.1)	0.4 (0.1)	0.3 (0.1)	0.2 (0)	0.7 (1.0)	0.2 (0.1)
FeO	7.0 (0.7)	6.4 (0.5)	6.3 (0.8)	6.1	7.9	6.8 (1.0)	6.8 (0.5)	6.6 (0.5)	8.5 (0.4)	7.6 (1.0)	6.9 (0.4)
<b>Li</b>	435 (416)	174 (47)	273 (301)	1173	696	272 (231)	120 (56)	276 (138)	136 (92)	415 (331)	395 (355)
<b>Be</b>	125 (51)	71 (10)	345 (309)	719	37	141 (48)	117 (34)	104 (32)	148 (44)	158 (23)	157 (97)
<b>B</b>	758 (153)	416 (203)	517 (186)	3264	2333	359 (92)	641 (101)	531 (277)	392 (223)	434 (356)	518 (426)
<b>Rb</b>	90 (67)	75 (19)	37 (21)	292	193	45 (20)	94 (6)	91 (68)	97 (73)	140 (122)	146 (165)
<b>Sr</b>	5591 (1537)	6014 (1020)	3753 (1354)	1122	7070	3046 (1218)	4909 (29)	5507 (1908)	4860 (467)	3963 (2381)	3074 (219)
<b>Y</b>	1458 (464)	1171 (297)	1041 (546)	247	515	2400 (2899)	1513 (470)	1356 (379)	1696 (402)	1425 (528)	1198 (271)
<b>Zr</b>	456 (227)	415 (183)	134 (29)	55	2561	172 (56)	313 (155)	645 (220)	452 (141)	468 (90)	299 (120)
<b>Nb</b>	1671 (1552)	795 (498)	54 (33)	33	56	137 (85)	720 (688)	2209 (2297)	1047 (1143)	1083 (412)	832 (412)
<b>Cs</b>	488 (507)	285 (108)	226 (166)	687	1656	197 (208)	683 (40)	795 (1011)	228 (72)	404 (374)	286 (269)
<b>Ba</b>	126 (50)	63 (14)	61 (37)	247	172	119 (77)	108 (18)	390 (543)	114 (47)	739 (1102)	85 (33)
<b>La</b>	8035 (3900)	5241 (1166)	6070 (4894)	1826	8642	6839 (4180)	9418 (4766)	5857 (2766)	10322 (4312)	9799 (8262)	9340 (2024)
<b>Ce</b>	1042 (468)	1852 (426)	4900 (2108)	1815	16171	7233 (3101)	6422 (282)	1366 (438)	6133 (1787)	2820 (1849)	4105 (2590)
<b>Nd</b>	10105 (4433)	6999 (1940)	7019 (5889)	1643	8622	8510 (4875)	10934 (4607)	7950 (3450)	12620 (4504)	11882 (7596)	11638 (1700)
<b>Sm</b>	10203 (4403)	7264 (1843)	6863 (5511)	1625	8342	9057 (5129)	10842 (4220)	8740 (3241)	12534 (3982)	11194 (6264)	10861 (1878)
<b>Eu</b>	8571 (3241)	6031 (1012)	6989 (5547)	1716	7190	10014 (6658)	10620 (4323)	7085 (2156)	11082 (3654)	8978 (5178)	9221 (1396)
<b>Gd</b>	10973 (4458)	7909 (2351)	7169 (5518)	1518	7402	11037 (8192)	11442 (4451)	8954 (3213)	13269 (3202)	11633 (5512)	10676 (1777)
<b>Dy</b>	10743 (3893)	8297 (2238)	6654 (4731)	1351	5273	13834 (13450)	10927 (3668)	9414 (2950)	12742 (2974)	10976 (4422)	9443 (2449)
<b>Er</b>	12940 (4881)	9985 (2688)	7719 (5344)	1653	3394	15479 (17359)	12225 (3791)	11343 (3537)	14163 (3011)	12295 (4250)	9601 (2695)
<b>Yb</b>	11954 (4279)	9165 (2548)	6264 (4379)	1174	2274	11450 (11553)	9975 (2787)	11052 (3132)	12410 (2679)	10534 (3379)	7705 (2353)
<b>Lu</b>	9127 (3209)	7223 (2226)	4984 (3231)	848	1543	8042 (7500)	7834 (1896)	8757 (2629)	9807 (2279)	8205 (2667)	5690 (1886)
<b>Hf</b>	552 (177)	601 (274)	160 (108)	73	1440	216 (66)	420 (99)	798 (237)	654 (198)	683 (122)	397 (182)
<b>Ta</b>	1443 (1125)	743 (441)	38 (19)	50	53	121 (64)	752 (685)	1969 (1753)	1075 (1065)	1199 (504)	845 (412)
<b>Pb</b>	1763 (312)	1260 (182)	1360 (587)	573	1891	657 (247)	1493 (106)	1645 (222)	1646 (154)	1043 (320)	1107 (71)
<b>Th</b>	4145 (1204)	3185 (1023)	3643 (1693)	475	5097	3813 (1177)	4717 (532)	4156 (826)	5447 (1574)	3718 (657)	2856 (297)
<b>U</b>	4696 (1885)	3264 (946)	3746 (957)	577	4093	6408 (4853)	5381 (882)	5720 (1750)	6076 (1021)	4129 (944)	4206 (1171)

6. Supplement – Supplement II: Mantle metasomatism by sediment fluids

Table 3.3.13: Continued.

P (GPa) / T (°C)	3.5 / 700				4.5 / 700			
	0	5	15	15	0	5	10	15
Salinity (wt.% NaCl)								
Sample	DT21	DT24	DT20	DT23	DT11	DT12	DT13	DT14
Na <sub>2</sub> O	0.5 (0.6)	0.3 (0.1)	0.7 (0.5)	0.4 (0.2)	0.6 (0.4)	0.3 (0.2)	0.2 (0)	0.2 (0)
MgO	0.8 (0.3)	1.1 (0.3)	1.2 (0.2)	1.1 (0.4)	1.1 (0.2)	0.9 (0.2)	0.8 (0.1)	0.9 (0.1)
Al <sub>2</sub> O <sub>3</sub>	18.8 (1.2)	16.8 (0.6)	14.4 (2.4)	17.2 (0.6)	15.8 (0.7)	15.1 (1.0)	15.9 (2.3)	17.6 (0.5)
SiO <sub>2</sub> (int. standard)	3I	3I	3I	32	32	32	32	32
K <sub>2</sub> O	0.2 (0.1)	0.2 (0.1)	0.1 (0.2)	0.1 (0)	0.3 (0.2)	0.2 (0.1)	0.1	0 (0)
CaO	11.2 (2.0)	10.5 (1.5)	10.9 (2.4)	11.0 (2.2)	9.4 (1.7)	7.9 (0.5)	10.2 (1.3)	11.4 (1.1)
TiO <sub>2</sub>	0.3 (0.1)	0.2 (0)	0.2 (0.1)	0.3 (0.1)	0.3 (0)	0.4 (0.1)	0.2 (0)	0.3 (0)
FeO	4.7 (0.4)	5.1 (0.3)	6.2 (1.6)	7.5 (0.3)	8.1 (0.7)	8.2 (0.6)	8.7 (0.9)	8.1 (0.4)

Li	208 (196)	61 (21)	89 (32)	227 (137)	105 (59)	98 (63)	44 (10)	38 (28)
Be	199 (112)	102 (16)	112 (32)	65 (25)	131 (68)	51 (9)	33 (26)	48 (23)
B	335 (127)	435 (224)	226 (93)	603 (227)	342 (119)	289 (120)	83 (27)	168 (78)
Rb	32 (22)	108 (40)	83 (35)	147 (64)	87 (44)	64 (23)	30 (13)	58 (15)
Sr	10948 (1269)	6906 (1097)	3721 (916)	5138 (551)	6335 (51)	6098 (562)	5726 (718)	4788 (241)
Y	1127 (118)	1297 (80)	1485 (439)	1708 (331)	593 (102)	622 (130)	424 (29)	746 (139)
Zr	95 (14)	215 (54)	294 (115)	394 (157)	48 (18)	79 (32)	26 (13)	120 (28)
Nb	169 (37)	414 (166)	652 (552)	1001 (556)	25 (19)	73 (46)	18 (4)	186 (59)
Cs	129 (49)	409 (185)	264 (208)	346 (166)	293 (154)	142 (43)	55 (29)	115 (30)
Ba	69 (22)	137 (46)	41 (34)	62 (34)	123 (32)	107 (35)	56 (28)	61 (20)
La	4707 (1021)	7896 (2031)	10120 (6432)	10858 (1749)	12936 (595)	12758 (1563)	13452 (1873)	11061 (1361)
Ce	6544 (256)	5300 (986)	3077 (1062)	5347 (1441)	37119 (1403)	34764 (4857)	43255 (6582)	33826 (3903)
Nd	5465 (868)	8712 (1492)	10678 (4955)	13715 (1590)	13046 (834)	13113 (1860)	13111 (2187)	11596 (1526)
Sm	5612 (899)	8393 (1191)	10044 (3596)	13381 (1210)	11335 (1034)	11575 (1635)	11315 (2056)	10490 (1463)
Eu	5027 (601)	8270 (1861)	7922 (3290)	9761 (1339)	10733 (520)	10194 (1217)	10017 (1499)	10022 (1115)
Gd	5710 (1391)	8600 (801)	9745 (3282)	14036 (703)	8971 (395)	9360 (1308)	8223 (1186)	9444 (1398)
Dy	5368 (1247)	8157 (1088)	9440 (3162)	12783 (850)	4233 (414)	5073 (1096)	3221 (500)	5453 (951)
Er	5067 (1542)	8956 (1717)	9931 (3290)	14163 (1921)	2474 (395)	3847 (1323)	1104 (148)	3984 (1230)
Yb	3866 (1112)	7517 (1535)	8144 (2966)	11802 (1925)	1802 (413)	2922 (1239)	555 (42)	3160 (1044)
Lu	2857 (790)	5812 (1348)	6207 (2180)	9460 (1690)	1292 (218)	2210 (926)	358 (28)	2399 (814)
Hf	70 (34)	271 (91)	319 (87)	519 (156)	50 (19)	90 (34)	29 (10)	185 (48)
Ta	132 (11)	362 (133)	639 (585)	1035 (555)	21 (16)	69 (55)	16 (5)	179 (50)
Pb	1345 (159)	1427 (697)	727 (370)	1216 (448)	1482 (97)	955 (159)	1314 (62)	889 (43)
Th	2781 (556)	3738 (858)	4429 (2363)	6108 (927)	7701 (744)	7434 (1265)	9252 (1997)	6836 (895)
U	3702 (661)	4750 (726)	4412 (1630)	6684 (792)	8372 (16)	8561 (984)	10235 (1924)	7958 (726)

6. Supplement – Supplement II: Mantle metasomatism by sediment fluids

**Table 3.3.14:** Rutile major and trace element compositions, as measured by LA-ICP-MS. ‘\*\*\*’ phosphorous test run with 1.1 wt.% of P<sub>2</sub>O<sub>5</sub> (per weight of solids) introduced via the fluid as diluted H<sub>3</sub>PO<sub>4</sub>. When no standard deviation is specified, then the measurement value was above detection limit in only one analysis. ‘b.d.l.’ below detection limit. ‘n.a.’ not analyzed. ‘(1)’ one analysis. ‘-’ grains too small for analysis.

P (GPa) / T (°C)	2.5 / 600					3.5 / 600					
Salinity (wt.% NaCl)	10	15	0	0	0	5	5	10	10	15	15
Sample	DT16	DT6 (1)	DT1	DT7 (1)	***DT17	DT2	DT9 (1)	DT3	DT10	DT4	DT8
Na <sub>2</sub> O	-	0.7	0.2 (0.2)	0.1	0.1 (0.1)	-	0.2	0.2 (0.1)	-	-	-
MgO	-	0.2	0.1 (0.1)	0.1	0.1	-	0.2	0.2 (0.1)	-	-	-
Al <sub>2</sub> O <sub>3</sub>	-	1.3	1.0 (1.3)	3.8	0.2 (0.1)	-	0.4	0.8 (1.0)	-	-	-
SiO <sub>2</sub>	-	8.2	6.8 (5.5)	4.3	b.d.l.	-	7.5	3.1 (1.0)	-	-	-
K <sub>2</sub> O	-	b.d.l.	0.1	0.2	b.d.l.	-	n.a.	0.2 (0.1)	-	-	-
CaO	-	1.8	b.d.l.	4.7	b.d.l.	-	b.d.l.	1.0 (1.8)	-	-	-
TiO <sub>2</sub> (int. standard)	-	88	98	98	99	-	98	98	-	-	-
FeO	-	3.5	1.2 (1.2)	1.9	1.2 (0.5)	-	1	0.9 (0.7)	-	-	-
Li	-	707	54	77	157	-	b.d.l.	344 (471)	-	-	-
Be	-	177	148	113	b.d.l.	-	b.d.l.	b.d.l.	-	-	-
B	-	677	118 (59)	225	188 (46)	-	b.d.l.	431 (505)	-	-	-
Rb	-	67	38 (19)	21	12 (2)	-	42	83 (52)	-	-	-
Sr	-	721	280 (364)	698	12 (13)	-	49	477 (396)	-	-	-
Y	-	10	10	16	b.d.l.	-	b.d.l.	14	-	-	-
Zr	-	320	134 (66)	11	200 (57)	-	142	178 (61)	-	-	-
Nb	-	26283	3660 (4504)	1195	1490 (1650)	-	2255	1807 (2674)	-	-	-
Cs	-	460	103 (87)	15	137 (59)	-	39	354 (227)	-	-	-
Ba	-	33	105 (113)	19	60	-	68	178 (174)	-	-	-
La	-	28	15 (3)	9	68 (84)	-	2	48 (66)	-	-	-
Ce	-	43	39 (49)	109	52 (61)	-	9	117 (188)	-	-	-
Nd	-	23	23	b.d.l.	25	-	b.d.l.	20 (17)	-	-	-
Sm	-	28	25	14	b.d.l.	-	b.d.l.	10	-	-	-
Eu	-	15	13 (15)	8	5	-	4	49	-	-	-
Gd	-	b.d.l.	8	31	39	-	b.d.l.	61	-	-	-
Dy	-	19	33	64	12	-	18	45	-	-	-
Er	-	b.d.l.	84	86	27 (13)	-	8	56	-	-	-
Yb	-	b.d.l.	23	126	38	-	b.d.l.	71	-	-	-
Lu	-	25	35	122	15 (4)	-	9	29 (34)	-	-	-
Hf	-	124	41 (44)	17	b.d.l.	-	25	14 (3)	-	-	-
Ta	-	25027	4098 (5048)	1100	1334 (1308)	-	2691	1235 (1685)	-	-	-
Pb	-	448	192 (215)	167	102 (62)	-	120	113 (160)	-	-	-
Th	-	10	5	b.d.l.	7	-	b.d.l.	12 (15)	-	-	-
U	-	9	37 (50)	31	6 (3)	-	13	29 (36)	-	-	-

6. Supplement – Supplement II: Mantle metasomatism by sediment fluids

Table 3.3.14: Continued.

P (GPa) / T (°C)	3.5 / 700				4.5 / 700			
	0	5	15	15	0	5	10	15
Salinity (wt.% NaCl)	0	5	15	15	0	5	10	15
Sample	DT21 (1)	DT24	DT20	DT23	DT11 (1)	DT12	DT13	DT14
Na <sub>2</sub> O	0.1	0.1	0.1 (0.1)	0.1	1.0	0 (0)	0.2 (0.1)	0.5 (0.6)
MgO	0.1	b.d.l.	0	0.3	0.7	0 (0.1)	0.2 (0.1)	0.3 (0.3)
Al <sub>2</sub> O <sub>3</sub>	1.6	1	0.7 (0.2)	1.5	2.4	0.4 (0.6)	1.3 (0.4)	1.4 (1.2)
SiO <sub>2</sub>	b.d.l.	b.d.l.	2.9	b.d.l.	4.5	1.7	4.2 (0.1)	3.4
K <sub>2</sub> O	0.4	0.2	0.2 (0.2)	b.d.l.	1.3	0.2 (0.2)	0.3 (0.1)	b.d.l.
CaO	b.d.l.	3.9	b.d.l.	b.d.l.	4.6	2.8	b.d.l.	3.9
TiO <sub>2</sub> (int. standard)	<b>93</b>	<b>94</b>	<b>93</b>	<b>93</b>	<b>93</b>	<b>98</b>	<b>93</b>	<b>93</b>
FeO	2.3	1.7	1.7 (0.7)	2.4	2.7	0.8 (1.0)	2.3 (0.1)	2.3 (0.5)

Li	135	46	84 (36)	237	b.d.l.	47 (62)	85 (41)	37 (11)
Be	b.d.l.	158	106 (79)	b.d.l.	252	178	95	66
B	b.d.l.	b.d.l.	247 (81)	b.d.l.	205	10	192 (187)	271
Rb	245	51	91 (50)	166	321	52 (72)	219 (76)	100 (49)
Sr	b.d.l.	11	92 (31)	229	101	239	96 (9)	71 (6)
Y	b.d.l.	b.d.l.	5	5	b.d.l.	b.d.l.	4 (2)	9
Zr	236	211	152 (59)	120	77	212 (26)	89 (13)	81 (41)
Nb	26843	25880	14225 (1819)	19203	22328	12716 (17922)	19257 (1006)	16423 (311)
Cs	104	27	162 (58)	376	459	77 (108)	280 (199)	112 (90)
Ba	187	82	65 (52)	141	520	130 (181)	86 (25)	50 (20)
La	b.d.l.	b.d.l.	b.d.l.	64	13	18	78 (15)	3
Ce	b.d.l.	3	5	174	14	73 (103)	271 (15)	5
Nd	b.d.l.	b.d.l.	b.d.l.	17	b.d.l.	47	92 (52)	b.d.l.
Sm	b.d.l.	b.d.l.	55	24	b.d.l.	b.d.l.	63 (7)	b.d.l.
Eu	b.d.l.	12	b.d.l.	38	b.d.l.	16	51 (25)	2
Gd	b.d.l.	b.d.l.	b.d.l.	28	b.d.l.	b.d.l.	45 (19)	b.d.l.
Dy	48	12	5	17	b.d.l.	b.d.l.	19 (3)	9
Er	b.d.l.	b.d.l.	b.d.l.	19	b.d.l.	b.d.l.	9 (1)	44
Yb	b.d.l.	b.d.l.	b.d.l.	b.d.l.	b.d.l.	18	15 (15)	7
Lu	13	b.d.l.	b.d.l.	9	b.d.l.	0	8 (6)	26
Hf	90	139	136 (17)	127	b.d.l.	14 (5)	53 (14)	76 (3)
Ta	27496	28460	13853 (4329)	20922	26586	15010 (21221)	19833 (1569)	15537 (799)
Pb	52	15	127 (92)	b.d.l.	174	16	163 (56)	312 (310)
Th	b.d.l.	3	4	13	b.d.l.	28	49 (14)	b.d.l.
U	b.d.l.	b.d.l.	13	34	36	16 (21)	76 (24)	24 (5)

6. Supplement – Supplement II: Mantle metasomatism by sediment fluids

**Table 3.3.15:** Major and trace element compositions of other accessory phases, as measured by LA-ICP-MS. ‘\*\*\*’ phosphorous test run with 1.1 wt.% of P<sub>2</sub>O<sub>5</sub> (per weight of solids) introduced via the fluid as diluted H<sub>3</sub>PO<sub>4</sub>. When no standard deviation is specified, then the measurement value was above detection limit in only one analysis. ‘b.d.l.’ below detection limit. ‘n.a.’ not analyzed.

P (GPa) / T (°C)	3.5 / 600	3.5 / 700	
Salinity (wt.% NaCl)	0	0	15
Sample	***DT17	DT21	DT23
Mineral	Ap	Ttn	Zrc
Na <sub>2</sub> O	0.2 (0.1)	0.2 (0.2)	0.1
MgO	1.0 (0.9)	0.2 (0.3)	0
Al <sub>2</sub> O <sub>3</sub>	0.2 (0.3)	2.6 (0.5)	0.2
SiO <sub>2</sub>	2.4 (1.7)	30 (i.s.)	37 (i.s.)
K <sub>2</sub> O	0.2 (0.1)	0.1 (0)	b.d.l.
CaO	54 (i.s.)	23.9 (5.3)	0.3
TiO <sub>2</sub>	0 (0)	23.8 (2.4)	0
FeO	0.8 (0.4)	0.4 (0.3)	0.1
P <sub>2</sub> O <sub>5</sub>	15.7 (2.1)	n.a.	n.a.

Li	71 (93)	75 (81)	147
Be	275	b.d.l.	17
B	505 (337)	79	156
Rb	84 (137)	39 (46)	31
Sr	10582 (1324)	1269 (152)	94
Y	206 (221)	663 (231)	90
Zr	6 (7)	151 (58)	443544
Nb	33 (29)	5697 (2477)	28
Cs	53 (63)	18 (12)	58
Ba	199 (171)	32 (27)	8
La	417 (126)	20 (10)	1
Ce	666 (592)	191 (54)	5
Nd	554 (175)	215 (111)	4
Sm	697 (407)	576 (188)	b.d.l.
Eu	865 (659)	908 (332)	2
Gd	1109 (987)	1062 (390)	19
Dy	1369 (1255)	2186 (553)	25
Er	1424 (1016)	2227 (820)	84
Yb	992 (295)	1183 (551)	84
Lu	677 (117)	640 (259)	92
Hf	11 (0)	111 (58)	14909
Ta	29 (30)	9444 (3418)	59
Pb	1748 (267)	139 (33)	32
Th	47 (14)	6 (2)	58
U	166 (83)	204 (104)	328

6. Supplement – Supplement II: Mantle metasomatism by sediment fluids

**Fluid compositions**

**Table 3.3.16:** Fluid major and trace element compositions, as measured by LA-ICP-MS. ‘\*\*\*’ phosphorous test run with 1.1 wt.% of P<sub>2</sub>O<sub>5</sub> (per weight of solids). ‘n.a.’ not analyzed. ‘TDS’ Total Dissolved Solids. ‘cont.’ values overestimated by more than an order of magnitude due to Zr contamination in the MEDIA diamond powder; a comparative test was performed at 3.5 GPa, 700 °C and 15 wt.% NaCl (DT20 and DT23) using a pristine Alfa Aesar diamond aggregate.

P (GPa) / T (°C)	2.5 / 600				3.5 / 600							
Salinity (wt.% NaCl)	10	15	0	0	0	5	5	10	10	15	15	
Sample	DT16	DT6	DT1	DT7	***DT17	DT2	DT9	DT3	DT10	DT4	DT8	
Na <sub>2</sub> O	2.1 (0.8)	4.7 (0)	0.5 (0.1)	0.9 (0)	0.4 (0)	0.3 (0)	1.4 (0.4)	3.0 (0.3)	1.5 (0)	4.5 (0.7)	3.9 (1.0)	
MgO	0.2 (0.2)	0.7 (0)	0.04 (0.01)	0.23 (0)	0.07 (0.01)	0.01 (0)	0.55 (0.26)	0.04 (0.02)	0.02 (0.01)	0.05 (0.01)	0.26 (0.27)	
Al <sub>2</sub> O <sub>3</sub>	0.5 (0.4)	1.7 (0)	0.1 (0)	0.3 (0)	0.2 (0)	0.1 (0)	1.0 (0.4)	0.1 (0)	0.1 (0)	0.1 (0)	0.5 (0.6)	
SiO <sub>2</sub>	4.3 (0.1)	10.9 (0.2)	5.3 (0.4)	6.8 (0.5)	47.1 (3.7)	5.2 (0.5)	12.5 (2.5)	13.9 (2.2)	6.3 (0.1)	9.8 (2.2)	12.2 (2.8)	
Cl	2.6 (1.1)	6.4 (0.1)	n.a.	n.a.	n.a.	0.2 (0)	0.8 (0.3)	5.0 (0.2)	2.3 (0.5)	8.3 (1.5)	6.9 (1.0)	
K <sub>2</sub> O	0.4 (0.1)	0.6 (0)	0.4 (0)	0.4 (0)	0.3 (0.1)	0.4 (0)	0.5 (0)	1.1 (0)	1.3 (0.4)	2.4 (0.2)	2.3 (0.3)	
CaO	0.5 (0.4)	1.8 (0)	0.2 (0)	0.4 (0.1)	1.0 (0.7)	0.1 (0)	1.3 (0.5)	0.6 (0)	0.8 (0.8)	0.8 (0.1)	0.9 (0.5)	
TiO <sub>2</sub>	0.02 (0.01)	0.06 (0)	0.004 (0.001)	0.015 (0)	0.072 (0.016)	0.002 (0.001)	0.044 (0.014)	0.002 (0.001)	0.002 (0.001)	0.003 (0)	0.019 (0.021)	
FeO	0.4 (0.3)	1.3 (0)	0.2 (0)	1.0 (0.1)	0.1 (0)	0.1 (0)	1.3 (0.6)	1.5 (0.4)	0.1 (0)	0.8 (0.1)	0.6 (0.7)	
P <sub>2</sub> O <sub>5</sub>	n.a.	n.a.	n.a.	n.a.	0.7 (0.4)	n.a.	n.a.	n.a.	n.a.	n.a.	n.a.	
TDS	11.1 (2.7)	28.0 (2.8)	6.8 (2.8)	9.9 (2.6)	50.1 (12.1)	6.4 (2.9)	19.3 (4.1)	25.1 (3.5)	12.4 (2.8)	26.7 (3.7)	27.6 (4.8)	
<b>Li</b>	234 (82)	574 (8)	387 (44)	570 (92)	310 (16)	164 (25)	380 (90)	740 (74)	176 (14)	399 (53)	376 (32)	
<b>Be</b>	43 (24)	106 (1)	80 (2)	59 (2)	27 (1)	57 (5)	123 (21)	18 (8)	69 (1)	49 (14)	103 (18)	
<b>B (**int. standard)</b>	930 (138)	1280 (2)	1736 (136)	1531 (217)	<b>1097 (73)</b>	1531 (71)	1601 (104)	1965 (78)	2542 (80)	1875 (211)	2648 (55)	
<b>Rb</b>	137 (27)	229 (19)	167 (3)	138 (1)	124 (13)	216 (7)	255 (22)	365 (13)	473 (32)	549 (7)	697 (4)	
<b>Sr</b>	150 (37)	489 (3)	209 (24)	96 (4)	473 (46)	415 (70)	298 (10)	857 (37)	731 (337)	1001 (139)	659 (134)	
<b>Y</b>	cont.	cont.	cont.	cont.	cont.	cont.	cont.	cont.	cont.	cont.	cont.	
<b>Zr</b>	cont.	cont.	cont.	cont.	cont.	cont.	cont.	cont.	cont.	cont.	cont.	
<b>Nb</b>	1.9 (0.1)	5.1 (0.2)	6.4 (1.3)	3.3 (0.7)	19.8 (2.3)	4.8 (0.6)	4.5 (0.9)	3.0 (0.7)	4.8 (0.2)	4.2 (0.4)	3.7 (1.2)	
<b>Cs (int. standard)</b>	<b>610 (23)</b>	<b>816 (0)</b>	<b>1265 (8)</b>	<b>1116 (6)</b>	324 (49)	<b>1460 (9)</b>	<b>1518 (70)</b>	<b>1354 (159)</b>	<b>1971 (36)</b>	<b>1100 (49)</b>	<b>1311 (89)</b>	
<b>Ba</b>	143 (16)	302 (4)	102 (3)	66 (9)	187 (29)	350 (60)	390 (5)	678 (41)	746 (66)	888 (78)	913 (68)	
<b>La</b>	0.2 (0.1)	0.9 (0.3)	0.14 (0.10)	0.03 (0)	6.29 (3.60)	0.21 (0.10)	0.25 (0.12)	11.20 (18.32)	1.93 (0.44)	4.14 (3.03)	1.60 (0.03)	
<b>Ce</b>	0.7 (0.3)	4.2 (1.1)	0.2 (0)	0.5 (0.1)	14.9 (8.5)	1.1 (0.5)	1.1 (0.4)	3.5 (2.3)	6.8 (0.8)	7.7 (1.3)	5.4 (0.5)	
<b>Nd</b>	0.2 (0.1)	0.9 (0.3)	0.1 (0)	0.1 (0)	8.8 (5.6)	0.3 (0.1)	0.5 (0.1)	0.5 (0.2)	1.5 (0.2)	2.4 (0.3)	1.2 (0.1)	
<b>Sm</b>	0.2 (0.1)	1.6 (0.3)	0.1 (0)	0.3 (0)	12.3 (8.5)	0.3 (0.2)	1.1 (0.3)	0.5 (0.1)	1.7 (0.4)	2.7 (0.6)	1.6 (0.1)	
<b>Eu</b>	0.3 (0.1)	1.4 (0.3)	0.2 (0)	0.5 (0)	18.0 (11.8)	1.0 (0.2)	2.4 (0.6)	0.7 (0.3)	2.5 (0.4)	3.9 (0.1)	3.5 (0.4)	
<b>Gd</b>	0.2 (0.1)	1.4 (0.3)	0.2 (0)	0.5 (0.1)	19.2 (13.7)	0.5 (0.2)	3.1 (0.6)	0.4 (0)	1.7 (0.3)	3.4 (0.4)	2.4 (0.8)	
<b>Dy</b>	0.8 (0.3)	3.7 (0.3)	1.1 (0.1)	2.3 (0)	35.1 (27.8)	1.1 (0.3)	9.6 (3.2)	0.9 (0.1)	2.9 (0.3)	5.1 (0.1)	6.4 (2.6)	
<b>Er</b>	2.9 (1.4)	12.9 (0.2)	3.8 (0.3)	7.4 (0.2)	59.1 (55.4)	3.1 (0.4)	21.3 (7.0)	3.5 (0.9)	7.2 (0.3)	14.5 (2.9)	16.9 (4.2)	
<b>Yb</b>	7.4 (2.5)	32.1 (1.2)	8.9 (2.7)	14.9 (2.4)	78.1 (74.9)	5.3 (1.0)	24.2 (5.5)	11.2 (1.6)	12.0 (2.1)	28.1 (7.0)	35.4 (7.4)	
<b>Lu</b>	8.2 (2.7)	37.8 (1.3)	6.6 (1.3)	11.0 (1.8)	61.7 (65.7)	4.5 (0.9)	19.1 (5.3)	8.9 (1.9)	10.4 (0.1)	28.7 (7.3)	31.4 (4.7)	
<b>Hf</b>	cont.	cont.	cont.	cont.	cont.	cont.	cont.	cont.	cont.	cont.	cont.	
<b>Ta</b>	3.3 (0.4)	9.0 (0.2)	7.1 (2.4)	3.3 (0.8)	23.1 (6.3)	5.6 (1.1)	3.6 (0.6)	5.6 (1.3)	6.1 (0.8)	7.4 (1.5)	5.7 (1.2)	
<b>Pb</b>	315 (247)	192 (10)	94 (11)	100 (19)	148 (29)	23 (2)	273 (31)	176 (37)	527 (471)	222 (6)	708 (579)	
<b>Th</b>	0.04 (0.02)	0.19 (0.05)	0.07 (0.02)	0.09 (0.01)	7.58 (8.19)	0.08 (0.03)	0.16 (0.08)	0.12 (0.06)	0.12 (0.02)	0.62 (0.21)	0.37 (0.07)	
<b>U</b>	2.1 (0.1)	14.7 (0.2)	10.9 (3.5)	20.7 (3.0)	40.4 (41.0)	8.2 (1.4)	11.5 (3.1)	3.9 (0.7)	11.1 (0.5)	17.6 (5.3)	19.4 (1.7)	

6. Supplement – Supplement II: Mantle metasomatism by sediment fluids

Table 3.3.16: Continued.

P (GPa) / T (°C)	3.5 / 700				4.5 / 700			
	0	5	15	15	0	5	10	15
Salinity (wt.% NaCl)	0	5	15	15	0	5	10	15
Sample	DT21	DT24	DT20	DT23	DT11	DT12	DT13	DT14
Na <sub>2</sub> O	1.0 (0.1)	0.6 (0)	4.2 (2.1)	3.4 (0.3)	0.7 (0.1)	0.7 (0.1)	1.4 (0.4)	2.3 (0.2)
MgO	0.02 (0)	0.10 (0.12)	0.02 (0.01)	0.04 (0.02)	0.02 (0)	0.02 (0.01)	0.03 (0.01)	0.07 (0.01)
Al <sub>2</sub> O <sub>3</sub>	0.3 (0)	0.2 (0)	0.1 (0.0)	0.1 (0)	0.23 (0.03)	0.12 (0.03)	0.06 (0.01)	0.13 (0.01)
SiO <sub>2</sub>	12.8 (1.3)	10.6 (2.3)	7.8 (2.1)	2.2 (0.8)	9.9 (1.1)	13.8 (3.4)	5.7 (0.9)	8.1 (1.0)
Cl	n.a.	0.5 (0)	8.3 (2.3)	7.8 (0.7)	n.a.	0.3 (0.1)	3.6 (0.3)	6.5 (0.3)
K <sub>2</sub> O	1.2 (0.1)	0.9 (0.1)	3.6 (1.1)	2.7 (0.1)	1.9 (0.2)	2.2 (0.2)	1.9 (0.6)	4.9 (0.1)
CaO	0.3 (0.1)	1.5 (1.4)	0.7 (0.1)	1.4 (0.4)	0.4 (0)	0.5 (0.1)	2.2 (0)	1.5 (0.8)
TiO <sub>2</sub>	0.015 (0.005)	0.008 (0.002)	0.004 (0.001)	0.003 (0.002)	0.015 (0.002)	0.015 (0.002)	0.006 (0)	0.009 (0.002)
FeO	0.1 (0)	0.4 (0.2)	0.2 (0.1)	0.1 (0.1)	0.1 (0)	0.2 (0.2)	0.1 (0)	0.3 (0)
P <sub>2</sub> O <sub>5</sub>	n.a.	n.a.	n.a.	n.a.	n.a.	n.a.	n.a.	n.a.
TDS	15.7 (2.8)	14.8 (3.9)	25.0 (4.7)	17.7 (2.7)	13.3 (2.7)	17.9 (8.3)	15.0 (2.8)	23.8 (2.8)

Li	530 (121)	311 (81)	365 (51)	877 (27)	602 (56)	682 (102)	518 (56)	378 (17)
Be	136 (30)	72 (10)	73 (29)	27 (10)	311 (37)	251 (74)	132 (6)	176 (23)
<b>B (**int. standard)</b>	2107 (444)	2202 (485)	3130 (1550)	1340 (631)	2496 (96)	3323 (337)	1828 (317)	4020 (451)
Rb	730 (241)	579 (96)	1330 (239)	1092 (15)	817 (27)	1274 (157)	1412 (221)	2435 (247)
Sr	427 (27)	1803 (1267)	1.3 (0.7)	2710 (67)	647 (49)	1098 (182)	1552 (253)	1346 (434)
Y	0.4 (0)	1.2 (0.6)	cont.	0.6 (0.3)	cont.	cont.	cont.	cont.
Zr	2.2 (2.3)	3.7 (0.9)	cont.	3.7 (1.7)	cont.	cont.	cont.	cont.
Nb	27.8 (4.8)	9.6 (2.6)	5.9 (1.6)	1.0 (0.3)	26.8 (2.1)	22.2 (2.8)	7.1 (0.6)	8.3 (1.0)
<b>Cs (int. standard)</b>	<b>2277 (35)</b>	<b>2133 (84)</b>	<b>2050 (76)</b>	<b>2144 (10)</b>	<b>2509 (27)</b>	<b>2500 (96)</b>	<b>2663 (12)</b>	<b>2213 (16)</b>
Ba	131 (4)	353 (142)	1109 (229)	1252 (15)	356 (55)	617 (99)	615 (75)	2040 (314)
La	0.2 (0.1)	0.8 (0.7)	1.6 (0.4)	0.8 (0.3)	1.0 (0.4)	0.6 (0.2)	2.8 (0.1)	3.9 (1.4)
Ce	1.0 (0.4)	3.2 (1.8)	5.0 (1.7)	4.1 (1.4)	5.0 (0.5)	4.6 (0.8)	11.5 (1.0)	19.2 (8.5)
Nd	0.2 (0)	0.6 (0.1)	1.2 (0.1)	0.6 (0.3)	1.1 (0.1)	0.8 (0.3)	2.7 (0.2)	4.7 (2.9)
Sm	0.2 (0)	0.5 (0.2)	0.9 (0.9)	0.7 (0.5)	1.6 (0.3)	0.9 (0.4)	2.9 (0.7)	5.7 (3.6)
Eu	0.3 (0.1)	1.2 (0.9)	0.8 (0.6)	1.1 (1.0)	3.0 (0.4)	2.5 (0.6)	6.6 (0.3)	11.0 (6.2)
Gd	0.3	1.3 (1.3)	1.3 (0.9)	0.6 (0.3)	2.7 (0.6)	1.7 (0.8)	4.2 (0.5)	5.0 (1.3)
Dy	0.3 (0)	1.1 (0.2)	1.0 (0.3)	0.4 (0.1)	3.2 (0.5)	2.3 (0.5)	3.3 (0.5)	3.9 (0.5)
Er	0.7 (0.1)	0.7 (0.1)	1.5 (0.7)	0.6 (0.2)	3.4 (0.8)	1.4 (0.5)	2.0 (0.2)	2.4 (0.7)
Yb	1.4 (0.5)	0.7 (0.1)	2.5 (1.8)	0.6 (0.3)	2.5 (0.3)	2.1 (1.2)	1.1 (0)	1.0 (0.4)
Lu	0.5 (0)	0.3 (0.1)	0.9 (0.2)	0.3 (0.2)	1.7 (0.4)	0.7 (0.4)	0.8 (0)	0.9 (0.2)
Hf	0.8 (1.0)	0.8 (0.3)	cont.	1.2 (1.2)	cont.	cont.	cont.	cont.
Ta	1.7 (0)	1.0 (0.1)	0.8 (0.4)	0.3 (0.1)	6.3 (0.4)	4.3 (1.7)	1.4 (0.2)	1.6 (0.3)
Pb	111 (38)	345 (241)	1256 (431)	879 (551)	287 (55)	117 (20)	486 (17)	1128 (348)
Th	0.04 (0)	0.31 (0.25)	0.06 (0.03)	0.19 (0.19)	0.37 (0.03)	0.12 (0.04)	0.27 (0.09)	0.36 (0.15)
U	2.3 (0.4)	2.7 (2.6)	1.7 (0.4)	1.7 (2.1)	13.5 (1.2)	25.2 (15.0)	7.0 (0.8)	8.8 (0.2)

**Mineral proportions**

**Table 3.3.17:** Major mineral proportions, expressed in wt.% of the solid residues. Mineral proportions are estimated from an iterative mass balance calculation, using the least fluid-soluble major element oxide concentrations in minerals (EPMA) and the fluid (LA-ICP-MS). ‘\*\*\*’ phosphorous test run with 1.1 wt.% of P<sub>2</sub>O<sub>5</sub> (per weight of solids) introduced via the fluid as diluted H<sub>3</sub>PO<sub>4</sub>. ‘\*\*’ values calculated using the lawsonite composition from run DT21. ‘\*’ zoisite and quartz stable in 2.5 GPa experiments. ‘-’ no overgrowth on garnet seeds.

P (GPa) / T (°C)	2.5 / 600					3.5 / 600					
	10	15	0	0	0	5	5	10	10	15	15
Sample	DT16	DT6	DT1	DT7	***DT17	DT2	DT9	DT3	DT10	DT4	DT8
Cpx	37.5 (8.6)	41.4 (6.8)	35.7 (3.3)	31.0 (2.7)	43.9 (7.1)	43.3 (3.3)	35.2 (3.7)	47.1 (5.4)	44.7 (3.3)	56.0 (4.0)	44.1 (5.3)
Pheng	26.5 (5.0)	25.7 (3.1)	23.0 (3.1)	24.5 (2.5)	27.1 (7.1)	20.8 (2.8)	24.3 (3.1)	20.9 (3.7)	19.8 (2.1)	19.7 (2.6)	20.0 (4.1)
Laws / *Zo	*11.9 (5.1)	*11.7 (3.6)	15.0 (2.1)	17.3 (2.0)	19.9 (3.5)	12.5 (2.1)	16.2 (2.3)	12.3 (3.3)	12.1 (2.0)	12.3 (2.1)	16.3 (3.0)
Grt	-	-	-	-	7.8 (2.8)	-	-	-	-	-	-
Coe / *Qtz	*24.1 (5.5)	*21.1 (3.9)	26.3 (2.2)	27.3 (2.1)	1.3 (0.3)	23.5 (2.6)	24.3 (2.5)	19.7 (3.5)	23.4 (2.1)	12.0 (2.2)	19.6 (3.3)

Table 3.3.17: Continued.

P (GPa) / T (°C)	3.5 / 700				4.5 / 700			
	0	5	15	15	0	5	10	15
Sample	DT21	DT24	DT20	DT23	DT11	DT12	DT13	DT14
Cpx	31.1 (2.7)	**32.3	**44.0	**38.7	21.2 (2.2)	32.2 (8.1)	32.9 (5.9)	39.8 (5.4)
Pheng	22.1 (3.5)	**24.2	**20.9	**19.7	19.6 (2.6)	14.9 (4.3)	18.1 (5.5)	15.3 (4.8)
Laws / *Zo	6.5 (1.7)	**4.7	**7.8	**4.2	16.5 (1.4)	13.4 (4.7)	11.9 (3.2)	11.2 (2.3)
Grt	12.7 (1.6)	**12.4	**7.6	**12.9	12.6 (1.5)	12.4 (2.9)	10.8 (1.9)	11.1 (2.1)
Coe / *Qtz	27.6 (2.5)	**26.4	**19.9	**24.6	30.0 (2.0)	27.1 (5.3)	26.4 (4.5)	22.7 (3.9)

**Preferred literature values for peridotite/melt partition coefficients**

**Table 3.3.18:** A summary of literature sources for the mineral/basalt partition coefficients that were used to calculate the peridotite/melt partition coefficients.

Reference	D <sub>ol/basalt</sub>	D <sub>opx/basalt</sub>	D <sub>cpx/basalt</sub>	D <sub>grt/basalt</sub>
Chaussidon & Libourel (1993)	B	B		
Dunn & Sen (1993)	Li, Be	Li, Be		
Hart & Brooks (1974)	Rb, Cs, Sr, Ba			
Hart & Dunn (1993)			Li, Be, Er, Yb, Lu	
Hauri et al. (1994)			Eu	
Johnson (1998)			Dy	La, Ce, Nd, Sm, Eu, Dy, Er, Yb, Lu
Kennedy et al. (1993)	La, Ce, Nd, Sm, Eu, Gd, Dy, Er, Yb, Lu	Sr, Ba, Nb, La, Ce, Nd, Sm, Eu, Gd, Dy, Er, Yb, Lu		
Klemme et al. (2002)			B, Rb, Cs, Sr, Ba, Ta, La, Gd	Li, Be, B, Rb, Cs, Sr, Ta, Gd
Salteras et al. (2002)	Nb, Pb, Th, U	Pb, Th, U	Nb, Ce, Nd, Sm, Pb, Th, U	Ba, Nb, Pb, Th, U
<i>empty reservoir</i>	<i>Ta</i>	<i>Rb, Cs, Ta</i>		

**Table 3.3.19:** A list of peridotite/melt partition coefficients, estimated assuming a mantle mineralogy of 70 wt.% olivine, 20 wt.% orthopyroxene, 5 wt.% clinopyroxene and 5 wt.% garnet. The given values were used to model the composition of primitive arc melts.

D <sub>peridotite/melt</sub>	
Li	0.3445
Be	0.0951
B	0.0317
Rb	0.0003
Cs	0.0004
Sr	0.0057
Ba	0.0015
Nb	0.0069
Ta	0.0008
La	0.0029
Ce	0.0030
Nd	0.0075
Sm	0.0200
Eu	0.0446
Gd	0.0544
Dy	0.1347
Er	0.2096
Yb	0.3698
Lu	0.3991
Pb	0.0050
Th	0.0015
U	0.0040

## **7. Appendix: Kinetics of nanolite crystallization in alkaline silicate melts from the Eifel Volcanic Fields (Germany)**

### **7.1. Introduction**

The final stages of groundmass crystallization in volcanic rocks can record the physical and chemical conditions of the magma shortly before, during, or after the eruption. Investigations of the finest crystal size fraction in volcanic products may provide useful insights on eruption dynamics. These late-stage crystallization products are typically nanoscale, and can be sub-divided further into nanolites (1  $\mu\text{m}$  to 30 nm) and ultrananolites ( $< 30$  nm), following the definition by Mujin et al. (2017).

Sharp et al. (1996), who originally introduced the term nanolite, were able to infer the cooling history of rhyolitic glasses from the Taupo Volcanic Center (New Zealand) by studying the composition and microstructures of  $< 0.6$   $\mu\text{m}$  clinopyroxene crystals. Mujin and Nakamura (2014) demonstrated that the microlite/nanolite record could preserve the transition point in eruption style of the 2011 eruption of Shinmoedake volcano (Japan) from sub-Plinian to intermittent Vulcanian explosions with effusion of lavas in the crater. The transition was observed as a change in the microlite mineral assemblage, and the different nanolite assemblages within the products of the same eruption style were related to varying near-surface magma residence periods.

In addition to providing a record of eruption dynamics, nanolite crystallization may also have an active role in modifying physical properties of magmas. Di Genova et al. (2017) and Di Genova et al. (2020) experimentally showed that the viscosity of both rhyolitic and basaltic melts may increase dramatically upon precipitation of nanoparticles. More recently, Cáceres et al. (2021) suggested that nanolites provide sites for heterogeneous nucleation of gas bubbles. Both bubble formation and melt viscosity influence the conditions of magma fragmentation, and nanolite crystallization is thought to control the style of some volcanic eruptions. The examples from previous studies provide an incentive for further research of nanolite crystallization.

The mechanisms of crystal nucleation and growth are thought to depend on the physical and chemical properties of the parent melt. We, therefore, decided to investigate the kinetics of nanolite crystallization in highly alkaline silicate melts, produced by historic eruptions of the Eifel Volcanic Fields (Germany). Due to high concentrations of network modifying alkali, considerable volatile budgets, and predominantly ultramafic and mafic compositions (Ch. 7.2), these melts have extremely low viscosities, such that favor high nucleation rates and rapid crystal growth. Because of the exotic composition and low melt viscosity, we initially hypothesized that nanolites from alkaline silicate melts likely represent a natural end-member with respect to crystal nucleation and growth mechanisms.

Indeed, we observed a rare nanolite growth mechanism in the groundmass of ultramafic eruptive products from the Eifel. We confirmed that magnetite nanoparticles coarsened as a result of oriented attachment (e.g. Penn and Banfield, 1999). The oriented attachment of magnetite nanoparticles may be restricted to ultramafic alkaline melts. Already in the more viscous mafic and intermediate samples, other nanolite crystallization mechanisms were observed (Ch. 7.4.1). We consider that longer timescales and very low melt viscosities are necessary conditions for the oriented attachment to occur, which places additional constraints on magma fragmentation mechanisms in maar-diatreme volcanoes (Ch. 7.5).

## **7.2. Volcanic activity in the Eifel**

The Quaternary Eifel Volcanic Fields (EVFs) – the Westeifel and Easteifel Volcanic Field (WEVF and EEVF) – are situated in central western Germany. The area is a part of the Rhenish Shield, and is characterized by volcanic deposits and numerous geomorphological features related to volcanic activity. The latest eruption in the geologic record of the Eifel Volcanic Fields occurred approximately 11 ka, and had formed the Ulmener Maar (Schmincke, 2009). Despite a long period of volcanic quiescence, continuous volcanic degassing and local microseismicity, accompanied by high rates of regional uplift (Schmincke, 2007; Kreemer et al., 2020), suggest that the Eifel may still be volcanically active. Most eruptions in the Eifel Volcanic Fields were not voluminous in terms of magma production, but many had formed fallout deposits that extend for kilometers with respect to the volcanic centers of origin (Schmincke, 2007). Given the population density in the

region, even eruptions of limited scale may present a potential hazard, although another volcanic event is likely not imminent.

The volcanic activity in the EVFs may be related to the uplift of a mantle plume located beneath central Europe. The existence of large-scale asthenosphere upwelling is supported by the isotopic and geochemical studies of central-European mantle-derived melts, the observation of low velocity seismic anomalies beneath Europe, as well as unusually high rates of uplift in the Eifel region (Hoernle et al., 1995; Wedepohl and Baumann, 1999; Ritter et al., 2001; Schmincke, 2007; Kreemer et al., 2020). However, due to the absence of a clear “hot-spot track” that correlates with the motion of the Eurasian plate, some authors prefer to attribute the Cenozoic and Quaternary volcanic centers in Europe to passive upwelling of the asthenosphere (Lustrino and Carminati, 2007; Schmincke, 2007).

The composition of magmas erupting in the Eifel Volcanic Fields is highly alkaline and predominantly potassic (Schmincke, 2007). Most eruptive products are SiO<sub>2</sub>-undersaturated (e.g. Mertes and Schmincke, 1985). Based on the modal mineralogy, the volcanic rocks can typically be classified as one of the mafic or ultramafic members of the alkaline series (foidites, basanites or tephrites). In addition, some volcanic centers, such as the Laacher See, also erupted the more evolved intermediate products – phonolites (Schmincke, 2007).

The predominant type of volcanoes in the Eifel are scoria cones and maar-diatreme volcanoes. The eruption mechanisms of the maar-diatreme type volcanoes are not entirely understood, and two different views on maar formation were proposed in literature (e.g. White and Ross, 2011). The ‘magmatic’ (or ‘fluidization’) model initially considered that the diatreme structure, and its surface expression – the maar, are formed by vigorous degassing of low-viscosity melts during rapid transport through the crust. The sudden devolatilization was attributed mostly to exolution of CO<sub>2</sub>. However, explosive magma-groundwater interaction at a shallow level could also explain many features of maar eruptions (e.g. Schmincke, 2007 and ref. therein). It is still debated which of the two proposed eruption mechanisms – the magmatic/fluidization or phreatomagmatic – is more prevalent in the Eifel Volcanic Fields. Schmincke (2007) notes that most scoria cones appear to

have a multiphase eruption history, typically beginning with an initial phreatic or phreatomagmatic maar/tephra ring stage, followed by pyroclastic eruptions and the formation of a cone structure.

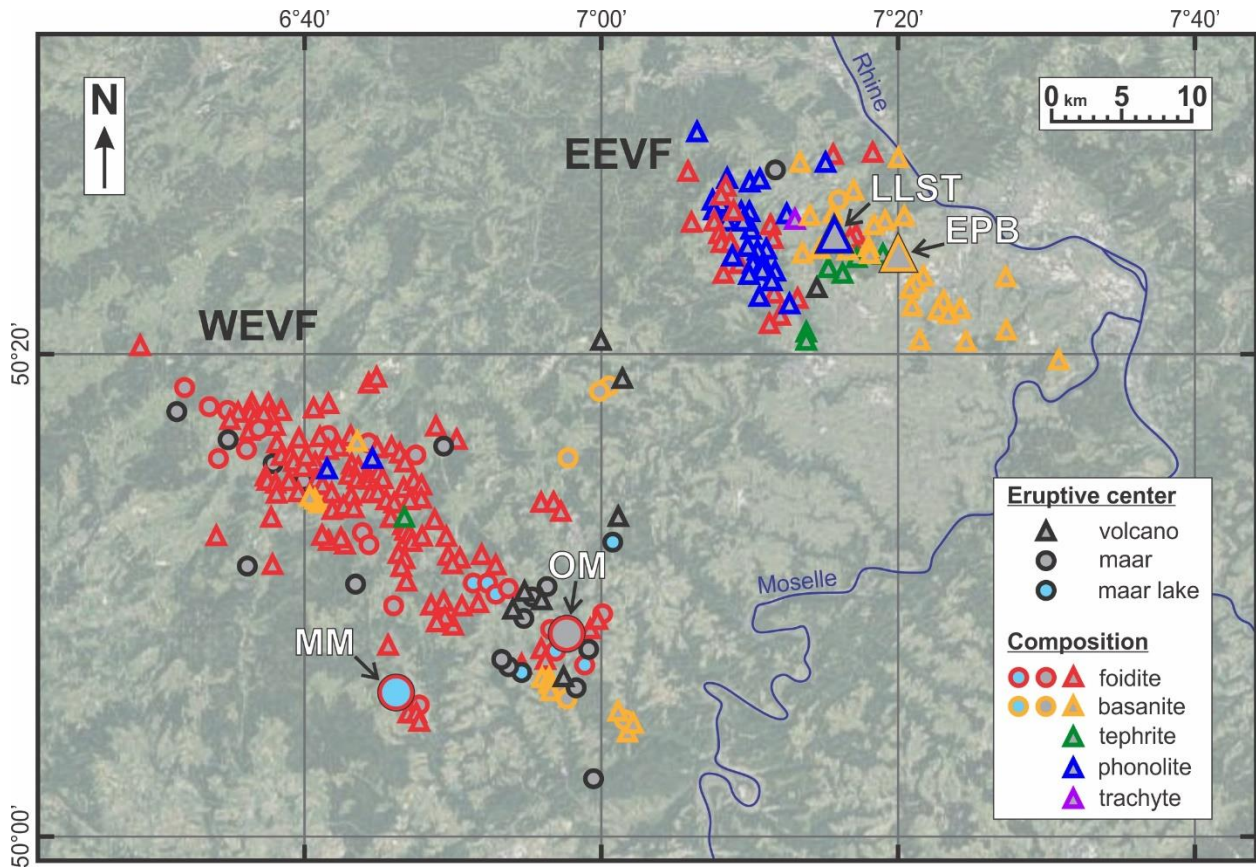


**Figure 7.2.1:** Distribution of eruptive centers in the Eifel Volcanic Fields (EVF) after Schmincke (2007) and Rausch et al. (2015). Symbol shapes indicate morphology of the volcanic centers, and the color specifies the dominant composition of the erupted material. Sampling locations from this study are shown with enlarged symbols, and are listed in Table 7.4.1. Abbreviations: EEVF – Easteifel Volcanic Field, WEVF – Westeifel Volcanic Field, EPB – Epplesberg, LLST – Lower Laacher See Tephra, OM – Oberwinkler Maar, MM – Meerfelder Maar.

### 7.3. Methods

Polished thin sections of all samples were first examined with standard polarized light microscopy, and the nanolite petrography was then observed in detail using a combination of FE-SEM and STEM systems at Tohoku University and the Bayerisches Geoinstitut. The images were processed using ImageJ software.

FE-SEM observation of the thin sections was carried out at an acceleration voltage of 15 kV and with a beam current of 1 nA, using a JEOL JSM7100F microscope at Tohoku University, equipped with a JEOL JED2300F energy dispersive spectrometer. Some samples were additionally examined at the Bayerisches Geoinstitut using a Zeiss LEO 1530 FE-SEM. Several target areas from three samples (MM, OM-1-2 and EPB) were selected for further TEM study.

TEM lamellae were extracted from target areas and thinned to transparency against a 200 kV electron beam. We used dual-beam focused ion beam / scanning electron microscopes (FIB/SEM) for TEM lamella preparation. The FIB system at the Bayerisches Geoinstitut is a FEI Scios, equipped with a FEI Easylift sample-lift-out manipulator system, a gallium ion source and a field-emission electron gun. At Tohoku University we used the FEI Quanta 3D 200i Dual Beam FIB/SEM system, with a gallium ion source and a thermal-emission electron gun. In addition, an electron transparent sample was prepared by milling the thin section of scoria fragment MM, using a conventional Ar milling machine at the Bayerisches Geoinstitut.

The lamellae were studied in detail at an acceleration voltage of 200 kV with a JEOL JEM-7100F scanning transmission electron microscope (STEM) at Tohoku University, equipped with a Gatan Orius 200D CCD camera and a JEOL JED2300 EDS system. A FEI Titan G2 80-200 STEM was used for observation at the Bayerisches Geoinstitut. Nanolites were imaged in conventional bright-field (BF) and dark-field (DF) mode. Selected-area electron diffraction (SAED) was used to confirm the identical orientation of magnetite particles in the nanorods, as well as the orientation of nanorods with respect to host crystals (Ch. 7.4.2). High-resolution transmission electron microscopy (HRTEM) allowed imaging of the dislocations within nanorods at the former attachment sites (Ch. 7.4.2). We also obtained sample images in scanning TEM mode with different detectors including BF, annular dark-field (ADF) and high-angle annular dark-field (HAADF). The overviews of the whole lamellae are composites of HAADF images.

Both FE-SEM and STEM semi-quantitative EDS mapping was used to distinguish different nanoparticle species (Fig. 7.4.7c), and we additionally confirmed the presence of magnetite in the nanolite populations with Raman spectroscopy (e.g. Di Genova et al., 2017).

## 7.4. Results

Samples were collected from four volcanic centers in the Eifel (Fig. 7.2.1), and a summary of sample information is given in Table 7.4.1. The samples include mafic and ultramafic eruptive products of the Meerfelder Maar, Oberwinkler Maar and the Eppelsberg volcano. In addition, one evolved sample, a phonolite from the Lower Laacher See Tephra (LLST), was collected as well.

**Table 7.4.1:** A summary of sample information. ‘\*’ phase composition was determined from optical properties and FE-SEM/EDS analyses. ‘\*\*’ phase composition was determined from optical properties, FE-SEM/EDS analyses and TEM/SAED. ‘\*\*\*’ phase composition was inferred using a combination of semi-quantitative FE-SEM/EDS, Raman spectroscopy and TEM/SAED. ‘?’ indicates that microlites/nanolites were observed, but were not studied in detail due to high sensitivity of the phonolitic glass to electron beam damage. Abbreviations: Amp – amphibole, Ap – apatite, AF – alkali feldspar, Cpx – clinopyroxene, Mc – mica, Leu – leucite, Mel – melilite, Mgt – magnetite, Ne – nepheline, Ol – olivine, Plag – plagioclase, Sod – sodalite group mineral (usually hauyne), S-melt – sulfide melt droplets.

Sample name	MM	OM-1-1	OM-1-2	OM-2	EPB	LLST
<b>Volcanic center</b>	Meerfelder Maar	Oberwinkler Maar	Oberwinkler Maar	Oberwinkler Maar	Eppelsberg volcano	Lacher See crater lake
<b>W/E Eifel</b>	West Eifel	West Eifel	West Eifel	West Eifel	East Eifel	East Eifel
<b>Material</b>	scoria	scoria	scoria	scoria	volcanic glass	pumice
<b>Fragment size</b>	≈ 2 cm	≈ 2 cm	≈ 0.5 cm	≈ 0.5 cm	≈ 2 cm	≈ 2 cm
<b>Rock</b>	foidite	basalt	foidite	foidite	basanite	phonolite
<b>Vesicular</b>	+	+	+	+	-	+
<b>Phenocrysts*</b>	Ol, Cpx, Sod, Mgn	Ol, Cpx	Ol, Cpx, Sod, Mgn	Ol, Cpx, Sod, Mgn	Cpx, Ol, Mc, Amp	AF
<b>Microlites**</b>	Mgt, Mel, Ol, Ap, Sod, Cpx, Ne	Cpx, Ol	Mgt, Mel, Ol, Ap, Sod, Cpx, Ne	Mgt, Mel, Ol, Ap, Sod, Cpx, Ne	Cpx, Leu, Mgn, Plag, Ap	?
<b>Nanoparticles***</b>	Mgt, Ap, S-melt, Ne	Cpx, TiFe-oxides	Mgt, Ap, S-melt, Ne	Mgt, Ap, S-melt, Ne	Mgt, Ap, S-melt	?

### 7.4.1. The FE-SEM study: an overview of nanolites in alkaline silicate melts

#### 7.4.1.1. Ultramafic foidite samples

Ultramafic samples were collected from two localities in the Westeifel Volcanic Field, the Meerfelder and Oberwinkler Maar (Fig. 7.2.1). All of the studied foidites have the same microlite mineral assemblage consisting of magnetite + melilite + olivine + apatite + sodalite-group mineral + clinopyroxene + nepheline (Fig. 7.4.1. and 7.4.2). The nanolite assemblage, as defined by Mujin et al. (2017), consists of magnetite + apatite + nepheline. Exolution of nanoscale sulfide melt droplets is commonly observed in foidite samples, as well (Fig. 7.4.1a, Fig. 7.4.6).

The most abundant nanolite species is magnetite. Magnetite nucleates both from the silicate melt, and heterogeneously on different mineral substrates. The most common substrates for heterogeneous magnetite nucleation are melilite and magnetite microlites. A specific spatial relationship of magnetite nanolites, with respect to bubble and microlite distribution, was observed in foidite MM. The highest number densities and smallest magnetite nanoparticle sizes appear to be restricted to the compositional boundary layers (CBLs) (Zellmer et al., 2016) of melilite microlites. With increasing distance from the melilite microlites, the number density of magnetite nanoparticles typically decreases, while the average crystal size increases (Fig. 7.4.3a, Fig. 7.4.7b, Fig. 7.4.10). The nanolite number density adjacent to gas bubbles is often low, or magnetite nanoparticles are entirely absent around the bubble-melt interfaces (Fig. 7.4.2a, Fig. 7.4.3c and d).

FE-SEM observation of WEVF foidites revealed a peculiar morphology of magnetite nanoparticles. The nanoparticles appear to grow preferentially in one crystallographic direction, resulting in formation of nanorod structures (Fig. 7.4.1). If a magnetite nanoparticle had initially nucleated heterogeneously on a microlite substrate, a topotaxial relationship between the host mineral and the magnetite nanorods is typically observed (Fig. 7.4.1b, Fig. 7.4.6b). Even detached from a particular host microlite, magnetite nanoparticles tend to aggregate in one direction and form rod-like structures. The magnetite nanorods are usually <200 nm in width, and may be as long as  $\approx 5 \mu\text{m}$ . The nanorods appear to form an interconnected three-dimensional network structure that has self-repeating rod orientations (Fig. 7.4.1a). These network structures may be locally interconnected at a scale of up to  $\approx 10 \mu\text{m}$ . The observed branching angles suggest that

nanorod networks have an overall lower symmetry, that is not consistent with  $Fd\bar{3}m$  magnetite (Fig. 7.4.9).

In addition to nanorod formation, magnetite crystal growth may occur by other mechanisms. Typical dendritic magnetite can occasionally be observed in both ultramafic and mafic samples (Fig. 7.4.2). Numerous short and robust branches that form  $90^\circ$  angles, characterize the dendritic magnetite. Nanorod branches are considerably finer and longer, and branching is not as frequent, as compared to dendrites. Unlike the nanorods, which preferentially develop away from gas bubbles, the dendritic magnetite is often located on bubble rims (Fig. 7.4.2). Semi-quantitative FE-SEM/EDS mapping showed that both nanorods and dendrites have a similar Ti- and Mg-rich composition (Fig. 7.4.1).

The second most common nanoparticles in Eifel foidites are sulfide melt droplets. The droplet size is typically in the ultrananolite-size range (<30 nm), but rare larger sulfide particles can be observed within the foidite volcanic glasses. Shaw (1997) studied the metasomatized mantle xenoliths from the Eifel, and described similar larger sulfide ‘blebs’. The sulfide droplets are homogeneously distributed throughout the volcanic glass. They may nucleate both heterogeneously – most often on magnetite nanorods – and homogeneously (Fig. 7.4.6). The sulfide droplets often provide nucleation sites for bubbles (e.g. Cáceres et al., 2021), and a ‘crescent moon’ structure may form as a result of surface tension between the silicate, sulfide and gas phase (Fig. 7.4.1a and 7.4.6). Subsequent TEM investigation revealed that some sulfide droplets have recrystallized to iron sulfides that were not studied in detail.

Apatite nanolites and ultrananolites are common in foidite samples as well. Homogeneous nucleation of apatite appears to predominate. However, apatite nanoparticles have occasionally been observed to incorporate into magnetite nanorods, so heterogeneous nucleation may not be excluded. Unlike magnetite, apatite nanolites are generally isometric and do not show any evidence of directional growth. Nepheline nanolites are rare and, were observed to nucleate exclusively on olivine microlites (Fig. 7.4.2.a).

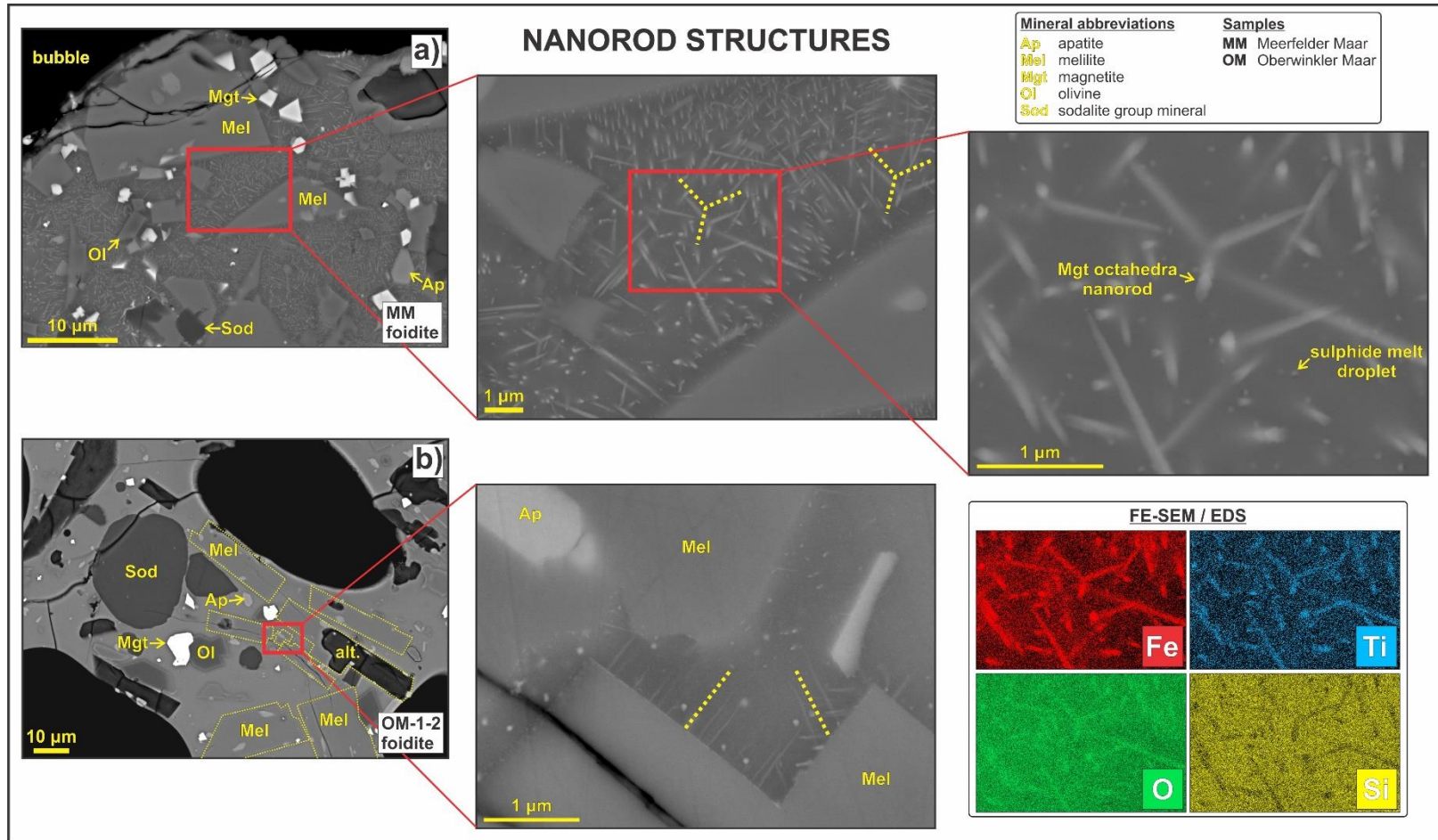


**Figure 7.4.1: a)** Representative BSE images from the Meerfelder Maar foidite show extensive development of magnetite nanorods. The self-repeating orientations of nanorods at a scale of approximately 5 µm are indicated by dashed yellow lines in the magnified image (center). The nanorods consist of linked magnetite nanoparticles, which are well resolved in TEM images (Ch. 7.4.2), but may occasionally be observed using FE-SEM as well; a nanorod with at least three visible octahedral magnetite grains is indicated in the magnified image on the right. Results of FE-SEM/EDS chemical mapping from the same area are shown below. **b)** Representative BSE images of OM-1-2 foidite from the Oberwinkler Maar. The glasses in scoria fragments from the Oberwinkler Maar exhibit variable crystallinity. Sample OM-1-2 is an example of low degree nanorod development.

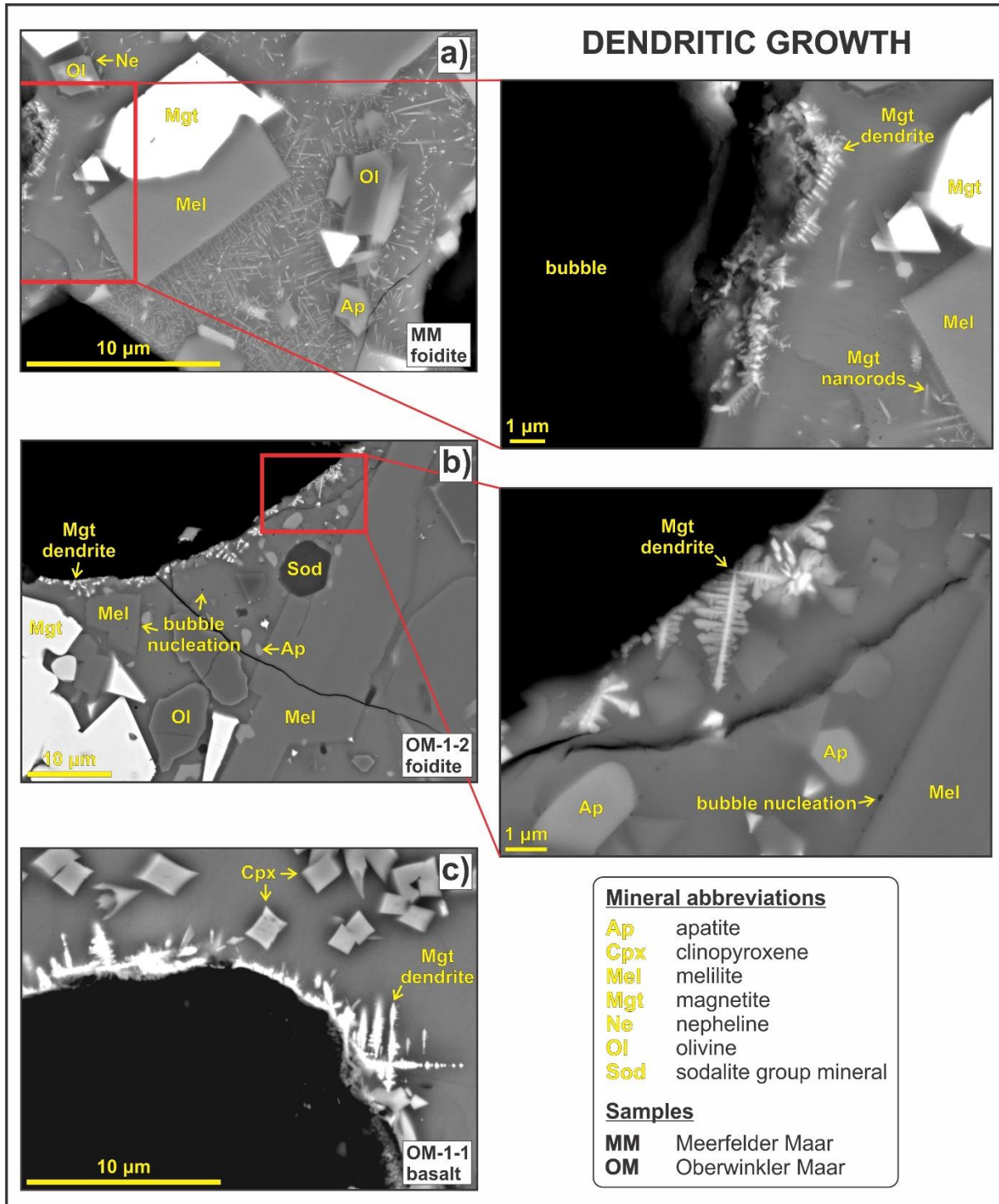


**Figure 7.4.2:** Examples of dendritic magnetite forming on gas bubble rims, both in foidites (**a and b**) and a basalt (**c**) sample. A typical spatial distribution of magnetite nanorods with respect to gas bubbles can be seen as well (**a**).

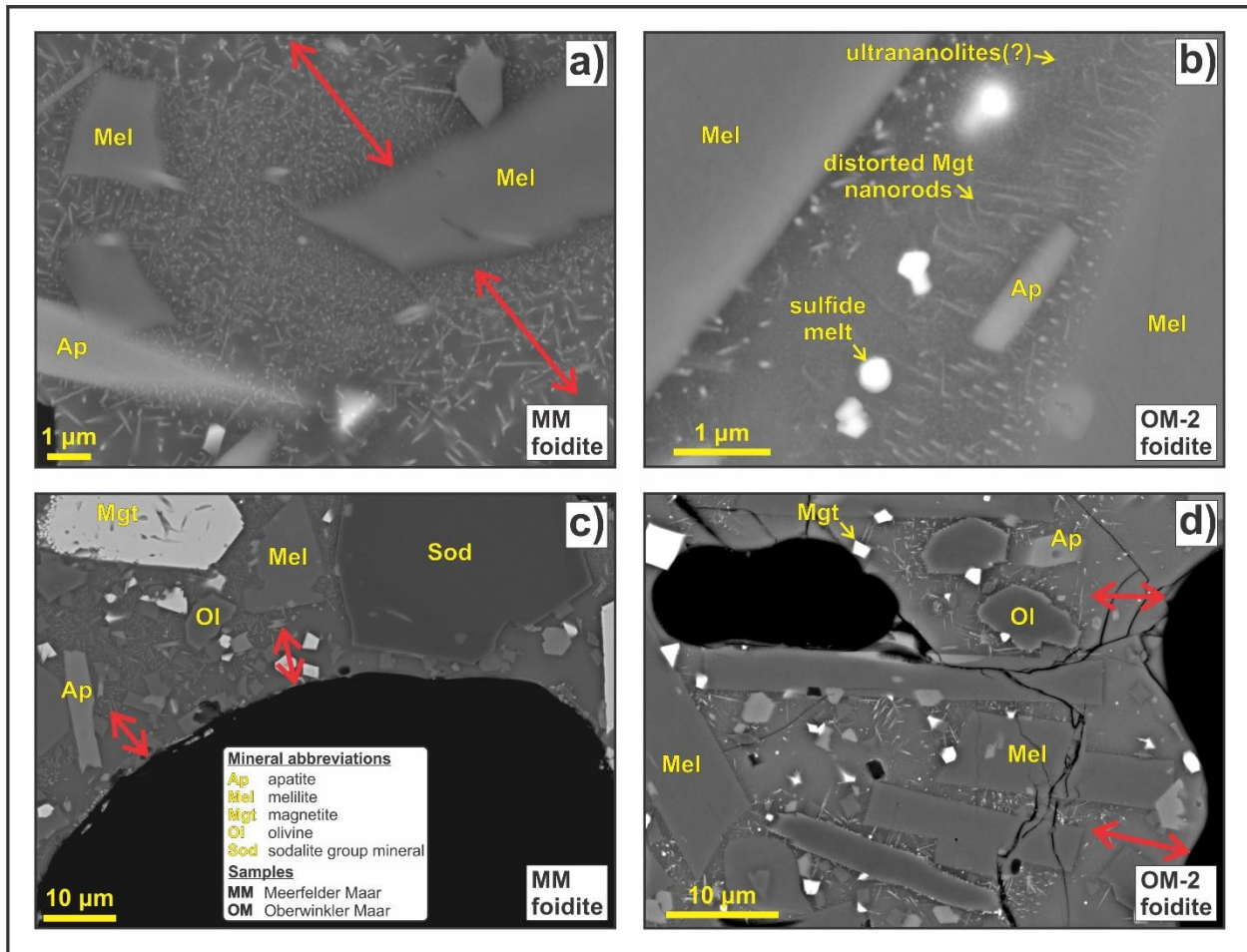


**Figure 7.4.3:** **a)** Coarsening of magnetite nanorods with increasing distance from a melilite microlite is indicated with red arrows. **b)** Low crystallinity foidites from the Oberwinkler Maar often contain distorted magnetite nanorods. **c)** and **d)** Examples of the spatial distribution of nanorods with respect to gas bubbles. Regions with low number density of nanorods are indicated with red arrows.

#### 7.4.1.2. Mafic and intermediate samples

One of the samples from Oberwinkler Maar (OM-1-1) was classified as a basalt, based on phenocryst optical properties. The sample is characterized by abundant clinopyroxene microlites, and a nanolite assemblage of TiFe-oxides + clinopyroxene (Fig. 7.4.4). The observed nanolite number density is generally lower, as compared to foidite samples. The clinopyroxene microlites and nanolites have normal chemical zoning (Fe- and Ca- rich cores; Mg- and Al- rich rims) and habits indicative of rapid crystallization. In addition, we observed radial aggregates of TiFe-oxides with a chemical composition similar to nanoscale magnetite from foidite samples. The morphology of aggregates suggests initial precipitation of nearly isometric iron oxide nanoparticles from the melt (“oxide 1”), followed by radial growth of another unknown lath-shaped (“oxide 2”) phase

(Fig. 7.4.4). An increase in number density of radial aggregates and extensive precipitation of dendritic magnetite around gas bubbles was observed in some regions of the thin section.

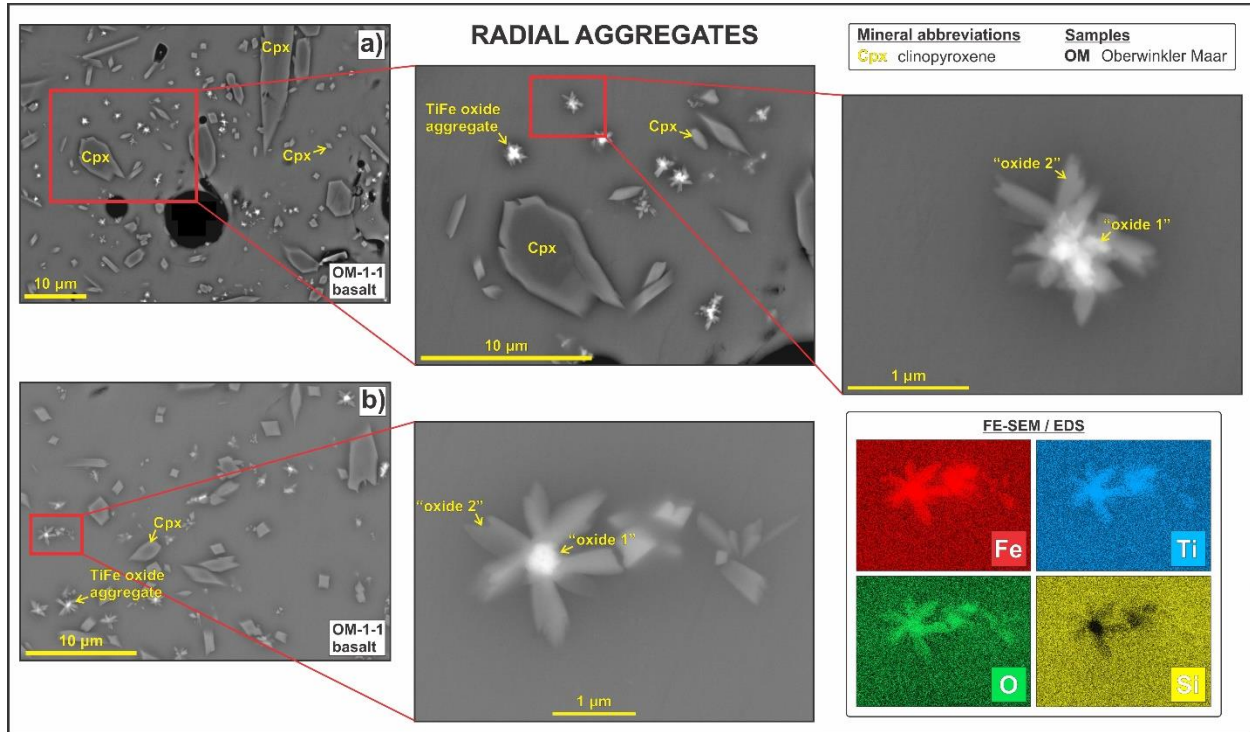


**Figure 7.4.4:** Radial aggregates of TiFe-oxides in the basalt sample OM-1-1. The aggregates are thought to form by two-stage crystallization. The growth of “oxide 1” is followed by development of a lath-shaped “oxide 2” phase.

The basanite sample, collected at the Epplesberg volcano, has a similar nanolite mineral assemblage as foidites (magnetite + apatite, with nanoscale sulfide melt droplets), but differs in microlite composition (clinopyroxene + leucite + magnetite + plagioclase + apatite). Based on FE-SEM examination, the nanolite nucleation and crystal growth mechanisms in sample EPB resembled foidites from the Westeifel Volcanic Field. In the absence of melilite microlites, which are common in foidites, the preferred host minerals for heterogenous magnetite nucleation in EPB were leucite and plagioclase (Fig. 7.4.5).

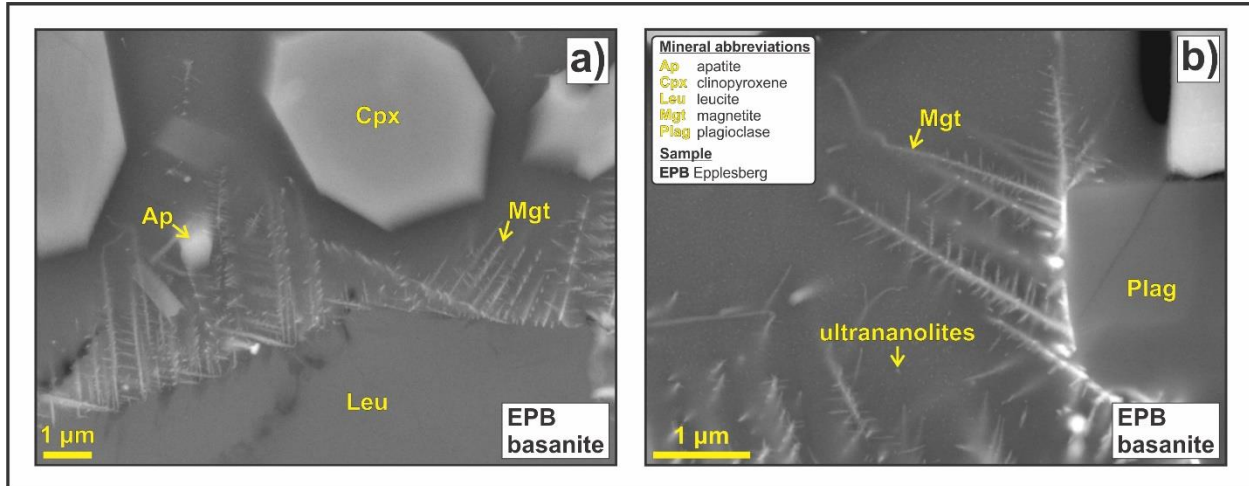


**Figure 7.4.5:** Fine-branching magnetite structures from the Epplesberg basanite. Magnetite typically nucleates heterogeneously on leucite (a) and plagioclase (b) microlites, and the crystal growth mechanism resembles nanorods from foidite samples.

The phonolite sample from the Laacher See crater lake is a highly degassed and mostly pristine volcanic glass, with rare alkali feldspar phenocrysts. At least two different phases in the nanolite size range ( $<1 \mu\text{m}$ ) were sporadically observed, but were not studied in detail due to high sensitivity of the phonolitic glass to beam damage. The nanolites were isometric, and no evidence of crystal aggregation or growth in a preferred orientation was found.

#### 7.4.2. Oriented attachment of magnetite nanoparticles

The TEM study primarily focused on the crystal growth mechanism of magnetite nanorods. For TEM observation, we selected foidite scoria fragments MM (Meerfelder Maar) and OM-1-2 (Oberwinkler Maar). In addition, we examined the fine-branching magnetite structures from the Epplesberg (EPB) basanite.

The morphology of magnetite nanorods from Westeifel foidites is consistent with oriented attachment (OA). Oriented attachment is a relatively rare non-classical crystal growth mechanism. It occurs when pre-existing nanoparticles translate and rotate unimpeded in a liquid medium in order to achieve crystallographic alignment prior to aggregation (e.g. De Yoreo et al., 2015). This allows reduction of the total surface energy of the system by eliminating the energy related to the attachment surfaces (Penn and Banfield, 1999). A notable characteristic of oriented attachment is the preferred one-directional crystal aggregation, which results in assembly of nanorod structures (Penn and Banfield, 1999). The nanorods are coherent single crystals, but observable dislocations can often be found at the former attachment sites (Penn and Banfield, 1998). Such dislocations are diagnostic of the oriented assembly of primary nanoparticles, as opposed to nanorod growth by dissolution-precipitation. Under certain conditions, the nanorods may form extensive superstructures with unexpected symmetries (Penn, 2004).

The highly developed nanorods from sample MM consist of either octahedral or anhedral (round) magnetite nanoparticles. We observed that entire sections of nanorods may be simultaneously aligned in diffraction condition, suggesting internal crystallographic coherence. The obtained SAED are consistent with  $Fd\bar{3}m$  magnetite structure (Fig. 7.4.6a). Neighboring nanorods that aggregated in different spatial directions may also have a common crystallographic orientation (7.4.6b). This supports the idea of interconnected three-dimensional nanorod networks on a scale of several  $\mu\text{m}$ , initially inferred from FE-SEM observation (Ch. 7.4.1, Fig. 7.4.1a). In addition, HRTEM imaging confirmed the existence of dislocations at the attachment sites within a coarse magnetite nanorod from sample MM (Fig. 7.4.7b1. and b2).

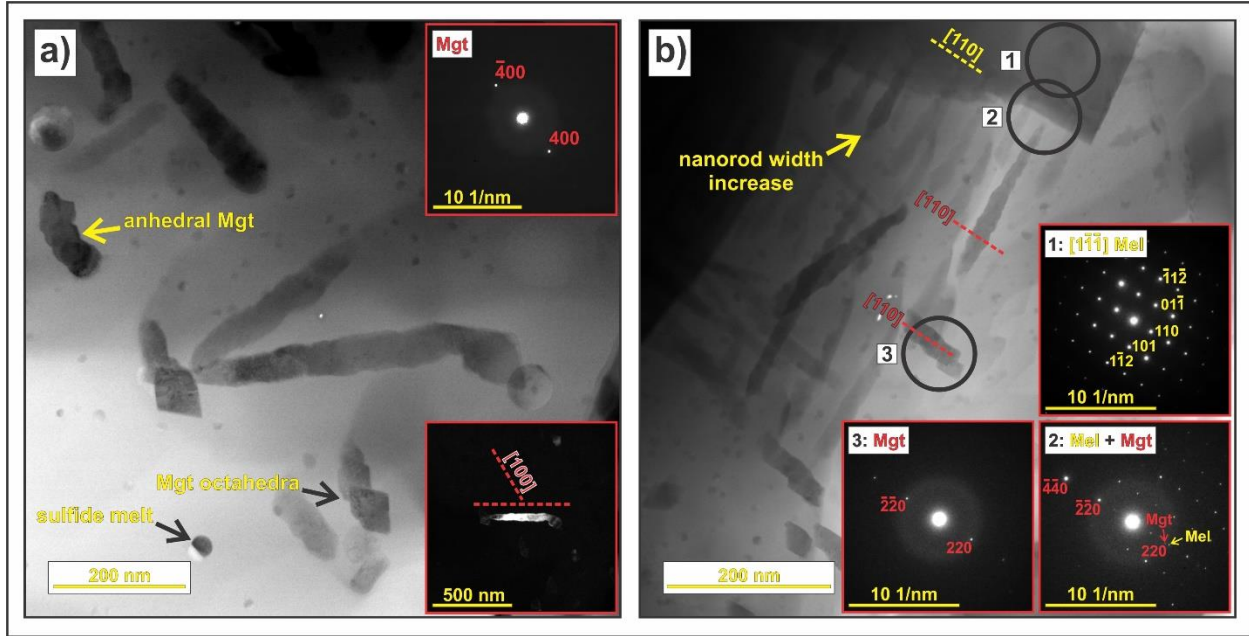


**Figure 7.4.6:** STEM annular dark field (ADF) images of the Meerfelder Maar (MM) scoria fragment. The sample was thinned to electron transparency using the conventional Ar-milling method. **a)** An example of typical nanorod morphologies, with nanorods consisting of either octahedral or anhedra (round) nanoparticles. The nanorods are coherent single crystals (visible in the conventional DF image) and consistent with  $Fd\bar{3}m$  magnetite structure, according to the selected area diffraction (SAED). The  $[100]$  crystallographic direction closes an approximately  $60^\circ$  angle with the apparent elongation direction of the nanorod. **b)** An example of a topotaxial relationship between a magnetite nanorod and the melilite host crystal. The  $[110]$  of the melilite substrate (1) is nearly aligned with the  $[110]$  of the magnetite nanorod (2). A neighbouring nanorod, which developed in a different spatial direction, has a similar crystallographic alignment as the melilite-hosted nanorod (3). Sulfide-melt droplets and gas bubbles with crescent-moon textures are visible in both images.

The nanorods in sample OM-1-2 are assembled exclusively from anhedra nanoparticles, and they have a distorted morphology (Fig. 7.4.3b, Fig. 7.4.8b). The distortion may have occurred as a result of eruption-related events (i.e. magma fragmentation), but it may also be a primary feature. Liao et al. (2012) performed in-situ TEM observation of  $Pt_3Fe$  nanorod assembly in organic solvents. The in-situ observations show initial assembly of distorted flexible nanorods that eventually straighten into rigid shapes, such as the ones commonly encountered in the volcanic glass of MM scoria fragment. We observed co-existing straight and distorted nanorods in sample MM, which suggests that the morphology observed in OM-1-2 may indeed be primary and unrelated to the eruption.

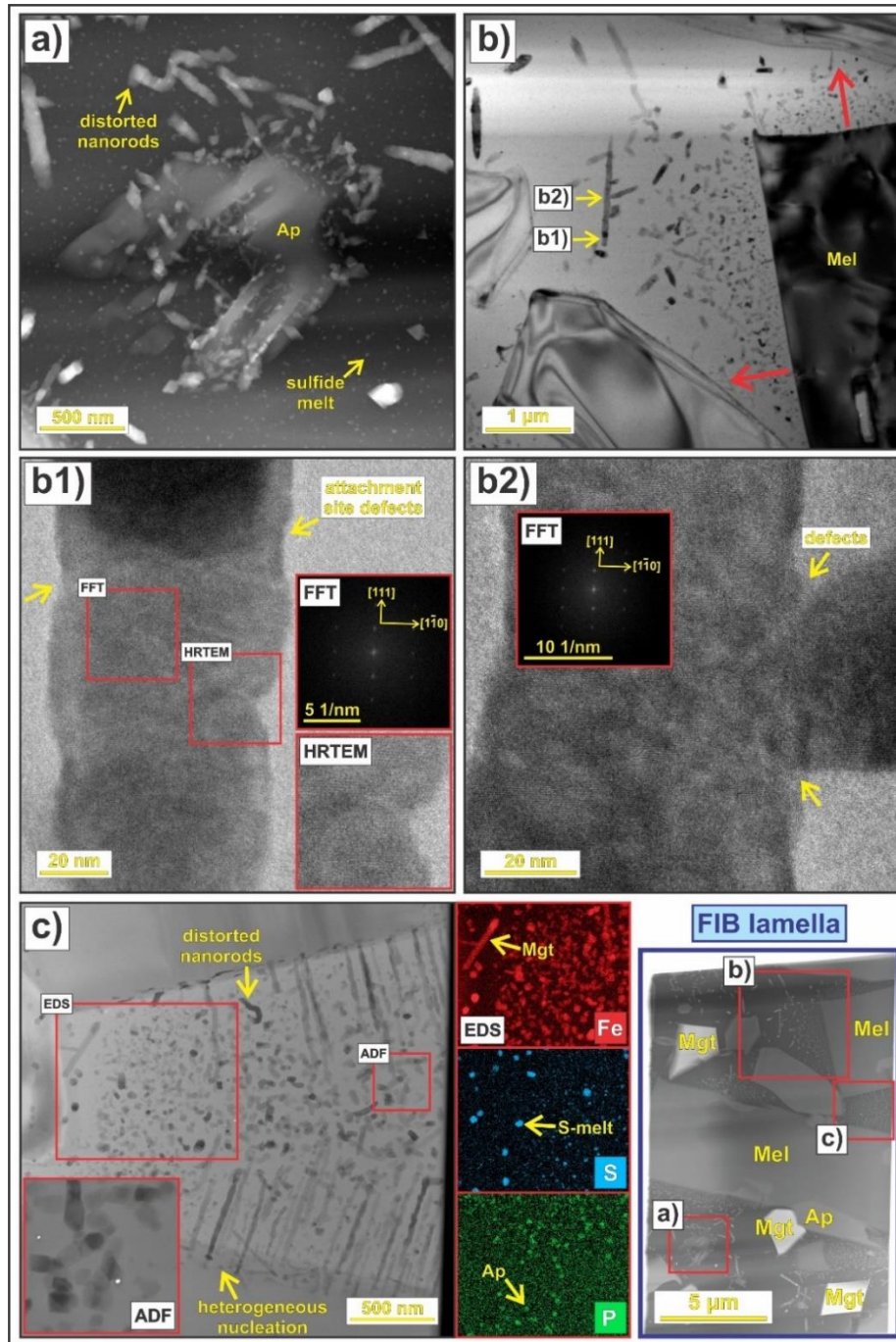


**Figure 7.4.7:** An overview of the FIB lamella (lower right corner) extracted from the MM scoria fragment. **a)** High angle annular dark field (HAADF) image of an apatite microlite as host for heterogeneous magnetite nucleation. Both distorted and rigid nanorods are visible. **b)** A conventional bright field (BF) image showing the variation in magnetite nanoparticles with increasing distance from the melilite host (red arrows). Areas observed in HRTEM mode are indicated as well (b1 and b2). **b1)** High resolution TEM (HRTEM) image of a magnetite nanorod with visible dislocations at the former attachment sites. **b2)** HRTEM image of the connection between a primary and secondary nanorod branch. A dislocation was observed at the branching site. Fast Fourier transform (FFT) indicates that the entire nanorod is in crystallographic alignment, with the primary branch assembling normal to a  $\{111\}$  plane. **c)** An ADF image of an area between two melilite hosts with high ultrananolite number density. Heterogeneous nucleation sites are visible at the inclined melilite surface. Distorted and straight nanorods co-exist in the same area. The EDS mapping demonstrates the presence of at least three different ultrananolite species: magnetite, sulfide melt droplets and apatite. The short magnetite chains (e.g. ADF image detail in the lower left corner) may occasionally incorporate other ultrananolite species.

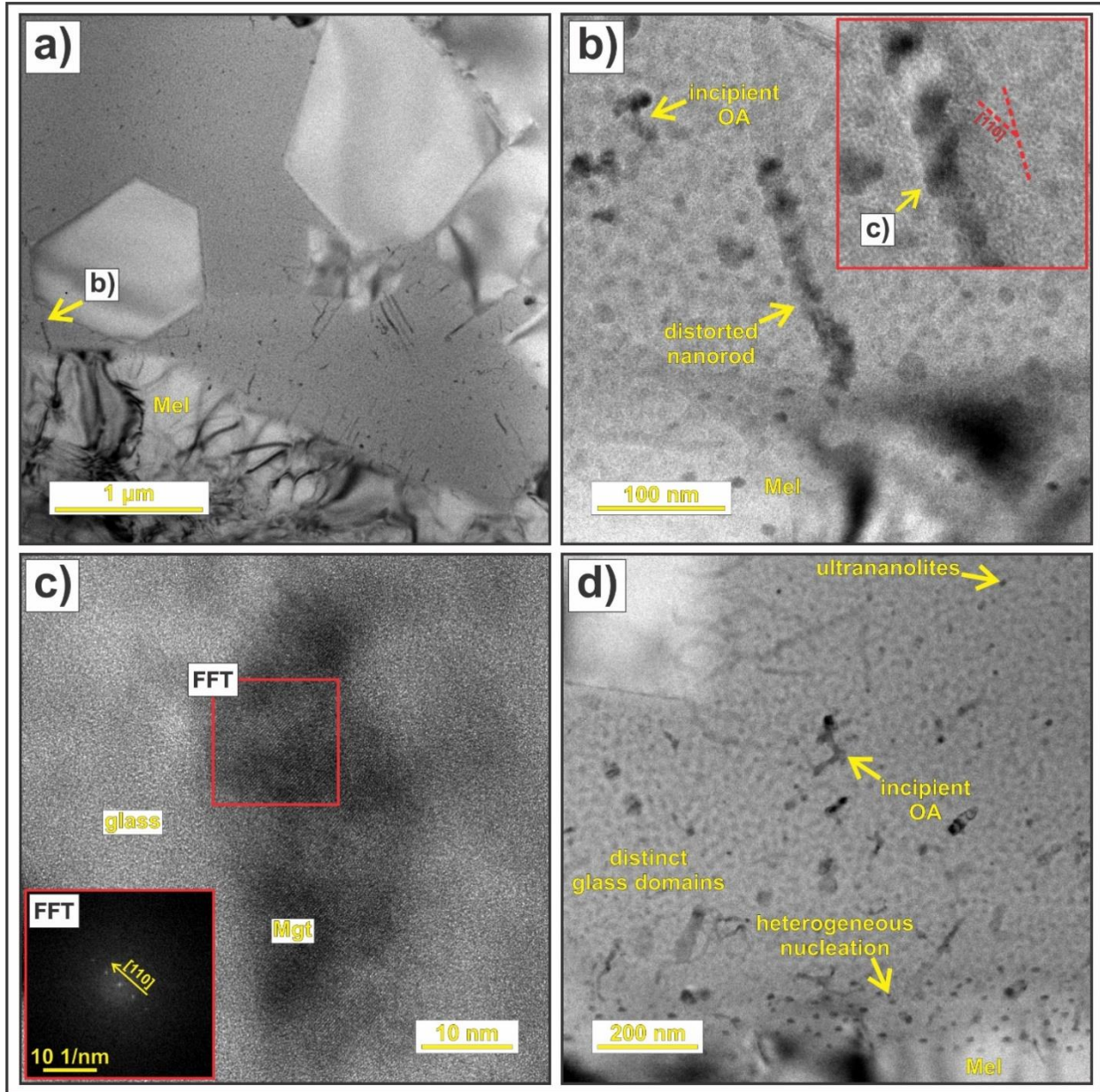


**Figure 7.4.8:** *a)* A conventional BF image showing an overview of the FIB lamella extracted from an OM-1-2 scoria fragment. *b)* A conventional BF image and a HRTEM image (upper right) of a distorted melilite-hosted magnetite nanorod. *c)* A higher magnification HRTEM image, with visible magnetite lattice fringes. *d)* A BF image of the volcanic glass. Formation of short incipient nanorods is visible. Nucleation of un-attached ultrananolites, likely magnetite, and separation of distinct structural and/or compositional domains in the melt is indicative of a rapid quench, following the nanorod assembly.

The volcanic glasses rapidly deteriorated in interaction with the 200 kV electron beam, and we collected limited crystallographic information about internal nanorod organization. In one instance, HRTEM images indicate that the nanorod elongation direction is normal to a {111} magnetite plane. In other cases, we were able to obtain SAED with one set of crystal planes aligned

into diffraction condition. We measured the apparent angles between nanorod elongation and a normal to the diffracting planes. We observed that the nanorods close angles of approximately  $0^\circ$  and  $60^\circ$  with a normal to  $\{100\}$ , as well as  $0^\circ$ ,  $35^\circ$  and  $90^\circ$  with a normal to  $\{110\}$  planes. In addition, we performed measurements of apparent branching angles of nanorods in a series of FE-SEM BSE images from sample MM. The branching angles have an approximately normal distribution around  $70.2^\circ$  and  $111.5^\circ$  (Fig. 7.4.9). The measurement was performed only when the connection between the two branches was in focus, as shown in Figure 7.4.9. The measured values are generally consistent with the dihedral angle of a regular octahedron (i.e.  $\{111\}$  in  $Fd\bar{3}m$ ). We conclude that the  $\{111\}$  planes are the most plausible attachment surfaces for the majority of nanorods, based on the  $\mu\text{m}$ -scale nanorod geometry and the available crystallographic information.

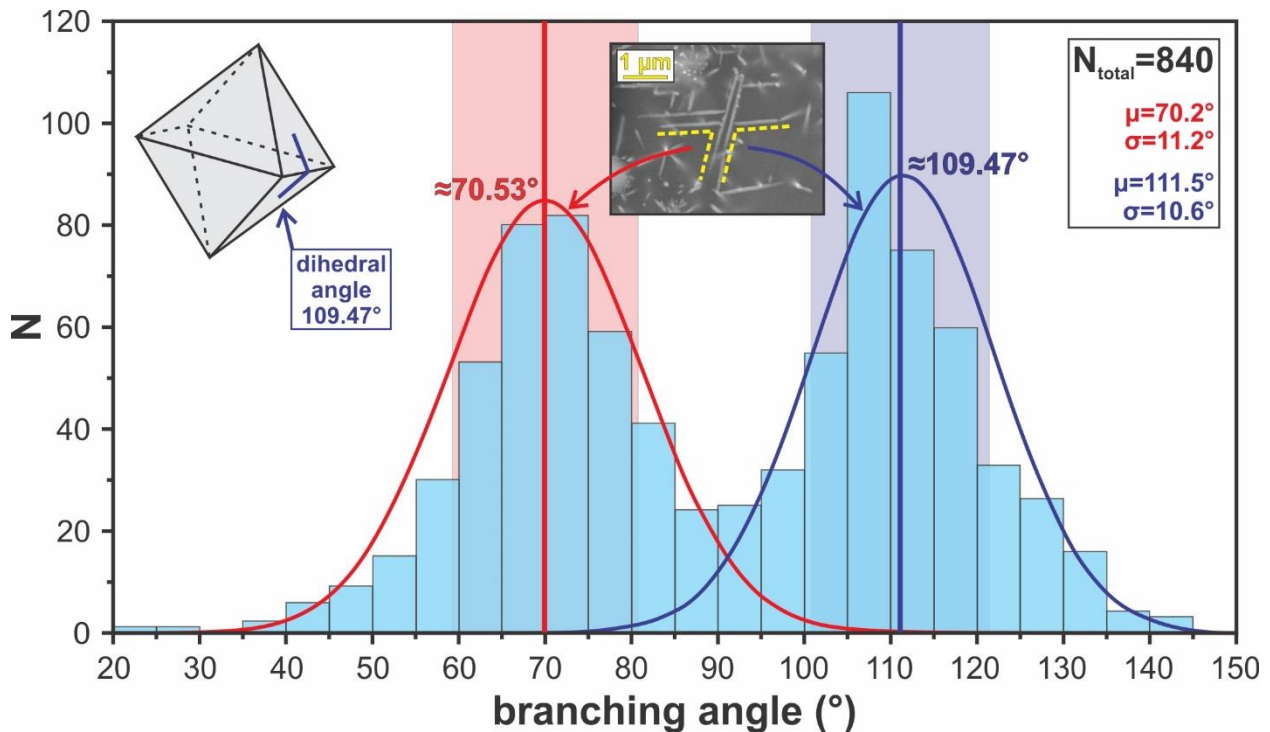


**Figure 7.4.9:** Measurement of the apparent nanorod branching angles in scoria fragment MM. The observed branching angles have an approximately normal distribution around  $70.2^\circ$  and  $111.5^\circ$ , consistent with the dihedral angle of a regular octahedron (upper left corner). The angles are measured only when the connection between the branches is clearly in focus (an example of a measurement is shown in the BSE image). The sample-beam interaction volume exceeds the average nanorod size, thus the BSE images provide a three-dimensional view of nanorods and the probability of directly observing the true branching angle is reduced (see standard deviations).

As discussed in Chapter 7.4.1, the primary nucleation and attachment sites of magnetite nanoparticles are surfaces and compositional boundary layers (CBLs) of melilite microlites. The relationships between the average magnetite nanoparticle size, with respect to the distance from

the melilite host crystal, were measured (Fig. 7.4.10a and c). The measurements were obtained from the FIB lamellae, where the relationships were clearly visible. We include both the diameters of un-attached nanoparticles within the melilite CBLs, as well as the widths of nanorods at the apparent half-length. The apparent lengths of melilite-hosted nanorods were measured in both TEM and FE-SEM images (Fig. 7.4.10b. and d). The nanorod lengths (Fig. 7.4.10b. and d) and the size-distance relationships (Fig. 7.4.10a and c) were used to estimate an average number of attachment events required to assemble the observed nanorods (Fig. 7.4.10b and d).

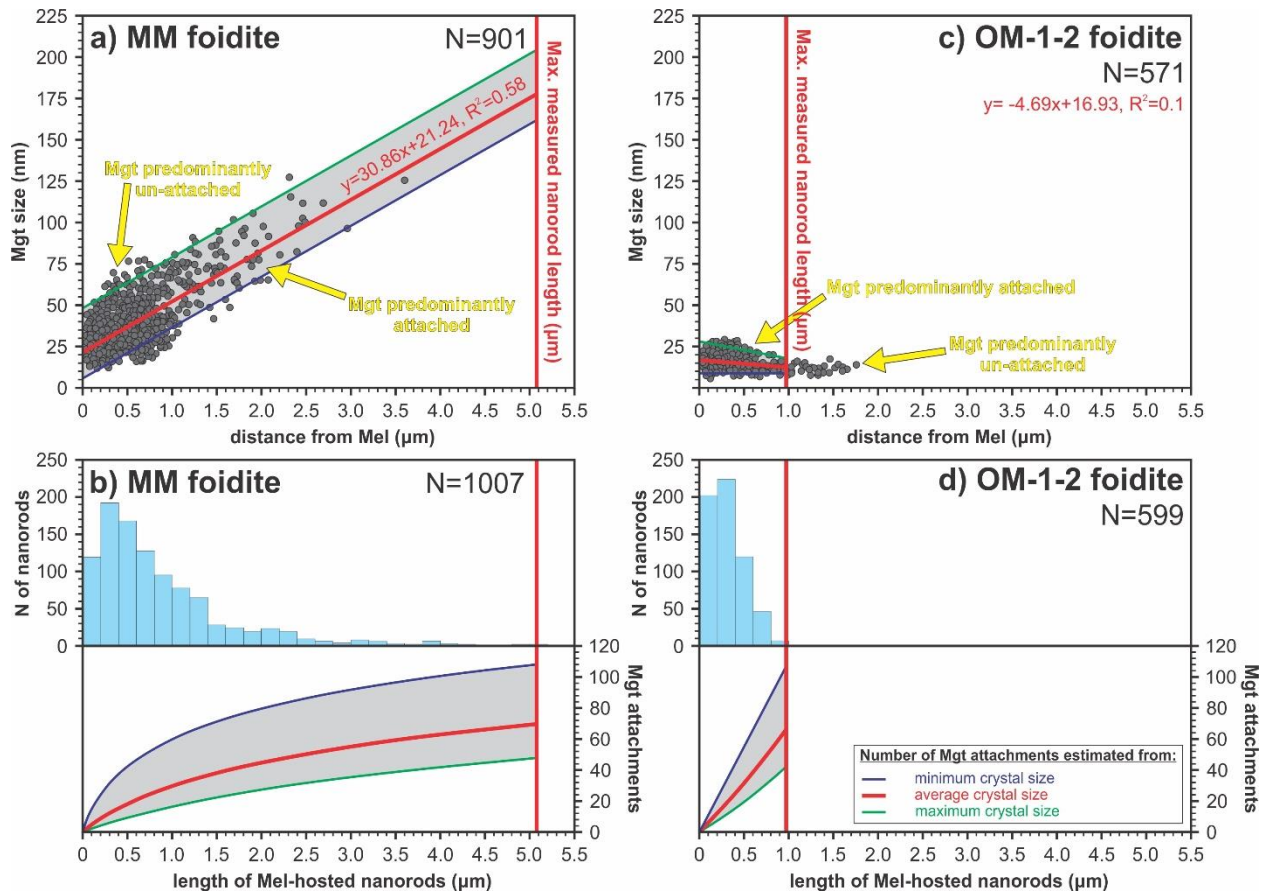


**Figure 7.4.10:** Characterization and comparison of melilite-hosted nanorods in samples MM and OM-1-2. **a) and c)** Measurements of average magnetite size with distance from the nearest melilite host. Average magnetite nanoparticle size in MM increases with distance from melilite surfaces. In OM-1-2, the average magnetite nanoparticle size remains nearly constant with distance from the host microlite (see weak negative correlation in the upper right corner of image c). **b) and d)** Histograms of the measured melilite-attached nanorod lengths, compared with the estimated number of attachment events necessary to produce a nanorod of a given length. The length of nanorods in MM is variable, with maximum length of 5  $\mu\text{m}$ . Nanorods in OM-1-2 have uniform length, with a maximum value of 1  $\mu\text{m}$ . The estimated numbers of attachment events are similar for both samples, and the differences in nanorod morphology arise mainly from different initial crystal size distributions of nanorod-forming nanoparticles.

The average size of magnetite nanoparticles in sample MM increases systematically with distance from the nearest melilite surface. At any given distance from the melilite host, the nanoparticle size may vary by approximately 50 nm. The lengths of melilite-hosted nanorods in sample MM are variable as well, with the majority of nanorods consisting of approximately 20 to 30 pre-existing nanoparticles and reaching lengths of 0.3 to 0.6  $\mu\text{m}$ . Nanorods with lengths up to 2.5  $\mu\text{m}$ , assembled by approximately 60 attachment events, are commonly observed as well. The longest measured nanorod was  $\approx 5 \mu\text{m}$ , and is estimated to consist of up to 70 primary particles. The nanorods usually have a particular morphology, where the width of the nanorod increases with distance from the melilite surface (Fig. 7.4.6b). These features suggest that magnetite nanoparticles preferentially attach to nearest-neighbors, as opposed to having long translation trajectories prior to assembly. The final attachments (at the nanorod ends) often include magnetite particles with octahedral habits (Fig. 7.4.6a), which may be interpreted as a result of Ostwald ripening occurring before and/or simultaneously with nanorod assembly, possibly with preferential coarsening of un-attached particles. It should be noted, however, that nanorod-forming particles may coarsen by dissolution-precipitation following the attachment (Liao et al., 2012). The considerable variability of magnetite nanoparticle size and shape, as well as differing nanorod lengths, are suggestive of multiple nucleation-ripening-assembly episodes.

The morphology of nanorods from sample OM-1-2 is indicative of a shorter one-stage assembly process. The average magnetite sizes and nanorod widths are both nearly constant with increasing distance from the melilite host. The observed nanorod lengths are uniform. Majority of nanorods consist of approximately 20 primary particles and are between 0.2 and 0.4  $\mu\text{m}$  long. The longest observed nanorod reached nearly 1  $\mu\text{m}$  length and is estimated to contain about 70 magnetite individuals. Interestingly, the estimated number of attachment events for both the average and maximum observed nanorod lengths in MM and OM-1-2 are similar. The differences in nanorod morphologies seen in MM, as compared to OM-1-2, arise mainly due to contrasting devolatilization/cooling histories and variable crystallization timescales, which initially produced magnetite nuclei of different sizes. The nanorod-forming particles in sample OM-1-2 are uniform in size (15-30 nm), and somewhat coarser than the un-attached magnetite nuclei ( $\approx 10 \text{ nm}$ ) in the surrounding glass. The sample OM-1-2 likely underwent one episode of magnetite nucleation and

nanorod assembly, followed by a rapid quench event that precipitated the 10 nm ultrananolites and produced distinct structural/compositional domains in the volcanic glass (Fig.7.4.8d).

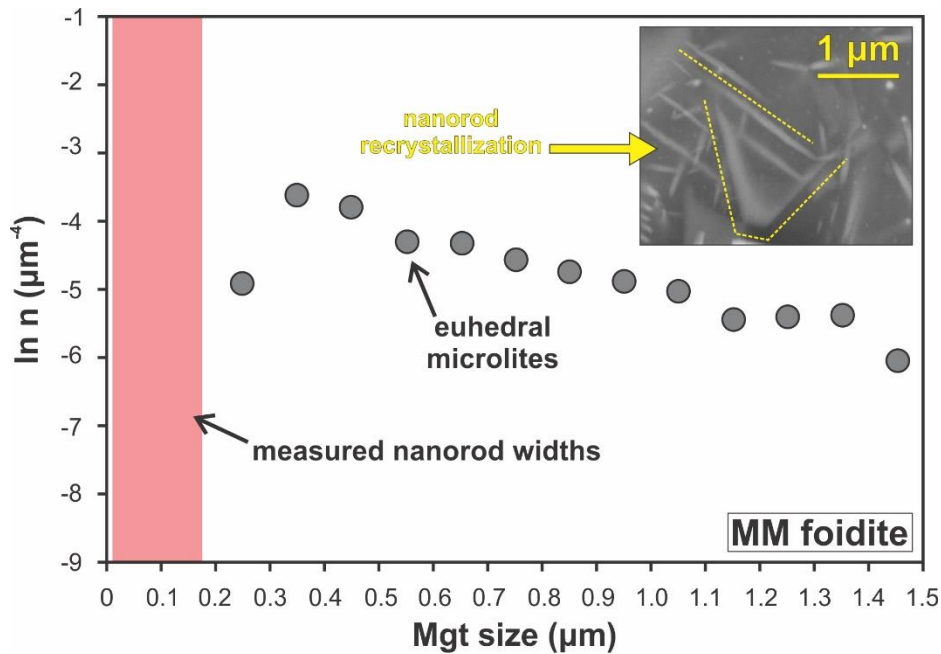


**Figure 7.4.11:** Conventional CSD plots of euhedral magnetite from scoria fragment MM, compared with the observed nanorod widths. The volumetric population densities of euhedral crystals are plotted against 0.1  $\mu\text{m}$  crystal size bins. Note the reduction in population density of euhedral nanoparticles with 200 to 300 nm size, and the example of a partial annealing of nanorods into a  $\approx 1.2 \mu\text{m}$  equilibrium-shaped crystal. These features are suggestive of a hiatus in crystallization just prior to nanorod assembly, potentially with an additional quiescent period that overlapped with the time of oriented attachment and allowed partial annealing into equilibrium-shaped crystals.

Crystal size distributions (CSD) of euhedral magnetite microlites and nanolites were measured in scoria fragments MM, OM-1-2 and OM-2 on approximately  $360 \times 180 \mu\text{m}$  areas. This resulted in 200 to 1600 measurements per sample, depending on crystallinity. The measurements were summarized in conventional plots of volumetric population density ( $n$ ) (Higgins, 2000). The CSD of the nanorod-forming nanoparticle population could not be re-constructed, but we compared the observed nanorod widths with population densities of euhedral crystals. Nanorod widths in OM-2 were measured only by FE-SEM, and are less reliable. A marked reduction in population density of  $\approx 200$  to 300 nm magnetite nanoparticles was observed in samples MM (Fig. 7.4.11), OM-1-2, and in 4 out of 6 scoria fragments collected from the OM-2 eruptive layer. We also note that annealing of magnetite nanorods into equilibrium-shaped crystals is possible via dissolution-precipitation of iron oxide (Fig. 7.4.11). These features are suggestive of a hiatus in crystallization just prior to nanorod assembly, potentially with an additional quiescent period that overlapped

with the time of oriented attachment and allowed partial annealing into equilibrium-shaped crystals.

In addition to foidite samples, we briefly studied the fine-branching magnetite structures from basanite sample EPB. Numerous secondary and tertiary branches can be resolved in STEM annular dark field (ADF) images (Fig. 4.7.12b), consistent with typical dendritic growth. The primary branches are relatively fine and long, and often grow at a specific angle with respect to the host crystal (Fig. 7.4.5. and Fig.7.4.12a). It is, therefore, possible that these magnetite structures initiated as nanorods, and then transitioned into dendritic growth. In addition, ultrananolites and short nanorod-like structures were observed in the volcanic glass, away from the dendritic magnetite (Fig. 7.4.12c).

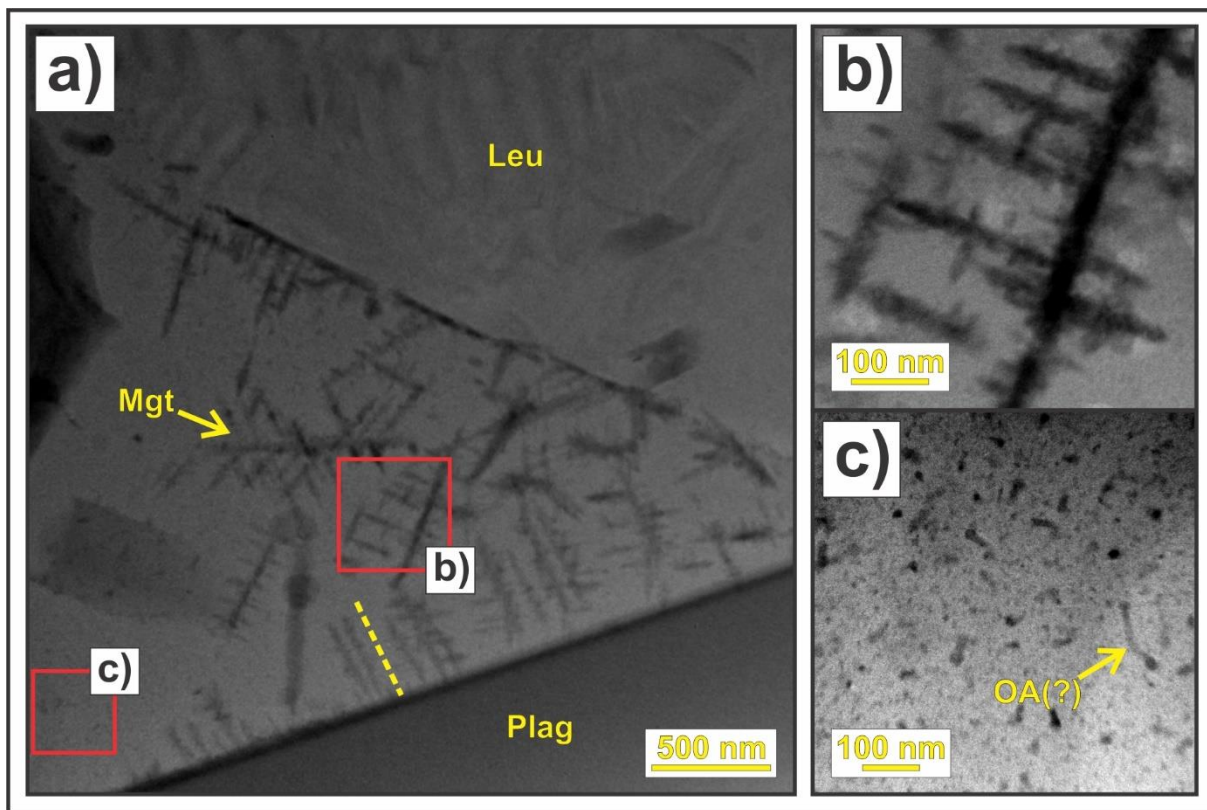


**Figure 7.4.12:** **a)** An overview ADF image of the FIB lamella extracted from the Epplesberg basanite (EPB). The dashed yellow line indicates the preferred orientation of the primary magnetite branches with respect to the plagioclase host. **b)** A high magnification ADF image showing secondary and tertiary branches of the magnetite structure, consistent with dendritic growth. **c)** Ultrananolites and nanorod-like structures in the volcanic glass of the EPB basanite, resembling the incipient nanorod formation from OM-1-2 foidite.

## 7.5. Discussion

Non-classical nucleation and crystal growth pathways control the kinetics of nanolite precipitation in alkaline silicate melts (Ch. 7.4.1) from the Eifel. The most abundant species in late-stage mineral assemblages is magnetite. We observed that different growth mechanisms may govern magnetite crystallization, and had resulted in formation of various nano-scale morphologies that include dendrites, nanorods and euhedral crystals.

We found compelling evidence that nanorod magnetite structures formed by oriented attachment (OA) of primary nanoparticles (Ch. 7.4.2). Oriented attachment has been reported in a number of synthetic systems (Penn, 2004; DeYoreo et al., 2015), as well as in biomineralization-related aquatic environments (e.g. Banfield et al., 2000), but to our knowledge this is the first observation in a natural magmatic system.

Better understanding of oriented attachment could allow advances in nanomaterial design and synthesis (Liao et al., 2012; DeYoreo et al., 2015), and has attracted considerable interest over the last several decades. However, the physics and chemistry of the liquid-nanoparticle interfaces, and the forces that govern particle motion and assembly are not well known (DeYoreo et al., 2015). Our findings demonstrate that oriented attachment may occur in a silicate liquid medium, which potentially offers new constraints for understanding the nanoparticle assembly processes on a fundamental level. In addition, it shows that nanoparticle attachment should be expected in a wide range of natural environments, including the extreme conditions of magmatic systems.

We suspect that viscosity of the liquid medium may be a limiting factor for oriented nanoparticle assembly in silicate systems. Silicate melts have orders of magnitude higher viscosities than the liquid media in both experimental and natural systems where oriented attachment was originally recognized (e.g. Penn and Banfield, 1998; Banfield et al., 2000). Within our own dataset, nanorod formation by oriented attachment could be confirmed only in the foidite scoria fragments, while different crystal growth mechanisms were observed in the more viscous mafic and intermediate melts (Ch. 7.4.1. and 7.4.2). In addition, previous studies of nanoparticles in silicate melts of higher viscosities – rhyolites, andesites and basalts – had not revealed obvious nanorod structures (Sharp

et al., 1996; Mujin and Nakamura, 2014; Mujin et al., 2017; Mujin and Nakamura, 2020; Di Genova et al., 2018; Di Genova et al., 2020).

Mujin et al. (2021) recently performed in-situ FE-SEM observation of Fe and Pt nanoparticle coalescence in rhyolitic melts at magmatic temperatures. Although the crystallographic alignment of nanoparticles could not be directly confirmed, and no nanorod structures developed, both Fe and Pt clearly coarsened by particle attachment mechanisms. The particle movements in the melt appeared to be limited by viscosity and surface tension phenomena. Overall, this suggests that crystal growth by particle attachment may be a common process in magmatic systems. However, development of complex and highly organized nanorod structures appears to be limited to extremely low-viscosity ultramafic – and possibly mafic – melt compositions, such as the Eifel foidites.

Direct observation of oriented attachment from in-situ TEM and FE-SEM experiments demonstrates that nanoparticle alignment and aggregation is not instantaneous. Experiments at near-ambient conditions in organic (Liao et al., 2012) and aqueous (Li et al., 2012) environments show that initial attachment events typically occur after several minutes. Following the initial attachments, Liao et al. (2012) additionally observe formation of Pt<sub>3</sub>Fe nanorods with morphologies strikingly similar to magnetite from foidite OM-1-2. Interestingly, the Pt<sub>3</sub>Fe nanorods would require ≈10 min, or longer, to assemble and straighten.

Mujin et al. (2021) report that initial coalescence of Fe nanoparticles in rhyolitic melts occurred between 10 and 75 minutes after the final run temperatures (950 to 1000 °C) were achieved. This suggests that nanoparticles may be able to attach at a similar frequency in different liquid media, and over a wide range of temperature (and pressure) conditions.

The morphology of nanorods from foidite MM is indicative of multiple nucleation-assembly episodes, accompanied by Ostwald ripening and partial attainment of nanoparticle crystal faces. These features resemble the morphology of titania nanorods, synthesized by Penn and Banfield (1999) under hydrothermal conditions (15 to 40 bar, 100 to 250 °C), with typical run durations between several hours and two weeks.

Considering the available constraints from experimental studies, we believe that assembly of magnetite nanorod structures observed in OM-1-2 scoria fragments may occur on timescales of minutes. The morphological features of magnetite nanorods in MM appear to be more consistent with timescales in the order of hours or days.

We observed remarkable preservation of nanorod structures in WEVF foidites, as well as preservation of spatial distributions of nanorods with respect to gas bubbles and melilite microlites (Ch. 7.4.1). The systematic increase in magnetite nanoparticle size, as well as nanorod coarsening away from the melilite host crystals (Ch. 7.4.2), indicates relatively stagnant conditions in the melt during the assembly process. Major perturbations of the liquid medium might disrupt alignment and subsequent attachment to neighboring particles. Following the nanoparticle assembly, limited relative movement of microlites with respect to one another is a necessary condition to preserve the three-dimensional nanorod networks.

Schmincke (2007) and Rausch (2014) describe upper mantle and lower crustal xenoliths, coated by agglutinate particles, in many eruptive layers from the Westeifel Volcanic Fields. These features are attributed to deep magma fragmentation, likely caused by vigorous CO<sub>2</sub> exolution. However, the high degree of preservation of fine nanorod structures in Westeifel foidites suggests that the assembly occurred after the transport from upper mantle/lower crustal depths.

We consider that nanorod formation likely takes place immediately prior, or at the time of the eruption. Two possible scenarios of nanorod formation are discussed: 1) *syn-eruptive* (in-flight nanoparticle attachment within the eruptive column) and 2) *pre-eruptive* (nanorod attachment during a period of shallow magma emplacement).

The scoria fragments from the Westefiel maar-diatreme volcanoes have variable macroscopic morphological features. Two types of fragments may be distinguished. Rausch et al. (2015), who performed a detailed analysis of scoria fragment shapes, use the terms ‘subround’ (OM-1-2) and ‘rugose’ (MM) to describe samples that have low and high degrees of matrix crystallinity, respectively.

The syn-eruptive scenario requires that melt viscosity remains low at a scale of average distance between pre-existing nanoparticles, and simultaneously that magma is nearly rigid on a scale of scoria fragment size in order to preserve the nanorods. Both conditions should be maintained for a sufficiently long time to allow nanorod assembly.

Di Genova et al. (2020) demonstrate that the presence of nanolites may increase bulk magma viscosity (e.g. at a scale of average fragment size). In the case of scoria fragments with high degrees of matrix crystallinity, and containing abundant magnetite nanoparticle population, it is possible that ideal conditions for both nanorod assembly and preservation are established immediately after the fragmentation. However, given the time constraints provided by in-situ observations of OA, the favorable conditions may not persist long enough to fully explain the multiphase growth of nanorods and partial attainment of nanoparticle crystal faces, such that was observed in sample MM.

The syn-eruptive origin of nanorods in ‘subround’ fragments (OM-1-2) is discussed next. These fragments are essentially nanolite-free, except for the magnetite within narrow melilite compositional boundary layers. The ‘subround’ fragments apparently maintained low melt viscosity just prior to quenching, as evidenced by the rounded bubble (Fig. 7.4.1b) and fragment (Rausch et al., 2015) geometry. It is questionable whether the conditions for brittle fragmentation could have been achieved, if the low melt viscosity was maintained for minutes during aerial transport, and the final quench occurred within the eruptive column.

Instead, both nano-scale and macroscopic features of OM-1-2 are more consistent with a rapid quench, and can be understood in terms of the ‘phreatomagmatic’ model (Ch. 7.2). Assuming a pre-eruptive origin, the nanorods are thought to assemble during the final shallow-level magma emplacement. The subsequent rapid quench, the separation of distinct domains in the volcanic glass (Fig. 7.4.8d), and the brittle fragmentation could have been facilitated by interaction with external water. Rausch et al. (2015) compare the shapes of ‘subround’ scoria fragments from the Eifel to the eruptive material produced by other phreatomagmatic eruptions, as well as to the run products from water-magma interaction experiments (Zimanowski et al., 1991). They conclude

that ‘subround’ fragments have characteristics typical of material produced by phreatomagmatic eruptions.

We favor the pre-eruptive nanorod assembly scenario. A shallow-level magma emplacement period could allow sufficient time for nanoparticle alignment and attachment, and the residual dissolved volatile species would additionally reduce melt viscosity and promote the frequency of attachment events (e.g. Leshner and Spera, 2015). The pre-eruptive scenario reconciles the timescales that may be required to produce morphological features of nanorods from ‘rugose’ scoria fragments. In addition, the spatial distribution of dendrites and nanorods in samples with higher matrix crystallinity suggests that magnetite crystallization can be devolatilization-driven, and not necessarily due to cooling (in air). Finally, we observed a crystallization hiatus, marked by a reduced population density of magnetite nanoparticles with 200-300 nm sizes, in a number of examined scoria fragments (Ch. 7.4.2., Fig.7.4.11). The pause in crystallization and partial annealing of nanorods into euhedral crystals could be due to periods of shallow level magma stagnation prior to, and overlapping with the time of nanorod assembly.

In the case of ‘rugose’ fragments, the mechanism of fragmentation is inconclusive. In the absence of external water, abundant precipitation of magnetite nanoparticles may eventually increase magma viscosity (e.g. Di Genova et al., 2017) and contribute to a devolatilization-driven fragmentation (‘magmatic’ model), possibly with nanorod assembly continuing even after the onset of the eruption. However, if the high matrix crystallinity is mostly pre-eruptive, the presence of magnetite nanoparticles may influence the fragment shape, even if the fragmentation mechanism is the same as for the ‘subround’ fragments (i.e. ‘phreatomagmatic’ model).

The observed differences in nanolite morphology in ‘rugose’ and ‘subround’ scoria fragments may be because of different undecooling histories, likely related to conduit geometries and initial melt volatile contents, and due to varying timescales of final magma emplacement before the eruption.

The physical conditions necessary for the oriented attachment to occur (high temperature and low melt viscosity), and the timescales required for nanorod assembly, suggest that shallow magma emplacement prior to eruption may be common in maar-diatreme volcanoes of the Eifel. At least

two fragmentation events may be involved in maar formation: one deep CO<sub>2</sub>-related event that initiates upward migration of the magma, followed by another shallow fragmentation that occurs either due to degassing of magmatic water or in interaction with external water sources.

## 7.6. List of references

Banfield, J. F., Welch, S. A., Zhang, H., Ebert, T. T., Penn, R. L. (2000). Aggregation-based crystal growth and microstructure development in natural iron oxyhydroxide biomineralization products. *Science*, 289(5480), 751–754.

Cáceres, F., Wadsworth, F.B., Scheu, B., Colombier, M., Madonna, C., Cimarelli, C., Hess, K.U., Kaliwoda, M., Ruthensteiner, B., Dingwell, D.B. (2020). Can nanolites enhance eruption explosivity? *Geology*, 48, 997-1001.

De Yoreo, J.J., Gilbert, P.U., Sommerdijk, N.A., Penn, R.L., Whitlam, S., Joester, D., Zhang, H., Rimer, J.D., Navrotsky, A., Banfield, J.F., Wallace, A.F., Michel, F.M., Meldrum, F.C., Cölfen, H., Dove, P.M. (2015). Crystallization by particle attachment in synthetic, biogenic, and geologic environments. *Science*, 349 (6247).

Di Genova, D., Brooker, R. A., Mader, H. M., Drewitt, J., Longo, A., Deubener, J., Neuville, D. R., Fanara, S., Shebanova, O., Anzellini, S., Arzilli, F., Bamber, E. C., Hennet, L., La Spina, G., Miyajima, N. (2020). In situ observation of nanolite growth in volcanic melt: A driving force for explosive eruptions. *Science advances*, 6(39).

Di Genova, D., Caracciolo, A., Kolzenburg, S. (2018). Measuring the degree of “nanotilization” of volcanic glasses: Understanding syn-eruptive processes recorded in melt inclusions. *Lithos*, 318-319, 209-218.

Di Genova, D., Kolzenburg, S., Wiesmaier, S., Dallanave, E., Neuville, D. R., Hess, K. U., Dingwell, D. B. (2017). A compositional tipping point governing the mobilization and eruption style of rhyolitic magma. *Nature*, 552(7684), 235–238.

Higgins, M.D. (2000). Measurement of crystal size distributions. *American Mineralogist*, 85, 1105–1116.

Hoernle, K., Zhang, Y., Graham, D.W. (1995). Seismic and geochemical evidence for large-scale mantle upwelling beneath the eastern Atlantic and western and central Europe. *Nature*, 374, 34-39.

K.H. Wedepohl, A. Baumann (1999). Central European Cenozoic plume volcanism with OIB characteristics and indications of a lower mantle source. *Contrib. Miner. Petrol.*, 136, 225-239.

Kreemer, C., Blewitt, G., Davis, P.M. (2020). Geodetic evidence for a buoyant mantle plume beneath the Eifel volcanic area, NW Europe. *Geophysical Journal International*, 222, 1316-1332.

Leshner, C.E., Spera, F.J. (2015). Thermodynamic and Transport Properties of Silicate Melts and Magma. *The Encyclopedia of Volcanoes* (2nd Ed.), 113-141.

Li, D., Nielsen, M.H., Lee, J., Frandsen, C., Banfield, J.F., De Yoreo, J.J. (2012). Direction-Specific Interactions Control Crystal Growth by Oriented Attachment. *Science*, 336, 1014 - 1018.

Liao, H., Cui, L., Whitlam, S., Zheng, H. (2012). Real-Time Imaging of Pt<sub>3</sub>Fe Nanorod Growth in Solution. *Science*, 336, 1011 - 1014.

Mertes, H., Schmincke, H.-U. (1985). Mafic potassic lavas of the Quaternary West Eifel volcanic field, I. Major and trace elements. *Contrib. Miner. Petrol.*, 89, 330-345.

Michele Lustrino, Eugenio Carminati (2007). Phantom plumes in Europe and the circum-Mediterranean region. *GSA Special Papers: Plates, Plumes and Planetary Processes* (Eds. Foulger, G.R., Jurdy, D.M.)

Mujin, M., Nakamura, M. (2014). A nanolite record of eruption style transition. *Geology*, 42, 611-614.

Mujin, M., Nakamura, M. (2020). Late-stage groundmass differentiation as a record of magma stagnation, fragmentation, and rewelding. *Bulletin of Volcanology*, 82, 1-17.

Mujin, M., Nakamura, M., Matsumoto, M. (2021). In-situ FE-SEM observation of the growth behaviors of Fe particles at magmatic temperatures. *Journal of Crystal Growth*, 560-561, [126043].

Mujin, M., Nakamura, M., Miyake, A. (2017). Eruption style and crystal size distributions: Crystallization of groundmass nanolites in the 2011 Shinmoedake eruption. *American Mineralogist*, 102(12), 2367-2380.

Penn, R. L., Banfield, J. F. (1998). Imperfect oriented attachment: dislocation generation in defect-free nanocrystals. *Science*, 281(5379), 969–971.

Penn, R.L. (2004). Kinetics of Oriented Aggregation. *Journal of Physical Chemistry B*, 108, 12707-12712.

Penn, R.L., Banfield, J.F. (1999). Morphology development and crystal growth in nanocrystalline aggregates under hydrothermal conditions: insights from titania. *Geochimica et Cosmochimica Acta*, 63, 1549-1557.

Rausch, J. (2014). Eifel maars: external water vs. magmatic volatiles (Eifel Volcanic Field, Germany). PhD thesis, University of Fribourg, Switzerland.

Rausch, J., Grobéty, B.H., Vonlanthen, P. (2015). Eifel maars: Quantitative shape characterization of juvenile ash particles (Eifel Volcanic Field, Germany). *Journal of Volcanology and Geothermal Research*, 291, 86-100.

Ritter, J.R., Jordan, M.I., Christensen, U.R., Achauer, U. (2001). A mantle plume below the Eifel volcanic fields, Germany. *Earth and Planetary Science Letters*, 186, 7-14.

Schmincke, H.-U. (2007). Quaternary volcanism of the East and West Eifel (Central Europe). In: *Geol. Soc. London, Geology of Central Europe* (Ed. McCann, T.).

Schmincke, H.-U. (2009). *Vulkane der Eifel*. Spektrum Akademischer Verlag, Heidelberg.

Sharp, T., Stevenson, R., Dingwell, D. (1996). Microlites and "nanolites" in rhyolitic glass: microstructural and chemical characterization. *Bull. Volcanol.*, 57, 631–640.

Shaw, C.S.J. (1997). Origin of sulfide blebs in variably metasomatized mantle xenoliths, Quaternary West Eifel Volcanic Field, Germany. *The Canadian Mineralogist*, 35, 1453-1463.

White, J., Ross, P.S. (2011). Maar-diatreme volcanoes: a review. *Journal of Volcanology and Geothermal Research*, 201, 1-29.

Zellmer, G.F., Sakamoto, N., Hwang, S., Matsuda, N., Iizuka, Y., Moebis, A., Yurimoto, H. (2016). Inferring the Effects of Compositional Boundary Layers on Crystal Nucleation, Growth Textures, and Mineral Chemistry in Natural Volcanic Tephra through Submicron-Resolution Imaging. *Frontiers in Earth Science*, 4, 88.

Zimanowski, B., Büttner, R., Lorenz, V. (1997). Premixing of magma and water in MFCI experiments. *Bull. Volcanol.*, 58 (6), 491–495.

## **(Eidesstattliche) Versicherungen und Erklärungen**

(§ 9 Satz 2 Nr. 3 PromO BayNAT)

*Hiermit versichere ich eidesstattlich, dass ich die Arbeit selbstständig verfasst und keine anderen als die von mir angegebenen Quellen und Hilfsmittel benutzt habe (vgl. Art. 64 Abs. 1 Satz 6 BayHSchG).*

(§ 9 Satz 2 Nr. 3 PromO BayNAT)

*Hiermit erkläre ich, dass ich die Dissertation nicht bereits zur Erlangung eines akademischen Grades eingereicht habe und dass ich nicht bereits diese oder eine gleichartige Doktorprüfung endgültig nicht bestanden habe.*

(§ 9 Satz 2 Nr. 4 PromO BayNAT)

*Hiermit erkläre ich, dass ich Hilfe von gewerblichen Promotionsberatern bzw. -vermittlern oder ähnlichen Dienstleistern weder bisher in Anspruch genommen habe noch künftig in Anspruch nehmen werde.*

(§ 9 Satz 2 Nr. 7 PromO BayNAT)

*Hiermit erkläre ich mein Einverständnis, dass die elektronische Fassung meiner Dissertation unter Wahrung meiner Urheberrechte und des Datenschutzes einer gesonderten Überprüfung unterzogen werden kann.*

(§ 9 Satz 2 Nr. 8 PromO BayNAT)

*Hiermit erkläre ich mein Einverständnis, dass bei Verdacht wissenschaftlichen Fehlverhaltens Ermittlungen durch universitätsinterne Organe der wissenschaftlichen Selbstkontrolle stattfinden können.*

Bayreuth, 24th August 2022

.....  
Ort, Datum, Unterschrift